

Applied Mathematical Sciences

Volume 142

Editors

J.E. Marsden L. Sirovich

Advisors

S. Antman J.K. Hale

P. Holmes T. Kambe J. Keller

B.J. Matkowsky C.S. Peskin

Springer-Science+Business Media, LLC

Applied Mathematical Sciences

1. *John*: Partial Differential Equations, 4th ed.
2. *Sirovich*: Techniques of Asymptotic Analysis.
3. *Hale*: Theory of Functional Differential Equations, 2nd ed.
4. *Percus*: Combinatorial Methods.
5. *von Mises/Friedrichs*: Fluid Dynamics.
6. *Freiberger/Grenander*: A Short Course in Computational Probability and Statistics.
7. *Pipkin*: Lectures on Viscoelasticity Theory.
8. *Giacaglia*: Perturbation Methods in Non-linear Systems.
9. *Friedrichs*: Spectral Theory of Operators in Hilbert Space.
10. *Stroud*: Numerical Quadrature and Solution of Ordinary Differential Equations.
11. *Wolovich*: Linear Multivariable Systems.
12. *Berkovitz*: Optimal Control Theory.
13. *Bluman/Cole*: Similarity Methods for Differential Equations.
14. *Yoshizawa*: Stability Theory and the Existence of Periodic Solution and Almost Periodic Solutions.
15. *Braun*: Differential Equations and Their Applications, 3rd ed.
16. *Lefschetz*: Applications of Algebraic Topology.
17. *Collatz/Wetterling*: Optimization Problems.
18. *Grenander*: Pattern Synthesis: Lectures in Pattern Theory, Vol. I.
19. *Marsden/McCracken*: Hopf Bifurcation and Its Applications.
20. *Driver*: Ordinary and Delay Differential Equations.
21. *Courant/Friedrichs*: Supersonic Flow and Shock Waves.
22. *Rouche/Habets/Laloy*: Stability Theory by Liapunov's Direct Method.
23. *Lamperti*: Stochastic Processes: A Survey of the Mathematical Theory.
24. *Grenander*: Pattern Analysis: Lectures in Pattern Theory, Vol. II.
25. *Davies*: Integral Transforms and Their Applications, 2nd ed.
26. *Kushner/Clark*: Stochastic Approximation Methods for Constrained and Unconstrained Systems.
27. *de Boor*: A Practical Guide to Splines.
28. *Keilson*: Markov Chain Models—Rarity and Exponentiality.
29. *de Veubeke*: A Course in Elasticity.
30. *Śniatycki*: Geometric Quantization and Quantum Mechanics.
31. *Reid*: Sturmian Theory for Ordinary Differential Equations.
32. *Meis/Markowitz*: Numerical Solution of Partial Differential Equations.
33. *Grenander*: Regular Structures: Lectures in Pattern Theory, Vol. III.
34. *Kevorkian/Cole*: Perturbation Methods in Applied Mathematics.
35. *Carr*: Applications of Centre Manifold Theory.
36. *Bengtsson/Ghil/Källén*: Dynamic Meteorology: Data Assimilation Methods.
37. *Saperstone*: Semidynamical Systems in Infinite Dimensional Spaces.
38. *Lichtenberg/Lieberman*: Regular and Chaotic Dynamics, 2nd ed.
39. *Piccinini/Stampacchia/Vidossich*: Ordinary Differential Equations in \mathbb{R}^n .
40. *Naylor/Sell*: Linear Operator Theory in Engineering and Science.
41. *Sparrow*: The Lorenz Equations: Bifurcations, Chaos, and Strange Attractors.
42. *Guckenheimer/Holmes*: Nonlinear Oscillations, Dynamical Systems, and Bifurcations of Vector Fields.
43. *Ockendon/Taylor*: Inviscid Fluid Flows.
44. *Pazy*: Semigroups of Linear Operators and Applications to Partial Differential Equations.
45. *Glashoff/Gustafson*: Linear Operations and Approximation: An Introduction to the Theoretical Analysis and Numerical Treatment of Semi-Infinite Programs.
46. *Wilcox*: Scattering Theory for Diffraction Gratings.
47. *Hale et al.*: An Introduction to Infinite Dimensional Dynamical Systems—Geometric Theory.
48. *Murray*: Asymptotic Analysis.
49. *Ladyzhenskaya*: The Boundary-Value Problems of Mathematical Physics.
50. *Wilcox*: Sound Propagation in Stratified Fluids.
51. *Golubitsky/Schaeffer*: Bifurcation and Groups in Bifurcation Theory, Vol. I.
52. *Chipot*: Variational Inequalities and Flow in Porous Media.
53. *Majda*: Compressible Fluid Flow and System of Conservation Laws in Several Space Variables.
54. *Wasow*: Linear Turning Point Theory.
55. *Yosida*: Operational Calculus: A Theory of Hyperfunctions.
56. *Chang/Howes*: Nonlinear Singular Perturbation Phenomena: Theory and Applications.
57. *Reinhardt*: Analysis of Approximation Methods for Differential and Integral Equations.
58. *Dwyer/Hussaini/Voigt (eds)*: Theoretical Approaches to Turbulence.
59. *Sanders/Verhulst*: Averaging Methods in Nonlinear Dynamical Systems.
60. *Ghil/Childress*: Topics in Geophysical Dynamics: Atmospheric Dynamics, Dynamo Theory and Climate Dynamics.

(continued following index)

Peter J. Schmid Dan S. Henningson

Stability and Transition in Shear Flows

With 222 figures



Springer

Peter J. Schmid
Applied Mathematics Department
University of Washington
Seattle, WA 98195-0001
USA
pjs@amath.washington.edu

Dan S. Henningson
Department of Mechanics
Royal Institute of Technology (KTH)
Stockholm, S-100 44
Sweden
henning@mech.kth.se

Editors

J.E. Marsden
Control and Dynamical Systems, 107-81
California Institute of Technology
Pasadena, CA 91125
USA

L. Sirovich
Division of Applied Mathematics
Brown University
Providence, RI 02912
USA

Mathematics Subject Classification (2000): 34E02, 35B35, 76EXX, 7602

Library of Congress Cataloging-in-Publication Data

Schmid, Peter J.

Stability and transition in shear flows / Peter J. Schmid, Dan S. Henningson.

p. cm. — (Applied mathematical sciences ; 142)

Includes bibliographical references and index.

ISBN 978-1-4612-6564-1 ISBN 978-1-4613-0185-1 (eBook)

DOI 10.1007/978-1-4613-0185-1

1. Shear flow. 2. Stability. I. Henningson, Dan S. II. Title. III. Applied mathematical sciences (Springer-Verlag New York, Inc.) ; v. 142.

QA1 .A647 no. 142

[QA922]

510 s—dc21

[532'.051]

00-022795

Printed on acid-free paper.

© 2001 Springer Science+Business Media New York

Originally published by Springer-Verlag New York in 2001

Softcover reprint of the hardcover 1st edition 2001

All rights reserved. This work may not be translated or copied in whole or in part without the written permission of the publisher (Springer-Science+Business Media, LLC), except for brief excerpts in connection with reviews or scholarly analysis. Use in connection with any form of information storage and retrieval, electronic adaptation, computer software, or by similar or dissimilar methodology now known or hereafter developed is forbidden.

The use of general descriptive names, trade names, trademarks, etc., in this publication, even if the former are not especially identified, is not to be taken as a sign that such names, as understood by the Trade Marks and Merchandise Marks Act, may accordingly be used freely by anyone.

Production managed by Michael Koy; manufacturing supervised by Erica Bresler.

Photocomposed copy prepared from the authors' TeX files.

9 8 7 6 5 4 3 2 1

ISBN 978-1-4612-6564-1

SPIN 10659102

Contents

Preface	xi
1 Introduction and General Results	1
1.1 Introduction	1
1.2 Nonlinear Disturbance Equations	2
1.3 Definition of Stability and Critical Reynolds Numbers	3
1.3.1 Definition of Stability	3
1.3.2 Critical Reynolds Numbers	5
1.3.3 Spatial Evolution of Disturbances	6
1.4 The Reynolds-Orr Equation	7
1.4.1 Derivation of the Reynolds-Orr Equation	7
1.4.2 The Need for Linear Growth Mechanisms	9
I Temporal Stability of Parallel Shear Flows	
2 Linear Inviscid Analysis	15
2.1 Inviscid Linear Stability Equations	15
2.2 Modal Solutions	17
2.2.1 General Results	17
2.2.2 Dispersive Effects and Wave Packets	33
2.3 Initial Value Problem	38
2.3.1 The Inviscid Initial Value Problem	38
2.3.2 Laplace Transform Solution	42

2.3.3	Solutions to the Normal Vorticity Equation	46
2.3.4	Example: Couette Flow	48
2.3.5	Localized Disturbances	50
3	Eigensolutions to the Viscous Problem	55
3.1	Viscous Linear Stability Equations	55
3.1.1	The Velocity-Vorticity Formulation	55
3.1.2	The Orr-Sommerfeld and Squire Equations	56
3.1.3	Squire's Transformation and Squire's Theorem	58
3.1.4	Vector Modes	59
3.1.5	Pipe Flow	61
3.2	Spectra and Eigenfunctions	64
3.2.1	Discrete Spectrum	64
3.2.2	Neutral Curves	71
3.2.3	Continuous Spectrum	74
3.2.4	Asymptotic Results	78
3.3	Further Results on Spectra and Eigenfunctions	85
3.3.1	Adjoint Problem and Bi-Orthogonality Condition	85
3.3.2	Sensitivity of Eigenvalues	89
3.3.3	Pseudo-Eigenvalues	93
3.3.4	Bounds on Eigenvalues	94
3.3.5	Dispersive Effects and Wave Packets	96
4	The Viscous Initial Value Problem	99
4.1	The Viscous Initial Value Problem	99
4.1.1	Motivation	99
4.1.2	Derivation of the Disturbance Equations	102
4.1.3	Disturbance Measure	102
4.2	The Forced Squire Equation and Transient Growth	103
4.2.1	Eigenfunction Expansion	103
4.2.2	Blasius Boundary Layer Flow	105
4.3	The Complete Solution to the Initial Value Problem	106
4.3.1	Continuous Formulation	106
4.3.2	Discrete Formulation	108
4.4	Optimal Growth	111
4.4.1	The Matrix Exponential	111
4.4.2	Maximum Amplification	112
4.4.3	Optimal Disturbances	119
4.4.4	Reynolds Number Dependence of Optimal Growth .	120
4.5	Optimal Response and Optimal Growth Rate	126
4.5.1	The Forced Problem and the Resolvent	126
4.5.2	Maximum Growth Rate	131
4.5.3	Response to Stochastic Excitation	133
4.6	Estimates of Growth	139
4.6.1	Bounds on Matrix Exponential	139

4.6.2	Conditions for No Growth	141
4.7	Localized Disturbances	144
4.7.1	Choice of Initial Disturbances	144
4.7.2	Examples	147
4.7.3	Asymptotic Behavior	149
5	Nonlinear Stability	153
5.1	Motivation	153
5.1.1	Introduction	153
5.1.2	A Model Problem	154
5.2	Nonlinear Initial Value Problem	155
5.2.1	The Velocity-Vorticity Equations	155
5.3	Weakly Nonlinear Expansion	160
5.3.1	Multiple-Scale Analysis	160
5.3.2	The Landau Equation	164
5.4	Three-Wave Interactions	167
5.4.1	Resonance Conditions	167
5.4.2	Derivation of a Dynamical System	168
5.4.3	Triad Interactions	172
5.5	Solutions to the Nonlinear Initial Value Problem	177
5.5.1	Formal Solutions to the Nonlinear Initial Value Problem	177
5.5.2	Weakly Nonlinear Solutions and the Center Manifold	179
5.5.3	Nonlinear Equilibrium States	180
5.5.4	Numerical Solutions for Localized Disturbances	185
5.6	Energy Theory	188
5.6.1	The Energy Stability Problem	188
5.6.2	Additional Constraints	191

II Stability of Complex Flows and Transition

6	Temporal Stability of Complex Flows	197
6.1	Effect of Pressure Gradient and Crossflow	198
6.1.1	Falkner-Skan (FS) Boundary Layers	198
6.1.2	Falkner-Skan-Cooke (FSC) Boundary layers	203
6.2	Effect of Rotation and Curvature	207
6.2.1	Curved Channel Flow	207
6.2.2	Rotating Channel Flow	211
6.2.3	Combined Effect of Curvature and Rotation	213
6.3	Effect of Surface Tension	216
6.3.1	Water Table Flow	216
6.3.2	Energy and the Choice of Norm	218
6.3.3	Results	221
6.4	Stability of Unsteady Flow	223

6.4.1	Oscillatory Flow	223
6.4.2	Arbitrary Time Dependence	229
6.5	Effect of Compressibility	237
6.5.1	The Compressible Initial Value Problem	237
6.5.2	Inviscid Instabilities and Rayleigh's Criterion	240
6.5.3	Viscous Instability	246
6.5.4	Nonmodal Growth	249
7	Growth of Disturbances in Space	253
7.1	Spatial Eigenvalue Analysis	253
7.1.1	Introduction	253
7.1.2	Spatial Spectra	255
7.1.3	Gaster's Transformation	264
7.1.4	Harmonic Point Source	266
7.2	Absolute Instability	270
7.2.1	The Concept of Absolute Instability	270
7.2.2	Briggs' Method	273
7.2.3	The Cusp Map	278
7.2.4	Stability of a Two-Dimensional Wake	281
7.2.5	Stability of Rotating Disk Flow	284
7.3	Spatial Initial Value Problem	290
7.3.1	Primitive Variable Formulation	290
7.3.2	Solution of the Spatial Initial Value Problem	291
7.3.3	The Vibrating Ribbon Problem	294
7.4	Nonparallel Effects	300
7.4.1	Asymptotic Methods	301
7.4.2	Parabolic Equations for Steady Disturbances	309
7.4.3	Parabolized Stability Equations (PSE)	318
7.4.4	Spatial Optimal Disturbances	329
7.4.5	Global Instability	337
7.5	Nonlinear Effects	344
7.5.1	Nonlinear Wave Interactions	344
7.5.2	Nonlinear Parabolized Stability Equations	346
7.5.3	Examples	349
7.6	Disturbance Environment and Receptivity	351
7.6.1	Introduction	351
7.6.2	Nonlocalized and Localized Receptivity	353
7.6.3	An Adjoint Approach to Receptivity	363
7.6.4	Receptivity Using Parabolic Evolution Equations .	367
8	Secondary Instability	373
8.1	Introduction	373
8.2	Secondary Instability of Two-Dimensional Waves	374
8.2.1	Derivation of the Equations	374
8.2.2	Numerical Results	378

8.2.3	Elliptical Instability	381
8.3	Secondary Instability of Vortices and Streaks	383
8.3.1	Governing Equations	383
8.3.2	Examples of Secondary Instability of Streaks and Vortices	389
8.4	Eckhaus Instability	394
8.4.1	Secondary Instability of Parallel Flows	394
8.4.2	Parabolic Equations for Spatial Eckhaus Instability .	397
9	Transition to Turbulence	401
9.1	Transition Scenarios and Thresholds	401
9.1.1	Introduction	401
9.1.2	Three Transition Scenarios	403
9.1.3	The Most Likely Transition Scenario	411
9.1.4	Conclusions	413
9.2	Breakdown of Two-Dimensional Waves	414
9.2.1	The Zero Pressure Gradient Boundary Layer	414
9.2.2	Breakdown of Mixing Layers	420
9.3	Streak Breakdown	425
9.3.1	Streaks Forced by Blowing or Suction	425
9.3.2	Freestream Turbulence	429
9.4	Oblique Transition	436
9.4.1	Experiments and Simulations in Blasius Flow	436
9.4.2	Transition in a Separation Bubble	441
9.4.3	Compressible Oblique Transition	445
9.5	Transition of Vortex-Dominated Flows	446
9.5.1	Transition in Flows with Curvature	446
9.5.2	Direct Numerical Simulations of Secondary Instabil- ity of Crossflow Vortices	450
9.5.3	Experimental Investigations of Breakdown of Cross- flow Vortices	455
9.6	Breakdown of Localized Disturbances	456
9.6.1	Experimental Results for Boundary Layers	459
9.6.2	Direct Numerical Simulations in Boundary Layers .	460
9.7	Transition Modeling	465
9.7.1	Low-Dimensional Models of Subcritical Transition .	465
9.7.2	Traditional Transition Prediction Models	469
9.7.3	Transition Prediction Models Based on Nonmodal Growth	471
9.7.4	Nonlinear Transition Modeling	474

III Appendix

A Numerical Issues and Computer Programs

479

A.1	Global versus Local Methods	479
A.2	Runge-Kutta Methods	480
A.3	Chebyshev Expansions	483
A.4	Infinite Domain and Continuous Spectrum	486
A.5	Chebyshev Discretization of the Orr-Sommerfeld Equation .	487
A.6	MATLAB Codes for Hydrodynamic Stability Calculations .	489
A.7	Eigenvalues of Parallel Shear Flows	503
B	Resonances and Degeneracies	509
B.1	Resonances and Degeneracies	509
B.2	Orr-Sommerfeld-Squire Resonance	511
C	Adjoint of the Linearized Boundary Layer Equation	515
C.1	Adjoint of the Linearized Boundary Layer Equation	515
D	Selected Problems on Part I	519
	Bibliography	529
	Index	551

Preface

The field of hydrodynamic stability has a long history, going back to Reynolds and Lord Rayleigh in the late 19th century. Because of its central role in many research efforts involving fluid flow, stability theory has grown into a mature discipline, firmly based on a large body of knowledge and a vast body of literature. The sheer size of this field has made it difficult for young researchers to access this exciting area of fluid dynamics.

For this reason, writing a book on the subject of hydrodynamic stability theory and transition is a daunting endeavor, especially as *any* book on stability theory will have to follow into the footsteps of the classical treatises by Lin (1955), Betchov & Criminale (1967), Joseph (1971), and Drazin & Reid (1981). Each of these books has marked an important development in stability theory and has laid the foundation for many researchers to advance our understanding of stability and transition in shear flows.

A task every author has to face is the choice of material to include in a book, while being fully aware of the fact that full justice cannot be done to all areas. The past two decades have seen a great deal of development in hydrodynamic stability theory. For this reason we chose to devote a substantial fraction of this book to recent developments in stability theory which, among others, include nonmodal analysis, spatial growth, adjoint techniques, parabolized stability equations, secondary instability theory and direct numerical simulations. Some more classical theories are included for completeness, but are treated in less detail, especially if they are covered elsewhere in the literature. Other topics such as, critical layer theory, advanced asymptotic methods, bifurcation and chaos theory, have been omitted altogether due to space constraints. We sincerely hope that the reader

will find our choice of material interesting and stimulating. Throughout the text references are provided that will guide the interested reader to more details, different applications and various extensions, but no attempt has been made to compile an exhaustive bibliography.

The book is foremost intended for researchers and graduate students with a basic knowledge of fundamental fluid dynamics. We particularly hope it will help young researchers at the beginning of their scientific careers to quickly gain an overview as well as detailed knowledge of the recent developments in the field. Various sections of the text have been used in graduate courses on hydrodynamic stability at the University of Washington, Seattle and the Royal Institute of Technology, Stockholm, Sweden.

The book consists of an introduction and two parts. The first part (Chapters 2-5) develops the fundamental concepts underlying stability theory. Chapter 2 deals with the temporal evolution of disturbances in an inviscid fluid. The linear theory for viscous fluids is developed in Chapters 3 and 4 with Chapter 3 concentrating on a modal description and Chapter 4 introducing the nonmodal framework. In Chapter 5 we discuss finite-amplitude effects and study various nonlinear stability theories.

The second part of the book (Chapters 6-9) covers more advanced topics. In Chapter 6 we will study the influence of various physical effects (such as rotation, curvature, compressibility, etc.) on the stability behavior of parallel shear flows. Chapter 7 is devoted to spatial stability theory covering such topics as absolute stability theory, weakly nonparallel effects, parabolized stability equations, and receptivity. Secondary instability theory is treated in Chapter 8 with applications to Tollmien-Schlichting waves, streaks, and vortical flows. In Chapter 9 many of the concepts introduced in the previous chapters are used to explain the transition process from laminar to turbulent fluid motion in a variety of shear flows. This chapter introduces and analyzes different transition scenarios observed in experiments and direct numerical simulations.

The appendices provide helpful hints on numerical methods, present more detailed derivations, and suggest some practice problems.

Over the course of the past years many colleagues and friends have contributed to this book through preprints of latest results, reprints of past results, insightful comments on the manuscript and moral support.

We wish to thank Larry Sirovich and Kenny Breuer who got us started on this demanding, but rewarding, project. Their comments and encouragement are appreciated greatly. We also thank Håkan Gustavsson for his contributions to an earlier review article that served as a starting point for this book.

We are deeply indebted to Alex Bottaro for his insightful comments on all parts of the book and to Philip Drazin for his careful proofreading of the manuscript. We thank Nick Trefethen for his detailed comments and his interest, encouragement and enthusiasm.

Many colleagues have generously provided comments and material from their past and current research. We especially wish to thank Henrik Al-fredsson, David Ashpis, Martin Berggren, Alex Bottaro, Carlo Cossu, Bill Criminale, Jeffrey Crouch, Ardeshir Hanifi, J. Healey, Werner Koch, Re-becca Lingwood, Satish Reddy, Ulrich Rist, Michael Rogers, Jerry Swearin-gen, Nick Trefethen, Anatoli Tumin, and Akiva Yaglom.

A large part of the writing was done during the first author's many visits to the Department of Mechanics at the Royal Institute of Technology (KTH) in Stockholm, during the second author's visit to the Department of Applied Mathematics at the University of Washington, and during a visit to the Center for Turbulence Research at Stanford University. We would like to thank the chairs of these institutions, Arne Johansson (KTH), K.K. Tung (UW), and Parviz Moin (CTR), for their warm hospitality and support. In particular, the first author is greatly indebted to the faculty and students at KTH and will always treasure the interesting discussions, memorable activities, and Swedish hospitality. The second author gratefully acknowledges the support of the Aeronautical Research Institute of Sweden.

Finally, we wish to thank our editor, Achi Dosanjh, and the staff at Springer-Verlag for their support and patience.

Last, but certainly not least, we wish to thank our families for supporting this effort and for enduring the many sacrifices it took.

Seattle and Stockholm, July 2000

Peter Schmid
Dan Henningson

Part I

Temporal Stability of Parallel Shear Flows

In this part of the book we will discuss the linear and nonlinear temporal stability of simple parallel shear flows. We will cover the linear stability of simple shear flows in the absence of viscosity, address the evolution of disturbances in viscous fluids, from both the modal and nonmodal (initial value) point of view, and present selected theories and results that describe the stability of shear flows to finite-amplitude disturbances.

Many of the concepts introduced in this part will be generalized in the subsequent sections of the book when more complex flows and various additional physical effects will be investigated.

1

Introduction and General Results

1.1 Introduction

Hydrodynamic stability theory is concerned with the response of a laminar flow to a disturbance of small or moderate amplitude. If the flow returns to its original laminar state one defines the flow as stable, whereas if the disturbance grows and causes the laminar flow to change into a different state, one defines the flow as unstable. Instabilities often result in turbulent fluid motion, but they may also take the flow into a different laminar, usually more complicated state. Stability theory deals with the mathematical analysis of the evolution of disturbances superposed on a laminar base flow. In many cases one assumes the disturbances to be small so that further simplifications can be justified. In particular, a linear equation governing the evolution of disturbances is desirable. As the disturbance velocities grow above a few percent of the base flow, nonlinear effects become important and the linear equations no longer accurately predict the disturbance evolution. Although the linear equations have a limited region of validity they are important in detecting physical growth mechanisms and identifying dominant disturbance types.

In this section we will derive the nonlinear equations governing the development of a disturbance on a laminar base flow, define various types of stability, and discuss some general concepts and results.

1.2 Nonlinear Disturbance Equations

The equations governing the general evolution of fluid flow are known as the Navier-Stokes equations. They describe the conservation of mass and momentum. For an incompressible fluid, using Cartesian tensor notation, the equations read

$$\frac{\partial u_i}{\partial t} = -u_j \frac{\partial u_i}{\partial x_j} - \frac{\partial p}{\partial x_i} + \frac{1}{Re} \nabla^2 u_i \quad (1.1)$$

$$\frac{\partial u_i}{\partial x_i} = 0 \quad (1.2)$$

where u_i are the velocity components, p is the pressure, and x_i are the spatial coordinates. In these equations, the convention of summation over identical indices has been assumed. For most flows presented in this text the streamwise direction will be denoted x_1 or x with velocity component u_1 or u , the normal direction is x_2 or y with corresponding velocity u_2 or v and the spanwise direction is x_3 or z with associated velocity u_3 or w .

These equations have to be supplemented with boundary and initial conditions, typically of the form

$$u_i(x_i, 0) = u_i^0(x_i) \quad (1.3)$$

$$u_i(x_i, t) = 0 \quad \text{on solid boundaries.} \quad (1.4)$$

The equations have been nondimensionalized by a velocity scale that is, for example, the centerline velocity (U_{CL}) for channel flows or the freestream velocity (U_∞) for boundary layer flows. The corresponding length scales are the channel half-height (h) or the boundary layer displacement thickness (δ_*). The Reynolds number is then given as $Re = U_{CL}h/\nu$ and $Re = U_\infty\delta_*/\nu$, respectively, with ν as the kinematic viscosity.

The evolution equations for the disturbance can then be derived by considering a basic state (U_i, P) and a perturbed state $(U_i + u'_i, P + p')$, both satisfying the Navier-Stokes equations. Subtracting the equations for the basic and perturbed state and omitting the primes for the disturbance quantities, we find the following nonlinear disturbance equations

$$\frac{\partial u_i}{\partial t} = -U_j \frac{\partial u_i}{\partial x_j} - u_j \frac{\partial U_i}{\partial x_j} - \frac{\partial p}{\partial x_i} + \frac{1}{Re} \nabla^2 u_i - u_j \frac{\partial u_i}{\partial x_j} \quad (1.5)$$

$$\frac{\partial u_i}{\partial x_i} = 0 \quad (1.6)$$

which constitute an initial/boundary value problem for the evolution of a disturbance $u_i^0 = u_i(t = 0)$.

To describe the development of an initial perturbation we also introduce a measure of its size. In most cases the disturbance kinetic energy is a natural choice. The kinetic energy of the disturbance contained in a volume V is

$$E_V = \frac{1}{2} \int_V u_i u_i \, dV. \quad (1.7)$$

The choice of the volume V is dependent on the flow geometry. For example, for flow over a flat plate the infinite half-space or for flow in a plane channel a box containing one period of the disturbance may be an appropriate choice.

1.3 Definition of Stability and Critical Reynolds Numbers

1.3.1 *Definition of Stability*

Before launching into some fundamental issues of hydrodynamic stability theory, we need to start with a formal definition of stability. We will follow Joseph (1976) and present four concepts based on the kinetic energy E_V of a disturbance.

The first definition introduces the concept of stability as an asymptotic limit for large times.

1 DEFINITION (STABILITY) A solution U_i to the Navier-Stokes equations is stable to perturbations if the perturbation energy satisfies

$$\lim_{t \rightarrow \infty} \frac{E_V(t)}{E_V(0)} \rightarrow 0. \quad (1.8)$$

The second definition deals with the fact that stability or instability may depend on the initial energy of the perturbation, which leads to the concept of conditional stability.

2 DEFINITION (CONDITIONAL STABILITY) If there exists a threshold energy $\delta > 0$ such that U_i is stable when $E(0) < \delta$, then the solution U_i is said to be conditionally stable.

A special case of conditional stability results in the definition of global stability.

3 DEFINITION (GLOBAL STABILITY) If the threshold energy is infinite, i.e. $\delta \rightarrow \infty$, the solution is said to be globally stable.

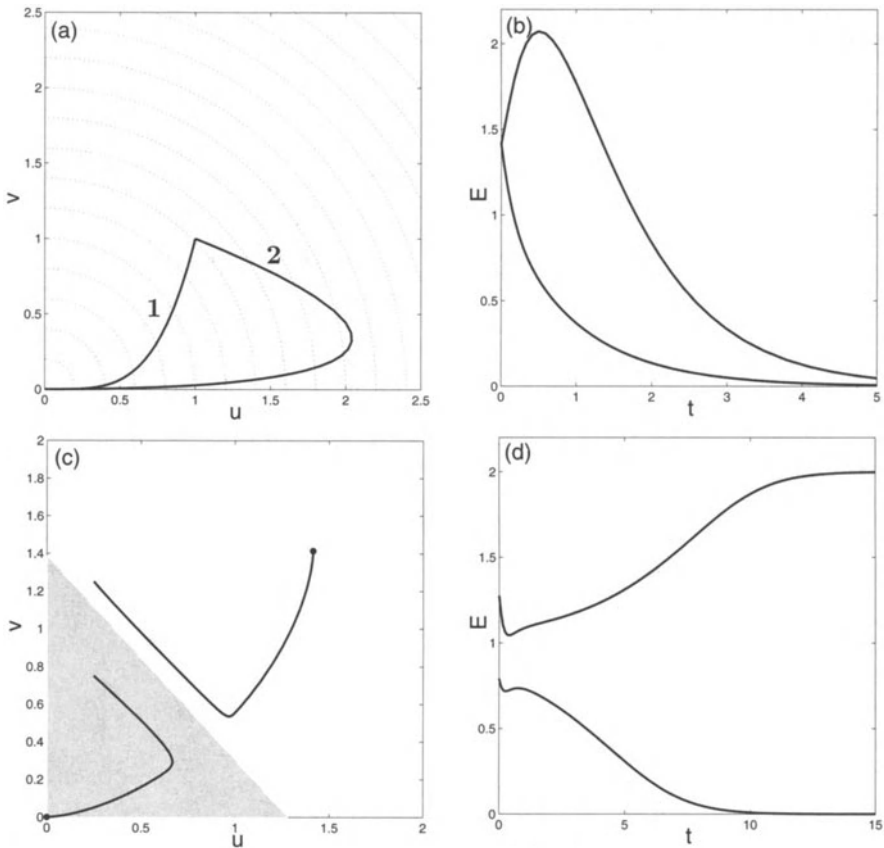


FIGURE 1.1. Sketch demonstrating different stability definitions. (a,b) Monotonic versus non-monotonic stability. The fixed point $(0,0)$ is stable. (c,d) Conditional stability. The fixed point $(0,0)$ is conditionally stable. For initial conditions outside the gray triangular area the fixed point $(0,0)$ is unstable.

Finally, the definition of monotonic stability adds further restrictions by requiring the energy of the perturbation to decrease for all times, not only in the asymptotic limit of large times.

4 DEFINITION (MONOTONIC STABILITY) If

$$\frac{dE_V}{dt} < 0 \quad \text{for all } t > 0, \quad (1.9)$$

then the solution is said to be monotonically stable.

These definitions of stability may be demonstrated with the help of a system of two ordinary differential equations $\dot{u} = f(u, v)$, $\dot{v} = g(u, v)$ and their solution in the two-dimensional phase space. An illustration is given in Figure 1.1. In Figure 1.1(a) we observe two phase curves originating at $(u, v) = (1, 1)$. Both cases describe stable behavior as defined in Definition 1, because the two curves tend toward the origin as $t \rightarrow \infty$. Solution 1 approaches the origin monotonically, whereas solution 2 first increases in energy before approaching the zero-energy asymptotic state. The evolution of energy versus time (see Figure 1.1(b)) further illustrates this behavior. The second set of figures (Figures 1.1(c) and 1.1(d)) demonstrates the concept of conditional stability. For initial conditions in the gray area, solutions approach the origin, whereas for initial conditions outside this area, we observe the evolution into a steady state at higher energy.

1.3.2 Critical Reynolds Numbers

Based on the definitions of stability it is appropriate to introduce the following critical Reynolds numbers.

5 DEFINITION (Re_E) For $Re < Re_E$ the flow is monotonically stable.

This is the critical Reynolds number given by energy theory (see Joseph, 1976) and derived using the Reynolds-Orr equation (1.11) in Section 5.6.

6 DEFINITION (Re_G) For $Re < Re_G$ the flow is globally stable.

This critical Reynolds number is difficult to derive analytically but may be determined by bifurcation analysis. One assumption sometimes made is that Re_G corresponds to the lowest Reynolds number for which turbulence can be sustained. This assumption, however, does not hold for all flows, in which case it is necessary to introduce a separate critical Reynolds number Re_T below which the flow will relaminarize.

7 DEFINITION (Re_L) For $Re > Re_L$ the flow is linearly unstable or not conditionally stable.

Flow	Re_E	Re_G	Re_T	Re_L
Hagen-Poiseuille	81.5	—	2000	∞
Plane Poiseuille	49.6	—	1000	5772
Plane Couette	20.7	125	360	∞

TABLE 1.1. Critical Reynolds numbers for a number of wall-bounded shear flows compiled from the literature (see, e.g., Joseph, 1976; Drazin & Reid, 1981).

In this Reynolds number regime there exists at least one infinitesimal disturbance that is unstable.

Figure 1.2 gives a schematic view of the different Reynolds number regimes based on the preceding definitions. In region I, that is, for $\text{Re} < \text{Re}_E$, all disturbances exhibit monotonic decay. Region II is characterized by global, but not necessarily monotonic stability. In this region, disturbances may grow, but they will ultimately decay as time evolves. For $\text{Re} > \text{Re}_G$ we can encounter instabilities. For Re between Re_G and Re_L we have a conditionally stable flow: for energies below the curve separating regions III and IV the disturbance will decay; for energies above this curve we observe instabilities. The intersection of this curve with the Re -axis defines the Reynolds number above which there exist instabilities of infinitesimal disturbances.

Examples of critical Reynolds numbers compiled from the literature are shown in Table 1.1 (see, e.g., Joseph, 1976; Drazin & Reid, 1981). We observe that in plane Couette flow Re_G and Re_T are different, implying that there exist stable nonturbulent equilibrium solutions (see Section 5.5.3 for more details). These solutions were first found by Nagata (1990) and later verified to be stable by use of direct numerical simulations (see Lundbladh, 1993a). For plane Poiseuille flow and circular pipe flow no such nonturbulent equilibrium solutions have been found for Reynolds numbers lower than Re_T . We will discuss this issue in more detail in Section 5.5.3. For the Blasius boundary layer it is difficult to define Re_E and Re_G unless one assumes parallel flow. The stability characteristics of the type of shear flows listed in Table 1.1 will be studied in detail in Part I.

1.3.3 Spatial Evolution of Disturbances

The definition of stability given earlier relates to growth of disturbances in time. This assumes that one is either considering a localized disturbance where V is a volume large enough to include the complete disturbance development during the time of interest, or a spatially periodic disturbance where the volume V contains one or more complete periods.

For disturbances that are generated at a fixed position in space the concept of temporal growth is not appropriate and the definitions of stability have to be modified. In this case one is interested in the growth of dis-

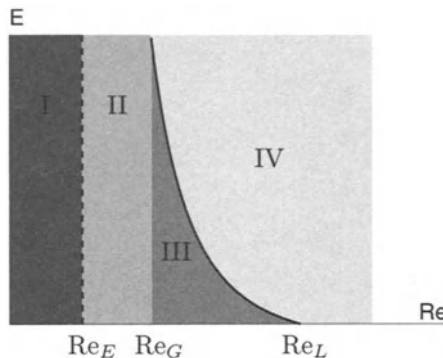


FIGURE 1.2. Sketch illustrating critical Reynolds numbers. Region I: monotonic stability; region II global stability, but not necessarily monotonic stability; between Re_G and Re_L : conditional stability; above Re_L : possible instability.

turbances in space, usually downstream of the disturbance generator. A disturbance is then said to be unstable if it grows without bound as the streamwise distance tends to infinity. Formally the spatial stability concept is somewhat more difficult to define than its temporal counterpart because it is not clear how one should measure the size of the disturbances. If the kinetic energy in a plane perpendicular to the flow direction is chosen, for example, one may encounter positions where this measure is identically zero although the disturbance does not vanish further downstream. An example of such a disturbance is a standing wave in the downstream direction. In practice, one may avoid this type of disturbance if only downstream propagating instabilities are considered, and in physical experiments it often suffices to use a simple disturbance measure such as the maximum of the streamwise velocity.

Figure 1.3 summarizes the different types of evolution that will be considered in this text. The top panel describes the evolution of disturbances that are localized in space, whereas the middle panel illustrates the evolution of an unstable wavelike disturbance in time. In the lower panel we depict an oscillatory disturbance localized in space that exhibits (spatial) growth as it propagates downstream.

1.4 The Reynolds-Orr Equation

1.4.1 Derivation of the Reynolds-Orr Equation

The previous section introduced the definitions of stability and critical Reynolds numbers based on the disturbance energy. It thus seems instruc-

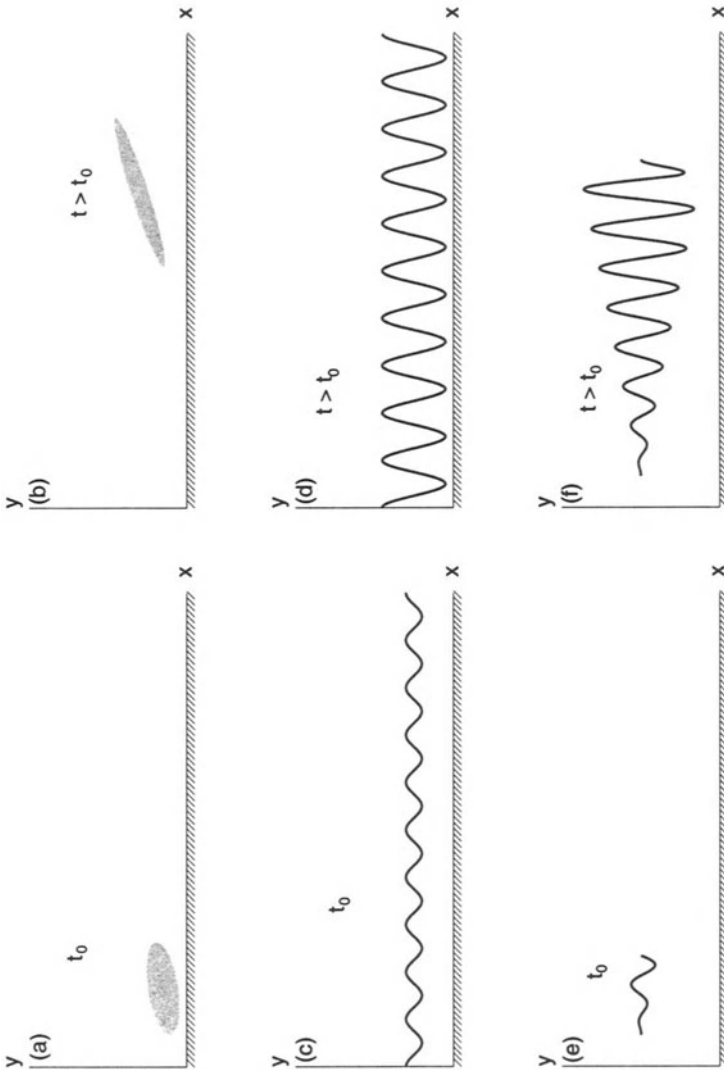


FIGURE 1.3. Evolution of disturbances in shear flows. (a,b) Temporal evolution of a localized disturbance; (c,d) temporal evolution of a global periodic disturbance; (e,f) spatial evolution of a disturbance created by an oscillatory source.

tive to derive an evolution equation for the kinetic disturbance energy. We start with scalar multiplication of the nonlinear disturbance equations by u_i and find that

$$\begin{aligned} u_i \frac{\partial u_i}{\partial t} &= -u_i u_j \frac{\partial U_i}{\partial x_j} - \frac{1}{\text{Re}} \frac{\partial u_i}{\partial x_j} \frac{\partial u_i}{\partial x_j} \\ &+ \frac{\partial}{\partial x_j} \left[-\frac{1}{2} u_i u_i U_j - \frac{1}{2} u_i u_i u_j \right. \\ &\quad \left. - u_i p \delta_{ij} + \frac{1}{\text{Re}} u_i \frac{\partial u_i}{\partial x_j} \right] \end{aligned} \quad (1.10)$$

where we have used the condition that the flow is divergence free. Integrating the equation over the volume V , assuming that the disturbance is localized or spatially periodic, and using Gauss' theorem, we find the Reynolds-Orr equation

$$\frac{dE_V}{dt} = - \int_V u_i u_j \frac{\partial U_i}{\partial x_j} dV - \frac{1}{\text{Re}} \int_V \frac{\partial u_i}{\partial x_j} \frac{\partial u_i}{\partial x_j} dV. \quad (1.11)$$

All the terms that can be written as gradients vanish when integrated over the volume V . In particular, it is important to realize that the nonlinear terms have dropped out. Due to the multiplication by u_i linear terms in (1.6) result in quadratic terms in (1.10); a nonlinear term in (1.6) thus corresponds to a cubic term in (1.10). The two remaining terms on the right-hand side of (1.11) represent the exchange of energy with the base flow and energy dissipation due to viscous effects, respectively.

1.4.2 The Need for Linear Growth Mechanisms

The Reynolds-Orr equation (1.11) can be used to draw an important conclusion about the nature of growth mechanisms possible for disturbances on base flows that are solutions to the Navier-Stokes equations.

From (1.11) we observe that the instantaneous growth rate, $\frac{1}{E_V} \frac{dE_V}{dt}$, is independent of the disturbance amplitude (see Henningson, 1996). In other words, the growth rate of a finite-amplitude disturbance can, at each instant of its evolution, be found from an infinitesimal disturbance with an identical shape. Thus, the instantaneous growth rate of a finite-amplitude disturbance is given by mechanisms that are present in the linearized equations, and the total growth of a finite-amplitude disturbance can be regarded as a sum of growth rates associated with the linear mechanisms. This is a consequence of the conservative nature of the nonlinear terms in the Navier-Stokes equations.

This argument about the need for a linear energy source assumes that the total disturbance energy is based on deviations from a laminar base flow

(U_i) that satisfies the Navier-Stokes equations. Alternatively, it is possible and common to measure the disturbance energy based on a mean flow modified by the disturbances, as, e.g., in the Reynolds averaging procedure frequently used in turbulence research. However, one of the advantages of using the decomposition leading to the nonlinear disturbance equation (1.6), is that in transition research one is frequently interested in measuring the departure of the disturbed flow from the initial laminar state.

2

Linear Inviscid Analysis

2.1 Inviscid Linear Stability Equations

We begin this section by deriving the stability equations for infinitesimal disturbances when effects due to viscosity are negligible. Stability calculations of this sort were among the first in the field of hydrodynamic stability theory. We will assume parallel flow. Let $U_i = U(y)\delta_{1i}$ be the base flow, i.e., a flow in the x -direction that varies with y (see Figure 2.1). If this flow is substituted into the disturbance equations (1.6) and the nonlinear and viscous terms are omitted, the resulting equations can be written as

$$\frac{\partial u}{\partial t} + U \frac{\partial u}{\partial x} + v U' = - \frac{\partial p}{\partial x} \quad (2.1)$$

$$\frac{\partial v}{\partial t} + U \frac{\partial v}{\partial x} = - \frac{\partial p}{\partial y} \quad (2.2)$$

$$\frac{\partial w}{\partial t} + U \frac{\partial w}{\partial x} = - \frac{\partial p}{\partial z} \quad (2.3)$$

and the continuity equation is

$$\frac{\partial u}{\partial x} + \frac{\partial v}{\partial y} + \frac{\partial w}{\partial z} = 0. \quad (2.4)$$

A prime ($'$) denotes a y -derivative. Taking the divergence of the linearized momentum equations, and using the continuity equation yields an equation for the perturbation pressure,

$$\nabla^2 p = -2U' \frac{\partial v}{\partial x}. \quad (2.5)$$

This may be used with equation (2.2) to eliminate p , resulting in an equation for the normal velocity, v :

$$\left[\left(\frac{\partial}{\partial t} + U \frac{\partial}{\partial x} \right) \nabla^2 - U'' \frac{\partial}{\partial x} \right] v = 0. \quad (2.6)$$

In order to describe the complete flow field, a second equation is needed. This is most conveniently the equation for the normal vorticity, which is defined as

$$\eta = \frac{\partial u}{\partial z} - \frac{\partial w}{\partial x}. \quad (2.7)$$

An equation for the evolution of the normal vorticity can be derived by differentiating (2.1) with respect to z , differentiating (2.3) with respect to x , and subtracting both equations, which results in

$$\left(\frac{\partial}{\partial t} + U \frac{\partial}{\partial x} \right) \eta = -U' \frac{\partial v}{\partial z}. \quad (2.8)$$

This pair of equations, together with the boundary conditions

$$v = 0 \quad \text{at a solid wall and/or the far field} \quad (2.9)$$

and the initial conditions

$$v(x, y, z, 0) = v_0(x, y, z) \quad (2.10)$$

$$\eta(x, y, z, 0) = \eta_0(x, y, z) \quad (2.11)$$

form a complete description of the evolution in both space and time of an arbitrary infinitesimal disturbance in an inviscid fluid.

One of the advantages of the formulation in terms of normal velocity and normal vorticity is the absence of the pressure term in the governing equations. If the disturbance pressure is needed, it can be easily recovered from the normal velocity by using the equation

$$\frac{\partial}{\partial t} \left[\frac{\partial u}{\partial x} + \frac{\partial w}{\partial z} \right] + U \frac{\partial}{\partial x} \left[\frac{\partial u}{\partial x} + \frac{\partial w}{\partial z} \right] + U' \frac{\partial v}{\partial x} = - \left[\frac{\partial^2}{\partial x^2} + \frac{\partial^2}{\partial z^2} \right] p \quad (2.12)$$

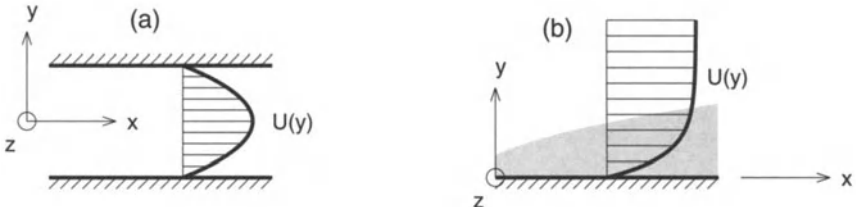


FIGURE 2.1. Geometry and coordinate system for (a) channel and (b) boundary layer flow.

which, after using the continuity equation (2.4), reduces to a Poisson equation in the x - z plane for the disturbance pressure

$$\left[\frac{\partial^2}{\partial x^2} + \frac{\partial^2}{\partial z^2} \right] p = \frac{\partial^2 v}{\partial t \partial y} + U \frac{\partial^2 v}{\partial x \partial y} - U' \frac{\partial v}{\partial x}. \quad (2.13)$$

2.2 Modal Solutions

2.2.1 General Results

The Rayleigh equation

Our interest lies in a specific form of disturbance. We will analyze the stability of the mean flow with respect to wavelike velocity and pressure perturbations. We assume

$$v(x_i, t) = \tilde{v}(y) e^{i(\alpha x + \beta z - \alpha c t)} \quad (2.14)$$

with $c \in \mathbb{C}$ as the phase speed and $\alpha, \beta \in \mathbb{R}$ as the streamwise and spanwise wave numbers. The choice of a complex frequency $\omega = \alpha c$ and real wave numbers is known as the temporal problem where the spatial structure of the wavelike perturbation is unchanged and the amplitude of the wave grows or decays as time progresses (see Figure 1.3). In Chapter 7 we will treat the more complicated spatial problem where the amplitude of a perturbation grows in space while the frequency of the wave is constant.

By substituting the wavelike disturbances into equation (2.6), which is equivalent to taking the Fourier transform, we obtain an equation known as the *Rayleigh equation* (see Rayleigh, 1880, 1887)

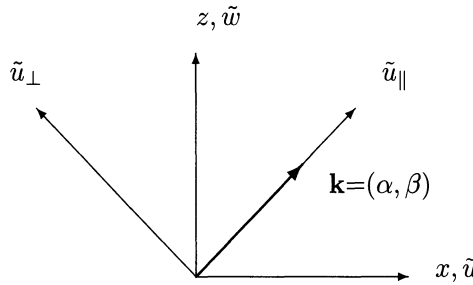


FIGURE 2.2. Illustration of the coordinate system aligned with the wave number vector.

$$(U - c)(\mathcal{D}^2 - k^2)\tilde{v} - U''\tilde{v} = 0 \quad (2.15)$$

with $k^2 = \alpha^2 + \beta^2$ and the boundary conditions

$$\tilde{v} = 0 \quad \text{for } y = \pm 1 \quad (\text{solid boundaries}) \quad (2.16)$$

where we take a bounded domain, $y \in [-1, 1]$. For other flow geometries, e.g., a semi-infinite or infinite domain, the boundary conditions have to be adjusted accordingly. The symbol \mathcal{D} stands for differentiation with respect to the inhomogeneous coordinate direction y .

The Rayleigh equation (2.15) poses an eigenvalue problem of a second-order differential operator with c as the complex eigenvalue. Because the coefficients of this differential equation are real, any complex eigenvalue will appear in complex conjugate pairs, that is, if c is an eigenvalue of the Rayleigh equation, so is the complex conjugate c^* .

Interpretation of modal results

To gain insight into the nature of the solution we consider a single Rayleigh wave with the spatial wave number vector $\mathbf{k} = (\alpha, \beta)$

$$\begin{aligned} v &= \text{Real}\{|\tilde{v}(y)| e^{i\phi(y)} e^{i[\alpha x + \beta z - \alpha(c_r + i c_i)t]}\} \\ &= |\tilde{v}(y)| e^{\alpha c_i t} \cos[\alpha(x - c_r t) + \beta z + \phi(y)]. \end{aligned} \quad (2.17)$$

If $\alpha c_i > 0$ the disturbance grows exponentially; for negative αc_i we encounter exponential decay. In the preceding expression c_r denotes the phase

speed in the x -direction, $|\tilde{v}(y)|$ stands for the absolute value and $\phi(y)$ for the phase of the solution to (2.15).

Let us define the horizontal velocities u_{\parallel}, u_{\perp} parallel and perpendicular to the wave number vector \mathbf{k} , as defined in Figure 2.2,

$$\tilde{u}_{\parallel} = \frac{1}{k} \begin{pmatrix} \alpha \\ \beta \end{pmatrix} \cdot \begin{pmatrix} \tilde{u} \\ \tilde{w} \end{pmatrix} = \frac{1}{k} (\alpha \tilde{u} + \beta \tilde{w}) = -\frac{1}{ik} \frac{d\tilde{v}}{dy} \quad (2.18)$$

$$\tilde{u}_{\perp} = \frac{1}{k} \begin{pmatrix} -\beta \\ \alpha \end{pmatrix} \cdot \begin{pmatrix} \tilde{u} \\ \tilde{w} \end{pmatrix} = \frac{1}{k} (\alpha \tilde{w} - \beta \tilde{u}) = -\frac{1}{ik} \tilde{\eta} \quad (2.19)$$

with $k = \|\mathbf{k}\|$. Thus, u_{\parallel} is proportional to the derivative of the normal velocity; u_{\perp} is determined by the normal vorticity. For the special case of two-dimensional disturbances with $i\beta = 0$

$$\tilde{u}_{\parallel} = -\frac{1}{i\alpha} \frac{d\tilde{v}}{dy} \quad (2.20)$$

which is the two-dimensional version of the continuity equation (2.4).

Critical layers and Tollmien's inviscid solutions

The Rayleigh equation (2.15) has a regular singular point in the complex y -plane where the phase velocity equals the mean velocity, $U(y) = c$. The corresponding real part of this location y_r defines the so-called critical layer where $U(y_r) = c_r$. The singularity is of logarithmic type, and the solution around this point can be expressed in the form of a Frobenius series.

Let us denote the location of the regular singular point by y_c and expand the velocity profile about this critical point in a Taylor series. Substituting into the Rayleigh equation (2.15), we obtain

$$\begin{aligned} \tilde{v}'' - \tilde{v} \{ k^2 [U'_c(y - y_c) + \dots] + U''_c + U'''_c(y - y_c) + \dots \\ + U'_c(y - y_c) + \frac{U''_c}{2}(y - y_c)^2 + \dots \} = 0 \end{aligned} \quad (2.21)$$

where the subscript c denotes the evaluation of the respective function at $y = y_c$.

Dropping terms of order $(y - y_c)^2$ and higher yields the equation

$$(y - y_c)\tilde{v}'' - \tilde{v} \left[\frac{U''_c}{U'_c} + \left(\frac{U'''_c}{U'_c} + k^2 - \frac{U''_c^2}{2U'^2_c} \right) (y - y_c) \right] = 0 \quad (2.22)$$

which is of the form

$$z\hat{v}'' + q(z)\hat{v} = 0 \quad (2.23)$$

with $z = y - y_c$ and $q(z)$ as the coefficient in the square brackets in equation (2.22).

A Frobenius series around the regular singular point $z = 0$ takes the form

$$\tilde{v} = \sum_{n=0}^{\infty} a_n z^{n+\lambda}. \quad (2.24)$$

Substituting into equation (2.22), expanding $q(z)$ in a power series $q(z) = \sum_{n=0}^{\infty} q_n z^n$, and collecting terms of equal power in z we get the indicial equation for the lowest power of z ,

$$a_0 \lambda(\lambda - 1) = 0 \quad (2.25)$$

which leads to $\lambda = 0, \lambda = 1$ as the indices of the Frobenius series. The case $\lambda = 1$ yields one of two linearly independent solutions, and it is not possible to find a solution of the same form for $\lambda = 0$. However, a second linearly independent solution can be found if a term containing a logarithm is introduced. It is then straightforward to show that the two linearly independent solutions to the Rayleigh equation (2.15) are of the form

$$\tilde{v}_1(y) = (y - y_c) P_1(y) \quad (2.26)$$

$$\tilde{v}_2(y) = P_2(y) + \frac{U_c''}{U_c'} \tilde{v}_1(y) \ln(y - y_c) \quad (2.27)$$

with $P_1(y)$ and $P_2(y)$ being analytic functions that have to be determined by enforcing the boundary conditions. The above equations are known as Tollmien's inviscid solutions (see Tollmien, 1929).

It follows from the preceding expression that the second fundamental solution is multivalued due to the appearance of a logarithmic term. This can easily be seen when $c_i = 0$, i.e., the critical layer is on the real axis and $y < y_c$. The logarithmic term yields

$$\ln(y - y_c) = \ln|y - y_c| \pm i\pi \quad \text{for } \operatorname{Im}(y_c) > 0. \quad (2.28)$$

In Section 2.3.2 we will return to the question of how to choose the sign of the imaginary part. We will also address the question of how to take the logarithmic singularity into account when numerically solving the Rayleigh equation.

Starting from the Rayleigh equation (2.15), a few general results can be derived without specifying a particular mean velocity profile. Three of these results will be presented here: Rayleigh's inflection point criterion, Fjørtoft's criterion, and Howard's semicircle theorem.

Rayleigh's inflection point criterion

Rayleigh's inflection point criterion (Rayleigh, 1880) relates the existence of an unstable mode to the occurrence of an inflection point in the mean velocity profile. We will assume a bounded flow domain with $y \in [-1, 1]$.

8 THEOREM (RAYLEIGH'S INFLECTION POINT CRITERION) If there exist perturbations with $c_i > 0$, then $U''(y)$ must vanish for some $y_s \in [-1, 1]$.

The proof of this theorem is given by multiplying the Rayleigh equation (2.15) by the complex conjugate of the normal velocity, \tilde{v}^* , and integrating in y from -1 to 1 . After integrating by parts we obtain the equation

$$\int_{-1}^1 |\mathcal{D}\tilde{v}|^2 + k^2|\tilde{v}|^2 dy + \int_{-1}^1 \frac{U''}{U - c} |\tilde{v}|^2 dy = 0. \quad (2.29)$$

The first integral is real and positive definite, and the second integral is in general complex-valued. Taking the imaginary part of the above expression yields

$$\text{Im} \left\{ \int_1^1 \frac{U''}{U - c} |\tilde{v}|^2 dy \right\} = \int_{-1}^1 \frac{U'' c_i |\tilde{v}|^2}{|U - c|^2} dy = 0. \quad (2.30)$$

Both $|\tilde{v}|^2$ and $|U - c|^2$ are nonnegative and c_i has been assumed positive. It follows that U'' has to change sign to render the integral zero. The theorem follows immediately from this conclusion. Rayleigh's inflection point criterion only gives a necessary condition for instability.

Fjørtoft's criterion

An extension of the inflection point criterion (2.30) due to Fjørtoft (1950) provides an improved necessary condition for instability.

9 THEOREM (FJØRTOFT'S CRITERION) Given a monotonic mean velocity profile $U(y)$, a necessary condition for instability is that $U''(U - U_s) < 0$ for $y \in [-1, 1]$, with $U_s = U(y_s)$ as the mean velocity at the inflection point, i.e., $U''(y_s) = 0$.

This means that the inflection point has to be a maximum (rather than a minimum) of the spanwise mean vorticity. Fjørtoft's criterion can be derived by considering the real part of equation (2.29). We get

$$\int_{-1}^1 \frac{U''(U - c_r)}{|U - c|^2} |\tilde{v}|^2 dy = - \int_{-1}^1 |\mathcal{D}\tilde{v}|^2 + k^2|\tilde{v}|^2 dy. \quad (2.31)$$

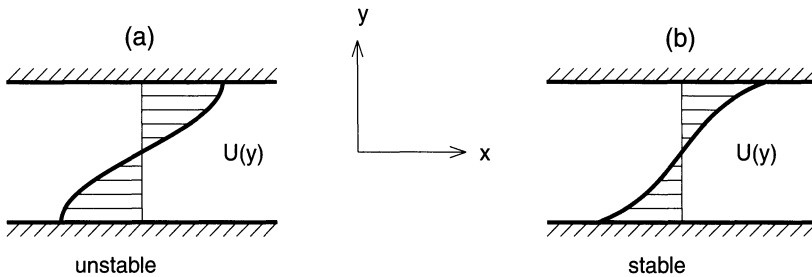


FIGURE 2.3. Demonstration of Fjørtoft's criterion as a necessary condition for instability in inviscid flow. (a) unstable according to Fjørtoft, (b) stable according to Fjørtoft.

Next, we add the expression

$$(c_r - U_s) \int_{-1}^1 \frac{U''}{|U - c|^2} |\tilde{v}|^2 dy \quad (2.32)$$

to the left side of the equation. This expression is identically zero due to the inflection point criterion (2.30). We then obtain

$$\int_{-1}^1 \frac{U''(U - U_s)}{|U - c|^2} |\tilde{v}|^2 dy = - \int_{-1}^1 |\mathcal{D}\tilde{v}|^2 + k^2 |\tilde{v}|^2 dy. \quad (2.33)$$

For the integral on the left to be negative, we have to require the expression $U''(U - U_s)$ to be negative somewhere in the flow field. This concludes the proof of Fjørtoft's theorem.

Figure 2.3 demonstrates Rayleigh's and Fjørtoft's criteria as necessary conditions for instability of inviscid fluid flow. Both mean velocity profiles show an inflection point in the center of the channel, and thus they satisfy Rayleigh's necessary condition for an inviscid instability. However, only the velocity profile on the left fulfills Fjørtoft's criterion in addition to Rayleigh's. The mean velocity profile on the right has a minimum (rather than a maximum) of the spanwise mean vorticity and therefore does not satisfy Fjørtoft's criterion.

Howard's semicircle theorem

Yet another general stability condition was introduced by Howard (1961) in the form of a semicircle that bounds the eigenvalues of the Rayleigh equation.

10 THEOREM (HOWARD'S SEMICIRCLE THEOREM) The unstable eigenvalues of the Rayleigh equation satisfy

$$\left[c_r - \frac{1}{2} (U_{\max} + U_{\min}) \right]^2 + c_i^2 \leq \left[\frac{1}{2} (U_{\max} - U_{\min}) \right]^2. \quad (2.34)$$

To derive this result we will introduce the variable ¹

$$\tilde{V} = \frac{\tilde{v}}{U - c} \quad (2.35)$$

and rewrite the Rayleigh equation (2.15) as

$$\mathcal{D} \left[(U - c)^2 \mathcal{D}\tilde{V} \right] - k^2 (U - c)^2 \tilde{V} = 0. \quad (2.36)$$

We then multiply by \tilde{V}^* , the complex conjugate of \tilde{V} , and integrate over the domain (in our case from -1 to 1), which after integration by parts yields

$$\int_{-1}^1 (U - c)^2 \underbrace{\left(|\mathcal{D}\tilde{V}|^2 + k^2 |\tilde{V}|^2 \right)}_{Q \geq 0} dy = 0. \quad (2.37)$$

Splitting this expression into real and imaginary parts results in

$$\int_{-1}^1 [(U - c_r)^2 - c_i^2] Q dy = 0 \quad (2.38)$$

and

$$2c_i \int_{-1}^1 (U - c_r) Q dy = 0. \quad (2.39)$$

From equation (2.39), it immediately follows that $U - c_r$ has to change sign in the interval $[-1, 1]$ or that c_r is bounded by the minimum and maximum mean velocity,

$$U_{\min} < c_r < U_{\max}. \quad (2.40)$$

¹This new variable \tilde{V} is the solution of the adjoint Rayleigh equation corresponding to the eigenvalue c .

It also follows that

$$\int_{-1}^1 UQ \, dy = c_r \int_{-1}^1 Q \, dy. \quad (2.41)$$

We will now direct our attention to equation (2.38) and use the above relation to obtain

$$\int_{-1}^1 U^2 Q \, dy = \int_{-1}^1 (c_r^2 + c_i^2) Q \, dy. \quad (2.42)$$

It then follows that

$$\begin{aligned} 0 &\geq \int_{-1}^1 (U - U_{\min})(U - U_{\max})Q \, dy \\ &\geq \int_{-1}^1 [(c_r^2 + c_i^2) - (U_{\max} + U_{\min})c_r + U_{\max}U_{\min}] Q \, dy \end{aligned} \quad (2.43)$$

from which we get

$$c_r^2 + c_i^2 - (U_{\max} + U_{\min}) c_r + U_{\max}U_{\min} \leq 0. \quad (2.44)$$

Howard's semicircle theorem follows from there. It states that the eigenvalues of the Rayleigh equation are confined to a disk of radius $(U_{\max} - U_{\min})/2$ centered at $c_r = (U_{\max} + U_{\min})/2$ and $c_i = 0$.

Figure 2.4 illustrates the semicircle in the complex c -plane. The Rayleigh equation has been solved numerically for the mean velocity $U = \operatorname{sech}(y)$, which approximates a jet profile. Unstable eigenvalues are found, which are confined to the semicircle shown in Figure 2.4(b). The curve inside the circle displays the location of the eigenvalues as the streamwise wave number varies.

Solution for piecewise linear velocity profiles

Now that we have derived general results for unspecified mean velocity profiles, we will compute the eigenvalues and eigenfunctions for simple base flows. Before computers were available to researchers in the field of hydrodynamic stability theory, a common technique to solve inviscid stability problems was to approximate continuous mean velocity profiles by piecewise linear profiles. Although this technique is rather outdated today, it is still instructive to learn about the fundamental characteristics of inviscid stability problems by considering piecewise linear velocity profiles because it allows the analytical derivation of the dispersion relation $c(\alpha, \beta)$ and the

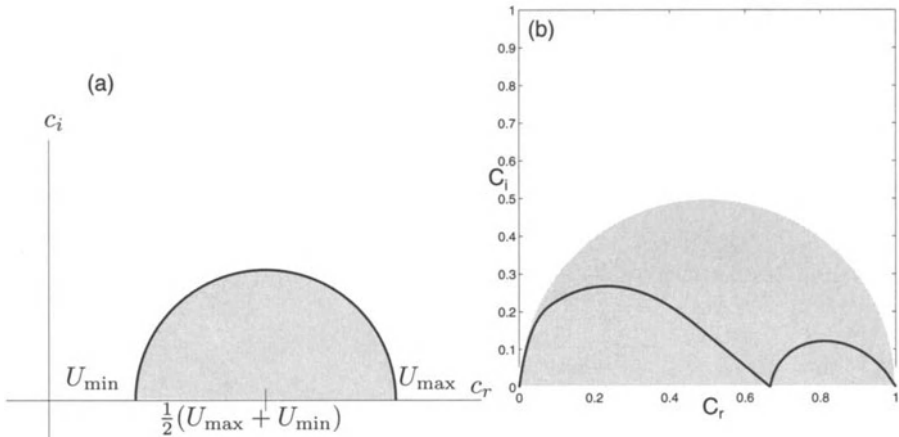


FIGURE 2.4. Howard's semicircle theorem. (a) Sketch of Howard's semicircle. (b) Example: inviscid spectrum for the Bickley jet. The unstable eigenvalues (solid line) fall inside Howard's semicircle (shaded area).

eigenfunctions. We will present two classical examples that will demonstrate the essential features of inviscid stability theory before we move on to an example that requires numerical techniques.

Let us first develop the tools to attack problems with piecewise linear velocity profiles. Piecewise linear velocity profiles have the advantage that the second derivative term U'' in the Rayleigh equation (2.15) vanishes for each section of the profiles, thus leading to a simple equation to solve for the eigenfunction \tilde{v} . However, we expect difficulties at points in the velocity profiles where the second derivative is discontinuous. At these locations we have to use a matching procedure, which will be outlined below before we show some examples.

Rewriting the Rayleigh equation (2.15) in the form

$$\mathcal{D}[(U - c)\mathcal{D}\tilde{v} - U'\tilde{v}] = (U - c)k^2\tilde{v} \quad (2.45)$$

and integrating over the discontinuity in U and/or U' located at y_D we get

$$[(U - c)\mathcal{D}\tilde{v} - U'\tilde{v}]_{y_D-\epsilon}^{y_D+\epsilon} = k^2 \int_{y_D-\epsilon}^{y_D+\epsilon} (U - c)\tilde{v} dy. \quad (2.46)$$

The integral on the right-hand side vanishes as ϵ approaches zero, which leaves us with the first jump condition that has to be satisfied by the eigenfunction

$$[(U - c)\mathcal{D}\tilde{v} - U'\tilde{v}] = 0 \quad (2.47)$$

where $\llbracket \cdot \rrbracket$ denotes the jump in the quantity enclosed in the brackets. This first constraint for the eigenfunction \tilde{v} is equivalent to matching the pressure across the discontinuity, as can be seen by recalling equation (2.13) for the disturbance pressure in inviscid flow, which in Fourier-transformed form reads

$$\tilde{p} = \frac{i\alpha}{k^2} (U' \tilde{v} - (U - c)\mathcal{D}\tilde{v}). \quad (2.48)$$

A second jump condition is easily derived by dividing this expression for the pressure by $i\alpha(U - c)^2/k^2$, which yields

$$-\frac{k^2 \tilde{p}}{i\alpha(U - c)^2} = \frac{\mathcal{D}\tilde{v}}{U - c} - \frac{U'}{(U - c)^2} = \mathcal{D} \left[\frac{\tilde{v}}{U - c} \right]. \quad (2.49)$$

Integrating over the discontinuity in the velocity profile results in

$$\left[\frac{\tilde{v}}{U - c} \right]_{y_D - \epsilon}^{y_D + \epsilon} = -\frac{k^2}{i\alpha} \int_{y_D - \epsilon}^{y_D + \epsilon} \frac{\tilde{p}}{(U - c)^2} dy. \quad (2.50)$$

Using the same arguments as earlier, the integral on the right-hand side vanishes as ϵ goes to zero, resulting in the second matching condition across the discontinuity

$$\left[\frac{\tilde{v}}{U - c} \right] = 0 \quad (2.51)$$

which for continuous U corresponds to matching the vertical velocity. To solve the Rayleigh equation (2.15) for a piecewise linear approximation to a continuous velocity profile, we need to solve

$$(\mathcal{D}^2 - k^2)\tilde{v} = 0 \quad (2.52)$$

in each subdomain. Imposing the boundary and matching conditions will determine the coefficients of the fundamental solutions in each subdomain and result in an expression for c as a function of k , which is the desired dispersion relation.

Piecewise linear mixing layer

As a first example of piecewise linear velocity profiles we consider the stability of a mixing layer where the velocity profile has been approximated by straight lines, as shown in Figure 2.5. The velocity profile is given as

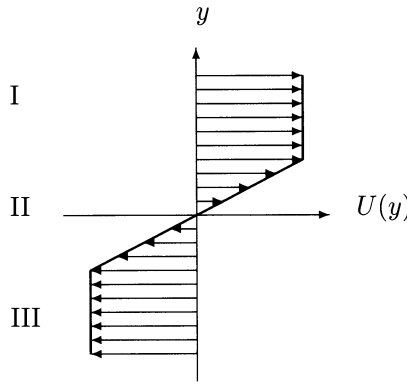


FIGURE 2.5. Sketch of the piecewise linear mixing layer.

$$U(y) = \begin{cases} 1 & \text{for } y > 1 \\ y & \text{for } -1 \leq y \leq 1 \\ -1 & \text{for } y < -1. \end{cases} \quad (2.53)$$

We will denote the upper part of the velocity profile ($y > 1$) region I, the middle part ($-1 \leq y \leq 1$) region II, and the lower part ($y < -1$) region III (see Figure 2.5). Because the second derivative term for the mean velocity profile vanishes, the Rayleigh equation (2.15) reduces to the simpler equation

$$(\mathcal{D}^2 - k^2)\tilde{v} = 0 \quad (2.54)$$

which has to be solved in all regions subject to the boundary conditions

$$\tilde{v} \rightarrow 0 \quad \text{as} \quad y \rightarrow \pm\infty \quad (2.55)$$

and the appropriate matching conditions.

The solution of (2.54) satisfying the boundary condition in regions I and III is found to be

$$\tilde{v}_I = A \exp(-ky) \quad \text{for } y > 1 \quad (2.56)$$

$$\tilde{v}_{II} = B \exp(-ky) + C \exp(ky) \quad \text{for } -1 \leq y \leq 1 \quad (2.57)$$

$$\tilde{v}_{III} = D \exp(ky) \quad \text{for } y < -1. \quad (2.58)$$

The constants A, B, C , and D have to be found by enforcing the matching conditions across the points $y = \pm 1$. From matching the velocity and pressure across the point $y = 1$, we get

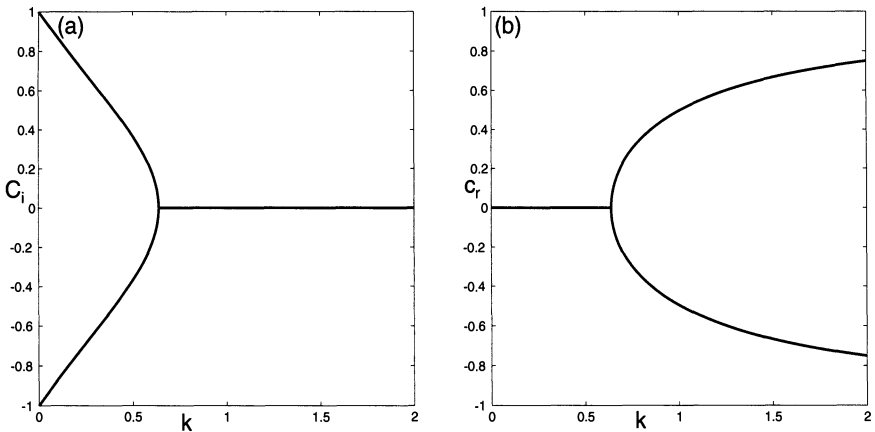


FIGURE 2.6. Eigenvalues for the piecewise linear mixing layer. (a) Imaginary part of the eigenvalue (growth rate) as a function of wave number. (b) Real part of the eigenvalue (phase speed) as a function of wave number.

$$2Ck(1 - c) \exp(k) = B \exp(-k) + C \exp(k) \quad (2.59)$$

and from matching across the point $y = -1$, we obtain

$$2Bk(1 + c) \exp(k) = B \exp(k) + C \exp(-k). \quad (2.60)$$

Both unknown coefficients B and C can be eliminated from these equations, leaving us with a condition on the eigenvalue c of the form

$$c = \pm \sqrt{\left(1 - \frac{1}{2k}\right)^2 - \left(\frac{1}{4k^2}\right) \exp(-4k)}. \quad (2.61)$$

A plot of the dispersion relation is given in Figure 2.6. For the range of wave numbers $0 \leq k \leq 0.6392$ the expression under the square root is negative, resulting in purely imaginary eigenvalues c . For wave numbers larger than $k = 0.6392$ the eigenvalues are real, and all disturbances are neutral. The eigenfunctions are displayed in Figure 2.7. As the wave number goes to zero, the wavelength associated with the disturbances is much larger than the length scale associated with the mean velocity profile. The limit of small wave numbers is thus equivalent to the limit of a zero thickness of region II. In this case we recover the stability results for a Kelvin-Helmholtz instability, namely,

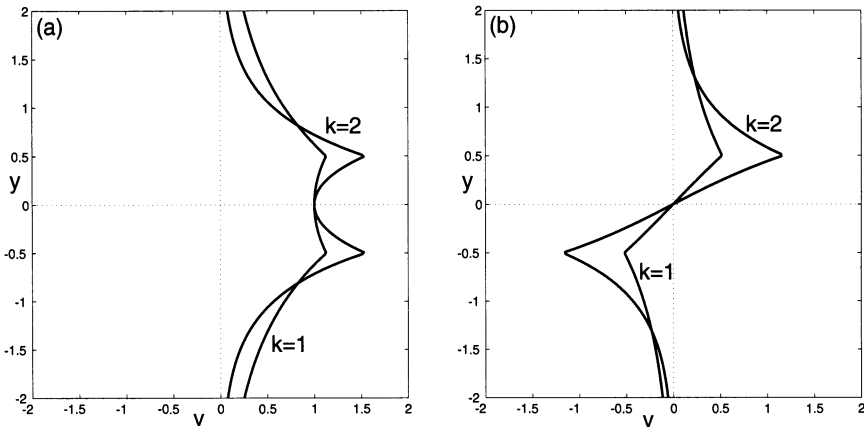


FIGURE 2.7. Eigenfunctions for the piecewise linear mixing layer for $k = 1$ and $k = 2$. (a) Symmetric eigenfunction; (b) antisymmetric eigenfunction.

$$\lim_{k \rightarrow 0} c^2(k) = \lim_{k \rightarrow 0} \frac{4k^2 - 4k + 1 - \exp(-4k)}{4k^2} = -1 \quad (2.62)$$

or

$$c = \pm i \quad (2.63)$$

which states that the eigenvalues for this case are independent of the wave number. Thus, wavelike perturbations on an unbounded vortex sheet in an inviscid fluid do not show any dispersion, i.e., all wave components travel at the same (zero) speed.

Piecewise linear boundary layer

Another interesting problem is given by approximating parallel boundary layer flow by piecewise linear velocity segments. We will split the boundary layer into three regions with the following velocity profile:

$$U(y) = \begin{cases} 2b y & \text{for } 0 \leq y \leq 1/2 \\ 2(1-b)y + (2b-1) & \text{for } 1/2 < y \leq 1 \\ 1 & \text{for } y > 1. \end{cases} \quad (2.64)$$

A sketch of the velocity profile for two choices of parameter b is given in Figure 2.8. By varying parameter b , we can simulate the effect of an adverse or favorable pressure gradient and even investigate the inviscid stability properties of separated flows (for negative b).

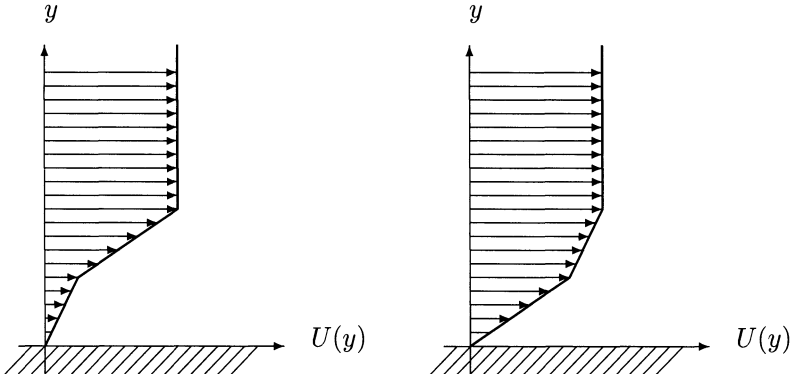


FIGURE 2.8. Sketch of two piecewise linear boundary layer profiles. Left: $b < 1/2$; right: $b > 1/2$.

Computing the eigenfunctions and dispersion relation for this type of flow proceeds along the same way as before, but the algebraic manipulations rapidly become unwieldy. The dispersion relation is given by a quadratic polynomial

$$A(k)c^2 + B(k; b)c + C(k; b) = 0 \quad (2.65)$$

with

$$A(k) = 2k^2(\xi + 1) \quad \xi = \coth(k/2) \quad (2.66)$$

$$\begin{aligned} B(k; b) = & 2k(1 - \xi)(1 - b)e^{-k} \\ & - 2k\{(\xi + 1)[k(1 + b) - (1 - b)] + 2(1 - 2b)\} \end{aligned} \quad (2.67)$$

and

$$\begin{aligned} C(k; b) = & 2(1 - b)[bk(\xi - 1) + 2(1 - 2b)]e^{-k} \\ & - 2(1 - b - k)[bk(\xi + 1) + 2(1 - 2b)]. \end{aligned} \quad (2.68)$$

We note that only for a limited range of values of b and k are the resulting eigenvalues c_1, c_2 purely real. In this range the flow does not accommodate growing or decaying solutions. All wavelike perturbations are neutrally stable, but they travel at different phase velocities depending on their wave number. Outside this range, on the other hand, we encounter complex conjugate eigenvalues, which indicate an inviscid instability mechanism. The

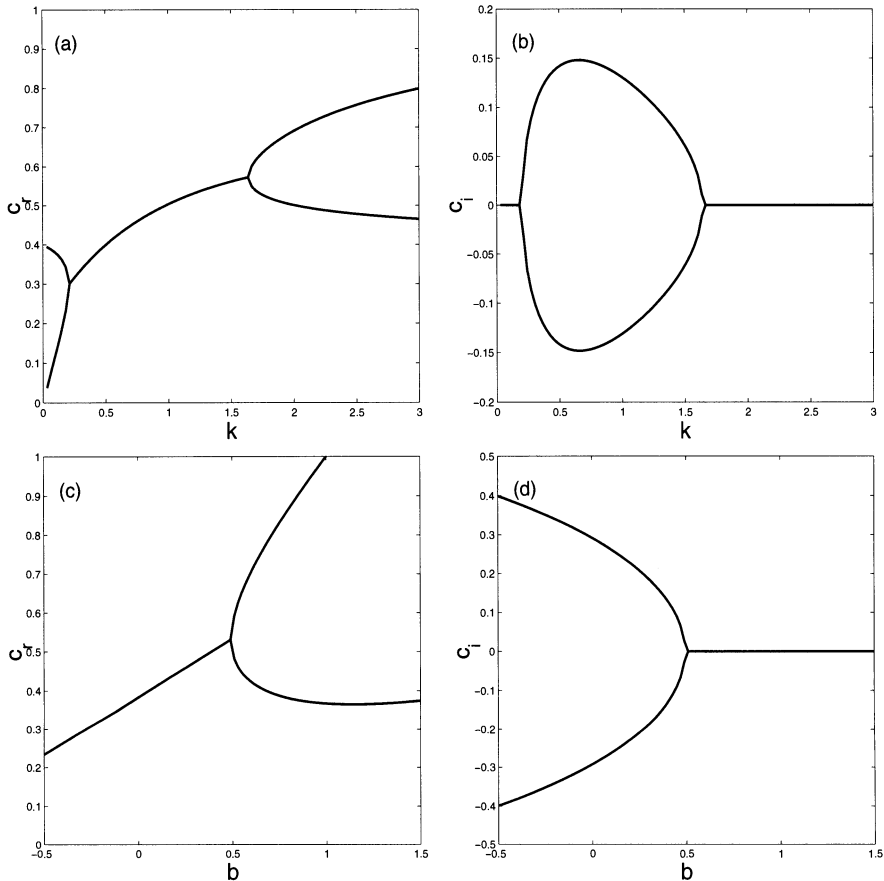


FIGURE 2.9. Dispersion relation for the piecewise linear boundary layer flow approximation. Phase velocity (a) and growth rate (b) as a function of wave number for $b = 0.4$. Phase velocity (c) and growth rate (d) as a function of parameter b for wave number $k = 1$.

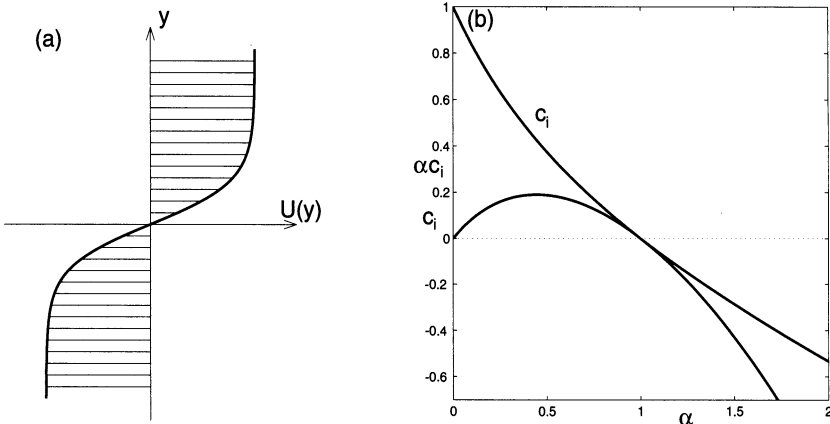


FIGURE 2.10. The hyperbolic tangent mixing layer. (a) Sketch of the velocity profile; (b) growth rate c_i for the mixing layer as a function of streamwise wave number α .

eigenvalues for varying wave number k and parameter b are displayed in Figure 2.9. We observe exponential instabilities for value of $b < 1/2$ which is in agreement with Rayleigh's inflection point criterion.

Mixing layer

As a final example we will discuss the solution of the two-dimensional Rayleigh equation for a continuous velocity profile (see also Appendix D). To contrast it to the piecewise linear mixing layer discussed previously, we will now choose an approximation of the mixing layer based on the hyperbolic tangent (Figure 2.10(a)):

$$U(y) = \tanh(y) \quad -\infty < y < \infty. \quad (2.69)$$

For this profile we will solve the Rayleigh equation (2.15) numerically using a shooting method. We choose a location on the negative real axis and guess the eigenvalue c , after which we integrate the Rayleigh equation in y along the real axis. At a specified location on the positive y -axis we compare the result of the integration to the boundary condition for an eigenfunction, namely,

$$\tilde{v}(y) \sim \exp(-\alpha y) \quad (2.70)$$

which represents the asymptotic behavior of solutions to the Rayleigh equation for $y \rightarrow \infty$. Any deviation from this behavior is then used to adjust the eigenvalue estimate until the integration of the Rayleigh equation (2.15)

yields the correct behavior at the specified y -location. The new guess for the eigenvalue c is determined by the secant method. The result of this procedure yields the eigenvalues for the mixing layer as displayed in Figure 2.10(b).

All eigenvalues found have zero real part, i.e., $c_r = 0$. For streamwise wave numbers α less than one, we obtain eigenvalues with positive imaginary part; for larger streamwise wave numbers, damped solutions exist. The numerical procedure described earlier holds true for eigenvalues with positive growth rates $c_i > 0$ but needs to be modified to obtain damped solutions for the mixing layer problem. For neutral and damped solutions we encounter the branch cut associated with the logarithmic singularity (see (2.27)) when integrating along the real y -axis and the problem of choosing the correct integration path needs to be addressed. This problem is treated in Section 2.3.2, where we will return to the mixing layer example.

2.2.2 Dispersive Effects and Wave Packets

Method of stationary phase

Because c is in general a complicated function of k , a perturbation decomposed into discrete eigenmodes will gradually change its shape due to dispersive effects. For real dispersion relations these effects can be determined by applying the method of stationary phase to the solution of the initial value problem. For more general complex dispersion relations, which will be covered in Chapter 3, we have to use the method of steepest descent.

We are interested in the long-time evolution of disturbances in inviscid flow. After solving the Rayleigh equation (2.15) for \tilde{v} , we are still faced with the task of inverting the Fourier transform, i.e., solving the integral

$$v(x, y, z, t) = \frac{1}{4\pi^2} \iint \tilde{v}(y, \alpha, \beta) \exp[i(\alpha \frac{x}{t} + \beta \frac{z}{t} - \omega)t] d\alpha d\beta, \quad \omega = \alpha c. \quad (2.71)$$

Because our interest is mostly in the behavior of the solution for large times, we can use asymptotic methods to evaluate the integral (2.71) approximately for $t \rightarrow \infty$. We notice that for large times the integrand oscillates rapidly and cancels itself over most of the integration range. Figure 2.11 illustrates this fact by displaying the real part of a general function $\exp[i\text{tp}(x)]$ versus x for a large given value of t . The function $p(x)$, symbolized by the dashed line in Figure 2.11, varies smoothly over the interval of integration. Because we wish to evaluate the integral of this function over the displayed interval, we experience, due to the rapid oscillations, cancellation effects near the ends of the interval. Only the part of the interval near the extremum of the smooth (dashed) function $p(x)$ contributes

$p(x)$, $\exp[itp(x)]$

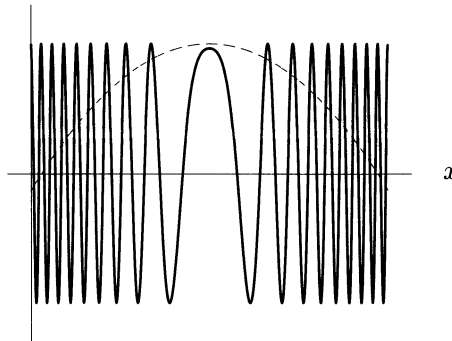


FIGURE 2.11. Sketch demonstrating the concept of stationary phase asymptotics. The dashed line symbolizes a smoothly varying function $p(x)$. The solid line represents the real part of $\exp[itp(x)]$ for large t .

to the value of the integral. As t tends to infinity, the oscillations become more and more rapid, and we can approximate the integral by quantities evaluated at the extreme point of the smooth function only. Applying this technique to our integral (2.71), we can concentrate on the parts of the integral where $\nabla\Psi = 0$, with

$$\Psi = \alpha \frac{x}{t} + \beta \frac{z}{t} - \omega. \quad (2.72)$$

We therefore have to solve for the wave numbers (α_0, β_0) that satisfy the set of equations

$$\frac{\partial\Psi}{\partial\alpha} = \frac{x}{t} - \frac{\partial\omega}{\partial\alpha} = 0 \quad (2.73)$$

$$\frac{\partial\Psi}{\partial\beta} = \frac{z}{t} - \frac{\partial\omega}{\partial\beta} = 0. \quad (2.74)$$

The expressions

$$\frac{\partial\omega}{\partial\alpha}(\alpha_0, \beta_0) \equiv c_{gx} = \frac{x}{t} \quad (2.75)$$

$$\frac{\partial\omega}{\partial\beta}(\alpha_0, \beta_0) \equiv c_{gz} = \frac{z}{t} \quad (2.76)$$

are known as the group velocities of the disturbance. A disturbance composed of a group of dispersive waves will propagate with the group velocity

although every individual wave component will travel with the corresponding phase velocity.

Expanding Ψ about the stationary point and evaluating the integral (2.71) gives the following result (see Gaster, 1975)

$$v = \frac{\tilde{v}(y; \alpha_0, \beta_0) \exp(i\Psi_0 t)}{2\pi i t \sqrt{\left| \frac{\partial^2 \omega_0}{\partial \alpha^2} \frac{\partial^2 \omega_0}{\partial \beta^2} - \left(\frac{\partial^2 \omega_0}{\partial \alpha \partial \beta} \right)^2 \right|}} \quad (2.77)$$

where

$$\Psi_0 t = \left(\alpha_0 \frac{x}{t} + \beta_0 \frac{z}{t} - \omega(\alpha_0, \beta_0) \right) t \quad (2.78)$$

and α_0 and β_0 satisfy (2.75) and (2.76).

This result is valid along the corresponding group velocity rays and describes a three-dimensional wave packet that propagates in both the streamwise and spanwise directions.

Wave areas

We will now apply the method of stationary phase to the evolution of wave packets in an inviscid fluid in the asymptotic limit of large times. For a homogeneous medium the wave numbers are found to be constant along group velocity rays. We have

$$\omega = \alpha c(k) \quad \text{with} \quad k^2 = \alpha^2 + \beta^2 \quad (2.79)$$

and introducing the wave angle θ , we can write

$$\alpha = k \cos \theta \quad \beta = k \sin \theta. \quad (2.80)$$

Substituting into the expression for the group velocities (2.75) and (2.76) we arrive at

$$c_{gx} = \frac{x}{t} = \frac{\partial \omega}{\partial \alpha} = c + \frac{\alpha^2}{k} \frac{dc}{dk} = c + (\cos(2\theta) + 1) \frac{k}{2} \frac{dc}{dk} \quad (2.81)$$

$$c_{gz} = \frac{z}{t} = \frac{\partial \omega}{\partial \beta} = \frac{\alpha \beta}{k} \frac{dc}{dk} = \sin(2\theta) \frac{k}{2} \frac{dc}{dk}. \quad (2.82)$$

Eliminating the wave angle or the wave numbers α and β , we get

$$\left(\frac{x}{t} - c - \frac{k}{2} \frac{dc}{dk} \right)^2 + \left(\frac{z}{t} \right)^2 = \left(\frac{k}{2} \frac{dc}{dk} \right)^2 \quad (2.83)$$

which describes circles in the $(x/t, z/t)$ plane, on which waves with wave number $k = \sqrt{\alpha^2 + \beta^2}$ appear. The center of the circles is at $c + \frac{k}{2} \frac{dc}{dk}$ and their radius is $\frac{k}{2} \frac{dc}{dk}$.

From expression (2.83) one can calculate the curve describing their envelope. The region inside the envelope curve will then indicate where wave solutions can be found. Gustavsson (1978) derived such an expression by differentiating the expression for the circles with respect to k . From this expression and the original one describing the circles (2.83) one can solve for the envelope in the $(x/t, z/t)$ plane. We have

$$\frac{x}{t} = c + \frac{kc'^2}{3c' + kc''} \quad (2.84)$$

$$\frac{z}{t} = \pm \frac{kc'}{3c' + kc''} \sqrt{c'(2c' + kc'')} \quad (2.85)$$

where the prime denotes differentiation with respect to the wave number k . For the piecewise linear approximation of the boundary layer (2.64) with $b = 1/2$, this envelope curve is shown in Figure 2.12, together with the circles for selected wave numbers.

The opening angle of the envelope at the origin is given as

$$\sin \phi = \lim_{k \rightarrow 0} \frac{\frac{k}{2} \frac{dc}{dk}}{c + \frac{k}{2} \frac{dc}{dk}}. \quad (2.86)$$

If we have a dispersion relation that asymptotically behaves like a power law for small wave numbers, that is, $c \approx k^\sigma$, as $k \rightarrow 0$, we can determine the opening angle of the envelope as

$$\sin \phi = \frac{\sigma}{\sigma + 2}. \quad (2.87)$$

Another fact worth noting is that the maximum spanwise group velocity

$$c_{gz} = \sin(2\theta) \frac{k}{2} \frac{dc}{dk} \quad (2.88)$$

that governs the spanwise spreading of the wave packet is achieved for a wave angle of $\theta = \frac{\pi}{4}$, which means that the edge of the wave packet consists of oblique waves inclined at an angle of 45° .

Example

Let us now apply the preceding asymptotic analysis to one of the piecewise linear velocity profiles for which we computed the dispersion relation in

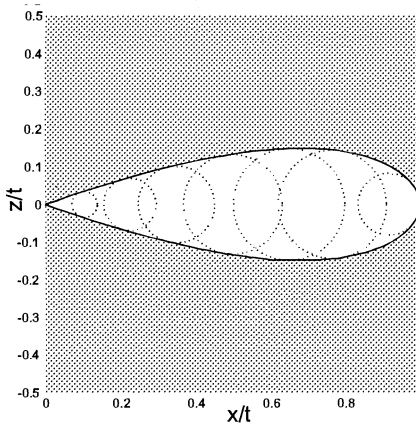


FIGURE 2.12. Location of wave-like solutions in the (x/t) - (z/t) -plane for a piecewise linear boundary layer.

closed form. We choose the piecewise linear approximation to the boundary layer flow $U(y) = \min(y, 1)$, i.e., the special case of $b = 1/2$ for the example given earlier (see equation (2.64)). The dispersion relation can be calculated as

$$c(k) = 1 - \exp(-k) \frac{\sinh(k)}{k}. \quad (2.89)$$

In this particular example, the dispersion relation for small wave numbers k is of power-law type

$$c(k) = k - \frac{2}{3}k^2 + \mathcal{O}(k^3) \quad \text{as } k \rightarrow 0 \quad (2.90)$$

which results in an opening angle for the envelope of the wave area of

$$\phi = \arcsin\left(\frac{1}{3}\right) \approx 19.47^\circ. \quad (2.91)$$

As an example we will also invert expressions (2.75) and (2.76) for the dispersion relation of the piecewise approximation to the boundary layer flow. We will assume that the Fourier-transformed normal velocity is given by a Gaussian distribution centered around the wave numbers $\alpha = \beta = 0$. The computational procedure is as follows: For a given time t and a given streamwise (x) and spanwise (z) location we solve the nonlinear system

$$c_{gx} = 1 - e^{-k} \left[\frac{\sinh k}{k} - \frac{\alpha^2}{k^2} \left(\sinh k - \cosh k + \frac{\sinh k}{k} \right) \right] = \frac{x}{t} \quad (2.92)$$

$$c_{gz} = \frac{\alpha\beta}{k^2} e^{-k} \left[\sinh k - \cosh k + \frac{\sinh k}{k} \right] = \frac{z}{t} \quad (2.93)$$

for the streamwise and spanwise wave numbers (α_0, β_0) . These wave numbers will then be used to evaluate the expression

$$v \approx \frac{\hat{v}(\alpha_0, \beta_0)}{2\pi it \sqrt{\left| \frac{\partial^2 \omega_0}{\partial \alpha^2} \frac{\partial^2 \omega_0}{\partial \beta^2} - \left(\frac{\partial^2 \omega_0}{\partial \alpha \partial \beta} \right)^2 \right|}} \exp[i(\alpha_0 \frac{x}{t} + \beta_0 \frac{z}{t} - \omega(\alpha_0, \beta_0)t)]. \quad (2.94)$$

We take the Fourier-transformed vertical velocity of the form

$$\hat{v}(\alpha_0, \beta_0) = \exp[-\chi k_0^2] \quad k_0^2 = \alpha_0^2 + \beta_0^2 \quad (2.95)$$

where we have chosen χ to be 0.3. The results of this calculation are displayed in Figures 2.13-2.15. It is apparent that real solutions of the nonlinear system of equations (2.92) and (2.93) exist only for locations in the (x/t) - (z/t) plane that fall inside the region covered by the circles given by equation (2.83).

2.3 Initial Value Problem

2.3.1 The Inviscid Initial Value Problem

We will now return to equations (2.6) and (2.8) governing the evolution of infinitesimal disturbances in an inviscid fluid. Because the coordinates x and z are homogeneous and the system is linear, it is possible to work in wave number space and consider the behavior of single Fourier components

$$v(x, y, z, t) = \hat{v}(y, t) e^{i(\alpha x + \beta z)} \quad (2.96)$$

$$\eta(x, y, z, t) = \hat{\eta}(y, t) e^{i(\alpha x + \beta z)}. \quad (2.97)$$

Introducing this decomposition into (2.6) and (2.8) results in the following pair of equations for \hat{v} and $\hat{\eta}$

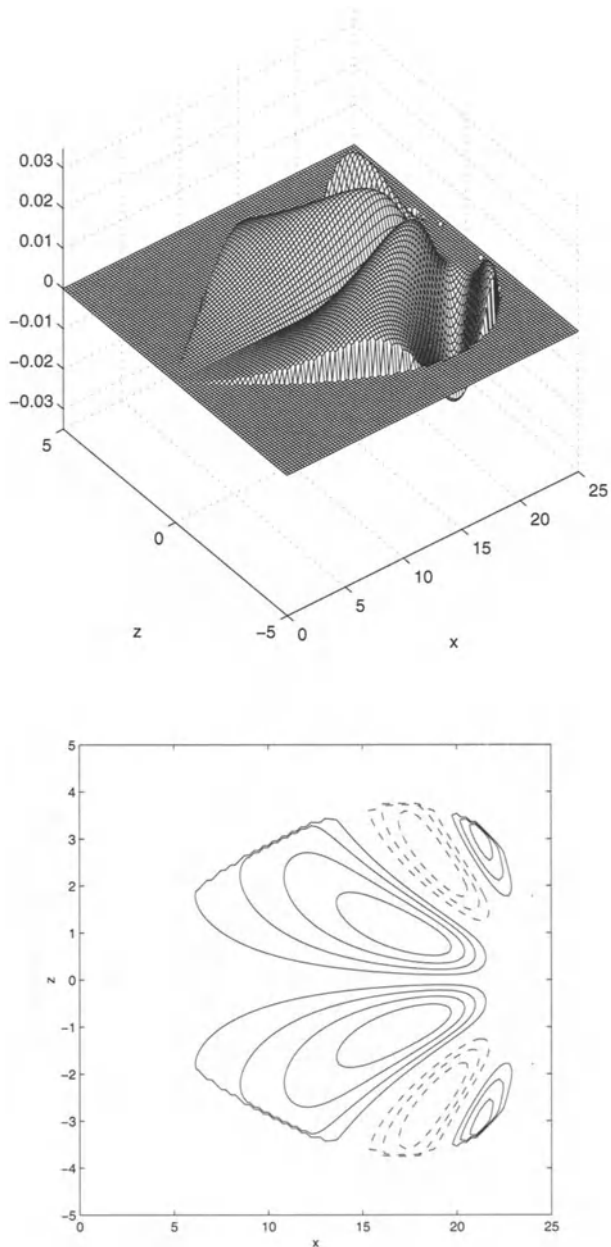


FIGURE 2.13. Evolution of a point-like disturbance in an inviscid piecewise linear boundary layer at time $t = 25$.

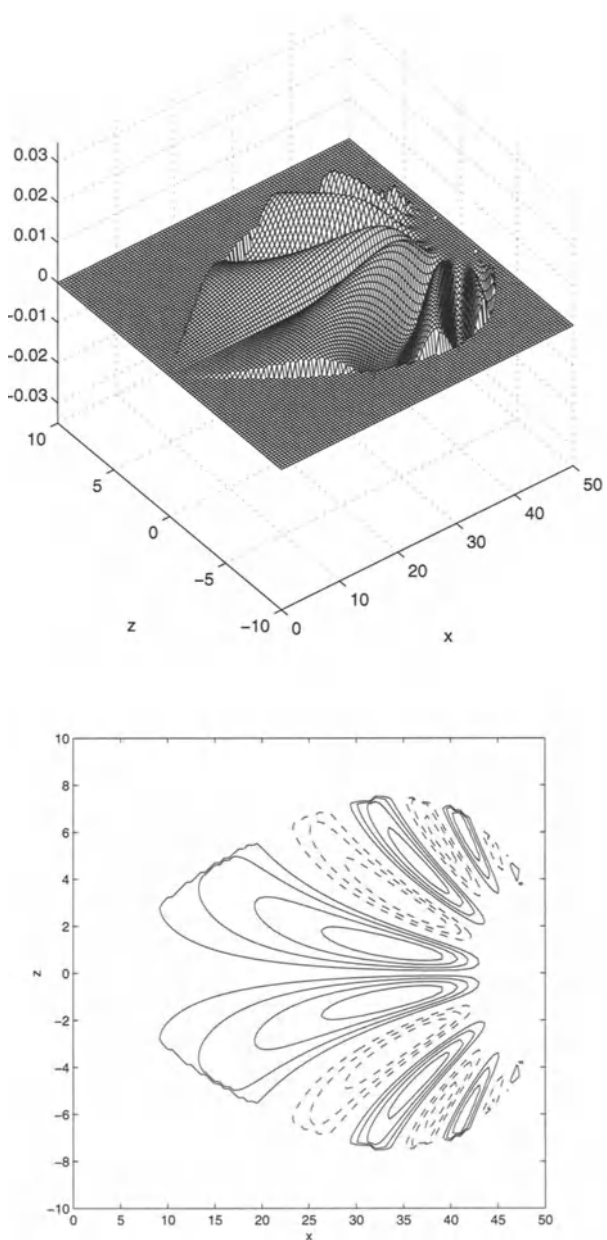


FIGURE 2.14. Evolution of a point-like disturbance in an inviscid piecewise linear boundary layer at time $t = 50$.

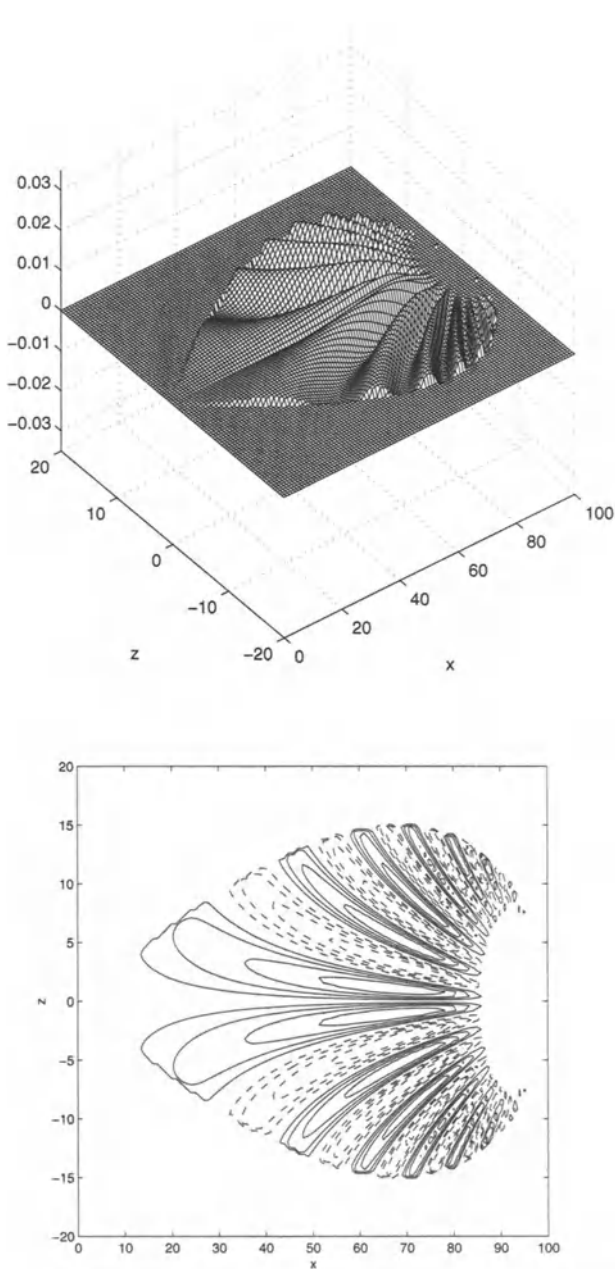


FIGURE 2.15. Evolution of a point-like disturbance in an inviscid piecewise linear boundary layer at time $t = 100$.

$$\left[\left(\frac{\partial}{\partial t} + i\alpha U \right) (\mathcal{D}^2 - k^2) - i\alpha U'' \right] \hat{v} = 0 \quad (2.98)$$

$$\left(\frac{\partial}{\partial t} + i\alpha U \right) \hat{\eta} = -i\beta U' \hat{v}. \quad (2.99)$$

Again, the symbol $\mathcal{D} = '$ denotes a y -derivative, α and β are the components of the wave number vector in the streamwise and spanwise directions, respectively, and $k = \sqrt{\alpha^2 + \beta^2}$ is its modulus. Equivalently, the same equations can be found by taking Fourier transforms in the horizontal directions

$$\hat{v}(\alpha, y, \beta, t) = \iint_{-\infty}^{\infty} v(x, y, z, t) e^{-i(\alpha x + \beta z)} dx dz \quad (2.100)$$

with the corresponding definition for the normal vorticity.

The boundary conditions for the normal velocity are

$$\hat{v} = 0 \quad (2.101)$$

at a solid wall and/or the far field.

Once \hat{v} and $\hat{\eta}$ are known, the horizontal velocities, \hat{u} and \hat{w} , may be obtained from

$$\hat{u} = \frac{i}{k^2} (\alpha \mathcal{D} \hat{v} - \beta \hat{\eta}) \quad (2.102)$$

$$\hat{w} = \frac{i}{k^2} (\beta \mathcal{D} \hat{v} + \alpha \hat{\eta}). \quad (2.103)$$

2.3.2 Laplace Transform Solution

Derivation of the Laplace transform solution

Further insight into the mathematical properties of the solutions of the Rayleigh equation (2.15) can be found by applying the Laplace transformation to the inviscid initial value problem (2.98). Defining

$$\tilde{v}(\alpha, y, \beta, s) = \mathcal{L}(\hat{v}) = \int_0^{\infty} \hat{v}(\alpha, y, \beta, t) e^{-st} dt \quad s = -i\alpha c \quad (2.104)$$

and recalling that $\mathcal{L}(d\hat{v}/dt) = s\tilde{v} - \hat{v}_0$, we find the Laplace-transformed equation (2.98)

$$(\mathcal{D}^2 - k^2)\tilde{v} - \frac{U''\tilde{v}}{U - c} = \frac{\hat{\phi}_0}{i\alpha(U - c)} \quad (2.105)$$

where $\hat{\phi}_0 = (\mathcal{D}^2 - k^2)\hat{v}_0$.

The solution to this inhomogeneous problem can be found by the method of variation of parameters (see, e.g., Boyce & DiPrima, 1997). Introducing a Green's function, we have

$$\tilde{v} = \int_{-1}^1 G(y, y') \hat{\phi}_0 dy'. \quad (2.106)$$

The Green's function is defined as

$$\begin{aligned} G(y, y') &= \frac{\tilde{v}_2(y)\tilde{v}_1(y')}{i\alpha[U(y') - c]W(c)} & y' < y \\ &= \frac{\tilde{v}_1(y)\tilde{v}_2(y')}{i\alpha[U(y') - c]W(c)} & y' > y \end{aligned} \quad (2.107)$$

where \tilde{v}_1 and \tilde{v}_2 are solutions to the homogeneous part of (2.105) satisfying $\tilde{v}_1(-1) = 0$ and $\tilde{v}_2(1) = 0$, and $W(c) = \tilde{v}_1\mathcal{D}\tilde{v}_2 - \tilde{v}_2\mathcal{D}\tilde{v}_1$ is the associated Wronskian.

Inversion of the Laplace and Fourier transforms results in the normal velocity field in physical space, according to

$$\hat{v}(\alpha, y, \beta, t) = \frac{1}{2\pi i} \int_{-\infty+i\gamma}^{\infty+i\gamma} \tilde{v}(\alpha, y, \beta, c) e^{-i\alpha c} dc \quad (2.108)$$

and

$$v(x, y, z, t) = \iint_{-\infty}^{\infty} \hat{v}(\alpha, y, \beta, t) e^{i(\alpha x + \beta z)} d\alpha d\beta. \quad (2.109)$$

The Laplace-transformed solution can be calculated by closing the contour in the lower half of the c -plane and using the method of residues. Each pole in the Green's function will then contribute to the full solution. The first type of poles are zeros of the Wronskian. These correspond to discrete eigenvalues of the Rayleigh equation because \tilde{v}_1 and \tilde{v}_2 will not be linearly independent if c is an eigenvalue of the homogeneous part of (2.105), thus resulting in a zero Wronskian. The second type of poles consist of values of c such that $U(y') = c$, i.e., a continuous spectrum for which the phase velocity is equal to the local mean velocity.

The existence of damped solutions of noninflectional profiles

At first sight, Rayleigh's inflection point criterion seems to exclude purely damped solutions for profiles without inflection points, because the eigenvalues to the Rayleigh equation come in complex conjugate pairs. This would prohibit a dispersive solution in inviscid Poiseuille and boundary layer flows, for example. The fact that such solutions exist has in the past generated some controversy, making it worthwhile to consider that question here.

Using the Frobenius method, it is straightforward to show that the homogeneous solutions \tilde{v}_1 and \tilde{v}_2 in (2.106) are linear combinations of Tollmien's solutions (2.26) and (2.27). The most important feature of these functions is the logarithmic term that appears in one of them. Otherwise the solutions are analytical functions of y . The logarithm has a branch point at $U(y) = c$ and the branch can be specified by interpreting the inviscid solutions as the limit of the viscous solutions for vanishing viscosity (Lin, 1961). Applying the inverse Laplace transform to (2.106), a typical term has the form

$$\hat{v} = \frac{1}{2\pi i} \int_{-1}^1 \int_{-\infty+i\gamma}^{\infty+i\gamma} f(y, y') \frac{(y' - y_c) \ln(y' - y_c) e^{-i\alpha ct}}{[U(y') - c]W(c)} dc dy' \quad (2.110)$$

where $f(y, y')$ represents the remaining part of the Green's function. When the integral in the c -plane is evaluated the contour has to be closed in the lower half-plane in order for the solution to remain bounded for $t > 0$. Thus when the argument of the logarithm is considered as a function of c the branch cut has to be placed in the lower part of the c -plane so that the solution is analytic in the upper half. Now consider the implication of this choice to the location of the branch cut in the y -plane. If $c_i \approx 0$, the behavior around the real y -axis can be found by Taylor expanding the mean flow around y_{cr} . We find

$$U(y_c) = U(y_{cr}) + U'(y_{cr})iy_{ci} + \dots = c_r + ic_i. \quad (2.111)$$

Close to the real axis the logarithmic term can be written as

$$\ln(y - y_c) \approx \ln \left[y_r + iy_i - y_{cr} - \frac{ic_i}{U'(y_{cr})} \right]. \quad (2.112)$$

The analyticity of the solution in the upper half of the c -plane implies that the logarithm has to be defined for positive values of c_i . Thus when (2.110) is integrated over y' we have to choose a path around the singularity such that y_i has the same sign as for the case $c_i > 0$. This implies that the branch cut in the complex y -plane has the following location:

$$\begin{aligned} U'(y_{cr}) &> 0 \Rightarrow y_i < 0 \text{ analytic} \Rightarrow \text{branch cut above singularity,} \\ U'(y_{cr}) &< 0 \Rightarrow y_i > 0 \text{ analytic} \Rightarrow \text{branch cut below singularity.} \end{aligned}$$

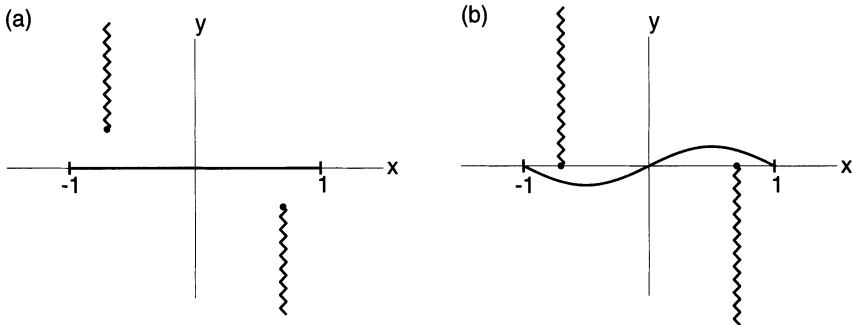


FIGURE 2.16. Singularities and branch cut structure for inviscid Poiseuille flow. The singularities are located at $(y_{cr}, -c_i/2y_{cr})$, where $2y_{cr}^2 = 1 - c_r + [(1 - c_r)^2 + c_i^2]^{1/2}$ and $c_i \leq 0$.

Away from the real y -axis we choose the direction of the branch cut in the same manner to ensure that all solutions use the same branch of the logarithm. The argument presented here essentially follows that of Dikii (1960).

As a first example consider a parabolic mean profile ($U = 1 - y^2$) for which Rayleigh's inflection point criterion prohibits exponential growth. Figure 2.16 shows the location of the singularities and branch cuts for that case. The branch cuts cross the real y -axis, resulting in a deflection into the complex plane of the paths along which the solution is defined. It is possible to find two dispersive solutions for the parabolic mean flow using the indicated integration paths. This does not violate the inflection point criterion because the criterion (see equation (2.30) and resulting argumentation) no longer holds when y is allowed to take on complex values.

The tanh-mixing layer revisited

We now return to the example of the tanh-mixing layer and describe how the damped eigenvalues shown in Figure 2.10(b) were calculated. The mean shear U is positive for all values of y for the tanh-mixing layer. Thus, based on the preceding analysis, the integration path has to be chosen below the singularity. Because $c_r = 0$ for the modes calculated, we have to select an integration contour that passes *under* the logarithmic singularity. As a result of this integration contour, we obtain eigenfunctions corresponding to damped eigenvalues that show discontinuities in their real and imaginary parts across the critical layer at $y = 0$. Figure 2.17 shows two eigenfunctions corresponding to an amplified and a damped eigenvalue.

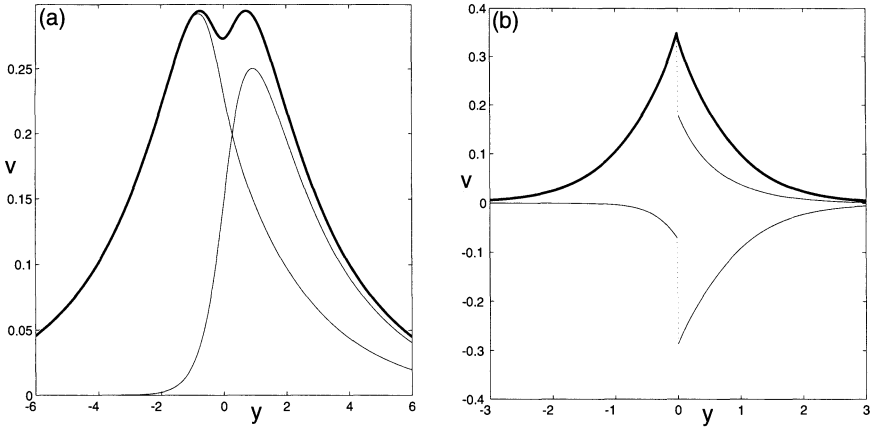


FIGURE 2.17. Eigenfunctions for the hyperbolic tangent mixing layer. (a) Eigenfunction for unstable flow with $\alpha = 0.4$. (b) Eigenfunction for stable flow with $\alpha = 1.5$. Note the discontinuity of the eigenfunction at $y = 0$. The thick line represents the absolute value of the eigenfunction, the thin lines represent the real and imaginary part.

2.3.3 Solutions to the Normal Vorticity Equation

Lift-up effect

When $\beta \neq 0$ the disturbance is three-dimensional, and we must also consider its normal vorticity. Equation (2.99) can be integrated to yield

$$\hat{\eta} = \hat{\eta}_0 e^{-i\alpha Ut} - i\beta U' e^{-i\alpha Ut} \int_0^t \hat{v}(y, t') e^{i\alpha Ut'} dt'. \quad (2.113)$$

The first term represents the advection of the initial normal vorticity field by the mean field, while the second term represents the integrated effect of the normal velocity, the so-called lift-up effect (see Landahl, 1980). This term represents the generation of horizontal velocity perturbations by the lifting-up of fluid elements in the presence of the mean shear. If a single Fourier component is considered, this process can be illustrated as follows. First we make a coordinate transformation such that one axis, x_1 , is aligned with the wave number vector \mathbf{k} : see Figure 2.18(a). The other axis, z_1 , will then be perpendicular to the wave number vector. The mean flow along the new coordinate axis will be denoted U_1 and W_1 , respectively, and is easily found to be

$$U_1 = \frac{\alpha}{k} U \quad (2.114)$$

$$W_1 = -\frac{\beta}{k} U. \quad (2.115)$$

Using equations (2.18) and (2.19) the disturbance velocities along the same axis become

$$\hat{u}_1 = \frac{i}{k} \mathcal{D} \hat{v} \quad (2.116)$$

$$\hat{w}_1 = \frac{i}{k} \hat{\eta}. \quad (2.117)$$

It is interesting that the velocity along the wave number vector is given by the two-dimensional continuity equation in that direction, and the velocity perpendicular to the wave number vector is determined by the normal vorticity component. The lift-up process can be easily visualized by considering the change in the \hat{w}_1 velocity during a short time Δt . Equations (2.113), (2.115), and (2.117) give

$$\Delta w_1 = -W'_1 \hat{v} \Delta t \quad (2.118)$$

where terms of $\mathcal{O}(\Delta t^2)$ have been neglected and it is assumed that the observer is moving with the wave. This expression for Δw_1 is readily identified as the induced horizontal velocity disturbance resulting from the lift-up of a fluid particle by the normal velocity such that the horizontal momentum in the direction perpendicular to the wave number vector is conserved. This is illustrated in Figure 2.18(b). Even if the normal velocity decays, this process can give rise to large amplitude perturbations in the horizontal velocity components.

Algebraic instability

For Fourier components with $\alpha = 0$ the growth may be calculated explicitly. In that case the Rayleigh equation (2.15) implies that \hat{v} is not a function of time, and (2.113) gives

$$\hat{\eta} = \hat{\eta}_0 - i\beta U' \hat{v}_0 t. \quad (2.119)$$

We will refer to this growth as an *algebraic instability* (see also Ellingsen & Palm, 1975).

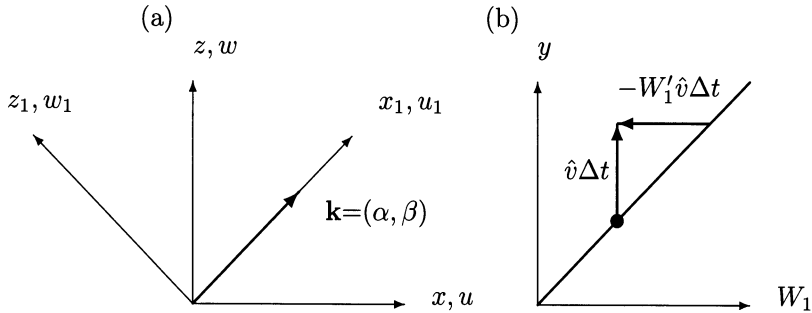


FIGURE 2.18. Illustration of the *lift-up* effect. (a) Definition of the coordinate system aligned with the wave number vector. (b) Creation of a horizontal velocity defect in the z_1 -direction by the lift-up of a fluid element that maintains its horizontal momentum.

2.3.4 Example: Couette Flow

The continuous spectrum and the convective part

When the Rayleigh equation (2.15) is solved for the velocity profile of plane Couette flow ($U = y$) no dispersive solution is obtained. Thus, only the continuous spectrum exists for that case as was first found by Case (1960). The Laplace-transformed equation for Couette flow becomes

$$(\mathcal{D}^2 - k^2)\hat{v} = \frac{\hat{\phi}_0}{i\alpha(U - c)}. \quad (2.120)$$

Taking the inverse Laplace and Fourier transforms we obtain the following simple expression for Couette flow

$$(\mathcal{D}^2 - k^2)\hat{v} = \hat{\phi}_0 e^{-i\alpha yt} \quad (2.121)$$

or

$$\nabla^2 v = \phi_0(x - \alpha y t, y, z, t) \quad (2.122)$$

which shows that the continuous spectrum corresponds to a solution that is advected by the local mean velocity (see Gustavsson, 1978). The continuous spectrum does not propagate with a phase coherence in the y -direction, nor does it spread out in the spanwise direction as dispersive waves: instead it spreads only in the streamwise direction with velocities dependent on the y -position. For a velocity profile with curvature, the solution for \hat{v} will contain both the dispersive and the convective parts.

The Case solution for Couette flow

To further illustrate the nondispersive aspects of the inviscid solution we will consider the solution for inviscid Couette flow in more detail. The solution to (2.121) for $U = y$ is readily obtained and can conveniently be written (see Case, 1960) as

$$\hat{v}(y) = \int_{-1}^1 G(y, y') \hat{\phi}_0(y') e^{-i\alpha t y'} dy' \quad (2.123)$$

where

$$G(y, y') = \begin{cases} \frac{-\sinh k(1-y)\sinh k(1+y)'}{k \sinh k} & y' < y \\ \frac{-\sinh k(1+y)\sinh k(1-y')}{k \sinh k} & y' > y. \end{cases} \quad (2.124)$$

$G(y, y')$ is the inverse Laplace-transformed Green's function. The effect of the continuous spectrum is represented by the factor $e^{-i\alpha t y'}$ in the integral.

With \hat{v} determined, the solution for $\hat{\eta}$ becomes

$$\hat{\eta} = \hat{\eta}_0 e^{-i\alpha t y} + i\beta \int_{-1}^1 G(y, y') \hat{\phi}_0 \frac{e^{-i\alpha t y} - e^{-i\alpha t y'}}{i\alpha(y - y')} dy' \quad (2.125)$$

where $\hat{\eta}_0$ is the initial value of $\hat{\eta}$.

Of particular interest is the small and large time behavior of these solutions. To leading order in αt , (2.123) is found to recover \hat{v}_0 whereas for large αt partial integration shows that the leading order term in \hat{v} is $\mathcal{O}(1/(\alpha t)^2)$. Hence, v is expected to decay in time.

For $\hat{\eta}$, however, the temporal behavior is different. For small times, a Taylor expansion shows that

$$\frac{e^{-i\alpha t y'} - e^{-i\alpha t y}}{i\alpha(y - y')} \sim t \left(1 + \frac{i\alpha t}{2}(y + y') + \dots \right) \quad (2.126)$$

which reduces (2.125) to

$$\hat{\eta} \sim \hat{\eta}_0 e^{-i\alpha t y} - i\beta \hat{v}_0 t - \frac{i\alpha \beta t^2}{2} \left[y \hat{v}_0(y) + \int_{-1}^1 \frac{\partial G}{\partial y'} \hat{v}_0 dy' \right]. \quad (2.127)$$

This demonstrates that $\hat{\eta}$, aside from the convected initial value, contains an induced term growing linearly for short times, which is due to the spanwise

variation of \hat{v}_0 . This is the previously mentioned lift-up effect for three-dimensional disturbances.

The algebraic growth is moderated for large times, as can be recognized by evaluating the integral in (2.125) as $at \rightarrow \infty$. The main contribution to the integral in (2.125) comes from the region around $y' = y$ and an expansion around this point gives the following result to leading order

$$\hat{\eta} \sim \hat{\eta}_0 e^{-i\alpha y t} - i\pi \frac{\beta \sinh k(1+y) \sinh k(1-y)}{k \sinh k} \hat{\phi}_0 e^{-i\alpha t y} \quad (2.128)$$

which shows that the forcing by the normal velocity leads to a *permanent scar* convecting downstream with the local mean velocity. This result is originally due to Landahl (1975), derived for a more general case. It was also derived for the piecewise linear boundary layer profile by Gustavsson (1978).

The expression (2.128) is infinite for $\alpha = 0$, which is in agreement with the explicit expression for the normal vorticity obtained earlier. Equation (2.119) shows that $\hat{\eta} \rightarrow \infty$ as $t \rightarrow \infty$. Consequently, disturbances that have wave number components with $\alpha = 0$ will have a different asymptotic behavior than those with only $\alpha \neq 0$ components.

2.3.5 Localized Disturbances

Evolution of the energy

Landahl (1980) discussed the implications of the algebraic instability for inviscid localized disturbances. He found that the growth of the energy and velocities are moderated by the spreading of the disturbance in the horizontal directions.

To see the effect of localization we first introduce an average of the normal velocity in the streamwise direction

$$\bar{v} = \int_{-\infty}^{\infty} v \, dx. \quad (2.129)$$

If we take the streamwise average of the inviscid linear stability equations (2.1), (2.2), and (2.5) and assume a localized disturbance, we obtain

$$\frac{\partial \bar{u}}{\partial t} = \bar{v} U' \quad (2.130)$$

$$\frac{\partial \bar{v}}{\partial t} = -\frac{\partial \bar{p}}{\partial y} \quad (2.131)$$

$$\nabla^2 \bar{p} = 0. \quad (2.132)$$

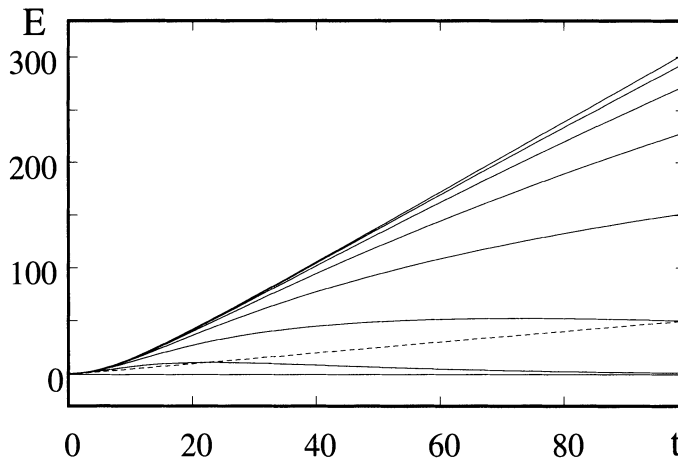


FIGURE 2.19. Disturbance energy history for Reynolds numbers 250 (bottom curve), 1000, 4000, 16000, 64000, 256000, and 1024000 (top). The dashed line shows the inviscid energy estimate (2.139) integrated in time. From Lundbladh (1993b).

We conclude from the equation for the pressure that $\bar{p} = 0$ because any solution of the Laplace equation vanishing at infinity necessarily has to be zero. Using this fact we can integrate the equation for \bar{v} and then the equation for \bar{u} :

$$\bar{v} = \bar{v}_0 \quad (2.133)$$

$$\bar{u} = \bar{u}_0 + \bar{v}_0 U' t. \quad (2.134)$$

We have an algebraic instability in the streamwise integral of the velocity component u . This does not mean, however, that the streamwise velocity itself grows, because we also may have a lengthening of the disturbance. Landahl (1993) estimated that the streamwise length l of the disturbance increases proportionally to the difference between the maximum and minimum values of the mean velocity. We have

$$l = (U_{\max} - U_{\min})t \equiv [U]t \quad (2.135)$$

which may be directly related to the shearing effect of the inviscid continuous spectrum discussed in the Couette flow example. Recall that we found that the inviscid continuous spectrum results in a disturbance that is convected by the local mean velocity of the base flow.

Using the integral inequality

$$\left| \int_{-\infty}^{\infty} f(x)g(x)dx \right|^2 \leq \int_{-\infty}^{\infty} |f(x)|^2 dx \int_{-\infty}^{\infty} |g(x)|^2 dx, \quad (2.136)$$

letting $f = u$ and

$$g = \begin{cases} 1 & \text{for } U_{\min}t - \Delta < x < U_{\max}t + \Delta \\ 0 & \text{otherwise} \end{cases} \quad (2.137)$$

where the initial disturbance is assumed to be exponentially small for $|x| > \Delta$ we find

$$[(U_{\max} - U_{\min})t + 2\Delta] \int_{-\infty}^{\infty} u^2 dx \geq \bar{u}^2 \quad (2.138)$$

where we used the solution obtained for \bar{u} . Assuming that t is large enough for the t^2 -term to dominate and disregarding the 2Δ term, we find

$$E \geq \frac{1}{2[U]} \bar{v}_0^2 U'^2 t. \quad (2.139)$$

The total energy of the disturbance now increases at least linearly in time, not necessarily as t^2 , as in the case of the algebraic instability for single waves.

Lundbladh (1993b) gave a numerical example of the predicted behavior for a localized disturbance in inviscid plane Couette flow. The initial disturbance chosen was

$$\begin{aligned} \psi &= 0.3232(1 - y^2)^2 z e^{-(x/2)^2 - (z/2)^2} \\ (u_0, v_0, w_0) &= (0, \psi_z, -\psi_y) \end{aligned} \quad (2.140)$$

with a total initial perturbation energy E equal to unity and a nonzero net normal momentum \bar{v} . He solved the linearized Navier-Stokes equations for increasingly higher Reynolds numbers, so that the inviscid nature of the disturbance evolution could be predicted. Figure 2.19 shows the perturbation energy as a function of time for various Reynolds numbers. There is a clear convergence to an inviscid limit where the energy grows linearly in time for large times. The result of the inequality derived by Landahl is also shown.

Evolution of the maximum streamwise velocity

The evolution of the maximum streamwise velocity was also considered by Lundbladh (1993b). Figure 2.20 shows the maximum modulus of the

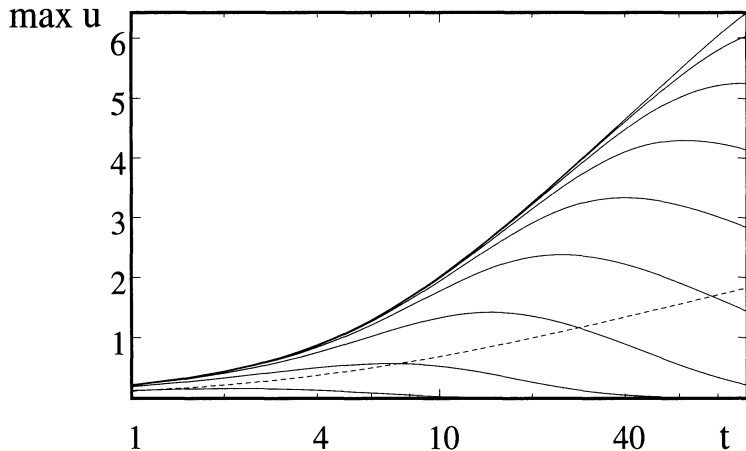


FIGURE 2.20. Maximum modulus of streamwise velocity for Reynolds numbers 16 (bottom curve), 62, 250, 1000, 4000, 16000, 64000, 256000, and 1024000 (top). The dashed line shows the amplitude estimate neglecting pressure. From Lundbladh (1993*b*).

streamwise perturbation amplitude as a function of time. This shows that the streamwise velocity amplitude growth is logarithmic in time after about $t = 20$ in the inviscid limit. For the highest Reynolds number the growth is logarithmic for $t \in [20, 80]$. This growth was not predicted by theory before the numerical simulations by Lundbladh (1993*b*), but an argument can be made for the logarithmic growth in time.

3

Eigensolutions to the Viscous Problem

3.1 Viscous Linear Stability Equations

3.1.1 The Velocity-Vorticity Formulation

We will consider the governing equations for infinitesimal disturbances in parallel flows. Let $U_i = U(y)\delta_{1i}$ be the parallel base flow, i.e., a flow in the x -direction that only depends on the wall-normal direction y (see Figure 2.1 defining the coordinate system and base flow). If this mean velocity profile is introduced into the disturbance equations (1.6) and the nonlinear terms are neglected, the resulting equations can be written:

$$\frac{\partial u}{\partial t} + U \frac{\partial u}{\partial x} + v U' = -\frac{\partial p}{\partial x} + \frac{1}{Re} \nabla^2 u \quad (3.1)$$

$$\frac{\partial v}{\partial t} + U \frac{\partial v}{\partial x} = -\frac{\partial p}{\partial y} + \frac{1}{Re} \nabla^2 v \quad (3.2)$$

$$\frac{\partial w}{\partial t} + U \frac{\partial w}{\partial x} = -\frac{\partial p}{\partial z} + \frac{1}{Re} \nabla^2 w. \quad (3.3)$$

This set of equations is completed by the continuity equation

$$\frac{\partial u}{\partial x} + \frac{\partial v}{\partial y} + \frac{\partial w}{\partial z} = 0. \quad (3.4)$$

A prime ('') denotes a y -derivative. Taking the divergence of the linearized momentum equations (3.1)-(3.3) and using the continuity equation (3.4) yields an equation for the perturbation pressure:

$$\nabla^2 p = -2U' \frac{\partial v}{\partial x}. \quad (3.5)$$

This equation may be used with equation (3.2) to eliminate p , resulting in an equation for the normal velocity, v :

$$\left[\left(\frac{\partial}{\partial t} + U \frac{\partial}{\partial x} \right) \nabla^2 - U'' \frac{\partial}{\partial x} - \frac{1}{Re} \nabla^4 \right] v = 0. \quad (3.6)$$

To describe the complete three-dimensional flow field, a second equation is needed. This is most conveniently the equation for the normal vorticity,

$$\eta = \frac{\partial u}{\partial z} - \frac{\partial w}{\partial x} \quad (3.7)$$

where η satisfies

$$\left[\frac{\partial}{\partial t} + U \frac{\partial}{\partial x} - \frac{1}{Re} \nabla^2 \right] \eta = -U' \frac{\partial v}{\partial z}. \quad (3.8)$$

This pair of equations with the boundary conditions

$$v = v' = \eta = 0 \quad \text{at a solid wall and in the far field} \quad (3.9)$$

and the initial conditions

$$v(x, y, z, t = 0) = v_0(x, y, z) \quad (3.10)$$

$$\eta(x, y, z, t = 0) = \eta_0(x, y, z) \quad (3.11)$$

provides a complete description of the evolution of an arbitrary disturbance in both space and time.

3.1.2 The Orr-Sommerfeld and Squire Equations

Following the derivation of the Rayleigh equation we introduce wavelike solutions of the form

$$v(x, y, z, t) = \tilde{v}(y) e^{i(\alpha x + \beta z - \omega t)} \quad (3.12)$$

$$\eta(x, y, z, t) = \tilde{\eta}(y) e^{i(\alpha x + \beta z - \omega t)} \quad (3.13)$$

where α and β denote the streamwise and spanwise wave numbers, respectively, and ω stands for the frequency.

Introducing this representation into (3.6) and (3.8), or equivalently taking the Fourier transform in the horizontal directions, results in the following pair of equations for \tilde{v} and $\tilde{\eta}$

$$\left[(-i\omega + i\alpha U)(\mathcal{D}^2 - k^2) - i\alpha U'' - \frac{1}{\text{Re}}(\mathcal{D}^2 - k^2)^2\right] \tilde{v} = 0 \quad (3.14)$$

$$\left[(-i\omega + i\alpha U) - \frac{1}{\text{Re}}(\mathcal{D}^2 - k^2)\right] \tilde{\eta} = -i\beta U' \tilde{v} \quad (3.15)$$

with the boundary conditions $\tilde{v} = \mathcal{D}\tilde{v} = \tilde{\eta} = 0$ at solid walls and in the free stream.

The equation for the normal velocity (3.14) is the classical Orr-Sommerfeld equation (Orr, 1907; Sommerfeld, 1908) and the equation for the normal vorticity (3.15) is known as the Squire equation (Squire, 1933). Although there is no general restriction to real or complex wave numbers or frequencies, in this chapter we will consider the temporal problem, where the spatial wave numbers α and β are assumed real. The frequency ω , or alternatively $c = \omega/\alpha$, appears as the eigenvalue in the Orr-Sommerfeld equation, and together with the associated eigenfunctions \tilde{v} is generally complex. The same holds true for the Squire equation. The Orr-Sommerfeld equation (3.14) can be thought of as the viscous extension of the Rayleigh equation (2.15). It is important to notice that the Orr-Sommerfeld equation is homogeneous. On the other hand, the Squire equation for the normal vorticity is forced by solutions of the Orr-Sommerfeld equation.

The solutions to the Orr-Sommerfeld and Squire equations can be divided into two classes of eigenmodes. The first class is the set of Orr-Sommerfeld (OS) modes denoted as

$$\{\tilde{v}_n, \tilde{\eta}_n^p, \omega_n\}_{n=1}^N \quad (3.16)$$

where \tilde{v}_n and ω_n are found by solving the Orr-Sommerfeld equation (3.14) and $\tilde{\eta}_n^p$ is found by solving the inhomogeneous Squire equation (3.15) with \tilde{v}_n on the right-hand side. We use the symbol $\tilde{\eta}^p$ for the normal vorticity component of the Orr-Sommerfeld mode to emphasize that it is equivalent to a particular solution of the driven Squire equation. For flows in a bounded domain all eigenvalues are discrete and infinite in number, whereas for unbounded domains there is usually only a finite number of discrete modes, complemented by a continuous spectrum (see Section 3.2.3).

The second class of eigenmodes is the set of Squire (SQ) modes denoted as

$$\{\tilde{v} = 0, \tilde{\eta}_m, \omega_m\}_{m=1}^M. \quad (3.17)$$

In this case the solution to the Orr-Sommerfeld equation (3.14) is identically zero, implying that the Squire equation (3.15) is homogeneous and thus constitutes an eigenvalue problem for $\tilde{\eta}_m$ and ω_m . The set of Orr-Sommerfeld eigenvalues $\{\omega_n\}_{n=1}^N$ are in general different from the set of Squire eigenvalues $\{\omega_m\}_{m=1}^M$.

3.1.3 Squire's Transformation and Squire's Theorem

Relation between the two-dimensional and three-dimensional solutions

Instead of considering the complex frequency ω as the eigenvalue one often uses the complex phase speed c , where

$$\omega = \alpha c \quad (3.18)$$

which results in the following slightly different version of the Orr-Sommerfeld equation (3.14)

$$(U - c)(\mathcal{D}^2 - k^2)\tilde{v} - U''\tilde{v} - \frac{1}{i\alpha \text{Re}}(\mathcal{D}^2 - k^2)^2\tilde{v} = 0. \quad (3.19)$$

Squire's transformation is found by comparing this equation to the two-dimensional Orr-Sommerfeld equation, i.e., the Orr-Sommerfeld equation with $\beta = 0$, given as

$$(U - c)(\mathcal{D}^2 - \alpha_{2D}^2)\tilde{v} - U''\tilde{v} - \frac{1}{i\alpha_{2D} \text{Re}_{2D}}(\mathcal{D}^2 - \alpha_{2D}^2)^2\tilde{v} = 0. \quad (3.20)$$

Comparing these two equations, it is evident that they have identical solutions if the following relations hold

$$\alpha_{2D} = k = \sqrt{\alpha^2 + \beta^2} \quad (3.21)$$

$$\alpha_{2D} \text{Re}_{2D} = \alpha \text{Re} \quad (3.22)$$

from which it follows that

$$\text{Re}_{2D} = \text{Re} \frac{\alpha}{k} < \text{Re}. \quad (3.23)$$

This states that to each three-dimensional Orr-Sommerfeld mode corresponds a two-dimensional Orr-Sommerfeld mode at a *lower* Reynolds number.

Damped Squire modes

Before we state Squire's theorem, we will prove the following.

11 THEOREM (DAMPED SQUIRE MODES) The solutions to the Squire equation are always damped, i.e., $c_i < 0$ for all α, β , and Re .

The theorem is proved by first multiplying the homogeneous Squire equation (3.15) by $\tilde{\eta}^*$, the complex conjugate of the normal vorticity, and integrating in the y -direction across the fluid domain, which for simplicity we take from -1 to 1 . We find

$$c \int_{-1}^1 \tilde{\eta}^* \tilde{\eta} dy = \int_{-1}^1 U \tilde{\eta}^* \tilde{\eta} dy - \frac{i}{\alpha \text{Re}} \int_{-1}^1 \tilde{\eta}^* (-\mathcal{D}^2 + k^2) \tilde{\eta} dy. \quad (3.24)$$

Taking the imaginary part of equation (3.24) and integrating by parts, we obtain

$$\begin{aligned} c_i \int_{-1}^1 |\tilde{\eta}|^2 dy &= -\frac{1}{\alpha \text{Re}} \int_{-1}^1 (-\tilde{\eta}^* \mathcal{D}^2 \tilde{\eta} + k^2 |\tilde{\eta}|^2) dy \\ &= -\frac{1}{\alpha \text{Re}} \int_{-1}^1 |\mathcal{D}\tilde{\eta}|^2 + k^2 |\tilde{\eta}|^2 dy < 0 \end{aligned} \quad (3.25)$$

which concludes the proof.

Squire's theorem

12 THEOREM (SQUIRE'S THEOREM) Given Re_L as the critical Reynolds number for the onset of linear instability for a given α, β , the Reynolds number Re_c below which no exponential instabilities exist for any wave numbers satisfies

$$\text{Re}_c \equiv \min_{\alpha, \beta} \text{Re}_L(\alpha, \beta) = \min_{\alpha} \text{Re}_L(\alpha, 0). \quad (3.26)$$

Thus parallel shear flows first become unstable to two-dimensional wavelike perturbations at a value of the Reynolds number that is smaller than any value for which unstable three-dimensional perturbations exist.

The proof of this theorem follows directly from Squire's transformation: If a three-dimensional mode is unstable, a two-dimensional mode is unstable at a lower Reynolds number.

3.1.4 Vector Modes

In the previous section we looked at the individual linear stability equations for parallel shear flows. In this section we will consider them as one

system, which will result in more compact notation and easier algebraic manipulations when general results are derived.

We will start by introducing the vector quantity

$$\begin{pmatrix} \tilde{v} \\ \tilde{\eta} \end{pmatrix} \quad (3.27)$$

which allows us to write the Orr-Sommerfeld and Squire equations (3.14) and (3.15) in matrix form as

$$-i\omega \begin{pmatrix} k^2 - \mathcal{D}^2 & 0 \\ 0 & 1 \end{pmatrix} \begin{pmatrix} \tilde{v} \\ \tilde{\eta} \end{pmatrix} + \begin{pmatrix} \mathcal{L}_{OS} & 0 \\ i\beta U' & \mathcal{L}_{SQ} \end{pmatrix} \begin{pmatrix} \tilde{v} \\ \tilde{\eta} \end{pmatrix} = 0 \quad (3.28)$$

where

$$\mathcal{L}_{OS} = i\alpha U(k^2 - \mathcal{D}^2) + i\alpha U'' + \frac{1}{Re}(k^2 - \mathcal{D}^2)^2 \quad (3.29)$$

$$\mathcal{L}_{SQ} = i\alpha U + \frac{1}{Re}(k^2 - \mathcal{D}^2). \quad (3.30)$$

The solution to this system, including boundary conditions, gives the eigenmodes discussed earlier. The off-diagonal coupling term, $i\beta U'$, in the matrix implies that the Squire equation is driven by solutions to the Orr-Sommerfeld equation, unless \tilde{v} or β is zero.

The eigenfunctions of the complete system can be divided into the two families of Orr-Sommerfeld and Squire modes previously defined. In the vector formulation they take the form

$$\begin{pmatrix} \tilde{v} \\ \tilde{\eta}^p \end{pmatrix} \quad \text{OS modes} \quad \begin{pmatrix} 0 \\ \tilde{\eta} \end{pmatrix} \quad \text{SQ modes.} \quad (3.31)$$

We like to emphasize that they are formally all eigenfunctions of the same system. It is only due to the zero off-diagonal term that they can be separated into two distinct families.

We now introduce a more compact notation. This is most easily accomplished by defining the vector

$$\tilde{\mathbf{q}} = \begin{pmatrix} \tilde{v} \\ \tilde{\eta} \end{pmatrix}. \quad (3.32)$$

The eigenvalue problem (3.28) now becomes

$$\mathbf{L}\tilde{\mathbf{q}} = i\omega \mathbf{M}\tilde{\mathbf{q}} \quad \text{or} \quad \mathbf{L}_1\tilde{\mathbf{q}} \equiv \mathbf{M}^{-1}\mathbf{L}\tilde{\mathbf{q}} = i\omega\tilde{\mathbf{q}} \quad (3.33)$$

where

$$\mathbf{M} = \begin{pmatrix} k^2 - \mathcal{D}^2 & 0 \\ 0 & 1 \end{pmatrix} \quad (3.34)$$

$$\mathbf{L} = \begin{pmatrix} \mathcal{L}_{OS} & 0 \\ i\beta U' & \mathcal{L}_{SQ} \end{pmatrix} \quad (3.35)$$

with \mathbf{M} as a positive definite operator.

3.1.5 Pipe Flow

Linear eigenvalue problem and vector formulation

Pipe flow is a parallel flow of considerable interest. Because the geometry is not Cartesian we will have to slightly modify the derivation of the linear stability equations.

Our starting point for the analysis of infinitesimal disturbances in circular pipe flow is the linearized Navier-Stokes equation for incompressible flow in circular coordinates, where an axial base flow of the form $U = U(r)$ has been assumed:

$$\frac{\partial u}{\partial t} + U \frac{\partial u}{\partial z} = -v U' - \frac{\partial p}{\partial z} + \frac{1}{\text{Re}} \left[\frac{1}{r} \frac{\partial}{\partial r} \left(r \frac{\partial u}{\partial r} \right) + \frac{1}{r^2} \frac{\partial^2 u}{\partial \theta^2} + \frac{\partial^2 u}{\partial z^2} \right] \quad (3.36)$$

$$\frac{\partial v}{\partial t} + U \frac{\partial v}{\partial z} = -\frac{\partial p}{\partial r} + \frac{1}{\text{Re}} \left[\frac{1}{r} \frac{\partial}{\partial r} \left(r \frac{\partial v}{\partial r} \right) + \frac{1}{r^2} \frac{\partial^2 v}{\partial \theta^2} + \frac{\partial^2 v}{\partial z^2} - \frac{v}{r^2} - \frac{2}{r^2} \frac{\partial w}{\partial \theta} \right] \quad (3.37)$$

$$\frac{\partial w}{\partial t} + U \frac{\partial w}{\partial z} = -\frac{1}{r} \frac{\partial p}{\partial \theta} + \frac{1}{\text{Re}} \left[\frac{1}{r} \frac{\partial}{\partial r} \left(r \frac{\partial w}{\partial r} \right) + \frac{1}{r^2} \frac{\partial^2 w}{\partial \theta^2} + \frac{\partial^2 w}{\partial z^2} + \frac{2}{r^2} \frac{\partial v}{\partial \theta} - \frac{w}{r^2} \right] \quad (3.38)$$

$$0 = \frac{\partial u}{\partial z} + \frac{1}{r} \frac{\partial (rv)}{\partial r} + \frac{1}{r} \frac{\partial w}{\partial \theta}. \quad (3.39)$$

Here u, v , and w are the perturbation velocities in the axial (z), radial (r), and azimuthal (θ) directions, respectively; p denotes the perturbation pressure; and ' stands for a differentiation with respect to r . The preceding equations have been nondimensionalized by the pipe radius a and the centerline velocity U_{CL} and the Reynolds number Re is defined as $U_{CL}a/\nu$, with ν as the kinematic viscosity. Because the flow is periodic in the azimuthal direction and will be assumed periodic in the streamwise direction, the dependence of all flow quantities on these coordinates will be taken to be of the form

$$\begin{pmatrix} u \\ v \\ w \\ p \end{pmatrix} = \begin{pmatrix} \tilde{u} \\ \tilde{v} \\ \tilde{w} \\ \tilde{p} \end{pmatrix} \exp(i\alpha z + in\theta - i\omega t) \quad (3.40)$$

with α as the streamwise wave number and n as the discrete azimuthal wave number. The presence of two homogeneous directions allows us to further reduce the equations to the more convenient radial velocity (\tilde{v}) - radial vorticity ($\tilde{\eta}$) form as suggested by Burridge & Drazin (1969)

$$(-i\omega + i\alpha U)\mathcal{T}\tilde{\Phi} - \frac{i\alpha}{r}(\frac{U'}{k^2 r})'\tilde{\Phi} = \frac{1}{Re}\mathcal{T}(k^2 r^2 \mathcal{T})\tilde{\Phi} + \frac{2}{Re}\alpha n^2 \mathcal{T}\tilde{\Omega} \quad (3.41)$$

$$k^2 r^2 (-i\omega + i\alpha U)\tilde{\Omega} + \frac{iU'}{r}\tilde{\Phi} = \frac{1}{Re}\mathcal{S}\tilde{\Omega} + \frac{2\alpha}{Re}\mathcal{T}\tilde{\Phi} \quad (3.42)$$

where

$$k^2 = \alpha^2 + \frac{n^2}{r^2} \quad (3.43)$$

$$\mathcal{T} = \frac{1}{r^2} - \frac{1}{r} \frac{d}{dr} \left(\frac{1}{k^2 r} \frac{d}{dr} \right) \quad (3.44)$$

$$\mathcal{S} = k^4 r^2 - \frac{1}{r} \frac{d}{dr} \left(k^2 r^3 \frac{d}{dr} \right) \quad (3.45)$$

$$\tilde{\Phi} \equiv -ir\tilde{v} \quad (3.46)$$

$$\tilde{\Omega} \equiv \frac{\alpha r\tilde{w} - n\tilde{u}}{nk^2 r^2} = \frac{\tilde{\eta}}{ink^2 r}. \quad (3.47)$$

The variables $\tilde{\Phi}$ and $\tilde{\Omega}$ describe the problem completely; the streamwise velocity \tilde{u} and the azimuthal velocity \tilde{w} can be recovered by

$$\tilde{u} = -\frac{\alpha}{k^2 r} \frac{d\tilde{\Phi}}{dr} - n^2 \tilde{\Omega} \quad (3.48)$$

$$\tilde{w} = -\frac{n}{k^2 r^2} \frac{d\tilde{\Phi}}{dr} + \alpha n r \tilde{\Omega} \quad (3.49)$$

where the continuity equation (3.39) and the definition of the radial vorticity have been used.

We now reformulate the pipe flow equations in matrix form by introducing the vector quantity $\tilde{\mathbf{q}} = (\tilde{\Phi} \ \tilde{\Omega})^T$, which results in the linear eigenvalue problem

$$\mathbf{L}\tilde{\mathbf{q}} = i\omega \mathbf{M}\tilde{\mathbf{q}} \quad (3.50)$$

where

$$\mathbf{M} = \begin{pmatrix} \mathcal{T} & 0 \\ 0 & k^2 r^2 \end{pmatrix} \quad (3.51)$$

$$\mathbf{L} = \begin{pmatrix} \mathcal{L}_{OS}^{pipe} & \frac{1}{\text{Re}} 2\alpha n^2 \mathcal{T} \\ \frac{-iU'}{r} - \frac{1}{\text{Re}} 2\alpha \mathcal{T} & \mathcal{L}_{SQ}^{pipe} \end{pmatrix} \quad (3.52)$$

and

$$\mathcal{L}_{OS}^{pipe} = -i\alpha U \mathcal{T} + \frac{i\alpha}{r} \left(\frac{U'}{k^2 r} \right)' + \frac{1}{\text{Re}} \mathcal{T} (k^2 r^2 \mathcal{T}) \quad (3.53)$$

$$\mathcal{L}_{SQ}^{pipe} = -k^2 r^2 i\alpha U + \frac{1}{\text{Re}} \mathcal{S}. \quad (3.54)$$

In addition to the inviscid coupling term, $-iU'/r$, which in its analogous form is also present in plane flows, viscous coupling terms appear that stem from the nonzero off-diagonal terms in the vector Laplacian for cylindrical coordinate systems. These terms are zero for disturbances that do not depend on the streamwise direction ($\alpha = 0$). For disturbances that are independent of the azimuthal direction ($n = 0$), the coupling term in the $\tilde{\Phi}$ equation disappears and the equations have a form similar to that of the Orr-Sommerfeld and Squire equations (3.28).

Boundary conditions

Boundary conditions have to be imposed on $\tilde{\Phi}$ and $\tilde{\Omega}$ in order to uniquely determine the solution to the physical problem. The boundary conditions for the solid wall at $r = 1$ are given by the no-slip assumption and can be written in the form

$$\tilde{\Phi} = \tilde{\Phi}' = \tilde{\Omega} = 0 \quad \text{at } r = 1. \quad (3.55)$$

The boundary conditions for the pipe centerline ($r = 0$) can be derived using the fact that the velocity vector has a vanishing azimuthal dependence as the centerline is approached (Khorrami *et al.*, 1989), i.e.,

$$\lim_{r \rightarrow 0} \frac{\partial}{\partial \theta} (u \mathbf{e}_z + v \mathbf{e}_r + w \mathbf{e}_\theta) = 0, \quad (3.56)$$

where \mathbf{e}_z , \mathbf{e}_r , and \mathbf{e}_θ denote the unit vectors in the axial, radial and azimuthal directions, respectively. For cylindrical coordinates

$$\frac{\partial \mathbf{e}_z}{\partial \theta} = 0 \quad \frac{\partial \mathbf{e}_r}{\partial \theta} = \mathbf{e}_\theta \quad \frac{\partial \mathbf{e}_\theta}{\partial \theta} = -\mathbf{e}_r \quad (3.57)$$

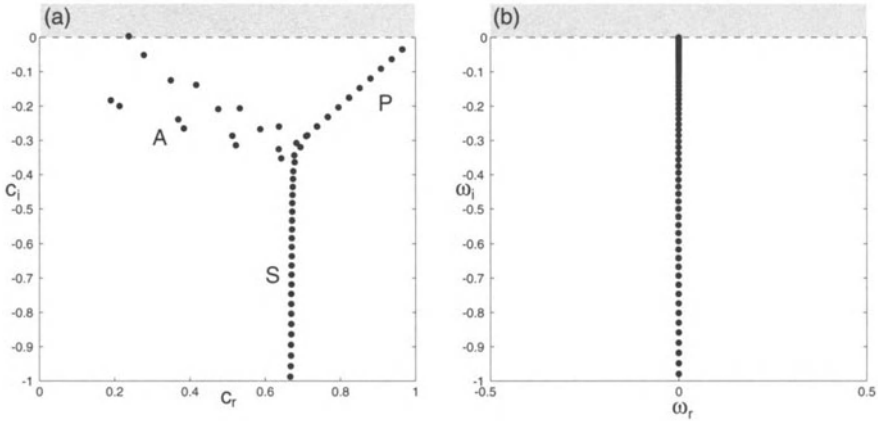


FIGURE 3.1. Orr-Sommerfeld spectrum of plane Poiseuille flow for $\text{Re} = 10000$: (a) wave numbers $\alpha = 1, \beta = 0$; (b) wave numbers $\alpha = 0, \beta = 1$.

and the restriction that each individual component has to vanish yields the required boundary conditions for $\tilde{\Phi}$ and $\tilde{\Omega}$ at $r = 0$

$$\text{for } n = 0 \quad \tilde{\Phi} = \tilde{\Phi}' = 0 \quad (3.58)$$

$$\text{for } n = \pm 1 \quad \tilde{\Phi} = \tilde{\Omega} = 0 \quad \text{and} \quad \tilde{\Phi}' \text{ finite} \quad (3.59)$$

$$\text{for } n \geq 2 \quad \tilde{\Phi} = \tilde{\Phi}' = \tilde{\Omega} = 0. \quad (3.60)$$

3.2 Spectra and Eigenfunctions

3.2.1 Discrete Spectrum

Plane Poiseuille flow

The eigenvalues of the Orr-Sommerfeld equation (3.14) for plane Poiseuille flow are shown in Figure 3.1. The Orr-Sommerfeld equation is solved using a spectral collocation technique described in Appendix A. Figure 3.1(a) shows a portion of the set of discrete eigenvalues c_n for nonzero α . The eigenvalues are located on three main branches which have been labeled A ($c_r \rightarrow 0$), P ($c_r \rightarrow 1$), and S ($c_r \approx 2/3$) by Mack (1976). The number of eigenvalues along the respective branches depends on the parameters. In this example there is one slightly unstable eigenmode on the A branch, which may be surprising because the parabolic base flow does not contain an inflection point. According to Rayleigh's inflection point criterion the Poiseuille profile is stable as $\text{Re} \rightarrow \infty$, so one must conclude that viscosity is in this case destabilizing. This unstable eigenmode is called a Tollmien-Schlichting wave (Tollmien, 1935; Schlichting, 1933) in honor of the researchers who first showed that the Orr-Sommerfeld equation has unstable

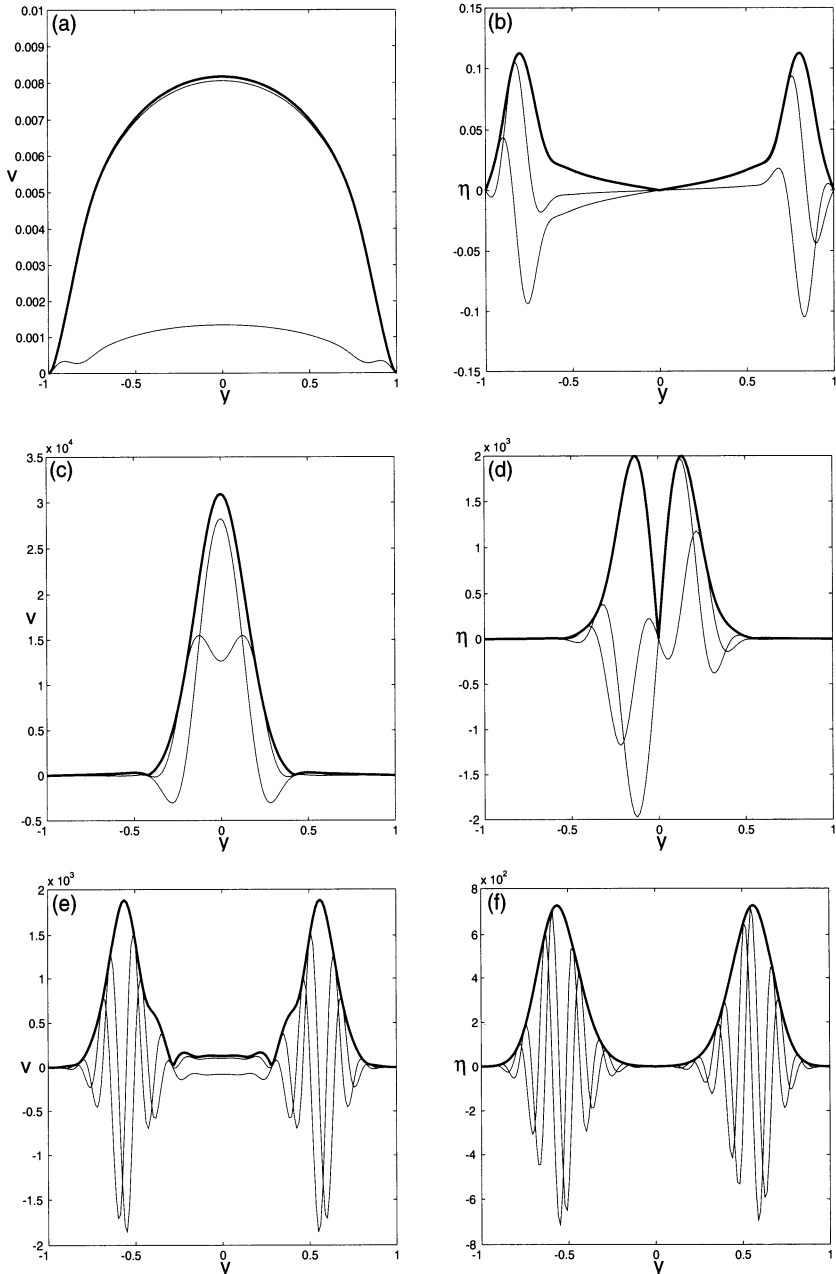


FIGURE 3.2. Orr-Sommerfeld eigenfunctions for plane Poiseuille flow with $Re = 5000, \alpha = 1, \beta = 1$. (a,b) A-branch (left: normal velocity, right: normal vorticity); (c,d) P-branch; (e,f) S-branch. The thick line represents the magnitude of normal velocity or vorticity; the thin lines are the real and imaginary parts.

disturbances for flows without inflection points. Typical shapes of eigenfunctions are shown in Figure 3.2. Both the normal velocity component and the normal vorticity component are given. These are eigenfunctions associated with three eigenvalues, one from each of the three branches. It is apparent from the shape of the eigenfunctions why one usually designates the A modes as wall modes and the P modes as center modes. The A modes, which have their largest variation close to the wall, have rather small phase velocities, whereas the P modes, which have their maxima close to the center of the channel, have much higher phase speeds. The S modes, which are highly damped, have a phase speed that is nearly equal to $2/3$.

Further characteristics of these modes are given in Section 3.2.4 on asymptotic results.

When considering disturbances with a vanishing streamwise dependence, i.e., $\alpha = 0$, the shape of the spectrum is markedly different; see Figure 3.1(b). In this case it is necessary to consider ω rather than c as the eigenvalue. The spectrum consists of just one branch originating close to the origin. One can easily show that these eigenvalues are always damped, using the same technique that was used to prove that all the Squire modes are damped (see Appendix D).

For the special case of zero streamwise wave number the dispersion relation and the eigenfunctions can be determined analytically because the Orr-Sommerfeld and Squire equations (3.14) and (3.15) reduce to a constant-coefficient differential equation. For the Orr-Sommerfeld modes we get

$$\omega = -\frac{i}{Re} (\beta^2 - \mu^2) \quad (3.61)$$

where μ is the solution of the transcendental equations

$$\mu \tan \beta + \beta \tan \mu = 0 \quad (\text{odd modes}) \quad (3.62)$$

$$\mu \cot \beta + \beta \cot \mu = 0 \quad (\text{even modes}) \quad (3.63)$$

and for the Squire equation we have

$$\omega = -\frac{i}{Re} \left(\beta^2 - \left(n - \frac{1}{2} \right)^2 \pi^2 \right). \quad (3.64)$$

For reference, eigenvalues for plane Poiseuille flow are listed in Appendix A.

Couette, pipe, and Blasius boundary layer flows

Spectra for other parallel shear flows have structures similar to the one described for plane Poiseuille flow, although there are some noteworthy differences. In Figure 3.3 the spectra for plane Couette and pipe flow are

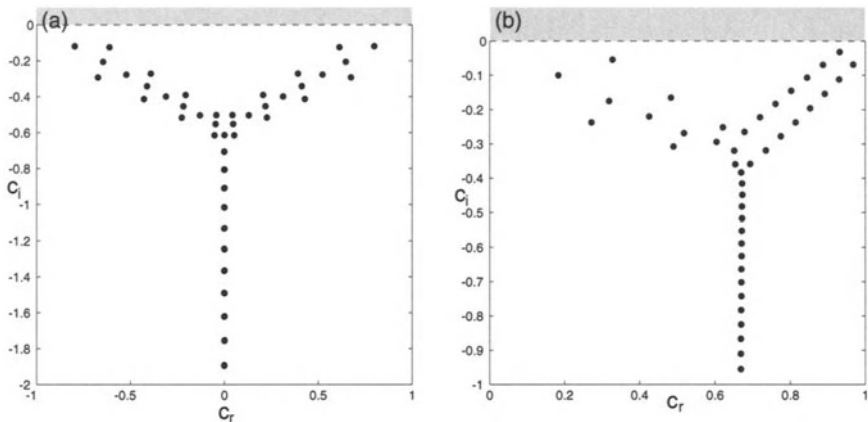


FIGURE 3.3. Spectrum of plane Couette and pipe flow. (a) Plane Couette flow for $\alpha = 1, \beta = 1, \text{Re} = 1000$; (b) Pipe flow for $\alpha = 1, n = 1, \text{Re} = 5000$.

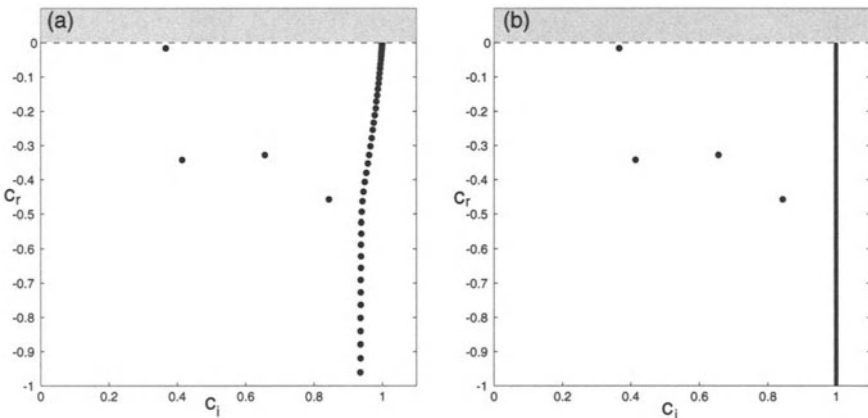


FIGURE 3.4. Spectrum for Blasius boundary layer flow for $\alpha = 0.2, \text{Re} = 500$. (a) Numerically obtained spectrum displaying a discrete representation of the continuous spectrum with a particular choice of discretization parameters. (b) Exact spectrum displaying the discrete and continuous part.

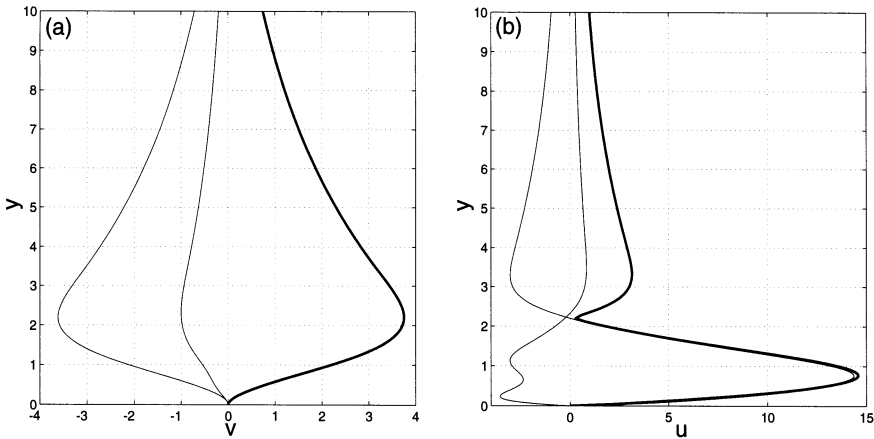


FIGURE 3.5. Eigenfunctions for Blasius boundary layer flow. (a,b) Eigenfunction of the discrete spectrum; vertical (a) and streamwise (b) velocity component for $\alpha = 0.2$, $Re = 500$. The thick line represents the absolute value of v or u , the thin lines represent the real and imaginary part.

shown. Pipe flow has the same three-branch structure as plane Poiseuille flow. The plane Couette flow spectrum, on the other hand, does not contain a P branch, but has two A branches; for every eigenfunction on one A branch there exists a corresponding eigenfunction on the other branch that is the exact image of the former reflected about the channel centerline. Neither Couette nor pipe flow supports unstable eigenvalues for any parameter combination. This is discussed further in the next section. The S branch in both of these flows corresponds to a phase speed equal to the average speed of the mean flow.

The eigenspectrum of the Blasius boundary layer (see Figure 3.4) has more significant differences compared to the other parallel shear flows considered so far.

The mean flow for Blasius boundary layer flow is not known explicitly, but it is given as the solution to the nonlinear ordinary differential equation

$$f''' + f f'' = 0 \quad (3.65)$$

subject to the boundary conditions $f(0) = f'(0) = 0$, $f'(\infty) = 1$. The superscript ' denotes differentiation with respect to the similarity variable $\eta = Re_\delta y \sqrt{\nu/U_\infty} x$. The mean velocity profile is then given as $U(y) = U_\infty f'(\eta)$. Figure 3.4(a) shows a small number of modes on the A branch in addition

to an almost vertical line with closely spaced eigenvalues resembling a combination of the P and S branches. Depending on the numerical method and numerical parameters used (e.g., resolution, domain truncation, freestream boundary condition), the eigenvalues on this vertical line will vary but will qualitatively agree with the spectrum shown in Figure 3.4(a). What we observe is a discrete representation of the continuous spectrum; its derivation and implication will be explored in Section 3.2.3. The boundary layer has at most one unstable mode, also denoted a Tollmien-Schlichting (TS) wave. The Tollmien-Schlichting mode is always on the A branch and is stable for the parameter combination shown here. The eigenfunction corresponding to the Tollmien-Schlichting wave is shown in Figure 3.5. It has a rather low phase speed and thus has its maximum amplitude close to the wall.

For each of these flows a set of numerically calculated eigenvalues can be found in Appendix A.

Spectrum of the continuous stability operator

For plane Poiseuille flow we observe a purely discrete set of eigenvalues for any given set of parameters α , β , and Re . As the streamwise and spanwise wave numbers α and β vary, the complex frequencies ω change accordingly but are restricted to a region in the complex ω -plane, which they densely fill. This subset of the complex ω -plane can be interpreted as the spectrum of the continuous linear stability operator. Assuming wavelike solutions will transform this continuous spectrum into a discrete point spectrum.

For plane Poiseuille flow the spectrum of the continuous stability operator has been computed by Trefethen *et al.* (1993) and is shown as the shaded area in Figure 3.6. For plane Poiseuille flow the spectrum is contained in the lower half-plane only for small Reynolds numbers; for larger Reynolds numbers two bumps appear, which protrude into the upper half-plane for $\text{Re} > 5772$.

The spectrum of the continuous stability operator for pipe flow is significantly different due to the fact that the azimuthal wave number takes on only integer values. Rather than covering an area in the complex ω -plane, the spectrum for pipe flow consists of continuous lines as shown in Figure 3.7 taken from Trefethen *et al.* (1999). Points in the complex plane that do not fall on one of the lines do not represent eigenvalues for any wave number combination.

Taking the Fourier transform of the continuous linear stability operator changes the continuous spectrum to a discrete one. Whereas this change is complete for the case of plane Poiseuille, plane Couette, and pipe flows, for boundary layer flow the Fourier transform cannot completely discretize the spectrum of the continuous operator resulting in a continuous remainder as shown in Figure 3.4.

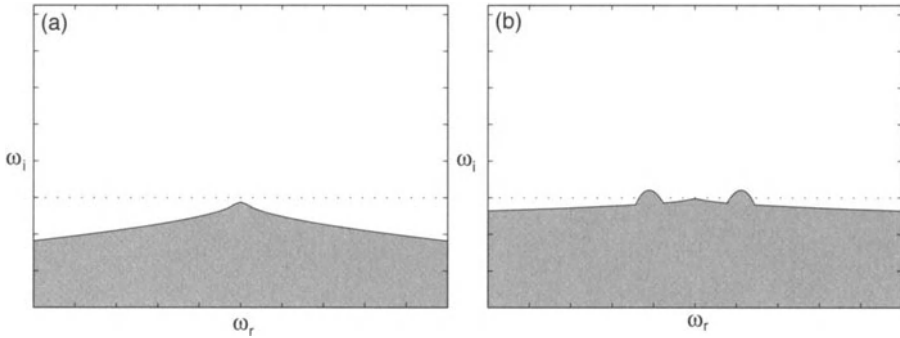


FIGURE 3.6. Spectrum of the continuous operator for plane Poiseuille flow. The shaded area marks the spectrum. (a) $Re = 1000$; (b) $Re = 10000$. From Trefethen *et al.* (1993).

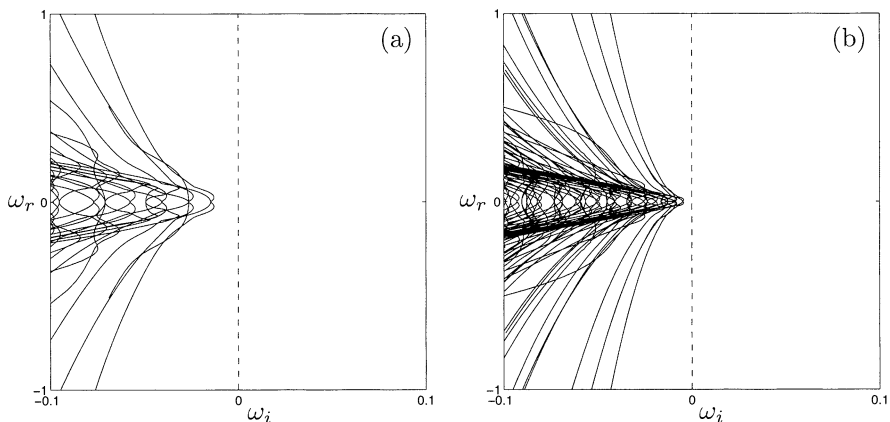


FIGURE 3.7. Spectrum of the continuous operator for pipe Poiseuille flow. The lines mark the spectrum. (a) $Re = 1000$; (b) $Re = 3000$. From Trefethen *et al.* (1999).

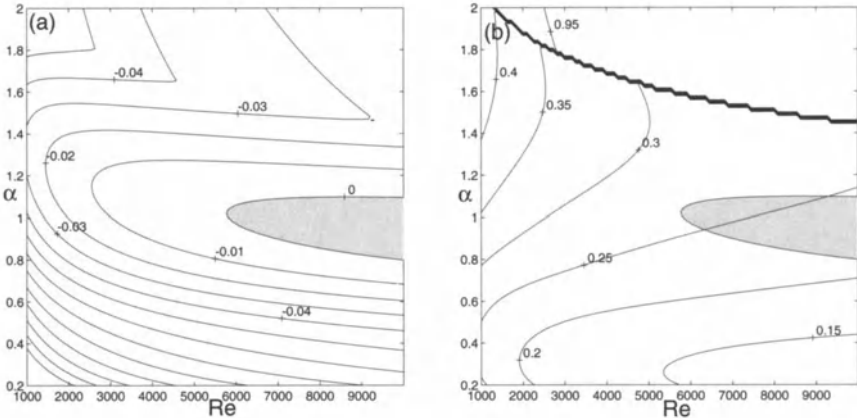


FIGURE 3.8. Neutral curve for plane Poiseuille flow: (a) contours of constant growth rate c_i ; (b) contours of constant phase velocity c_r . The shaded area represents the region of parameter space where unstable solutions exist.

3.2.2 Neutral Curves

Plane Poiseuille and Blasius Flows

The curve that defines the boundary between areas in parameter space where exponentially growing solutions exist and where they do not, is called the neutral curve. Such a neutral curve for plane Poiseuille flow is shown in Figure 3.8(a), together with contours of constant nonzero growth rates c_i . The region in which unstable waves exist is shaded. The left-most tip of this shaded region defines the lowest Reynolds number for which an exponentially unstable eigenvalue exists. This Reynolds number is called the critical Reynolds number, Re_{crit} . The growth rates of the unstable waves are quite small compared to the decay rates of the damped waves outside of the shaded region. The maximum exponential growth rate of plane Poiseuille flow is $\omega_i \approx 0.007688$, which is achieved for a streamwise wave number of $\alpha \approx 0.782$ and a Reynolds number of $\text{Re} \approx 46950$. This implies that it takes 90.2 time units for the wave to double in amplitude. During this time it has propagated about 14.3 channel half-heights in the downstream direction. These small viscous growth rates should be compared to the ones obtained for inviscidly unstable flows discussed in Chapter 2.

Figure 3.8(b) presents a contour plot of the phase speed for the least stable eigenmode of plane Poiseuille flow. For the unstable waves the phase speed is about 20 to 25 percent of the centerline velocity. The thick line at the top of the figure, which represents a discontinuity of the phase speed contours, signifies a change of the least stable eigenmode from a wall mode on the A branch at the lower end of the figure to a center mode on the P branch in the upper part of the figure.

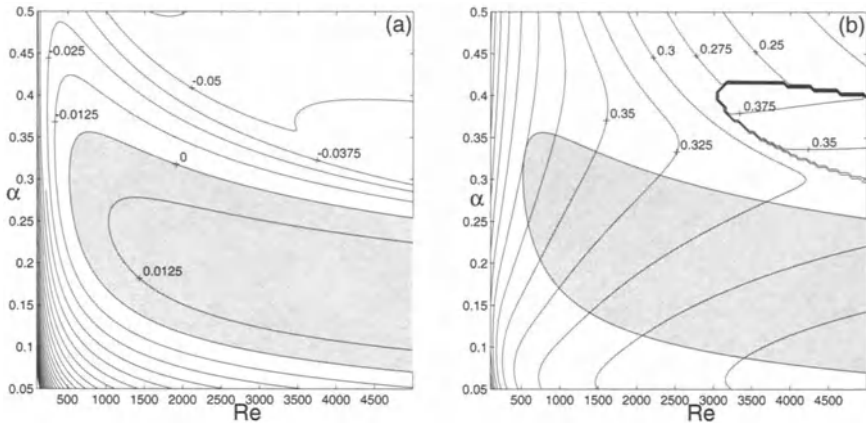


FIGURE 3.9. Neutral curve for Blasius boundary layer flow: (a) contours of constant growth rate c_i ; (b) contours of constant phase velocity c_r . The shaded area represents the region in parameter space where unstable solutions exist.

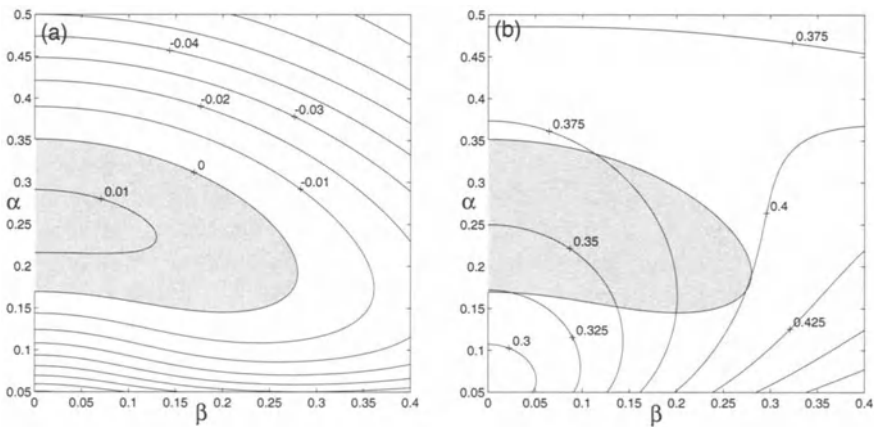


FIGURE 3.10. Neutral curve for Blasius boundary layer flow $Re = 1000$ in the α - β -plane: (a) contours of constant growth rate c_i ; (b) contours of constant phase velocity c_r .

Flow	α_{crit}	Re_{crit}	$c_r _{crit}$
Plane Poiseuille flow	1.020	5772.2	0.2639
Blasius boundary layer flow	0.303	519.4	0.3965

TABLE 3.1. Critical parameters for plane Poiseuille and Blasius boundary layer flows.

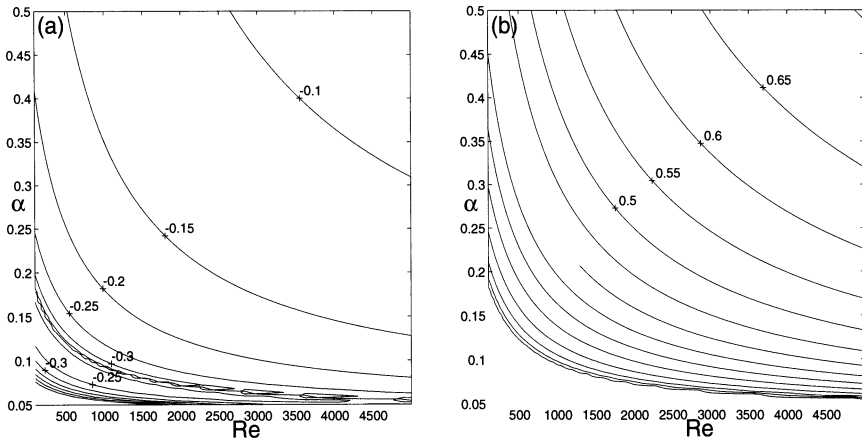


FIGURE 3.11. Contours of constant growth rate (a) and phase speed (b) for plane Couette flow.

Figure 3.9 shows contours of the imaginary and real parts of the phase speed for the Blasius boundary layer, which have a similar shape to those presented for plane Poiseuille flow. There is a region close to the upper right-hand corner of the figure where the least stable mode changes identity.

For $\text{Re} > \text{Re}_{crit}$ a line of constant Reynolds number intersects the neutral stability curve in two locations, which in turn divides the neutral curve into two parts: the upper branch (or branch II) and the lower branch (or branch I). We will refer back to this definition in later parts of this chapter.

Figure 3.10 displays the contours of the growth rate and phase speed for three-dimensional waves in Blasius boundary layer flow. As expected, the maximum growth rate is found for two-dimensional waves. According to Squire's transformation this will be the case for all Reynolds numbers that are below the Reynolds number for which the maximum exponential growth rate occurs.

In Table 3.1 critical parameters for plane Poiseuille and Blasius boundary layer flows are presented to aid in the validation of numerical Orr-Sommerfeld solvers.

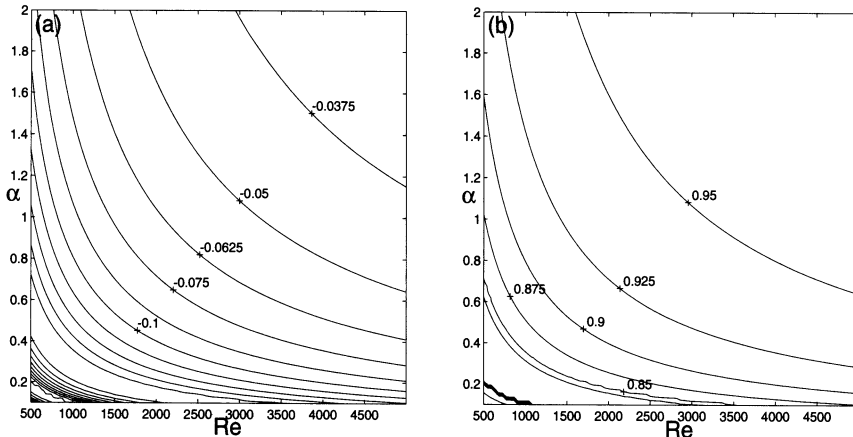


FIGURE 3.12. Contours of constant growth rate (a) and phase speed (b) for pipe Poiseuille flow.

Plane Couette and Pipe Flows

The spectra of plane Couette flow and pipe flow do not contain any unstable eigenvalues for any parameter combinations. This is perhaps the most important difference between these flows and plane Poiseuille and boundary layer flows. For Couette flow the nonexistence of unstable eigenvalues has been proven by Romanov (1973) but for pipe flow only “numerical proofs” are available. Figures 3.11 and 3.12 show contours of the growth rate and phase speed for plane Couette and pipe flows.

3.2.3 Continuous Spectrum

An example

When solving the Orr-Sommerfeld equation (3.14) for an infinite or semi-infinite domain, we generally encounter a discrete (point) spectrum and a continuous spectrum. In this section, we will investigate the nature and properties of the continuous spectrum. But first we will motivate its existence by a simple example.

Suppose we wish to solve the linear one-dimensional wave equation

$$\frac{\partial^2 u}{\partial t^2} = \frac{\partial^2 u}{\partial x^2} \quad (3.66)$$

in a bounded domain $x \in [0, 1]$ subject to the boundary conditions

$$u(0, t) = u(1, t) = 0 \quad (3.67)$$

and appropriate initial conditions. We seek solutions of the form

$$u(x, t) = f(x) \exp(i\omega t) \quad (3.68)$$

that results in an infinite set of discrete eigenvalues and eigenfunctions

$$\omega_n = n\pi \quad f_n(x) = \frac{1}{\sqrt{2}} \sin(n\pi x) \quad n = 1, 2, 3, \dots \quad (3.69)$$

These eigenfunctions form a complete set. If we repeat the same computation for the infinite domain $x \in [0, \infty)$ with the boundary conditions

$$u(0, t) = 0 \quad \text{and} \quad u(x, t) \rightarrow 0 \quad \text{as} \quad x \rightarrow \infty \quad (3.70)$$

we find that there are no discrete eigenvalues. If, on the other hand, the boundary condition at infinity is relaxed to

$$u(x, t) \quad \text{is bounded} \quad \text{as} \quad x \rightarrow \infty \quad (3.71)$$

we obtain a continuous spectrum

$$\omega \geq 0 \quad \text{or} \quad \omega \in \mathbb{R}_0^+ \quad (3.72)$$

and the corresponding eigenfunctions are

$$f(x; \omega) = \frac{1}{\sqrt{2\pi}} \sin(\omega x). \quad (3.73)$$

These eigenfunctions are not square-integrable.

Another example of a discrete spectrum changing into a continuum arises from the Fourier representation of a solution to a differential equation when the domain changes from a finite to an infinite one. For finite periodic domains one may use a sum over a discrete set of Fourier modes to represent the solution. In contrast, in an infinite domain a continuous set of Fourier modes is necessary to represent the solution.

Relaxation of the boundary condition at infinity

Applying a similar technique to the Orr-Sommerfeld equation (3.14) on a semi-infinite domain (see Grosch & Salwen, 1978) suggests the use of the modified boundary condition

$$\hat{v}, \mathcal{D}\hat{v} \quad \text{bounded} \quad \text{as} \quad y \rightarrow \infty. \quad (3.74)$$

In the limit as $y \rightarrow \infty$ the Orr-Sommerfeld equation (3.14) can be written as

$$(\mathcal{D}^2 - k^2)^2 \hat{v} = i\alpha \text{Re} [(U_\infty - c) (\mathcal{D}^2 - k^2)] \hat{v} \quad (3.75)$$

which is a fourth-order differential equation with *constant* coefficients. In this asymptotic limit the fundamental solutions of the Orr-Sommerfeld equation can be written as

$$\hat{v}_n = \exp(\lambda_n y) \quad (3.76)$$

with

$$\lambda_1 = -\sqrt{i\alpha \text{Re}(U_\infty - c) + k^2} \quad (3.77)$$

$$\lambda_2 = +\sqrt{i\alpha \text{Re}(U_\infty - c) + k^2} \quad (3.78)$$

$$\lambda_3 = -k \quad (3.79)$$

$$\lambda_4 = +k. \quad (3.80)$$

The first two solutions corresponding to \hat{v}_1, \hat{v}_2 are referred to as the *viscous* solutions or the vorticity modes, whereas \hat{v}_3, \hat{v}_4 are called the *inviscid* solutions or the pressure modes.

Assume that $i\alpha \text{Re}(U_\infty - c) + k^2$ is real and negative. We then obtain

$$\alpha \text{Re} c_i + k^2 < 0 \quad \alpha \text{Re}(U_\infty - c_r) = 0 \quad (3.81)$$

or

$$c_i < -\frac{k^2}{\alpha \text{Re}} \quad (3.82)$$

which can be rewritten as

$$c_i = -(1 + \xi^2) \frac{k^2}{\alpha \text{Re}} \quad \xi \in \mathbb{R}^+. \quad (3.83)$$

Finally, the spectrum is given as

$$c = U_\infty - i(1 + \xi^2) \frac{k^2}{\alpha \text{Re}} \quad (3.84)$$

and the corresponding eigenfunctions behave like

$$\hat{v} \sim A \exp(-i\xi ky) + B \exp(i\xi ky) + C \exp(-ky). \quad (3.85)$$

This form of the solution in the free stream can be used as the starting condition for computing modes in the continuous spectrum. Given α and β , choose c to be part of the continuous spectrum; then use the three linearly independent solutions obtained in the free stream and integrate them toward the wall. We have three free constants and two boundary conditions at the wall. As the third condition an arbitrary normalization condition can be applied. This produces the spectrum displayed in Figure 3.4(b), which is contrasted to the discrete approximation of the continuous spectrum obtained from a global numerical scheme (see Figure 3.4(a)).

Laplace transform and branch cuts

An alternative interpretation of the continuous spectrum was given by Gustavsson (1979) using Laplace transform methods.

Applying the Laplace transform to the normal velocity equation (3.6) we obtain the following inhomogeneous Orr-Sommerfeld equation

$$(U - c)(\mathcal{D}^2 - k^2)\tilde{v} - U''\tilde{v} - \frac{1}{i\alpha \text{Re}}(\mathcal{D}^2 - k^2)^2\tilde{v} = \frac{1}{i\alpha}\hat{\Phi}_0 \quad (3.86)$$

with

$$c = -\frac{s}{i\alpha}, \quad \hat{\Phi}_0 = (\mathcal{D}^2 - k^2)\hat{v}|_{t=0}. \quad (3.87)$$

The boundary conditions are

$$\tilde{v} = \mathcal{D}\tilde{v} = 0 \quad \text{at} \quad y = 0 \quad \text{and} \quad y \rightarrow \infty. \quad (3.88)$$

The general solution of this equation is

$$\tilde{v} = \sum_{n=1}^4 A_n(y)\tilde{v}_n(y) \quad (3.89)$$

where $\tilde{v}_n(y)$ are the four independent solutions of the homogeneous problem. The coefficients $A_n(y)$ can be determined by the method of variation of parameters (see, e.g., Boyce & DiPrima, 1997), which leads to a system of equations for the derivatives of the coefficients $A_n(y)$ which can readily be solved using Cramer's rule. One obtains

$$A_n = \text{Re} \int_y \frac{D_n \hat{\Phi}_0}{W} dy \quad n = 1, 2, 3, 4 \quad (3.90)$$

where D_n is the co-factor of $\mathcal{D}^3 \tilde{v}_n$ with reversed sign and W stands for the Wronskian.

Because the next-highest derivative is absent in the (fourth-order) Orr-Sommerfeld equation (3.86), the Wronskian is a constant and can be evaluated at infinity. We obtain

$$W = -4k\sqrt{k^2 + i\alpha\text{Re}(1-c)^2} [i\alpha\text{Re}(1-c)]^2. \quad (3.91)$$

The coefficients $A_n(y)$ determine the Laplace-transformed normal velocity. To obtain \hat{v} , we have to invert the Laplace transform:

$$\hat{v} = \frac{1}{2\pi i} \int_{\gamma-i\infty}^{\gamma+i\infty} e^{st} \tilde{v} \, ds \quad (3.92)$$

with the constant γ chosen such that the path of integration in the complex s -plane is to the right of all singularities of \tilde{v} . The singularities of \tilde{v} are given by the zeros of W and the zeros of the dispersion relation. The latter are simply associated with the discrete modes of the Orr-Sommerfeld equation; the zeros of the Wronskian W are given by

$$k^2 + i\alpha\text{Re}(1-c)^2 = 0. \quad (3.93)$$

Recall that this is exactly the expression used to define the continuous spectrum in the previous subsection. In addition, $W = 0$ when $c = 1$, which can be shown to result from the particular representation of the solution in the free stream when evaluating the Wronskian. The four fundamental solutions $\tilde{v}_n(y)$ become linearly dependent as $c \rightarrow 1$.

The required path for the Laplace inversion thus becomes the one shown in Figure 3.13. Gustavsson (1979) used this expression to determine an explicit expression for the continuous spectrum in terms of integrals of the four linearly independent solutions of the Orr-Sommerfeld equation. The discrete spectrum results from evaluating the poles in the complex plane using residue theory; the continuous spectrum is associated with the contributions of the branch cut when inverting the Laplace transform.

3.2.4 Asymptotic Results

Critical layers

In many high Reynolds number flow situations the inviscid approximation is accurate in most of the domain and the effects of viscosity enter only in thin boundary and internal layers. This is also the case for solutions of the Orr-Sommerfeld equation as $\text{Re} \rightarrow \infty$.

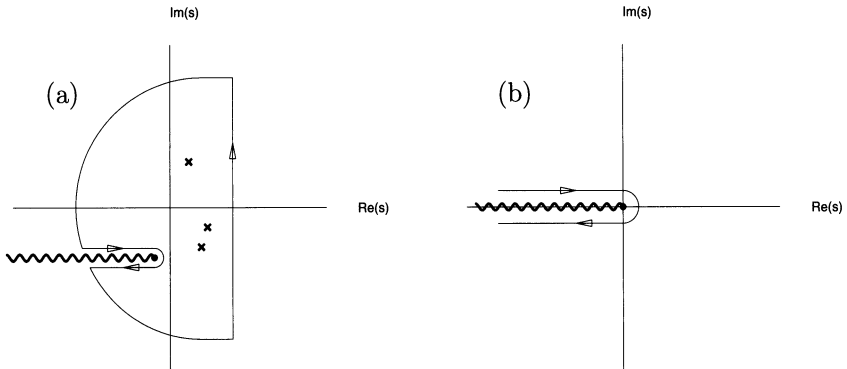


FIGURE 3.13. Inversion contour for the Laplace transform: (a) for non-zero streamwise wave number; (b) for zero streamwise wave number.

In the limit of large Reynolds numbers there are two regions where viscosity is important and they can easily be deduced from the nature of Tollmien's inviscid solutions of the Rayleigh equation, which are

$$\tilde{v}_1(y) = (y - y_c)P_1(y) \quad (3.94)$$

$$\tilde{v}_2(y) = P_2(y) + (U_c''/U_c')\tilde{v}_1(y) \ln(y - y_c) \quad (3.95)$$

where $P_1(y)$ and $P_2(y)$ are analytic at y_c with $P_1(y_c) = P_2(y_c) = 1$ and $P'_2(y_c) = 0$. We recall that y_c is the location of the critical layer where $U(y_c) = c$; the above solutions were discussed in Section 2.2.1.

These two solutions do not satisfy the viscous boundary conditions and can thus be expected to have viscous modifications close to the boundary. In addition, there is a logarithmic singularity at the critical layer, due to the regular singular point of the Rayleigh equation. Because the Orr-Sommerfeld equation is not singular at the critical layer, there also has to be a viscous modification close to that region.

In addition to using viscous effects to determine matching conditions for the inviscid solution on both sides of the critical layer, nonlinearities can be used to find matching conditions. For a thorough review of this technique, known as nonlinear critical layers, the interested reader is referred to Maslowe (1986).

The boundary layer near a wall

Let us consider the nature of the viscous solution when the term with the highest-order derivative $(i\alpha\text{Re})^{-1}\mathcal{D}^4\tilde{v}$ balances the dominant inviscid term. In the region close to the wall, the mean velocity approaches zero and we have the following boundary-layer approximation to the Orr-Sommerfeld equation (3.14)

$$(i\alpha \text{Re})^{-1} \mathcal{D}^4 \tilde{v} = -c \mathcal{D}^2 \tilde{v}. \quad (3.96)$$

The boundary layer solution to this equation, i.e., the solution that decays as we move away from the boundary, is

$$\tilde{v}_3(y) = C \exp\{-(y - y_1)(i\alpha \text{Re})^{1/2} e^{-\pi i/4}\}. \quad (3.97)$$

This shows, as we may expect, that the boundary layer close to the wall is of order $(\alpha \text{Re})^{-1/2}$. The reason we call this solution \tilde{v}_3 is that it may be used as an approximation to the third linearly independent solution when an asymptotic form of the dispersion relation is derived. The first two linearly independent solutions are taken as Tollmien's inviscid solutions (2.26), (2.27).

Local turning point approximation at the critical layer

To obtain approximations to the viscous solution at the critical layer we expand the coefficients of the Orr-Sommerfeld equation (3.14) around y_c in a Taylor series, which implies that $U - c \approx U'_c(y - y_c)$. The dominant terms in the Orr-Sommerfeld equation thus become

$$(i\alpha \text{Re})^{-1} \mathcal{D}^4 \tilde{v} = U'_c(y - y_c) \mathcal{D}^2 \tilde{v}. \quad (3.98)$$

This equation can be simplified by the introduction of

$$\tilde{v}(y) = V(\xi) \quad \text{where} \quad \xi = (y - y_c)/\epsilon \quad \text{and} \quad \epsilon = (i\alpha \text{Re} U'_c)^{-1/3} \quad (3.99)$$

which results in

$$\left(\frac{d^2}{d\xi^2} - \xi \right) \frac{d^2}{d\xi^2} V = 0. \quad (3.100)$$

This is an Airy equation for V'' and the solutions are known as generalized Airy functions, which are discussed at length in Drazin & Reid (1981). Two of the linearly independent solutions to this fourth-order equation are the leading terms of Tollmien's inviscid solutions (2.26), (2.27) at the critical layer, and the two remaining are the viscous solutions at the critical layer.

It follows from the scaling of ξ that the internal layer thickness around the critical layer is of order $(\alpha \text{Re})^{-1/3}$. An interesting question is the vertical separation of the two layers. Two possibilities are shown in Figure 3.14. It is clear that under some circumstances the internal layer at the critical layer can overlap with the (thinner) boundary layer at the wall. It can be shown

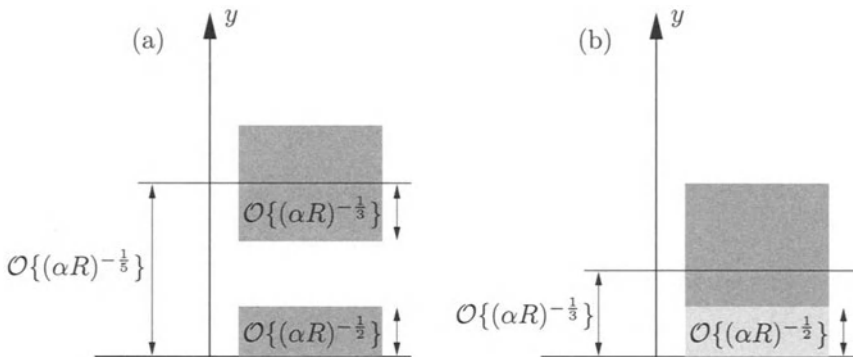


FIGURE 3.14. Critical and viscous layer scaling for (a) upper branch, (b) lower branch of neutral stability curve.

that approximations for the upper branch of the neutral stability curve as $\alpha Re \rightarrow \infty$ have well separated boundary layers, whereas approximations for the lower branch have only one boundary layer of order $(\alpha Re)^{-1/3}$ close to the wall. We will return to this topic later in this section.

Asymptotics of eigenvalues for plane Poiseuille flow

The asymptotic behavior of the eigenvalues on the *A*-branch is governed by $(\alpha Re)^{-1/3}$ and the eigenvalues are related to the zeros of the (generalized) Airy function. The eigenfunctions will have large amplitudes close to the wall and are therefore called wall-modes. On the *P*-branch the asymptotic behavior of the eigenvalues is governed by $(\alpha Re)^{-1/2}$ and the real and imaginary parts of c are, to leading order, related:

$$c_r - c_i = 1 + \mathcal{O}\left((\alpha Re)^{-1/2}\right). \quad (3.101)$$

The eigenfunctions have large amplitudes close to the centerline, and are thus called center-modes; they are related to the parabolic cylinder function (see Abramowitz & Stegun, 1973). In contrast to the other branches the number of eigenvalues on the *S*-branch is infinite. These eigenvalues are governed by $(\alpha Re)^{-1}$ asymptotically.

For plane Couette flow the structure is changed in that only the *A*- and *S*-branches are present and for the Blasius boundary layer only the *A*-branch exists (see the discussion about unbounded flows). For the techniques used to obtain the asymptotic expressions for the eigenvalues see Drazin & Reid (1981).

Lower-branch asymptotics for Blasius flow

Using the asymptotic approximations of the previous section we can derive scaling laws for various regions of the wall-normal coordinates where the fluid flow is well approximated by simplified equations taking into account the most dominant effect. These scaling laws constitute the starting point of triple-deck theory. We will follow Healey (1998).

We will apply methods of singular perturbation theory to the Orr-Sommerfeld equation (3.14) for a Blasius boundary layer. In the limit of large Reynolds numbers viscous effects only play a role in a very thin layer adjacent to the wall. Outside this layer, the flow is governed by the inviscid equation, i.e., the Rayleigh equation (2.15).

The method of approach is standard. We will first solve the Rayleigh equation (2.15) to obtain the outer solution for the inviscid regime away from the wall. The freestream boundary condition is applied and the limit of the outer solution as it approaches the boundary layer is determined. To satisfy the boundary condition at the wall, a boundary layer of appropriate thickness is introduced, and the governing equation is reformulated in terms of inner variables. The solution to this inner problem is then matched to the outer solution to yield a uniformly valid approximation for all values of the wall-normal coordinate.

For the outer (inviscid) problem we express the solution as a linear combination of Tollmien's solutions (2.26, 2.27). The boundary condition at infinity, namely,

$$\tilde{v} \sim \exp(-\alpha y) \quad \text{as } y \rightarrow \infty \quad (3.102)$$

is then imposed, which leads us to the outer solution (see Drazin & Howard, 1962)

$$\tilde{v}_{outer} = \tilde{v}_1 + \frac{\alpha}{U_c'^2} \tilde{v}_2 \quad (3.103)$$

where \tilde{v}_1 and \tilde{v}_2 denote Tollmien's two fundamental solutions (2.26, 2.27) of the Rayleigh equation (2.15). In the limit as the normal coordinate y tends to zero, the outer solution approaches

$$\lim_{y \rightarrow 0} \tilde{v}_{outer} = y - y_c + \frac{\alpha}{U_c'^2} \left(1 + \frac{U_c''}{U_c'} [\ln |y - y_c| - i\pi] \right). \quad (3.104)$$

Continuing, we need to determine the inner solution. We will introduce inner variables (Y, V, A, C) and assume a general scaling of the form

$$y = \text{Re}_x^{-p} Y \quad (3.105)$$

$$\tilde{v} = \text{Re}_x^{-q} V \quad (3.106)$$

$$\alpha = \text{Re}_x^r A \quad (3.107)$$

$$c = \text{Re}_x^{-s} C \quad (3.108)$$

where Re_x is the Reynolds number based on the distance x from the leading edge and the exponents (p, q, r, s) will be determined by balancing appropriate terms in the Orr-Sommerfeld equation (3.14). Before proceeding, we will limit the range of the exponents (p, q, r, s) by making the following assumptions:

1. We will restrict the viscous wall layer to lie inside the Blasius boundary layer, which results in $p > 1/2$.
2. We restrict ourselves to streamwise waves that are short compared to the distance to the leading edge but long compared to the boundary layer thickness. This assumption leads to $0 < r < 1/2$.
3. We will assume that the phase speed is small compared to the freestream velocity, which will ensure the existence of a critical layer close to the wall. This is ensured by taking $s > 0$.

Before balancing terms, we also need to determine the asymptotic behavior of the mean velocity U as we approach the wall. Using the Blasius equation (3.65), we arrive at

$$U \sim f_0'' \eta - \frac{1}{48} f_0''^2 \eta^4 \quad f_0'' = 0.33206 \dots \quad (3.109)$$

or in terms of the wall-normal coordinate y (rather than the similarity variable η)

$$U \sim f_0'' \text{Re}_x^{1/2} y - \frac{f_0''^2 \text{Re}_x^2}{48} y^4 \quad U'' \sim -\frac{f_0''^2 \text{Re}_x^2}{4} y^2. \quad (3.110)$$

We then substitute the velocity profile into the Orr-Sommerfeld equation (3.14) and express dependent and independent variables in terms of the inner variables (3.105)-(3.108). We obtain

$$\begin{aligned} & \left(f_0'' \text{Re}_x^{1/2-p} Y - f_0''^2 \text{Re}_x^{2-4p} Y^4 - C \text{Re}_x^{-s} \right) (\text{Re}_x^{2p} V'' - \text{Re}_x^{2r} A^2 V) \\ & + f_0''^2 \text{Re}_x^{2-2p} Y^2 V \\ & = \frac{1}{i4\text{Re}_x^{1+r}} (\text{Re}_x^{4p} V''' - 2A^2 \text{Re}_x^{2p+2r} V'' + A^4 \text{Re}_x^{4r} V). \end{aligned} \quad (3.111)$$

We will concentrate on the lower branch of the neutral curve by retaining the term stemming from $(U - c)$ and the most dominant viscous term. We get to leading order

$$\left(f'' \text{Re}_x^{1/2-p} Y - C \text{Re}_x^{-s} \right) \text{Re}_x^{2p} V'' = \frac{1}{iA} \text{Re}_x^{4p-1-r} V'''. \quad (3.112)$$

A consistent balance can be ensured by requiring

$$\frac{1}{2} = p - s \quad \text{and} \quad 1 = 2p - r + s. \quad (3.113)$$

Introducing the variable

$$\xi = (iA f_0'')^{1/3} \left(Y - \frac{C}{f_0''} \right) \quad (3.114)$$

the Orr-Sommerfeld equation to leading order simplifies to a generalized Airy equation with the solution

$$V(\xi) = k_1 \left[\xi \int_{\xi_0}^{\xi} Ai(s) \, ds - Ai'(\xi) + Ai'(\xi_0) \right] \quad (3.115)$$

where ξ_0 denotes ξ for $Y = 0$, and Ai stands for the Airy function. The term containing Bi , the associated Airy function, has been removed to ensure nonsingular behavior at infinity. The constant k_1 is found by matching the inner solution to the outer solution. We obtain

$$\begin{aligned} k_1 \text{Re}_x^{-q} \left[\xi \int_{\xi_0}^{\infty} Ai(s) \, ds + Ai'(\xi_0) \right] &= -\frac{C \text{Re}_x^{-p} \xi}{\xi_0 f_0''} \\ &+ \frac{A \text{Re}_x^{-1+r}}{f_0''^2} \left[1 + \frac{C^3 \text{Re}_x^{1/2-2s-p}}{4 f_0''^2 \xi_0} \xi \left(\ln \left| \frac{C \text{Re}_x^{-p} \xi}{f_0'' \xi_0} \right| - i\pi \right) \right] \end{aligned} \quad (3.116)$$

which yields, after assuming $1/2 - 2s - p < 0$, the following two constraints on the scaling exponents

$$1 = q + r \quad \text{and} \quad q = p. \quad (3.117)$$

Solving the four constraints (3.113), (3.117) on the scaling exponents results in

$$p = q = \frac{5}{8} \quad r = \frac{3}{8} \quad s = \frac{1}{8}. \quad (3.118)$$

We have determined the proper scalings for the inner solutions of the matching problem. We will return to these scalings when we outline an asymptotic method for incorporating effects due to weakly nonparallel flow. These scalings were first derived by Lin (1946).

3.3 Further Results on Spectra and Eigenfunctions

3.3.1 Adjoint Problem and Bi-Orthogonality Condition

In a number of applications one needs a set of functions that are orthogonal to the set of Orr-Sommerfeld eigenfunctions, i.e., each function in this set is required to be orthogonal to all but one eigenfunction of the Orr-Sommerfeld problem. It is easy to derive an eigenvalue problem with these functions as its solutions; this is known as the *adjoint* Orr-Sommerfeld problem. In this section, we will derive the adjoint Orr-Sommerfeld equation and investigate the orthogonality relation between regular and adjoint eigenfunctions. In certain cases the adjoint equation is identical to the original equation, and hence the problem is called selfadjoint. Eigenvalue problems governing the stability of shear flows are in many cases non-selfadjoint.

The form of the adjoint problem is dependent on the inner product one uses. In the following derivation we will start with a definition and a derivation of the adjoint problem after which we will obtain the inner product one must use to ensure orthogonality between regular and adjoint solutions.

We define the two-dimensional adjoint Orr-Sommerfeld equation in the following manner

$$\int_{-1}^1 \tilde{\xi}^* \mathcal{L}_{OS} \tilde{v} dy = \int_{-1}^1 \tilde{v} (\mathcal{L}_{OS}^+ \tilde{\xi})^* dy \quad (3.119)$$

where we assumed a bounded geometry. For other geometries, the integration limits have to change accordingly. The derivation of the adjoint Orr-Sommerfeld equation in two dimensions is an exercise in integration by parts. We will first concentrate on the terms including the mean velocity profile $U(y)$ such as

$$\int_{-1}^1 \xi^* [U(\mathcal{D}^2 - \alpha^2) \tilde{v} - U'' \tilde{v}] dy. \quad (3.120)$$

Integrating by parts twice yields the following expression

$$\begin{aligned} \left[\tilde{\xi}^* U \mathcal{D} \tilde{v} \right]_{-1}^1 - \left[(\tilde{\xi}^* U)' v \right]_{-1}^1 + \int_{-1}^1 \tilde{v} (\tilde{\xi}^* U)'' dy \\ - \alpha^2 \int_{-1}^1 \tilde{\xi}^* U \tilde{v} dy - \int_{-1}^1 \tilde{\xi}^* U'' \tilde{v} dy. \end{aligned} \quad (3.121)$$

Using the boundary conditions on \tilde{v} and $D\tilde{v}$ and simplifying the expression results in

$$\int_{-1}^1 \tilde{v} \left[U(\mathcal{D}^2 - \alpha^2) \tilde{\xi}^* + 2U' \mathcal{D} \tilde{\xi}^* \right] dy. \quad (3.122)$$

To complete the derivation of the adjoint Orr-Sommerfeld equation we need to derive adjoint boundary conditions. This is done by integrating by parts the terms involving the highest derivative. We get

$$\begin{aligned} \frac{1}{Re} \int_{-1}^1 \tilde{\xi}^* \mathcal{D}^4 \tilde{v} dy = & \underbrace{\frac{1}{Re} \left[\tilde{\xi}^* \mathcal{D}^3 \tilde{v} \right]_{-1}^1}_{\boxed{1}} - \underbrace{\frac{1}{Re} \left[\mathcal{D} \tilde{\xi}^* \mathcal{D}^2 \tilde{v} \right]_{-1}^1}_{\boxed{2}} \\ & + \underbrace{\frac{1}{Re} \left[\mathcal{D}^2 \tilde{\xi}^* \mathcal{D} \tilde{v} \right]_{-1}^1}_{\boxed{3}} - \underbrace{\frac{1}{Re} \left[\mathcal{D}^3 \tilde{\xi}^* \tilde{v} \right]_{-1}^1}_{\boxed{4}} + \frac{1}{Re} \int_{-1}^1 \mathcal{D}^4 \tilde{\xi}^* \tilde{v} dy. \end{aligned} \quad (3.123)$$

The terms labeled $\boxed{3}$ and $\boxed{4}$ are identically zero due to the boundary conditions imposed on the Orr-Sommerfeld eigenfunctions. We can further simplify the expression by choosing the boundary conditions for the adjoint problem as

$$\mathcal{D} \tilde{\xi} = \tilde{\xi} = 0 \quad \text{at} \quad y = \pm 1 \quad (3.124)$$

which eliminates the terms labeled as $\boxed{1}$ and $\boxed{2}$. We finally can write the adjoint Orr-Sommerfeld equation for two-dimensional disturbances as

$$(i\alpha U - i\omega)(\mathcal{D}^2 - \alpha^2)\tilde{\xi} + 2i\alpha U' \mathcal{D} \tilde{\xi} + \frac{1}{Re} (\mathcal{D}^2 - \alpha^2)^2 \tilde{\xi} = 0. \quad (3.125)$$

We now proceed to derive the orthogonality relations between the regular and adjoint Orr-Sommerfeld modes by evaluating the expression

$$\int_{-1}^1 \tilde{\xi}_j^* (\mathcal{L}_{OS} \tilde{v}_i) - \tilde{v}_i (\mathcal{L}_{OS}^+ \tilde{\xi}_j)^* dy = 0 \quad (3.126)$$

where the regular and adjoint Orr-Sommerfeld operators \mathcal{L}_{OS} and \mathcal{L}_{OS}^+ are now known. Integration by parts similar to the procedure employed to derive the adjoint Orr-Sommerfeld equation results in

$$(\omega_i - \omega_j^*) \int_{-1}^1 \tilde{\xi}_j^* (\alpha^2 - \mathcal{D}^2) \tilde{v}_i dy = 0. \quad (3.127)$$

From the definition of the adjoint it is apparent that the eigenvalues of the adjoint problem are complex conjugate to the eigenvalues of the regular equation. This leads to the orthogonality relation

$$\int_{-1}^1 \tilde{\xi}_j^* (\alpha^2 - \mathcal{D}^2) \tilde{v}_i dy = C \delta_{ij} \quad (3.128)$$

where δ_{ij} denotes the Kronecker delta symbol, and the constant C can be taken as one for properly normalized eigenfunctions. The integral in the expression can be interpreted as a weighted inner product between two functions with $\alpha^2 - \mathcal{D}^2$ as the weight operator.¹ Expression (3.128) then states that the eigenfunctions of the regular and adjoint Orr-Sommerfeld equations are mutually orthogonal under this inner product. Because the Orr-Sommerfeld eigenfunctions are not orthogonal to each other, but rather to a second set, the orthogonality condition (3.128) is often referred to as the bi-orthogonality condition.

In an analogous way, one can show that the Squire modes are nonorthogonal. A similar analysis then shows that the equation adjoint to the homogeneous Squire equation reads

$$(i\alpha U - i\omega^*) \tilde{\zeta} + \frac{1}{\text{Re}} (\mathcal{D}^2 - \alpha^2) \tilde{\zeta} = 0 \quad (3.129)$$

and the corresponding scalar product under which the regular eigenfunctions $\tilde{\eta}$ and adjoint eigenfunctions $\tilde{\zeta}$ are bi-orthogonal is given as

$$\int_{-1}^1 \tilde{\zeta}_i^* \tilde{\eta}_j dy = C \delta_{ij}. \quad (3.130)$$

¹We have chosen the positive definite form $\alpha^2 - \mathcal{D}^2$ as the weight operator rather than $\mathcal{D}^2 - \alpha^2$.

It will also be useful to know the adjoint modes in the vector formulation. They are derived in a similar manner, although one has to scalar multiply the vector formulation of the Orr-Sommerfeld and Squire equations with the vector $(\tilde{\xi}^* \tilde{\zeta}^*)$ before one performs the integration by parts. Henningson & Schmid (1992) derived the following adjoint system for three-dimensional disturbances

$$-i\omega \begin{pmatrix} k^2 - \mathcal{D}^2 & 0 \\ 0 & 1 \end{pmatrix} \begin{pmatrix} \tilde{\xi} \\ \tilde{\zeta} \end{pmatrix} + \begin{pmatrix} \mathcal{L}_{OS}^+ & -i\beta U' \\ 0 & \mathcal{L}_{SQ}^+ \end{pmatrix} \begin{pmatrix} \tilde{\xi} \\ \tilde{\zeta} \end{pmatrix} = 0 \quad (3.131)$$

with

$$\mathcal{L}_{OS}^+ = -i\alpha U(k^2 - \mathcal{D}^2) + 2i\alpha U' \mathcal{D} + \frac{1}{Re}(k^2 - \mathcal{D}^2)^2 \quad (3.132)$$

$$\mathcal{L}_{SQ}^+ = -i\alpha U + \frac{1}{Re}(k^2 - \mathcal{D}^2). \quad (3.133)$$

The adjoint system (3.131) is subject to the same boundary conditions as the regular system. It is interesting that the off-diagonal term has moved to the adjoint normal velocity equation implying that the adjoint vector modes have the form

$$\begin{pmatrix} \tilde{\xi} \\ 0 \end{pmatrix} \quad \text{Adj. OS-modes} \quad \begin{pmatrix} \tilde{\xi}^p \\ \tilde{\zeta} \end{pmatrix} \quad \text{Adj. SQ-modes.} \quad (3.134)$$

We will also introduce the compact notation for the adjoint problem. We define

$$\tilde{\mathbf{q}}^+ = \begin{pmatrix} \tilde{\xi} \\ \tilde{\zeta} \end{pmatrix}. \quad (3.135)$$

The adjoint eigenvalue problem now becomes

$$\mathbf{L}^+ \tilde{\mathbf{q}}^+ = i\omega \mathbf{M} \tilde{\mathbf{q}}^+ \quad \text{or} \quad \mathbf{L}_1^+ \tilde{\mathbf{q}}^+ \equiv \mathbf{M}^{-1} \mathbf{L}^+ \tilde{\mathbf{q}}^+ = i\omega \tilde{\mathbf{q}}^+ \quad (3.136)$$

where \mathbf{M} is the same as previously defined and

$$\mathbf{L}^+ = \begin{pmatrix} \mathcal{L}_{OS}^+ & -i\beta U' \\ 0 & \mathcal{L}_{SQ}^+ \end{pmatrix}. \quad (3.137)$$

We can deduce the bi-orthogonality condition from the definition of the regular and adjoint problems; we find

$$(\mathbf{M}\tilde{\mathbf{q}}_p, \tilde{\mathbf{q}}_r^+) = C\delta_{pr} \quad (3.138)$$

where the eigenfunctions can be normalized so that $C = 1$. The orthogonality relations are derived for the inner product

$$(\mathbf{M}\tilde{\mathbf{q}}, \tilde{\mathbf{q}}^+) = (\tilde{\mathbf{q}}, \mathbf{M}\tilde{\mathbf{q}}^+) = \int_{-1}^1 \left(\mathcal{D}\tilde{\xi}^* \mathcal{D}\tilde{v} + k^2 \tilde{\xi}^* \tilde{v} + \tilde{\zeta}^* \tilde{\eta} \right) dy. \quad (3.139)$$

This is the most natural inner product to use from a physical point of view, because the associated norm, $\|\tilde{\mathbf{q}}\|^2 = (\mathbf{M}\tilde{\mathbf{q}}, \tilde{\mathbf{q}})$, is directly proportional to the disturbance energy, as we will show in the next chapter (Chapter 4).

3.3.2 Sensitivity of Eigenvalues

Sensitivity of individual eigenvalues

When numerically determining the eigenvalues of the Orr-Sommerfeld and Squire equations, the issue of their sensitivity to small perturbations in the stability equations needs to be addressed. The two main sources of these perturbations are the approximation of the continuous equations by a discrete representation and the solution of the equations in finite-precision arithmetic on a computer. As we will show in this section, the effect of these approximations on the spectra are quite distinct. But first we will develop general means to investigate the sensitivity of the entire spectrum and the sensitivity of individual eigenvalues to random perturbations.

The mathematical problem we want to address is a very familiar one in numerical linear algebra and is easily stated as follows. Given our eigenvalue problem

$$\mathbf{L}_1 \tilde{\mathbf{q}}_j = \lambda_j \tilde{\mathbf{q}}_j \quad (3.140)$$

with $\lambda_j = i\omega_j$, what is the change in the eigenvalues once the operator \mathbf{L}_1 is perturbed by an operator \mathbf{P} of norm $\varepsilon \ll 1$, i.e., what is the size of $\delta\lambda_j$ for the problem

$$(\mathbf{L}_1 + \mathbf{P})(\tilde{\mathbf{q}}_j + \delta\tilde{\mathbf{q}}_j) = (\lambda_j + \delta\lambda_j)(\tilde{\mathbf{q}}_j + \delta\tilde{\mathbf{q}}_j) \quad \|\mathbf{P}\| = \varepsilon \ll 1. \quad (3.141)$$

Although it is straightforward to also compute the perturbation of the eigenvectors, we will be mainly concerned with the perturbation of the eigenvalues. Simplifying the above equation and using (3.140) we obtain

$$(\mathbf{L}_1 - \lambda_j \mathbf{I})\delta\tilde{\mathbf{q}}_j + \mathbf{P}\tilde{\mathbf{q}}_j = \delta\lambda_j \tilde{\mathbf{q}}_j, \quad (3.142)$$

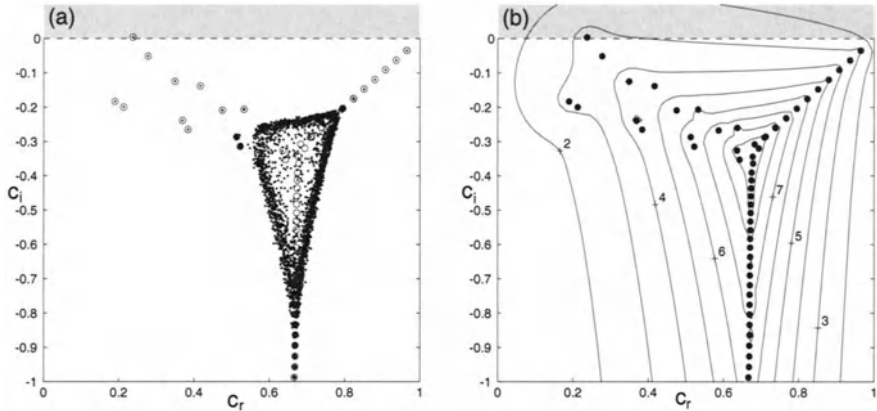


FIGURE 3.15. Pseudospectrum for plane Poiseuille flow for $\alpha = 1$, $\text{Re} = 10000$. (a) Based on random perturbations of the operator, (b) based on the resolvent norm (the contour levels are spaced logarithmically).

where we have dropped the terms $\mathbf{P}\delta\tilde{\mathbf{q}}_j$ and $\delta\lambda_j\delta\tilde{\mathbf{q}}_j$ that are negligible (i.e., of higher order in ε) compared to the size of the terms retained. The operator \mathbf{I} denotes the identity operator. We proceed by multiplying on the left by the eigenvectors $\tilde{\mathbf{q}}^+$ of the unperturbed operator \mathbf{L}_1^+ , which solve the adjoint equation

$$\mathbf{L}_1^+ \tilde{\mathbf{q}}_j^+ = \lambda_j^* \tilde{\mathbf{q}}_j^+. \quad (3.143)$$

Because we are interested in measuring the size of the perturbation \mathbf{P} in a physically meaningful way, we choose as the scalar product the one derived in the previous section (see (3.139)). We get

$$(\mathbf{M}\tilde{\mathbf{q}}_j^+, (\mathbf{L}_1 - \lambda_j \mathbf{I})\tilde{\mathbf{q}}_j) + (\mathbf{M}\tilde{\mathbf{q}}_j^+, \mathbf{P}\tilde{\mathbf{q}}_j) = \delta\lambda_j (\mathbf{M}\tilde{\mathbf{q}}_j^+, \tilde{\mathbf{q}}_j) \quad (3.144)$$

The first term on the left-hand side is identically zero using the definition of \mathbf{L}_1 and equation (3.143). We are left with an expression for the deviation $\delta\lambda_j$ of the j th eigenvalue from its unperturbed location:

$$\delta\lambda_j = \frac{(\mathbf{M}\tilde{\mathbf{q}}_j^+, \mathbf{P}\tilde{\mathbf{q}}_j)}{(\mathbf{M}\tilde{\mathbf{q}}_j^+, \tilde{\mathbf{q}}_j)} = (\mathbf{M}\tilde{\mathbf{q}}_j^+, \mathbf{P}\tilde{\mathbf{q}}_j). \quad (3.145)$$

where we assumed appropriately normalized eigenvectors. At this point we exploit the fact that \mathbf{M} is a symmetric, positive definite operator and thus can be factored into $\mathbf{M} = \mathbf{F}^H \mathbf{F}$. Our expression for the eigenvalue deviation is therefore

$$\delta\lambda_j = (\mathbf{F}^H \mathbf{F} \tilde{\mathbf{q}}_j^+, \mathbf{P} \tilde{\mathbf{q}}_j) = (\mathbf{F} \tilde{\mathbf{q}}_j^+, \mathbf{F} \mathbf{P} \mathbf{F}^{-1} \mathbf{F} \tilde{\mathbf{q}}_j). \quad (3.146)$$

Using the Schwartz inequality we arrive at an upper bound for the eigenvalue deviation

$$|\delta\lambda_j| \leq \|\mathbf{F} \tilde{\mathbf{q}}_j^+\| \|\mathbf{F} \mathbf{P} \mathbf{F}^{-1}\| \|\mathbf{F} \tilde{\mathbf{q}}_j\| \quad (3.147)$$

$$\leq \|\tilde{\mathbf{q}}_j^+\|_E \|\mathbf{P}\|_E \|\tilde{\mathbf{q}}_j\|_E \quad (3.148)$$

where the subscript $_E$ denotes the energy norm based on the standard definition of weighted norms; a detailed discussion of the energy norm is given in Chapter 3.

The quantity $s = \|\tilde{\mathbf{q}}_j^+\|_E \|\tilde{\mathbf{q}}_j\|_E$ can be interpreted as the sensitivity of a selected eigenvalue because it appears as the proportionality constant between the size of the perturbation and the size of the eigenvalue deviation.

It is worth pointing out that the sensitivity of the eigenvalues to random perturbations is a property of the underlying stability operator rather than a property of the chosen numerical scheme. We will further develop this concept in this section, which will lead us to ε -pseudo-eigenvalues, a generalization of eigenvalues. But first we will present results from a sensitivity study of the Orr-Sommerfeld eigenvalues using these measures. Table 3.2 lists selected eigenvalues for plane Poiseuille flow from the A -, P -, and S -branches of the spectrum together with their sensitivity measures. It is immediately apparent that the eigenvalues near the junction point of the three branches exhibit the largest sensitivity and thus react considerably to small perturbations of the operator. Fortunately, the least stable mode (on the P -branch for the parameter combinations chosen) shows rather little sensitivity.

Sensitivity of the complete spectrum

To verify and further illustrate this result we perturb the stability matrix artificially by adding to it a matrix with random entries chosen from a normal distribution of mean zero and standard deviation one that is subsequently scaled to a norm of 10^{-5} . The perturbed eigenvalue problem has then been solved for 100 of these random matrices. Figure 3.15 shows the superposition of the 100 spectra. As expected, the eigenvalues in the vicinity of the junction point of the three branches experience significant deviations from their unperturbed location whereas the eigenvalues closer to the neutral line are rather insensitive to small perturbations. Eigenvalues in the junction point move by an order one amount, even though the perturbations imposed on the matrix are five orders of magnitude smaller in norm.

c_r	c_i	sensitivity s
A-branch		
0.26813	-0.01750	4.51
0.50275	-0.16921	99.93
0.42658	-0.22346	162.93
P-branch		
0.94996	-0.04961	3.11
0.82949	-0.16797	334.39
0.71481	-0.29109	35014.47
S-branch		
0.68368	-0.34720	102763.87
0.66889	-0.84601	2144.02
0.66858	-0.97773	1169.87

TABLE 3.2. Sensitivities of eigenvalues for plane Poiseuille flow at $\alpha = 1, \beta = 0, \text{Re} = 5000$.

The reason for this large sensitivity of parts of the spectrum is the presence of nonorthogonal eigenvectors. In case of a set of orthogonal eigenvectors all of the sensitivity measures would be identically one, resulting in a one-to-one relation between the size of the perturbation and the amount of deviation from the unperturbed location. In this case, the deviation of the eigenvalues would be bounded by 10^{-5} and, within plotting accuracy, Figure 3.15 would display the unperturbed spectrum.

Matrices with nonorthogonal eigenvectors are known as nonnormal matrices, and a similar condition defines nonnormal operators. We can therefore conclude that the presence of sensitive parts of the spectrum is a reflection of the nonnormal property of the stability operator and its discretized matrix analog. Eigenvalue sensitivity, however, is only one symptom associated with a nonnormal stability operator. The next chapter (Chapter 4) will further explore the implications of a nonnormal stability operator.

Discretization errors

Errors in the spectrum introduced by an insufficient resolution of the eigenvectors have a qualitatively different behavior. Looking at the real and imaginary parts of the eigenfunctions corresponding to one of the eigenvalues on the S -branch one observes that with decreasing imaginary part the eigenfunctions become increasingly oscillatory. At a certain point on the S -branch, the numerical resolution is insufficient to represent these oscillations. At this point the eigenvalue corresponding to this ill-represented eigenfunction fails to follow the asymptotic behavior of the S -branch and a characteristic splitting of the S -branch is observed. Figure 3.16 compares the spectrum for plane Poiseuille flow with sufficient and insufficient numerical resolution. For increasingly insufficient resolution the oscillatory

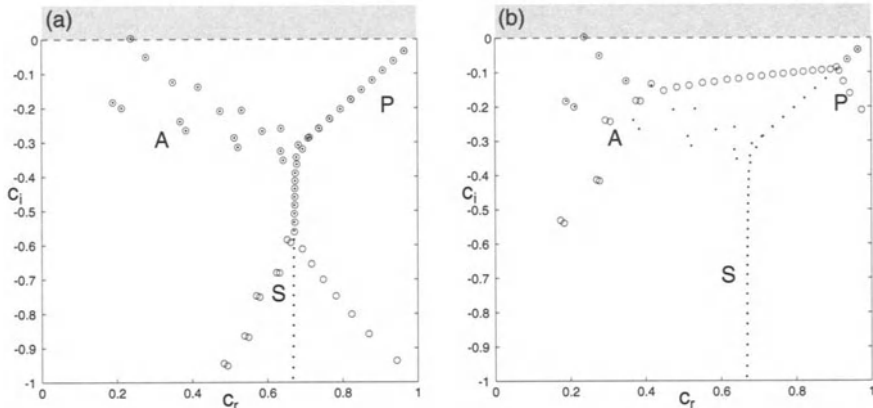


FIGURE 3.16. Insufficiently resolved Orr-Sommerfeld spectrum for plane Poiseuille flow for $\text{Re} = 10000, \alpha = 1, \beta = 0$. The number of Chebyshev polynomials is (a) $N = 100$, (b) $N = 50$.

behavior of the A - and P -modes cannot be resolved either, which results in a similar splitting along the A - and P -branches of the spectrum as shown in the right-hand side of Figure 3.16. A hybrid spectral collocation method based on Chebyshev polynomials (see Appendix A for a detailed description of this numerical method) has been used to produce the plots.

3.3.3 Pseudo-Eigenvalues

As demonstrated in the previous section, parts of the Orr-Sommerfeld spectrum exhibit a significant sensitivity to small perturbations. It has been found that the sensitivity is caused by the presence of nonorthogonal eigenfunctions. This determines the phenomenon of sensitivity as a property of the operator rather than an artifact of the numerical scheme.

The presence of nonorthogonal eigenfunctions is in turn a consequence of the nonnormal nature of the underlying operator. Nonnormal operators are operators that do not commute with their associated adjoint operators, i.e.,

$$\mathcal{L}\mathcal{L}^+ \neq \mathcal{L}^+\mathcal{L}. \quad (3.149)$$

As we will see in Chapter 4, the nonnormality of the Orr-Sommerfeld operator has not only consequences for the sensitivity of the spectrum, but it also influences the dynamics of disturbances governed by the linearized Navier-Stokes equations. These influences prompted Trefethen (1992) to introduce the concept of ε -pseudo-eigenvalues to analyze the behavior of evolution processes governed by nonnormal operators or matrices. Here we will present the definition for matrices.

A number $z \in \mathbb{C}$ lies in the ε -pseudospectrum of a matrix A , which we denote by $\Lambda_\varepsilon(A)$, if either of the following equivalent conditions is satisfied.

13 DEFINITION (ε -PSEUDO-EIGENVALUES I) z is an ε -pseudo-eigenvalue of A if it is an eigenvalue of $\tilde{A} = A + E$ for some perturbation matrix E with $\|E\| \leq \varepsilon$.

14 DEFINITION (ε -PSEUDO-EIGENVALUES II) z is an ε -pseudo-eigenvalue of A if it satisfies $\|(zI - A)^{-1}\| \geq \varepsilon^{-1}$.

The definitions for operators are essentially the same. For the details, see Reddy *et al.* (1993).

The first definition relates the ε -pseudospectrum to the spectrum of a randomly perturbed matrix. z is considered an ε -pseudo-eigenvalue of A if it is an exact eigenvalue of a matrix \tilde{A} that is perturbed by a random matrix E of norm less than or equal to ε .

The second definition uses the norm of the resolvent $R(z) = (zI - A)^{-1}$, which is continuously defined in the complex plane with the exception of the spectrum of A . The point spectrum of A will correspond to the locations where the norm of the resolvent tends to infinity. For finite but large resolvent norms, z will be defined as an ε -pseudo-eigenvalue of A with $\varepsilon = 1/\|R(z)\|$. In Figure 3.15(b) contours of the resolvent norm are plotted for plane Poiseuille flow.

3.3.4 Bounds on Eigenvalues

Bounds on the eigenvalues for the Orr-Sommerfeld and Squire operators can be obtained by multiplying the equations with the complex conjugate of their respective eigenfunctions, integrating over the y -interval, identifying real and imaginary parts, and using variational inequalities.

As an example we will use plane Poiseuille flow. Davis & Reid (1977) obtained for the Squire modes

$$U_{\min} < c_r < U_{\max} \quad (3.150)$$

$$c_i < -\frac{\pi^2/4 + k^2}{\alpha \text{Re}}. \quad (3.151)$$

These modes are thus always damped, as also noted by Squire. For the Orr-Sommerfeld eigenvalues the following bounds were obtained by Joseph (1968) for plane channel flow

$$(a) \quad U''_{\min} > 0 \quad (3.152)$$

$$U_{\min} < c_r < U_{\max} + \frac{2U''_{\max}}{\pi^2 + 4\alpha^2} \quad (3.153)$$

$$(b) \quad U''_{\min} \leq 0 \leq U''_{\max} \quad (3.154)$$

$$U_{\min} + 2U''_{\min}\pi^2 + 4\alpha^2 < c_r < \frac{2U''_{\max}}{\pi^2 + 4\alpha^2} \quad (3.155)$$

$$(c) \quad U''_{\max} \leq 0 \quad (3.156)$$

$$U_{\min} + \frac{2U''_{\min}}{\pi^2 + 4\alpha^2} < c_r < U_{\max} \quad (3.157)$$

$$c_i \leq \frac{q}{2\alpha} - \left\{ \frac{\pi^2(\pi^2 + \alpha^2)}{\pi^2 + 4\alpha^2} + \alpha^2 \right\} / \alpha \operatorname{Re} \quad (3.158)$$

where q is given as

$$q = \max_{y \in [0,1]} |U'(y)|. \quad (3.159)$$

The propagation speeds of small disturbances are thus essentially restricted to the range set by the mean flow, whereas the growth rate is always bounded from above.

No amplified disturbances exist if

$$\alpha \operatorname{Re} q < f(\alpha) \equiv \max[M_1, M_2] \quad (3.160)$$

with

$$M_1 = (2.365)^2\pi + 2^{3/2}\alpha^3, \quad M_2 = (2.365)^2\pi + \alpha^2\pi. \quad (3.161)$$

The number $(2.365)^4$ is the smallest eigenvalue of a vibrating rod with displacement ϕ satisfying $\phi(-1) = \phi(1) = \phi'(-1) = \phi'(1) = 0$.

We have

$$I_2^2 \geq (2.365)^4 I_0^2 \quad (3.162)$$

with

$$I_2^2 = \int_{-1}^1 |\phi''|^2 dy, \quad I_{-1}^2 = \int_0^1 |\phi'|^2 dy. \quad (3.163)$$

Figure 3.17 compares the bound given by Joseph (1968) to the exact solution.

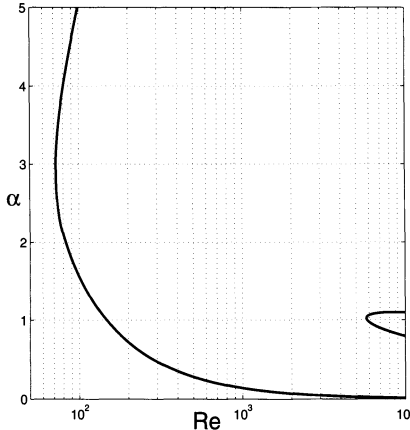


FIGURE 3.17. Bound on the critical Reynolds number for plane Poiseuille flow (left) according to Joseph (1968) and exact result (right).

3.3.5 Dispersive Effects and Wave Packets

The method of steepest descent

As in the inviscid case analyzed in Chapter 2, the discrete eigenmodes will represent dispersion that can be analyzed by using the method of steepest descent – a generalization to complex frequencies of the method of stationary phase used in Chapter 2. In addition, some approximations and extensions of the steepest descent solutions will be discussed in this section.

For large times, one can assume that all higher eigenmodes of the Orr-Sommerfeld equation (3.14) are exponentially small in comparison to the least-stable mode, in which case the form of v (in physical space) is given by the Fourier inversion integral

$$v(x, y, z, t) = \frac{1}{4\pi^2} \int_{\alpha} \int_{\beta} \tilde{v}(y; \alpha, \beta) e^{\Psi t} d\alpha d\beta \quad (3.164)$$

where the phase Ψ is defined

$$\Psi t = i(\alpha \frac{x}{t} + \beta \frac{z}{t} - \omega)t. \quad (3.165)$$

In the above expression \tilde{v} is the least-stable eigenmode of the Orr-Sommerfeld equation for each value of (α, β) and $\omega = \omega(\alpha, \beta)$ is the dispersion relation.

We can evaluate the integral in (3.164) using the method of steepest descent, where we expand the integrand about the stationary point of Ψ , in the same manner as was done for the method of stationary phase. The only

difference is that the stationary point of the phase function Ψ in general now occurs for complex values of α . The stationary points are defined by the two conditions

$$c_{gx} = \frac{\partial \omega^S}{\partial \alpha} = \frac{x}{t} \quad (3.166)$$

$$c_{gz} = \frac{\partial \omega^S}{\partial \beta} = \frac{z}{t}. \quad (3.167)$$

Here c_{gx} and c_{gz} are the components of the group velocity in the x - and z -directions, respectively, and a superscript S denotes evaluation at the stationary point (α^S, β^S) . Again, α^S and β^S may be complex-valued and are defined by the above relations such that the group velocity is real. The interpretation of this result is that an observer moving along the rays defined by the group velocity will follow waves with a wave number vector equal to the real part of (α^S, β^S) .

Expanding Ψ about the stationary point and evaluating the integral in (3.164) gives the following result (see Gaster, 1975)

$$v = \frac{\tilde{v}(y; \alpha^S, \beta^S) \exp(\Psi^S t)}{2\pi i t \sqrt{\left| \frac{\partial^2 \omega^S}{\partial \alpha^2} \frac{\partial^2 \omega^S}{\partial \beta^2} - \left(\frac{\partial^2 \omega^S}{\partial \alpha \partial \beta} \right)^2 \right|}} \quad (3.168)$$

where

$$\Psi^S t = i \left(\alpha^S \frac{x}{t} + \beta^S \frac{z}{t} - \omega(\alpha^S, \beta^S) \right) t. \quad (3.169)$$

This result is valid along the corresponding group velocity ray and describes a three-dimensional wave packet that propagates in both the streamwise and spanwise directions. The exponential growth of the disturbance is given by the imaginary part of the phase, $\text{Im}(\Psi^S)t$, and has the form

$$\text{Im}(\Psi^S)t = \text{Im}(\omega^S)t - \text{Im}(\alpha^S)x - \text{Im}(\beta^S)z \quad (3.170)$$

$$= (\text{Im}(\omega^S) - \text{Im}(\alpha^S)c_{gx} - \text{Im}(\beta^S)c_{gz})t \quad (3.171)$$

which may be interpreted as a combination of both spatial and temporal growth.

The real axis approximation

If the stationary point (α^S, β^S) has a small imaginary part one may approximate the steepest descent solution by expanding the phase (3.165)

around a nearby point with a real wave number vector, say (α^R, β^R) . This will make the group velocity as it is defined in (3.166), (3.167) complex-valued. In the real axis approximation one neglects the imaginary part of the group velocity, instead using the definition

$$c_{gx} = \frac{\partial \omega_r^R}{\partial \alpha} = \frac{x}{t} \quad (3.172)$$

$$c_{gz} = \frac{\partial \omega_r^R}{\partial \beta} = \frac{z}{t} \quad (3.173)$$

where ω_r is the real part of the dispersion relation. Using this definition the phase at the new stationary point is denoted

$$\Psi^R t = i(\alpha^R \frac{x}{t} + \beta^R \frac{z}{t} - \omega^R) t \quad (3.174)$$

where the superscript R denotes evaluation at (α^R, β^R) . One may proceed to evaluate the integral in (3.164) by the method of stationary phase. The result is similar to (3.168) except that all quantities are evaluated at the approximate stationary point (α^R, β^R) .

To analyze the error made in the real axis approximation we let ϵ be a small parameter and assume that the following holds

$$\alpha^S - \alpha^R = \mathcal{O}(\epsilon) \quad \beta^S - \beta^R = \mathcal{O}(\epsilon) \quad (3.175)$$

which implies that the stationary point is close to the real axis. If we further assume that the group velocity is the same for the two cases it is straightforward to show that the error in the phase using the real axis approximation is $\mathcal{O}(\epsilon^2)$, i.e.,

$$\Psi^S t = [\Psi^R + \mathcal{O}(\epsilon^2)] t \quad (3.176)$$

Thus if $t = \mathcal{O}(1/\epsilon)$ or smaller the error in the approximation is negligible and the real axis approximation may be used. One has to be careful, however, because the solution (3.168) is an asymptotic result and formally valid only as $t \rightarrow \infty$. The quantitative usefulness of the approximate solution for finite values of t and ϵ must thus be experimentally verified, as is the case with all asymptotic results. Gaster (1982b) showed that the errors may indeed be large in the real axis approximation when t exceeds $\mathcal{O}(1/\epsilon)$.

4

The Viscous Initial Value Problem

4.1 The Viscous Initial Value Problem

4.1.1 Motivation

This chapter will reexamine the equations governing the evolution of small disturbances in a viscous fluid. The emphasis will be different, though. Rather than concentrating on the eigenvalue problem, we will investigate the equations in the form of an initial value problem. What may seem to be merely a question of formalism or notation will turn out to have significant implications on the way we characterize the behavior of infinitesimal disturbances and the tools we use to study them.

To motivate the approach taken in this chapter, we will first draw our attention to a small model problem that will illustrate the principal differences between the initial value and eigenvalue approach (see also Appendix D). Let us study the evolution problem

$$\frac{d}{dt} \begin{pmatrix} v \\ \eta \end{pmatrix} = \begin{pmatrix} -\frac{1}{Re} & 0 \\ 1 & -\frac{2}{Re} \end{pmatrix} \begin{pmatrix} v \\ \eta \end{pmatrix} \quad (4.1)$$

with initial conditions $v(0) = v_0$ and $\eta(0) = \eta_0$. This system of equations strongly resembles the structure of the Orr-Sommerfeld and Squire equations. The important feature in this system is the off-diagonal term in the matrix, indicating that the evolution equation for η is driven by v .

System (4.1) can be solved exactly and the general solution is given as

$$\begin{pmatrix} v \\ \eta \end{pmatrix} = v_0 \begin{pmatrix} 1 \\ \text{Re} \end{pmatrix} \exp[-t/\text{Re}] + (\eta_0 - v_0 \text{Re}) \begin{pmatrix} 0 \\ 1 \end{pmatrix} \exp[-2t/\text{Re}] \quad (4.2)$$

using the eigenvalues and eigenvectors of the evolution matrix.

Judging from the eigenvalues $\{-1/\text{Re}, -2/\text{Re}\}$ alone, one may be tempted to conclude that both v and η are decaying exponentially because both terms on the right-hand side of (4.2) exhibit exponential decay. While this is certainly true for the v -component, for η we have to be more careful. Looking at the η -variable separately, we have

$$\eta(t) = \eta_0 \exp[-2t/\text{Re}] + \text{Re } v_0 (\exp[-t/\text{Re}] - \exp[-2t/\text{Re}]). \quad (4.3)$$

The first term on the right-hand side describes the evolution of the initial condition η_0 in time, and the second term represents the response in η to the driving by v . This second term can be expanded for small times by replacing the exponentials by their respective Taylor series. We obtain

$$\begin{aligned} \text{Re } v_0 (\exp[-t/\text{Re}] - \exp[-2t/\text{Re}]) \\ &= v_0 \text{Re} \left(-\frac{t}{\text{Re}} + \frac{t^2}{\text{Re}^2} - \dots + \frac{2t}{\text{Re}} - \frac{4t^2}{\text{Re}^2} + \dots \right) \\ &= v_0 t - \frac{3v_0}{\text{Re}} t^2 + \dots \end{aligned} \quad (4.4)$$

which shows that for small times $t < \mathcal{O}(\text{Re})$ the η -component can experience algebraic growth. This example demonstrates that the superposition of two decaying exponentials in the preceding way can generate short-time algebraic growth in time. This phenomenon – as will be analyzed in detail in later sections of this chapter – is caused by the nonorthogonality of the eigenvectors. A closer look at the normalized eigenvectors

$$\frac{1}{\sqrt{1 + \text{Re}^2}} \begin{pmatrix} 1 \\ \text{Re} \end{pmatrix} \quad \begin{pmatrix} 0 \\ 1 \end{pmatrix} \quad (4.5)$$

reveals that as Re increases the two eigenvectors approach each other. In other words, the scalar product of the two eigenvectors approaches one as $\text{Re} \rightarrow \infty$, making the angle ϕ between the eigenvectors tend to zero:

$$\cos \phi = \frac{\text{Re}}{\sqrt{1 + \text{Re}^2}} \quad \lim_{\text{Re} \rightarrow \infty} \phi = 0. \quad (4.6)$$

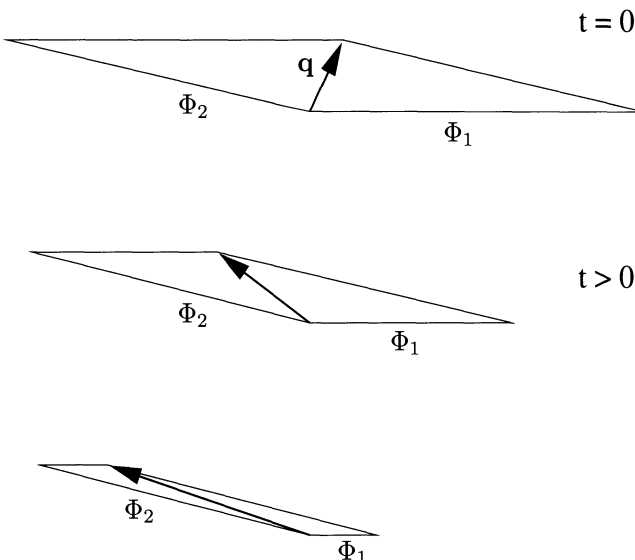


FIGURE 4.1. Sketch illustrating transient growth due to nonorthogonal superposition of two vectors that decay at different rates as time evolves.

A geometric view may illustrate this behavior more clearly. Let the two eigenfunctions be represented by the two vectors Φ_1 and Φ_2 in Figure 4.1. A general initial condition q is then expressed as a nonorthogonal superposition of the two eigenvectors. The solution at all times is geometrically represented by the diagonal of the parallelogram. While each side of the parallelogram decreases exponentially according to its respective eigenvalue, the diagonal increases in length before it decays exponentially according to the larger of the two eigenvalues.

It is thus clear that in the description of the dynamics of general initial conditions, eigenvectors (specifically the angle between them) are as important as eigenvalues. A spectral analysis, i.e., a study of the eigenvalues only, cannot capture the full dynamics of the system of equations in this case.

It is the objective of this chapter to analyze the viscous initial value problem as to its potential to exhibit transient algebraic growth and to introduce tools to detect and quantify short-time behavior. This transient behavior will be identified as the viscous version of the algebraic instability (see equation (2.119)) discussed in Chapter 2.

4.1.2 Derivation of the Disturbance Equations

The derivation of the disturbance equation follows the same path as outlined in Chapter 3. We exploit the homogeneous nature of the streamwise and spanwise coordinate directions by assuming solutions of the form

$$v(x, y, z, t) = \hat{v}(y, t) e^{i(\alpha x + \beta z)} \quad (4.7)$$

$$\eta(x, y, z, t) = \hat{\eta}(y, t) e^{i(\alpha x + \beta z)}. \quad (4.8)$$

Contrary to Chapter 3, we do not assume an exponential time-dependence, which leaves us with the following pair of equations for \hat{v} and $\hat{\eta}$

$$\left[\left(\frac{\partial}{\partial t} + i\alpha U \right) (\mathcal{D}^2 - k^2) - i\alpha U'' - \frac{1}{Re} (\mathcal{D}^2 - k^2)^2 \right] \hat{v} = 0 \quad (4.9)$$

$$\left[\left(\frac{\partial}{\partial t} + i\alpha U \right) - \frac{1}{Re} (\mathcal{D}^2 - k^2) \right] \hat{\eta} = -i\beta U' \hat{v} \quad (4.10)$$

with boundary conditions

$$\hat{v} = \mathcal{D}\hat{v} = \hat{\eta} = 0 \quad (4.11)$$

at solid walls and/or the far field.

As before, the horizontal velocities, \hat{u} and \hat{w} , can be recovered from the normal velocity \hat{v} and normal vorticity $\hat{\eta}$ according to

$$\hat{u} = \frac{i}{k^2} (\alpha \mathcal{D}\hat{v} - \beta \hat{\eta}) \quad (4.12)$$

$$\hat{w} = \frac{i}{k^2} (\beta \mathcal{D}\hat{v} + \alpha \hat{\eta}). \quad (4.13)$$

The evolution of \hat{v} is described by the homogeneous equation (4.9) with homogeneous boundary conditions and can be determined once the initial data are given. In contrast, the equation for $\hat{\eta}$ is inhomogeneous, where the spanwise variation of \hat{v} and the mean shear combine in the forcing term. Because (4.10) is the linearized form of the evolution equation for normal vorticity, and because the forcing term stems from the linearized vortex tilting term, it may be appropriate to denote the forcing mechanism as vortex tilting. In the chapter on inviscid disturbance development (Chapter 2) it was this effect that gave rise to an algebraic instability (see equation (2.119)).

4.1.3 Disturbance Measure

In order to quantify the size of a disturbance we need to introduce a disturbance measure. A natural choice is the kinetic energy of the perturbation.

Using Parseval's equality, (4.12), and (4.13), the kinetic energy can be written in terms of the Fourier coefficients of the disturbance variables as follows (Gustavsson, 1986):

$$\begin{aligned} E_V &= \int_{\alpha} \int_{\beta} E \, d\alpha \, d\beta \\ &= \int_{\alpha} \int_{\beta} \frac{1}{2k^2} \int_{-1}^1 (|\mathcal{D}\hat{v}|^2 + k^2|\hat{v}|^2 + |\hat{\eta}|^2) \, dy \, d\alpha \, d\beta \end{aligned} \quad (4.14)$$

where E is the energy density in Fourier space.

The energy measure can be related to the weighted inner product derived in Section 3.3.1. We have

$$E = \frac{1}{2k^2} \int_{-1}^1 \begin{pmatrix} \hat{v} \\ \hat{\eta} \end{pmatrix}^H \begin{pmatrix} k^2 - \mathcal{D}^2 & 0 \\ 0 & 1 \end{pmatrix} \begin{pmatrix} \hat{v} \\ \hat{\eta} \end{pmatrix} \, dy. \quad (4.15)$$

4.2 The Forced Squire Equation and Transient Growth

4.2.1 Eigenfunction Expansion

The viscous solution

In addition to the dispersive effects discussed in the previous sections, the viscous initial value problem allows for the possibility of initial transient growth that, in many cases, overshadows the asymptotic behavior predicted by the eigenmodes. The most striking example is the viscous counterpart of the inviscid algebraic instability. For simplicity we assume that only the l th Orr-Sommerfeld mode is excited initially. We then have the following solution for the normal velocity

$$\hat{v} = \tilde{v}_l e^{-i\alpha c_l t} \quad (4.16)$$

after which we solve the equation for the normal vorticity (4.10) using (4.16) on the right-hand side. The solution consists of a homogeneous and a particular solution, which is given in the following form

$$\hat{\eta} = \hat{\eta}_{hom} + \tilde{\eta}_l^p e^{-i\alpha c_l t} \quad (4.17)$$

where the time dependence of the particular solution has been written in explicit form. In order to solve for $\hat{\eta}_{hom}$ and $\tilde{\eta}_l^p$ we assume that both

can be expanded in the eigenmodes of the homogeneous part of the normal vorticity equation, i.e., in Squire modes. For the homogeneous part we have the expansion

$$\hat{\eta}_{hom} = \sum_j C_j \tilde{\eta}_j e^{-i\alpha\sigma_j t} \quad (4.18)$$

where C_j are the expansion coefficients and $\tilde{\eta}_j$ are the Squire modes corresponding to the eigenvalues of the Squire equation, σ_j . For the particular vorticity $\tilde{\eta}_l^p$ we assume a similar expansion as (4.18) without the exponential time dependence. When these expansions are substituted into equation (4.10) the following expression for the normal vorticity results

$$\hat{\eta} = \sum_j C_j \tilde{\eta}_j e^{-i\alpha\sigma_j t} + \sum_l D_{jl} \frac{e^{-i\alpha c_l t} - e^{-i\alpha\sigma_j t}}{\alpha c_l - \alpha\sigma_j} \quad (4.19)$$

where the expansion coefficients are

$$C_j = \int_{-1}^1 \hat{\eta}_0 \tilde{\eta}_j dy \quad (4.20)$$

$$D_{jl} = \beta \int_{-1}^1 U' \tilde{v}_l \tilde{\eta}_j dy. \quad (4.21)$$

These expressions are equivalent to the solution that can be derived using Laplace transform techniques.

The inviscid limit

To illustrate the connection to the inviscid case we can consider finite times and assume that the Reynolds number tends to infinity. For $\alpha \rightarrow 0$ we find that

$$\omega_l^{OS} = \alpha c_l = -i\mu_l/\text{Re} \quad (4.22)$$

$$\omega_j^{SQ} = \alpha\sigma_j = -i\nu_j/\text{Re} \quad (4.23)$$

where μ_l and ν_j are both positive quantities of order one, defined in terms of integrals over the eigenfunctions. These expressions can be derived in the same manner as was used to prove the theorem on the stability of the Squire modes (3.24): One multiplies the equations with their respective complex conjugates, integrates over the domain and uses integration by parts.

Expressions (4.22) and (4.23) show that the angular frequencies for these waves are inversely proportional to the Reynolds number and that they

coalesce as the Reynolds number approaches infinity. If these expressions are substituted into (4.21) and the exponents are Taylor expanded for small t/Re we find

$$\begin{aligned}\hat{\eta} = & \sum_j C_j \tilde{\eta}_j \left[1 - \nu_j t/\text{Re} + \mathcal{O} \left(\frac{t^2}{\text{Re}^2} \right) \right] \\ & - \sum_j i D_{jl} \tilde{\eta}_j t \left[1 - (\nu_l + \mu_j) \frac{t}{2\text{Re}} + \mathcal{O} \left(\frac{t^2}{\text{Re}^2} \right) \right].\end{aligned}\quad (4.24)$$

The $\mathcal{O}(1)$ terms in the series can be summed. We find

$$\hat{\eta} = \hat{\eta}_0 - i\beta U' \hat{v}_0 t + \mathcal{O} \left(\frac{t}{\text{Re}} \right) \quad (4.25)$$

which demonstrates that the limit of the viscous solution (4.19) as the Reynolds number approaches infinity for $\alpha = 0$ is identical to the inviscid algebraic instability (see equation (2.119)).

4.2.2 Blasius Boundary Layer Flow

A similar result is obtained in boundary layers for perturbations with zero streamwise dependence, i.e., $\alpha = 0$. For this case, the governing equation for the streamwise disturbance velocity is

$$\frac{\partial u}{\partial t} - \frac{1}{\text{Re}} \left(\frac{\partial^2}{\partial y^2} + \frac{\partial^2}{\partial z^2} \right) u = -U' v. \quad (4.26)$$

For small times, $t/\text{Re} \ll 1$, it can be shown by Fourier-Laplace transform methods that the vertical velocity v remains constant

$$v(y, z, t) = v_0(y, z) + \mathcal{O}(t/\text{Re}). \quad (4.27)$$

The streamwise velocity component can then be obtained as the solution to a forced diffusion equation. For small times $t/\text{Re} \ll 1$, application of standard asymptotic techniques (see Hultgren & Gustavsson, 1981) gives

$$\begin{aligned}u(y, z, t) \sim & u_0(y, z) + \mathcal{O}(t/\text{Re}) \\ & - \int_0^t \left[v U' + \frac{\tau}{\text{Re}} \left(\frac{\partial^2}{\partial y^2} + \frac{\partial^2}{\partial z^2} \right) v U' \right] d\tau.\end{aligned}\quad (4.28)$$

We focus our attention on the first term in the integrand because it leads to algebraic growth in time

$$u(y, z, t) \sim -v_0(y, z)U't. \quad (4.29)$$

This recovers the inviscid result of Ellingsen & Palm (1975). Their result was derived for bounded flows, but it is valid for semibounded flows as well.

4.3 The Complete Solution to the Initial Value Problem

4.3.1 Continuous Formulation

Eigenfunction expansion

Because the Orr-Sommerfeld and Squire eigenmodes for a bounded flow form a complete set (see Chapter 3) they can be used to express a solution of the three-dimensional initial value problem. The solution to the system (4.9), (4.10) can be written

$$\begin{pmatrix} \hat{v} \\ \hat{\eta} \end{pmatrix} = \sum_l K_l \begin{pmatrix} \tilde{v}_l \\ \tilde{\eta}_l^p \end{pmatrix} e^{-i\omega_l^{OS}t} + \sum_j B_j \begin{pmatrix} 0 \\ \tilde{\eta}_j \end{pmatrix} e^{-i\omega_j^{SQ}t}. \quad (4.30)$$

The expansion coefficients K_l and B_j can be calculated at $t = 0$, using the initial values and the solutions of the adjoint system (3.131). If the energy inner product is formed between the expansion (4.30) and the adjoint Orr-Sommerfeld and Squire modes, using the bi-orthogonality relations derived in Chapter 3, we find

$$\begin{aligned} K_l &= \frac{1}{2k^2} \int_{-1}^1 \begin{pmatrix} \tilde{\xi}_l \\ 0 \end{pmatrix}^H \begin{pmatrix} k^2 - \mathcal{D}^2 & 0 \\ 0 & 1 \end{pmatrix} \begin{pmatrix} \hat{v}_0 \\ \hat{\eta}_0 \end{pmatrix} dy \\ &= \int_{-1}^1 \tilde{\xi}_l^*(k^2 - \mathcal{D}^2) \hat{v}_0 dy \end{aligned} \quad (4.31)$$

$$\begin{aligned} B_j &= \frac{1}{2k^2} \int_{-1}^1 \begin{pmatrix} \tilde{\xi}_j^p \\ \tilde{\zeta}_j \end{pmatrix}^H \begin{pmatrix} k^2 - \mathcal{D}^2 & 0 \\ 0 & 1 \end{pmatrix} \begin{pmatrix} \hat{v}_0 \\ \hat{\eta}_0 \end{pmatrix} dy \\ &= \int_{-1}^1 \left[\tilde{\xi}_j^{p*}(k^2 - \mathcal{D}^2) \hat{v}_0 + \tilde{\zeta}_j^* \hat{\eta}_0 \right] dy. \end{aligned} \quad (4.32)$$

The coefficients B_j for the Squire modes are dependent on the initial normal velocity. This is a consequence of the forcing term in equation (4.10) and represents the lift-up effect in terms of a modal decomposition. The potential for growth can be seen directly from equation (4.30). Suppose that we expand an initial condition with zero normal vorticity. This will

excite a number of Orr-Sommerfeld modes to represent the initial normal velocity. Each Orr-Sommerfeld mode has an associated particular normal vorticity η_j^p , which now needs to be cancelled by an appropriate combination of Squire modes. Thus both Orr-Sommerfeld and Squire modes are excited by an initial condition of zero normal vorticity. As the disturbance evolves downstream, each mode evolves in time according to its eigenvalue. Because the phase speeds and decay rates are different the modes will propagate apart and the cancellation that was enforced for $t = 0$ will not persist. Consequently, the disturbance will experience transient growth in the normal vorticity component. It is worth noting that the particular normal vorticity in an Orr-Sommerfeld mode is typically orders of magnitude larger than the normal velocity, as can be seen from the large off-diagonal term (proportional to βRe) in the second component of the system (3.28). This large particular vorticity needs to be cancelled out by Squire-modes, thus generating large expansion coefficients B_j . As time evolves we observe large transient growth in the vorticity.

It is not difficult to show that the normal vorticity part of (4.30) is equivalent to expression (4.19). This can be seen if the particular adjoint normal velocity and the particular normal vorticity are expanded in eigenmodes of their respective homogeneous operators.

Treatment of the continuous spectrum

In the case of semibounded flows, for example, Blasius boundary layer flow, the spectrum consists of both a discrete and a continuous part. In this case, special care has to be taken when expanding arbitrary disturbances in terms of eigenfunctions. Following Salwen & Grosch (1981), we expand a perturbation as follows:

$$\mathbf{q}(y, t) = \sum_{j=1}^N \kappa_j(t) \tilde{\mathbf{q}}_j(y) + \int_0^\infty \kappa(t; s) \tilde{\mathbf{q}}(y; s) \, ds. \quad (4.33)$$

The sum represents a linear combination of the N discrete eigenfunctions $\tilde{\mathbf{q}}_j$, whereas the integral is associated with the eigenfunctions $\tilde{\mathbf{q}}(y; s)$ of the continuous spectrum. The number N of discrete eigenfunctions strongly depends on the streamwise and spanwise wave numbers, α and β , as well as the Reynolds number Re , and for certain parameter combinations (e.g., for $\alpha = 0$) may be zero.

To find the expansion coefficients κ_j and $\kappa(s)$ we make use of the bi-orthogonality conditions

$$(\mathbf{M}\tilde{\mathbf{q}}_j, \tilde{\mathbf{q}}_k^+) = \delta_{jk} \quad (4.34)$$

$$(\mathbf{M}\tilde{\mathbf{q}}(s), \tilde{\mathbf{q}}^+(\sigma)) = \delta(s - \sigma) \quad (4.35)$$

with δ_{jk} as the Kronecker symbol and $\delta(s - \sigma)$ as the Dirac delta function. The superscript $+$ denotes the adjoint eigenfunctions. We have assumed that the discrete and continuous eigenfunctions have been normalized to unit length based on the energy inner product. We then obtain

$$\kappa_j(t) = (\mathbf{M}\mathbf{q}, \tilde{\mathbf{q}}_k^+) \quad (4.36)$$

$$\kappa(t; s) = (\mathbf{M}\mathbf{q}, \tilde{\mathbf{q}}^+(s)) \quad (4.37)$$

for the expansion coefficients. In the next section we will introduce an all-discrete formulation that approximates the integral in the preceding expression by a corresponding sum.

4.3.2 Discrete Formulation

Eigenfunction expansion

It will greatly simplify further analysis if we use a discrete approximation of the continuous norm and scalar product associated with the energy. We will also introduce a more compact notation by using the vector quantities defined in Chapter 3.

The linear initial value problem can be written as

$$\mathbf{M} \frac{\partial \mathbf{q}}{\partial t} = \mathbf{L}\mathbf{q} \quad \text{or} \quad \frac{\partial \mathbf{q}}{\partial t} = \mathbf{M}^{-1}\mathbf{L}\mathbf{q} = \mathbf{L}_1\mathbf{q} \quad (4.38)$$

where \mathbf{M} and \mathbf{L} are defined in (3.34), (3.35). Assuming solutions of the form

$$\mathbf{q} = \tilde{\mathbf{q}} \exp(-i\omega t) \quad \omega \in \mathbb{C} \quad (4.39)$$

will transform the initial value problem (4.38) into a generalized eigenvalue problem of the form

$$\mathbf{L}\tilde{\mathbf{q}} = -i\omega\mathbf{M}\tilde{\mathbf{q}}. \quad (4.40)$$

Restricting ourselves to the space \mathbb{S}^N spanned by the first N eigenfunctions of \mathbf{L}_1

$$\mathbb{S}^N = \text{span}\{\tilde{\mathbf{q}}_1, \tilde{\mathbf{q}}_2, \dots, \tilde{\mathbf{q}}_N\} \quad (4.41)$$

and expanding the vector functions $\mathbf{q} \in \mathbb{S}^N$ in the basis $\{\tilde{\mathbf{q}}_1, \dots, \tilde{\mathbf{q}}_N\}$

$$\mathbf{q} = \sum_{n=1}^N \kappa_n(t)\tilde{\mathbf{q}}_n \quad \mathbf{q} \in \mathbb{S}^N \quad (4.42)$$

we can restate the initial value problem (4.38) in a particularly simple form as

$$\frac{d\kappa}{dt} = -i\Lambda\kappa \quad \Lambda \in \mathbb{C}^{N \times N} \quad \kappa \in \mathbb{C}^N \quad (4.43)$$

with

$$\kappa = (\kappa_1, \kappa_2, \dots, \kappa_N)^T \quad \Lambda = \text{diag}\{\omega_1, \omega_2, \dots, \omega_N\}. \quad (4.44)$$

The operator Λ represents the linear evolution operator, \mathbf{L}_1 , projected onto the space \mathbb{S}^N . Henceforth, we can focus our attention on analysis of the initial value problem (4.43) and describe the evolution of infinitesimal disturbances by the expansion coefficients κ_j instead of the state vector \mathbf{q} . It is important to keep in mind that the expansion coefficients κ_j are associated with both Orr-Sommerfeld and Squire modes.

In the preceding expansion we have assumed that we have distinct eigenvalues and eigenvectors. For particularly chosen parameter combinations, we can also encounter degenerate eigenvalues. The mathematical details of degenerate eigenvalues will be dealt with in Appendix B. The following analysis and formulation will also hold for the degenerate case once the proper adjustments (detailed in Appendix B) have been made.

Discrete formulation and the completeness of the eigenfunctions

We have chosen a simplified formulation of the initial value problem that assumes that both the eigenvalues are discrete and the corresponding eigenvectors form a complete set. The first assumption is only true for flows that have bounded domains in the normal direction. For unbounded flows, such as the Blasius boundary layer, we have already seen that the spectrum consists of both a discrete and a continuous part. However, for practical or computational purposes it is often possible to use a discretized approximation of the continuous spectrum when solutions to the initial value problem are sought. An example of a discretized approximation of the continuous spectrum can be found in Figure 3.4(a). Although the eigenvalues of this spectrum differ from the exact representation of the continuous spectrum, particularly as the decay rate increases, their sum has been found to correctly describe the solutions to the initial value problem (by, e.g., Butler & Farrell, 1992). It is possible to formally expand the solution to the initial value problem using integrals over the continuous spectrum, as shown by Gustavsson (1979) and Salwen & Grosch (1981). However, the added computational complexity, without any significant gain in computational accuracy, justifies the use of the current simpler formulation. A note of caution has to be made, however: It is important to verify that the computed results do not depend on the approximation of the continuous spectrum.

This usually means varying the extent of the domain in the normal direction, ensuring that the results are independent of this computational parameter.

The second assumption relates to the possibility of approximating solutions by using the eigenfunctions of the linear operator; this raises the question of completeness of the spectrum. For bounded domains completeness has been proven by Schensted (1961) and DiPrima & Habetler (1969). The proof proceeds in the following fashion. One divides the linear operator \mathbf{L}_1 into the selfadjoint part \mathbf{L}_S and the remaining part \mathbf{B} . It is straightforward to prove that the eigenfunctions of \mathbf{L}_S form an orthogonal set and are complete in the appropriate Hilbert space. It then remains to be shown that the eigenfunctions of the operator $\mathbf{L}_S + \mathbf{B}$ form a complete set. This is accomplished by perturbation theory (the operator \mathbf{B} being a perturbation of the operator \mathbf{L}_S) which introduces additional restrictions on the properties of \mathbf{B} . The results of Gustavsson (1979) show that the discrete modes and the continuous spectrum form a complete representation of the solution to the initial value problem for boundary layer flows.

Inner product and energy norm

To complete the transformation from the vector quantities \mathbf{q} to the expansion coefficients κ , we also have to reformulate the scalar product and its associated norm.

If $\mathbf{q}_1, \mathbf{q}_2 \in \mathbb{S}^N$, it follows from (3.138) that

$$(\mathbf{q}_1, \mathbf{q}_2)_E = \frac{1}{k^2} \int_{-1}^1 \mathbf{q}_2^H \mathbf{M} \mathbf{q}_1 \, dy = \kappa_2^H M \kappa_1 \quad M \in \mathbb{C}^{N \times N} \quad (4.45)$$

where M is the matrix whose elements are given by

$$M_{ij} = (\tilde{\mathbf{q}}_i, \tilde{\mathbf{q}}_j)_E = \frac{1}{k^2} \int_{-1}^1 \tilde{\mathbf{q}}_j^H \mathbf{M} \tilde{\mathbf{q}}_i \, dy. \quad (4.46)$$

We observe that M is both Hermitian and positive definite. We can therefore factor M according to $M = F^H F$. The scalar product $(\cdot, \cdot)_E$ can then be defined as

$$\begin{aligned} (\mathbf{q}_1, \mathbf{q}_2)_E &= \kappa_2^H M \kappa_1 \\ &= \kappa_2^H F^H F \kappa_1 = (F \kappa_1, F \kappa_2)_2 \\ &= (\kappa_1, \kappa_2)_E \end{aligned} \quad (4.47)$$

and its associated vector norm satisfies

$$\|\mathbf{q}\|_E = \|F\kappa\|_2 = \|\kappa\|_E \quad \mathbf{q} \in \mathbb{S}^N \quad (4.48)$$

where

$$\|\mathbf{q}\|_E^2 = (\mathbf{q}, \mathbf{q})_E \quad (4.49)$$

$$\|\kappa\|_E^2 = (\kappa, \kappa)_E. \quad (4.50)$$

For matrices $B \in \mathbb{C}^{N \times N}$, the energy norm is induced by the vector norm according to

$$\begin{aligned} \|B\|_E &= \max_{\mathbf{q}} \frac{\|B\mathbf{q}\|_E}{\|\mathbf{q}\|_E} \\ &= \max_{\mathbf{q}} \frac{\|FB\mathbf{q}\|_2}{\|F\mathbf{q}\|_2} = \max_{\mathbf{q}} \frac{\|FBF^{-1}F\mathbf{q}\|_2}{\|F\mathbf{q}\|_2} \\ &= \|FBF^{-1}\|_2. \end{aligned} \quad (4.51)$$

In what follows we will, if not otherwise stated, use the discrete scalar product and norm based on the energy density and will, therefore, omit the subscript E hereafter.

The adjoint operator

We will also need the representation of the adjoint operator in the space \mathbb{S}^N using the eigenvectors of \mathbf{L}_1 as a basis. We use the standard definition of the adjoint and find

$$\begin{aligned} (\kappa, \Lambda\kappa) &= \kappa^H M \Lambda \kappa = \kappa^H M \Lambda M^{-1} M \kappa \\ &= (M^{-1} \Lambda^H M \kappa)^H M \kappa = (M^{-1} \Lambda^H M \kappa, \kappa). \end{aligned} \quad (4.52)$$

The adjoint of Λ is therefore equal to

$$\Lambda^+ = M^{-1} \Lambda^H M. \quad (4.53)$$

4.4 Optimal Growth

4.4.1 *The Matrix Exponential*

In the previous sections we have introduced a compact notation based on the eigenfunctions of the linear stability operator. We will now return to

the initial value problem and use this notation to develop techniques for the quantitative and qualitative description of transient effects.

The formal solution of the initial value problem can be written as

$$\mathbf{q} = e^{i\mathbf{L}_1 t} \mathbf{q}_0 \quad \mathbf{q}_0 = \mathbf{q}(t = 0). \quad (4.54)$$

which introduces the matrix exponential. A common definition of the matrix exponential is by a Taylor series, i.e.,

$$e^{i\mathbf{L}_1 t} = \mathbf{I} + i\mathbf{L}_1 t - \frac{1}{2}\mathbf{L}_1^2 t^2 + \dots \quad (4.55)$$

The advantages of the discrete formulation introduced in the previous section now become apparent as we solve the temporal evolution problem for the coefficients κ in terms of the matrix exponential.

We assume that $\mathbf{q} \in \mathbb{S}^N$, which allows the solution of the initial value problem

$$\kappa = e^{-it\Lambda} \kappa_0 \quad \kappa_0 = \kappa(t = 0) \quad (4.56)$$

in the simple form

$$e^{-it\Lambda} = \begin{pmatrix} e^{-i\omega_1 t} & & \\ & \ddots & \\ & & e^{-i\omega_N t} \end{pmatrix}. \quad (4.57)$$

This form of the solution can easily be verified by direct substitution into equation (4.43).

4.4.2 Maximum Amplification

Derivation of the result

We have now derived the solution of the complete initial value problem in a simple form. This can be used to consider the development of general solutions, not just single eigenmodes of the system. In particular, we wish to search for initial disturbances that maximize short-term growth. We have already seen that large transient growth can occur when the normal velocity forces the normal vorticity. We will now investigate this issue from a more general point of view.

We define the maximum possible amplification G of initial energy density as

$$\begin{aligned}
G(t) &= \max_{\mathbf{q}_0 \neq 0} \frac{\|\mathbf{q}(t)\|^2}{\|\mathbf{q}_0\|^2} \\
&= \|e^{i\mathbf{L}_1 t}\|^2 \\
&= \max_{\kappa_0 \neq 0} \frac{\|\kappa\|^2}{\|\kappa_0\|^2} \\
&= \|\exp(-it\Lambda)\|^2 \\
&= \|F \exp(-it\Lambda) F^{-1}\|_2^2 \\
&= \sigma_1^2(F \exp(-it\Lambda) F^{-1})
\end{aligned}$$

with σ_1 denoting the principal singular value. Both the continuous and discrete formulation of the problem has been stated, and for the equality to hold we have to assume that $\mathbf{q} \in \mathbb{S}^N$.

It is important to keep in mind that the curve given by $\|\exp(-it\Lambda)\|^2$ represents the maximum possible energy amplification, which for each instant in time is optimized over all possible initial conditions with unit energy norm. The initial condition that optimizes the amplification factor might be different for different times so that $\|\exp(-it\Lambda)\|^2$ should be thought of as the envelope of the energy evolution of individual initial conditions with unit energy norm (see Figure 4.2).

Plane Poiseuille flow

We start by comparing the growth functions $G(t)$ for stable and unstable flows. Figure 4.3(a) plots the growth function for $\alpha = 1, \beta = 0$ for $\text{Re} = 5000$ and $\text{Re} = 8000$. For small values of t , the growth function is qualitatively the same in the two cases. In this transient phase, the behavior of the growth function does not depend on the stability or instability of the flow; the stability of the flow is only revealed as $t \rightarrow \infty$. The least stable eigenvalues govern the behavior of the growth function only for large time. The transient growth for stable flows is a short-time phenomenon compared to the infinite growth for unstable flows. The third curve in Figure 4.3(a) shows the energy of the perturbation velocity \hat{v} when the initial velocity is the normalized eigenfunction associated with the unstable eigenvalue for $\alpha = 1$ and $\text{Re} = 8000$. The unstable mode does not achieve the greatest possible energy growth; the initial condition that achieves the maximum growth is a linear combination of several eigenfunctions.

Let us now examine the maximum growth function $G_{\max} = \max_t G(t)$ for two-dimensional plane Poiseuille flow in the (α, Re) -plane. If there exists an unstable eigenvalue, $G_{\max} = \infty$. This region is indicated by the gray area in Figure 4.3(b). Outside of this region the figure shows contours of G_{\max} . We see that there can be significant transient growth at subcritical Reynolds numbers.

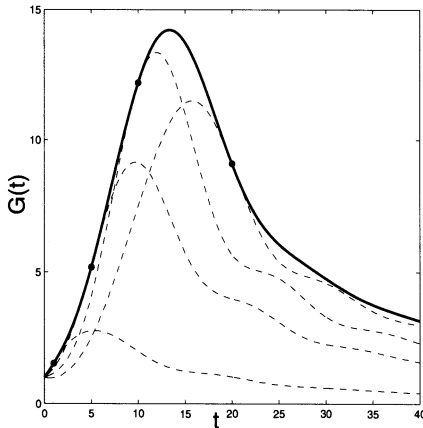


FIGURE 4.2. Amplification $G(t)$ for Poiseuille flow with $\text{Re} = 1000$, $\alpha = 1$ (solid line) and growth curves of selected initial conditions (dashed lines).

Figure 4.4 investigates the dependence of G_{\max} on the streamwise and spanwise wave numbers and shows the level curves of G_{\max} for $\text{Re} = 1000$ in the region where G_{\max} is largest. We find that the optimum of G_{\max} is about 196 and that this growth is achieved for $\alpha = 0$ and $\beta \approx 2.05$. In addition, we find that it occurs at a time of about 76.

Hagen-Poiseuille flow

Pipe flow also exhibits substantial transient growth as reported in an early investigation by Boberg & Brosa (1988). The maximum amplification of initial energy G_{\max} is displayed in Figure 4.5 in the $(\alpha\text{Re}, \text{Re})$ -plane for two different azimuthal wave numbers ($n = 0, 1$).

In the axisymmetric case (Figure 4.5(a)) we observe an increasing value of G_{\max} as αRe becomes larger. A minimum value of $\alpha\text{Re} \approx 369.7$, which has been found to be Reynolds number independent for the values of Re shown in Figure 4.5(a), has to be surpassed in order to experience transient growth. Below this value the energy density exhibits decay for all times. The $G_{\max} = 1$ contour is hence the curve that separates parameter combinations for which transient growth may occur from ones for which energy decay is assured.

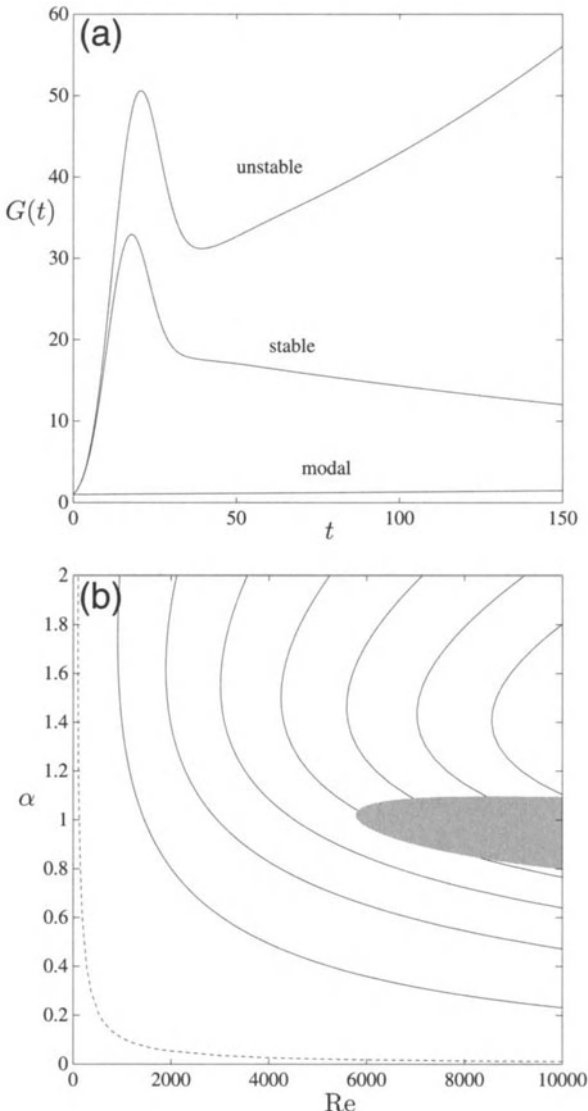


FIGURE 4.3. Level curves of $G_{max}(\alpha, 0, Re)$ for Poiseuille flow (a). The dashed curve corresponds to $G_{max}(\alpha, 0, Re) = 1$. The solid curves, from left to right, correspond to $G_{max}(\alpha, 0, Re) = 10, 20, 30, \dots, 70$. In the shaded region the flow is linearly unstable. Plot of $G(\alpha, 0, Re, t)$ for stable and unstable Poiseuille flow (b). The stable case corresponds to $\alpha = 1$ and $Re = 5000$, and the unstable to $\alpha = 1$ and $Re = 8000$. The curve labeled *modal* is a plot of the perturbation energy in the case that the initial velocity is the normalized eigenfunction corresponding to the unstable eigenvalue for $\alpha = 1$ and $Re = 8000$. From Reddy & Henningson (1993).

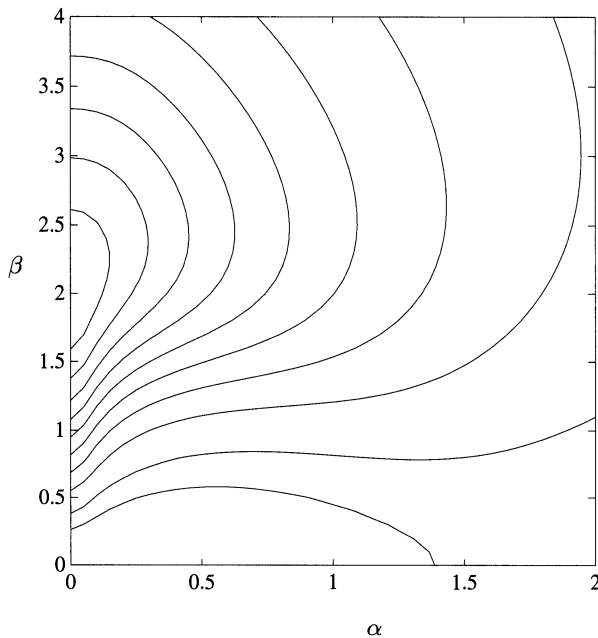


FIGURE 4.4. Contours of G_{max} for Poiseuille flow with $Re = 1000$. The curves from outer to inner correspond to $G_{max} = 10, 20, 40, \dots, 140, 160, 180$. From Reddy & Henningson (1993).

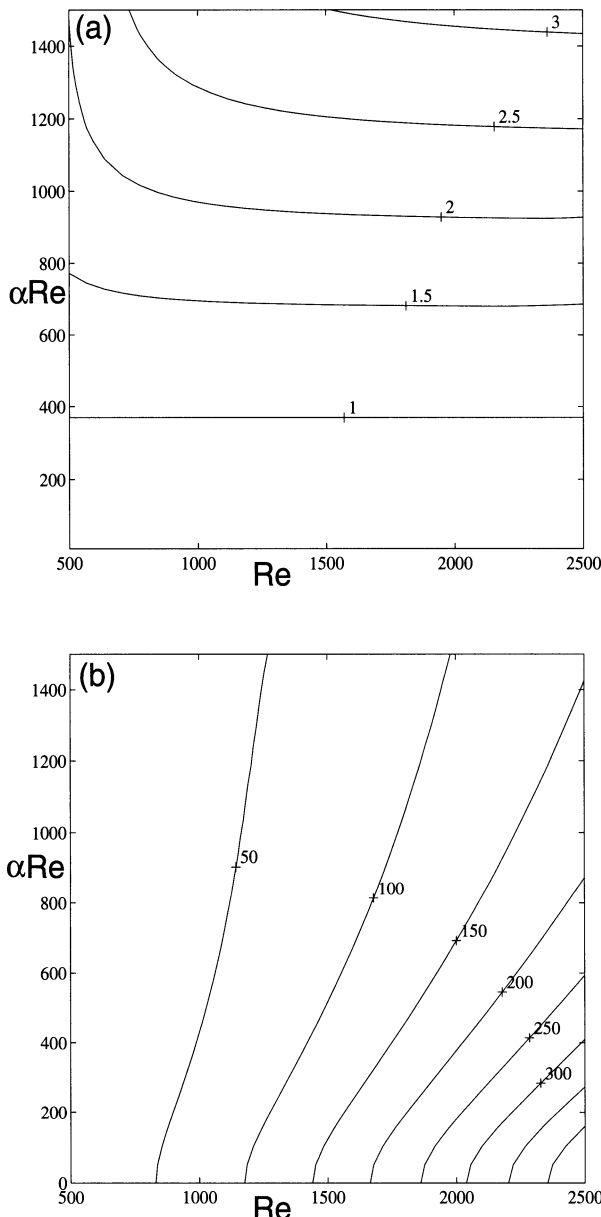


FIGURE 4.5. Contours of maximum transient growth in the αRe - Re -plane for selected azimuthal wavenumbers. (a) Contours of G_{\max} for azimuthal wavenumber $n = 0$, (b) for $n = 1$. From Schmid & Henningson (1994).

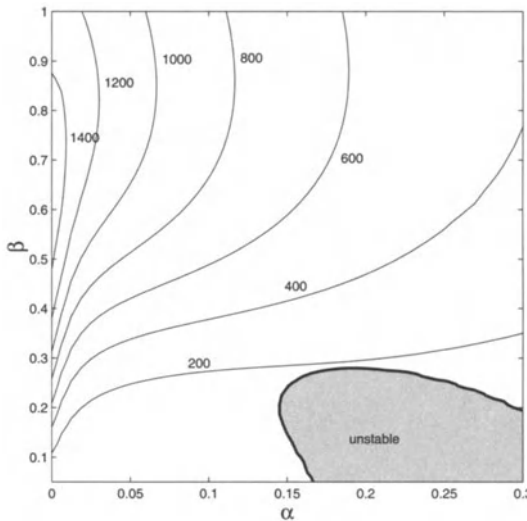


FIGURE 4.6. Contours of maximum transient growth G_{\max} for Blasius boundary layer flow at $Re_\delta = 1000$. From Schmid (2000).

The nonaxisymmetric case (Figure 4.5(b)) differs even qualitatively from the axisymmetric case. It shows that the maximum possible amplification G_{\max} is obtained for disturbances with vanishing streamwise wave numbers.

Similar results were found by Bergström (1993) and O'Sullivan & Breuer (1994).

Blasius boundary layer flow

A contour plot of the maximum amplification G_{\max} as a function of the streamwise and spanwise wave numbers is presented in Figure 4.6 for Blasius boundary layer flow at a Reynolds number, based on the displacement thickness, of 1000. Substantial transient growth is observed for disturbances with no streamwise dependence, i.e., $\alpha = 0$. Two-dimensional disturbances (with $\beta = 0$) exhibit far less transient growth potential. In transition scenarios where the dominant linear energy growth is provided by a nonmodal mechanisms, we should therefore expect to observe structures that are elongated in the streamwise direction.

Figure 4.6 has been computed using an eigenfunction expansion in discrete and (discretized) continuous modes. Alternatively, one may use a technique based on the regular and adjoint initial value problem which avoids any modal representation; see Corbett & Bottaro (2000b) or Section 6.4.2 for details.

4.4.3 Optimal Disturbances

It is not difficult to determine the initial condition that will reach the maximum possible amplification at a given time t_0 and will be tangent to $\|\exp(-it\Lambda)\|$ at t_0 . The procedure is best understood in terms of the singular value decomposition (SVD).

Let us denote the (yet unknown) initial condition that will constitute the perturbation with the maximum possible amplification at a time t_0 by \mathbf{q}_0 . Assuming the initial condition has unit energy norm, it will have an energy of $\|F \exp(-it_0\Lambda) F^{-1}\|$ at a later time t_0 because it has been chosen to be the optimal perturbation at this specific time. We therefore have the equation

$$B\kappa_0 = \mu\kappa_{t_0} \quad (4.58)$$

with

$$B = F \exp(-it_0\Lambda) F^{-1} \quad \mu = \|B\| \quad (4.59)$$

and κ_{t_0} denoting the normalized perturbation after it evolved t_0 time units. Realizing that μ is equal to the largest singular value of B , we can solve for the optimal initial condition κ_0 (and the perturbation κ_{t_0}) by decomposing the matrix B into

$$BV = U\Sigma \quad (4.60)$$

where V and U are unitary matrices and Σ is a diagonal matrix consisting of the singular values, $\Sigma = \text{diag}\{\sigma_1, \dots, \sigma_N\}$, $\sigma_j \in \mathbb{R}_0^+$, which are ordered in size, i.e., $\sigma_1 \geq \sigma_2 \geq \dots \geq \sigma_N$.

The 2-norm of B , equivalent to the energy norm of $\exp(-it\Lambda)$, is given by the largest singular value σ_1 . Concentrating only on the column vectors of V and U corresponding to σ_1 , which are referred to as the principal right and left singular vectors respectively, one obtains

$$Bv_1 = \sigma_1 u_1. \quad (4.61)$$

This describes a mapping B of an input vector v_1 onto an output vector u_1 that is also stretched by a factor of σ_1 equal to the 2-norm of B . Therefore, v_1 describes the initial condition that will be amplified by a factor of $\sigma_1 = \|B\|_2$ due to the mapping $F \exp(-it_0\Lambda) F^{-1}$ where t_0 is the time at which this amplification will be reached. To extract the optimal initial condition \mathbf{q}_0 we have to express it in the basis $\{\tilde{\mathbf{q}}_1, \dots, \tilde{\mathbf{q}}_N\}$ with the coefficients given by the N components of the principal vector v_1 . The square of the largest singular value of B is equivalent to the largest eigenvalue of $B^H B$ and the

principal singular vector v_1 of B corresponds to the principal eigenvector of $B^H B$.

An alternative method to compute optimal disturbances is based on the calculus of variations (see Butler & Farrell, 1992) and another one uses repeated integrations of the regular and adjoint equations in a power iteration procedure (see Andersson *et al.* (1997), Luchini (2000), Corbett & Bottaro (2000b)).

It should be noted that the initial condition κ_1 may reach higher energies after t_0 , but at time t_0 it will be the initial disturbance among all unit energy initial disturbances that will reach the maximum possible energy amplification. The phrase “maximum possible amplification at t_0 ” is thus an optimization over initial conditions with unit energy norm rather than an optimization over time.

Optimal disturbances for plane Poiseuille flow are displayed in Figure 4.7. The top two figures show the two-dimensional optimal disturbance and the perturbation after $t = t_{\max}$ time units with $G(t_{\max}) = G_{\max}$. The initial disturbance is characterized by flow patterns that oppose the mean shear. As time evolves the disturbance will tilt into the mean shear direction thus causing transient growth of energy. This mechanism is often associated with the inviscid Orr mechanism (Orr, 1907) which describes short-term instabilities due to the tilting of initial disturbances into the direction of the mean shear. The lower two figures depict the optimal disturbance for $\alpha = 0$ and $\beta = 2$ for $t = 0$ and $t = t_{\max}$. Streamwise vortices are observed that change little as time evolves. However, high-energy streaks will form due to the lift-up effect.

4.4.4 Reynolds Number Dependence of Optimal Growth

Scaling laws for optimal growth

To get a complete understanding of the behavior of $G_{\max}(\alpha, \beta, \text{Re})$ it is necessary to compute the growth throughout the three-dimensional $(\alpha, \beta, \text{Re})$ parameter space. This approach is computationally expensive. We can get a better understanding of the behavior of $G_{\max}(\alpha, \beta, \text{Re})$ for small αRe by employing a scaling used by Gustavsson (1991) in his analysis of the growth of the vorticity.

Let us define

$$\bar{t} = t/\text{Re}, \quad \bar{\eta}(y, \bar{t}) = \hat{\eta}(y, t/\text{Re})/\beta\text{Re}, \quad \bar{v}(y, \bar{t}) = \hat{v}(y, t/\text{Re}). \quad (4.62)$$

Then we have $\bar{\mathbf{q}}(y, t/\text{Re}) = [\bar{v}(y, \bar{t}) \quad \beta\text{Re}\bar{\eta}(y, \bar{t})]^T$. The evolution equations for \bar{v} and $\bar{\eta}$ can be put into a vector form similar to (4.38). We have

$$\mathbf{M} \frac{\partial \bar{\mathbf{q}}}{\partial \bar{t}} = \bar{\mathbf{L}} \bar{\mathbf{q}} \quad \text{or} \quad \frac{\partial \bar{\mathbf{q}}}{\partial \bar{t}} = \bar{\mathbf{L}}_1 \bar{\mathbf{q}} \quad (4.63)$$

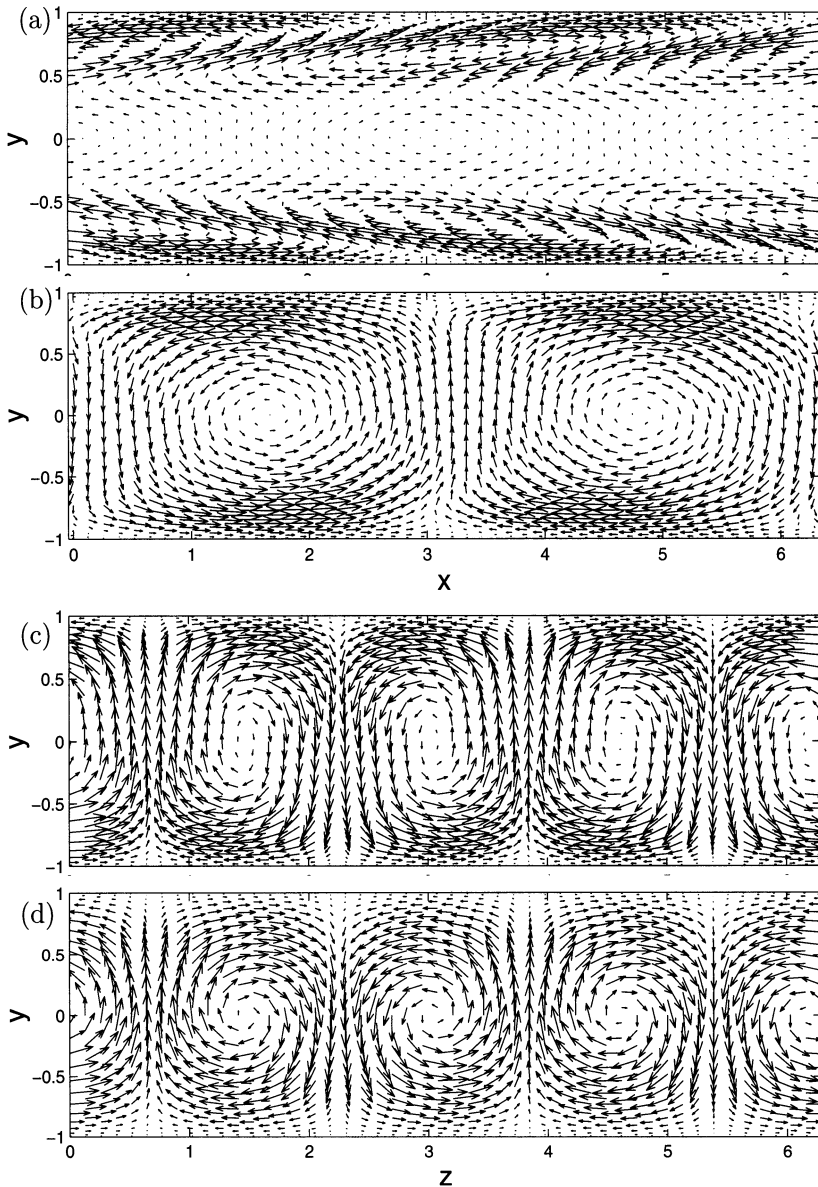


FIGURE 4.7. Optimal disturbances for plane Poiseuille flow. (a,b) Two-dimensional optimal initial condition for $\alpha = 1$, $Re = 1000$, and at time $t = t_{\max}$; (c,d) three-dimensional optimal initial condition for $\alpha = 0$, $\beta = 2$, $Re = 1000$, and at time $t = t_{\max}$.

where $\bar{\mathbf{L}}_1 = \mathbf{M}^{-1}\bar{\mathbf{L}}$ and

$$\bar{\mathbf{L}} = \begin{pmatrix} -\alpha \text{Re}U(k^2 - \mathcal{D}^2) + \alpha \text{Re}U'' - i(k^2 - \mathcal{D}^2)^2 & 0 \\ U' & \alpha \text{Re}U - i(k^2 - \mathcal{D}^2) \end{pmatrix}. \quad (4.64)$$

The advantage of the scaling is that the operator $\bar{\mathbf{L}}_1$ depends on only two parameters: $k^2 = \alpha^2 + \beta^2$ and αRe . The energy $E(\bar{t})$ of the perturbation $(\bar{v} \ \bar{\eta})^T$ in the new variables is given by

$$\begin{aligned} E(\bar{t}) &= E_v(\bar{t}) + \beta^2 \text{Re}^2 E_\eta(\bar{t}) \\ &= \int_{-1}^1 (|\mathcal{D}\bar{v}|^2 + k^2 |\bar{v}|^2) dy + \beta^2 \text{Re}^2 \int_1^1 |\bar{\eta}|^2 dy. \end{aligned} \quad (4.65)$$

Here, E_v and $\beta^2 \text{Re}^2 E_\eta$ are the energies in the velocity and normal vorticity, respectively.

The advantage of the new formulation is not clear at this point because of the reappearance of a third parameter, βRe , in (4.65). To motivate the scaling let us consider growth for Poiseuille flow with $\alpha = 0$ and $\beta = \mathcal{O}(1)$. As shown in the previous subsection, the maximum growth can be quite large for these parameters. The large growth is due entirely to the forcing of the normal vorticity by the velocity, because all of the individual eigenmodes decay for these parameter values.

This implies that to achieve a large energy growth the initial perturbation $(\bar{v}(y, 0) \ \bar{\eta}(y, 0))^T$ should be chosen so that most of the initial energy is in the velocity

$$E_v(0) \gg \beta^2 \text{Re}^2 E_\eta(0). \quad (4.66)$$

Let \bar{t}_{\max} denote the time at which the energy of the perturbation has increased by a factor $G_{\max}(0, \beta, \text{Re})$. Because $E_v(\bar{t})$, the energy in the velocity, does not grow, it follows that the perturbation that experiences the maximal energy growth satisfies

$$\beta^2 \text{Re}^2 E_\eta(\bar{t}) \gg E_v(\bar{t}) \quad \text{for } t \approx \bar{t}_{\max}. \quad (4.67)$$

These last inequalities and the definition of the growth function imply

$$G_{\max}(0, \beta, \text{Re}) = \sup_{\hat{v}(y, 0) \neq 0, \bar{t} \geq 0} \frac{E_v(\bar{t}) + \beta^2 \text{Re}^2 E_\eta(\bar{t})}{E_v(0) + \beta^2 \text{Re}^2 E_\eta(0)} \quad (4.68)$$

$$\approx \beta^2 \text{Re}^2 \sup_{\bar{v}(y, 0) \neq 0, \bar{t} \geq 0} \frac{E_\eta(\bar{t})}{E_v(0)}. \quad (4.69)$$

The optimization problem depends on k and αRe . Hence, if the three-dimensional growth is large, we have

$$G_{\max}(\alpha, \beta, \text{Re}) \approx \frac{\beta^2 \text{Re}^2}{k^2} H_2(k, \alpha\text{Re}) \quad (4.70)$$

for some function H_2 . The k^2 term in the denominator ensures that H_2 is nonsingular as $k \rightarrow 0$. Again, (4.70) becomes more accurate as Re increases.

Plane Poiseuille and plane Couette flow

Figure 4.8 verifies (4.70) by plotting the level curves of the expression $k^2 G_{\max}(\alpha, \beta, \text{Re}) / (\beta^2 \text{Re}^2)$ for Couette and Poiseuille flow in the αRe - k plane. Comparing results for the two Reynolds numbers, we see that the scaling relation becomes more accurate as $\alpha\text{Re} \rightarrow 0$.

For Poiseuille flow, $S(\text{Re}) = \sup_{\alpha, \beta} G_{\max}(\alpha, \beta, \text{Re})$ is achieved for a point on the β -axis for $\text{Re} < \text{Re}_{\text{crit}}$, as we saw in the previous subsection. Hence, we can use the scaling relation (4.70). It follows that S scales like Re^2 . We find that

$$S(\text{Re}) \approx 1.96 \times 10^{-4} \text{Re}^2 \quad (4.71)$$

for large subcritical Re . This growth is achieved at $t \approx 0.076\text{Re}$.

For Couette flow, the maximum growth in the α - β plane is achieved near the β -axis. The scaling relation (4.70) and the results in Figure 4.8(a) imply that the largest growth in the α - β plane is achieved for $k \approx C_1$ and $\alpha\text{Re} \approx C_2$, where C_1 and C_2 are constants. If we substitute these constants into (4.70) and use the fact that $\beta^2 = k^2 - \alpha^2$, we find that

$$\frac{\beta^2 \text{Re}^2}{k^2} H_2(k, \alpha\text{Re}) = \text{Re}^2 \left(1 - \frac{C_2^2}{C_1^2 \text{Re}^2}\right) H_2(C_1, C_2). \quad (4.72)$$

Hence, the growth scales like Re^2 as $\text{Re} \rightarrow \infty$. This result verifies the results in Butler & Farrell (1992), where it is shown that

$$S(\text{Re}) \approx 1.18 \times 10^{-3} \text{Re}^2 \quad (4.73)$$

and that the maximum growth occurs at $t \approx 0.117\text{Re}$. We find that $C_1 \approx 1.6$, $C_2 \approx 35$.

Pipe flow

A similar scaling as was shown to hold for the plane channel flows can be used in pipe flow to make an argument for the Re^2 -dependence of the maximum growth (see Schmid & Henningson, 1994).

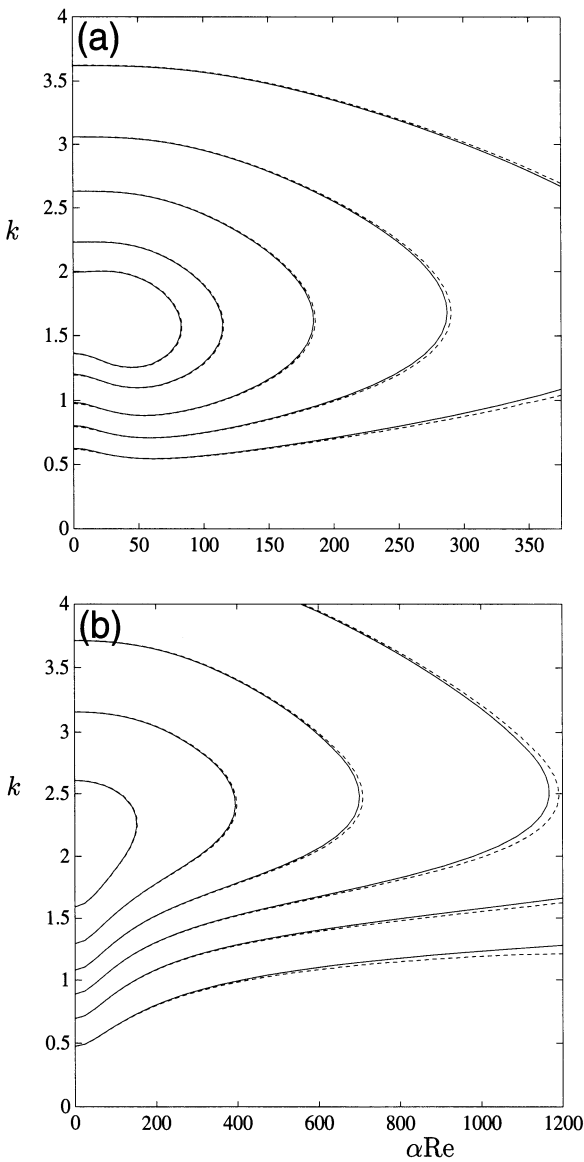


FIGURE 4.8. Contours of $k^2 G_{max}(\alpha, \beta, \text{Re}) / (\beta^2 \text{Re}^2)$. For Couette flow (a), the contours from outer to inner correspond to $0.4, 0.6, 0.8, 1.0, 1.1$ ($\times 10^{-3}$). The dashed and solid contours are for $\text{Re} = 500$ and $\text{Re} = 1000$, respectively. For Poiseuille flow (b), the contours from outer to inner correspond to $0.3, 0.6, 0.9, 1.2, 1.5, 1.8$ ($\times 10^{-4}$). The dashed and solid lines are for $\text{Re} = 1500$ and $\text{Re} = 3000$, respectively. From Reddy & Henningson (1993).

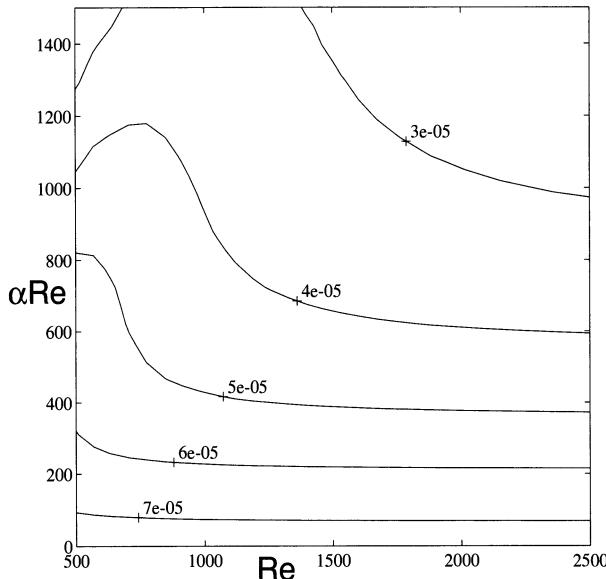


FIGURE 4.9. Contours of the ratio of maximum transient growth to the square of the Reynolds number G_{\max}/Re^2 in the αRe - Re -plane for azimuthal wave number $n = 1$. From Schmid & Henningson (1994).

In Figure 4.9 the ratio of maximum growth G_{\max} and the square of the Reynolds number Re^2 is plotted for pipe flow. A vanishing dependence of this ratio on the Reynolds number for large Re is observed, which implies a quadratic scaling of the maximum energy amplification with the Reynolds number as $Re \rightarrow \infty$. Thus the behavior is similar to that observed for plane Poiseuille and Couette flow.

Summary for wall-bounded shear flow

We summarize the results of the dependence of the optimal growth on the Reynolds number in Table 4.1. It can be seen that independent of the flow

Flow	$G_{\max} (10^{-3})$	t_{\max}	α	β
plane Poiseuille	$0.20 Re^2$	$0.076 Re$	0	2.04
plane Couette	$1.18 Re^2$	$0.117 Re$	$35/Re$	1.6
circular pipe	$0.07 Re^2$	$0.048 Re$	0	1
Blasius boundary layer	$1.50 Re^2$	$0.778 Re$	0	0.65

TABLE 4.1. Reynolds number dependence of G_{\max} and t_{\max} for a number of wall-bounded shear flows. Results for plane Couette and Poiseuille flow from Tre-fethen *et al.* (1993), for pipe flow from Schmid & Henningson (1994) and for boundary layer flow from Butler & Farrell (1992).

the maximum growth occurs at essentially zero streamwise wave number and a spanwise wave number of order one. The maximum growth in energy is of order Re^2 occurring at a time proportional to Re .

It is interesting to note that although these characteristics are so similar, the modal (exponential) stability behavior differs widely, from linearly stable flows such as pipe and plane Couette flows to unstable flows such as plane Poiseuille and Blasius boundary layer flows.

4.5 Optimal Response and Optimal Growth Rate

4.5.1 The Forced Problem and the Resolvent

The solution to the forced problem

Consider the harmonically forced problem with frequency ω

$$\frac{\partial \mathbf{q}}{\partial t} = i\mathbf{L}_1 \mathbf{q} + \mathbf{f} \quad \text{with} \quad \mathbf{f} = \mathbf{q}_f e^{i\omega t} \quad \omega \in \mathbb{R} \quad (4.74)$$

The general solution to this problem consists of a homogeneous and a particular part and reads

$$\mathbf{q}(t) = \exp(it\mathbf{L}_1)\mathbf{q}_0 - i(\mathbf{L}_1 - \omega\mathbf{I})^{-1}\mathbf{q}_f e^{i\omega t} \quad (4.75)$$

which, assuming that the eigenvalues of \mathbf{L}_1 are confined to the stable half-plane, has the asymptotic long-time response

$$\mathbf{q} = -i(\mathbf{L}_1 - \omega\mathbf{I})^{-1}\mathbf{q}_f e^{i\omega t}. \quad (4.76)$$

The quantity $(\mathbf{L}_1 - \omega\mathbf{I})^{-1}$ is known as the resolvent, which we already encountered when studying the sensitivity of eigenvalues.

The solution of the Laplace-transformed problem

The resolvent also appears as the solution of the Laplace-transformed initial value problem

$$s\tilde{\mathbf{q}} - \mathbf{q}_0 = i\mathbf{L}_1 \tilde{\mathbf{q}}. \quad (4.77)$$

Solving for $\tilde{\mathbf{q}}$ we have

$$\tilde{\mathbf{q}} = (\mathbf{L}_1 - s\mathbf{I})^{-1}\mathbf{q}_0. \quad (4.78)$$

Using an expansion of the Laplace-transformed solution in the eigenfunctions of \mathbf{L}_1 and assuming $\mathbf{q} \in \mathbb{S}^N$, we find the following expression

$$\tilde{\mathbf{q}} = \sum_{n=1}^N \frac{-i\kappa_n^f}{s - i\omega_n} \tilde{\mathbf{q}}_n \quad (4.79)$$

where $\kappa_f = \{\kappa_1^f, \kappa_2^f, \dots, \kappa_N^f\}^T$ is the vector of expansion coefficients of \mathbf{q}_f in terms of the eigenvectors of \mathbf{L}_1 . Let κ be the vector of expansion coefficients of the Laplace-transformed solution, the preceding then implies

$$\kappa = (i\Lambda - s\mathbf{I})^{-1} \kappa_f. \quad (4.80)$$

Maximum response from a forcing function

Similarly to defining the maximum growth of an initial condition, we can define the maximum response of the system due to a forcing at a frequency ω according to

$$\begin{aligned} R(\omega) &= \max_{\mathbf{q}_f} \frac{\|(\mathbf{L}_1 - \omega\mathbf{I})^{-1} \mathbf{q}_f\|}{\|\mathbf{q}_f\|} \\ &= \|(\mathbf{L}_1 - \omega\mathbf{I})^{-1}\| \\ &= \max_{\kappa_f} \frac{\|\kappa\|}{\|\kappa_f\|} \\ &= \|(\Lambda - \omega\mathbf{I})^{-1}\| \\ &= \|F \operatorname{diag}\left(\frac{1}{\lambda_1 - \omega}, \dots, \frac{1}{\lambda_N - \omega}\right) F^{-1}\|_2. \end{aligned}$$

This quantity is a measure of the maximum possible response of a linear system described by \mathbf{L}_1 to a harmonic forcing at a real frequency ω . The maximum response can easily be extended to a complex forcing frequency.

For our case, the norm of the resolvent is most conveniently calculated by the singular value decomposition as

$$\|(\Lambda - \omega I)^{-1}\| = \sigma_1 \left\{ F \operatorname{diag} \left(\frac{1}{\lambda_1 - \omega}, \dots, \frac{1}{\lambda_N - \omega} \right) F^{-1} \right\} \quad (4.81)$$

where σ_1 denotes the largest singular value.

Figure 4.10 displays the maximum response to a harmonic forcing for plane Poiseuille flow. We observe a pronounced peak in the response curve for steady forcing in the case displayed in Figure 4.10(a). For non-zero streamwise wave numbers we see two peaks stemming from a near-resonance with eigenvalues from the A- and P-branch. The maximum response increases with increasing Reynolds number.

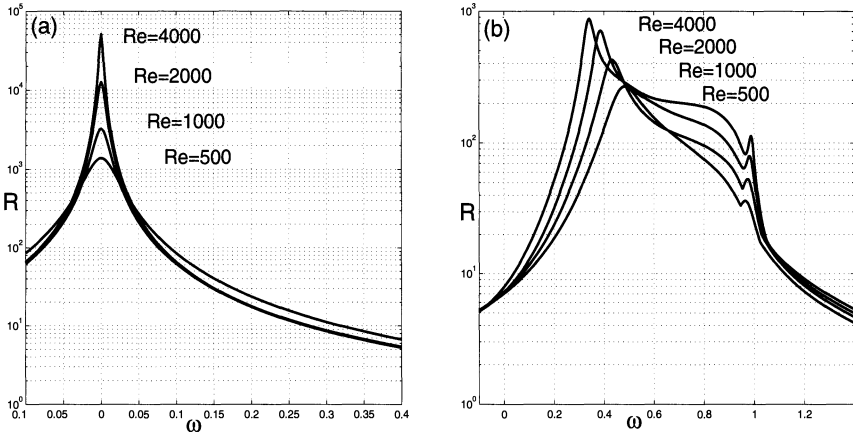


FIGURE 4.10. Resolvent norm versus frequency for plane Poiseuille flow (a) for wave numbers $\alpha = 0, \beta = 2$, (b) for wave numbers $\alpha = 1, \beta = 1$.

Bounds on the maximum response

It is instructive to bound the maximum response $R(\omega)$. From the preceding expression of $R(\omega)$ in terms of the 2-norm we readily obtain

$$\frac{1}{\text{dist}(\{\lambda\} - \omega)} \leq R(\omega) \leq \frac{\text{cond}(F)}{\text{dist}(\{\lambda\} - \omega)} \quad (4.82)$$

where $\text{cond}(F)$ is the condition number of the matrix F and $\text{dist}(\{\lambda\} - \omega)$ denotes the closest distance between ω and the eigenvalues $\{\lambda\}$ of \mathbf{L}_1 .

It follows from expression (4.82) that there are in principle two distinct ways to get a large response: Either the forcing frequency ω is close to an eigenvalue of the linear operator or there is a large condition number $\text{cond}(F)$ that indicates that the underlying linear operator has a set of highly nonorthogonal eigenvectors. The first case is the more familiar one; we force the linear system “at resonance.” In the second case, the forcing frequency can be “off-resonance,” i.e., the distance between the forcing frequency and the spectrum can be large, and yet we can exhibit a large response. For normal systems, $F = I$ and the only possibility to get a large response is by resonant or near-resonant forcing.

Most responsive disturbances

The operator $F^{-1}(\Lambda - \omega \mathbf{I})^{-1}F$ maps a certain forcing function κ_f to its response κ_{resp} . We can therefore ask the question for the most-responsive disturbance

$$B\kappa_f = \mu\kappa_{\text{resp}} \quad B = F^{-1}(\Lambda - \omega \mathbf{I})^{-1}F \quad (4.83)$$

where μ is a measure of the response given by the amplitude of the input to the amplitude of the output. The largest possible response we can get is

$$\mu = \|B\|. \quad (4.84)$$

We are interested in determining the forcing κ_f that results in this largest possible response. Following an argument similar to the one for determining the optimal disturbance, the singular-value decomposition (SVD) can be used to determine this most responsive disturbance. We get

$$Bv_1 = \sigma_1 u_1 \quad (4.85)$$

where v_1 is the principal right singular vector of B , u_1 is the principal left singular vector, and σ_1 is the largest singular value of B equal to $\|B\| = \mu$. The most responsive forcing is therefore given as the principal right singular vector and is expressed in the eigenvector basis $\{\tilde{q}_1, \dots, \tilde{q}_N\}$ with the coefficients given by the N components of v_1 .

An alternative method based on the calculus of variations can be used to determine the most responsive forcing.

Reynolds number dependence of maximum response

The Reynolds number dependence for the norm of the resolvent can be found by rescaling the linearized problem in the same way as given in Section 4.4.4. In addition to the scalings introduced earlier

$$\bar{t} = t/\text{Re}, \quad \bar{\eta} = \tilde{\eta}/\beta\text{Re}, \quad \bar{v} = \tilde{v} \quad (4.86)$$

we have to rescale s as

$$\bar{s} = s\text{Re}. \quad (4.87)$$

In the new variables the resolvent can be written as

$$\|(sI - \mathbf{L}_1)^{-1}\| = \text{Re}\|(\bar{s}I - \bar{\mathbf{L}}_1)^{-1}\|. \quad (4.88)$$

For $\alpha\text{Re} = 0$, it can be shown that $\|(\bar{s}I - \bar{\mathbf{L}}_1)^{-1}\|$ scales like Re in the limit as $\text{Re} \rightarrow \infty$. The proof is contained in Kreiss *et al.* (1994) and is only outlined here. Using the definition of the scaled energy norm and the scaled norm of the resolvent we find

$$\|(\bar{s}I - \bar{\mathbf{L}}_1)^{-1}\| = \max_{\hat{\mathbf{a}}_0} \frac{E_v(\bar{s}) + \beta^2 \text{Re}^2 E_\eta(\bar{s})}{E_v(0) + \beta^2 \text{Re}^2 E_\eta(0)} \quad (4.89)$$

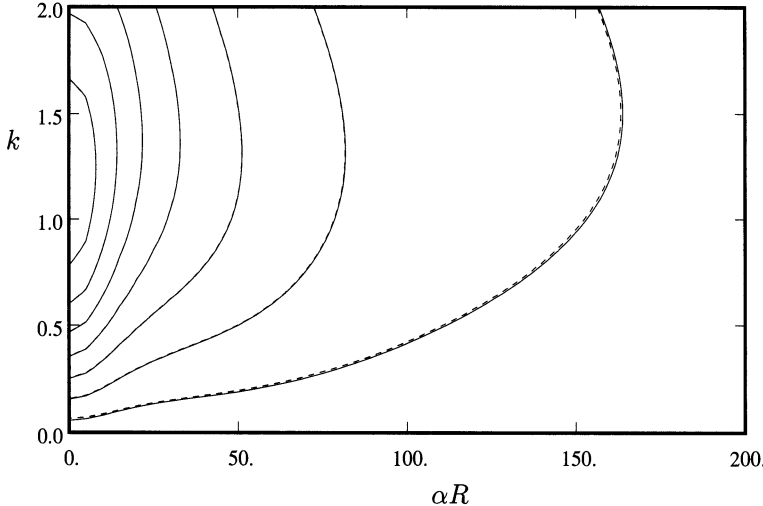


FIGURE 4.11. $k\|\mathbf{L}_1^{-1}\|/(\beta\text{Re}^2)$ for $\text{Re} = 500$ (solid lines) and $\text{Re} = 1000$ (dashed lines). The maximum is 0.0152 which occurs at $\alpha\text{Re} = 0$ and $k = 1.18$. Contour spacing is 0.002. From Kreiss *et al.* (1993).

where $E_v(\bar{s})$ and $E_\eta(\bar{s})$ denotes the energy of the Laplace-transformed solution of the Orr-Sommerfeld and Squire equations, respectively. One may argue that the maximum of this expression will occur for initial values that do not contain any normal vorticity and values of \bar{s} that are dominated by the normal vorticity, similar to the argument for motivating the Re^2 -scaling of the maximum growth in Section 4.4.4.

Alternatively, one may formally estimate $E_v(\bar{s})$ and $E_\eta(\bar{s})$ using the resolvent of the Orr-Sommerfeld and Squire operators. Because both operators are normal for $\alpha\text{Re} = 0$, the value of their resolvent norm is equal to the distance from the point \bar{s} to the nearest value of the spectrum of the respective operators (see the bounds on $R(\omega)$ given in (4.82)). Using such estimates in equation (4.89) and the form of the Laplace-transformed solution one can derive the following inequality

$$\|(\bar{s}I - \bar{\mathbf{L}}_1)^{-1}\| \leq \frac{1}{(\delta + \bar{s}_r)^2 + \bar{s}_i^2} \left[1 + \frac{2k^{-2}\beta^2\text{Re}^2|U''_{max}|^2}{(\delta + \bar{s}_r)^2 + \bar{s}_i^2} \right] \quad (4.90)$$

where δ is the closest distance from \bar{s} to either the stable Orr-Sommerfeld or Squire eigenvalue.

The norm of the resolvent for $s = 0$ for plane Couette flow is shown in Figure 4.11, which shows that this scaling is not only valid for $\alpha\text{Re} = 0$

Flow	$\max_{\omega \in \mathbb{R}} R(\omega)$	α	β
plane Poiseuille	$(Re/17.4)^2$	0	1.62
plane Couette	$(Re/8.12)^2$	0	1.18
Blasius boundary layer	$(Re/1.83)^2$	0	0.21

TABLE 4.2. Reynolds number dependence of $R(\omega)$ for a number of wall-bounded shear flows.

but extends to larger values of αRe . For the Reynolds number dependence of the resolvent of other flows, see Table 4.2.

4.5.2 Maximum Growth Rate

Derivation of the maximum growth rate

In this subsection we will derive the maximum instantaneous growth rate that a disturbance may experience. We use both the continuous formulation of the solutions to the initial value problem and the one based on an expansion in a finite number of eigenfunctions of the linear operator.

It follows from the definition of the scalar product and its associated norm that the growth rate of a disturbance can be obtained as

$$\begin{aligned} \frac{\partial}{\partial t} \|\mathbf{q}\|^2 &= \left(\frac{\partial \mathbf{q}}{\partial t}, \mathbf{q} \right) + \left(\mathbf{q}, \frac{\partial \mathbf{q}}{\partial t} \right) \\ &= (-i\mathbf{L}_1 \mathbf{q}, \mathbf{q}) + (\mathbf{q}, -i\mathbf{L}_1 \mathbf{q}) \\ &= 2 \operatorname{Im} \{(\mathbf{L}_1 \mathbf{q}, \mathbf{q})\} \end{aligned} \quad (4.91)$$

or

$$\begin{aligned} \frac{\partial}{\partial t} \|\kappa\|^2 &= \left(\frac{\partial \kappa}{\partial t}, \kappa \right) + \left(\kappa, \frac{\partial \kappa}{\partial t} \right) \\ &= (-i\Lambda \kappa, \kappa) + (\kappa, -i\Lambda \kappa) \\ &= 2 \operatorname{Im} (\Lambda \kappa, \kappa). \end{aligned} \quad (4.92)$$

In what follows we will use the discrete eigenfunction expansion formulation. Using the adjoint we can rewrite expression (4.92) as

$$\frac{\partial}{\partial t} \|\kappa\|^2 = 2 \operatorname{Im} \{(\Lambda \kappa, \kappa)\} = \|L\kappa\|^2 \quad (4.93)$$

where $L^H L = -i(\Lambda - \Lambda^+)$. Thus, the maximum possible growth rate can be determined as

$$\max_{\|\kappa\|=1} \|L\kappa\|^2 = \|L\|^2. \quad (4.94)$$

The numerical range

The quantity $(\Lambda\kappa, \kappa)$ is known as the numerical range and is defined as the set of Rayleigh quotients of Λ :

$$\mathcal{F}(\Lambda) = \{z \in \mathbb{C} : z = (\Lambda\kappa, \kappa), \quad \|\kappa\| = 1\}. \quad (4.95)$$

The boundary of the numerical range is easily computed using the following formula (see Horn & Johnson, 1991). The complex number z given as

$$z = \frac{x^H Ax}{x^H x} \quad (4.96)$$

is a boundary point of the numerical range of a matrix A where x denotes the principal eigenvector (i.e., the eigenvector that corresponds to the largest eigenvalue) of the matrix

$$H(e^{i\theta} A) \quad (4.97)$$

where $H(M)$ stands for the Hermitian part of a matrix M or

$$H(M) = \frac{1}{2} (M + M^H) \quad (4.98)$$

and the angle θ ranges from 0 to 2π . In short, we multiply our original matrix by $e^{i\theta}$, take the Hermitian part, and calculate the Rayleigh quotient of the original matrix using the principal eigenvector. As the angle θ varies from 0 to 2π , the Rayleigh quotient traces the boundary of the numerical range of A .

It follows from the derivation of the maximum growth rate that a condition for energy growth can be obtained in terms of the numerical range: A necessary and sufficient condition for the growth of energy is that the numerical range $\mathcal{F}(\Lambda)$ extends into the upper complex half-plane. Thus, the critical Reynolds number below which no energy growth is possible is equivalent to the Reynolds number for which the numerical range is entirely confined to the stable half-plane with the boundary of the numerical range tangent to the real axis. This critical Reynolds number thus coincides with the one obtained by the energy stability method (Joseph & Carmi, 1969), which is based on a variational principle applied to (1.11). We will return to this topic in Section 5.6.

The bounds given in Chapter 3 do not only bound the eigenvalues but also the *numerical range* of the Orr-Sommerfeld and Squire operators. For the Squire operator the numerical range is the set of all complex values in the c -plane such that

$$c = \int_{-1}^1 \tilde{\eta}^* [U + \frac{1}{i\alpha \text{Re}} (-\mathcal{D}^2 + k^2)] \tilde{\eta} dy \quad (4.99)$$

under the conditions that $\int_{-1}^1 \tilde{\eta}^* \tilde{\eta} dy = 1$ and $\tilde{\eta}(\pm 1) = 0$. The quantity $\tilde{\eta}$ does not need to be an eigenfunction and the bounds (3.150) and (3.151) are readily derived from (4.99). For the Orr-Sommerfeld operator a similar relation holds. It can be shown that the eigenvalues of an operator are found within the numerical range and that the numerical range can be used to give a precise condition for no transient growth. *The energy of all initial disturbances decays monotonically if and only if the numerical range of the governing operator is confined to the lower half of the c-plane.* Thus (3.151) shows that solutions governed by the Squire operator alone not only decay asymptotically as $t \rightarrow \infty$ but decay monotonically. This is a much stronger condition, which has often been overlooked.

Plane shear flow examples

We will conclude this section by presenting examples of plane shear flows, analyzed by the mathematical techniques introduced in this and the previous chapter. These tools include the spectrum governing the time-asymptotic behavior of the particular flow. In addition, diagnostic tools addressing the short-time behavior are added; these include the resolvent norm contours characterizing and quantifying the degree of nonnormality of the operator for the chosen parameter combination. Furthermore, the optimal growth and optimal response are displayed by computing the energy norm of the appropriate operator as a function of time or frequency. Numerical values for maximum amplification and maximum response are given. Figure 4.12 displays the spectrum, optimal growth and optimal response to periodic forcing for two-dimensional plane Poiseuille flow; Figure 4.13 depicts the same quantities for the case of streamwise independent disturbances. As we have seen in previous sections, the largest transient growth and maximum response is observed for these special disturbances. Figure 4.14 summarizes the same results for two-dimensional plane Couette flow.

4.5.3 Response to Stochastic Excitation

The previous sections have shown a potential for significant energy amplification due to forcing. In this section we will address the issue of forcing by a stochastic field and present analytical expressions for the energy amplification of streamwise independent perturbations. The derivation follows the work of Farrell & Ioannou (1993) and Bamieh & Dahleh (1999).

We will start with the equations governing the evolution of streamwise independent ($\alpha = 0$) disturbances given in terms of their normal velocity and normal vorticity:

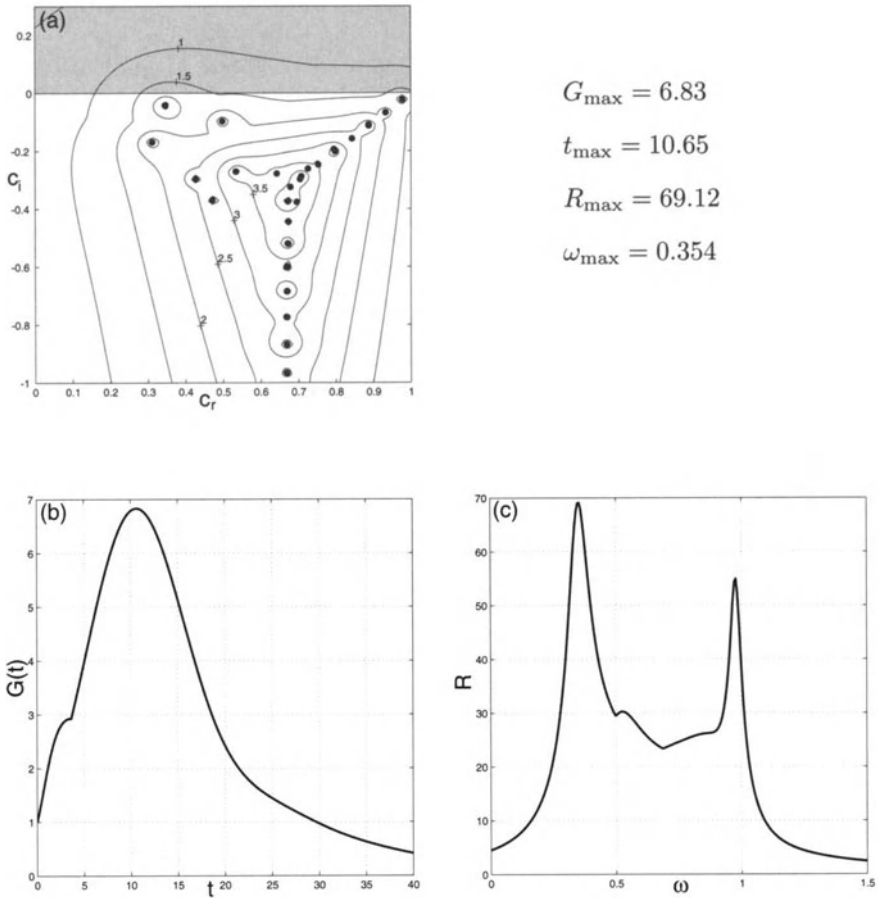


FIGURE 4.12. Resolvent norm contours and spectrum (a), transient growth $G(t)$ (b), and maximum response $R(\omega)$ to harmonic forcing (c) for plane Poiseuille flow at $\alpha = 1, \beta = 0, \text{Re} = 1000$.

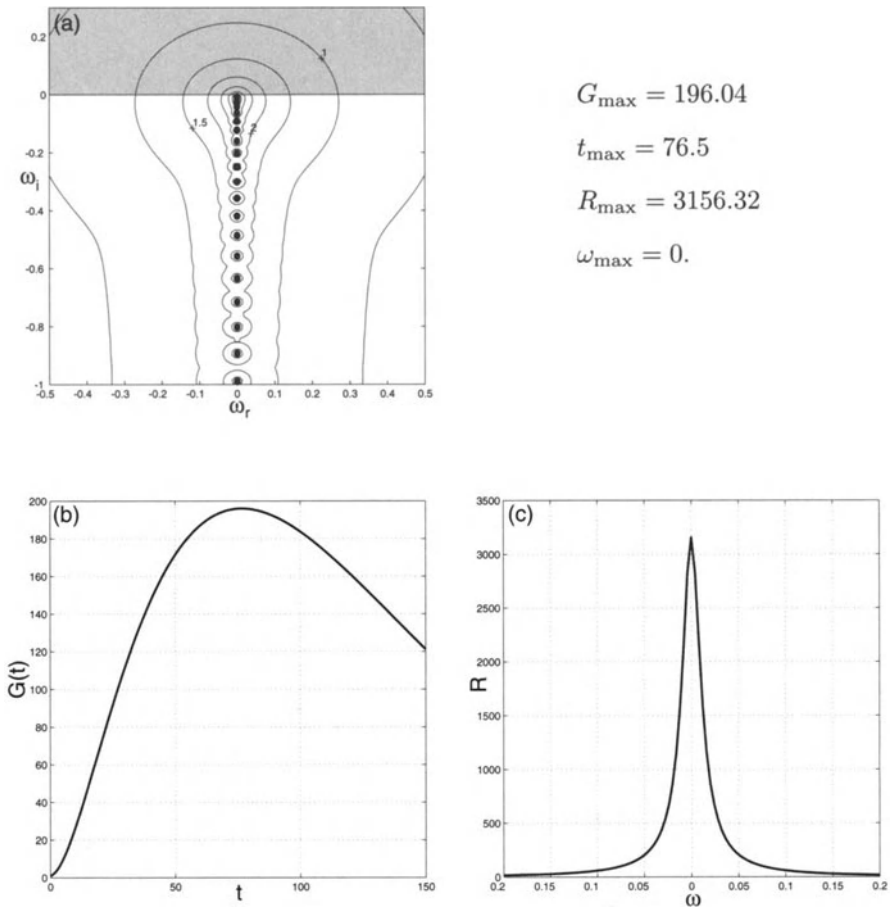


FIGURE 4.13. Resolvent norm contours and spectrum (a), transient growth $G(t)$ (b), and maximum response $R(\omega)$ to harmonic forcing (c) for plane Poiseuille flow at $\alpha = 0$, $\beta = 2$, $\text{Re} = 1000$.

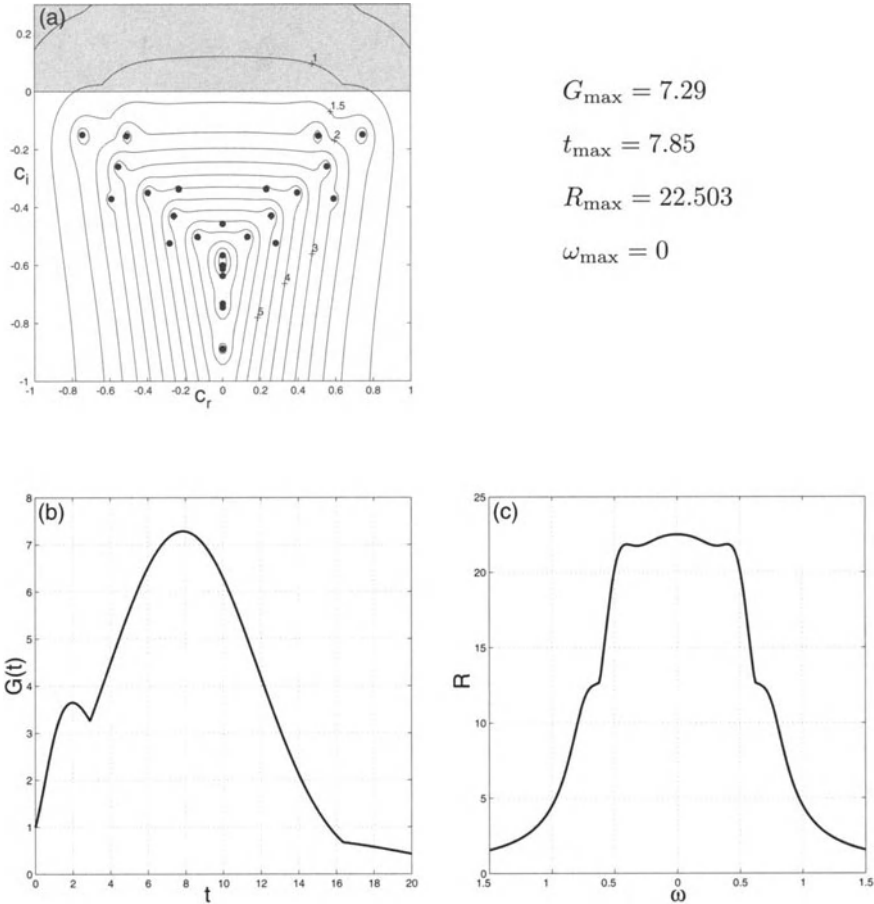


FIGURE 4.14. Resolvent norm contours and spectrum (a), transient growth $G(t)$ (b), and maximum response $R(\omega)$ to harmonic forcing (c) for plane Couette flow at $\alpha = 1$, $\beta = 0$, $\text{Re} = 500$.

$$\frac{\partial}{\partial t} \mathbf{M} \begin{pmatrix} v \\ \eta \end{pmatrix} = \begin{pmatrix} \mathcal{L}_{os} & 0 \\ \mathcal{C} & \mathcal{L}_{sq} \end{pmatrix} \begin{pmatrix} v \\ \eta \end{pmatrix} \quad (4.100)$$

with

$$\mathbf{M} = \begin{pmatrix} -\mathcal{D}^2 & 0 \\ 0 & \mathcal{I} \end{pmatrix} \quad \mathcal{L}_{os} = \frac{1}{\text{Re}} \mathcal{D}^4 \quad \mathcal{C} = -i\beta U' \quad \mathcal{L}_{sq} = \frac{1}{\text{Re}} \mathcal{D}^2. \quad (4.101)$$

We will again use the energy of the harmonic perturbation as a measure of disturbance size and perform a change of variables similar to the one introduced earlier to arrive at the initial value problem

$$\frac{\partial}{\partial t} \mathbf{p} = \mathbf{B} \mathbf{p} + \mathbf{f} \quad (4.102)$$

with

$$\mathbf{p} = \mathbf{F} \begin{pmatrix} v \\ \eta \end{pmatrix} \quad \mathbf{B} = \mathbf{F} \begin{pmatrix} \mathcal{L}_{os} & 0 \\ \mathcal{C} & \mathcal{L}_{sq} \end{pmatrix} \mathbf{F}^{-1} \quad \mathbf{F}^H \mathbf{F} = \mathbf{M}. \quad (4.103)$$

We have added a white noise stationary random field to this equation to model stochastic forcing. The random field \mathbf{f} has zero mean and unit variance. With such forcing, the velocity field becomes random and its statistics is governed by the dynamics of the system. We characterize the random velocity field by an ensemble averaged energy density, which takes the form of the stationary covariance operator \mathbf{V} of the vector \mathbf{p} and can be written as

$$\mathbf{V} = \int_0^t e^{\tau \mathbf{B}} e^{\tau \mathbf{B}^+} d\tau. \quad (4.104)$$

Differentiating this expression with respect to time we obtain an evolution equation for \mathbf{V}

$$\frac{d}{dt} \mathbf{V} = \mathbf{I} + \mathbf{B}^+ \mathbf{V} + \mathbf{V} \mathbf{B} \quad (4.105)$$

with \mathbf{I} as the identity matrix. In the limit of large times, the ensemble averaged energy density reaches a steady state, which we will denote by \mathbf{V}^∞ . It is given as the solution to the Lyapunov equation

$$\mathbf{B}^+ \mathbf{V}^\infty + \mathbf{V}^\infty \mathbf{B} = -\mathbf{I}. \quad (4.106)$$

Finally, the statistically steady-state variance maintained by stochastic forcing is related to \mathbf{V}^∞ through

$$\langle E^\infty \rangle = \text{trace}(\mathbf{V}^\infty). \quad (4.107)$$

The solution of the Lyapunov equation (4.106) requires standard methods of linear algebra and is not attempted here. We are more interested in the Reynolds number dependence of the steady-state variance. To this end, it is advantageous to write equation (4.106) in component form (omitting the superscript)

$$\mathbf{V} = \begin{pmatrix} V_{11} & V_0^* \\ V_0 & V_{22} \end{pmatrix} \quad (4.108)$$

$$\mathcal{L}_{os} V_{11} + V_{11} \mathcal{L}_{os}^* = -\mathcal{I} \quad (4.109)$$

$$\mathcal{L}_{sq} V_0 + V_0 \mathcal{L}_{os}^* = -\mathcal{C} V_{11} \quad (4.110)$$

$$\mathcal{L}_{sq} V_{22} + V_{22} \mathcal{L}_{sq}^* = -(\mathcal{I} + \mathcal{C} V_0^* + V_0 \mathcal{C}^*) \quad (4.111)$$

In this form it is now possible to determine the Reynolds number dependence of each individual component of \mathbf{V} . The first equation implies that V_{11} is $\mathcal{O}(\text{Re})$, because only the left-hand side contains the Reynolds number. This in turn results in $V_0 = \mathcal{O}(\text{Re}^2)$ from the second equation. These two results, combined with the third equation, imply that

$$V_{22} = g(\beta) \text{Re} + f_2(\beta) \text{Re}^3 \quad (4.112)$$

and

$$\text{trace}(\mathbf{V}) = \text{trace}(V_{11}) + \text{trace}(V_{22}) \quad (4.113)$$

$$= f_1(\beta) \text{Re} + f_2(\beta) \text{Re}^3. \quad (4.114)$$

A spectral decomposition using analytical expressions for the eigenfunctions of the operator \mathcal{D}^2 subject to appropriate boundary conditions yields the functions f_1 and f_2 as follows

$$f_1(\beta) = \frac{2\beta \coth(2\beta) - 1}{\beta^2} + \frac{1}{2} \frac{4\beta^2 + \beta \sinh(4\beta) - \cosh(4\beta) + 1}{\beta^2(8\beta^2 - \cosh(4\beta) + 1)} \quad (4.115)$$

$$f_2(\beta) = \frac{1}{2} \sum_{n=1}^{\infty} \frac{\beta^2}{\gamma_n^4} C_n \quad (4.116)$$

with

$$C_n = \frac{1}{2} + \frac{n^2\pi^2}{2\gamma_n} \left[\frac{2\beta(\cosh(2\beta) - 1)}{\gamma_n(\sinh(2\beta) - 2\beta)} - \frac{1}{4(\alpha_n \coth(\alpha_n) - \beta \coth(\beta))} \right] \quad (4.117)$$

for n even, and

$$C_n = \frac{1}{2} - \frac{n^2\pi^2}{2\gamma_n} \left[\frac{\beta(\cosh(2\beta) + 1)}{\gamma_n(\sinh(2\beta) + 2\beta)} + \frac{1}{4(\alpha_n \tanh(\alpha_n) - \beta \tanh(\beta))} \right] \quad (4.118)$$

for n odd. The coefficients α_n and γ_n are respectively given by

$$\alpha_n = \sqrt{2\beta^2 + \frac{n^2\pi^2}{4}} \quad (4.119)$$

$$\gamma_n = -\left(\frac{n^2\pi^2}{4} + \beta^2\right). \quad (4.120)$$

Figure 4.15 displays the steady-state variance as a function of the spanwise wave number β and the Reynolds number Re . One observes a distinct peak at a spanwise wave number of approximately $\beta \approx 1.5$, which monotonically increases for increasing Reynolds number.

Based on the results derived earlier using the resolvent norm to compute the response to a periodic forcing, it is interesting to note that randomness of the forcing reduces the Reynolds number dependence of the response to Re^3 , rather than Re^4 for a deterministic forcing. The response, however, is still very strong in the stochastic case.

For details on the derivation of the functions f_1 and f_2 , which involves state-space realizations borrowed from control theory, the reader is referred to Bamieh & Dahleh (1999).

4.6 Estimates of Growth

4.6.1 Bounds on Matrix Exponential

Bounds using condition number

The maximum growth possible for solutions to an initial value problem can be estimated by bounding the matrix exponential. Upper and lower bounds on the norm of the matrix exponential are given as follows:

$$\begin{aligned} \exp(\omega_i t) &\leq \|\exp(-it\Lambda)\| \\ &\leq \|F\|_2 \|F^{-1}\|_2 \exp(\omega_i t) = \text{cond}(F) \exp(\omega_i t) \end{aligned} \quad (4.121)$$

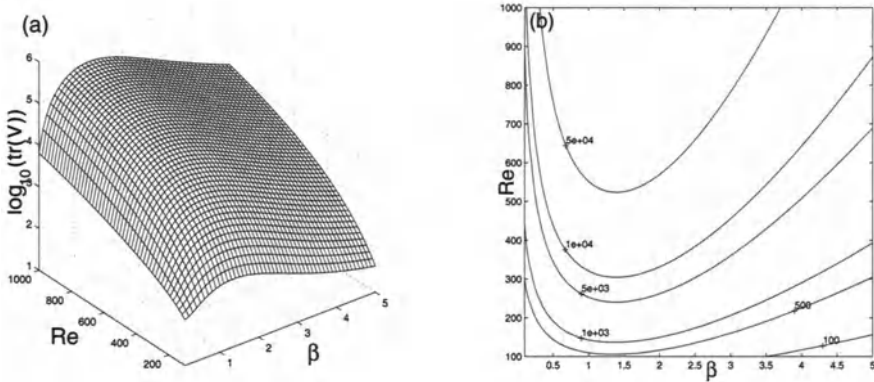


FIGURE 4.15. Response of streamwise independent disturbances to stochastic forcing as a function of spanwise wave number and Reynolds number.

where ω_i denotes the imaginary part of the least stable eigenvalue of Λ and the quantity $\text{cond}(F) = \|F\|_2 \|F^{-1}\|_2$ is known as the condition number of the matrix F and is greater than or equal to one.

Two cases have to be distinguished. If $\text{cond}(F)$ equals one, the upper and lower bounds coincide and the temporal evolution of $\|\exp(-it\Lambda)\|$ is dictated by the least stable eigenvalue for all times. If $\text{cond}(F)$ is substantially larger than one, then the behavior of $\|\exp(-it\Lambda)\|$ is determined by ω_i only in the asymptotic limit of large times. For short times, there may be substantial transient growth although $\omega_i < 0$.

Kreiss matrix theorem

A lower bound on the matrix exponential can be found from one of the equalities in the Kreiss matrix theorem for matrix exponentials. We show how this is obtained by using the definition of the Laplace transform

$$\tilde{\mathbf{q}} = \int_0^\infty e^{-st} \mathbf{q} dt. \quad (4.122)$$

Expressing the solution using the matrix exponential and the Laplace-transformed solution using the resolvent,

$$\mathbf{q} = e^{i\mathbf{L}_1 t} \mathbf{q}_0 \quad \tilde{\mathbf{q}} = (\mathbf{L}_1 - s\mathbf{I})^{-1} \mathbf{q}_0 \quad (4.123)$$

we can rewrite the integral in (4.122) as

$$(\mathbf{L}_1 - s\mathbf{I})^{-1} \mathbf{q}_0 = \int_0^\infty e^{-st} e^{i\mathbf{L}_1 t} \mathbf{q}_0 dt. \quad (4.124)$$

From this expression we can estimate the resolvent as follows

$$\begin{aligned} \|(\mathbf{L}_1 - s\mathbf{I})^{-1}\| &\leq \int_0^\infty |e^{-st}| \|e^{i\mathbf{L}_1 t}\| dt \\ &\leq \int_0^\infty e^{-\text{Real}\{s\}t} dt \max_{t>0} \|e^{i\mathbf{L}_1 t}\| \\ &\leq \frac{1}{\text{Real}\{s\}} \max_{t>0} \|e^{i\mathbf{L}_1 t}\|. \end{aligned} \quad (4.125)$$

This implies that a lower bound for the matrix exponential is

$$\max_{t>0} \|e^{i\mathbf{L}_1 t}\| \geq \max_{\text{Real}\{s\}>0} \text{Real}\{s\} \|(\mathbf{L}_1 - s\mathbf{I})^{-1}\| = \gamma \quad (4.126)$$

which means that growth can be estimated from the quantity γ that measures how far the resolvent contours reach into the unstable half-plane. Using the definition of G_{\max} we have

$$G_{\max} \geq \gamma^2. \quad (4.127)$$

4.6.2 Conditions for No Growth

Using the numerical range

We determine conditions for no energy growth by using the definition of the numerical range. To compute $(\mathbf{L}_1 \mathbf{q}, \mathbf{q})$ we note that

$$\mathbf{L}_1 \mathbf{q} = \begin{pmatrix} \mathcal{L}_{OS} \hat{v} \\ i\beta U' \hat{v} + \mathcal{L}_{SQ} \hat{\eta} \end{pmatrix}. \quad (4.128)$$

This result and the definition of the inner product imply that

$$\begin{aligned} (\mathbf{L}_1 \mathbf{q}, \mathbf{q}) &= -\frac{1}{\text{Re}} \int_{-1}^1 (|\hat{v}''|^2 + 2k^2 |\hat{v}'|^2 + k^4 |\hat{v}|^2 + |\hat{\eta}'|^2 + k^2 |\hat{\eta}|^2) dy \\ &\quad + \int_{-1}^1 U' (\alpha \hat{v}^* \hat{v}' dy - \beta \hat{v}^* \hat{\eta}) dy \end{aligned} \quad (4.129)$$

where ' denotes differentiation.

The first term in (4.129) is strictly negative for all Reynolds numbers and corresponds to dissipation of disturbance energy. The second term may be positive or negative and is related to the exchange of energy with the mean flow U .

There is no energy growth if $(\mathbf{L}_1 \mathbf{q}, \mathbf{q}) \leq 0$. The second term in (4.129) is bounded in magnitude. Hence, if the Reynolds number is sufficiently small, then the numerical range will lie in the lower half-plane. If $\text{Re}_1(\alpha, \beta)$ is the largest value of Re such that the numerical range lies in the lower half-plane, then

$$\frac{1}{\text{Re}_1(\alpha, \beta)} = \max_{\mathbf{q}} \frac{\int (\alpha U' \hat{v}^* \hat{v}' - \beta U' \hat{v}^* \hat{\eta}) dy}{\int (|\hat{v}''|^2 + 2k^2 |\hat{v}'|^2 + k^4 |\hat{v}|^2 + |\hat{\eta}|^2 + k^2 |\hat{\eta}|^2) dy}. \quad (4.130)$$

This optimization problem can be solved using calculus of variations. The Euler equations corresponding to (4.130) lead to the coupled eigenvalue problem

$$\hat{v}^{(iv)} - 2k^2 \hat{v}'' + k^4 \hat{v} + i\lambda(\alpha U' \hat{v}' + \frac{1}{2} \alpha U'' \hat{v} - \frac{1}{2} \beta U' \hat{\eta}) = 0 \quad (4.131)$$

$$-\hat{\eta}'' + k^2 \hat{\eta} - i\lambda \frac{1}{2} \beta U' \hat{v} = 0 \quad (4.132)$$

$$\hat{v}(\pm 1) = \hat{v}'(\pm 1) = \hat{\eta}(\pm 1) = 0. \quad (4.133)$$

The function $\text{Re}_1(\alpha, \beta)$ is the smallest positive eigenvalue λ of the system of equations (4.131), (4.132), and (4.133). If $\beta = 0$, then (4.132) is not required and $\text{Re}_1(\alpha, 0)$ is the smallest positive eigenvalue of

$$\hat{v}^{(iv)} - 2k^2 \hat{v}'' + k^4 \hat{v} + i\alpha\lambda(U' \hat{v}' + \frac{1}{2} U'' \hat{v}) = 0 \quad (4.134)$$

$$\hat{v}(\pm 1) = \hat{v}'(\pm 1) = 0. \quad (4.135)$$

This last eigenvalue problem was first derived by Orr (1907) using energy methods and was subsequently derived by Synge (1938) using a procedure similar to the one discussed earlier.¹

Using the Reynolds-Orr equation

Expression (4.129) gives the rate of change of energy of the perturbation \mathbf{q} for a particular mode in α - β -space. The rate of change of the total perturbation energy E_V of a perturbation of arbitrary size is given by the Reynolds-Orr equation, derived in Chapter 1. We have

$$\frac{dE_V}{dt} = - \int_V u_i u_j \frac{\partial U_i}{\partial x_j} dV - \frac{1}{\text{Re}} \int_V \frac{\partial u_i}{\partial x_j} \frac{\partial u_i}{\partial x_j} dV \quad (4.136)$$

¹The original goal of Synge's analysis was to determine a sufficient condition for linear stability.

where the integration is over the volume of the domain. The right-hand side of (4.136) is analogous to (4.129); the first term represents dissipation and the second term represents energy exchange with the mean flow.

Equation (4.136) is the starting point for energy methods, which will be dealt with in Chapter 5. Here we will briefly anticipate those results in order to draw an interesting conclusion. For parallel flows the Reynolds number Re_G , below which there is no energy growth, is given as

$$\frac{1}{\text{Re}_G} = \max_{u_i} \frac{- \int_V U'(y)uv \, dV}{\int_V \frac{\partial u_i}{\partial x_j} \frac{\partial u_i}{\partial x_j} \, dV} \quad (4.137)$$

where u_i is an admissible perturbation satisfying the no-slip boundary conditions on the plates.

Equation (4.129) can be derived from (4.136). Let $u = \text{Real}\{\hat{u}(y)e^{i\alpha x + i\beta z}\}$ and let us similarly define v , w , and η . As will be done in Chapter 5, we proceed by integrating and averaging over one period in the x - and z -directions. For the energy exchange term we obtain

$$-\frac{\alpha\beta}{4\pi^2} \int_{-1}^1 \int_0^{\frac{2\pi}{\alpha}} \int_0^{\frac{2\pi}{\beta}} U'uv \, dz \, dx \, dy = \frac{1}{2k^2} \int_{-1}^1 U'(\alpha\hat{v}^*\mathcal{D}\hat{v} - \beta\hat{v}^*\hat{\eta}) \, dy. \quad (4.138)$$

Except for the factor $2k^2$ in the denominator, which is constant for any fixed wave number combination, the right-hand side of (4.138) is the same as the second term in (4.129). Using the same procedure, it can be shown that the first term in (4.136) is the same as the dissipation term in (4.129), except for a factor of $2k^2$.

The key point of this analysis is that (4.129), which is based on the linear operator \mathbf{L}_1 and its numerical range, is equivalent to (4.136), which gives the rate of change of the total energy for a perturbation of arbitrary size. The equality occurs because the nonlinear term in the Navier-Stokes equation is not present in (4.136). For a complete derivation of the Euler equations associated with the variational problem for Re_G see Chapter 5.

These arguments imply that

$$\text{Re}_G = \min_{\alpha, \beta} \text{Re}_1(\alpha, \beta). \quad (4.139)$$

Equation (4.139) would have an interesting implication if \mathbf{L}_1 were normal for all α and β . In such a case, $\text{Re}_L \equiv \inf_{\alpha, \beta} \text{Re}_1(\alpha, \beta)$ by the Hille-Yosida theorem (see Kato, 1976). Coupled with (4.139), this would imply that there could be no transition at subcritical Reynolds numbers, which in turn implies that subcritical transition occurs for plane Poiseuille and Couette flows because \mathbf{L}_1 is nonnormal.

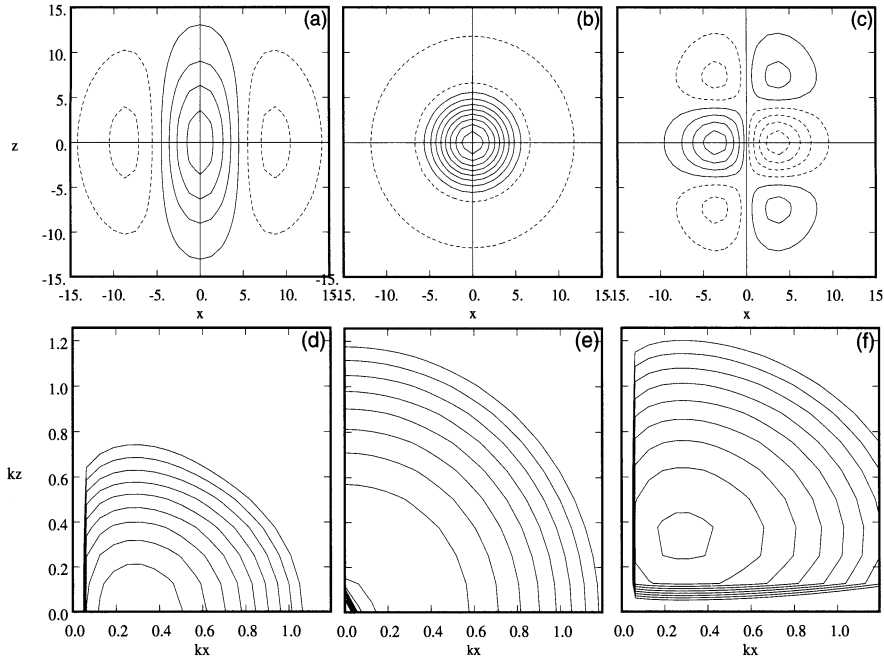


FIGURE 4.16. Velocity field and spectrum of initial conditions for three different disturbance types. (a,d) disturbance centered around a two-dimensional Tollmien-Schlichting wave; (b,e) axisymmetric jet disturbance; (c,f) counterrotating streamwise vortices. Top row: contours of normal velocity in the x - z -plane; bottom row: spectral representation in the (k_x, k_z) wave number plane.

4.7 Localized Disturbances

4.7.1 Choice of Initial Disturbances

Localized disturbances exemplifying different growth mechanisms

Localized disturbances are characterized by a rich stability behavior, and their development can give an interesting glance at the different growth mechanisms that are present in shear flows. We will consider three different disturbances, each one designed to excite a particular growth mechanism or demonstrate a typical behavior. The evolution of these three types of disturbances will be studied in channel and boundary layer flows.

The two primary growth mechanisms found in the analysis of linear disturbances are the exponential growth associated with Tollmien-Schlichting waves or inflectional instabilities and the transient growth associated with the lift-up effect. These mechanisms are dominant in different regions of wave number space. Fourier components that have a potential to experience exponential growth will unlikely experience large transient growth. Roughly speaking, most of the exponential growth is associated with two-

dimensional waves, i.e., $\beta = 0$, and transient growth is associated with streamwise independent disturbances, i.e., $\alpha = 0$. Transient growth is also strongly dependent on the distribution of normal velocity and normal vorticity in the initial Fourier components, and growth is associated only with the normal vorticity. For Fourier components where exponential growth is present the normal velocity and normal vorticity grow simultaneously and the least stable mode will emerge as long as the initial condition has a sufficient projection onto that mode.

Disturbances exciting the least stable mode

First, we consider a disturbance centered around the least stable two-dimensional Tollmien-Schlichting wave. The initial condition in physical space is nearly two-dimensional and the energy in Fourier space is centered around the least stable mode on the α -axis, see Figure 4.16(a,d).

This type of disturbance can be generated experimentally, for example, by the use of blowing and suction through perforated plates, as in the experiment by Cohen *et al.* (1991).

Axisymmetric disturbances with zero normal vorticity

Next, we consider a disturbance that contains no normal vorticity and has substantial energy in wave numbers associated with large transient growth. As shown by Gustavsson (1991), an axisymmetric disturbance in the x - z plane will have no normal vorticity and will be associated with an axisymmetric disturbance in wave number space, see Figure 4.16(b,e).

Experimentally this type of disturbance is close to what can be generated by axisymmetric jets injecting fluid perpendicular to the wall of a wind tunnel.

Counterrotating streamwise vortices

Finally, we consider a disturbance that was originally devised by Landahl (1983) but has subsequently been used in numerous studies of localized disturbances. It consists of two pairs of counterrotating streamwise vortices, does not contain Fourier components on the α - or β -axis, and is centered around a pair of oblique waves, see Figure 4.16(c,f). When we consider the nonlinear development of localized disturbances we will see additional reasons for choosing this type of disturbance.

Breuer & Haritonidis (1990) have generated this type of disturbance by membranes moving up and down in a localized region.

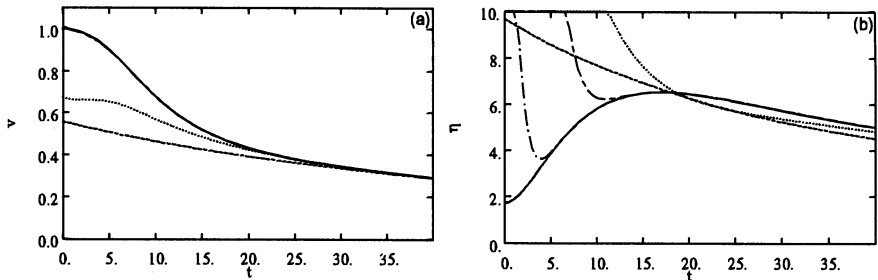


FIGURE 4.17. Time evolution of the integrated rms values for (a) the normal velocity and (b) the normal vorticity for a localized disturbance at $Re = 3000$. Solid curves represent an exact solution obtained from numerical simulations; the dashed, dotted, chain-dashed and chain-dotted curves represent the eigenfunction expansions using $L = J = 1, 4, 10$ and 15 respectively. From Henningson *et al.* (1993).

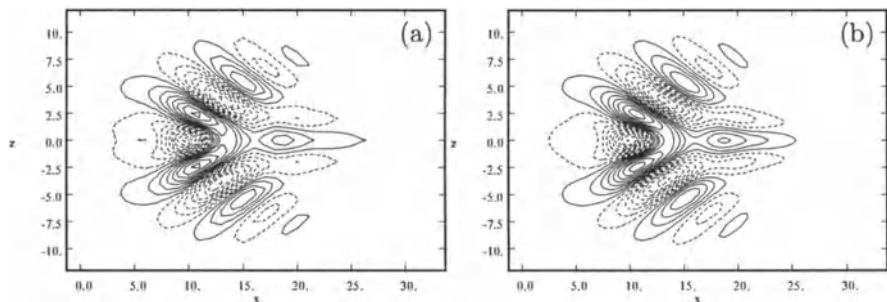


FIGURE 4.18. Normal velocity at $y = -0.56$ and $t = 30$ of a localized disturbance with $\theta = 0$. (a) Results from an eigenfunction expansion using $A1$ -modes only. (b) Results from direct numerical simulation. Contour spacing of 5.0×10^{-7} . From Henningson *et al.* (1993).

4.7.2 Examples

Eigenfunction expansion for plane Poiseuille flow

We begin our study of localized disturbances by applying an eigenfunction expansion (4.30) to an initial condition similar to that given in Figure 4.16(c). A number of streamwise and spanwise Fourier components have to be included to capture the streamwise and spanwise variations of the localized disturbance. For each such wave number a number of normal modes have to be used. Figure 4.17 shows the time evolution of the root-mean-square values of the normal velocity and the normal vorticity. Four modes for each wave number capture the behavior of the normal velocity after $t = 20$ whereas one mode is sufficient after $t = 30$. The convergence of the expansion for the normal vorticity is not as strong. We have to increase the number of modes per wave number to a total of 40 (20 Orr-Sommerfeld and 20 Squire modes) to be able to capture the initial transient growth phase. There is a large initial cancellation between nonorthogonal modes causing transient growth. After the peak in energy we observe mode-like behavior as the least stable eigenvalue governs the decay.

To demonstrate dispersive effects of localized disturbances we will investigate the behavior associated with the least stable Orr-Sommerfeld modes ($A1$) at $t = 30$, see Figure 4.18(a). At this time these modes capture all the qualitative effects of the normal velocity evolution. The agreement with direct numerical simulations (see Figure 4.18(b)) is good even without including the modes from the P -branch of the Orr-Sommerfeld spectrum since the expansion coefficients for the least damped P modes are approximately one order of magnitude lower than those for the $A1$ modes. Thus, using an eigenfunction expansion one may predict the development of the normal velocity for this disturbance with a small number of Orr-Sommerfeld modes. The normal vorticity component, on the other hand, requires a significantly larger number of modes.

DNS of small amplitude disturbances in plane Poiseuille flow

Transient growth may also play an important role in the growth of localized disturbances if these disturbances have initial energy in specific wave number combinations. Henningson *et al.* (1993) studied the development of the localized disturbances displayed in Figure 4.16(c,f) with small enough initial energy to ensure that nonlinear effects are negligible. Figure 4.19 shows the streamwise and normal velocities for times $t = 10$ and $t = 40$. The normal velocity shows the typical decaying wave packet pattern while the streamwise velocity shows large-amplitude streaky structures. Although the initial streamwise and normal velocity were of the same order, the amplitude of the streamwise velocity is about 30 times that of the normal velocity at $t = 40$. This is due to the lift-up effect and is mostly associated with the normal vorticity component.

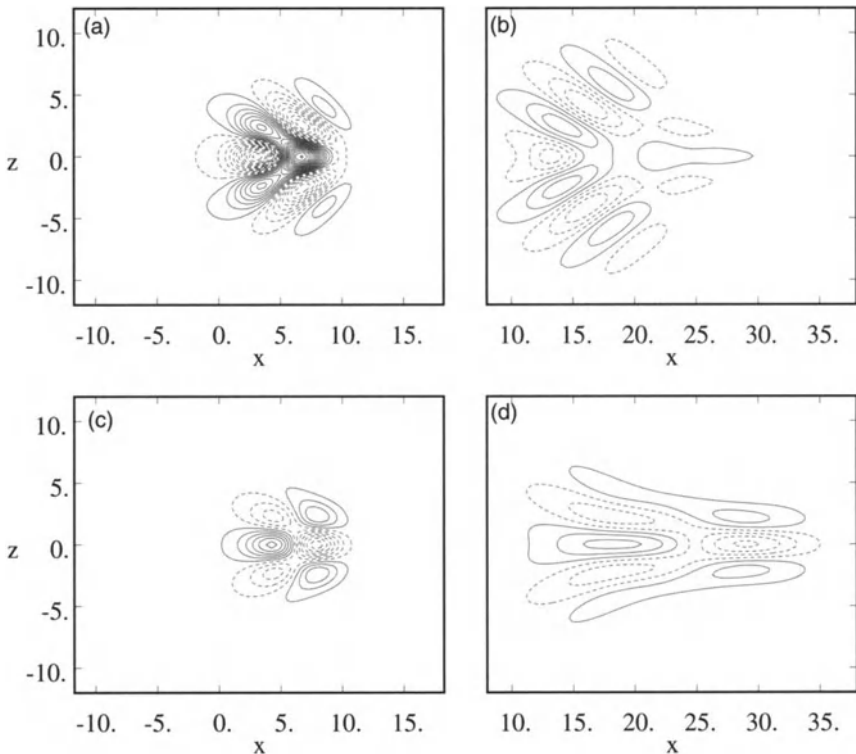


FIGURE 4.19. Velocity contours of a localized disturbance ($y = -0.56$). (a) Normal velocity at $t = 10$; (b) normal velocity at $t = 40$; (c) streamwise velocity at $t = 10$; (d) streamwise velocity at $t = 40$. The contour spacing of the streamwise velocity is 20 times that of the normal velocity. From Henningson *et al.* (1993).

DNS of small-amplitude disturbances in the Blasius boundary layer

Let us next compare the development of the wave packet (Figure 4.16(a,d)) and the jet disturbance (Figure 4.16(b,e)) in the Blasius boundary layer. Simulations were performed by directly solving the Navier-Stokes equations numerically with an initial disturbance amplitude low enough to ensure that nonlinear effects were negligible. The parallel flow assumption was made, but the boundary layer was allowed to grow in time to account for the spatial boundary layer growth. The qualitative features of the disturbance development were independent of the boundary layer growth.

As can be seen in Figure 4.20, the behavior of the normal velocity is similar for the two disturbances. On the other hand, two very different types of behavior are observed for the streamwise velocity. The normal velocity shows a wave packet pattern in both cases which stems from initial energy in the vicinity of the least stable mode. For the wave packet disturbance we see a corresponding wave packet in the streamwise velocity because no initial energy is present along the β -axis of the wave number space where algebraic growth dominates. For the axisymmetric disturbance, which has substantial energy along the β -axis, the wave packet behavior is overtaken by large-amplitude streaks produced by the lift-up effect.

4.7.3 Asymptotic Behavior

Localized disturbance calculations at high Reynolds numbers

Most studies on the asymptotic behavior of small-amplitude disturbances have concentrated on single waves or wave packets. To date little work has been done on the asymptotic behavior of general localized disturbances, particularly when nonmodal effects play an important role. We will therefore present results from a numerical simulation of the linearized Navier-Stokes equations for localized disturbances in plane Couette flow at high Reynolds numbers. We are particularly interested in the Reynolds number scaling of various flow quantities which we extract from the simulations as the Reynolds number is increased from moderate values to approximately $Re = 10^6$. We choose initial conditions that are known to be dominated by transient growth mechanisms. Again, all these simulations used low enough initial disturbance energies to ensure negligible nonlinear effects.

Evolution of energy and velocity maximum

Various flow quantities can be used to describe the evolution of localized disturbances; we will focus on the maximum disturbance energy, the maximum streamwise velocity, and the disturbance length. The results from the numerical simulations will be compared to results we obtained for single-wave disturbances. Table 4.3 summarizes the main findings for plane Couette flow.

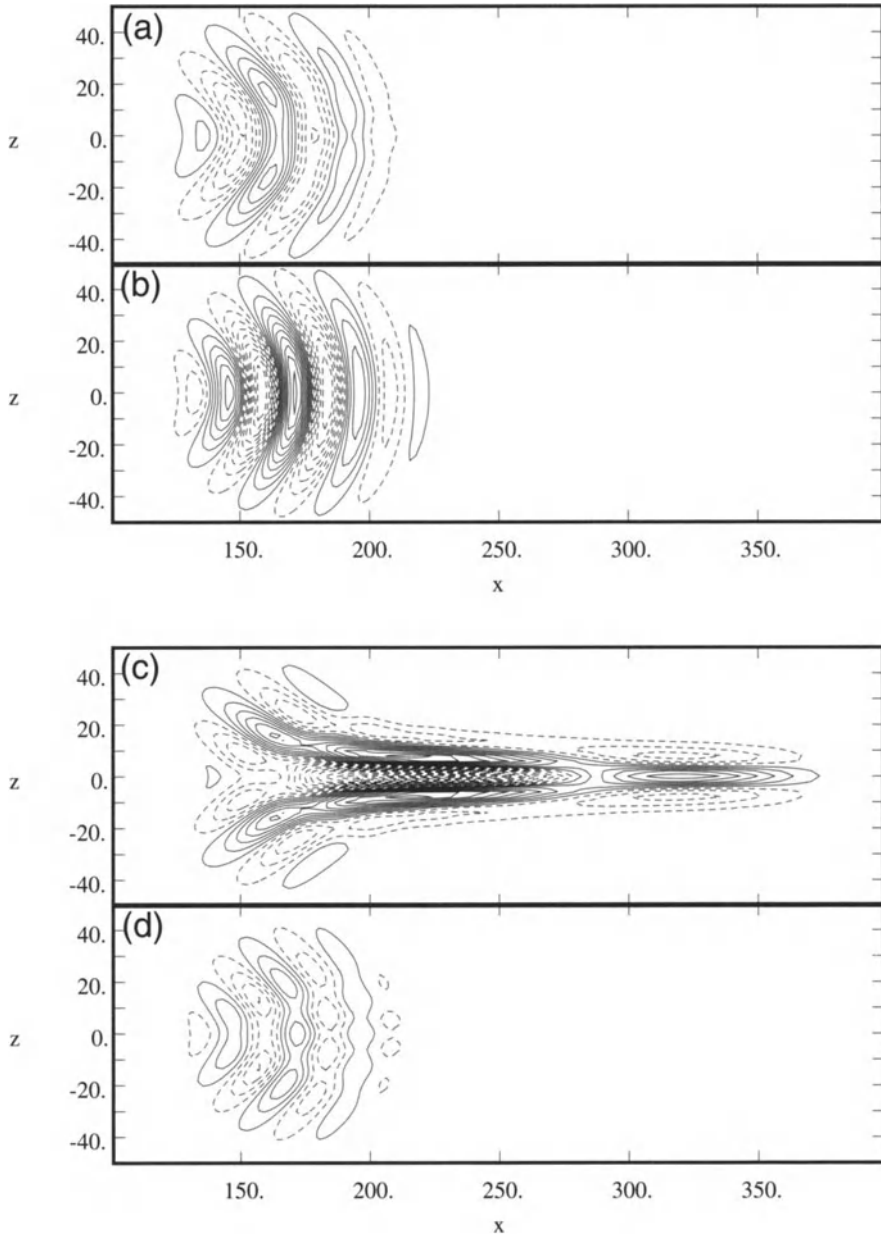


FIGURE 4.20. Temporal evolution of localized disturbances in Blasius boundary layer flow. Streamwise velocity (a,c) and normal velocity (b,d) at $t = 400$ for the wave packet (a,b) and the axisymmetric jet disturbance (c,d).

Quantity	Single waves	Localized disturbances
Energy growth at	$E_{max} \sim Re^2$ $t_{max} \sim Re$	$E_{max} \sim Re$ $t_{max} \sim Re$
Maximum of u at	$u_{max} \sim Re$ $t_{max} \sim Re$	$u_{max} \sim \log Re$ $t_{max} \sim Re^{1/3}$
Disturbance length		$l \approx ([U] - CRe^{-1/3})t$

TABLE 4.3. Comparison of Reynolds number dependence of characteristic flow quantities for localized and single-wave disturbances. Results from Lundbladh (1993b).

We see that both the energy and maximum streamwise velocity of localized disturbances scale significantly different with Reynolds number when compared to single-wave disturbances. The maximum of the total disturbance energy is proportional to Re for localized disturbances; for single waves the maximum energy shows a Re^2 -dependence. The time to reach the maximum remains the same for localized and single-wave disturbances. We find a similar behavior for the maximum of the streamwise velocity: The Reynolds number dependence is reduced from a linear scaling for single waves to a logarithmic scaling for localized disturbances. The time to reach this maximum is proportional to Re for waves but proportional to $Re^{1/3}$ for localized disturbances. Although the maximum of u is lower for the localized disturbance it is attained faster than for single waves. Most of the growth in energy and streamwise velocity is associated with the spreading of the localized disturbance; the Reynolds number scaling of the disturbance length is also reported in Table 4.3.

5

Nonlinear Stability

5.1 Motivation

5.1.1 Introduction

Nonlinear effects

The previous chapters have been devoted to the linear theory of hydrodynamic instabilities. This means that only the development of disturbances with infinitesimal amplitude can be described reliably. As soon as larger amplitudes are obtained (through an instability, for example), the linearized equations are rendered invalid, and nonlinear effects become important and have to be taken into account. For wavelike disturbances Fourier components no longer evolve independently but are all coupled together through wave-triad interactions. Typically this implies that waves with larger wave numbers than those included in the initial conditions are needed to describe the nonlinearly developing solution. In physical space smaller scales are introduced and the evolution of the disturbance becomes more complicated.

Choice of material included

Due to its complexity few general theories of nonlinear stability exist. Instead, a vast number of approximate techniques, often applicable only to special cases, have been developed. It would be impossible to cover all those techniques in this volume. The theories and techniques included here are chosen based on their applicability to shear flow transition and are mainly used as a vehicle to obtain understanding of physical mechanisms governing

different transition scenarios. For quantitative information about a specific nonlinear phenomena one often has to resort to numerical solutions of the full Navier-Stokes equations or to physical experiments, both of which will play an increasing role in the following chapters of this book.

After a model problem we start this chapter by deriving nonlinear results for two special cases. This will introduce important concepts such as nonlinear saturation, supercritical and subcritical bifurcation, and wave-triad interactions. Then we will tackle the complete nonlinear initial value problem and end with general results that can be derived from the full nonlinear problem.

5.1.2 A Model Problem

Burgers equation

First we will investigate the characteristics of nonlinear terms with the help of a model problem. We take the viscous Burgers equation

$$\frac{\partial u}{\partial t} + u \frac{\partial u}{\partial x} = \nu \frac{\partial^2 u}{\partial x^2} \quad (5.1)$$

which shows some resemblance to the Navier-Stokes equations. We will decompose the variable u into a mean ($U = \text{const}$) and a fluctuating ($u'(x, t)$) part and derive an equation for the fluctuating part only. We get (omitting the primes)

$$\frac{\partial u}{\partial t} + U \frac{\partial u}{\partial x} - \nu \frac{\partial^2 u}{\partial x^2} = -u \frac{\partial u}{\partial x}. \quad (5.2)$$

The term on the right-hand side represents the nonlinear interaction between the velocities and becomes important only when the velocity or its gradient are large enough for the product to be of the same order as any term on the left-hand side. To fully understand the effect of nonlinearities it is instructive to assume a periodic x -domain and expand the velocity in the form of waves

$$u = \sum_{k=-\infty}^{\infty} a_k(t) e^{ik\alpha x} \quad a_k = a_{-k}^* \quad (5.3)$$

which results in

$$\begin{aligned} & \sum_{k=-\infty}^{\infty} \left[\frac{da_k}{dt} + ik\alpha U a_k + \nu k^2 \alpha^2 a_k \right] e^{ik\alpha x} \\ &= \sum_{m=-\infty}^{\infty} \sum_{n=-\infty}^{\infty} [a_m(t) \text{ in } \alpha \text{ } a_n(t)] e^{i(m+n)\alpha x}. \end{aligned} \quad (5.4)$$

This expression represents a balance between solutions of the form

$$\sim e^{ik\alpha x} \quad \text{and} \quad \sim e^{i(m+n)\alpha x} \quad (5.5)$$

which can only be satisfied if

$$m + n = k. \quad (5.6)$$

We therefore can write

$$\frac{da_k}{dt} + ik\alpha U a_k + \nu k^2 \alpha^2 a_k = \sum_{m=-\infty}^{\infty} a_{k-m} im\alpha a_m. \quad (5.7)$$

The role of nonlinear terms

We can now determine the evolution of the wave coefficients $a_k(t)$ including nonlinear effects. Starting with one wave component only

$$a_{\pm 1} \neq 0, \quad a_0 = a_{\pm 2} = a_{\pm 3} = \dots = 0 \quad (5.8)$$

we see that waves with wave number 2α (known as the second harmonic) will be excited by a nonlinear interaction of two components a_1 . After a_2 acquires nonzero amplitude, one of the waves can interact with the remaining a_1 to nonlinearly excite a_3 , and so on. It is thus clear that the nonlinear terms (and *only* the nonlinear terms) are responsible for the propagation of energy from one harmonic to another.

5.2 Nonlinear Initial Value Problem

5.2.1 The Velocity-Vorticity Equations

Derivation of the equations

Before considering special cases where the nonlinear effects can be treated in a mathematically advantageous way, let us first concentrate on the nonlinear initial value problem that describes – without any simplifying assumptions – the temporal evolution of finite-amplitude disturbances in parallel shear flows.

Let x, y, z denote the streamwise, normal, and spanwise directions, respectively, while the velocity components in the respective directions are u, v , and w and η is the normal vorticity. If we eliminate the pressure we may write the governing equations in the velocity-vorticity formulation (see Benney & Gustavsson, 1981),

$$\left(\frac{\partial}{\partial t} + U \frac{\partial}{\partial x} \right) \nabla^2 v - U'' \frac{\partial v}{\partial x} - \frac{1}{Re} \nabla^4 v = N_v \quad (5.9)$$

$$\left(\frac{\partial}{\partial t} + U \frac{\partial}{\partial x} \right) \eta + U' \frac{\partial v}{\partial z} - \frac{1}{Re} \nabla^2 \eta = N_\eta \quad (5.10)$$

$$\frac{\partial u}{\partial x} + \frac{\partial v}{\partial y} + \frac{\partial w}{\partial z} = 0 \quad (5.11)$$

$$\eta = \frac{\partial u}{\partial z} - \frac{\partial w}{\partial x} \quad (5.12)$$

where the continuity equation (5.11) and the definition of normal vorticity (5.12) make the system complete. The initial conditions for these equations are

$$v(t=0) = v_0(x, y, z) \quad (5.13)$$

$$\eta(t=0) = \eta_0(x, y, z) \quad (5.14)$$

and the no-slip boundary conditions become

$$v(y = \pm 1) = 0 \quad (5.15)$$

$$\frac{\partial v}{\partial y}(y = \pm 1) = 0 \quad (5.16)$$

$$\eta(y = \pm 1) = 0. \quad (5.17)$$

for a bounded domain with $y \in [-1, 1]$.

The nonlinear terms are defined as follows,

$$N_v = - \left[\left(\frac{\partial^2}{\partial x^2} + \frac{\partial^2}{\partial z^2} \right) S_2 - \frac{\partial^2 S_1}{\partial x \partial y} - \frac{\partial^2 S_3}{\partial y \partial z} \right] \quad (5.18)$$

$$N_\eta = - \left(\frac{\partial S_1}{\partial z} - \frac{\partial S_3}{\partial x} \right) \quad (5.19)$$

with

$$S_1 = \frac{\partial(u^2)}{\partial x} + \frac{\partial(uv)}{\partial y} + \frac{\partial(uw)}{\partial z} \quad (5.20)$$

$$S_2 = \frac{\partial(uv)}{\partial x} + \frac{\partial(v^2)}{\partial y} + \frac{\partial(vw)}{\partial z} \quad (5.21)$$

$$S_3 = \frac{\partial(uw)}{\partial x} + \frac{\partial(vw)}{\partial y} + \frac{\partial(w^2)}{\partial z}. \quad (5.22)$$

The matrix formulation

Equations (5.9) and (5.10) can be put into matrix form, yielding

$$\begin{aligned} & \frac{\partial}{\partial t} \begin{pmatrix} -\nabla^2 & 0 \\ 0 & 1 \end{pmatrix} \begin{pmatrix} v \\ \eta \end{pmatrix} \\ & + \begin{pmatrix} -U\nabla^2 \frac{\partial}{\partial x} + U'' \frac{\partial}{\partial x} + \nabla^4 / \text{Re} & 0 \\ U' \frac{\partial}{\partial z} & U \frac{\partial}{\partial x} - \nabla^2 / \text{Re} \end{pmatrix} \begin{pmatrix} v \\ \eta \end{pmatrix} \\ & = - \begin{pmatrix} \frac{\partial^2}{\partial x \partial y} & -\frac{\partial^2}{\partial x^2} - \frac{\partial^2}{\partial z^2} & \frac{\partial^2}{\partial y \partial z} \\ \frac{\partial}{\partial z} & 0 & -\frac{\partial}{\partial x} \end{pmatrix} \begin{pmatrix} S_1 \\ S_2 \\ S_3 \end{pmatrix} \end{aligned} \quad (5.23)$$

where the nonlinear terms (5.20)-(5.22) take the form

$$\begin{pmatrix} S_1 \\ S_2 \\ S_3 \end{pmatrix}^T = \begin{pmatrix} \partial/\partial x \\ \partial/\partial y \\ \partial/\partial z \end{pmatrix}^T \left[\begin{pmatrix} u \\ v \\ w \end{pmatrix} \cdot \begin{pmatrix} u \\ v \\ w \end{pmatrix}^T \right]. \quad (5.24)$$

We proceed to expand the flow variables in Fourier series in the streamwise and spanwise directions. For example, the normal velocity is assumed to have the form

$$v = \sum_m \sum_n \hat{v}_{mn}(y, t) e^{i\alpha_m x + i\beta_n z} \quad (5.25)$$

where the wave numbers are defined as follows

$$\alpha_m = 2\pi m / L_x \quad (5.26)$$

$$\beta_n = 2\pi n / L_z \quad (5.27)$$

$$k_{mn}^2 = \alpha_m^2 + \beta_n^2 \quad (5.28)$$

and L_x and L_z are the lengths of the periodic domain in the streamwise and spanwise directions, respectively. If the Fourier series expansion of the dependent variables is introduced into equation (5.23) the following matrix equation results

$$\left(\mathbf{L}_{mn} + \frac{\partial}{\partial t} \mathbf{M}_{mn} \right) \hat{\mathbf{q}}_{mn} = \mathbf{A}_{mn} \sum_{k+p=m} \sum_{l+q=n} \left[\mathcal{D}_{mn}^T \left(\hat{\mathbf{u}}_{kl} \hat{\mathbf{u}}_{pq}^T \right) \right]^T \quad (5.29)$$

where the initial and boundary conditions are obtained from (5.13-5.17) using the Fourier-expanded variables. The expression $k + p = m$ in the convolution sum implies that the sum should be taken over all combinations of k and p such that their sum equals m . The matrix and vector quantities introduced are defined as follows:

$$\hat{\mathbf{q}}_{mn} = \begin{pmatrix} \hat{v}_{mn} \\ \hat{\eta}_{mn} \end{pmatrix} \quad \hat{\mathbf{u}}_{mn} = \begin{pmatrix} \hat{u}_{mn} \\ \hat{v}_{mn} \\ \hat{w}_{mn} \end{pmatrix} \quad \mathcal{D}_{mn} = \begin{pmatrix} i\alpha_m \\ \mathcal{D} \\ i\beta_n \end{pmatrix} \quad (5.30)$$

and

$$\mathbf{L}_{mn} = \begin{pmatrix} \mathcal{L}_{OS} & 0 \\ \mathcal{C} & \mathcal{L}_{SQ} \end{pmatrix} \quad (5.31)$$

$$\mathbf{M}_{mn} = \begin{pmatrix} k_{mn}^2 - \mathcal{D}^2 & 0 \\ 0 & 1 \end{pmatrix} \quad (5.32)$$

$$\mathbf{A}_{mn} = \begin{pmatrix} -i\alpha_m \mathcal{D} & -k_{mn}^2 & -i\beta_n \mathcal{D} \\ -i\beta_n & 0 & i\alpha_m \end{pmatrix} \quad (5.33)$$

$$\mathcal{L}_{OS} = -i\alpha_m U (\mathcal{D}^2 - k_{mn}^2) + i\alpha_m U'' + \frac{1}{Re} (\mathcal{D}^2 - k_{mn}^2)^2 \quad (5.34)$$

$$\mathcal{L}_{SQ} = i\alpha_m U - \frac{1}{Re} (\mathcal{D}^2 - k_{mn}^2) \quad (5.35)$$

$$\mathcal{C} = i\beta_n U' \quad (5.36)$$

where \mathcal{D} denotes differentiation in the normal direction. Finally, the relationship between $\hat{\mathbf{u}}_{mn}$ and $\hat{\mathbf{q}}_{mn}$ can be found from the Fourier-expanded versions of equations (5.11) and (5.12). We have

$$\hat{\mathbf{u}}_{mn} = \mathbf{C}_{mn} \hat{\mathbf{q}}_{mn} \quad (5.37)$$

where

$$\mathbf{C}_{mn} = \begin{pmatrix} i\alpha_m \mathcal{D}/k_{mn}^2 & -i\beta_n/k_{mn}^2 \\ 1 & 0 \\ i\beta_n \mathcal{D}/k_{mn}^2 & i\alpha_m/k_{mn}^2 \end{pmatrix}. \quad (5.38)$$

With the introduction of matrix operators this stability problem closely resembles the formulation used by DiPrima (1967) for the equations governing the stability of Taylor-Couette flow.

The wave numbers $\alpha = \beta = 0$

The preceding equations are not valid when $(\alpha, \beta) = (0, 0)$. Instead, we must use the Fourier-transformed streamwise and spanwise momentum equations to find \hat{u} and \hat{w} for this case. If we assume constant pressure gradient, allowing the mass flux to change, the streamwise momentum equation for wave number zero can be written

$$\frac{\partial \hat{u}_{00}}{\partial t} - \frac{1}{\text{Re}} \mathcal{D}^2 \hat{u}_{00} = - \sum_{k+p=0} \sum_{l+q=0} \mathcal{D}(\hat{u}_{kl} \hat{v}_{pq}) \quad (5.39)$$

with appropriate initial and boundary conditions. The equations for the spanwise velocity component for wave number zero can be found in an analogous manner:

$$\frac{\partial \hat{w}_{00}}{\partial t} - \frac{1}{\text{Re}} \mathcal{D}^2 \hat{w}_{00} = - \sum_{k+p=0} \sum_{l+q=0} \mathcal{D}(\hat{w}_{kl} \hat{v}_{pq}). \quad (5.40)$$

By extending the definition of the vector functions and matrix operators introduced in the previous subsection to the case $m = n = 0$, equation (5.29) can be made uniformly valid for all wave numbers. The following definitions complete the equations.

$$\hat{\mathbf{q}}_{00} = \begin{pmatrix} \hat{u}_{00} \\ \hat{w}_{00} \end{pmatrix} \quad (5.41)$$

$$\mathbf{L}_{00} = \begin{pmatrix} -\mathcal{D}^2/\text{Re} & 0 \\ 0 & -\mathcal{D}^2/\text{Re} \end{pmatrix} \quad (5.42)$$

$$\mathbf{M}_{00} = \begin{pmatrix} 1 & 0 \\ 0 & 1 \end{pmatrix} \quad (5.43)$$

$$\mathbf{A}_{00} = \begin{pmatrix} -1 & 0 & 0 \\ 0 & 0 & -1 \end{pmatrix} \quad (5.44)$$

$$\mathbf{C}_{00} = \begin{pmatrix} 1 & 0 \\ 0 & 0 \\ 0 & 1 \end{pmatrix} \quad (5.45)$$

Summary of complete equations

In summary, we have the following equations, giving the full solution to the nonlinear initial value problem in parallel shear flows

$$(\mathbf{L}_{mn} + \frac{\partial}{\partial t} \mathbf{M}_{mn}) \hat{\mathbf{q}}_{mn} = \sum_{k+p=m} \sum_{l+q=n} \gamma_{(k,l)(p,q)}^{(m,n)} \quad (5.46)$$

where the nonlinear terms on the right-hand side are given as

$$\gamma_{(k,l)(p,q)}^{(m,n)} = \mathbf{A}_{mn} [\mathbf{D}_{mn}^T (\hat{\mathbf{u}}_{kl} \hat{\mathbf{u}}_{pq}^T)]^T. \quad (5.47)$$

The linear part is equivalent to the equations stated in the previous chapter.

5.3 Weakly Nonlinear Expansion

5.3.1 Multiple-Scale Analysis

Introduction of a slow time scale

In this section we will derive equations that take into account the nonlinear interaction between modes of different wave numbers. Although this cannot be accomplished in the most general form, specialized cases can be treated once simplifying assumptions have been made. We will present the derivation of so-called weakly nonlinear equations by the method of multiple scales. Other approaches are available, such as ones based on amplitude expansions, the singular value decomposition, and the center manifold theorem. A brief reference to these alternative methods will be given.

Because of the absence of nonlinear terms in linear stability theory, any results, e.g., eigenfunctions, are independent of the amplitude of the disturbance. For this reason, no evolution equation for the amplitude A can be derived from the linear stability equations.

A first approach to incorporate nonlinear terms is based on the assumption that the amplitude is *weakly* time-dependent. The term “weakly” is further specified by the fact that the amplitude varies at a much slower time scale than the time scale of the wavelike part of the disturbance:

$$\mathbf{q} = \text{Re} \{ A(\tau) \mathbf{q}(y) \exp[i(\alpha x + \beta z - \omega t)] \} \quad \tau \ll t. \quad (5.48)$$

The amplitude $A(\tau)$ again factors out when considering the fast time scale t , but using a perturbation technique an evolution equation for the slowly varying amplitude $A(\tau)$ can be derived at higher order. The assumption of a slowly varying amplitude separated from the exponential time-dependence does not hold for all parameters but rather is restricted to values in the vicinity of a neutral state.

We will restrict our derivation to a two-dimensional neutral state although it is valid for any neutral state, i.e., we choose (α, R_0) such that

$c_i(\alpha, R_0) \approx 0$. The generalization to three-dimensional neutral states with (α, β, R_0) such that $c_i(\alpha, \beta, R_0) \approx 0$ is more complicated but conceptually equivalent to the two-dimensional calculation.

The governing equation for the evolution of two-dimensional perturbations can be derived from (5.46) and is given as

$$\begin{aligned} & (\mathcal{D}^2 - \alpha_m^2) \frac{\partial \hat{v}_m}{\partial t} + i\alpha_m U (\mathcal{D}^2 - \alpha_m^2) \hat{v}_m \\ & \quad - i\alpha_m U'' \hat{v}_m - \frac{1}{\text{Re}} (\mathcal{D}^2 - \alpha_m^2)^2 \hat{v}_m \\ & = i\alpha_m \mathcal{D} \sum_{k=-\infty}^{\infty} [\hat{u}_{m-k} i\alpha_k \hat{u}_k + \hat{v}_{m-k} \mathcal{D} \hat{u}_k] \\ & \quad + \alpha_m^2 \sum_{k=-\infty}^{\infty} [\hat{u}_{m-k} i\alpha_k \hat{v}_k + \hat{v}_{m-k} \mathcal{D} \hat{v}_k] \end{aligned} \quad (5.49)$$

$$i\alpha_m \hat{u}_m + \mathcal{D} \hat{v}_m = 0 \quad (5.50)$$

with $\alpha_m = m\alpha$. The terms on the right-hand side represent the nonlinear interactions between modes with different streamwise wave numbers.

A perturbation technique, known as multiple-scale analysis, will be used to derive an evolution equation for the slowly varying amplitude $A(\tau)$. If a state is slightly supercritical or slightly subcritical states, then

$$|\text{Re} - \text{Re}_0| \ll 1 \quad \text{with } c_i(\text{Re}_0) = 0. \quad (5.51)$$

We will choose a slightly supercritical state and thus let

$$\varepsilon^2 \equiv \frac{1}{\text{Re}_0} - \frac{1}{\text{Re}} \quad \text{for } \text{Re} \geq \text{Re}_0. \quad (5.52)$$

The linear growth rate at Reynolds numbers $\text{Re} > \text{Re}_0$ is of order ε^2 whereas the time scale on which nonlinear interactions affect the evolution of the fundamental mode is of order $(\text{linear growth rate})^{-1}$ (see Stuart, 1960). We therefore introduce a second time scale

$$\tau \equiv \varepsilon^2 t \quad (5.53)$$

which will affect the time derivative accordingly:

$$\frac{\partial}{\partial t} \rightarrow \frac{\partial}{\partial t} + \varepsilon^2 \frac{\partial}{\partial \tau}. \quad (5.54)$$

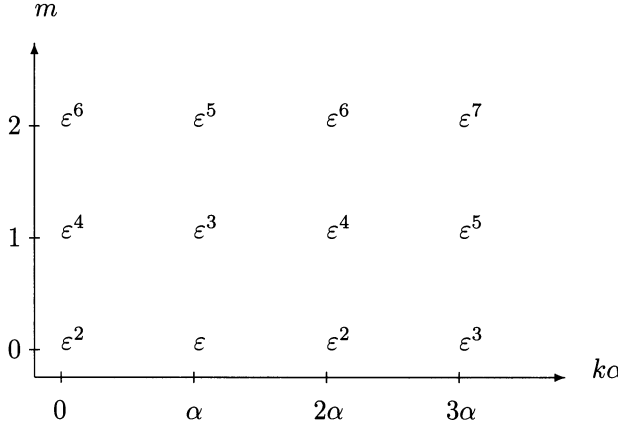


FIGURE 5.1. Scaling hierarchy for weakly nonlinear expansion based multiple-scale analysis.

The expansion

We proceed by expanding the normal velocity component as

$$v = \sum_{k=-\infty}^{\infty} \sum_{m=0}^1 \varepsilon^{1+|(|k|-1)|+2m} \hat{V}_{k,1+|(|k|-1)|+2m}(t, y) E^k \quad (5.55)$$

with $E \equiv \exp[i\alpha(x - ct)]$ and c as the *real* phase velocity obtained from the linear eigenvalue problem. Figure 5.1 illustrates the scaling hierarchy. We start with an amplitude of order ε in wave number α . Velocity components that are generated in higher wave numbers are scaled according to the number of nonlinear interactions it takes to generate them, e.g., 2α -disturbances require the interaction of two α -perturbations, thus the 2α velocity component is of order ε^2 , etc. Substituting the expansion, the expression for the time derivative and the deviation of the Reynolds number from the critical one into the two-dimensional Orr-Sommerfeld equation driven by nonlinear terms and equating like powers of $\varepsilon^j E^k$, we obtain a sequence of equations for the solution of the functions V_{kj} .

At $\mathcal{O}(\varepsilon^1)$ we get the regular Orr-Sommerfeld problem

$$L(\alpha_m, \text{Re}_0) \hat{V}_{1,1} = 0 \quad (5.56)$$

which yields the solution

$$\hat{V}_{1,1} = A(\tau) \tilde{V}_{1,1}. \quad (5.57)$$

At the next order, $\mathcal{O}(\varepsilon^2)$ we obtain solutions in the form

$$\hat{V}_{0,2} = A^2(\tau) \tilde{V}_{0,2} \quad (5.58)$$

$$\hat{V}_{2,2} = |A(\tau)|^2 \tilde{V}_{2,2}. \quad (5.59)$$

We have to proceed to $\mathcal{O}(\varepsilon^3)$ to derive an evolution equation for the amplitude $A(\tau)$. At this order, we get

$$L(\alpha_m, \text{Re}_0) \hat{V}_{1,3} = -\frac{dA}{d\tau} (\mathcal{D}^2 - \alpha^2) \hat{V}_{1,1} - A (\mathcal{D}^2 - \alpha^2)^2 \hat{V}_{1,1} + |A|^2 A N_{1,3} \quad (5.60)$$

where N stands for the nonlinear term. This equation is an inhomogeneous partial differential equation that has a unique solution if and only if a solvability condition (or the Fredholm alternative) is satisfied. The solvability condition states that the inhomogeneous term has to be orthogonal to the solution of the adjoint homogeneous problem. For our case this means that the right-hand side of equation (5.60) has to be orthogonal to solutions of the adjoint two-dimensional Orr-Sommerfeld equation (see Chapter 3). We finally obtain (see Stuart (1960) and Watson (1960))

$$\frac{dA}{d\tau} = \lambda_1 A + \lambda_2 |A|^2 A \quad (5.61)$$

with

$$\lambda_1 = -\frac{\int \tilde{\xi}^+ (\mathcal{D}^2 - \alpha^2)^2 \hat{V}_{1,1} dy}{\int \tilde{\xi}^+ (\mathcal{D}^2 - \alpha^2) \hat{V}_{1,1} dy} \quad (5.62)$$

$$\lambda_2 = \frac{\int \tilde{\xi}^+ N_{1,3} dy}{\int \tilde{\xi}^+ (\mathcal{D}^2 - \alpha^2) \hat{V}_{1,1} dy}. \quad (5.63)$$

The integrals are evaluated over the flow domain in the inhomogeneous direction, e.g., for plane Poiseuille flow from $y = -1$ to $y = 1$. For further details on the derivation and implication of (5.61) the reader is referred to Landau & Lifshitz (1959), Drazin & Reid (1981), and Craik (1985).

Tables 5.3.1 and 5.3.1 display the coefficients λ_1 and λ_2 for a variety of parameters for plane Poiseuille flow. They have been taken from Sen & Venkateswarlu (1983).

Re	c_r	$c_i \times 10^{-3}$	λ_2
5774	0.2639	-0.002068	-140.6 - 28.88 i
5750	0.2641	-0.04190	-140.2 - 28.74 i
5730	0.2644	-0.07541	-139.9 - 28.62 i
5710	0.2644	-0.09228	-139.8 - 28.56 i
5700	0.2645	-0.1092	-139.6 - 28.50 i

TABLE 5.1. Table of Landau coefficients for $c_i < 0, \alpha = 1.02$.

Re	α	c_r	$c_i \times 10^{-3}$	λ_2
5780	1.02	0.2639	0.006215	-140.7 - 28.91 i
6000	1.00	0.2598	0.3181	-133.2 - 21.42 i
6000	1.05	0.2656	0.1335	-162.9 - 47.00 i
7000	1.05	0.2584	1.106	-182.7 - 58.33 i
9000	0.83	0.2212	0.3771	-85.32 + 10.54 i

TABLE 5.2. Table of Landau coefficients for $c_i > 0$.

5.3.2 The Landau Equation

Steady states

The equation for the slowly varying amplitude $A(\tau)$ is known as the Landau equation and the coefficients λ_1 and λ_2 are referred to as Landau coefficients. It is instructive to investigate the steady states of this equation as a function of the coefficients λ_1 and λ_2 . Multiplying the Landau equation (5.61) by A^* and the complex conjugate Landau equation by A and summing the two equations we obtain

$$\begin{aligned} \frac{d}{d\tau}|A|^2 &= \mu_1|A|^2 + \mu_2|A|^4 \\ \mu_1 &= \lambda_1 + \lambda_1^* \\ \mu_2 &= \lambda_2 + \lambda_2^* \end{aligned} \tag{5.64}$$

which can be integrated to result in

$$|A|^2 = \frac{A_0^2 \exp(\mu_1 \tau)}{1 + \frac{\mu_2}{\mu_1} A_0^2 (1 - \exp(\mu_1 \tau))} \quad A_0 = A(\tau = 0). \tag{5.65}$$

Various cases are worth investigating. For $\mu_1 > 0$ and $\mu_2 < 0$ we reach a steady state as time increases at an equilibrium amplitude of

$$A_{equ} = \sqrt{-\frac{\mu_1}{\mu_2}} \tag{5.66}$$

which is independent of the initial amplitude A_0 . Keeping the second coefficient μ_2 negative but changing the sign on μ_1 , the only equilibrium state is the zero-amplitude state. Figure 5.2 displays the equilibrium amplitude for the case $\mu_2 < 0$. The bifurcation behavior pictured in Figure 5.2(a) is known as supercritical bifurcation, where finite-amplitude equilibrium states can be achieved after the infinitesimal state has become unstable. The behavior displayed in Figure 5.2(b) is referred to as subcritical bifurcation where finite-amplitude equilibrium states exist before the infinitesimal state has become unstable.

If $\mu_2 > 0$ and $\mu_1 < 0$ we have the equilibrium state as earlier, whereas for $\mu_1 > 0$ only the zero-amplitude state exists as a steady state.

Stability of steady states

In addition to determining the steady states, it is important to investigate their stability. Linearizing the Landau equation about a steady-state A_0 we obtain

$$\frac{dA'}{d\tau} = (\mu_1 + 2\mu_2 A_0) A' \quad (5.67)$$

where A' denotes the (small) deviation from the equilibrium state A_0 . Clearly, the sign of $\mu_1 + 2\mu_2 A_0$ governs the stability of the steady-state A_0 .

The stability of the zero-amplitude state $A_0 = 0$ is determined by the sign of μ_1 . For $\mu_1 < 0$ we have a stable zero-amplitude state, whereas for $\mu_1 > 0$ we have an unstable one. The finite-amplitude state given by $A_0 = \sqrt{-\mu_1/\mu_2}$ is stable for $\mu_2 < 0$, i.e., for the supercritical bifurcation; for the subcritical bifurcation with $\mu_2 > 0$ the finite-amplitude state is unstable.

Strictly speaking, the Landau equation is only valid for Reynolds numbers close to the critical one. At supercritical Reynolds numbers, or at subcritical Reynolds number for $\mu_2 > 0$, the amplitude $A(\tau)$ increases rapidly with the cubic amplitude term dominating the temporal evolution. In this case, higher-order terms need to be included, which can be calculated in a similar (though somewhat algebraic) way. The resulting equation is of the form

$$\frac{dA}{d\tau} = \lambda_1 A + \lambda_2 |A|^2 A + \lambda_3 |A|^4 A + \lambda_4 |A|^6 A + \dots \quad (5.68)$$

For growing amplitudes $A(\tau)$ the higher-order terms quickly become important and for an accurate description more terms need to be included. However, as Herbert (1983) pointed out, the higher Landau coefficients $\lambda_3, \lambda_4, \dots$ increase in magnitude, such that even a higher-order expansion

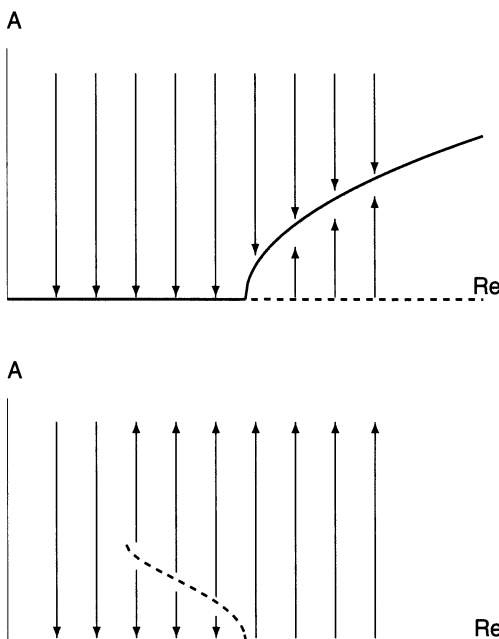


FIGURE 5.2. Bifurcation characteristics based on weakly nonlinear expansion.
(a) Supercritical bifurcation; (b) subcritical bifurcation.

quickly becomes impractical due to its rapidly decreasing radius of convergence.

Extensions

Various extensions of the above procedure have been considered. The introduction of more than two time scales according to

$$t_n \equiv \varepsilon^{2n} t \quad (5.69)$$

is conceivable resulting in higher-order corrections to the Landau equation. The interested reader is referred to Fujimura (1989, 1991).

Furthermore, it is possible to introduce a slowly varying space scale $X = \varepsilon^2 x$ that accounts for small spatial growth or decay of the disturbance amplitudes in the streamwise direction (see Stewartson & Stuart, 1971). The resulting partial differential equation for the slowly varying amplitude (in space and time) is known as the Ginzburg-Landau equation and reads

$$\frac{\partial A}{\partial \tau} = \lambda_0 \frac{\partial^2 A}{\partial X^2} + \lambda_1 A + \lambda_2 |A|^2 A. \quad (5.70)$$

5.4 Three-Wave Interactions

5.4.1 Resonance Conditions

General concept

Another nonlinear stability result that is tractable by asymptotic and analytical techniques is based on the resonant interaction of three waves of finite and comparable amplitude. This scenario has been investigated in detail by Craik (1971) and has been conjectured to play an important role in the transition to turbulent fluid motion due to its significant growth rates.

The amplification of the three waves stems from the fact that they force each other very effectively at resonant conditions. They can interact only if their wave numbers sum up to zero, i.e., $\alpha_1 = \alpha_2 + \alpha_3$, as we found in Section 5.1.2. If we include a third dimension we have the same relation for the wave number vectors. Let us assume the wave number vectors

$$\mathbf{k}_1 = \begin{pmatrix} \alpha_1 \\ \beta_1 \end{pmatrix}, \quad \mathbf{k}_2 = \begin{pmatrix} \alpha_2 \\ \beta_2 \end{pmatrix}, \quad \mathbf{k}_3 = \begin{pmatrix} \alpha_3 \\ \beta_3 \end{pmatrix}. \quad (5.71)$$

The second and third wave can only interact with the first one if the wave number vectors satisfy the relation

$$\mathbf{k}_1 = \mathbf{k}_2 + \mathbf{k}_3. \quad (5.72)$$

This relation is necessary for the interaction of the waves, but it does not specify any details about their temporal interaction. By imposing the additional constraint that the combined frequency of the two interacting waves matches the frequency of the third wave, i.e.,

$$\text{Real}(\omega_1) = \text{Real}(\omega_2) + \text{Real}(\omega_3) \quad (5.73)$$

we enforce resonance between the waves. Resonance can be a strong amplification mechanism in periodically driven systems.

Craik's triad

For the case considered by Craik (1971), we will concentrate on the interaction of two three-dimensional waves with wave number vectors

$$\mathbf{k}_2 = \begin{pmatrix} \alpha/2 \\ \beta \end{pmatrix} \quad \mathbf{k}_3 = \begin{pmatrix} \alpha/2 \\ -\beta \end{pmatrix} \quad (5.74)$$

with a two-dimensional wave with wave number vector

$$\mathbf{k}_1 = \begin{pmatrix} \alpha \\ 0 \end{pmatrix}. \quad (5.75)$$

The resonance condition then requires that

$$\text{Real}\{\omega(\alpha/2, \beta)\} + \text{Real}\{\omega(\alpha/2, -\beta)\} = \text{Real}\{\omega(\alpha, 0)\}. \quad (5.76)$$

Depending on the dispersion relation, there is only a limited set of wave number combinations that satisfies this resonance condition. We will discuss this condition further and give an example in the next section.

5.4.2 Derivation of a Dynamical System

The three linear eigenmodes

We assume a mean flow in the form $\mathbf{U} = [U(y), 0, 0]$. A two-dimensional perturbation is assumed and determined by the normal velocity component v_0 . The streamwise velocity component follows from the continuity equation; the spanwise velocity component is zero. We take the two-dimensional disturbance of the form

$$v_0 = \text{Real} \{ A_0(t) \tilde{v}_0(y) \exp[i\alpha(x - ct)] \} \quad c = c_r + ic_i \quad (5.77)$$

where \tilde{v}_0 satisfies the Orr-Sommerfeld equation (3.14)

$$\mathcal{L}(\tilde{v}_0) \equiv i\alpha [(U - c)(\mathcal{D}^2 - \alpha^2)\tilde{v}_0 - U''\tilde{v}_0] - \frac{1}{\text{Re}} (\mathcal{D}^2 - \alpha^2)^2 \tilde{v}_0 = 0 \quad (5.78)$$

with homogeneous boundary conditions. The three-dimensional perturbation is determined by its normal velocity ($v_{\pm 1}$) and normal vorticity ($\eta_{\pm 1}$) components. For the normal velocity component we assume a form similar to the one given earlier

$$v_{\pm 1} = \text{Real} \left\{ A_{\pm 1}(t) \tilde{v}_{\pm 1}(y) \exp[i(\frac{1}{2}\alpha x \pm \beta z - \frac{1}{2}\alpha \tilde{c}t)] \right\} \quad \tilde{c} = c_r + i\tilde{c}_i \quad (5.79)$$

where $\tilde{v}_{\pm 1}$ satisfies

$$\mathcal{L}'(\tilde{v}_{\pm 1}) \equiv i\frac{\alpha}{2} [(U - \tilde{c})(\mathcal{D}^2 - k^2)\tilde{v}_{\pm 1} - U''\tilde{v}_{\pm 1}] - \frac{1}{\text{Re}} (\mathcal{D}^2 - k^2)^2 \tilde{v}_{\pm 1} = 0 \quad (5.80)$$

with homogeneous boundary conditions and $k^2 = \frac{1}{4}\alpha^2 + \beta^2$.

The particular normal vorticity is expressed as

$$\eta_{\pm 1} = \text{Real} \left\{ A_{\pm 1}(t) \tilde{\eta}_{\pm 1}(y) \exp[i(\frac{1}{2}\alpha x \pm \beta z - \frac{1}{2}\alpha \tilde{c}t)] \right\} \quad (5.81)$$

where $\tilde{\eta}_{\pm 1}$ obeys

$$\mathcal{L}''(\tilde{\eta}_{\pm 1}) \equiv \frac{1}{2}i\alpha(U - \tilde{c})\tilde{\eta}_{\pm 1} - \frac{1}{\text{Re}} (\mathcal{D}^2 - k^2) \tilde{\eta}_{\pm 1} = \mp i\beta U' \tilde{v}_{\pm 1} \quad (5.82)$$

with homogeneous boundary conditions.

The nonlinear system

With the normal velocities and normal vorticities assumed in the above form, substitution into the nonlinear evolution equation, keeping only terms up to second order in the amplitude, results in

$$A_1(t)\mathcal{L}'(\tilde{v}_1) = -\frac{dA_1}{dt}(\mathcal{D}^2 - k^2)\tilde{v}_1 + A_0 A_{-1}^* \exp(\alpha c_i t) G_1(y) \quad (5.83)$$

$$A_{-1}(t)\mathcal{L}'(\tilde{v}_{-1}) = -\frac{dA_{-1}}{dt}(\mathcal{D}^2 - k^2)\tilde{v}_{-1} + A_0 A_1^* \exp(\alpha c_i t) G_{-1}(y) \quad (5.84)$$

$$A_0(t)\mathcal{L}'(\tilde{v}_0) = -\frac{dA_0}{dt}(\mathcal{D}^2 - k^2)\tilde{v}_0 + A_1 A_{-1}^* \exp[\alpha(\tilde{c}_i - c_i)t] G_0(y). \quad (5.85)$$

In the evaluation of the exponential factors on the right-hand side the resonance condition $\text{Real}(c) = \text{Real}(\tilde{c})$ has been used.

Solutions of this system of equations exist only if a solvability condition or Fredholm alternative is satisfied. This solvability condition requires that the right-hand side be orthogonal to the solution of the adjoint linear problem. We obtain

$$\frac{dA_1}{dt} \int \tilde{\xi}_1^+ (\mathcal{D}^2 - k^2) \tilde{v}_1 dy = A_0 A_{-1}^* \int \tilde{\xi}_1^+ G_1(y) dy \exp(\alpha c_i t) \quad (5.86)$$

$$\frac{dA_{-1}}{dt} \int \tilde{\xi}_{-1}^+ (\mathcal{D}^2 - k^2) \tilde{v}_{-1} dy = A_0 A_1^* \int \tilde{\xi}_{-1}^+ G_{-1}(y) dy \exp(\alpha c_i t) \quad (5.87)$$

$$\frac{dA_0}{dt} \int \tilde{\xi}_0^+ (\mathcal{D}^2 - \alpha^2) \tilde{v}_0 dy = A_1 A_{-1} \int \tilde{\xi}_0^+ G_0(y) dy \exp[\alpha(\tilde{c}_i - c_i)t]. \quad (5.88)$$

Introducing the new dependent variables

$$a_{\pm 1}(t) = A_{\pm 1}(t) \exp\left(\frac{1}{2}\alpha \tilde{c}_i t\right) \quad a_0(t) = A_0(t) \exp(\alpha c_i t) \quad (5.89)$$

the exponentials on the right-hand sides drop out and we arrive at

$$\frac{da_1}{dt} = \frac{1}{2}\alpha \tilde{c}_i a_1 + \lambda_1 a_0 a_{-1}^* \quad (5.90)$$

$$\frac{da_{-1}}{dt} = \frac{1}{2}\alpha \tilde{c}_i a_{-1} + \lambda_{-1} a_0 a_1^* \quad (5.91)$$

$$\frac{da_0}{dt} = \alpha c_i a_0 + \lambda_0 a_1 a_{-1} \quad (5.92)$$

with

Re_δ	α	β	αc_i	αc_r	$1/2\alpha\tilde{c}_i$
400	0.31664	0.18517	-0.21356E-2	0.13105	-0.57847E-2
600	0.29602	0.17057	0.93374E-3	0.11472	-0.29180E-2
800	0.28016	0.16014	0.23601E-2	0.10340	-0.14591E-2
1000	0.26758	0.15220	0.31330E-2	0.94981E-1	-0.59308E-3
1200	0.25727	0.14585	0.35885E-2	0.88407E-1	-0.29837E-4

TABLE 5.3. Parameter values for Craik's resonance condition for Blasius boundary layer flow.

$$\lambda_1 = \frac{\int \tilde{\xi}_1^+ G_1(y) dy}{\int \tilde{\xi}_1^+ (\mathcal{D}^2 - k^2) \tilde{v}_1 dy} \quad (5.93)$$

$$\lambda_{-1} = \frac{\int \tilde{\xi}_{-1}^+ G_{-1}(y) dy}{\int \tilde{\xi}_{-1}^+ (\mathcal{D}^2 - k^2) \tilde{v}_{-1} dy} \quad (5.94)$$

$$\lambda_0 = \frac{\int \tilde{\xi}_0^+ G_0(y) dy}{\int \tilde{\xi}_0^+ (\mathcal{D}^2 - \alpha^2) \tilde{v}_0 dy}. \quad (5.95)$$

Example

We will demonstrate resonant triad interactions for Blasius boundary layer flow. As a first step we need to determine wave number combinations (α, β) that satisfy the resonance condition (5.76) for a given Reynolds number. We first solve the Orr-Sommerfeld equation for the two-dimensional wave with streamwise wave number α and determine the phase velocity c_r of the least stable mode. We then solve the Orr-Sommerfeld equation for the three-dimensional wave with $(\alpha/2, \beta)$ and vary the spanwise wave number β until the phase velocity c_r of the three-dimensional perturbation matches the phase velocity of the two-dimensional disturbance, thus satisfying the resonance condition. Figure 5.3(a) shows the interaction of the two oblique waves and the two-dimensional wave superimposed on a contour plot of the phase velocity. As is apparent, the three-dimensional and two-dimensional waves share the same phase velocity contour ($c_r = 0.39$ or $c_r = 0.34$). The corresponding growth rates for the two- and three-dimensional waves can be extracted from Figure 5.3(b).

The linear growth rates for the two- and three-dimensional disturbance as a function of the streamwise wave number α and for two selected Reynolds numbers is presented in Figure 5.4. For the lower Reynolds number we observe a range of wave numbers where the two-dimensional wave is linearly unstable. The three-dimensional disturbance is linearly stable in this range. For higher Reynolds numbers, unstable two- and three-dimensional perturbations can coexist at the same streamwise wave number.

Table 5.3 shows wave number combinations for Blasius boundary layer flow that satisfy the resonance condition for five different Reynolds num-

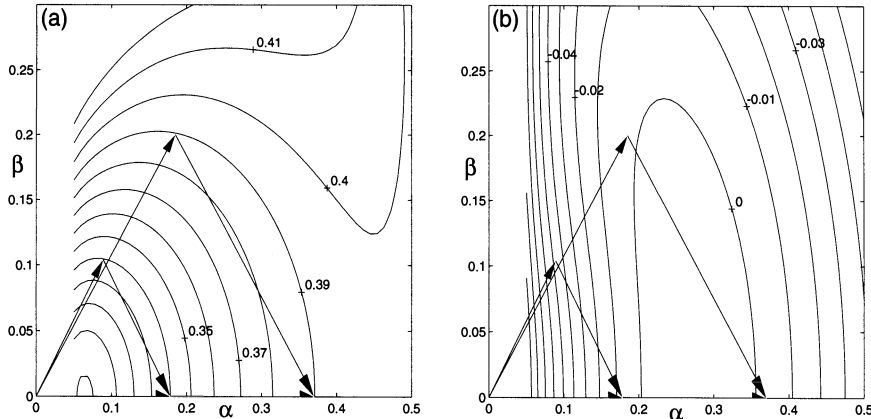


FIGURE 5.3. Contours of phase velocity (a) and growth rate (b) for Blasius boundary layer at $\text{Re}_\delta = 750$, and two selected resonant wave triads.

α	β	c	\tilde{c}	$\lambda_1 = \lambda_{-1}$	λ_0
0.1	0.0617	0.2859 -0.0461 i	0.2859 -0.0888 i	0.5473 +0.7013 i	0.6079 +0.5563 i
0.2	0.1209	0.3394 +0.0041 i	0.3394 -0.0294 i	3.7350 +1.1757 i	0.0083 -0.2471 i
0.3	0.1705	0.3685 +0.0083 i	0.3685 -0.0035 i	8.8249 -0.1495 i	0.4305 -0.3217 i
0.4	0.2098	0.3846 -0.0107 i	0.3846 +0.0035 i	18.8784 -3.7073 i	0.4962 -0.4081 i
0.5	0.1911	0.3834 -0.0444 i	0.3834 +0.0047 i	29.5892 -6.0644 i	0.0129 -0.9701 i

TABLE 5.4. Resonant triads, eigenvalues and second-order interaction coefficients for Blasius flow at $\text{Re} = 882$. From Usher & Craik (1975).

bers. Table 5.4, taken from Usher & Craik (1975), lists the interaction coefficients for the dynamical system (5.90)-(5.92) for a Blasius boundary layer with $\text{Re} = 882$.

5.4.3 Triad Interactions

Energy transfer and energy conservation

The nonlinear part of the Navier-Stokes operator on the right-hand side of equation (5.46) provides the propagation of energy in spectral space by an interaction of different wave numbers that form a triad. The sum over all triads contributing to a given wave number appears as a convolution sum in wave number space. For periodic and localized disturbances the propa-

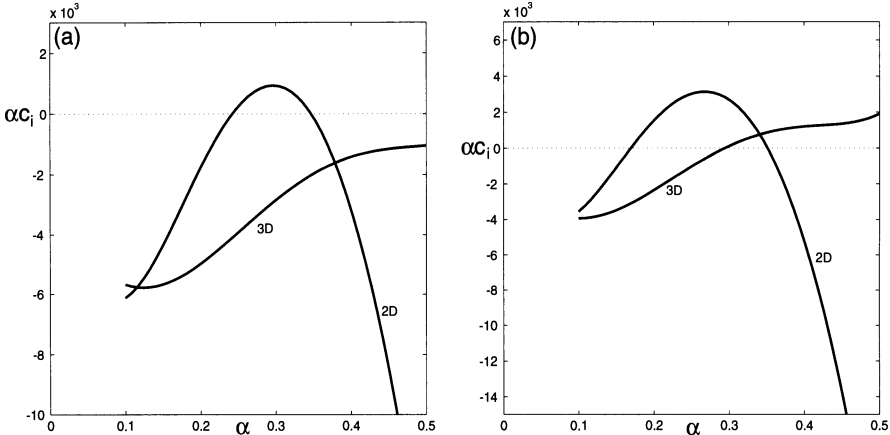


FIGURE 5.4. Growth/decay rate for two-dimensional and three-dimensional waves under resonant conditions. (a) $\text{Re}_\delta = 600$; (b) $\text{Re}_\delta = 1000$.

gation of energy by nonlinear action is conservative. This is an immediate consequence of the Reynolds-Orr equation.

The nonlinear terms of the Navier-Stokes equations are responsible for the exchange of energy between different wave numbers. This is accomplished by an interaction between three different wave numbers whose wave number vectors form a triangle.

Let us define the rate of energy transfer into wave number (α_m, β_n) by an interaction of (α_p, β_q) and (α_k, β_l) where $\alpha_m = \alpha_p + \alpha_k$ and $\beta_n = \beta_q + \beta_l$, as follows:

$$\dot{E}([m, n], [p, q], [k, l]) \equiv \frac{1}{k_{mn}^2} \text{Real} \left\{ \int_{-1}^1 \hat{\mathbf{q}}_{mn}^H \gamma_{(p, q)(k, l)}^{(m, n)} dy \right\}. \quad (5.96)$$

The short form $[m, n]$ has been introduced for (α_m, β_n) and the superscript H denotes the conjugate transpose. The preceding definition follows directly from the right-hand side of equation (5.46) by multiplying with $\hat{\mathbf{q}}_{mn}^H$ and integrating over the channel height. A sketch of the triad interaction in wave number space is given in Figure 5.5. The triangle labeled by 1 depicts the interaction of $[p, q]$ and $[k, l]$ to transfer energy into $[m, n]$.

It is easy to verify by integration by parts and the use of the triad relation between the wave numbers (e.g. Smyth, 1992) that

$$\dot{E}([m, n], [p, q], [k, l]) + \dot{E}([-k, -l], [p, q], [-m, -n]) = 0. \quad (5.97)$$

To continue, we will also define the net energy transfer T into wave number $[m, n]$ as

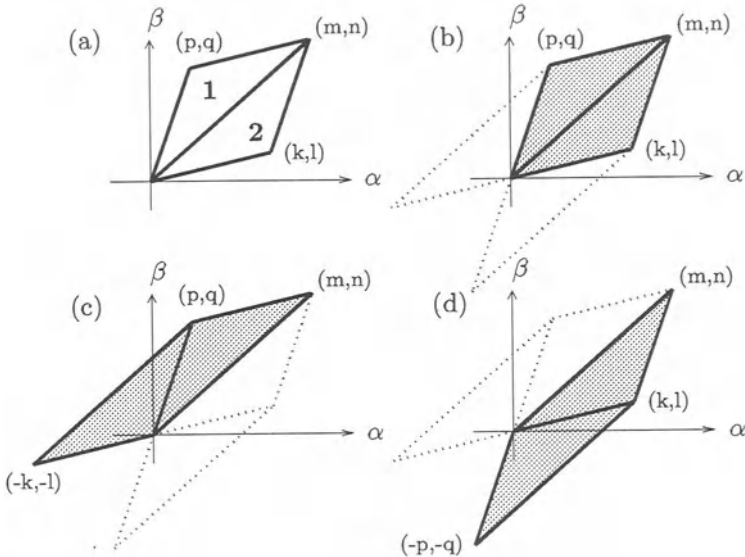


FIGURE 5.5. Sketch of wave number triads.

$$\begin{aligned}
 T([m, n], [p, q], [k, l]) &\equiv \dot{E}([m, n], [p, q], [k, l]) + \dot{E}([m, n], [k, l], [p, q]) \\
 &\equiv \frac{1}{k_{mn}^2} \text{Real} \left\{ \int_{-1}^1 \hat{\mathbf{q}}_{mn}^H [\gamma_{(p,q)(k,l)}^{(m,n)} + \gamma_{(k,l)(p,q)}^{(m,n)}] dy \right\}
 \end{aligned} \tag{5.98}$$

which is equivalent to summing the contributions of the two triad interactions labeled **1** and **2** in Figure 5.5(a). From the definition of T , the following invariances follow immediately:

$$T([m, n], [p, q], [k, l]) = T([m, n], [k, l], [p, q]) \tag{5.99}$$

and

$$T([m, n], [p, q], [k, l]) = T([-m, -n], [-p, -q], [-k, -l]). \tag{5.100}$$

Moreover, using equation (5.97) we can show that

$$\begin{aligned}
 T([m, n], [p, q], [k, l]) + T([p, q], [-k, -l], [m, n]) \\
 + T([k, l], [-p, -q], [m, n]) = 0.
 \end{aligned} \tag{5.101}$$

Therefore, the three net triad interactions given by equation (5.101) have a zero energy transfer rate. The three terms of expression (5.101) are displayed in Figures 5.5(b), 5.5(c), and 5.5(d), respectively. It should be noted

that a sum over all nonlinear triad interactions contains a given wave number triplet $([m, n], [p, q], [k, l])$ only once. For this reason, equation (5.101) implies that the conservation of energy by the nonlinear terms of the Navier-Stokes equations is not only present in a global sense as a sum over all wave numbers; energy is conserved by the nonlinear terms within groups of three net triads as shown in Figure 5.5(b-d). This renders the analysis of the nonlinear energy transfer and the design of nonlinear, highly truncated, but still conservative, model equations feasible.

A constant of motion

Equation (5.101) suggests the design of a generic set of energy-conserving equations based on nonlinear triad interactions shown in Figure 5.5(b-d):

$$\mathbf{M}_{mn} \frac{\partial}{\partial t} \hat{\mathbf{q}}_{mn} = \gamma_{(p,q)(k,l)}^{(m,n)} + \gamma_{(k,l)(p,q)}^{(m,n)} \quad (5.102)$$

$$\mathbf{M}_{pq} \frac{\partial}{\partial t} \hat{\mathbf{q}}_{pq} = \gamma_{(m,n)(-k,-l)}^{(p,q)} + \gamma_{(-k,-l)(m,n)}^{(p,q)} \quad (5.103)$$

$$\mathbf{M}_{kl} \frac{\partial}{\partial t} \hat{\mathbf{q}}_{kl} = \gamma_{(-p,-q)(m,n)}^{(k,l)} + \gamma_{(m,n)(-p,-q)}^{(k,l)}. \quad (5.104)$$

This set of equations can be derived from equation (5.46) by neglecting all linear terms of the evolution operator and including only the nonlinear terms associated with the energy-conserving triads in (5.101).

We will conclude this section by mentioning the existence of an integral of motion that can be derived in an abstract form due to the conservation of initial energy within a specific triad. We multiply the three equations (5.102)-(5.104) by $\hat{\mathbf{q}}_{mn}^H/k_{mn}^2$, $\hat{\mathbf{q}}_{pq}^H/k_{pq}^2$, and $\hat{\mathbf{q}}_{kl}^H/k_{kl}^2$, respectively, integrate over the domain, and sum the three equations. Using equation (5.101) and the definition of T we find

$$\begin{aligned} & \frac{1}{k_{mn}^2} \frac{\partial}{\partial t} \int_{-1}^1 \hat{\mathbf{q}}_{mn}^H \mathbf{M}_{mn} \hat{\mathbf{q}}_{mn} dy + \frac{1}{k_{pq}^2} \frac{\partial}{\partial t} \int_{-1}^1 \hat{\mathbf{q}}_{pq}^H \mathbf{M}_{pq} \hat{\mathbf{q}}_{pq} dy \\ & + \frac{1}{k_{kl}^2} \frac{\partial}{\partial t} \int_{-1}^1 \hat{\mathbf{q}}_{kl}^H \mathbf{M}_{kl} \hat{\mathbf{q}}_{kl} dy = \frac{1}{k_{mn}^2} \text{Real} \left\{ \int_{-1}^1 \hat{\mathbf{q}}_{mn}^H (\gamma_{(p,q)(k,l)}^{(m,n)} + \gamma_{(k,l)(p,q)}^{(m,n)}) dy \right\} \\ & + \frac{1}{k_{pq}^2} \text{Real} \left\{ \int_{-1}^1 \hat{\mathbf{q}}_{pq}^H (\gamma_{(m,n)(-k,-l)}^{(p,q)} + \gamma_{(-k,-l)(m,n)}^{(p,q)}) dy \right\} \\ & + \frac{1}{k_{kl}^2} \text{Real} \left\{ \int_{-1}^1 \hat{\mathbf{q}}_{kl}^H (\gamma_{(-p,-q)(m,n)}^{(k,l)} + \gamma_{(m,n)(-p,-q)}^{(k,l)}) dy \right\} = 0 \end{aligned} \quad (5.105)$$

which further simplifies to the integral of motion

$$\begin{aligned} \frac{1}{k_{mn}^2} \int_{-1}^1 \mathbf{q}_{mn}^H \mathbf{M}_{mn} \mathbf{q}_{mn} dy + \frac{1}{k_{pq}^2} \int_{-1}^1 \mathbf{q}_{pq}^H \mathbf{M}_{pq} \mathbf{q}_{pq} dy \\ + \frac{1}{k_{kl}^2} \int_{-1}^1 \mathbf{q}_{kl}^H \mathbf{M}_{kl} \mathbf{q}_{kl} dy = E_0 = \text{const} \end{aligned} \quad (5.106)$$

where E_0 denotes the initial energy. For the design of highly truncated dynamical systems, triads like the preceding one are fundamental energy-conserving building blocks.

Equations for complete energy dynamics

In the assessment of the role of linear and nonlinear processes in the finite-amplitude development of a disturbance it is useful to consider the total energy dynamics of a particular Fourier mode. Using (5.46) and (4.15) we have

$$\begin{aligned} \frac{d}{dt} E_{mn} = \frac{1}{k_{mn}^2} \text{Real} \left\{ \int_{-1}^1 \hat{\mathbf{q}}_{mn}^H \mathbf{L} \hat{\mathbf{q}}_{mn} dy \right\} \\ + \frac{1}{k_{mn}^2} \text{Real} \left\{ \sum_{k+i=m, l+j=n} \int_{-1}^1 \hat{\mathbf{q}}_{mn}^H \mathbf{N}(\hat{\mathbf{q}}_{kl}, \hat{\mathbf{q}}_{ij}) dy \right\}. \end{aligned} \quad (5.107)$$

The first integral represents the rate of energy transfer due to linear terms; the second integral accounts for nonlinear wave-triad interactions. When the time rate of change of the total disturbance energy is calculated by summing (5.107) over all wave numbers the second integral vanishes which follows from the preceding arguments:

$$\frac{dE}{dt} = \frac{d}{dt} \sum_{mn} E_{mn} = \sum_{mn} \frac{1}{k_{mn}^2} \text{Real} \left\{ \int_{-1}^1 \hat{\mathbf{q}}_{mn}^H \mathbf{L} \hat{\mathbf{q}}_{mn} dy \right\}. \quad (5.108)$$

This again shows that the relative change of the total energy is independent of the disturbance amplitude, i.e., at every instant the quantity $\frac{1}{E} \frac{dE}{dt}$ is unaffected by a rescaling of the amplitude. Hence, if all infinitesimal disturbances exhibit monotonic total energy decay, finite-amplitude disturbances will also decay monotonically. Conversely, if any finite-amplitude disturbance exhibits total energy growth there must exist an instantaneously growing infinitesimal disturbance. The latter statement can readily be confirmed by rescaling the finite-amplitude disturbance.

5.5 Solutions to the Nonlinear Initial Value Problem

5.5.1 Formal Solutions to the Nonlinear Initial Value Problem

Expansion in normal modes

We will expand the solution to the full nonlinear problem (5.46) in terms of eigenfunctions of equation (3.33), allowing the coefficients to be time-dependent. We introduce

$$\hat{\mathbf{q}}_{mn} = \sum_p K_{mnp}(t) \tilde{\mathbf{q}}_{mnp} \quad (5.109)$$

into equation (5.46). To find a system of ordinary differential equations governing the time-dependent coefficients K_{mnp} we multiply by the adjoint eigenfunctions and use the bi-orthogonality relations. We obtain

$$\frac{dK_{mns}}{dt} + i\omega_s K_{mns} = \sum_p \sum_r \sum_{k+q=m} \sum_{l+j=n} K_{klp} K_{qjr} \Gamma_{(klp)(qjr)}^{(mns)} \quad (5.110)$$

with the quadratic interaction coefficients given as

$$\Gamma_{(klp)(qjr)}^{(mns)} = \int_{-1}^1 \tilde{\mathbf{q}}_{mns}^H \mathbf{A}_{mn} \left\{ \mathcal{D}_{mn}^T \left[\mathbf{C}_{kl} \tilde{\mathbf{q}}_{klp} (\mathbf{C}_{qj} \tilde{\mathbf{q}}_{qjr})^T \right] \right\}^T dy. \quad (5.111)$$

We have assumed simple eigenvalues although degeneracies can be incorporated in a straightforward manner (see Appendix B). The initial conditions for the system are found by projecting the initial flow field $\hat{\mathbf{q}}_{mn}^0$ onto the linear eigenfunctions; we have

$$K_{mns}^0 = (\mathbf{M} \hat{\mathbf{q}}_{mn}^0, \tilde{\mathbf{q}}_{mns}^+). \quad (5.112)$$

For large Reynolds numbers the nonorthogonality of the eigenfunctions associated with the linear problem makes them unattractive as expansion functions and causes numerical difficulties in the calculation of the expansion coefficients (see Reddy *et al.*, 1993). For example, nearly linearly dependent eigenfunctions cause values of the expansion coefficients that may be orders of magnitude larger than the function they approximate. Orthogonal expansion functions that still retain some of the physical properties of the initial value problem can be computed from the selfadjoint part of the linear equation. Dolph & Lewis (1958) used this approach for the Orr-Sommerfeld problem in an early investigation of the linear stability of Poiseuille flow, and Nagata (1990) used a similar idea in his nonlinear study of Couette flow. In the following section we will generalize this approach using vector eigenfunctions.

Expansion in orthogonal modes and numerical solutions

We divide the linear operator \mathbf{L}_{mn} into a selfadjoint part, \mathbf{L}_{mn}^S , and a remaining non-selfadjoint operator denoted by \mathbf{B}_{mn} :

$$\mathbf{L}_{mn}^S = \begin{pmatrix} (\mathcal{D}^2 - k_{mn}^2)^2 / \text{Re} & 0 \\ 0 & -(\mathcal{D}^2 - k_{mn}^2) / \text{Re} \end{pmatrix} \quad (5.113)$$

$$\mathbf{B}_{mn} = \begin{pmatrix} -i\alpha_m U (\mathcal{D}^2 - k_{mn}^2) + i\alpha_m U'' & 0 \\ i\beta_n U' & i\alpha_m U \end{pmatrix}. \quad (5.114)$$

Although the selfadjoint eigenvalue problem associated with \mathbf{L}_{mn}^S has real eigenvalues and eigenfunctions we still introduce the complex eigenvalue $i\omega$ to conform to the previous notation. Realizing that ω will be purely imaginary, we will use expansion functions that are solutions to the following eigenvalue problem (where we have dropped the subscripts m and n for convenience)

$$(\mathbf{L}^S - i\omega \mathbf{M}) \tilde{\mathbf{q}} = 0. \quad (5.115)$$

The boundary conditions are identical to the non-selfadjoint case. One may easily verify that the new expansion functions satisfy the following orthogonality relations:

$$(\mathbf{M}\tilde{\mathbf{q}}_p, \tilde{\mathbf{q}}_r) = (\tilde{\mathbf{q}}_p, \mathbf{M}\tilde{\mathbf{q}}_r) = \delta_{pr} \quad (5.116)$$

$$(\mathbf{L}^S \tilde{\mathbf{q}}_p, \tilde{\mathbf{q}}_r) = (\tilde{\mathbf{q}}_p, \mathbf{L}^S \tilde{\mathbf{q}}_r) = i\omega_p \delta_{pr} \quad (5.117)$$

where ω_p are eigenvalues of equation (5.115).

We again assume an expansion of the form (5.109), now with the orthogonal set of functions. Upon substitution into equation (5.46) we find the following system of equations for the time-dependent coefficients:

$$\begin{aligned} \frac{dK_{mns}}{dt} + i\omega_s K_{mns} &= - \sum_p K_{mnp} (\mathbf{B}_{mn} \tilde{\mathbf{q}}_{mnp}, \tilde{\mathbf{q}}_{mns}) \\ &\quad + \sum_p \sum_r \sum_{k+q=m} \sum_{l+j=n} K_{klp} K_{qjr} \bar{\Gamma}_{(klp)(qjr)}^{(mns)} \end{aligned} \quad (5.118)$$

with

$$\bar{\Gamma}_{(klp)(qjr)}^{(mns)} = \int_{-1}^1 \tilde{\mathbf{q}}_{mns}^T \mathbf{A}_{mn} \left\{ \mathcal{D}_{mn}^T \left[\mathbf{C}_{kl} \tilde{\mathbf{q}}_{klp} (\mathbf{C}_{qj} \tilde{\mathbf{q}}_{qjr})^T \right] \right\}^T dy. \quad (5.119)$$

The system of equations is now coupled by the non-selfadjoint part of the linear operator as well as by the nonlinear terms.

5.5.2 Weakly Nonlinear Solutions and the Center Manifold

Given the nonlinear system (5.110), weakly nonlinear solutions can be extracted in an elegant manner with the help of center manifold theory (Carr, 1981). In general, center manifold theory uses the fact that – in the asymptotic limit of large times and in the absence of unstable modes – dynamical systems are governed by modes that are approximately neutrally stable; decaying modes, on the other hand, experience a functional dependence on the neutrally stable modes. In phase space, the center manifold is tangent to the space spanned by the neutrally stable eigenvectors and attracts the solution of the system as time progresses. The existence of neutral modes is essential to the applicability of center manifold theory. Because the dynamical system (5.110) describes disturbance evolution in plane Poiseuille flow, the finite-amplitude neutral stability surface calculated by Herbert (1977) constitutes the parameter subspace that assures the existence of a center manifold. This restriction to the neutral stability surface also indicates a connection to weakly nonlinear amplitude expansions. However, we like to emphasize that center manifold theory can be applied *anywhere* close to the finite-amplitude neutral surface and is by no means restricted to the nearly linear regime.

Although valid for infinite-dimensional systems, we apply center manifold theory to an N -dimensional representation of equation (5.110). Furthermore, we assume N distinct eigenvalues and choose the parameters such that one mode is close to the neutral stability surface. Assuming that the mode with expansion coefficient K_0 is neutrally stable we write (5.110) as

$$\frac{dK_0}{dt} + i\omega_0 K_0 = f(K_0, K_i) \quad (5.120)$$

$$\frac{dK_j}{dt} + i\omega_j K_j = g_j(K_0, K_i) \quad i, j = 1, 2, \dots, N-1 \quad (5.121)$$

with $\text{Imag}(\omega_j) \ll \text{Imag}(\omega_0) \approx 0$. The functions f and g are strictly quadratic polynomials in the expansion coefficients and represent the right-hand side of equation (5.110). In the preceding equations, i and j are assumed to span all three indices associated with the expansion coefficients. In the limit of large time the motion of the system will largely depend on the neutrally stable mode K_0 and the center manifold theorem (Carr, 1981) assures that all of the subdominant modes have the following expansion:

$$K_j = \gamma_j^{(2)} K_0^2 + \gamma_j^{(3)} K_0 K_0^* + \gamma_j^{(4)} K_0^{*2} + \dots \quad (5.122)$$

Substituting (5.122) into equation (5.121) yields

$$\begin{aligned} & \left[2\gamma_j^{(2)} K_0 + \gamma_j^{(3)} K_0^* + \dots \right] \left[-i\omega_0 K_0 + f(K_0, \gamma_i^{(2)} K_0^2 + \dots) \right] + \\ & \left[2\gamma_j^{(4)} K_0^* + \gamma_j^{(3)} K_0 + \dots \right] \left[i\omega_0^* K_0^* + f^*(K_0, \gamma_i^{(2)} K_0^2 + \dots) \right] + \quad (5.123) \\ & i\omega_j \left[\gamma_j^{(2)} K_0^2 + \dots \right] - g_j \left(K_0, \gamma_i^{(2)} K_0^2 + \dots \right) = 0. \end{aligned}$$

From this equation, the unknown coefficients $\gamma_j^{(m)}$ can easily be determined by matching terms of equal powers in K_0 and K_0^* . The equation for the asymptotic behavior of the system, i.e., the equation governing the motion on the center manifold is then given by

$$\frac{dK_0}{dt} + i\omega_0 K_0 = f(K_0, \gamma_i^{(2)} K_0^2 + \gamma_i^{(3)} K_0 K_0^* + \gamma_i^{(4)} K_0^{*2} + \dots). \quad (5.124)$$

This idea can readily be generalized for multidimensional center manifolds, including degenerate modes. One example is the Stuart-Watson expansion (see Stuart, 1960; Watson, 1960), resulting in the Landau equation (see, e.g., Fujimura, 1989, 1991).

Alternatively, (5.110) can be reduced to a low-dimensional dynamical system by truncating the number of modes (see Bergström (1999) for an example of plane Poiseuille flow).

5.5.3 Nonlinear Equilibrium States

General concept

In the previous sections of this chapter we have incorporated nonlinearities in the governing equations, but additional assumptions were necessary to obtain a mathematically tractable problem. For the case of weakly nonlinear theory (Section 5.3) we used a perturbation expansion near the neutral curve that quickly diverged for parameter values far from neutral. For resonant triad interactions (Section 5.4) we exploited the resonance condition between the wave number vector and the associated frequencies to arrive at a tractable problem. However, these resonance conditions do not hold throughout parameter space but are rather limited to a small subspace.

Advanced numerical techniques and powerful computers have made it feasible to attack the full nonlinear problem; as a result two techniques for investigating the nonlinear problem have emerged. The first is based on the initial value problem and studies selected initial conditions as they propagate in time. An alternative approach is based on a global numerical bifurcation analysis in parameter space, which will be discussed in this section. This second approach is equivalent to investigating a nonlinear dynamical system by studying its fixed points and classifying the local

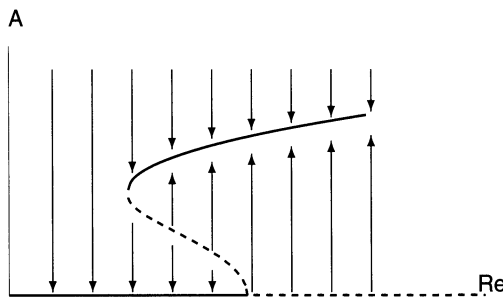


FIGURE 5.6. Sketch of nonlinear saturation for subcritical bifurcation behavior.

stability behavior near these equilibrium states. The first approach, on the other hand, would correspond to integrating the nonlinear dynamical system in time and describing the solution behavior for various parameter values and initial conditions.

Nonlinear equilibrium solutions provide important information on the dynamics of the nonlinear system; in fact, there is numerical and experimental evidence of a relation between these equilibrium states and coherent structures in transitional and turbulent flows. Even if equilibrium states are not observable due to their stability characteristics, they may have a pronounced influence on the overall dynamics of a nonlinear system of equations.

Based on the fact that most shear flows exhibit a subcritical bifurcation to finite-amplitude states, we expect a nonlinear equilibrium surface in the qualitative shape displayed in Figure 5.6.

Governing equations

The starting point for the analysis of nonlinear equilibrium states is the nonlinear initial value problem, which we reproduce here from (5.46)

$$(\mathbf{L}_{mn} + \frac{\partial}{\partial t} \mathbf{M}_{mn}) \hat{\mathbf{q}}_{mn} = \sum_{k+p=m} \sum_{l+q=n} \gamma_{(k,l)(p,q)}^{(m,n)}. \quad (5.125)$$

For the subsequent analysis we will assume a constant mean-pressure-gradient base flow.

Because we are interested in traveling-wave-type solutions it is advantageous to introduce a reference frame moving in the x -direction with a (yet unknown) wave speed C . The coordinate transformation

$$x' = x - ct \quad \frac{\partial}{\partial t} = -C \frac{\partial}{\partial x'} \rightarrow -i\alpha_m C \quad (5.126)$$

results in

$$(\mathbf{L}_{mn} - i\alpha_m C \mathbf{M}_{mn}) \hat{\mathbf{q}}_{mn} = \sum_{k+p=m} \sum_{l+q=n} \gamma_{(k,l)(p,q)}^{(m,n)}. \quad (5.127)$$

Defining

$$\hat{\mathbf{q}} = \{\hat{v}_{mn}, \hat{\eta}_{mn}, \hat{u}_{00}, C\} \quad (m, n) \neq (0, 0) \quad (5.128)$$

$$\lambda = \{\alpha, \beta, \text{Re}\} \quad (5.129)$$

we can write equation (5.127) symbolically as

$$\mathbf{F}(\hat{\mathbf{q}}, \lambda) = 0 \quad (5.130)$$

which represents a large system of nonlinear differential equations. After the normal direction has been discretized we obtain a nonlinear algebraic system of equations which is solved by Newton-Raphson iteration in conjunction with a pseudo-arclength continuation procedure (Keller, 1977).

The arclength continuation procedure parameterizes the solution to the nonlinear equation (5.130) by a scalar variable s and imposes an arclength condition of the form

$$\left(\frac{d\hat{\mathbf{q}}}{ds} \right)^2 + \left(\frac{d\lambda}{ds} \right)^2 = 1 \quad (5.131)$$

which after discretization in the s -direction results in the system of equations

$$N(\hat{\mathbf{q}}, \lambda, s) \equiv (\hat{\mathbf{q}}(s) - \hat{\mathbf{q}}(s_0)) \left. \frac{d\hat{\mathbf{q}}}{ds} \right|_{s_0} + (\lambda(s) - \lambda(s_0)) \left. \frac{d\lambda}{ds} \right|_{s_0} - (s - s_0) = 0 \quad (5.132)$$

where s_0 denotes a previously computed point. The extended system of equations

$$\mathbf{F}(\hat{\mathbf{q}}, \lambda) = 0 \quad N(\hat{\mathbf{q}}, \lambda, s) = 0 \quad (5.133)$$

avoids the singularity of ordinary parameter continuation at a turning point of the solution curve.

It is customary to use the total disturbance energy as a scalar measure of the nonlinear equilibrium state. Alternatively, an amplitude of the equilibrium state can be defined from its total disturbance energy.

To start the pseudo-arc length continuation procedure we need a known solution. In general neutral solutions of the linear problem are used as a starting point for equilibrium states of finite amplitude.

Two-dimensional analysis

Nonlinear equilibrium solutions to the system of equations (5.133) have been found for two-dimensional disturbances. With

$$\lambda = \{\alpha, 0, \text{Re}\} \quad (5.134)$$

and starting with the neutral linear stability curve, Zahn *et al.* (1974) and Herbert (1977) computed finite-amplitude solutions to the system of equations (5.133) for plane Poiseuille flow and Herbert (1977) extended the neutral linear stability curve to neutral finite-amplitude states. Figure 5.7 shows the two-dimensional nonlinear equilibrium surface reproduced by Ehrenstein & Koch (1991). We observe that the smallest Reynolds number that supports steady two-dimensional finite-amplitude states is $\text{Re} = 2702$, which is significantly lower than the critical Reynolds number of 5772 obtained from linear stability theory; this confirms a conjecture made by Landau (see Landau & Lifshitz, 1959). It also verifies the subcritical bifurcation behavior of linear neutral solutions based on the sign of the cubic Landau coefficient. Studies of equilibrium states have been found to be sensitive to the number N of Fourier components included. For highly accurate and reliable results, truncations with $N \gg 2$ are needed.

Three-dimensional analysis

Three-dimensional computations have been performed by Ehrenstein & Koch (1991) and Soibelman & Meiron (1991), who started from two-dimensional neutral solutions and solved (5.133) to determine three-dimensional steady states.

Results from Ehrenstein & Koch (1991) for plane Poiseuille flow are displayed in Figure 5.8. The neutral surface for finite-amplitude disturbances depends on four parameters – the streamwise and spanwise wave numbers, the Reynolds number, and the equilibrium amplitude/energy – and is thus difficult to visualize. Figure 5.8 presents slices through parameter space and gives a first indication of the convoluted structure of the neutral surface for plane Poiseuille flow.

Ehrenstein & Koch (1991) found finite-amplitude equilibrium solutions at Reynolds numbers as low as 1000 which is the experimentally observed Reynolds number below which turbulence cannot be sustained (see Table 1.1).

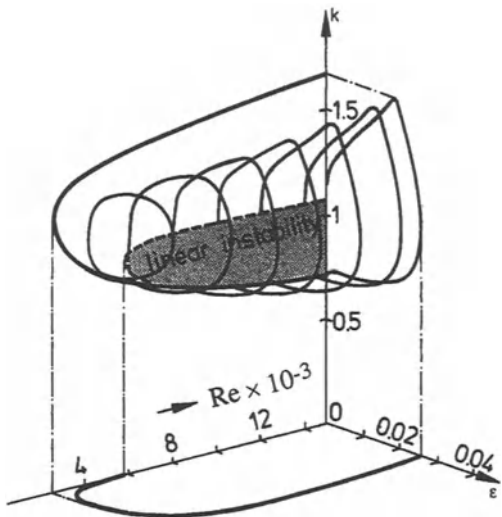


FIGURE 5.7. Perspective view and projection of two-dimensional ($\beta = 0$) non-linear equilibrium surface with $K = 20$ and $N = 2$. From Ehrenstein & Koch (1991).

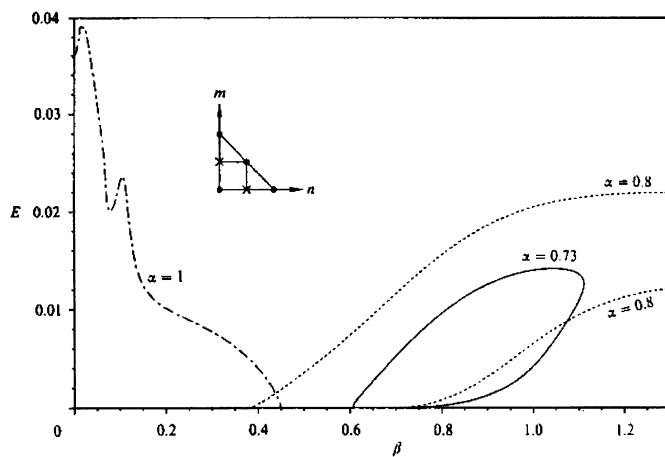


FIGURE 5.8. Three-dimensional primary equilibrium surface for $Re_p = 8000$ and various $\alpha = \text{const.}$ cuts with $K = 15$ and triangular modal cut off at $N = M = 2$. From Ehrenstein & Koch (1991).

Nagata (1990) computed steady three-dimensional finite-amplitude solutions for plane Couette flow by extending circular narrow-gap Couette flow between corotating cylinders to the case with zero average rotation rate. He found equilibrium states for Reynolds numbers as low as $\text{Re} = 125$ and refers to this type of bifurcation analysis as “bifurcation from infinity.”

Both analyses of Ehrenstein & Koch (1991) and Nagata (1990) used highly truncated versions of (5.133). Lundbladh (1993a) performed high-resolution direct numerical simulations and found Nagata’s solutions to be stable.

5.5.4 Numerical Solutions for Localized Disturbances

The difficulty in obtaining general solutions to the nonlinear initial value problem makes progress only possible by using numerical methods to solve the Navier-Stokes equations. In this section we will show numerical solutions for localized disturbances in plane Poiseuille flow at subcritical Reynolds numbers. We have seen that the dominating growth mechanism for such cases is nonmodal growth and we expect this mechanism to play an important role in the nonlinear development as well. In this section we will address the onset of nonlinearity, but will leave the simulation of the complete laminar-turbulent transition process to Chapter 9.

The results presented here are also qualitatively valid for single-wave disturbances. However, we have chosen localized disturbances to contrast our findings to the linear development of such disturbances studied in the previous chapter. In terms of single-wave disturbances, the transition scenario that most closely resembles the scenario considered here is referred to as oblique or O-type transition, see Chapter 9.

Amplitude expansion

An amplitude expansion has proven instrumental in studying the onset of nonlinear effects in numerical simulations of localized disturbances since it allows the decomposition of flow fields into linear, quadratic and cubic parts. We write the following expansion

$$u(\epsilon) = \sum_{j=0}^n u_k \epsilon^k + \mathcal{O}(\epsilon^{n+1}) \quad (5.135)$$

where u may represent any of the velocity or vorticity components and the dependence on x, y, z, t has not been explicitly indicated. In the preceding expansion we take u_0 to represent the parabolic mean flow. The remaining u_k -components can be found by evaluating $u(\epsilon)$ for various values of the amplitude ϵ and solving for the expansion coefficients in (5.135), neglecting the error term. Using the velocity field for three different values of ϵ we calculate u_1, u_2, u_3 as solutions to the following linear system

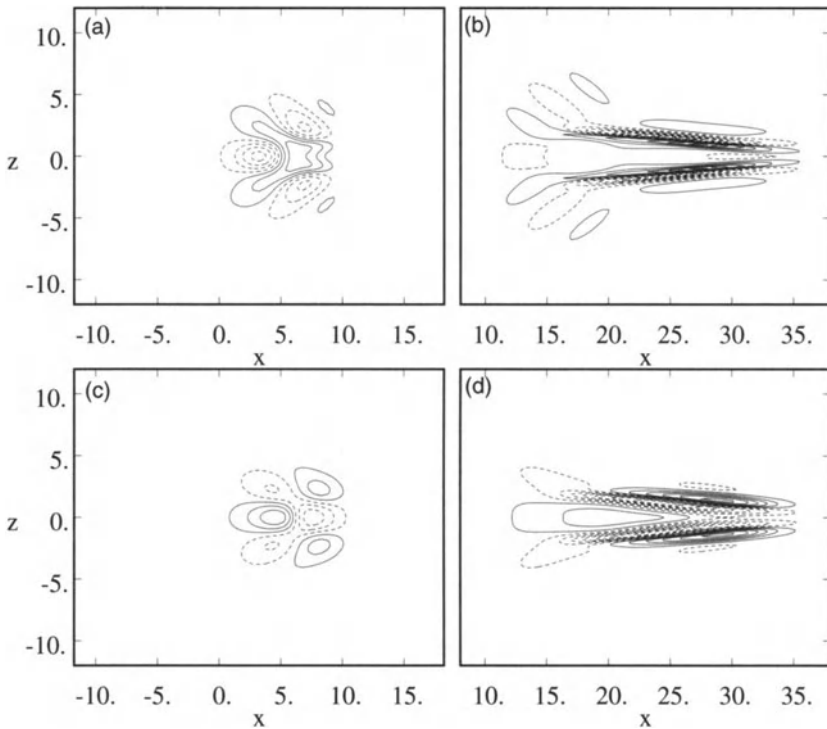


FIGURE 5.9. Temporal evolution of finite-amplitude localized disturbance. Velocity contours at $y = -0.56$: (a) normal velocity at $t = 10$; (b) normal velocity at $t = 40$; (c) streamwise velocity at $t = 10$; (d) streamwise velocity at $t = 40$. The contour spacing of the streamwise velocity is 10 times that of the normal velocity. From Henningson *et al.* (1993).

$$\begin{pmatrix} \epsilon_1 & \epsilon_1^2 & \epsilon_1^3 \\ \epsilon_2 & \epsilon_2^2 & \epsilon_2^3 \\ \epsilon_3 & \epsilon_3^2 & \epsilon_3^3 \end{pmatrix} \begin{pmatrix} u_1 \\ u_2 \\ u_3 \end{pmatrix} = \begin{pmatrix} u(\epsilon_1) \\ u(\epsilon_2) \\ u(\epsilon_3) \end{pmatrix}. \quad (5.136)$$

In our case we chose the amplitudes $\epsilon_1 = 0.0005$, $\epsilon_2 = 0.001$ and $\epsilon_3 = 0.002$ for the initial disturbance. This system has to be solved for each combination of x, y, z, t of interest.

Poiseuille example

The initial condition first presented in Section 4.7.1 is used in direct numerical simulations for plane Poiseuille flow.

The normal velocity field (Figure 5.9) is dominated by narrow elongated patterns. The wave packet (as observed in linear computations) is also

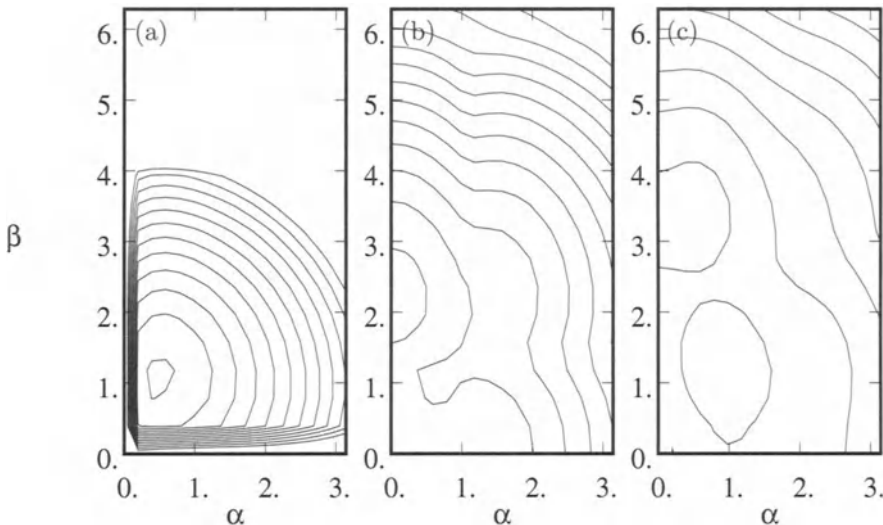


FIGURE 5.10. Energy spectra of localized disturbance at $t = 15$ obtained from an amplitude expansion. (a) Linear part; (b) quadratic part; (c) cubic part. Contour spacing of one decade. From Henningson *et al.* (1993).

present, but it plays a minor role because its amplitude is much smaller than the more localized and faster moving central part of the disturbance. The emerging streaks are associated with sharp spanwise gradients.

Signs of nonlinearity are first seen in the normal velocity, and only later in the horizontal velocities. Neither the normal nor the streamwise velocity decay in the moderate-amplitude case, in contrast to the linear case. During the nonlinear phase of the evolution the disturbance development is strongly influenced by the large spanwise shear associated with the formation of streaky structures.

The nature of the nonlinear interactions is illustrated in Figure 5.10, where the energy spectra of the first three terms of the amplitude expansion are plotted. The quadratic part of the spectrum has peaks along the streamwise and spanwise wave number axes, and the cubic term continues the cascade of energy to smaller spanwise scales, close to the β -axis. The linear part is dominated by the wave packet, whereas the quadratic part is responsible for the formation of streaky structures as energy is focused along the spanwise wave number axis.

The initial stages of finite-amplitude development can be understood by considering the action of the nonlinear terms in the Navier-Stokes equations in Fourier space. An initial energy distribution with peaks at $(\pm\alpha, \pm\beta)$ in the spectral plane will give rise to new peaks at $(\pm 2\alpha, \pm 2\beta)$, $(\pm 2\alpha, 0)$, $(0, \pm 2\beta)$, and $(0, 0)$. The last is a modification of the mean profile and the

first tends to vanish due to the large values of the exponential damping in that region of wave number space. Of the remaining two peaks, the one with zero streamwise wave number dominated which explains the tendency toward the formation of elongated patterns with roughly half the wavelength of the initial disturbance. First- and higher-order nonlinear interactions tend to propagate energy along the β -axis to $(0, \pm 2\beta)$ and further to $(\pm\alpha, \pm 3\beta)$, $(0, \pm 4\beta)$, etc. We will refer to this preferred propagation of energy along the spanwise wave number axis as the *β -cascade*.

5.6 Energy Theory

5.6.1 The Energy Stability Problem

The evolution of disturbance energy

As has already been alluded to in Chapter 1 and will be further discussed in this chapter, the nonlinear terms in the Navier-Stokes equations do not contribute to the increase or decrease of kinetic perturbation energy. This remarkable fact can be used to derive bounds on the evolution of energy. This section is devoted to a brief exposition of energy theory to describe the evolution and stability characteristics of finite-amplitude disturbances. Despite the fact that the governing stability equations are linear, we treat this branch of stability theory as a nonlinear theory, because it applies to disturbances of arbitrary amplitude; only the property of energy conservation of the nonlinear Navier-Stokes terms allows us to reduce it to a linear problem.

The nonlinear disturbance equations based on a mean velocity profile U_i are given by

$$\frac{\partial u_i}{\partial t} + u_j \frac{\partial U_i}{\partial x_j} + U_j \frac{\partial u_i}{\partial x_j} + u_j \frac{\partial u_i}{\partial x_j} + \frac{\partial p}{\partial x_i} - \frac{1}{\text{Re}} \frac{\partial^2 u_i}{\partial x_j \partial x_j} = 0 \quad (5.137)$$

$$\frac{\partial u_i}{\partial x_i} = 0 \quad (5.138)$$

with the boundary conditions

$$u_i = 0 \quad \text{on solid boundaries} \quad (5.139)$$

and the initial condition

$$u_i(t=0) = u_i^0(x_i). \quad (5.140)$$

We will measure the disturbance size in terms of the kinetic energy defined as

$$E(t) = \frac{1}{2} \int_V u_i u_i \, dV. \quad (5.141)$$

The evolution equation for the disturbance energy is known as the Reynolds-Orr equation and was already derived in Chapter 1:

$$\frac{dE}{dt} = - \int_V u_i u_j \frac{\partial U_i}{\partial x_j} \, dV - \frac{1}{Re} \int_V \frac{\partial u_i}{\partial x_j} \frac{\partial u_i}{\partial x_j} \, dV. \quad (5.142)$$

Several features are worth noting. First, the evolution of disturbance energy is governed by two terms. The first term describes an interaction with the mean shear and is responsible for the growth of energy, whereas the second term is negative and describes the decrease of disturbance energy by viscous dissipation. A more familiar formulation of the first term is given by

$$u_i u_j \frac{\partial U_i}{\partial x_j} = u_i u_j D_{ij} \quad (5.143)$$

with

$$D_{ij} = \frac{1}{2} \left[\frac{\partial U_i}{\partial x_j} + \frac{\partial U_j}{\partial x_i} \right] \quad (5.144)$$

as the mean strain rate.

Second, it is important to note that the terms stemming from the nonlinear terms of the Navier-Stokes equations are not present in the final evolution equation for the energy. We therefore conclude that the nonlinear terms of the Navier-Stokes equation preserve energy, a fact that has already been pointed out in previous chapters. The evolution of energy is solely determined by the linear terms of the Navier-Stokes equations. We like to stress, however, that this result crucially depends on the definition of the disturbance energy, as well as on the choice of the mean velocity profile.

The energy Reynolds number

We can now formulate the energy stability problem: We are interested in the critical Reynolds number, denoted by Re_E , below which the kinetic energy of *any* finite-amplitude disturbance decays monotonically. The mathematical formulation of this problem leads us to a variational principle

$$\frac{1}{Re_E} = \max_{u_i} - \frac{\int_V u_i u_j D_{ij} \, dV}{\int_V \frac{\partial u_i}{\partial x_j} \frac{\partial u_i}{\partial x_j} \, dV}. \quad (5.145)$$

Substituting into the evolution equation for the disturbance energy results in

$$\frac{dE}{dt} = \left[-\frac{\int_V u_i u_j D_{ij} dV}{\int_V \frac{\partial u_i}{\partial x_j} \frac{\partial u_i}{\partial x_j} dV} - \frac{1}{Re} \right] \int_V \frac{\partial u_i}{\partial x_j} \frac{\partial u_i}{\partial x_j} dV. \quad (5.146)$$

We assume that \tilde{u}_i maximizes this expression, and let $u_i(t=0) = \tilde{u}_i$. It then follows that

$$\frac{dE(0)}{dt} = \int_V \frac{\partial \tilde{u}_i}{\partial x_j} \frac{\partial \tilde{u}_i}{\partial x_j} dV \left[\frac{1}{Re_E} - \frac{1}{Re} \right] > 0 \quad \text{if } Re > Re_E \quad (5.147)$$

which means that for Reynolds numbers below Re_E all initial conditions monotonically decay.

Let us now solve the variational problem and determine the critical Reynolds number Re_E . Recasting the preceding problem as

$$\frac{1}{Re} = \max_{u_i} \frac{P(u_i)}{D(u_i)} \quad (5.148)$$

where $P(u_i)$ and $D(u_i)$ denote the production and dissipation functionals, we assume the velocity field u_i to be of the form

$$u_i = \tilde{u}_i + \epsilon \eta_i \quad (5.149)$$

where \tilde{u}_i maximizes the quotient and $\epsilon \eta_i$ denotes a small deviation from this velocity field.

The first variation of the quotient then becomes

$$\begin{aligned} \frac{\partial}{\partial \epsilon} \left(\frac{1}{Re} \right) \Big|_{\epsilon=0} &= \frac{1}{D} \left[\frac{\partial P}{\partial \epsilon} + \frac{P}{D} \frac{\partial D}{\partial \epsilon} \right]_{\epsilon=0} \\ &= \frac{1}{D} \left[\frac{\partial P}{\partial \epsilon} + \frac{1}{Re} \frac{\partial D}{\partial \epsilon} \right]_{\epsilon=0} = 0. \end{aligned} \quad (5.150)$$

Applying this technique to our problem requires the evaluation of the following terms

$$\frac{\partial}{\partial \epsilon} \left[- \int_V u_i u_j D_{ij} dV \right] = -2 \int_V u_j D_{ij} \frac{\partial u_i}{\partial \epsilon} dV \quad (5.151)$$

$$\frac{\partial}{\partial \epsilon} \left[\int_V \frac{\partial u_i}{\partial x_j} \frac{\partial u_i}{\partial x_j} dV \right] = -2 \int_V \frac{\partial^2 u_i}{\partial x_j \partial x_j} \frac{\partial u_i}{\partial \epsilon} dV \quad (5.152)$$

which results in the eigenvalue problem

$$u_j D_{ij} - \frac{1}{\text{Re}} \frac{\partial^2 u_i}{\partial x_j \partial x_j} = 0. \quad (5.153)$$

This equation has to be solved for the eigenvalue Re , and the largest eigenvalue yields the critical Reynolds number Re_E below which all initial conditions decay monotonically.

5.6.2 Additional Constraints

Restriction to divergence-free solutions

The critical Reynolds number resulting from the variational principle given earlier is a rather conservative estimate of the transition Reynolds number $\text{Re} \approx 1000$ (for plane Poiseuille flow) and can therefore be taken as a lower bound only. The reason for the large discrepancy between the transition Reynolds number and the critical Reynolds number Re_E is twofold. First, we require monotonic decay of the energy. This constraint seems to be unnecessarily stringent. Allowing the energy to grow for a limited amount of time but *ultimately* decay to zero would result in a more realistic setting and a more realistic critical Reynolds number. Second, the optimization procedure expressed as \max_{u_i} allows velocity fields that may be entirely unphysical. In other words, the range of functions used in the variational principle may be too large, and additional constraints on the functions enforcing *physical* properties may be appropriate. Many scientists have addressed this issue, and we will give the most simple, but obvious, additional constraint on the range of functions.

To incorporate additional constraints into the variational principle we add Lagrange multipliers. For example, the restriction to divergence-free test functions can be implemented as follows

$$\frac{1}{\text{Re}_E} = \max_{u_i} - \frac{\int u_i u_j D_{ij} dV}{\int \left(\frac{\partial u_i}{\partial x_j} \frac{\partial u_i}{\partial x_j} + \lambda \frac{\partial u_i}{\partial x_i} \right) dV} \quad (5.154)$$

where λ denotes the Lagrange multiplier. Because the vanishing divergence is a local constraint (rather than a global one) and thus has to be satisfied at any point x_i in the domain V , the Lagrange multiplier has to be a function of x_i . Proceeding as before and using the relation

$$\int \lambda \frac{\partial u_i}{\partial x_i} dV = - \int u_i \frac{\partial \lambda}{\partial x_i} dV + \underbrace{\int \lambda u_i n_i dA}_{=0} \quad (5.155)$$

we obtain

$$\delta u \ vU' + \delta v \ uU' - \frac{1}{\text{Re}} \left(2\delta u \ \nabla^2 u + 2\delta v \ \nabla^2 v + 2\delta w \ \nabla^2 w - \delta u \ \frac{\partial \lambda}{\partial x} - \delta v \ \frac{\partial \lambda}{\partial y} - \delta w \ \frac{\partial \lambda}{\partial z} \right) = 0 \quad (5.156)$$

which leads to the following Euler-Lagrange equations in component form

$$\text{Re } U'v - 2\nabla^2 u + \frac{\partial \lambda}{\partial x} = 0 \quad (5.157)$$

$$\text{Re } U'u - 2\nabla^2 v + \frac{\partial \lambda}{\partial y} = 0 \quad (5.158)$$

$$-2\nabla^2 w + \frac{\partial \lambda}{\partial z} = 0 \quad (5.159)$$

$$\frac{\partial u}{\partial x} + \frac{\partial v}{\partial y} + \frac{\partial w}{\partial z} = 0. \quad (5.160)$$

It is interesting to note at this stage that the Lagrange multiplier λ can be identified as directly proportional to the pressure; thus the pressure term in the Navier-Stokes equations can be thought of as the quantity that enforces divergence-free velocity fields.

Joseph (1976) showed that the largest Reynolds numbers Re_E result for disturbances that are independent of the streamwise direction. We therefore expand the variables in the preceding equations as

$$f = \hat{f}(y)e^{i\beta z} \quad (5.161)$$

which yields

$$\text{Re}U'\hat{v} - 2(\mathcal{D}^2 - \beta^2)\hat{u} = 0 \quad (5.162)$$

$$\text{Re}U'\hat{u} - 2(\mathcal{D}^2 - \beta^2)\hat{v} + \mathcal{D}\hat{\lambda} = 0 \quad (5.163)$$

$$-2(\mathcal{D}^2 - \beta^2)\hat{w} + i\beta\hat{\lambda} = 0 \quad (5.164)$$

$$\mathcal{D}\hat{v} + i\beta\hat{w} = 0. \quad (5.165)$$

Solving for the Lagrange multiplier $\hat{\lambda}$ in the third equation and substituting into the second equations leads to the final equation for the eigenvalue problem for Re :

$$2(\mathcal{D}^2 - \beta^2)^2\hat{v} + \beta^2\text{Re}U'\hat{u} = 0 \quad (5.166)$$

$$2(\mathcal{D}^2 - \beta^2)^2\hat{u} - \text{Re}U'\hat{v} = 0. \quad (5.167)$$

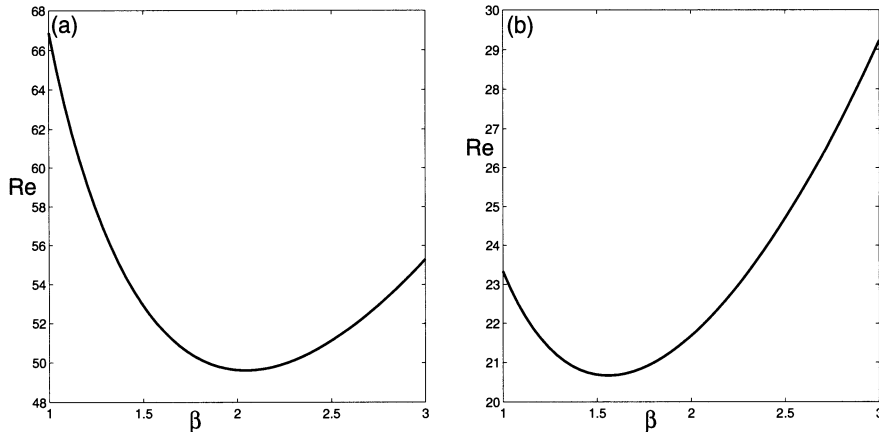


FIGURE 5.11. Critical Reynolds number versus spanwise wave number. (a) For plane Poiseuille flow: the lowest critical Reynolds number is obtained at $Re_E \approx 49$ for a spanwise wave number of $\beta \approx 2$. (b) For plane Couette flow: the lowest critical Reynolds number is obtained at $Re_E \approx 21$ for a spanwise wave number of $\beta \approx 1.5$.

Examples

This eigenvalue problem has to be solved for the smallest eigenvalue Re that corresponds to the critical Reynolds number below which no amplification in disturbance energy will be observed. Figure 5.11 displays the critical Reynolds number for the problem stated earlier for plane Poiseuille and plane Couette flows. For plane Poiseuille flow, the energy Reynolds number is approximately 49, which is realized for a spanwise wave number of $\beta \approx 2$, whereas plane Couette flow has an energy Reynolds number of about 21 at a spanwise wave number of $\beta \approx 1.5$.

These energy Reynolds numbers are far from the Reynolds numbers at which transition to turbulence is observed in experiments. This is mainly due to the monotonic decay requirement and the nonnormal nature of the linearized Navier-Stokes equations for shear flows (see also Section 4.6.2).

Part II

Stability of Complex Flows and Transition

The previous chapters of this book focused on a variety of mathematical and physical concepts in the field of hydrodynamic stability theory. These concepts have been exemplified using generic flow types that are void of additional complicating factors such as complex geometry, complex fluid properties, or a moving frame of reference. The emphasis has rather been on the development of mathematical tools to describe accurately the evolution of disturbances and general stability characteristics. The growth of disturbances has been monitored with respect to time and, except for a brief digression in Chapter 5, we have mainly dealt with the primary instability of infinitesimal wavelike and localized disturbances.

In the chapters that follow we will extend our scope by addressing the effects of selected complications (such as compressibility, rotation, curvature) on the stability of fluid flow (Chapter 6), by developing the more complicated – but sometimes more realistic – framework of spatially evolving disturbances (Chapter 7), and by studying the stability characteristics of mean velocity profiles that have been modified by a primary instability (Chapter 8). The last chapter of this book then applies the techniques of all previous chapters in studying the entire transition from laminar to turbulent flow. Various stages of transition to turbulence will be analyzed using the tools provided in this book, and our current understanding of transition for a variety of flows will be presented. Although we do not attempt to present a global picture of the transition process, the case studies in Chapter 9 should demonstrate the usefulness of hydrodynamic stability theory in better understanding transition from laminar to turbulent fluid.

6

Temporal Stability of Complex Flows

In previous chapters we developed a mathematical framework to analyze the stability characteristics of shear flows. We addressed instabilities of inviscid flows, and the effects of viscosity, transient behavior, and various effects of nonlinearities. The examples chosen have concentrated on the mathematical tools rather than an accurate modeling of realistic flow behavior. However, few applications of hydrodynamic stability theory deal with these idealized flow situations, and additional effects have to be taken into account. Varying pressure gradients, three-dimensionality of the mean flow, rotation and curvature, surface tension for free-surface flows and compressibility of the fluid medium are but a few of the effects that arise in realistic situations. Although the mathematical techniques introduced in previous chapters carry over to more complex flows, we will devote this chapter to the study of selected complications of the basic flow and their effect on the temporal growth of infinitesimal perturbations.

In Section 6.1 we will consider boundary layer flow with adverse and favorable pressure gradients and three-dimensional boundary layers with crossflow. Section 6.2 then addresses effects of rotation and curvature on the stability of flows, and in Section 6.3 we will look at an example of free-surface flows where surface tension is important. Unsteady flow phenomena, including oscillatory mean velocity profiles, will be dealt with in Section 6.4 where a technique for computing energy amplification for flows with arbitrary time dependence will be introduced. Section 6.5 focuses on the stability of compressible boundary layers.

6.1 Effect of Pressure Gradient and Crossflow

6.1.1 Falkner-Skan (FS) Boundary Layers

Mean velocity profiles

Pressure gradients influence the mean velocity profile as they accelerate or decelerate the freestream velocity. We will consider a special class of velocity profiles that allow the formulation of the mean flow in terms of similarity variables. These profiles are characterized by a power law dependence of the freestream velocity U_∞ on the streamwise coordinate direction. We have

$$U_\infty(x) = Cx^m \quad (6.1)$$

which is related to a freestream mean pressure gradient of the form

$$\frac{dP_\infty}{dx} = -U_\infty \frac{dU_\infty}{dx}. \quad (6.2)$$

Transforming the independent variables into a similarity variable according to

$$\eta = \sqrt{\frac{m+1}{2}} \frac{\text{Re}_{\delta^*}^2 \nu}{U_\infty x^{m-1}} y \quad (6.3)$$

and introducing a stream function Ψ of the form

$$\Psi = \sqrt{\frac{2U_\infty \nu x}{m+1}} f(\eta) \quad (6.4)$$

with

$$u = \frac{\partial \Psi}{\partial y} \quad v = -\frac{\partial \Psi}{\partial x} \quad (6.5)$$

results, after some algebra, in a nonlinear ordinary differential equation for the function $f(\eta)$

$$f''' + ff'' + \beta_H(1 - f'^2) = 0 \quad (6.6)$$

which has to be solved subject to the boundary conditions

$$f(0) = f'(0) = 0 \quad f'(\infty) = 1. \quad (6.7)$$

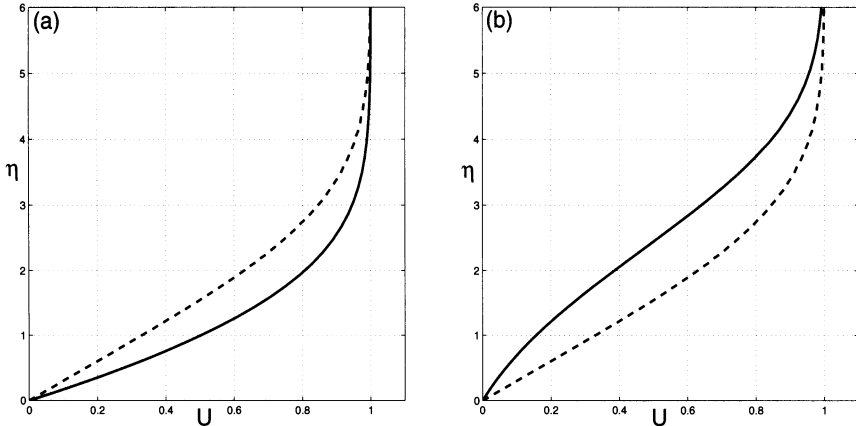


FIGURE 6.1. Mean velocity profile for accelerating and decelerating boundary layer flow. (a) Favorable pressure gradient, accelerating flow $\beta_H = 0.2$. (b) Adverse pressure gradient, decelerating flow $\beta_H = -0.085$. The dashed line represents the Blasius mean velocity profile with $\beta_H = 0$.

The ordinary differential equation for f was first derived by Falkner and Skan and now carries their names.

The parameter β_H , known as the Hartree parameter, is related to m by

$$\beta_H = \frac{2m}{m+1} \quad m = \frac{\beta_H}{2-\beta_H} \quad (6.8)$$

and is a measure of the acceleration or deceleration of the freestream, or the adverse or favorable nature of the mean pressure gradient.

In the case of an accelerating flow (Figure 6.1(a)), that is, $m > 0$, the mean velocity profile appears fuller than the Blasius velocity profile that is recovered for $m = 0$. For the case of a decelerating outer flow (Figure 6.1(b)), that is, $m < 0$, we observe a mean velocity profile with points of inflection. We therefore conclude already that, in the inviscid limit, the boundary layer with an adverse pressure gradient can exhibit exponentially growing solutions, whereas for zero and favorable pressure gradients these unstable inviscid solutions do not exist.

If the adverse pressure gradient increases beyond a critical level, the wall shear

$$\left. \frac{dU}{dy} \right|_{y=0} \sim f''(\eta = 0) \quad (6.9)$$

becomes negative, resulting in flow separation. The critical deceleration is given by

β_H	m	R_{crit}	α_{crit}
-0.1	-0.0476	400.0	0.338
-0.05	-0.0244	459.4	0.319
0	0	519.4	0.303
0.05	0.0256	582.5	0.289
0.1	0.0526	650.3	0.276

TABLE 6.1. Critical Reynolds numbers and streamwise wave numbers for boundary layer flow with adverse and favorable pressure gradient.

$$m_{crit} = -0.0905 \quad \beta_{H crit} = -0.199 \quad (6.10)$$

which is quite small. Thus, the laminar boundary layer can only support a rather small amount of deceleration without flow separation.

Physical situations where boundary layer profiles of this type occur include two-dimensional stagnation flow ($m = 1$) and, more generally, flow in the stagnation region of a two-dimensional wedge of opening angle $\beta_H \pi$.

Spectra and neutral curve

The neutral curves for accelerating and decelerating boundary layer flow are shown in Figure 6.2(a). For a negative pressure gradient (accelerating flow) it is evident that the critical Reynolds number Re_{crit} increases and the region of instability decreases. On the other hand, for the positive pressure gradient (decelerating flow) the critical Reynolds number Re_{crit} decreases and the region of instability increases. For high Reynolds numbers the upper and lower branches of the neutral curve for $m < 0$ do not asymptotically close, i.e., even in the limit of infinite Reynolds number there exists an instability. This is because the Falkner-Skan solutions for $m < 0$ have an inflection point and, according to Rayleigh's inflection point criterion, may exhibit an instability in the inviscid limit. To illustrate the strong effect of a pressure gradient on the critical Reynolds number: the critical Reynolds number Re_{crit} (based on displacement thickness) for $m = -0.075$ is approximately 130, whereas for $m = 0.075$ it is approximately 2000. Further values of the critical parameters are given in Table 6.1. Figure 6.2(b) displays the growth rates as a function of the Hartree parameter for selected streamwise wave numbers.

Optimal growth

Because the Orr-Sommerfeld and Squire equations governing the linear stability of boundary layer flow are nonnormal we expect a potential for transient energy growth. We have already seen that there can be substantial nonmodal energy growth outside the neutral stability curve for zero-pressure gradient (Blasius) boundary layers; the reader is referred back to

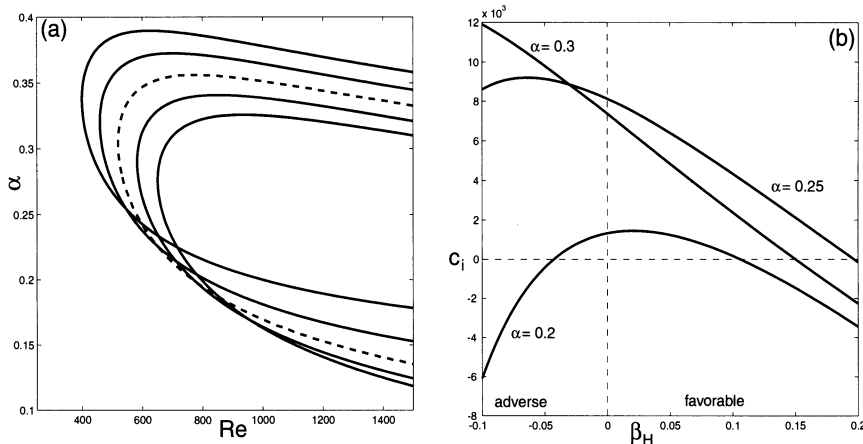


FIGURE 6.2. (a) Neutral stability curve for adverse, zero and favorable pressure gradient boundary layer flow with $\beta_H = \{-0.1, -0.05, 0, 0.05, 0.1\}$. (b) Growth rate of least stable mode for $Re = 800$ as a function of β_H for selected streamwise wave numbers.

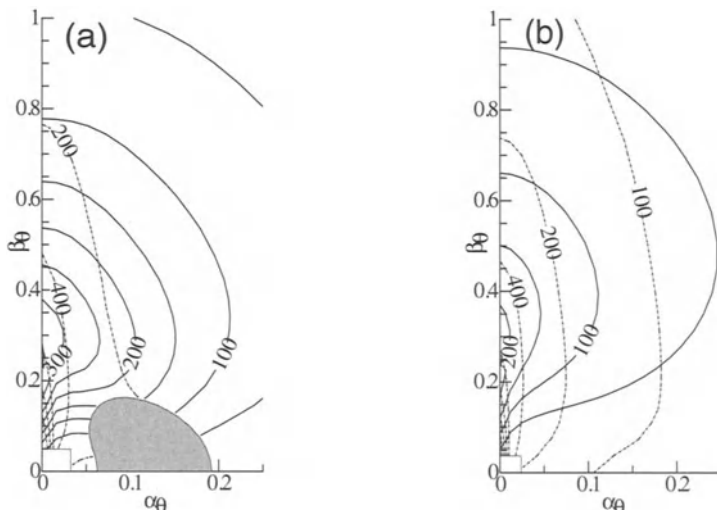


FIGURE 6.3. (a) Contours of maximum transient growth (solid lines) and time t_{max} at which maximum growth is achieved (dotted lines) in the wave number plane for $Re_\theta = 166$. (a) $m = -0.05$; disturbances in the shaded region are exponentially unstable. (b) $m = 0.1$. In all cases, the increment between level curves of t_{max} towards the origin is 400. Note the 4:1 axis ratio. From Corbett & Bottaro (2000b).

Figure 4.6. In what follows we will investigate the influence of the pressure gradient on the nonmodal stability characteristics such as the maximum transient energy growth.

Figure 6.3 shows contour plots of maximum transient energy growth G_{\max} as a function of the streamwise and spanwise wave numbers for a Reynolds number (based on the momentum thickness θ) of $Re_\theta = 166$. The shaded area denotes the region where an exponential instability exists, thus resulting in an infinite energy growth G_{\max} . The shape of these areas takes the form of the familiar kidney-shaped curves introduced in Chapter 3. Due to the largely destabilizing effect of an adverse pressure gradient, Figure 6.3(a) shows a larger exponential instability area than the zero-pressure gradient case. On the other hand, a favorable pressure gradient boundary layer (see Figure 6.3(b)) shows no modal instabilities for the chosen parameters. In both cases of adverse and favorable pressure gradients, we observe transient growth potential with substantial amplifications. The maximum occurs for disturbances that are independent of the streamwise direction (Corbett & Bottaro, 2000b).

Separated flow

Once the adverse pressure gradient becomes large enough, flow separation occurs. In this case, the pressure is strong enough to reverse the flow near the wall. Flow separation substantially alters the stability characteristics of boundary layer flow. Traditional stability analysis is hindered by the fact that the mean flow changes abruptly. In general, an absolute stability analysis (see Chapter 7) is called for. Instability of separated flow may also be studied using a local approximation of the mean flow if the separation bubble does not exhibit an absolute or global instability. Numerical simulations of the disturbance evolution in separated flows have shown that the disturbances which grow on the detached shear layer have their origin upstream of the separation point, where the flow exhibits unstable boundary layer profiles (Bestek *et al.*, 1989). When a boundary layer instability mode propagates into a separated shear layer its eigenfunction changes to that associated with the least stable mode on the shear layer (Dovgal *et al.*, 1994). Direct numerical simulations of instabilities on a separation bubble by Rist & Maucher (1994) show that the disturbance amplification rate may be an order of magnitude larger in the separation bubble than outside it. They also found that three-dimensional modes are nearly as amplified as two-dimensional waves. In addition amplification rates from an Orr-Sommerfeld equation with the basic flow taken from the steady separation bubble agreed surprisingly well with the full nonparallel simulations.

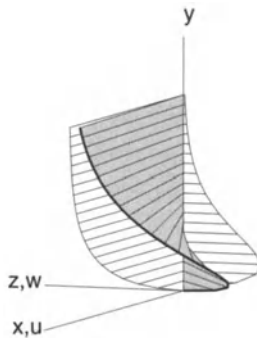


FIGURE 6.4. Sketch of three-dimensional boundary layer flow.

6.1.2 Falkner-Skan-Cooke (FSC) Boundary layers

Governing equations

Three-dimensional boundary layers, that is, boundary layers in which the direction of the mean flow is a function of the normal coordinate, arise in many relevant flow geometries such as swept wings, rotating discs, cones, spheres, and cones at an angle of attack. For this reason, a thorough understanding of their stability characteristics is particularly important.

The effect of three-dimensionality on boundary layers was first discovered for the classical aeronautical case of flow over a swept wing. Grey (1952) observed that wing sections that had substantial regions of laminar flow when unswept were almost fully turbulent when a sweep larger than 20 degrees was applied. This phenomenon was explained by Gregory *et al.* (1955) as an inviscid inflectional instability of the three-dimensional boundary layer profiles. The similarity between the three-dimensional boundary layer profiles on the swept wing and on a rotating disc was also pointed out, and, consequently, rotating disc flow has often been used as a model problem for flow over a swept wing. Mathematically, good approximations of velocity profiles in a three-dimensional boundary layer are given by the family of similarity solutions known as Falkner-Skan-Cooke (FSC) boundary layers (Cooke, 1950). Below we will discuss the stability of Falkner-Skan-Cooke flow.

We obtain the mean flow in a manner similar to the previous section on Falkner-Skan boundary layers. The introduction of a similarity variable η as well as a stream function Ψ follows the analysis of the previous section. In addition, we will introduce a velocity component in the spanwise direction that is induced by the sweep. We have

$$u = \frac{\partial \Psi}{\partial y} \quad v = -\frac{\partial \Psi}{\partial x} \quad w = W_\infty g(\eta). \quad (6.11)$$

After some algebra, we arrive at the ordinary differential equation for the function $g(\eta)$ governing the crossflow profile:

$$g'' + fg' = 0. \quad (6.12)$$

where f is the solution to the Falkner-Skan equation with specified Hartree parameter $\beta_H = 2m/(m+1)$. The boundary conditions are

$$g(0) = 0 \quad g(\infty) \rightarrow 1. \quad (6.13)$$

The Falkner-Skan-Cooke mean velocity profile is then given as

$$U(y) = f'[\eta(y)] \quad W(y) = \frac{W_\infty}{U_\infty} g[\eta(y)]. \quad (6.14)$$

We have used the freestream velocity in the streamwise direction to nondimensionalize the mean velocities. The preceding profiles will be used as the basic states in the stability investigations that follow.

If we assume that the parallel flow assumption holds, the mean velocity in a three-dimensional boundary layer can be written

$$U_i = U(y)\delta_{i1} + W(y)\delta_{i3} \quad (6.15)$$

where U is the velocity in the direction of the outer stream line and W is the component perpendicular to that direction. Figure 6.4 shows a typical example of such a mean velocity profile. Because the crossflow velocity component W is zero both at the wall and in the outer flow, the spanwise mean velocity W contains an inflection point.

We then rederive the linear initial value problem (4.9), (4.10) using the mean flow (6.15), resulting in the following equations for the Fourier-transformed normal velocity and normal vorticity

$$\left[\left(\frac{\partial}{\partial t} + i\alpha U + i\beta W \right) (\mathcal{D}^2 - k^2) - i\alpha U'' - i\beta W'' - \frac{1}{Re} (\mathcal{D}^2 - k^2)^2 \right] \hat{v} = 0 \quad (6.16)$$

$$\left[\left(\frac{\partial}{\partial t} + i\alpha U + i\beta W \right) - \frac{1}{Re} (\mathcal{D}^2 - k^2) \right] \hat{\eta} = (i\alpha W - i\beta U') \hat{v}. \quad (6.17)$$

Assuming exponential time dependence the equation for the normal velocity can be transformed into the two-dimensional Orr-Sommerfeld equation (3.20), using an extended form of Squire's transformation

$$U_1 = U + \frac{\beta}{\alpha} W \quad (6.18)$$

$$\alpha_1 \text{Re}_1 = \alpha \text{Re} \quad (6.19)$$

$$\alpha_1 = k. \quad (6.20)$$

The effective mean velocity U_1 in the two-dimensional Orr-Sommerfeld equation changes with the direction of the wave and represents the velocity component projected in the direction of the wave number vector. Because W always has an inflection point in Falkner-Skan-Cooke flow, one may expect to find a direction along which an unstable wave exists. In direct numerical simulations, these waves are found to grow rapidly to a nonlinearly saturated level, where they appear as longitudinal vortices when superimposed on the mean flow. These crossflow vortices are corotating and have been found on rotating discs (Gregory *et al.*, 1955), rotating cones (Kobayashi *et al.*, 1983), and yawed cylinders (Poll, 1985). Various attempts have been made to investigate the details of the crossflow instability; see the review article by Reed & Saric (1989).

In addition to instabilities associated with unstable crossflow eigenmodes, we will study nonmodal instabilities of three-dimensional boundary layer flow. Similar to two-dimensional boundary layers with pressure gradients, Corbett & Bottaro (2000a) investigated the possibility of transient energy growth. Their findings are summarized in Figure 6.5(a), where the maximum possible energy amplification G_{\max} has been plotted in the α - β plane. The Reynolds number based on the momentum thickness θ is $\text{Re}_\theta = 166$. We observe substantial amplification outside the region of exponential instability, which indicates that significant amplitude levels can be achieved transiently for subcritical parameter combinations. These nonmodal effects also play a role for the parameter combination where crossflow instabilities exist, because the formation of finite-amplitude crossflow vortices is accelerated by transient growth.

Breuer & Kuraishi (1994) found similar results by solving the initial value problem (6.16)-(6.17) starting with initial conditions without normal vorticity (similar to the work of Gustavsson (1991) in plane Poiseuille flow). They also found substantial transient growth in the subcritical parameter regime.

Swept Hiemenz flow

We will look at a special case of three-dimensional boundary layers that has received a great deal of attention in aerodynamics. This type of flow, known as swept Hiemenz flow, arises at the leading edge of swept wings. In

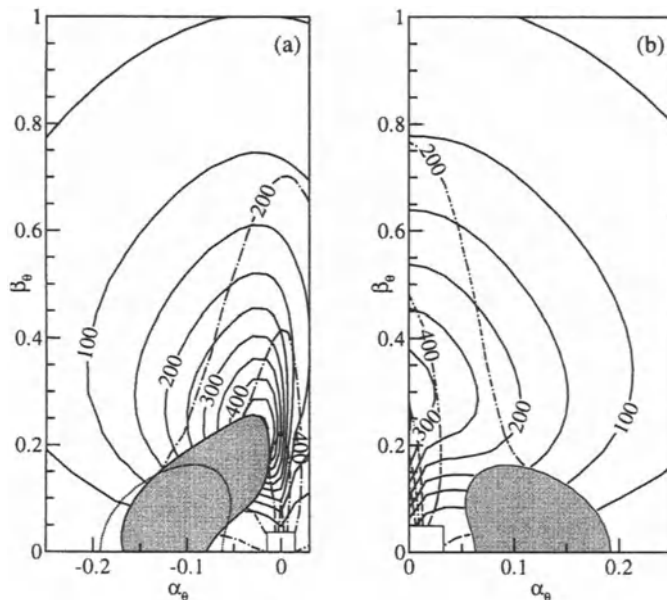


FIGURE 6.5. Maximum transient growth in a retarded three-dimensional boundary layer (left), solid lines G_{max} , dash-dotted lines t_{max} . The flow parameters are $Re_\theta = 166$, $m = -0.05$, $\phi = 45^\circ$. The shaded region indicates exponential instability, the dotted line represents its extent for two-dimensional flows. Transient growth in a two-dimensional boundary layer (right) subject to an identical pressure gradient. From Corbett & Bottaro (2000a).

addition to a stagnation point flow, the sweep of the wing induces a strong velocity component in the direction of the leading edge. Swept Hiemenz flow is a special case of the preceding equations with the Hartree parameter β_H set to one.

When solving the Orr-Sommerfeld equation using a Falkner-Skan-Cooke mean flow with Hartree parameter $\beta_H = 1$ the following stability characteristics – typical of many crossflow dominated flows – are observed.

The most amplified waves propagate approximately in the crossflow direction, thus establishing a crossflow instability. In the unstable region stationary disturbances (with $\omega_r = 0$) exist with an amplification rate slightly smaller than the maximum for traveling waves (with $\omega_r \neq 0$). The range of amplified wave numbers is rather large in the crossflow direction with the largest unstable range for stationary disturbances. Another general property of crossflow instabilities is the stabilizing (destabilizing) effect of an increase in the sweep angle for flows with adverse (favorable) pressure gradients (see Mack, 1984). The eigenfunctions associated with crossflow instabilities consist of counterrotating vortices. However, when the disturbances grow to finite amplitude they produce a system of corotating vortices. This is a result of the superposition of the growing eigensolution with the crossflow velocity profile. Once the crossflow vortices reach an amplitude of about 10 percent of the mean flow, they saturate and remain approximately aligned with the outer inviscid stream line.

6.2 Effect of Rotation and Curvature

Shear flows that are affected by body forces constitute an interesting class of stability problems. Two such forces of wide interest are body forces due to either streamline curvature (centrifugal forces) or system rotation (Coriolis forces). In engineering applications such effects may be of importance in flows along curved surfaces or in rotating machinery, but applications in geophysical fluid dynamics also encounter rotation and curvature effects. Instabilities in such flows are of entirely different character compared to Tollmien-Schlichting waves; the primary disturbance takes the form of stationary roll cells aligned in the streamwise direction. We will start to describe such instabilities for the simplified cases of curved channel flow and rotating channel flow. A discussion of the more complicated cases of curved and rotating boundary layer flows will be postponed to Chapters 7 and 8.

6.2.1 Curved Channel Flow

A centrifugal instability will occur if there is an imbalance between the centrifugal force acting on fluid elements and the pressure. In curved channel

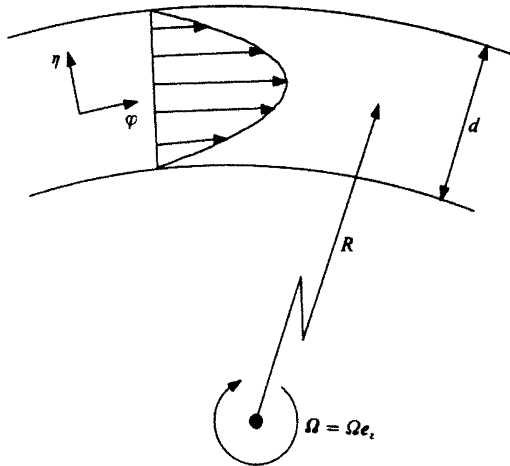


FIGURE 6.6. Sketch of curved and rotating channel flow.

flow this instability is governed by the so-called Dean number De defined as $Re\sqrt{\gamma}$, where $Re = U_b d / \nu$ and $\gamma = d/R$. The bulk flow velocity is denoted U_b , d is the channel width, R its radius of curvature at the channel centerline (see Figure 6.6). Furthermore, we assume $\gamma \ll 1$. The critical Dean number De_{crit} for curved channel flow is given in Drazin & Reid (1981) as 35.92.

Small curvature approximation

We start with the Navier-Stokes equations in radial geometry linearized about a mean flow of the form

$$U = U_\phi(r). \quad (6.21)$$

Because we are only interested in slightly curved channels, we will take the limit of small curvature as follows

$$r = R \left(1 + \frac{\gamma}{2}y\right) \quad R = \frac{2L}{\gamma} \quad y \in [-1, 1] \quad (6.22)$$

where γ measures the curvature of the channel and shall be taken as a small parameter. The nondimensional variable y then replaces the radial coordinate. We have

$$\frac{\partial}{\partial r} \rightarrow \frac{1}{L} \frac{\partial}{\partial y} \quad \frac{\partial}{\partial \phi} \rightarrow \frac{2L}{\gamma} \frac{\partial}{\partial x} \quad (6.23)$$

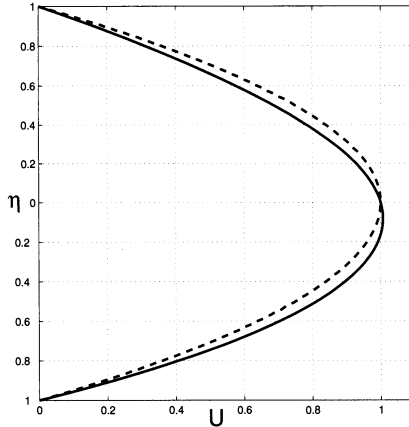


FIGURE 6.7. Mean velocity profile for curved Poiseuille flow with $\gamma = 0.5$. The dashed line represents plane Poiseuille flow.

$$u_\phi \rightarrow u \quad u_r \rightarrow v \quad u_z \rightarrow w \quad U_\phi(r) \rightarrow U(y) \quad (6.24)$$

$$\frac{1}{r} = \frac{\gamma}{2L} \frac{1}{1 + \frac{\gamma}{2}y} = \frac{\gamma}{2L} - \frac{\gamma^2}{4L}y + \mathcal{O}(\gamma^3). \quad (6.25)$$

We will also nondimensionalize the governing equations by the half-channel height L , the centerline velocity U_{CL} , and the kinematic viscosity ν , and we will base the Reynolds number on these parameters. Under these assumptions the mean flow is shown in Figure 6.7.

Governing equations

The transformed equations in primitive variables, taking into account curvature effects of first order in γ , are then

$$\begin{aligned} \frac{\partial u}{\partial t} + U \frac{\partial u}{\partial x} + U'v - \frac{\gamma}{2}yU \frac{\partial u}{\partial x} - \frac{\gamma}{2}Uv \\ = -\frac{\partial p}{\partial x} + \frac{\gamma}{2}y \frac{\partial p}{\partial x} + \frac{1}{Re} \left(\frac{\partial^2 u}{\partial x^2} + \frac{\partial^2 u}{\partial y^2} + \frac{\partial^2 u}{\partial z^2} - \gamma y \frac{\partial^2 u}{\partial x^2} + \frac{\gamma}{2} \frac{\partial u}{\partial y} - \gamma \frac{\partial u}{\partial x} \right) \end{aligned} \quad (6.26)$$

$$\begin{aligned} \frac{\partial v}{\partial t} + U \frac{\partial v}{\partial x} - \frac{\gamma}{2}yU \frac{\partial v}{\partial x} - \gamma U u \\ = -\frac{\partial p}{\partial y} + \frac{1}{Re} \left(\frac{\partial^2 v}{\partial x^2} + \frac{\partial^2 v}{\partial y^2} + \frac{\partial^2 v}{\partial z^2} - \gamma y \frac{\partial^2 v}{\partial x^2} + \frac{\gamma}{2} \frac{\partial v}{\partial y} - \gamma \frac{\partial u}{\partial x} \right) \end{aligned} \quad (6.27)$$

$$\begin{aligned} \frac{\partial w}{\partial t} + U \frac{\partial w}{\partial x} - \frac{\gamma}{2} y U \frac{\partial w}{\partial x} \\ = - \frac{\partial p}{\partial z} + \frac{1}{\text{Re}} \left(\frac{\partial^2 w}{\partial x^2} + \frac{\partial^2 w}{\partial y^2} + \frac{\partial^2 w}{\partial z^2} - \gamma y \frac{\partial^2 w}{\partial x^2} + \frac{\gamma}{2} \frac{\partial w}{\partial y} \right) \end{aligned} \quad (6.28)$$

and the continuity equation reads

$$\frac{\partial u}{\partial x} + \frac{\partial v}{\partial y} + \frac{\partial w}{\partial z} - \frac{\gamma}{2} y \frac{\partial u}{\partial x} + \frac{\gamma}{2} v = 0 \quad (6.29)$$

Normal velocity – normal vorticity formulation for vanishing streamwise dependence

The preceding equations can be brought into a formulation using the normal velocity and normal vorticity employing manipulations similar to the ones in the derivation of the Orr-Sommerfeld equation. Because the required calculations quickly become unwieldy, we restrict ourselves to the case of vanishing streamwise dependence. This choice is motivated by the fact that streamwise vortices are observed experimentally. The resulting equations are

$$\frac{\partial}{\partial t} (\beta^2 - \mathcal{D}^2) \hat{v} - \gamma \left(\frac{1}{2} \frac{\partial}{\partial t} \mathcal{D} \hat{v} + i \beta U \hat{\eta} \right) + \frac{1}{\text{Re}} ((\mathcal{D}^2 - \beta^2)^2 \hat{v} - \gamma \beta^2 \mathcal{D} \hat{v}) = 0 \quad (6.30)$$

$$\frac{\partial}{\partial t} \hat{\eta} + i \beta U' \hat{v} - \gamma \left(\frac{1}{2} i \beta U \hat{v} \right) - \frac{1}{\text{Re}} \left((\mathcal{D}^2 - \beta^2) \hat{\eta} + \gamma \left(\frac{1}{2} \mathcal{D} \hat{v} \right) \right) = 0. \quad (6.31)$$

Results

Figure 6.8 shows the results of modal and nonmodal calculations for curved channel flow for disturbances of vanishing streamwise dependence in the limit of small curvature. We see a surprisingly high sensitivity to small curvature. For curvature parameters γ of the order 10^{-3} we experience significant exponential growth throughout a large part of the parameter range. The growth rates are quite substantial, much larger than the growth rates for plane Poiseuille flow for the same wave numbers and Reynolds number.

Despite the dominance of exponential instabilities we also observe substantial transient growth. The influence of curvature on the maximum energy amplification is positive, resulting in larger amplification for slightly curved channels. These transient effects can be quite significant for subcritical parameter combinations, but they are less important for parameter combinations where exponential growth is strong. Nevertheless, finite-amplitude states are reached faster when an exponential instability is paired with transient growth.

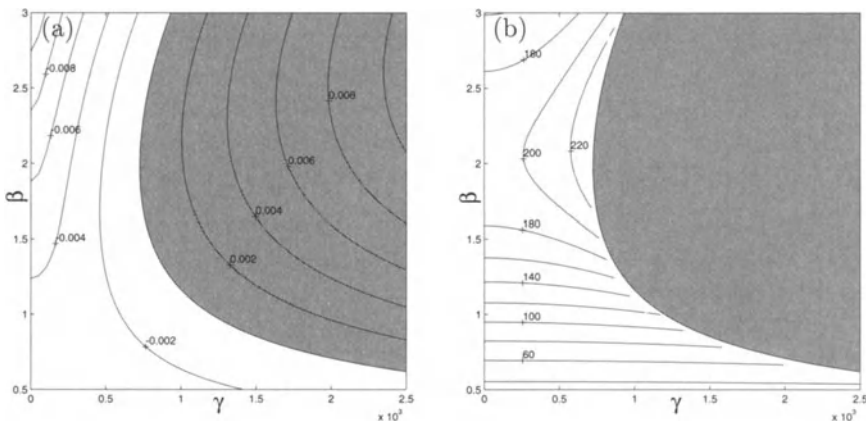


FIGURE 6.8. Asymptotic growth rates (a) and maximum transient amplification (b) for streamwise independent disturbances in curved channel flow.

Stability calculations for larger values of γ have been performed by Matsson & Alfredsson (1990).

6.2.2 Rotating Channel Flow

Effects of spanwise system rotation

Coriolis forces may affect the shear flows in a similar way as centrifugal forces do. For rotating channel flow two parameters are needed to characterize the stability of the flow, namely, the Reynolds number Re and the rotation number $Ro = \Omega d/U_b$, where Ω is the system angular velocity (see Figure 6.6). The instability mechanism may qualitatively be understood as follows. The Coriolis acceleration of a fluid particle in a rotating system is

$$\bar{a}_{Cor} = 2\bar{\Omega} \times \bar{U}. \quad (6.32)$$

This acceleration gives rise to a force in the opposite direction (normal to the walls in a rotating channel), because the basic flow is unidirectional and parallel to the walls. The force is directed toward the leading side of the channel. The basic flow for rotating channel flow has the standard parabolic profile, giving the largest force in the center of the channel, thus resulting in an unstable stratification of the Coriolis force on the leading side and a stable one on the trailing side. However, for large rotation rates the flow becomes stabilized by the rotation.

The governing equations can easily be derived by adding the above acceleration term to the linearized Navier-Stokes equations and following the procedure for the derivation of the Orr-Sommerfeld-Squire equations as outlined in Section 3.1.1. We obtain

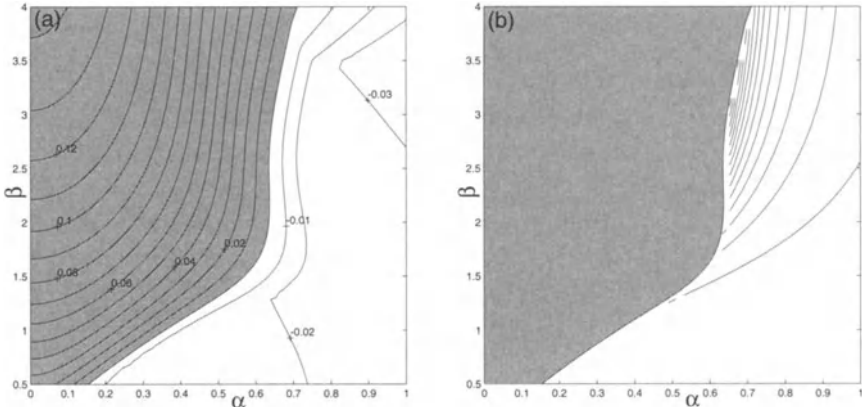


FIGURE 6.9. Asymptotic growth rates (a) and maximum transient amplification (b) for streamwise independent disturbances in rotating channel flow at $Re = 1000$, $Ro = 0.025$. The contours levels in (b) are $[200, 400, 600, \dots]$.

$$\frac{\partial}{\partial t}(k^2 - \mathcal{D}^2)\hat{v} + i\alpha U(k^2 - \mathcal{D}^2)\hat{v} + i\alpha U''\hat{v} - 2i \text{Ro} \beta \hat{\eta} + \frac{1}{\text{Re}}(k^2 - \mathcal{D}^2)^2\hat{v} = 0 \quad (6.33)$$

$$\frac{\partial}{\partial t}\hat{\eta} + i\alpha U\hat{\eta} - 2i \text{Ro} \beta \hat{v} + i\beta U'\hat{v} - \frac{1}{\text{Re}}(\mathcal{D}^2 - k^2)\hat{\eta} = 0. \quad (6.34)$$

Results

The Orr-Sommerfeld problem for rotating channel flow was solved numerically, and the results are shown in Figure 6.9(a). Analysis of the least stable mode shows a large area of exponential instability (shaded area) in the α - β plane. Eigenmodes close to the β -axis, i.e., disturbances with weak or vanishing streamwise dependence, show particularly large growth rates, well above growth rates for nonrotating channel flow. For parameter regimes where only damped solutions exist, we experience characteristic switching of the type of least stable modes that manifests itself in cusp formations in the contour lines of Figure 6.9(a).

Similar to the case of curved channel flow, the presence of significant exponential growth throughout a large part of the parameter space suggests that transient effects may play a rather subordinate role. Nevertheless, Figure 6.9(b) shows significant energy amplification in the vicinity of the neutral stability curve. A disturbance consisting of many Fourier components is expected to evolve into a structure elongated in the streamwise direction due to the presence of strong exponential instabilities near the spanwise wave number axis.

A simplified analysis of stabilization and destabilization is also given by Tritton & Davies (1985) through a displaced particle argument. Linear

theory determines the lowest critical Reynolds number as $\text{Re}_{\text{crit}} \approx 89$, which occurs at a rotation number Ro of 0.5. This is nearly two orders of magnitude smaller than the Reynolds number ($\text{Re}_{\text{crit}} = 7696$, based on the bulk velocity) for which Tollmien-Schlichting waves become unstable.

6.2.3 Combined Effect of Curvature and Rotation

The most striking feature in the stability analysis of curved and rotating channel flows is the marked sensitivity to small amounts of curvature and rotation resulting in substantial exponential growth rates. Because each body force has a distinct direction, it is particularly interesting to investigate the combined effects of curvature and rotation. We are especially interested in how destabilizing effects of curvature can be compensated by adding the correct amount of rotation, such as to generate an asymptotically neutral state. We follow Matsson & Alfredsson (1990) in their derivation of the stability equations. Based on experimental evidence we assume the neutrally stable disturbances to be independent of the streamwise coordinate direction. For small curvature we then get the following set of equations for the normal and streamwise velocity components

$$(\mathcal{D}^2 - \beta^2)^2 \tilde{v} + 2\gamma \mathcal{D}(\mathcal{D}^2 - \beta^2) \tilde{v} - 2\beta^2 \text{Re}(\gamma U + \text{Ro}) \tilde{u} = \mathcal{O}(\gamma^2) \quad (6.35)$$

$$(\mathcal{D}^2 - \beta^2) \tilde{u} + \gamma \mathcal{D} \tilde{u} - \text{Re}(U' + \gamma U + 2\text{Ro}) \tilde{v} = \mathcal{O}(\gamma^2) \quad (6.36)$$

with boundary conditions

$$\tilde{v}(\pm 1) = \mathcal{D}\tilde{v}(\pm 1) = \tilde{u}(\pm 1) = 0. \quad (6.37)$$

This system of equations constitutes an eigenvalue problem for β with the (small) curvature γ , the Reynolds number Re and the rotation number Ro as parameters. In the lowest-order approximation for curved channel flow, the parameter γ and the Reynolds number can be consolidated into one nondimensional number, the Dean number De , which is given in the form $\text{De} = \text{Re}\sqrt{\gamma}$. If all terms of order γ are kept, however, the stability behavior of curved and rotating channel flows is no longer solely dependent on the Dean number but weakly depends on the parameter γ .

For general disturbances that evolve both temporally and spatially the system of equations (6.35), (6.36) has to be supplemented by unsteady and streamwise dependent terms. Introducing the temporal and spatial growth rates, s and m , respectively, the governing stability equations read

$$\begin{aligned}
& (\mathcal{D}^2 - \beta^2)^2 \tilde{v} + 2\gamma \mathcal{D}(\mathcal{D}^2 - \beta^2) \tilde{v} - 2\beta^2 \operatorname{Re}(\gamma U + \operatorname{Ro}) \tilde{u} = \\
& s \operatorname{Re}(\mathcal{D}^2 - \beta^2 + \gamma \mathcal{D}) \tilde{v} + m \left\{ \operatorname{Re} [(\mathcal{D}^2 - \beta^2) - U'' - 2\operatorname{Ro}\mathcal{D}] \tilde{v} - 2\gamma\beta^2 \tilde{u} \right\} \\
& + \mathcal{O}(m^2, ms, \gamma^2)
\end{aligned} \tag{6.38}$$

$$\begin{aligned}
& (\mathcal{D}^2 - \beta^2) \tilde{u} + \gamma \mathcal{D} \tilde{u} - \operatorname{Re}(U' + \gamma U + 2\operatorname{Ro}) \tilde{v} = \\
& s \operatorname{Re} \tilde{u} + m \left\{ \operatorname{Re} U \tilde{u} + \frac{1}{\beta^2} [\mathcal{D}^3 + 2\gamma\mathcal{D}^2 - \beta^2\mathcal{D} - 3\gamma\beta^2] \tilde{v} \right\} \\
& + \mathcal{O}(m^2, s^2, ms, \gamma^2)
\end{aligned} \tag{6.39}$$

subject to (6.37).

Spectra and neutral curves

Figure 6.10(a) shows the neutral stability curves in the $(\beta, \operatorname{Re})$ plane for nonrotating channel flow with $\gamma = 0.025$. There are several differences compared to similar diagrams for Tollmien-Schlichting waves. Shown in the diagram are four eigenmodes, which all are unstable in the Reynolds number range of the figure. For Tollmien-Schlichting waves there is only one mode that can become unstable; in curved channel flow there are in principle infinitely many modes that may become unstable. It is also clear that the width of the band of unstable wave numbers increases as the Reynolds number increases. The corresponding eigenfunctions of the radial velocity component and the stream function for the most unstable mode at the critical spanwise wave number show a roll-cell structure and a displacement toward the unstable concave wall.

As the rotation number is changed to negative numbers, a complex interaction between various modes becomes apparent. This interaction takes the form of intersecting neutral stability curves for the different modes, and one has to keep in mind that the neutral stability curves are not associated with only one mode along its entire length but rather consist of the neutral curve of many different modes (as can be seen, for example, in Figure 6.10(e)). In Figure 6.10(f), merging and reconnection of neutral curves associated with two different modes have taken place. Neutral, but time-periodic solutions arise as the steady neutral solutions undergo a Hopf-bifurcation. These solutions can be found by solving (6.38), (6.39) and are indicated by the dotted lines in Figures 6.10(f-i). As can be seen in the remaining subplots of Figure 6.10, the development of the neutral curve is quite complicated.

For positive rotation numbers Matsson & Alfredsson (1990) report a smooth transition from curvature-dominated to rotation-dominated flow.

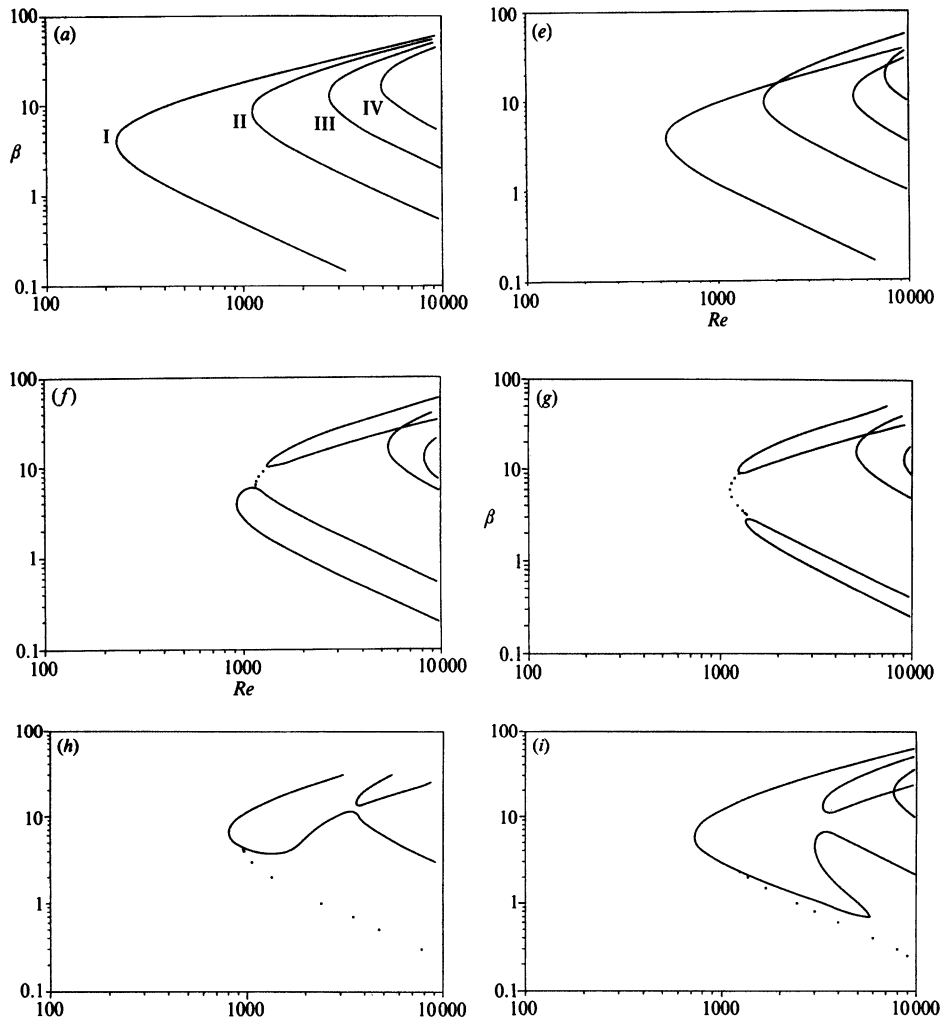


FIGURE 6.10. Neutral stability curves for curved channel flow for curvature parameter $\gamma = 0.025$ and various rotation numbers. (a) $\text{Ro} = 0$; (e) $\text{Ro} = -0.025$; (f) $\text{Ro} = -0.028$; (g) $\text{Ro} = -0.0254$; (h) $\text{Ro} = -0.032$; (i) $\text{Ro} = -0.0328$. From Matsson & Alfredsson (1990).

6.3 Effect of Surface Tension

In the previous sections we used the kinetic energy of the perturbation as a measure of disturbance size. Although additional terms were added to the governing equations to model various physical effects, and although significant changes in the stability characteristics have been observed, there was neither a mathematical nor a physical reason to adjust the measure of disturbance size. This is not always the case. The next two sections will give a convincing illustration that it is important to augment the norm in the calculations of nonmodal stability quantities to incorporate additional physical features. Failure to do so will result in diverging computations of nonmodal results. In this section we will analyze the stability of water table flow and probe the effects of surface tension.

6.3.1 Water Table Flow

Water table flow is the flow down an inclined plane driven by gravity and can be thought of as the prototypical flow describing industrial applications of thin films and coating flows.

An asymptotic stability analysis of water table flow reveals two distinct types of eigenmodes: surface modes and shear modes. Chin (1981) defined surface modes as those modes whose maximum amplitudes occur at the free surface, whereas shear modes have their amplitude maximum closer to the wall. An alternative definition is based on the phase velocities. All modes with phase velocities larger than the mean surface velocity are considered to be surface modes, while the slower modes are taken as shear modes (Floryan *et al.*, 1987). Benjamin (1961) and Yih (1963) showed that there are long surface waves present that propagate downstream at velocities twice that of the undisturbed surface.

Complete neutral stability curves for two-dimensional disturbances were calculated by Chin (1981) and Floryan *et al.* (1987). For a slightly inclined plane, Floryan *et al.* (1987) determined Re_{crit} for the shear and surface modes separately. Denoting the critical Reynolds numbers associated with shear modes and surface modes by Re_{shear} and $Re_{surface}$, respectively, they showed that for larger inclination angles, $Re_{surface} < Re_{shear}$. The magnitude of $Re_{surface}$ varies from $\mathcal{O}(10^4)$ at very small angles to $\mathcal{O}(10)$ for large angles. Re_{shear} is of the same magnitudes as Re_{crit} for plane Poiseuille flow. Gustavsson (1982) studied three-dimensional disturbances, and it is his formulation of the basic equations and the free-surface conditions that will be adopted here. The basic equations governing the evolution of a three-dimensional disturbance can be written in terms of the normal velocity and normal vorticity.

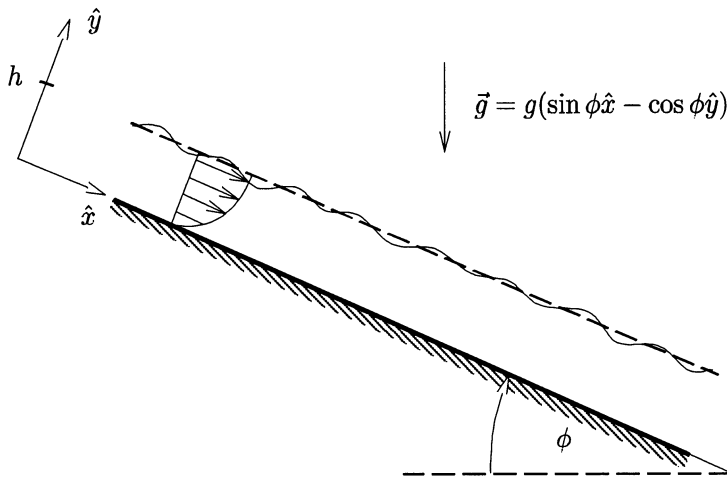


FIGURE 6.11. Watertable flow with the mean velocity profile corresponding to the dashed equilibrium position of the free surface (h). Also shown is the superimposed vertical deflection of the surface, $[1 + f(x, z, t)]h$. From Olsson & Henningson (1994).

Velocity-vorticity formulation

According to the physical setup as shown in Figure 6.11, the parabolic base flow is given as

$$U(y) = 2y - y^2. \quad (6.40)$$

The Fourier-transformed linearized equations governing the evolution of a small disturbance on this base flow are

$$\left(\frac{\partial}{\partial t} + i\alpha U \right) (\mathcal{D}^2 - k^2) \hat{v} - i\alpha U'' \hat{v} = \frac{1}{Re} (\mathcal{D}^2 - k^2)^2 \hat{v} \quad (6.41)$$

$$\left(\frac{\partial}{\partial t} + i\alpha U \right) \hat{\eta} + i\beta U' \hat{v} = \frac{1}{Re} (\mathcal{D}^2 - k^2) \hat{\eta} \quad (6.42)$$

where $k^2 = \alpha^2 + \beta^2$ and \mathcal{D} and $'$ denote the normal derivative.

Boundary conditions

The boundary conditions at the wall become

$$\hat{v} = \frac{\partial \hat{v}}{\partial y} = \hat{\eta} = 0, \quad \text{at } y = 0. \quad (6.43)$$

Special care is required for the boundary conditions at the free surface because the location of the surface is unknown and part of the solution. We obtain

$$k^2 S \hat{f} + \left[\frac{\partial}{\partial t} + i\alpha - \frac{1}{\text{Re}} (\mathcal{D}^2 - 3k^2) \right] \mathcal{D}\hat{v} = 0 \quad (6.44)$$

$$-(\mathcal{D}^2 + k^2)\hat{v} = 2i\alpha\hat{f} \quad (6.45)$$

$$\left(\frac{\partial}{\partial t} + i\alpha \right) \hat{f} = \hat{v} \quad (6.46)$$

$$\mathcal{D}\hat{\eta} = 2i\beta\hat{f} \quad (6.47)$$

all at $y = 1$.

The parameter S characterizing the influence of gravity and surface tension is the only extra parameter present when comparing the water table equations to the equations governing the evolution of disturbances in Poiseuille and Couette flows. This free-surface parameter is defined as

$$S = \frac{\cos \phi}{\text{Fr}^2} + \frac{k^2}{\text{We}} \quad (6.48)$$

where Fr and We are the Froude number and Weber number, respectively. The first free-surface boundary condition (6.44) is based on a balance of the normal stresses and surface tension, the second (6.45) and the fourth (6.47) equations use the condition of zero shear stress and the third boundary condition (6.46) stems from the kinematic equation defining the position of the interface.

6.3.2 Energy and the Choice of Norm

Kinetic energy

The energy is a convenient quantity of physical relevance when measuring the growth of a disturbance. In contrast to Poiseuille and Couette flows the energy of a disturbance in water table flow consists of kinetic energy and the potential energy of the displaced surface. The latter will be further divided into two components.

We will use

$$E_{kin} = \frac{1}{2k^2} \int_0^1 (|\mathcal{D}\hat{v}|^2 + k^2|\hat{v}|^2 + |\hat{\eta}|^2) dy \quad (6.49)$$

as a measure of the kinetic energy content in a given Fourier component (α, β) .

Energy associated with gravity and surface tension

The gravitational force can be decomposed into two components. The component parallel to the plane drives the flow and thereby governs the base flow. The component normal to the table influences the free surface.

The force per displaced volume at the surface is given by

$$\vec{X}_g = -\frac{\cos \phi}{Fr^2} \hat{y} \quad (6.50)$$

where \hat{y} is the unit vector in the normal direction. Integrating over the displaced volume with $y \in [1, 1+f]$ and then Fourier-transforming in space, we obtain the following energy

$$E_g = \frac{\cos \phi}{Fr^2} \frac{|\hat{f}|^2}{2}. \quad (6.51)$$

When the surface is displaced, work is done not only against gravity but also against forces stemming from surface tension. The energy involved is given by multiplying the surface tension σ by the change in the surface area due to the displacement (Landau & Lifshitz, 1959). In wave number space the corresponding energy is

$$E_\sigma = \frac{1}{2} \frac{k^2}{We} |\hat{f}|^2. \quad (6.52)$$

The total disturbance energy can now be defined as

$$\begin{aligned} E &= E_{kin} + E_\sigma + E_g \\ &= \frac{1}{2k^2} \left[\int_0^1 (|\mathcal{D}\hat{v}|^2 + k^2 |\hat{v}|^2) dy + \int_0^1 |\hat{\eta}|^2 dy + k^2 S |\hat{f}|^2 \right] \\ &= \frac{1}{2k^2} (E_v + E_\eta + k^2 S E_f). \end{aligned} \quad (6.53)$$

Inner product and energy norm

We base our definition for an inner product on the expression for the energy (6.53) and define

$$(\hat{\mathbf{q}}_1, \hat{\mathbf{q}}_2) = \frac{1}{2k^2} \left[\int_0^1 (\mathcal{D}\hat{v}_1^* \mathcal{D}\hat{v}_2 + k^2 \hat{v}_1^* \hat{v}_2 + \hat{\eta}_1^* \hat{\eta}_2) dy + k^2 S \hat{f}_1^* \hat{f}_2 \right] \quad (6.54)$$

where the superscript * denotes the complex conjugate and $\hat{\mathbf{q}} = (\hat{v} \ \hat{\eta} \ \hat{f})^T$. It is easily seen that if $\hat{\mathbf{q}}_1 = \hat{\mathbf{q}}_2$ in (6.54), we recover the expression for the energy. We then define the square of the energy norm as

$$\|\hat{\mathbf{q}}\|^2 = (\hat{\mathbf{q}}, \hat{\mathbf{q}}) = E. \quad (6.55)$$

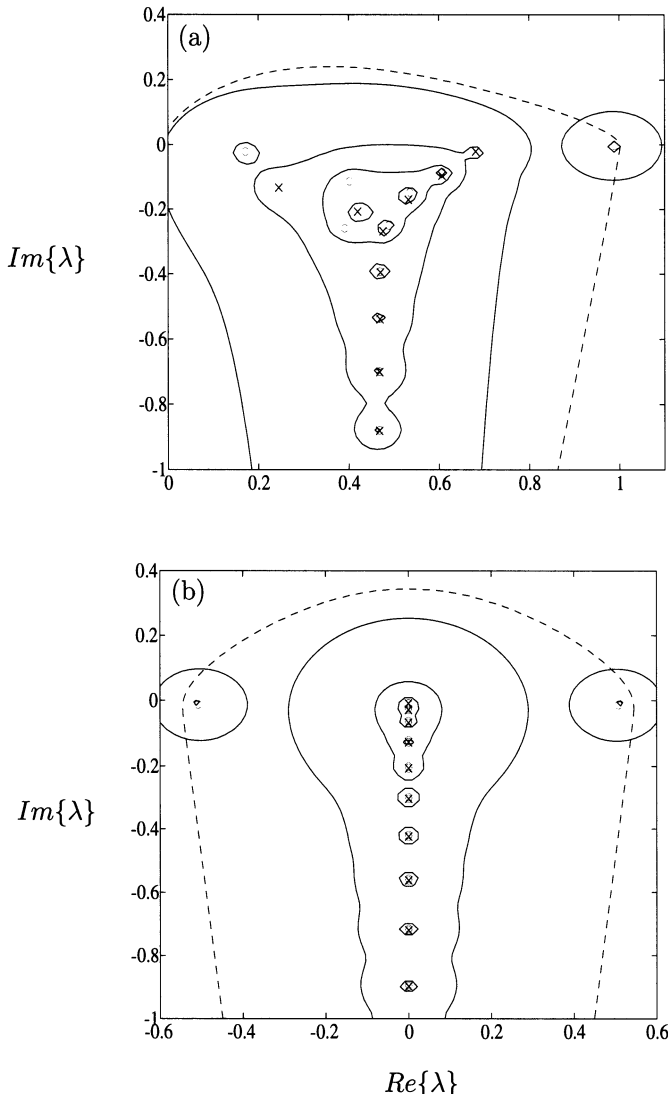


FIGURE 6.12. Spectra, pseudospectra (solid lines) and the numerical range (dashed line) for $\text{Re} = 1000$ and $S = 0.1$. The contour levels of the resolvent norm are (from outer to inner) 10, 100, 1000, 10000. The circles and the crosses represent the Orr-Sommerfeld and Squire eigenvalues, respectively. In (a) the streamwise wave number is $\alpha = 0.7$ and the spanwise wave number is $\beta = 1.3$; in (b) $\alpha = 0$ and $\beta = 2.625$. From Olsson & Henningson (1994).

6.3.3 Results

Spectra and pseudospectra

We will present results for two sets of parameters: a nonzero streamwise dependence given by $\alpha = 0.7$, $\beta = 1.3$ and a zero streamwise dependence with $\alpha = 0$, $\beta = 2.625$. In both cases the Reynolds number is $\text{Re} = 1000$ and the free-surface parameter has been set to $S = 0.1$.

Figure 6.12 shows the spectrum for both cases, together with the pseudospectrum represented in terms of contours of constant resolvent norm (as introduced in Chapter 4). In addition, we include the numerical range (the dashed line). Various conclusions can be drawn. Because all eigenvalues are confined to the lower half-plane, the asymptotic behavior in both cases is governed by exponential decay. The resolvent contours, on the other hand, reach into the upper half-plane, indicating the potential for transient growth despite asymptotic decay. The dashed line is the boundary of the numerical range (see Chapter 4), which also protrudes into the unstable domain. We therefore expect the existence of nonmodal growth, and the initial transient growth rate is directly related to the maximum distance the numerical range reaches into the unstable half-plane.

For both of the parameter combinations, surface modes constitute the bounds on the real part of the eigenvalues; i.e., they have the largest and smallest phase velocities c_r .

The eigenmode structure differs from that for plane Poiseuille flow. The least stable mode in Figure 6.12(a) has the largest positive phase velocity and is a surface mode. The second least stable mode is a Squire mode and is followed in growth rate by the second surface mode with the minimal phase velocity. The least stable mode in Figure 6.12(b) is a Squire mode, followed in terms of growth rate by the two surface modes having identical eigenfunctions and damping but different phase velocities. The eigenstructure of non-surface modes is similar to the one for plane Poiseuille flow.

Optimal growth

In Figure 6.13, the maximum energy growth G_{\max} is shown as a function of α and β for two values of the free-surface parameter S and a Reynolds number of $\text{Re} = 1000$. Figure 6.13(b) reveals that at small values of the free-surface parameter S an unstable region is introduced. In this region the surface mode with the largest positive c_r has become linearly unstable. This unstable area disappears as S increases. It is noteworthy that in Figure 6.13, the maximum of G_{\max} that occurs on the β -axis is nearly independent of the free-surface parameter S .

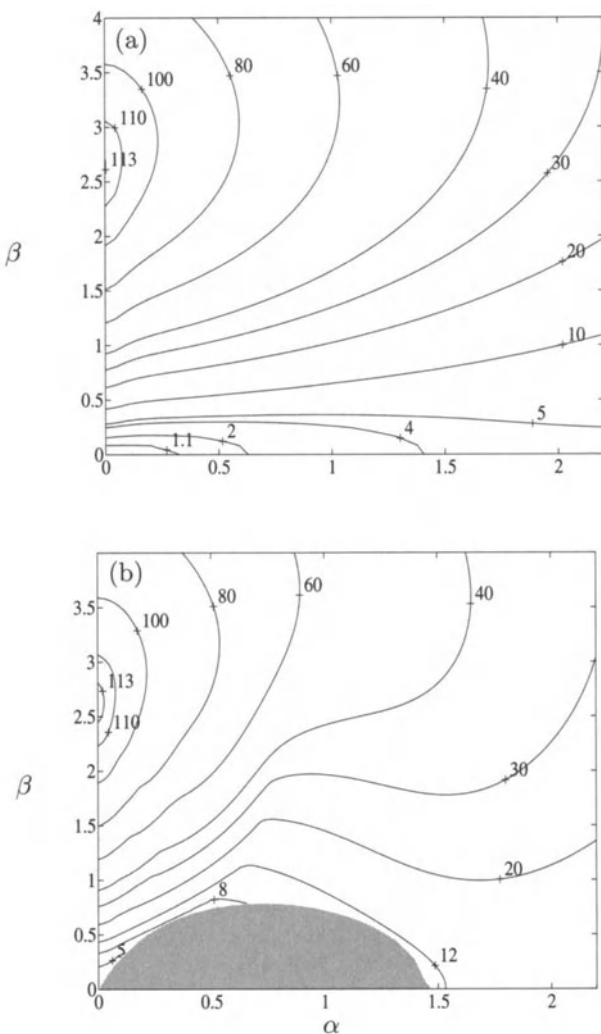


FIGURE 6.13. G_{max} for two different values of S with $Re = 1000$. In (a) $S = 100$. $G^{opt} = 113.13$ at $t^{opt} = 53.83$ at $\alpha = 0$ and $\beta = 2.644$. (b) $S = 0.1$. The shaded area is the linearly unstable area. $G^{opt} = 113.75$ at $t^{opt} = 55.04$ at $\alpha = 0$ and $\beta = 2.625$. From Olsson & Henningson (1994).

6.4 Stability of Unsteady Flow

In this section we will discuss a further extension of the standard approach to hydrodynamic stability theory as outlined in the first part of the book. In particular, we will investigate the effects of unsteadiness on the stability characteristics of selected flows. Little is known about the stability of fluid flows with a general time dependence.

6.4.1 Oscillatory Flow

Model problem: Mathieu's equation

To demonstrate techniques for analyzing oscillatory systems we will first investigate the stability characteristics of Mathieu's equation. This equation arises in many physical applications – among them free-surface waves – and has become the principal model equation for studying and illustrating the effects of parametric forcing. The equation reads

$$\frac{d^2y}{dt^2} + (\delta + \epsilon \cos t) y = 0 \quad (6.56)$$

with δ and ϵ as constant parameters. For $\epsilon = 0$, we recover the harmonic oscillator, which exhibits oscillatory solutions for positive δ and exponential solutions for negative δ . For nonzero ϵ we add an oscillatory forcing term of period $T = 2\pi$. Depending on the parameters δ and ϵ , this oscillatory term can have a destabilizing effect on the solutions to (6.56).

To investigate the stability characteristics of (6.56) we assume solutions of the form

$$y(t) = e^{\lambda t} \sum_k a_k e^{ikt} \quad (6.57)$$

which represents a decomposition into an exponential part and a purely oscillatory part. Introducing this approach into (6.56) and balancing terms of equal harmonic dependence we arrive at a nonlinear eigenvalue problem for λ :

$$(ik + \lambda)^2 a_k + \delta a_k + \frac{1}{2} \epsilon (a_{k-1} + a_{k+1}) = 0 \quad (6.58)$$

which can be reformulated as a linear eigenvalue problem

$$\lambda \begin{pmatrix} a_k \\ A_k \end{pmatrix} = \begin{pmatrix} A_k \\ (k^2 - \delta)a_k - 2ikA_k - \frac{1}{2}\epsilon(a_{k-1} + a_{k+1}) \end{pmatrix} \quad (6.59)$$

after introducing $A_k = \lambda a_k$. The appearance of a_{k-1} and a_{k+1} in the equation for the coefficients a_k and A_k indicates a coupling of the coefficients for nonzero ϵ . The oscillatory component of Mathieu's equation thus links all the frequencies, and a solution may contain frequencies other than the forcing or natural frequency. We can write the coupled system as

$$\gamma \begin{pmatrix} \mathbf{a} \\ \mathbf{A} \end{pmatrix} = \begin{pmatrix} \mathbf{0} & \mathbf{I} \\ \mathbf{P} & \mathbf{Q} \end{pmatrix} \begin{pmatrix} \mathbf{a} \\ \mathbf{A} \end{pmatrix} \quad (6.60)$$

with

$$\mathbf{a} = \begin{pmatrix} \vdots \\ a_k \\ \vdots \end{pmatrix} \quad \mathbf{A} = \begin{pmatrix} \vdots \\ A_k \\ \vdots \end{pmatrix} \quad (6.61)$$

$$\mathbf{P} = \begin{pmatrix} \ddots & & & & \\ & \ddots & & & \\ & & \ddots & & \\ & -\frac{1}{2}\epsilon & k^2 - \delta & \frac{1}{2}\epsilon & \\ & & \ddots & \ddots & \ddots \end{pmatrix} \quad \mathbf{Q} = \begin{pmatrix} \ddots & & & \\ & -2ik & & \\ & & \ddots & \\ & & & \ddots \end{pmatrix} \quad (6.62)$$

and **I** and **0** as the identity and zero matrices, respectively. Numerically, we have to truncate the vectors **a** and **A** and the corresponding matrices to arrive at a finite linear eigenvalue problem. Solving a truncated version of (6.60) for the least stable mode for a region of parameters ϵ and δ yields the familiar stability regions for Mathieu's equation displayed in Figure 6.14(a). For parameter combinations inside the instability areas, solutions to the Mathieu equation show exponential growth, whereas for (δ, ϵ) outside the instability regions, we get purely oscillatory (i.e., bounded) solutions.

Oscillating channel flow

A similar analysis to the one applied to Mathieu's equation can be used to investigate the stability of flows with an oscillatory mean velocity profile. Kerczek (1982) studied the effect of an oscillatory pressure gradient on the stability of plane Poiseuille flow using this technique, and we will follow his analysis here.

We start with an oscillatory pressure gradient of the form

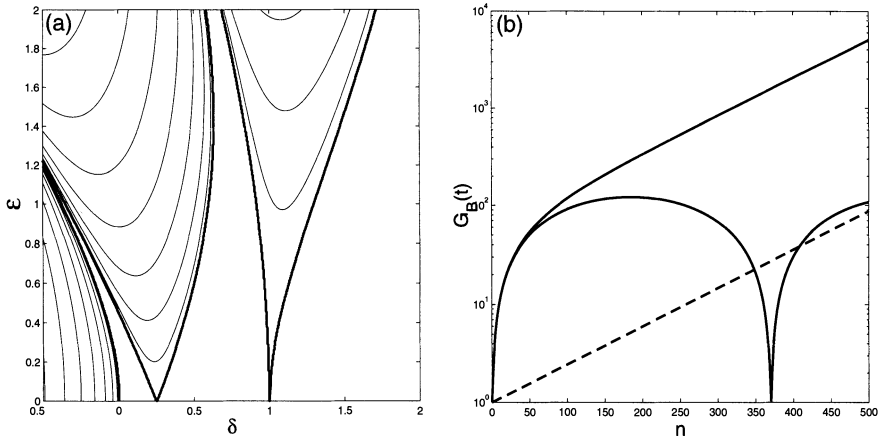


FIGURE 6.14. Stability diagram (a) for Mathieu's equation. Transient growth (b) for Mathieu's equation. $\epsilon = 1.47585, 1.4759, \delta = 1.5$. The dashed line represents the modal solution for the unstable parameter setting.

$$\frac{\partial P}{\partial x} = -\frac{2}{\text{Re}} (1 + \Lambda \cos \Omega t) \quad (6.63)$$

and an associated mean velocity profile

$$U(y, t) = U_0(y) + \frac{\Lambda}{\gamma^2} U_1(y, t) \quad (6.64)$$

$$U_0(y) = 1 - y^2 \quad (6.65)$$

$$U_1(y, t) = \text{Real} \left\{ \left[\frac{\cosh \gamma(1+i) - \cosh \gamma(1+i)y}{i \cos \gamma(1+i)} \right] e^{i\Omega t} \right\} \quad (6.66)$$

$$= \text{Real} \{ \bar{U}_1(y) e^{i\Omega t} \} \quad (6.67)$$

where the nondimensional parameters γ , Ω , and δ are the ratio of the half-channel height to the Stokes layer thickness, the frequency, and the Stokes layer thickness, respectively. All quantities are nondimensionalized by the channel half-height and the steady part of the centerline velocity.

Because Squire's theorem holds for oscillatory channel flow, it suffices to investigate the two-dimensional stability problem, which reads

$$\begin{aligned} \frac{\partial}{\partial t} (\mathcal{D}^2 - \alpha^2) \hat{v} &= \frac{1}{\text{Re}} (\mathcal{D}^2 - \alpha^2)^2 \hat{v} \\ &\quad - i\alpha (U_0 (\mathcal{D}^2 - \alpha^2) \hat{v} - U_0'' \hat{v}) \\ &\quad - i\alpha \frac{\Lambda}{\gamma^2} (U_1 (\mathcal{D}^2 - \alpha^2) \hat{v} - U_1'' \hat{v}) \end{aligned} \quad (6.68)$$

with boundary conditions $\hat{v} = \mathcal{D}\hat{v} = 0$ at the channel walls.

Recalling the approach in the previous chapter, we assume solutions of the form

$$\hat{v} = e^{\lambda t} \sum_k \tilde{v}_k(y) e^{ik\Omega t} \quad (6.69)$$

that upon substitution result in the coupled eigenvalue problem

$$\begin{aligned} & (\lambda + ik\Omega + i\alpha U_0)(\mathcal{D}^2 - \alpha^2)\tilde{v}_k + i\alpha U_0''\tilde{v}_k - \frac{1}{\text{Re}}(\mathcal{D}^2 - \alpha^2)^2\tilde{v}_k \\ &= -i\alpha \frac{\Lambda}{\gamma^2} [(\bar{U}_1(\mathcal{D}^2 - \alpha^2) - \bar{U}_1'')\tilde{v}_{k+1} + (\bar{U}_1^*(\mathcal{D}^2 - \alpha^2) - \bar{U}_1^{*\prime\prime})\tilde{v}_{k-1}]. \end{aligned} \quad (6.70)$$

Although considerably more complicated than the stability equations for Mathieu's equation, we recognize similarities between (6.59) and (6.70), most notably the coupling of the expansion coefficients represented by the right-hand side of equation (6.70). Again, we need to truncate the expansion (6.69) – neglecting higher frequency influences – to solve the stability equations numerically.

Kerczek (1982) solved a truncated system of equations (6.70) and demonstrated that the introduction of an oscillatory pressure gradient has a stabilizing effect on plane Poiseuille flow for moderate forcing frequencies. This was illustrated by comparing the neutral stability curve for steady and oscillatory channel flow, as shown in Figure 6.15. We notice an appreciable shift of the nose of the neutral stability curve due to oscillations. At very high and low values of imposed forcing frequency, the unsteady flow is only slightly less stable than the steady one.

Transient amplification in oscillatory systems

Considering the analysis of the previous section, the question arises whether the governing equations for periodic flows support transiently growing solutions. The existence of nonmodal behavior would be especially relevant for parameter regimes where modal analysis predicts stability.

The question of transient amplification in oscillatory systems has only been little explored for physical mean velocity profiles, although evidence for strong nonmodal solution behavior exists as reported by Kerczek (1982).

In this section we will outline a mathematical framework for analyzing nonmodal behavior in nonautonomous systems with periodic coefficients. We will first reformulate the solution of time-periodic systems using operator notation, after which we will apply these techniques to our model problem of Mathieu's equation. The analogous analysis for oscillatory channel or pipe flow is left for the future.

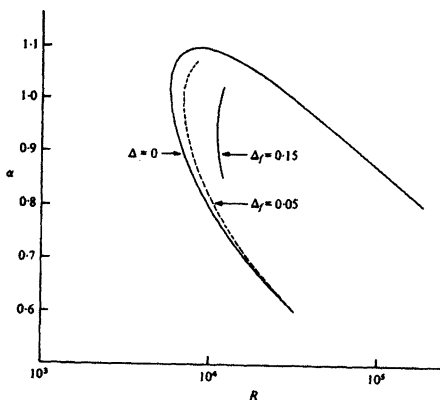


FIGURE 6.15. Neutral stability curve for oscillatory channel flow; shift of the nose due to oscillations. From Kerczek (1982).

We consider an evolution problem governed by a time-periodic linear operator

$$\frac{\partial}{\partial t} \mathbf{q} = \mathcal{L}(t) \mathbf{q} \quad \mathcal{L}(t+T) = \mathcal{L}(t). \quad (6.71)$$

We can write the solution formally as

$$\mathbf{q} = \mathcal{A} \mathbf{q}_0 \quad (6.72)$$

where \mathcal{A} denotes the fundamental solution operator that propagates the initial condition \mathbf{q}_0 forward in time. For steady evolution operators \mathcal{L} the fundamental solution operator \mathcal{A} is given by the operator exponential (see Chapter 4).

We will now separate the periodic dependence of the solution operator from the nonperiodic (exponential) behavior, as was done in the previous section. Let

$$\mathcal{A}(t+T) = \mathcal{A}(t)\mathcal{C}. \quad (6.73)$$

The operator \mathcal{C} , which describes the evolution over one time period, is referred to as the monodromy operator. We can then state the Floquet theorem for time-periodic linear systems.

Each fundamental solution operator $\mathcal{A}(t)$ can be written as the product of two operators

$$\mathcal{A}(t) = \mathcal{P}(t) \exp(\mathcal{B}t) \quad (6.74)$$

with $\mathcal{P}(t)$ T -periodic and \mathcal{B} a time-independent operator. It follows from this definition that

$$\mathcal{C} = \exp(\mathcal{B}T). \quad (6.75)$$

The eigenvalues of \mathcal{B} are referred to as Floquet exponents.

The Floquet theorem suggests that solutions of the equation consist of a product of polynomials in t and $\exp(\lambda t)$ and T -periodic terms, because the variable transformation

$$\mathbf{q} = \mathcal{P}(t)\mathbf{Q} \quad (6.76)$$

reduces (6.71) to the evolution equation

$$\frac{\partial}{\partial t} \mathbf{Q} = \mathcal{B}\mathbf{Q} \quad (6.77)$$

which is a constant-coefficient equation and has the solution

$$\mathbf{Q} = \exp(\mathcal{B}t)\mathbf{Q}_0. \quad (6.78)$$

We recall that we have already used the decomposition of the solution into a periodic and an exponential part in the stability analysis of the Mathieu equation and of the Orr-Sommerfeld equation for oscillatory channel flow. The more abstract derivation represents a more formal framework of the same analysis technique.

As far as the stability of time-periodic flows is concerned, the operator \mathcal{B} or the monodromy operator \mathcal{C} are to be investigated. A necessary and sufficient condition for *asymptotic* stability of the solution is that all Floquet exponents have negative real part.

Mathieu's equation revisited

We will now apply the operator-based method to our model problem (6.56). Computing the fundamental solution operator over one period $T = 2\pi$ we obtain the monodromy operator \mathcal{C} according to (see Gantmacher, 1959)

$$\mathcal{C} = \mathcal{A}(T) \approx \prod_{i=1}^N e^{\mathcal{L}(t_i)\Delta t} \quad t_i = i\Delta t \quad \Delta t = \frac{2\pi}{N} \quad (6.79)$$

where we have used an approximate technique to calculate $\mathcal{A}(t)$.

Using equation (6.75), we can solve for the time-independent part of the solution operator as

$$\mathcal{B} = \frac{1}{2\pi} \log \mathcal{C}. \quad (6.80)$$

This operator represents the nonoscillatory part of the fundamental solution operator and its eigenvalues govern the asymptotic stability of solutions to Mathieu's equation (6.56). Similar to the techniques introduced in Chapter 4, we can investigate the potential for transient, nonmodal amplification by computing the norm of the operator exponential

$$G_B(t) = \|\exp(t\mathcal{B})\|. \quad (6.81)$$

A plot of $G_B(t)$ is displayed in Figure 6.14(b) for two different parameter combinations (δ, ϵ) . The upper curve shows exponential growth for large times because the specific parameter combination (δ, ϵ) falls within the instability region of Figure 6.14(a). The lower periodic curve displays $G_B(t)$ for a stable parameter configuration. It is interesting to observe that both curves show a significant amount of transient growth (up to two orders of magnitude) before the asymptotic behavior can be identified. As a comparison, the modal curve (represented by a straight dashed line) for the unstable parameter setting has also been added to the figure. The discrepancy between the two curves can be entirely attributed to nonmodal effects.

6.4.2 Arbitrary Time Dependence

General formulation

Although the derivation of the stability equations governing infinitesimal perturbations imposed on an unsteady mean flow $U = U(y, t)$ follows the same principles as for a steady, equilibrated flow, the subsequent analysis differs quite significantly from the steady analog. We have the governing equations of the form

$$\frac{\partial}{\partial t} \mathbf{q} = \mathcal{L}(t) \mathbf{q} \quad \mathbf{q}(t = 0) = \mathbf{q}_0 \quad (6.82)$$

which is a nonautonomous linear initial value problem for the disturbance quantity \mathbf{q} . The time dependence of the evolution operator $\mathcal{L}(t)$ usually arises from an unsteady mean velocity profile.

Formally, the solution of this evolution equation can be written as

$$\mathbf{q}(t) = \mathcal{A}(t)\mathbf{q}_0 \quad (6.83)$$

with \mathcal{A} as the fundamental solution operator that satisfies the operator equation

$$\frac{\partial}{\partial t} \mathcal{A} = \mathcal{L}\mathcal{A} \quad \mathcal{A}(t=0) = \mathcal{I} \quad (6.84)$$

where \mathcal{I} denotes the identity operator. Equation (6.83) describes the action of the fundamental solution operator on the initial condition \mathbf{q}_0 , propagating it forward in time.

Although it is quite straightforward to formally give the solution (6.83) to the general initial value problem (6.82), determining the fundamental solution operator \mathcal{A} is – without further simplifying assumptions – quite difficult and only in very limited cases analytically accessible. Various approximations of the fundamental solution operator are well known; among the more common ones is the formulation of \mathcal{A} as a finite product of operator exponentials, i.e.,

$$\mathcal{A} \approx \prod_{i=1}^N e^{\mathcal{L}(t_i)\Delta t} \quad t_i = i\Delta t \quad \Delta t = \frac{T}{N}. \quad (6.85)$$

This approximation results from the solution of successive *autonomous* problems where the evolution operator $\mathcal{L}(t)$ is assumed constant over a small time interval Δt (see Schmid & Kytömaa, 1994). For practical applications, the computation of the fundamental solution operator is quite cumbersome though, and it is often plagued by numerical difficulties.

Nevertheless, a formalism similar to the one introduced in the first part of the book can be developed. We are interested in the evolution of a disturbance measure given by an appropriate norm (e.g., the energy norm) of the vector \mathbf{q} optimized over all initial conditions \mathbf{q}_0 , which leads us to the amplification

$$G(t) = \sup_{\|\mathbf{q}_0\| \neq 0} \frac{\|\mathcal{A}(t)\mathbf{q}_0\|}{\|\mathbf{q}_0\|} = \|\mathcal{A}(t)\|. \quad (6.86)$$

For the case of a steady underlying flow, the fundamental solution operator $\mathcal{A}(t)$ reduces to the operator exponential.

Optimal disturbances

We will now describe a simpler route to obtain the optimal growth and optimal disturbances if we are interested in the disturbance that is amplified most over a specified time interval. For this case, we will describe

a technique that avoids the explicit computation of the fundamental solution operator \mathcal{A} . This technique is based on the observation that in equation (6.86) the term $\mathcal{A}\mathbf{q}_0$ does not explicitly require the computation of the fundamental solution operator \mathcal{A} but rather requires the solution of the initial value problem (6.82) with \mathbf{q}_0 as the initial condition.

Evaluating (6.86), we get (using the notation introduced in Chapter 4)

$$\begin{aligned} G(t) &= \max_{\mathbf{q}_0} \frac{(\mathcal{A}\mathbf{q}_0, \mathcal{A}\mathbf{q}_0)}{(\mathbf{q}_0, \mathbf{q}_0)} \\ &= \max_{\mathbf{q}_0} \frac{(\mathcal{A}^+ \mathcal{A}\mathbf{q}_0, \mathbf{q}_0)}{(\mathbf{q}_0, \mathbf{q}_0)}. \end{aligned} \quad (6.87)$$

We have not yet specified an inner product in this equation; in fact, it is possible to define $G(t)$ based on different scalar products for the numerator and denominator.

The last expression in (6.87) defines a Rayleigh quotient for the operator $\mathcal{A}^+ \mathcal{A}$, and the solution of (6.87) is equivalent to the maximum eigenvalue of the associated eigenvalue problem

$$\mathcal{A}^+ \mathcal{A}\mathbf{q}_0 = \lambda \mathbf{q}_0. \quad (6.88)$$

The maximum eigenvalue of (6.88) will be computed by the power iteration method, i.e.,

$$\mathbf{q}_0^{(n+1)} = \rho^{(n)} \mathcal{A}^+ \mathcal{A}\mathbf{q}_0^{(n)} \quad (6.89)$$

where the superscript (n) denotes the n th iterate and ρ is used to scale the eigenfunction iterates $\mathbf{q}_0^{(n)}$ to keep the amplitudes reasonable. We assume that the initial guess is not orthogonal to the principal eigenvector of $\mathcal{A}^+ \mathcal{A}$.

We will now derive a numerical procedure to determine the optimal disturbance. We start with the identity

$$(\Psi, \mathcal{A}\mathbf{q}_0) = (\mathcal{A}^+ \Psi, \mathbf{q}_0) \equiv (\Phi, \mathbf{q}_0) \quad (6.90)$$

where we used the definition of the adjoint operator \mathcal{A}^+ in the second term and Ψ and Φ are (square) integrable functions. This expression allows the following observations. In the first term, the initial condition \mathbf{q}_0 is propagated forward (by the action of \mathcal{A}) up to a specified point in time, say $t = T$. The outcome of this evolution, i.e., $\mathcal{A}\mathbf{q}_0$, is then scalar multiplied by, or projected onto a test function Ψ . This test function is not specified at this point but represents quantities that we wish to observe at $t = T$. Looking at the second term in (6.90) we identify Ψ as the initial condition

for the adjoint operator \mathcal{A}^+ , which after evolving backward from $t = T$ to $t = 0$ is projected onto the initial condition \mathbf{q}_0 . The result of the action of \mathcal{A}^+ on Ψ_0 is denoted by Φ as defined by the third term in (6.90).

Up to this point we have identified Ψ as the input to the adjoint problem and Φ as the output of the adjoint operator. We have to continue by specifying the form of Φ and Ψ , which can be obtained from the derivation of the adjoint equations. Before proceeding, we consider a semi-infinite domain and choose the energy norm as defined in Chapter 4 for the following calculations. By integration by parts we have

$$\begin{aligned} 0 &= \int_0^T \int_0^\infty \mathbf{p}^H \mathbf{M} \left(\frac{\partial}{\partial t} - \mathcal{L} \right) \mathbf{q} \, dy \, dt \\ &= \int_0^T \int_0^\infty \mathbf{q}^H \mathbf{M} \left(\frac{\partial}{\partial t} - \mathcal{L}^+ \right) \mathbf{p} \, dy \, dt \\ &\quad + \int_0^\infty (\mathbf{M}\mathbf{p}(T))^H \mathbf{q}(T) \, dy - \int_0^\infty (\mathbf{M}\mathbf{p}(0))^H \mathbf{q}_0 \, dy \\ &\quad + \text{boundary terms in } y. \end{aligned} \tag{6.91}$$

The boundary terms in y can be eliminated by enforcing the given homogeneous boundary conditions on \mathbf{q} and by choosing homogeneous boundary conditions for the adjoint variables \mathbf{p} . The second line of (6.91) defines the adjoint equation

$$\frac{\partial \mathbf{p}}{\partial t} - \mathcal{L}^+ \mathbf{p} = 0. \tag{6.92}$$

Identifying terms in the third line of (6.91) and (6.90) we can find the initial conditions for the adjoint and action of the adjoint as follows:

$$\int_0^\infty (\mathbf{M}\mathbf{p}(T))^H \mathbf{q}(T) \, dy \longleftrightarrow (\Psi, \mathcal{A}\mathbf{q}_0) \tag{6.93}$$

$$\int_0^\infty (\mathbf{M}\mathbf{p}(0))^H \mathbf{q}_0 \, dy \longleftrightarrow (\Phi, \mathbf{q}_0) \tag{6.94}$$

which results in

$$\begin{aligned} \mathbf{p}(T) &= \mathbf{M}^{-1} \Psi \\ \Phi(0) &= \mathbf{M}\mathbf{p}(0). \end{aligned} \tag{6.95}$$

In Appendix C we give a specific example and a detailed derivation for the linearized boundary layer equations.

Equation (6.89), together with the above derivation, suggests the following solution strategy:

1. Start with an arbitrary initial condition \mathbf{q}_0 .
2. Integrate the governing equations forward in time up to $t = T$.
3. Determine the initial condition for the adjoint problem by computing $\mathbf{p} = \mathbf{M}^{-1}\Psi$ with $\Psi = \mathbf{q}(T)$.
4. Use this initial condition and integrate the adjoint problem backwards in time to $t = 0$ resulting in $\mathbf{p}(0)$.
5. Compute the new initial condition for the regular problem by evaluating $\Phi = \mathbf{M}\mathbf{p}(0)$.
6. Rescale the amplitude of the new initial condition, i.e., $\mathbf{q}_0 = \rho\Phi$ and goto to step 2.
7. Continue until converged.

This procedure in essence performs a power iteration on the operator $\mathcal{A}^+\mathcal{A}$ by solving two initial value problems in time. The resulting disturbance represents the initial condition that achieves the highest energy amplification over the specified time period T .

We wish to stress that the evolution operator \mathcal{L} can have any arbitrary time dependence for this procedure. For steady operators \mathcal{L} , this procedure reduces to the technique introduced in Chapter 4 for computing optimal disturbances.

Application to temporal boundary layers

Even for steady evolution operators \mathcal{L} , this procedure can have advantages. For example, in semibounded domains the technique introduced in Chapter 4 for computing optimal disturbances requires the representation of the entire spectrum (discrete and continuous), which can be computationally expensive; the preceding technique only requires the solution of two initial value problems regardless of their spectral representation. This is a great advantage when the continuous spectrum is difficult to compute or resolve.

As an illustration of the power iteration technique (6.89) we report on the investigation by Corbett & Bottaro (2000b), who determined optimal disturbances in parallel boundary layers with favorable and adverse pressure gradients.

Figure 6.16 displays the contours of $G(T)$ where T is chosen as the time when the maximum possible amplification (over all time) is reached. The Reynolds number has been chosen as $\text{Re} = 386$. By fixing the time over which $G(T)$ is optimized, we obtain amplification values for the region of modal instability. We recall that for unlimited time, solutions in this region of parameter space result in an infinite amplification due to an exponential instability (see Figure 4.6). For a fixed time, on the other hand, we can assess the competition and dominance of nonmodal and modal

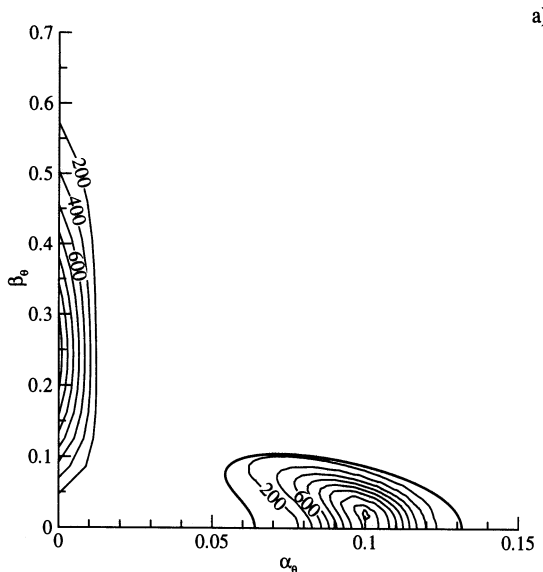


FIGURE 6.16. Contours of $G(t_r)$ for $Re = 386$ (local optimum growth). The critical stability limit is indicated by the thick line. The innermost level curve in the exponentially unstable area is $G = 1660$. From Corbett & Bottaro (2000b).

growth. Figure 6.16 demonstrates that nonmodal growth is certainly a strong mechanism for energy growth, but substantial growth also occurs in the linear instability region with the largest response obtained by an oblique Tollmien-Schlichting wave. For more details and additional results the reader is referred to Corbett & Bottaro (2000b).

A geophysical application: the Gulf Stream

Whereas Corbett & Bottaro (2000b) – by choosing a steady mean velocity profile – do not fully exploit the capability of the adjoint technique to analyze flows with arbitrary time dependence, Moore & Farrell (1993) applied a similar technique to study the linear evolution of perturbations superimposed on the time-dependent Gulf Stream flow. A nonlinear quasi-geostrophic model has been solved to predict the Gulf Stream flow, which was then used as the base flow in the linear stability equations. An iterative procedure using the regular and adjoint disturbance equations has been employed to determine perturbations that attain maximum energy over a specified period of time. The details of these computations are beyond the scope of this book; the interested reader is urged to consult the original reference.

Energy growth rate, Lyapunov exponents, and numerical range

The growth rate associated with the energy of the perturbation for unsteady flow can be derived as

$$\begin{aligned} \frac{d}{dt} \ln \left(\frac{E}{E_0} \right) &= \frac{1}{E} \frac{dE}{dt} \\ &= \frac{(\mathbf{q}, (\mathcal{L}^+ + \mathcal{L})\mathbf{q})}{(\mathbf{q}, \mathbf{q})} \end{aligned} \quad (6.96)$$

which again is in the form of a Rayleigh quotient for the operator

$$\mathcal{L}^+ + \mathcal{L}. \quad (6.97)$$

Determining the maximum possible energy growth, the Rayleigh quotient of the operator takes on its maximum value for \mathbf{q} being the principal eigenvector of (6.97). Similarly, the eigenvector corresponding to the smallest eigenvalue of (6.97) results in the smallest value of the Rayleigh quotient and thus in the smallest possible energy growth. We therefore get the bounds on the energy growth rate as

$$\lambda_{\min}(t) \leq \frac{d}{dt} \ln \left(\frac{E}{E_0} \right) \leq \lambda_{\max}(t) \quad (6.98)$$

where $\lambda_{\max, \min}$ are the largest and smallest eigenvalues of (6.97), respectively. We have already encountered the upper bound of the energy growth for steady evolution operators. Recalling the definition of the numerical range (4.91) and the outline of the computational technique (4.96)-(4.98), we see that the upper bound on the energy growth in (6.98) is equivalent to the top of the numerical range ($\theta = 0$ in (4.97)) for steady evolution operators. This analysis thus extends the concept of the numerical range to unsteady evolution operators.

A measure often used in general stability theory (see Farrell & Ioannou, 1996) is the Lyapunov exponent defined as

$$\Lambda = \lim_{t \rightarrow \infty} \sup \frac{\ln \|\mathcal{A}\|}{t} \quad (6.99)$$

where we used the appropriate energy measure for the norm. We can again cast this expression in terms of the eigenvalues of the operator (6.97). If we integrate (6.98) in time we find

$$\int_0^t \lambda_{\min}(s) \, ds \leq \ln \left(\frac{E}{E_0} \right) \leq \int_0^t \lambda_{\max}(s) \, ds \quad (6.100)$$

or, in terms of the Lyapunov exponent Λ ,

$$\limsup_{t \rightarrow \infty} \frac{\int_0^t \lambda_{\min}(s) ds}{2t} \leq \Lambda \leq \limsup_{t \rightarrow \infty} \frac{\int_0^t \lambda_{\max}(s) ds}{2t} \quad (6.101)$$

For the special case of a time-periodic evolution operator we obtain for the Lyapunov exponent

$$\begin{aligned} \Lambda &= \limsup_{t \rightarrow \infty} \frac{\ln \|\mathcal{A}\|}{t} \\ &= \limsup_{t \rightarrow \infty} \frac{\ln \|\mathcal{P}(t) \exp(t\mathcal{B})\|}{t} \\ &= \lim_{t \rightarrow \infty} \frac{\ln \|\mathcal{P}(t_{\max}) \exp(t\mathcal{B})\|}{t} \\ &= \lim_{t \rightarrow \infty} \frac{\ln \|\exp(t\mathcal{B})\|}{t} \\ &= \lambda_{\max}(\mathcal{B}) \end{aligned} \quad (6.102)$$

where t_{\max} is the time for which $\|\mathcal{P}(t)\|$ takes on its largest value.

For our model of Mathieu's equation, we determined the Lyapunov coefficient for the unstable configuration in Figure 6.14(b) and obtained a value of $\Lambda \approx 0.0014$, which was matched by the largest eigenvalue of the operator \mathcal{B} .

Bounding the Lyapunov exponent for Mathieu's equation yields

$$\frac{\int_0^{2\pi} \lambda_{\min}(s) ds}{4\pi} < \Lambda < \frac{\int_0^{2\pi} \lambda_{\max}(s) ds}{4\pi} \quad (6.103)$$

where $\lambda_{\min, \max}$ are the minimum and maximum eigenvalues of $\mathcal{L} + \mathcal{L}^+$. The eigenvalues of this operator are easily determined as

$$\lambda_{1,2} = \pm(1 - (\delta + \epsilon \cos t)). \quad (6.104)$$

It is interesting to note that for fixed time, the evolution operator \mathcal{L} can be transformed into a normal operator. However, due to the time-dependent term in \mathcal{L} normality cannot be ensured for *all* times. We therefore conclude that parametric instabilities in Mathieu's equation are a consequence of the nonnormality of the underlying evolution operator (see also Farrell & Ioannou, 1996).

6.5 Effect of Compressibility

6.5.1 The Compressible Initial Value Problem

Compressible flow equations

Effects of compressibility on the stability and transition of fluid flows are important in many applications, such as supersonic and transonic transport or flows in turbines and compressors. In this section we will focus on stability issues due to compressibility. Because compressibility significantly complicates the set of governing equations, the linear stability and modal structure of compressible fluids are rich in behavior and complexity. For this reason, we will only be able to give a brief introduction to compressible stability theory. For a more complete treatment we refer the interested reader to the references cited in this section.

We will start with the nondimensionalized compressible Navier-Stokes equations for boundary layer flow, which can be written in the form

$$\frac{\partial \rho}{\partial t} + u_j \frac{\partial \rho}{\partial x_j} = -\rho \frac{\partial u_i}{\partial x_i} \quad (6.105)$$

$$\begin{aligned} \rho \left(\frac{\partial u_i}{\partial t} + u_j \frac{\partial u_i}{\partial x_j} \right) &= -\frac{1}{\gamma Ma^2} \frac{\partial p}{\partial x_i} \\ &+ \frac{1}{Re} \frac{\partial}{\partial x_j} \left[\mu \left(\frac{\partial u_i}{\partial x_j} + \frac{\partial u_j}{\partial x_i} - \frac{2}{3} \frac{\partial u_k}{\partial x_k} \delta_{ij} \right) \right] \end{aligned} \quad (6.106)$$

$$\begin{aligned} \rho \left(\frac{\partial T}{\partial t} + u_j \frac{\partial T}{\partial x_j} \right) &= -(\gamma - 1)p \frac{\partial u_i}{\partial x_i} + \frac{\gamma}{Pr Re} \frac{\partial}{\partial x_j} \left(\kappa \frac{\partial T}{\partial x_j} \right) \\ &+ \gamma(\gamma - 1)Ma^2 \frac{1}{Re} \frac{\mu}{2} \\ &\times \left[2 \frac{\partial u_i}{\partial x_j} \frac{\partial u_i}{\partial x_j} + 2 \frac{\partial u_i}{\partial x_j} \frac{\partial u_j}{\partial x_i} - \frac{4}{3} \left(\frac{\partial v_k}{\partial x_k} \right)^2 \right] \end{aligned} \quad (6.107)$$

$$p = \rho T \quad (6.108)$$

where (6.105) is the continuity equation, (6.106) are the momentum equations, (6.107) is the energy equation, and (6.108) is the equation of state for a perfect gas. The dependent variables (ρ, u_i, p, T) are the density, velocities, pressure, and temperature, respectively. All quantities are nondimensionalized with their values at the boundary layer edge, Ma is the Mach number at the edge of the boundary layer, $\gamma = c_p/c_v$ is the ratio of the specific heats, $Re = U_e L \rho / \mu_e$ is the Reynolds number, and $Pr = \mu_e c_p / \kappa_e$ is the Prandtl number; μ_e and κ_e are the dynamic viscosity and thermal conductivity at the edge of the boundary layer, respectively. In these equations Stokes' hypothesis has also been used.

Linear stability equations

We then derive linear equations for the evolution of small disturbances imposed on a steady and parallel mean flow. In nondimensional form we have

$$\begin{aligned}\rho &\rightarrow \frac{1}{T(y)} + \rho \\ u_i &\rightarrow U_i + u_i = U(y)\delta_{1i} + W(y)\delta_{3i} + u_i \\ p &\rightarrow 1 + p \\ T &\rightarrow T(y) + \theta.\end{aligned}\tag{6.109}$$

Furthermore, we assume a temperature dependence of the dynamic viscosity and thermal conductivity and incorporate changes in thermal and viscous properties due to temperature as follows

$$\begin{aligned}\mu &\rightarrow \mu(T) + \frac{d\mu}{dT}(T)\theta \\ \kappa &\rightarrow \kappa(T) + \frac{d\kappa}{dT}(T)\theta.\end{aligned}\tag{6.110}$$

In this decomposition, the boundary-layer assumption of a constant pressure in the normal direction and the parallel flow assumption have been invoked. If we substitute this decomposition into the compressible Navier-Stokes equations, subtract the equation for the basic flow, and linearize, we obtain the disturbance equations

$$\frac{\partial \rho}{\partial t} + U_j \frac{\partial \rho}{\partial x_j} = -v \left(\frac{1}{T} \right)' - \frac{1}{T} \frac{\partial u_i}{\partial x_i} \quad (6.111)$$

$$\begin{aligned} \frac{\partial u_i}{\partial t} + U_j \frac{\partial u_i}{\partial x_j} &= -v U'_i - \frac{T}{\gamma Ma^2} \frac{\partial p}{\partial x_i} + \frac{T}{Re} \left\{ \mu \left[\nabla^2 u_i + \frac{1}{3} \frac{\partial}{\partial x_i} \frac{\partial u_j}{\partial x_j} \right] \right. \\ &\quad \left. + \frac{d\mu}{dT} \left[T' \left(\frac{\partial u_i}{\partial y} + \frac{\partial v}{\partial x_i} - \frac{2}{3} \frac{\partial u_j}{\partial x_j} \delta_{i2} \right) \right. \right. \\ &\quad \left. \left. + \theta U''_i + \frac{\partial \theta}{\partial y} U'_i + U_j \frac{\partial \theta}{\partial x_j} \delta_{i2} \right] + \frac{d^2 \mu}{dT^2} T' U'_i \theta \right\} \end{aligned} \quad (6.112)$$

$$\begin{aligned} \frac{\partial \theta}{\partial t} + U_j \frac{\partial \theta}{\partial x_j} &= -v T' - (\gamma - 1) T \frac{\partial u_i}{\partial x_i} + \frac{\gamma T}{Pr Re} [\kappa \nabla^2 \theta \\ &\quad + \frac{d\kappa}{dT} \left(2T' \frac{\partial \theta}{\partial y} + \theta T'' \right) + \frac{d^2 \kappa}{dT^2} T'^2 \theta] \\ &\quad + \gamma(\gamma - 1) Ma^2 \frac{T}{Re} \left[2\mu U'_j \left(\frac{\partial u_i}{\partial y} + \frac{\partial v}{\partial x_j} \right) + \frac{d\mu}{dT} \theta U'_i U'_i \right] \end{aligned} \quad (6.113)$$

$$p = \rho T + \frac{\theta}{T} \quad (6.114)$$

where appropriate boundary conditions have to be imposed; see, e.g., Mack (1984). If the pressure is eliminated from the above problem using the disturbance form of the equation of state (6.114), the set of equations can be written in the standard form of an initial value problem:

$$\frac{\partial \mathbf{q}}{\partial t} = \mathcal{L} \mathbf{q} \quad (6.115)$$

where $\mathbf{q}^T = (\rho, u, v, w, \theta)$ and \mathcal{L} is found from the terms of the disturbance equations.

Parallel flow assumption and relative Mach number

To further simplify the equations, we restrict ourselves to a *quasiparallel flow*, i.e., $V = 0$. The disturbances are taken to be harmonic waves

$$\mathbf{q} = \tilde{\mathbf{q}}(y) e^{i(\alpha x + \beta z - \omega t)} \quad (6.116)$$

where α and β are the wave numbers in the streamwise and spanwise direction, respectively, and ω represents the frequency of the disturbance. The stability equations then lead to an eigenvalue problem for ω or α , which serves as the starting point for further analysis. Before we proceed, some

additional quantities that will prove convenient in the analysis will be introduced. Following Mack (1984) let us define the *relative Mach number* as

$$\widehat{\text{Ma}} = \frac{\alpha U + \beta W - \omega}{\sqrt{\alpha^2 + \beta^2}} \frac{\text{Ma}}{\sqrt{T}}. \quad (6.117)$$

For neutral disturbances the physical meaning of $\widehat{\text{Ma}}$ can be better understood if it is rewritten as

$$\widehat{\text{Ma}} = \text{Ma}_{\parallel} - \frac{c_*}{a} \quad (6.118)$$

where Ma_{\parallel} is the local Mach number of the mean flow parallel to the wave number vector $\mathbf{k} = (\alpha, \beta)^T$ and a stands for the local speed of sound. The phase velocity, c , is defined in the standard way as

$$c = \frac{\omega}{k} \quad (6.119)$$

where $k = |\mathbf{k}|$ and the subscript $*$ denotes a dimensional quantity. The phase velocity c_* is now the phase velocity in the direction of the wave number vector rather than the x -direction.

Thus, $\widehat{\text{Ma}}$ denotes the local Mach number of the mean flow in the direction of \mathbf{k} relative to the phase velocity. With this definition, we can now classify the disturbances based on the value of $\widehat{\text{Ma}}$. A disturbance is called *subsonic*, *sonic*, or *supersonic* if $|\widehat{\text{Ma}}|$ at the boundary layer edge is less than, equal to, or greater than unity, respectively.

6.5.2 Inviscid Instabilities and Rayleigh's Criterion

Inviscid stability equations

The stability equations substantially simplify in the case of inviscid ($\text{Re} \rightarrow \infty$) flow. This simplification allows the analytical treatment of certain aspects of the linear stability behavior. The results discussed here follow the seminal work of Lees & Lin (1946) and Mack (1984).

The linear stability equations for a three-dimensional parallel compressible inviscid flow can be written

$$(-i\omega + i\alpha U + i\beta W) \tilde{\rho} = -\left(\frac{1}{T}\right)' \tilde{v} - \left(\frac{1}{T}\right) (\mathcal{D}\tilde{v} + ik\tilde{u}_\parallel) \quad (6.120)$$

$$(-i\omega + i\alpha U + i\beta W) k\tilde{u}_\parallel = -(\alpha U' + \beta W')\tilde{v} - ik^2 \frac{T}{\gamma Ma^2} \tilde{p} \quad (6.121)$$

$$(-i\omega + i\alpha U + i\beta W) \tilde{v} = -\frac{T}{\gamma Ma^2} \mathcal{D}\tilde{p} \quad (6.122)$$

$$(-i\omega + i\alpha U + i\beta W) k\tilde{u}_\perp = -(\alpha W' - \beta U')\tilde{v} \quad (6.123)$$

$$(-i\omega + i\alpha U + i\beta W) \tilde{\theta} = -T'\tilde{v} - (1 - \gamma)T(\mathcal{D}\tilde{v} + ik\tilde{u}_\parallel) \quad (6.124)$$

$$\tilde{p} = T\tilde{\rho} + \left(\frac{\tilde{\theta}}{T}\right) \quad (6.125)$$

where we have decomposed the streamwise momentum equations into a component parallel to the wave number vector and a component perpendicular to that direction, which allows the rather straightforward derivation of a compressible version of the Rayleigh equation.

Compressible Rayleigh equation

It is quite easy to derive a second-order equation for the normal velocity: First we eliminate the perturbation density $\tilde{\rho}$ and the perturbation temperature $\tilde{\theta}$ in the equation of state (6.125) using equations (6.120) and (6.124). The quantity \tilde{u}_\parallel is then eliminated with the help of equation (6.121). At this stage, we have derived an equation for the perturbation pressure \tilde{p} in terms of the perturbation normal velocity \tilde{v} . This expression is then substituted into equation (6.122) to yield the desired result. We find

$$\left[\frac{(U_\parallel - c)\tilde{v}' - U'_\parallel \tilde{v}}{(1 - \widehat{Ma}^2)} \frac{1}{T} \right]' = \frac{k^2}{T} (U_\parallel - c)\tilde{v} \quad (6.126)$$

where we have used the definition of the relative Mach number and where $U_\parallel = (\alpha U + \beta W)/k$ stands for the velocity component in the direction of the wave number vector. This equation is the three-dimensional compressible counterpart of the incompressible Rayleigh equation (2.15). It is important to notice that the inviscid instability is governed by U_\parallel , the mean flow in the direction of \mathbf{k} .

Generalized inflection point criterion

The compressible version of the Rayleigh equation (6.126) – in analogy with the incompressible case (2.15) – has a singularity of regular type at the location $y_c : U_\parallel(y_c) = c$, which defines the critical layer. This can best

be seen by rewriting equation (6.126) in the form given by Lees & Lin (1946). We have

$$\mathcal{D}(\xi \mathcal{D}\tilde{v}) - \left(\eta + \frac{k^2}{T} \right) \tilde{v} = 0 \quad (6.127)$$

with

$$\xi(y) = \frac{1}{1 - \widehat{\text{Ma}}^2} \frac{1}{T} \quad (6.128)$$

$$\eta(y) = \frac{1}{U_{\parallel} - c} \mathcal{D}(\xi U'_{\parallel}). \quad (6.129)$$

We observe that unless the quantity

$$\left[\mathcal{D}(\xi U'_{\parallel}) \right]_{U_{\parallel}=c} = \left[\mathcal{D}(U'_{\parallel}/T) \right]_{U_{\parallel}=c} \quad (6.130)$$

vanishes at the critical layer, the point $y = y_c$ in the complex plane is a regular singular point of equation (6.127). In this derivation we used the fact that $\widehat{\text{Ma}} = 0$ for $U_{\parallel} = c$.

Lees & Lin (1946) showed that the quantity $\mathcal{D}(U'_{\parallel}/T)$ plays the same role as U'' in incompressible flows. The location in the normal direction where $\mathcal{D}(U'_{\parallel}/T) = 0$ is called the *generalized inflection point*. The existence of a generalized inflection point in the boundary layer, such that $U_{\parallel}(y_c) > 1 - 1/\text{Ma}$, is a necessary condition for an inviscid wavelike disturbance to be unstable. In addition, it is a necessary condition for the existence of a *neutral subsonic* wave. This wave has a phase velocity, c_c , equal to the mean flow $U_{\parallel}(y_c)$ at the critical layer. Moreover, if $|\widehat{\text{Ma}}| < 1$ throughout the entire boundary layer, the condition is also a *sufficient* condition for the existence of such a wave with a unique wave number α_c .

As a result of the generalized inflection point criterion, the compressible boundary layer over an adiabatic flat plate is unstable in the inviscid limit, in contrast to the incompressible case.

Inward and outward propagating waves

The disturbance equation for the normal velocity \tilde{v} takes on a simplified form in the freestream (i.e., in the limit $y \rightarrow \infty$). We obtain

$$\tilde{v}'' = (1 - \widehat{\text{Ma}}^2) k^2 \tilde{v} \quad (6.131)$$

which can easily be solved, resulting in

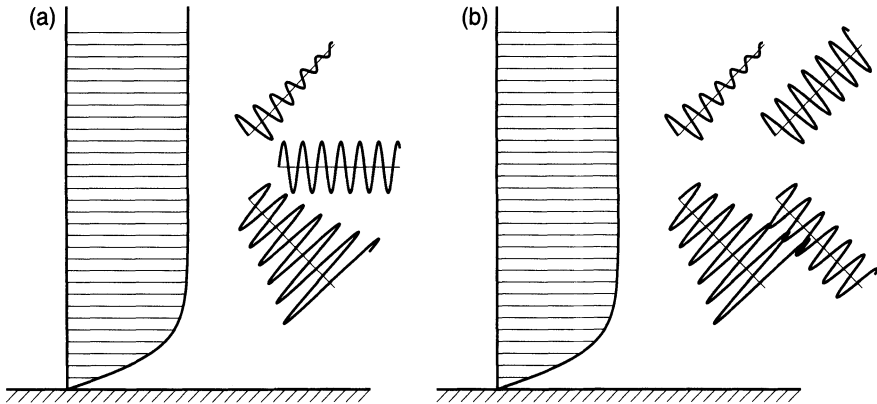


FIGURE 6.17. Sketch of wave propagation in the free stream for compressible flow. (a) Subsonic case; (b) supersonic case.

$$\tilde{v} \sim e^{\pm k\eta y} \quad \text{with} \quad \eta^2 = (1 - \widehat{\text{Ma}}^2). \quad (6.132)$$

Splitting the complete solution into real and imaginary parts yields

$$v = \tilde{v}(y) e^{k(c_i t + \eta_r y)} e^{ik(-c_r t + \eta_i y)} e^{i(\alpha x + \beta z)} \quad (6.133)$$

where we assumed that both $\widehat{\text{Ma}}$ and U_{\parallel} take on their respective freestream values.

Requiring the solution for the vertical velocity to be bounded at infinity, we conclude that η_r has to be negative. Additionally, for nonzero η_i , waves in the freestream propagate toward or away from the boundary layer, depending on the sign of η_i .

For the subsonic case with $\widehat{\text{Ma}} < 1$, we have

$$\eta = \pm \sqrt{1 - \text{Ma}^2(U_{\parallel} - c_r)^2} \pm i \frac{c_i \text{Ma}^2(U_{\parallel} - c_r)}{\sqrt{1 - \text{Ma}^2(U_{\parallel} - c_r)^2}} + \mathcal{O}(c_i^2) \quad (6.134)$$

whereas for the supersonic case with $\widehat{\text{Ma}} > 1$ we have

$$\eta = \pm \frac{c_i \text{Ma}^2(U_{\parallel} - c_r)}{\sqrt{\text{Ma}^2(U_{\parallel} - c_r)^2 - 1}} \pm i \sqrt{\text{Ma}^2(U_{\parallel} - c_r)^2 - 1} + \mathcal{O}(c_i^2). \quad (6.135)$$

This implies that damped subsonic and supersonic waves propagate away from the boundary layer and that amplified subsonic and supersonic waves propagate toward the boundary layer. In contrast, neutral subsonic waves

propagate parallel to the x -axis, whereas neutral supersonic waves propagate both in and out of the boundary layer (see Figure 6.17). Although the analysis by Lees & Lin (1946) only applies to subsonic waves, numerical calculations have shown that both types of neutral waves are inflectional, i.e., have their critical layer located at the generalized inflection point (see Mack, 1984).

Higher modes

As was mentioned earlier, the uniqueness of α_c was based on the condition that $|\widehat{Ma}| < 1$ throughout the entire boundary layer. Lees & Reshotko (1962) conjectured that α_c may not be unique for $|\widehat{Ma}| > 1$, allowing for multiple solutions. These multiple solutions were first found by Mack (1963, 1964, 1965) using extensive numerical computations. At about the same time, Gill (1965) independently found similar multiple solutions for top-hat jets and wakes. Alternatively, one can find evidence for the existence of multiple modes by studying the inviscid equation for a pressure disturbance (see Mack, 1984)

$$\tilde{p}'' - \left[\ln(\widehat{Ma}^2) \right]' \tilde{p}' - k^2(1 - \widehat{Ma}^2)\tilde{p} = 0 \quad (6.136)$$

which is the Rayleigh equation in terms of the disturbance pressure rather than the normal velocity perturbation. One can easily see that (6.136) changes its behavior when $(1 - \widehat{Ma}^2)$ changes sign. If the second term on the left-hand side is neglected (which can be justified based on numerical calculations), the remaining equation is a wave equation for the pressure \tilde{p} if $\widehat{Ma}^2 > 1$. Consequently, multiple solutions may be found. The least stable of these additional modes, usually called the *second* mode, is particularly interesting. The numerical studies of Mack showed that this mode is the most amplified mode for supersonic boundary layers at high Mach numbers; see Figure 6.18. He also found that the most unstable *first* mode, which is an extension of the incompressible Tollmien-Schlichting (TS) wave, is oblique rather than two-dimensional as in incompressible boundary layer flows; see Figure 6.19.

In addition to the mentioned multiple modes, Mack found another group of neutral waves with phase velocities in the range $1 \leq c \leq 1 + 1/\text{Ma}$. For each of these phase velocities there is an infinite number of corresponding wave numbers. The existence of these modes is not related to the inflection point; therefore these solutions are called *noninflectional* waves. According to Mack "... the importance of the $c = 1$ neutral waves is that in the absence of an interior generalized inflection point they are accompanied by a neighboring family of unstable waves with $c < 1$. Consequently, a compressible boundary layer is unstable to inviscid waves whenever $\widehat{Ma}^2 > 1$, regardless of any other feature of the velocity and temperature profiles."

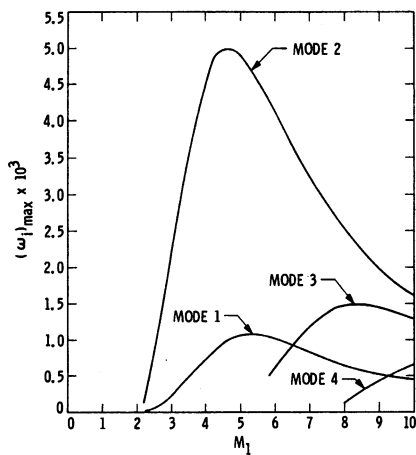


FIGURE 6.18. Effect of Mach number on maximum temporal amplification rate of two-dimensional waves for first four modes. Insulated wall, wind-tunnel temperatures. From Mack (1984).

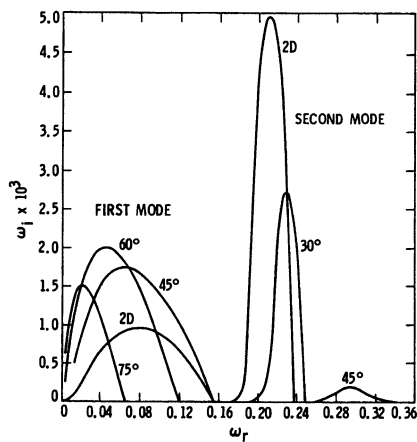


FIGURE 6.19. Temporal amplification rate of first and second modes versus frequency for several wave angles at $Ma_\infty = 4.5$. Insulated wall, $\bar{T}_\infty = 311$ K. From Mack (1984).

This family of modes does not have any counterpart in incompressible theory.

6.5.3 Viscous Instability

Exponential instabilities

Early results of viscous compressible stability investigations were based on the asymptotic theories of Lees & Lin (1946), Dunn & Lin (1955), and Lees & Reshotko (1962). None of these theories deals with the complete set of stability equations but rather makes various approximations. Brown (1961, 1962) solved the stability equations numerically, first based on the theory of Dunn & Lin (1955) and later using the complete set of equations. Mack (1965) presented detailed numerical results for Mach numbers up to 10. These results include both first and second viscous modes that are unstable. Similar to the inviscid results, the least stable of the first-mode disturbances were found to be oblique. For supersonic boundary layers over a flat plate, the wave angle ψ of these disturbances is about 50 to 60 degrees. Among the second-mode disturbances, the two-dimensional waves were shown to have the largest growth rate; see Figure 6.20. The lowest Mach number at which second-mode instabilities at finite Reynolds numbers exist is about $Ma = 3$. This occurs for a Reynolds number of approximately $Re = 13900$. Then, as the Mach number increases, the unstable region moves rapidly to lower Reynolds numbers. However, the *critical Reynolds number* for the second mode (the lowest Reynolds number for which an unstable disturbance exists) has a minimum for a Mach number of about $Ma = 4.5$. As shown in Figure 6.21, the first- and second-mode unstable regions are separated at this Mach number whereas at Mach numbers above $Ma = 4.6$ they have merged.

The general stability of a compressible boundary layer is governed by a viscous instability at lower Mach numbers, but at Mach numbers above $Ma = 3$ inviscid instabilities prevail. Viscous instabilities, as defined in Mack (1984), have the maximum amplification rate increase as the Reynolds number decreases. An indication of viscous instability is a neutral stability curve with an upper-branch wave number that increases as the Reynolds number decreases. In Figure 6.22 the neutral stability curves of two-dimensional waves for different Mach numbers are given. At $Ma = 1.6$, the neutral curve is similar to that of incompressible flow. The viscous instability weakens as the Mach number increases and at $Ma = 3.8$ has completely vanished. The same behavior has been observed for three-dimensional disturbances.

Effects of heat transfer on stability characteristics

Various additional effects can be added to the governing equations and their influence on the stability behavior can be investigated. As an example we will focus on the effects of heat transfer on the flow instability by examining

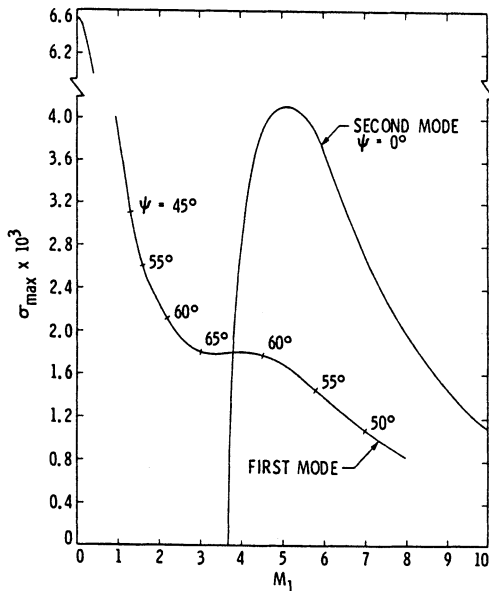


FIGURE 6.20. Maximum spatial growth rate, $\text{Re} = 1500$. From Mack (1984).

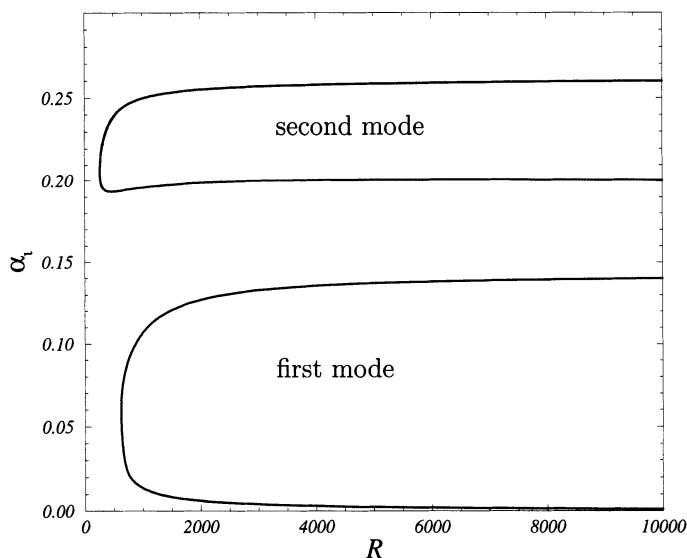


FIGURE 6.21. Neutral stability curve for compressible boundary layer flow at $Ma_e = 4.5$. From Hanifi (private communication).

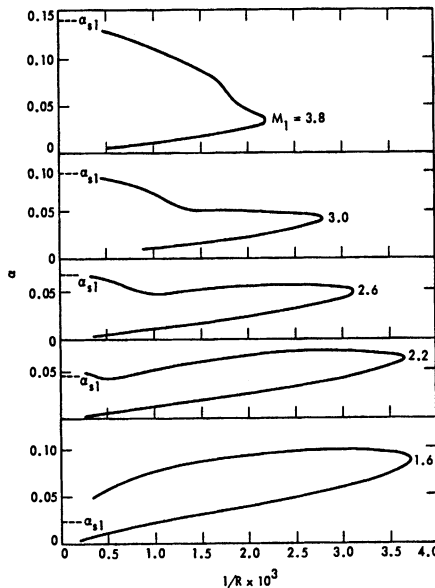


FIGURE 6.22. Effect of Mach number on the two-dimensional neutral stability curves. Insulated wall, wind tunnel temperature. From Mack (1984).

its effects on the boundary layer profiles. As mentioned before, a compressible flow is inviscidly unstable if it has a generalized inflection point at $y_c > y_0$ where $U(y_0) = 1 - 1/\text{Ma}$. A compressible boundary layer on an insulated surface contains only one generalized inflection point. As the surface temperature is reduced, another generalized inflection point appears inside the boundary layer at $y = y_{s2}$; see Figure 6.23. Because this point is located in the portion of the boundary layer where $U(y) < 1 - 1/\text{Ma}$, it does not modify an inviscid instability. The distance between y_c and y_{s2} decreases as the surface cooling increases. For a given Mach number, there is a level of cooling at which these two generalized inflection points cancel each other and consequently no unstable first-mode solutions will exist. However, existence of unstable higher modes depends only on a region of relative supersonic flow and cannot be eliminated by wall cooling.

This argument has been confirmed by numerical investigations (Mack, 1975; Malik, 1989; Masad *et al.*, 1992) that also showed that the maximum growth rate of the second-mode disturbances increases with increasing surface cooling. Thus, increasing surface cooling destabilizes the second mode and stabilizes the first mode.

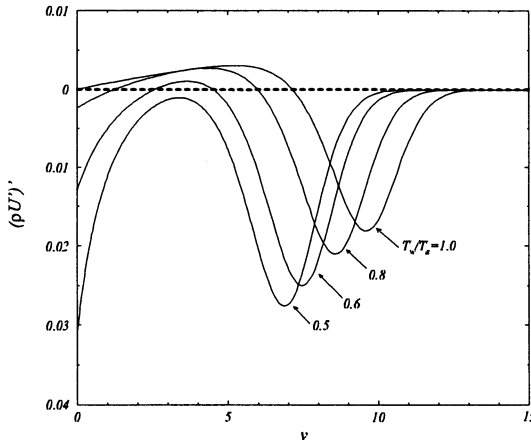


FIGURE 6.23. Effect of cooling on the distribution of $(U'/T)'$ through a flat-plate compressible boundary layer; $\text{Ma}_\infty = 4$ for $\bar{T}_\infty = 300 \text{ K}$ and $\text{Pr} = 0.72$. From Hanifi (private communication).

6.5.4 Nonmodal Growth

Inviscid algebraic instability

The nonmodal instability of incompressible flows was discussed in Chapter 4. We will now investigate the nonmodal behavior of disturbances in a compressible flow by directly looking at the initial value problem describing the evolution of infinitesimal disturbances in compressible boundary layers.

Let us start by considering an inviscid compressible parallel shear flow independent of the streamwise and spanwise directions. Furthermore, let the perturbations be independent of the streamwise coordinate. It is easily verified that the incompressible solution of Ellingsen & Palm (1975) also satisfies the linearized equations of motion under these assumptions, with the addition that ρ and T grow algebraic in time. We have

$$u = -v_0 \frac{\partial U}{\partial y} t \quad (6.137)$$

$$v = v_0 \quad (6.138)$$

$$w = w_0 \quad (6.139)$$

$$p = 0 \quad (6.140)$$

$$\rho = \rho_0 - v_0 \frac{\partial \bar{\rho}}{\partial y} t \quad (6.141)$$

$$T = T_0 - v_0 \frac{\partial \bar{T}}{\partial y} t. \quad (6.142)$$

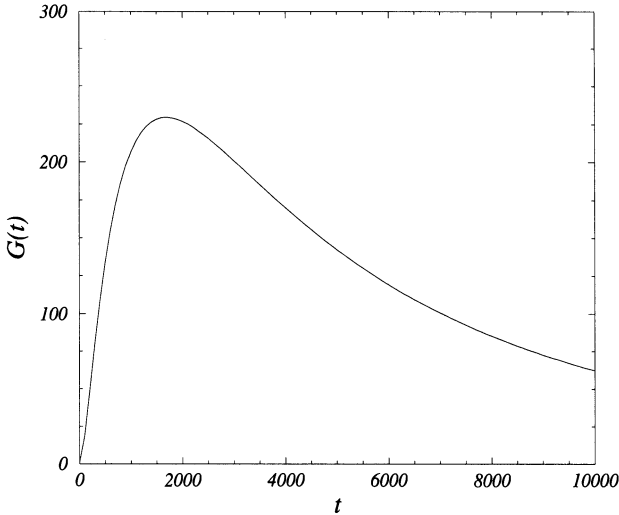


FIGURE 6.24. Transient growth as a function of time for compressible viscous boundary layer flow. $\text{Re} = 300$, $\text{Ma} = 2.5$, $\alpha = 0$ and $\beta = 0.1$. For these parameters all eigenmodes are stable. From Hanifi *et al.* (1996).

Not only the streamwise momentum but also the perturbation density and temperature are conserved as a fluid particle is lifted up by the normal velocity. It is still necessary for the initial condition to be incompressible in order to satisfy the equation of state.

Transient growth

Infinitesimal perturbations in an inviscid compressible fluid may experience unbounded algebraic growth. However, this growth is bounded when viscosity is present. Once we define a disturbance measure for compressible flow, we can investigate transient growth. In the case of compressible flows, there is no obvious definition of disturbance measure. The following quantity

$$E = \int_V \left\{ \bar{\rho}(|\hat{u}|^2 + |\hat{w}|^2 + |\hat{v}|^2) + \frac{\bar{T}}{\bar{\rho}\gamma\text{Ma}^2} |\hat{\rho}|^2 + \frac{\bar{\rho}}{\gamma(\gamma-1)\bar{T}\text{Ma}^2} |\hat{T}|^2 \right\} dV \quad (6.143)$$

was first suggested by Mack (1969) and later rederived by Hanifi *et al.* (1996).

Using this measure and the method described in Section 4.4, Hanifi *et al.* (1996) showed that the largest transient growth occurs for $\alpha = 0$. They

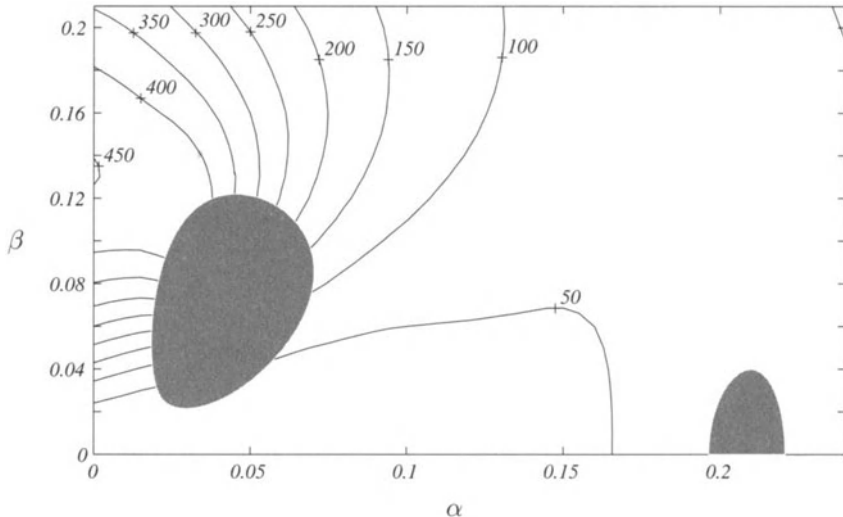


FIGURE 6.25. Contours of maximum transient growth for compressible viscous boundary layer flow at $\text{Re} = 300$ and $\text{Ma} = 4.5$. The shaded region corresponds to the parameter space where the flow is linearly unstable. The shaded region at the left corresponds to the first-mode unstable disturbances and at the right to the second-mode unstable disturbances. From Hanifi *et al.* (1996).

also showed that the maximum transient growth scales with Re^2 while t_{\max} varies linearly with Re where t_{\max} is the time at which the maximum growth is reached. The optimal disturbances, those which give the largest growth, are initially streamwise vortices with small streamwise velocity. All of these characteristics agree well with those found for incompressible shear flows. Figure 6.25 shows contours of the maximum transient growth G_{\max} . The region of the unstable first- and second-mode disturbances are also shown in this figure. The transient growth is largest for low streamwise wave numbers.

The relation between transient growth and the algebraic instability of compressible streamwise independent disturbances was investigated by Hanifi & Henningson (1998). They showed that for small times, when viscosity effects are small, the optimal transient growth is close to the optimal growth of inviscid disturbances given by (6.137)-(6.142).

Figure 6.26 displays transient growth curves for increasingly higher Reynolds numbers compared to the inviscid result. Good agreement between viscous and inviscid results is observed for small times, but at large times viscous effects dominate and bound the inviscid algebraic growth.

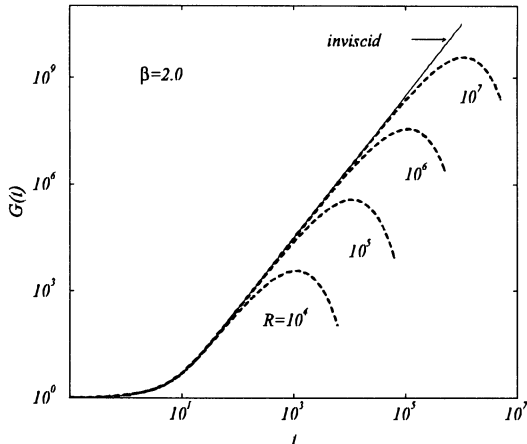


FIGURE 6.26. Comparison of transient growth for viscous and inviscid disturbances. $\text{Ma}_e = 2.5$, $\alpha = 0$, $\beta = 2$. From Hanifi & Henningson (1998).

Oblique transition

Because the most unstable first-mode disturbances are oblique, small-amplitude three-dimensional disturbances can create streamwise vortices through nonlinear interaction. These vortices may then induce rapidly growing streaks. Figure 6.25 shows that the most unstable first-mode disturbance has a spanwise wave number approximately half the one for the optimally growing streak. Thus, a pair of the most unstable oblique first-mode waves can transfer energy into the Fourier component where optimal transient growth occurs. This condition is approximately satisfied over a range of Mach numbers, and in Chapter 9 we investigate its importance in so-called oblique transition of compressible flows.

7

Growth of Disturbances in Space

7.1 Spatial Eigenvalue Analysis

7.1.1 Introduction

Up to now we have only been concerned with the temporal evolution of disturbances. However, it is conceivable that the physical situation requires the modeling of the disturbance amplitude/energy as a spatially growing quantity. Vibrating ribbons or harmonic point sources are only two of many situations where a spatial framework is more appropriate than a temporal one. In this section we develop the mathematical basis for a spatial linear stability analysis and discuss the relation between the temporal and spatial settings.

The derivation of the spatial stability equations is analogous to the temporal equations, with the exception that we assume a complex streamwise wave number α and a real frequency ω rather than a real wave number α and a complex frequency ω :

$$\omega \in \mathbb{C} \quad \alpha \in \mathbb{R} \quad \text{temporal setting} \quad (7.1)$$

$$\omega \in \mathbb{R} \quad \alpha \in \mathbb{C} \quad \text{spatial setting.} \quad (7.2)$$

Although this change does not influence the general form of the equations, the problem of determining the spatial stability is given by an eigenvalue problem where the eigenvalue appears *nonlinearly* (up to the fourth power).

Throughout this section we will use simple model problems (such as the linearized viscous Burgers equation or the constant-coefficient two-

dimensional Navier-Stokes equation) to demonstrate the general analysis required for the spatial framework before applying it to the full Navier-Stokes equations. It is hoped that this will result in a more lucid exposition of spatial stability techniques.

A model problem

To demonstrate the concept of spatial stability and its relation to the temporal approach it will be instructive to investigate the linearized viscous Burgers equation as a model problem:

$$\frac{\partial u}{\partial t} + U \frac{\partial u}{\partial x} = \epsilon \frac{\partial^2 u}{\partial x^2}. \quad (7.3)$$

Choosing the temporal framework we take a Fourier transform in the x -direction after which we assume the time dependence in the form $\exp(-i\omega t)$, which results in the dispersion relation

$$\omega = \alpha U - i\epsilon\alpha^2 \quad \text{with } \alpha \in \mathbb{R}. \quad (7.4)$$

In the spatial approach we assume a real frequency ω resulting in

$$-i\omega \hat{u} + U \frac{\partial \hat{u}}{\partial x} = \epsilon \frac{\partial^2 \hat{u}}{\partial x^2} \quad (7.5)$$

which, after introducing $\hat{v} = \partial \hat{u} / \partial x$, yields

$$\frac{\partial}{\partial x} \begin{pmatrix} \hat{u} \\ \hat{v} \end{pmatrix} = \begin{pmatrix} 0 & 1 \\ -\frac{i\omega}{\epsilon} & \frac{U}{\epsilon} \end{pmatrix} \begin{pmatrix} \hat{u} \\ \hat{v} \end{pmatrix}. \quad (7.6)$$

We then assume solutions in the form

$$\begin{pmatrix} \hat{u} \\ \hat{v} \end{pmatrix} = \begin{pmatrix} \tilde{u} \\ \tilde{v} \end{pmatrix} \exp(i\alpha x) \quad \text{with } \alpha = \alpha_r + i\alpha_i \quad (7.7)$$

where $\alpha_i < 0$ means spatially growing solutions. This yields the dispersion relation

$$-\det \begin{pmatrix} -i\alpha & 1 \\ -\frac{i\omega}{\epsilon} & \frac{U}{\epsilon} - i\alpha \end{pmatrix} = \alpha^2 + \frac{iU}{\epsilon}\alpha - \frac{i\omega}{\epsilon} = 0 \quad (7.8)$$

which is identical to the one obtained for the temporal setting (see equation (7.4)). Solving for the (complex) streamwise wave number α yields

$$\begin{aligned}\alpha &= -\frac{iU}{2\epsilon} \pm \sqrt{\frac{i\omega}{\epsilon} - \frac{U^2}{4\epsilon^2}} \\ &= \frac{iU}{2\epsilon} \pm \frac{iU}{2\epsilon} \left[1 - \frac{2i\omega\epsilon}{U^2} + \frac{2\omega^2\epsilon^2}{U^4} + \mathcal{O}(\epsilon^3) \right]\end{aligned}\quad (7.9)$$

where an expansion for small ϵ has been applied. Two modal solutions emerge from this analysis: The first mode

$$\alpha = \frac{\omega}{U} + i\frac{\omega^2}{U^3}\epsilon \quad (7.10)$$

is a slowly decaying mode with a phase speed $c_r = U$. The second mode

$$\alpha = -\frac{\omega}{U} - i\frac{U}{\epsilon} \quad (7.11)$$

represents a rapidly growing mode with phase speed $c_r = -U$. The group velocity of the waves is given as

$$c_g = \frac{\partial \omega}{\partial \alpha} \quad (7.12)$$

and evaluates to

$$\text{mode 1: } c_g = U \quad \text{mode 2: } c_g = -U. \quad (7.13)$$

Therefore, mode 1 is a downstream propagating slowly decaying wave, whereas mode 2 represents an upstream propagating decaying wave; see Figure 7.1.

7.1.2 Spatial Spectra

Constant-coefficient Navier-Stokes equations

We will now consider the two-dimensional Navier-Stokes equations and assume the normal direction y as homogeneous. A Fourier transformation in t and y leads to

$$\hat{u}_x + i\gamma\hat{v} = 0 \quad (7.14)$$

$$-i\omega\hat{u} + U\hat{u}_x + U_x\hat{u} + i\gamma V\hat{u} + U_y\hat{v} = -\hat{p}_x + \frac{1}{\text{Re}} (\hat{u}_{xx} - \gamma^2\hat{u}) \quad (7.15)$$

$$-i\omega\hat{v} + U\hat{v}_x + V_x\hat{u} + i\gamma V\hat{v} + V_y\hat{v} = -i\gamma\hat{p} + \frac{1}{\text{Re}} (\hat{v}_{xx} - \gamma^2\hat{v}) \quad (7.16)$$

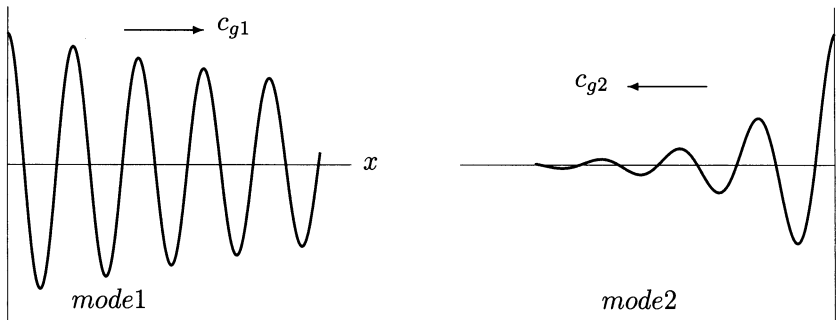


FIGURE 7.1. Sketch of mode 1 and mode 2 for viscous Burgers equation.

where γ denotes the normal wave number and ω the frequency. For simplicity we will restrict ourselves to a constant mean flow, which yields the disturbance equations in matrix form

$$\frac{d}{dx} \begin{pmatrix} \hat{u} \\ \hat{v} \\ \hat{v}_x \\ \hat{p} \end{pmatrix} = \begin{pmatrix} 0 & -i\gamma & 0 & 0 \\ 0 & 0 & 1 & 0 \\ 0 & c_2 & U\text{Re} & i\gamma\text{Re} \\ c_3 & i\gamma U & -i\gamma/\text{Re} & 0 \end{pmatrix} \begin{pmatrix} \hat{u} \\ \hat{v} \\ \hat{v}_x \\ \hat{p} \end{pmatrix} \quad (7.17)$$

with

$$c_2 = (-i\omega + i\gamma V)\text{Re} + \gamma^2 \quad c_3 = i\omega - i\gamma V - \frac{\gamma^2}{\text{Re}}. \quad (7.18)$$

We have eliminated the \hat{u}_{xx} -term using the x -derivative of the continuity equation (7.14). We then assume perturbations of the form

$$\begin{pmatrix} \hat{u} \\ \hat{v} \\ \hat{v}_x \\ \hat{p} \end{pmatrix} = \begin{pmatrix} \tilde{u} \\ \tilde{v} \\ \tilde{v}_x \\ \tilde{p} \end{pmatrix} \exp(i\alpha x) \quad (7.19)$$

which results in an eigenvalue problem for the complex streamwise wave number α . We obtain

$$\alpha \begin{pmatrix} \tilde{u} \\ \tilde{v} \\ \tilde{v}_x \\ \tilde{p} \end{pmatrix} = \begin{pmatrix} 0 & -\gamma & 0 & 0 \\ 0 & 0 & -i & 0 \\ 0 & -ic_2 & -iU\text{Re} & \gamma\text{Re} \\ -ic_3 & \gamma U & -\gamma/\text{Re} & 0 \end{pmatrix} \begin{pmatrix} \tilde{u} \\ \tilde{v} \\ \tilde{v}_x \\ \tilde{p} \end{pmatrix}. \quad (7.20)$$

Due to the various simplifications (constant mean flow and periodic y -dependence), we can compute analytical expressions for the eigenvalues and their corresponding eigenvectors:

$$\alpha_{1,2} = \pm i\gamma \quad (7.21)$$

$$\alpha_{3,4} = \frac{-iU\text{Re} \pm i\sqrt{U^2\text{Re}^2 + 4c_2}}{2} \quad (7.22)$$

and

$$\Phi_1 = \begin{pmatrix} i \\ 1 \\ -\gamma \\ \frac{\omega}{\gamma} - V - iU \end{pmatrix} \quad \Phi_2 = \begin{pmatrix} -i \\ 1 \\ \gamma \\ \frac{\omega}{\gamma} - V + iU \end{pmatrix} \quad (7.23)$$

$$\Phi_3 = \begin{pmatrix} i\gamma \\ -\alpha_3 \\ -\alpha_3^2 \\ 0 \end{pmatrix} \quad \Phi_4 = \begin{pmatrix} i\gamma \\ -\alpha_4 \\ -\alpha_4^2 \\ 0 \end{pmatrix}. \quad (7.24)$$

As we will learn later in this chapter, it is desirable to obtain a parabolic approximation to the governing equations. A characteristic feature of a parabolic system is that the information propagates in one direction only, and the solution at any given point is only influenced by the solution upstream of the current position. This allows us to calculate the solution to such a system by marching in the propagation direction. The propagation directions of the eigenmodes are given by their group velocities, which can be obtained by differentiation of the expressions for the eigenvalues; see (7.12). The first two eigenvalues, $\alpha_{1,2}$, are associated with the disturbance pressure as the pressure component in the eigenvectors is nonzero. Because these eigenvalues are independent of ω , resulting in $\partial\alpha/\partial\omega = 0$, the corresponding group velocity can be thought of as infinite, propagating information instantaneously upstream and downstream. The group velocities associated with the third and fourth eigenvalues contain the frequency ω , hence yielding finite group velocities. A Taylor series expansion of $\alpha_{3,4}$ for large $U\text{Re}$ results in

$$\alpha_3 \approx \frac{i\gamma^2}{U\text{Re}} - \frac{\gamma V}{U} + \frac{\omega}{U} \quad (7.25)$$

$$\alpha_4 \approx -iU\text{Re} - \frac{i\gamma^2}{U\text{Re}} + \frac{\gamma V}{U} - \frac{\omega}{U} \quad (7.26)$$

which yields

$$c_{g3} \approx U \quad c_{g4} \approx -U. \quad (7.27)$$

These expressions imply that α_3 and α_4 correspond to downstream and upstream propagating disturbances, respectively. In order to obtain a set of equations that are parabolic in nature, the two eigenvalues that propagate upstream must be removed or suppressed. This will be further discussed in Section 7.4.3.

Variable coefficients: velocity-vorticity formulation

The preceding example (with a constant mean flow) has been included to demonstrate analytically the behavior of infinitesimal disturbances using eigenvalue analysis. We will now drop the simplification of a constant mean flow and rederive the equations governing the spatial linear evolution of wavelike perturbations. We will again employ eigenvalue or normal mode analysis to describe the spatial behavior of disturbances. To compute spatial normal modes for parallel shear flows we will start with the Orr-Sommerfeld and Squire equations (3.14), (3.15). As mentioned earlier, the distinction between temporal and spatial spectra does not affect the derivation of the linearized stability equations. Therefore, the Orr-Sommerfeld and Squire equations govern both temporal and spatial modes; it is only a matter of which quantity we prescribe and which we solve for. We have

$$\left[(-i\omega + i\alpha U)(\mathcal{D}^2 - \alpha^2 - \beta^2) - i\alpha U'' - \frac{1}{\text{Re}}(\mathcal{D}^2 - \alpha^2 - \beta^2)^2 \right] \tilde{v} = 0 \quad (7.28)$$

$$\left[(-i\omega + i\alpha U) - \frac{1}{\text{Re}}(\mathcal{D}^2 - \alpha^2 - \beta^2) \right] \tilde{\eta} = -i\beta U' \tilde{v} \quad (7.29)$$

with the boundary conditions $\tilde{v} = \tilde{v}' = \tilde{\eta} = 0$ at solid walls (and in the freestream, in the case of, e.g., boundary layer flow).

For the spatial spectrum we wish to solve the set of equations for α given a real frequency ω . We observe that these equations constitute a generalized eigenvalue problem where the eigenvalue α appears up to the fourth power in the normal velocity and up to the second power in the normal vorticity equation. A closer look at the viscous terms reveals that the eigenvalue appears equidimensional with respect to the differential operator \mathcal{D} . This suggests a transformation of the independent variable y of the form (see Haj-Hariri, 1988)

$$\begin{pmatrix} \tilde{v} \\ \tilde{\eta} \end{pmatrix} = \begin{pmatrix} \tilde{V} \\ \tilde{E} \end{pmatrix} \exp(-\alpha y) \quad (7.30)$$

which will reduce the order of the nonlinear eigenvalue problem by two. The reduced equations then read

$$(i\omega - i\alpha U)(\mathcal{D}^2 - 2\alpha\mathcal{D} - \beta^2)\hat{V} + i\alpha U''\hat{V} + \frac{1}{Re}(\mathcal{D}^2 - 2\alpha\mathcal{D} - \beta^2)^2\hat{V} = 0 \quad (7.31)$$

$$(i\omega - i\alpha U)\hat{E} - i\beta U'V + \frac{1}{Re}(\mathcal{D}^2 - 2\alpha\mathcal{D} - \beta^2)\hat{E} = 0. \quad (7.32)$$

Although we have been able to reduce the power of the eigenvalue problem by two, we are still faced with a nonlinear generalized eigenvalue problem. Similar to reducing an n th-order ordinary differential equation to an n -dimensional system of first-order differential equations, we can reduce the higher-order eigenvalue problem to a linear one by introducing the vector quantity $(\alpha\hat{V}, \hat{V}, \hat{E})^T$, which leads to

$$\begin{pmatrix} -R_1 & -R_0 & 0 \\ I & 0 & 0 \\ 0 & -S & -T_0 \end{pmatrix} \begin{pmatrix} \alpha\hat{V} \\ \hat{V} \\ \hat{E} \end{pmatrix} = \alpha \begin{pmatrix} R_2 & 0 & 0 \\ 0 & I & 0 \\ 0 & 0 & T_1 \end{pmatrix} \begin{pmatrix} \alpha\hat{V} \\ \hat{V} \\ \hat{E} \end{pmatrix} \quad (7.33)$$

with

$$R_2 = \frac{4}{Re}\mathcal{D}^2 + 2iU\mathcal{D} \quad (7.34)$$

$$R_1 = -2i\omega\mathcal{D} - \frac{4}{Re}\mathcal{D}^3 + \frac{4}{Re}\beta^2\mathcal{D} - iU\mathcal{D}^2 + iU\beta^2 + iU'' \quad (7.35)$$

$$R_0 = i\omega\mathcal{D}^2 - i\omega\beta^2 + \frac{1}{Re}\mathcal{D}^4 - \frac{2}{Re}\beta^2\mathcal{D}^2 + \frac{1}{Re}\beta^4 \quad (7.36)$$

$$T_1 = \frac{2}{Re}\mathcal{D} + iU \quad (7.37)$$

$$T_0 = -i\omega - \frac{1}{Re}\mathcal{D}^2 + \frac{1}{Re}\beta^2 \quad (7.38)$$

$$S = i\beta U'. \quad (7.39)$$

These equations have to be solved for the spatial spectrum of parallel shear flows given by the streamwise mean velocity profile $U(y)$.

It is worth mentioning that the variable transformation (7.30) reducing the order of the eigenvalue problem by two is only of advantage for profiles that do not have any symmetries. If the mean velocity profile is symmetric such that even and odd modes can be computed separately and on half the computational domain, it is of no particular advantage to reduce the order of the eigenvalue problem by two.

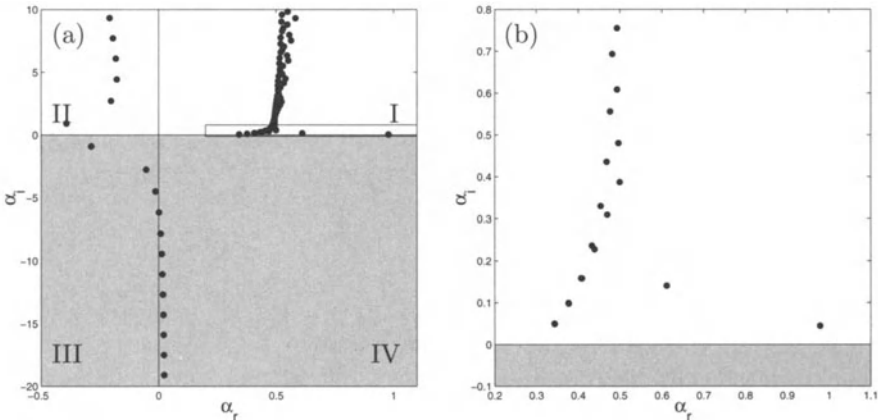


FIGURE 7.2. Spatial Orr-Sommerfeld spectrum for $\omega = 0.3$, $\beta = 0$, and $\text{Re} = 2000$. (a) Entire spectrum, (b) blow-up of region indicated in (a).

α_r	α_i
0.97875	0.044394
0.34312	0.049677
0.61167	0.140492

TABLE 7.1. Selected spatial eigenvalues α for plane Poiseuille flow for $\omega = 0.3$, $\text{Re} = 2000$, and $\beta = 0$.

Example: Plane Poiseuille flow

As an example we will compute the spatial spectrum for plane Poiseuille flow. The spectrum is displayed in Figure 7.2; in the shaded region spatially growing solutions are found. Table 7.1 lists selected spatial eigenvalues.

The spatial spectrum shows a more complicated structure than the temporal one. In particular, we notice eigenvalues in all four quadrants. Eigenvalues in quadrants one and four have positive phase velocities; eigenvalues in the second and third quadrants have negative phase velocities. The eigenvalues in the first and some in the second quadrant will be relevant for computing the downstream response to a forcing at the origin, whereas most eigenvalues in the third and fourth quadrants will influence the perturbation dynamics upstream of the source of the disturbance. We will see an application of this in a later section, when we compute the response of a vibrating ribbon in a boundary layer.

Example: Boundary layer flow

The spectrum for Blasius boundary layer flow is shown in Figure 7.3(a). Similar to the temporal case, we observe a combination of discrete eigenvalues and a continuous spectrum. We will analyze the structure of the spec-

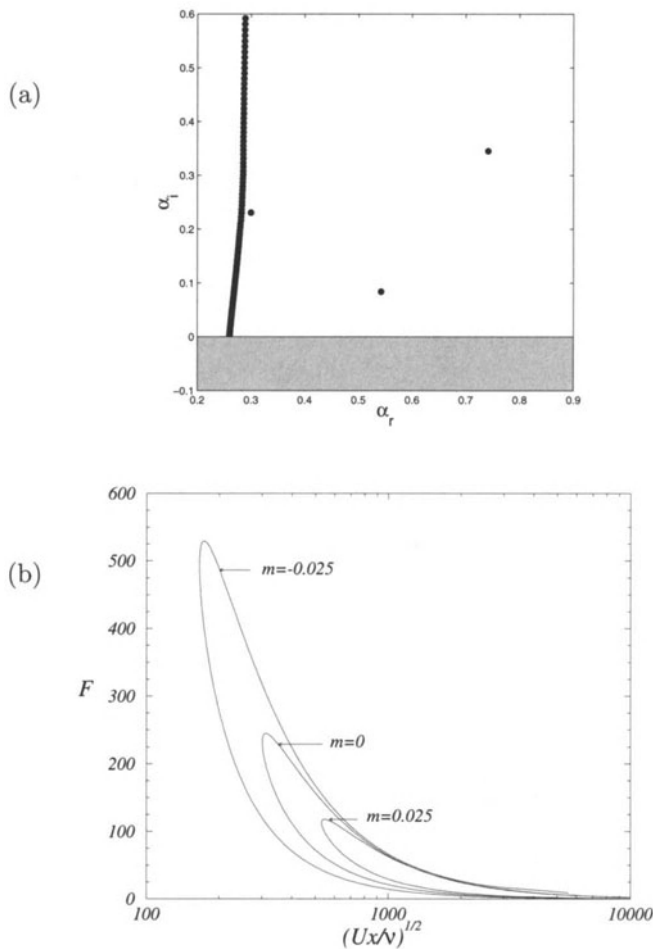


FIGURE 7.3. Spatial Orr-Sommerfeld spectrum for Blasius boundary layer flow. (a) Spectrum with $\omega = 0.26$, $\beta = 0$, and $Re_\delta = 1000$, (b) neutral curve in the $(\sqrt{Re_x}, F)$ -plane. The spectrum in (a) corresponds to $F = 260$ and $\sqrt{Re_x} = 581$. From Hanifi (private communication).

α_r	α_i
0.54213	0.083968
0.29967	0.230773
0.74155	0.345132

TABLE 7.2. Selected spatial discrete eigenvalues α for Blasius boundary layer flow for $\omega = 0.26$, $Re_\delta = 1000$, and $\beta = 0$.

trum, especially the part associated with freestream contributions (i.e., the spatial continuous spectrum) in the next subsection. Table 7.2 lists selected spatial eigenvalues for Blasius boundary layer flow.

Figure 7.3(b) shows neutral curves for Blasius boundary layer flow. Although the shape of the neutral curve is independent of a spatial or temporal viewpoint, we would like to direct our attention to the scaling of the axes. Rather than choosing the Reynolds number Re_δ based on the displacement thickness and the frequency ω we have plotted the neutral curve in the $\sqrt{Re_x}$ - F plane. The Reynolds number Re_x is based on the distance x from the leading edge and thus directly relates to a specific downstream location. It is related to Re_δ through $Re_\delta = 1.72\sqrt{Re_x}$. The frequency F defined as $F = 10^6 \omega \nu / U_\infty^2$ is related to the frequency based on the displacement thickness through $F = 10^6 \omega / Re_\delta$. This choice of scaling avoids the Reynolds number dependence of the displacement thickness, and therefore leaves us with a frequency that is constant for various downstream positions. The type of scaling displayed in Figure 7.3(b) is rather convenient for spatially evolving flows and, for this reason, is often used when theoretical results are compared with experiments. The figure also includes neutral curves for adverse and favorable pressure gradients as indicated by the parameter m (see Section 6.1.1 for an explanation). The neutral curves for adverse and favorable pressure gradients exhibit the same behavior as found in Chapter 6.

Continuous spectrum

Similar to the temporal case (see Section 3.2.3), we expect the presence of a continuous spectrum for flow in unbounded geometry. This part of the spectrum manifests itself as a branch cut in the complex wave number plane after the equations have been Fourier-Laplace-transformed. We will investigate the singularity structure of the solutions to the Orr-Sommerfeld equation in the limit as $y \rightarrow \infty$. We have

$$U \rightarrow U_\infty \quad U'' \rightarrow U''_\infty = 0 \quad (7.40)$$

and the two-dimensional Orr-Sommerfeld equation (3.14) in this limit reads

$$(\mathcal{D}^2 - \alpha^2)(\mathcal{D}^2 - \mu^2)\tilde{v} = 0 \quad (7.41)$$

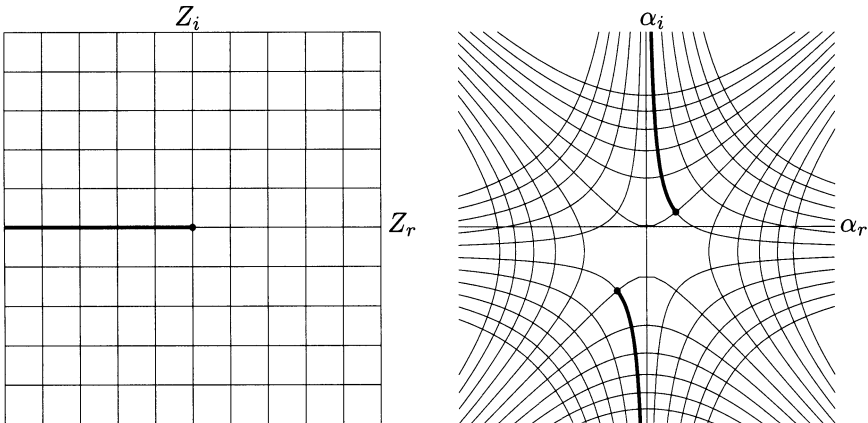


FIGURE 7.4. Mapping of the complex Z -plane into the complex α -plane used in computing the spatial continuous spectrum.

where $\mu = \alpha^2 + i\alpha \text{Re}(1 - c)$. This constitutes a constant-coefficient fourth-order ordinary differential equation. This equation has already been encountered in the derivation of the temporal continuous spectrum (see equation (3.75)). The four fundamental solutions are given in exponential form

$$\tilde{v}_j = \exp(r_j y) \quad j = 1, \dots, 4 \quad (7.42)$$

with

$$r_{1,3} = \pm(\mu^2)^{1/2} \quad r_{2,4} = \pm(\alpha^2)^{1/2}. \quad (7.43)$$

Two pairs of branch cuts arise, which we will treat separately. For the first pair, associated with $r_{1,3}$, we define the auxiliary function (see Ashpis & Reshotko, 1990)

$$Z = \alpha^2 + i\text{Re}(\alpha U_\infty - \omega) \quad (7.44)$$

which redefines

$$\mu = Z^{1/2} \quad \text{and} \quad r_{1,3} = \pm\mu. \quad (7.45)$$

Because of the appearance of a square root function we need to decide on a branch of the multivalued function; we choose the branch of μ such that the real part of μ is positive for all values of Z . The branch cut is chosen along the negative real axis in the Z plane.

The real Z -axis maps to the hyperbola in the complex α plane given by

$$\alpha_r^2 - \left(\alpha_i + \frac{\text{Re}U_\infty}{2} \right)^2 = Z_r \quad (7.46)$$

and the imaginary Z -axis maps to the hyperbola

$$2\alpha_r \left(\alpha_i + \frac{\text{Re}U_\infty}{2} \right) = Z_i + \text{Re}\omega. \quad (7.47)$$

The branch points are given by

$$Z = \alpha^2 + i\text{Re}(\alpha U_\infty - \omega) = 0 \quad \text{or} \quad \omega = \alpha U_\infty - i\frac{\alpha^2}{\text{Re}}. \quad (7.48)$$

Solving for α we find the two branch points seen in Figure 7.4, and solving for ω we confirm the branch point in the ω plane given in (3.84). For the continuous spectrum associated with $r_{2,4}$ we define the auxiliary function

$$Z = (\alpha - i\epsilon)(\alpha + i\epsilon) \quad (7.49)$$

then let $\zeta = \sqrt{Z}$ and thus

$$r_{2,4} = \pm \lim_{\epsilon \rightarrow 0} \zeta. \quad (7.50)$$

The branch cuts that make ζ single-valued are sections of the imaginary α -axis, from the branch points $\pm i\epsilon$ to $\pm\infty$, because they are mapped into the negative real ζ -axis. As $\epsilon \rightarrow 0$ the branch points approach the origin, and the branch cuts span the imaginary axis, excluding the point of origin $\alpha = 0$, which remains a regular point.

7.1.3 Gaster's Transformation

The preceding analysis demonstrates that the spatial framework is mathematically more challenging. It is therefore not surprising that a transformation due to Gaster (1962) is quite frequently used to convert temporal growth rates to spatial ones and vice versa. Unfortunately, this transformation is only valid in a rather restricted region of the parameter space, and for general settings of the governing parameters solutions or approximations have to be based on the spatial rather than the temporal initial value problem.

Derivation of Gaster's transformation

We start with the same dispersion relation but solve for different quantities. On the neutral curve we have $\alpha_i = \omega_i = 0$ or $\alpha \in \mathbb{R}$ and $\omega \in \mathbb{R}$. For small imaginary parts we can use a Taylor series expansion in the neighborhood of the neutral curve.

Gaster's transformation gives a relation between growth rates obtained by temporal analysis and growth rates from spatial analysis. Assuming a dispersion relation of the general form

$$D(\alpha, \omega, \text{Re}) = 0 \quad (7.51)$$

we obtain the total differential in the form

$$dD = \frac{\partial D}{\partial \alpha} d\alpha + \frac{\partial D}{\partial \omega} d\omega + \frac{\partial D}{\partial \text{Re}} d\text{Re} = 0. \quad (7.52)$$

With α_0, ω_0 , and Re_0 on the neutral stability curve we get

$$d\omega|_{\alpha_0} = -d\text{Re} \frac{\partial D}{\partial \text{Re}} \Big/ \frac{\partial D}{\partial \omega} \quad (7.53)$$

$$d\alpha|_{\omega_0} = -d\text{Re} \frac{\partial D}{\partial \text{Re}} \Big/ \frac{\partial D}{\partial \alpha} \quad (7.54)$$

$$d\omega|_{\text{Re}_0} = -d\alpha \frac{\partial D}{\partial \alpha} \Big/ \frac{\partial D}{\partial \omega} = \frac{\partial \omega}{\partial \alpha} \Big|_{\text{Re}_0} d\alpha. \quad (7.55)$$

From there it follows that

$$d\omega|_{\alpha_0} = d\alpha|_{\omega_0} \frac{\partial D / \partial \alpha}{\partial D / \partial \omega} = \left(-\frac{\partial \omega}{\partial \alpha} \Big|_{\text{Re}_0} \right) d\alpha|_{\omega_0} = -c_g d\alpha|_{\omega_0}. \quad (7.56)$$

The last equation relates a small change in α to a small change in ω through the group velocity.

It is important to realize that Gaster's transformation (7.56) makes use of the fact that the dispersion relation is evaluated for parameters near the neutral stability curve and thus only holds for small temporal or spatial growth rates (see Gaster, 1962).

Example: Model problem

Going back to the model problem we considered in the beginning of this chapter, we can verify that Gaster's transformation (7.56), to first order in ϵ , gives the correct relation between the temporal and spatial growth rates. We have the temporal and spatial eigenvalues,

$$\omega = \alpha U - i\epsilon\alpha^2 \quad \alpha = \frac{\omega}{U} + i\frac{\omega^2}{U^3}\epsilon. \quad (7.57)$$

Using the definition of the group velocity

$$c_g = U - 2i\epsilon\alpha \quad (7.58)$$

Gaster's transformation (7.56) gives the following relation between the temporal and spatial growth rates

$$d\omega_i = -c_g d\alpha_i = -\frac{\omega^2 \epsilon}{U^2} = -\alpha^2 \epsilon \quad (7.59)$$

which is easily verified to be correct to leading order in ϵ .

7.1.4 Harmonic Point Source

We will now consider the spatial counterpart of the wave packet solution (2.77) and study the spatial evolution of a harmonic point source.

Three-dimensional problem

The wave pattern created by the least stable downstream propagating mode can be evaluated using the inverse Fourier transform. The normal velocity field resulting from the least stable spatial mode \tilde{v}_1 takes the form

$$v(x, y, z, t) = \iint \kappa_1(\omega, \beta) \tilde{v}_1(y, \omega, \beta) \exp[i(\alpha_1(\omega, \beta)x + \beta z - \omega t)] d\omega d\beta. \quad (7.60)$$

We will consider the special case of a harmonic point source, i.e., $\kappa_1(\omega, \beta) = \delta(\omega - \omega_0)$. We find

$$v(x, y, z, t) = \int \tilde{v}_1(y, \omega_0, \beta) \exp[i(\alpha_1(\omega_0, \beta)x + \beta z - \omega_0 t)] d\beta. \quad (7.61)$$

We wish to evaluate the Fourier integral asymptotically for the limit of large streamwise position. The asymptotic behavior of the wave train for large x can be found using the method of steepest descent, in analogy with the analysis of wave packets in Chapter 2. Let

$$\Psi = i \left(\alpha_1 + \beta \frac{z}{x} - \omega_0 \frac{t}{x} \right) \quad (7.62)$$

which implies that the saddle point satisfies the condition

$$\frac{\partial \Psi}{\partial \beta} = 0 \quad \tan \phi = \frac{z}{x} = -\frac{\partial \alpha_1}{\partial \beta}. \quad (7.63)$$

The saddle point condition implies that the group velocity angle of the waves has to be real. Along a direction in the x - z plane given by the angle ϕ we define β^S such that

$$\tan \phi = -\frac{\partial \alpha_1}{\partial \beta}(\beta^S). \quad (7.64)$$

In the neighborhood of the saddle point the exponent can then be expanded as

$$x\Psi \approx x\Psi^S + \frac{1}{2}x(\beta - \beta^S)^2 \frac{\partial^2 \Psi}{\partial \beta^2}(\beta^S). \quad (7.65)$$

Along any descending path the quadratic term in the expansion near the saddle point has negative real part, implying that the asymptotic solution of the integral becomes

$$v(x, y, z, t) = \tilde{v}_1(y, \omega, \beta^S) \exp(\Psi^S x) \sqrt{\frac{2\pi}{\frac{\partial^2 \Psi^S}{\partial \beta^2}}} \sqrt{-x \frac{\partial \beta^S}{\partial \beta^2}} \quad (7.66)$$

where

$$\Psi^S x = i (\alpha_1^S x + \beta^S z - \omega_0 t). \quad (7.67)$$

For the nonparallel case Mack (1984) modified this method along the lines of Gaster (1982a). Examples of such calculations can be found in Mack (1984).

Example: piecewise linear boundary layer

We will demonstrate the asymptotic result (7.66) of the previous section by computing the development of a disturbance emanating from an oscillating point source. As a mean flow we will choose a piecewise linear approximation of a boundary layer velocity profile ((2.64) with $b = 1/2$). This mean flow was introduced in Chapter 2 where we computed the time-asymptotic dynamics of a localized disturbance (2.77). The advantage of this flow lies in the explicit nature of the dispersion relation

$$D(\alpha, \beta, \omega) = \alpha\xi(k) - \omega = 0 \quad k^2 = \alpha^2 + \beta^2 \quad (7.68)$$

with

$$\xi(k) = 1 - \exp(-k) \frac{\sinh(k)}{k}. \quad (7.69)$$

For the asymptotic analysis we need the first derivative of the streamwise wave number with respect to the spanwise wave number to compute the critical β^S at the saddle point. We also need to compute the second derivative of the phase function with respect to α . Because the dispersion relation (7.68) is a transcendental equation in α we need to differentiate implicitly. We obtain

$$\frac{\partial\alpha}{\partial\beta} = -\frac{D_\beta}{D_\alpha} \quad \frac{\partial^2\alpha}{\partial\beta^2} = -\frac{D_\alpha^2 D_{\beta\beta} - 2D_\alpha D_\beta D_{\alpha\beta} + D_\beta^2 D_{\alpha\alpha}}{D_\alpha^3} \quad (7.70)$$

where the various terms in the above expressions are

$$\begin{aligned} D_\alpha &= \xi + \frac{\alpha^2}{k}\xi' & D_\beta &= \frac{\alpha\beta}{k}\xi' \\ D_{\alpha\alpha} &= \frac{2\alpha^3 + 3\alpha\beta^2}{k^3}\xi' + \frac{\alpha^3}{k^2}\xi'' & & \\ D_{\beta\beta} &= \frac{\alpha^3}{k^3}\xi' + \frac{\alpha\beta}{k^2}\xi'' & D_{\alpha\beta} &= \frac{\beta^3}{k^3}\xi' + \frac{\alpha^2\beta}{k^2}\xi''. \end{aligned} \quad (7.71)$$

The computational procedure is as follows: For chosen streamwise and spanwise positions, x and z , respectively, and a chosen forcing frequency ω we solve equation (7.64) for the spanwise wave numbers β^S that correspond to a stationary point of the phase function. For the case of a piecewise linear boundary layer, we obtain two solutions, as long as the group velocity angle is different from zero or the maximum angle. For each of the spanwise wave numbers β^S we solve the dispersion relation (7.68) for the corresponding streamwise wave number α^S , and evaluate the integral (7.66). Similar to Chapter 2 we take the forcing profile \tilde{v}_1 to be a Gaussian in wave number space. The result of this procedure is shown in Figure 7.5.

By evaluating the maximum half-angle of the wedge for various forcing frequencies, we recover the result $\phi \approx 19.47^\circ$ in the limit of a zero frequency, which coincides with the temporal evolution of a wave packet (2.77) under the same dispersion relation.

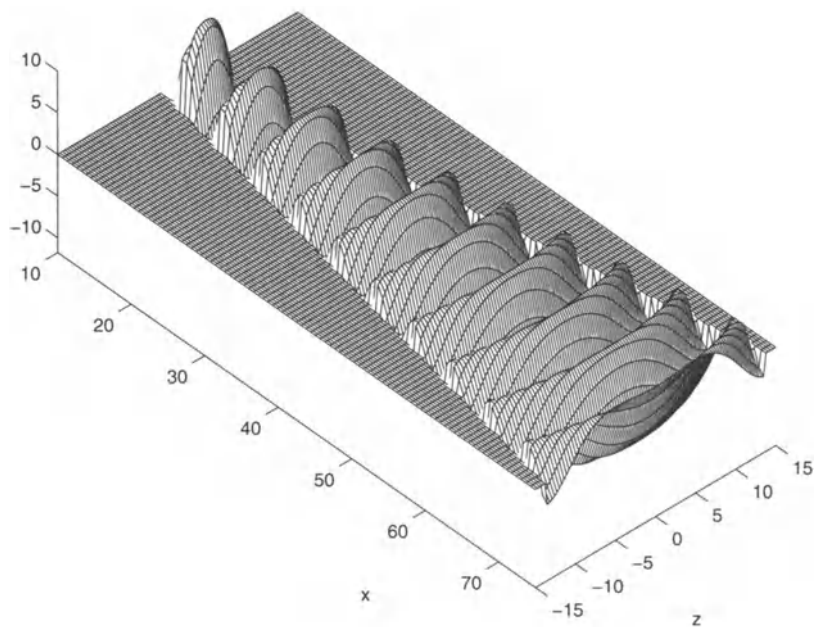


FIGURE 7.5. Asymptotic response to a harmonic point source in a piecewise linear boundary layer. The forcing frequency is $\omega = 0.5$.

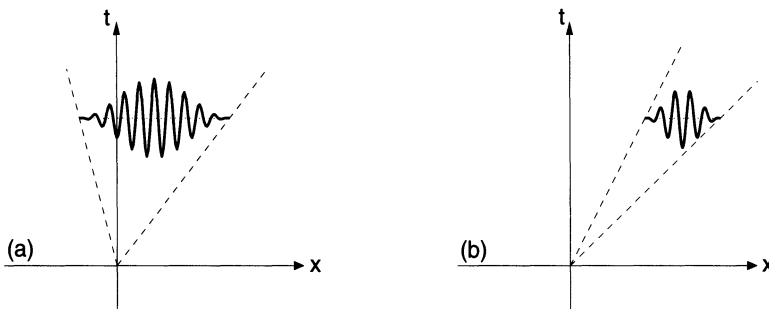


FIGURE 7.6. Sketch of convective and absolute stability. (a) x - t -plane diagram of an absolutely unstable disturbance; (b) x - t -plane diagram of a convectively unstable disturbance.

7.2 Absolute Instability

7.2.1 *The Concept of Absolute Instability*

In the previous section we encountered situations where disturbances grow in both time and space. Here, we will address an important aspect associated with the evolution of perturbations in space *and* time and introduce specific tools for the quantitative description of the spatio-temporal dynamics of these perturbations. In particular, we will investigate the impulse response of a linear system at various streamwise locations. If the localized disturbance generated by the impulse spreads both upstream and downstream of the location where it originated, the flow is considered absolutely unstable. In case the disturbance is swept downstream or upstream of the source, the flow is convectively unstable. Figure 7.6 demonstrates the concept of absolute and convective instability in form of an x - t diagram. On the left the wave packet created at the origin spreads in both the negative and positive x -directions and, in the limit of large time, contaminates the entire domain. On the other hand, the x - t diagram on the right demonstrates the case of a convectively unstable disturbance that is being swept away from the origin. At any location x for the convectively unstable case, the flow will return to its original state as $t \rightarrow \infty$.

In the following section we will develop theoretical tools and criteria to distinguish between convective and absolute instability behavior. We will only concentrate on local instability concepts, that is, instabilities of the local velocity profile. The issue of global instability behavior, i.e., instability of the entire flow field, and its relation to absolute instability behavior is

treated in Section 7.4.5 and in more detail in the review by Huerre & Monkewitz (1990).

Dispersion relation

Let us first mathematically define convective and absolute instability by introducing the general dispersion relation

$$D(\alpha, \omega) = 0 \quad (7.72)$$

which associates dynamic behavior in space (expressed by the wave number α) and time (characterized by the frequency ω). For example, the dispersion relation for parallel shear flows is obtained by solving the Orr-Sommerfeld equation. More simple basic flows, such as the piecewise linear velocity profiles we encountered in Chapter 2, may have explicit dispersion relations. In general, both α and ω could be complex. Any solution of the dispersion relation where α is given and a complex frequency ω is determined from equation (7.72) is known as a temporal branch of the dispersion relation, whereas solutions for which ω is given and a complex α is computed from the dispersion relation are referred to as spatial branches. The differential equation associated with the dispersion relation (7.72) is given as

$$D\left(-i\frac{\partial}{\partial x}, i\frac{\partial}{\partial t}\right)v(x, t) = 0. \quad (7.73)$$

We are interested in the response of the linear system governed by equation (7.73) – or, alternatively, by the dispersion relation (7.72) – to an impulse at the origin of the x - t diagram. The response to this impulse is given by the Green's function $G(x, t)$, which satisfies

$$D\left(-i\frac{\partial}{\partial x}, i\frac{\partial}{\partial t}\right)G(x, t) = \delta(x)\delta(t). \quad (7.74)$$

The definition of linear stability and convective and absolute instability are then expressed in terms of the impulse response $G(x, t)$ as follows.

Definitions

The basic flow is *linearly stable* if

$$\lim_{t \rightarrow \infty} G(x, t) = 0 \quad \text{along all rays } \frac{x}{t} = \text{constant}. \quad (7.75)$$

The basic flow is *linearly unstable* if

$$\lim_{t \rightarrow \infty} G(x, t) \rightarrow \infty \quad \text{along at least one ray } \frac{x}{t} = \text{constant}. \quad (7.76)$$

Among linearly unstable flows, we must further distinguish between convectively and absolutely unstable flows.

The basic flow is *convectively unstable* if

$$\lim_{t \rightarrow \infty} G(x, t) = 0 \quad \text{along the ray } \frac{x}{t} = 0. \quad (7.77)$$

The basic flow is *absolutely unstable* if

$$\lim_{t \rightarrow \infty} G(x, t) \rightarrow \infty \quad \text{along the ray } \frac{x}{t} = 0. \quad (7.78)$$

These definitions are the mathematical analog of the x - t diagrams displayed in Figure 7.6.

Integral representation of the Green's function solution

We will next derive general mathematical criteria based on the singularity structure of the dispersion relation in the complex ω and α planes to classify instabilities as convective or absolute. We will start with the solution to the stability problem in Fourier-Laplace space. If we Fourier- and Laplace-transform (7.74) and formally revert back to physical space, we have

$$G(x, t) = \frac{1}{4\pi^2} \int_L \int_F \frac{\exp[i(\alpha x - \omega t)]}{D(\alpha, \omega)} d\alpha d\omega \quad (7.79)$$

where L and F denote the inversion contour in the Laplace- ω plane and the Fourier- α plane, respectively. Although the Fourier-Laplace integral (7.79) could be determined for all x and t , the complexity of the dispersion relation suggests a time-asymptotic solution of the integral. Moreover, the definition of convective and absolute instability as a limit process for large time also warrants an asymptotic approach in evaluating the Fourier-Laplace integral (7.79). The time-asymptotic evaluation of the integral expression for the Green's function will involve the deformation of the integration contours in the complex α and ω planes. By deforming the integration path through a saddle point in the α plane, we can use the method of steepest descent to evaluate the time-asymptotic behavior (see Section 3.3.5). If this evaluation will result in a divergent integral, the flow under investigation is considered absolutely unstable according to the definition. If the asymptotic limit results in a convergent integral (in fact, in a zero integral), the flow is convectively unstable. Lingwood (1997) points out that special care has to be taken when applying the method of steepest descent. We will come

back to this issue later. Careful evaluation of the time-asymptotic behavior of the Fourier-Laplace integral (7.79) is accomplished using a method introduced by Briggs.

7.2.2 Briggs' Method

Inversion of the Green's function integrals

In Briggs' method (see Briggs, 1964) the wave number integral is chosen first

$$\tilde{G}(x, \omega) = \frac{1}{2\pi} \int_F \frac{\exp[i\alpha x]}{D(\alpha, \omega)} d\alpha \quad (7.80)$$

which is followed by the ω -inversion

$$G(x, t) = \frac{1}{2\pi} \int_L \tilde{G}(x, \omega) \exp[-i\omega t] d\omega. \quad (7.81)$$

The method of analytic continuation is used to deflect the original L -contour in an attempt to lower it below the real ω -axis. If this is achieved, the exponent in the ω -inversion integral (7.81) forces the integrand to vanish as $t \rightarrow \infty$; if not, the time-asymptotic discrete response is governed by the highest discrete singularity in the ω plane. Lowering the ω -contour could fail if a singularity above the real ω -axis is encountered. Because of the interconnection through the dispersion relation this singularity in the ω plane will have an associated singularity in the α plane.

We start by choosing the real α -axis as the inversion contour for the spatial part. This integration path maps through the dispersion relation (7.72) to a curve in the ω plane denoted by $\omega(F)$ in Figure 7.7. The temporal inversion contour (labeled L in Figure 7.7) has to lie above this curve in order to satisfy causality: The integration path for $t < 0$, which involves closure in the upper half-plane, cannot encircle any singularities, or, in other words, the integrand of the ω integral (7.81) has to be analytic in the half-space $\omega_i > \max \text{Im}(\omega(F))$. The temporal contour L can also be mapped back into the α plane, resulting in the branches labeled $\alpha^+(L)$ and $\alpha^-(L)$ in Figure 7.7. The spatial branch above the real axis is associated with the dynamics downstream of the origin, while the branch below the real α -axis governs the perturbation behavior upstream of the source. By analytic continuation we will try to lower the ω inversion contour below the real axis. As we deform the ω contour, its image in the α plane will also deform. At some point, the original α contour will be squeezed between the two branches, which will necessitate the deformation of the original α contour as well. This will in turn modify the ω contour. By constantly adjusting the inversion contours and their maps into the associated plane, we may arrive

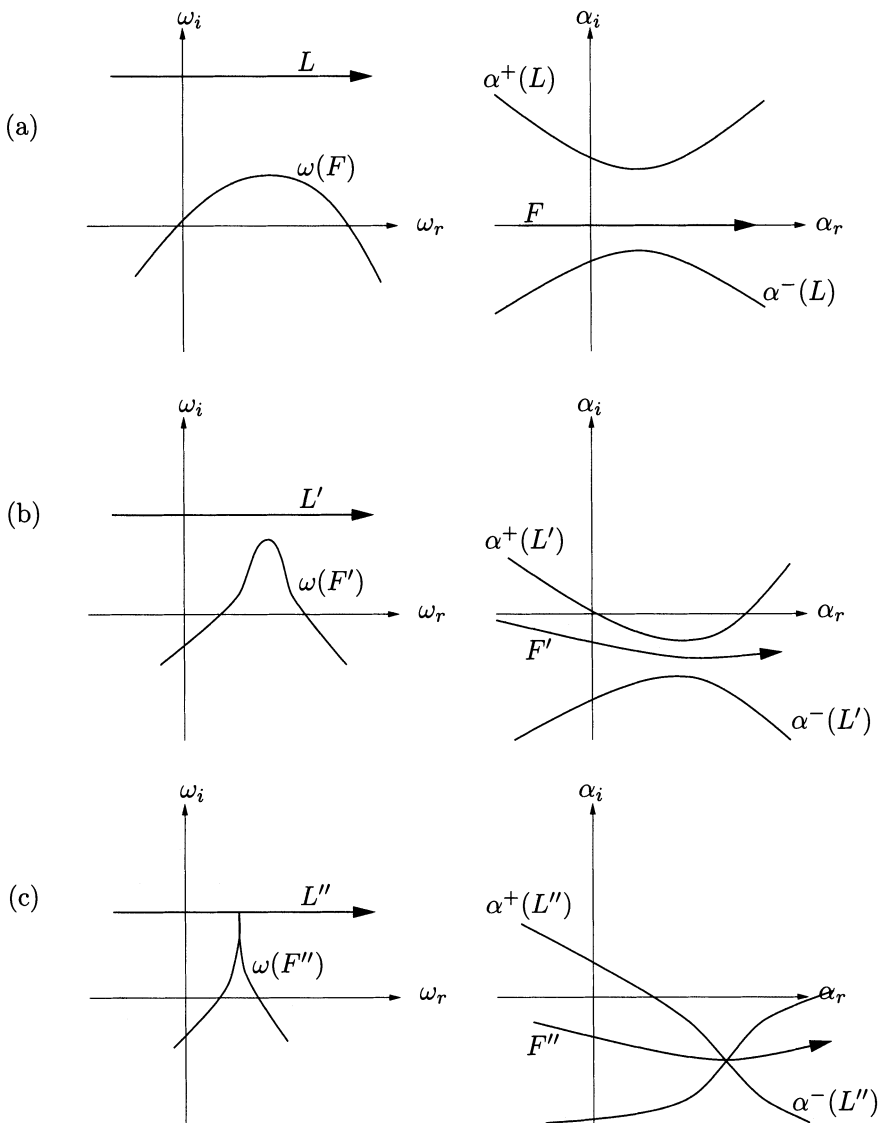


FIGURE 7.7. Sketch of contour deformation procedure for Briggs' method. Left: complex ω -plane; right: complex α -plane.

at a situation where the spatial inversion contour is pinched between the two spatial branches, therefore prohibiting any further deformation without crossing singularities. If this occurs, the temporal inversion contour cannot be lowered any further due to formation of a branch point in the ω plane.

Branch points and pinch points

The simultaneous occurrence of a pinch point in the α plane and a branch point in the ω plane can be explained as follows. A pinch point α_0 in the complex α plane (which is a special kind of saddle point) satisfies the relation¹

$$D(\alpha_0, \omega_0) = 0 \quad \frac{\partial D}{\partial \alpha}(\alpha_0, \omega_0) = 0 \quad \frac{\partial^2 D}{\partial \alpha^2}(\alpha_0, \omega_0) \neq 0. \quad (7.82)$$

A Taylor series expansion of the dispersion relation (7.72) in the neighborhood of the singularity (α_0, ω_0) then leads to

$$0 = \left. \frac{\partial D}{\partial \omega} \right|_0 (\omega - \omega_0) + \frac{1}{2} \left. \frac{\partial^2 D}{\partial \alpha^2} \right|_0 (\alpha - \alpha_0)^2 + \mathcal{O}((\omega - \omega_0)^2, (\alpha - \alpha_0)^3). \quad (7.83)$$

This expression gives a relation between the neighborhood of ω_0 in the ω plane and the neighborhood of α_0 in the α plane. The quadratic nature of the local map between the α and ω planes results in a square root singularity for the local map between the ω and α planes.

If the contour deformation procedure results in a pinch point in the α plane, we are dealing with an absolute instability if the associated branch point in the ω plane lies above the real ω -axis. From the definition of absolute instability and the conceptual view in Figure 7.6, it is clear that such an instability depends on the existence of an unstable wave with zero group velocity. At an unstable pinch/branch point we have

$$c_g = \frac{\partial \omega}{\partial \alpha} = \frac{\partial D}{\partial \alpha} / \frac{\partial D}{\partial \omega} = 0, \quad (7.84)$$

thus satisfying this criterion.

Outline of Briggs' method

As outlined earlier, a crucial step in detecting absolute instabilities is locating pinch points in the complex α plane. A systematic way of accomplishing

¹Higher-order saddle points can be treated analogously (see Lingwood, 1997).

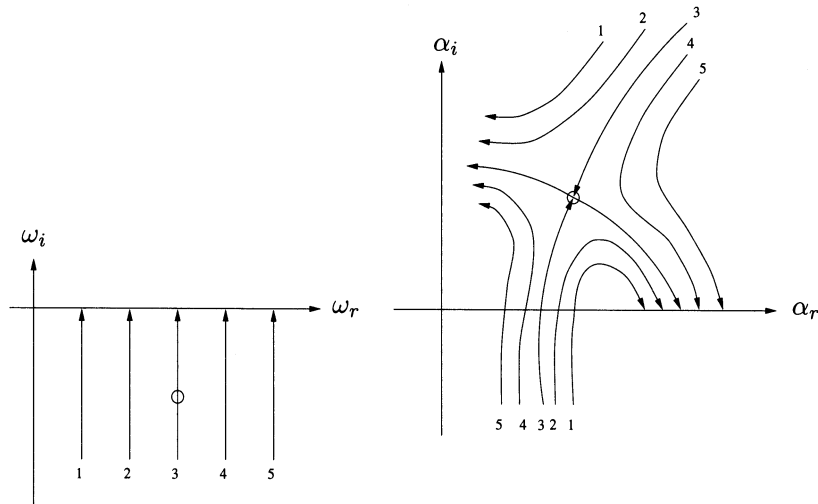


FIGURE 7.8. Illustration of numerical procedure for detecting saddle points in the α -plane used in Briggs' method.

this was suggested by Briggs (1964), where we repeatedly solve for the spatial branches of the dispersion relation (7.72) for frequencies ω given along specified paths in the complex ω plane. For simplicity, we choose straight lines parallel to the imaginary ω -axis. Mapping points along these ω paths into the α plane traces out spatial branches of the dispersion relation associated with the given temporal branches in the ω plane. By varying the real part of the ω lines, we gradually visualize the map of the ω plane into the α plane under the dispersion relation $D(\alpha, \omega) = 0$. It should then be fairly straightforward to locate saddle points in the α plane. An important restriction to keep in mind is that the saddle point has to consist of spatial branches that originate in different half-spaces. Figure 7.8 shows schematically the procedure just outlined. A saddle point clearly forms in the α plane as the ω lines are varied accordingly. Moreover, the two spatial branches forming the saddle point originate in two different half-spaces. The corresponding branch point in the ω plane, marked by a circle along the third ray, lies below the real ω -axis and thus does not constitute an absolute instability, according to Briggs' criterion.

An example

To further demonstrate this important method, we will introduce a sample dispersion relation (taken from Kupfer *et al.* (1987)) and apply Briggs' method. The dispersion relation is a mathematical one; it is used here for demonstration purposes only. Its simplicity allows explicit solutions for the pinch point and branch point locations. We consider

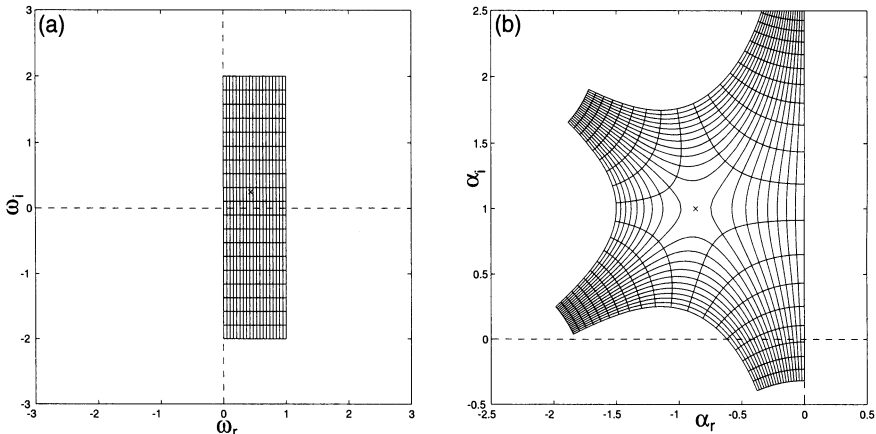


FIGURE 7.9. Mapping of the complex ω -plane into the complex α -plane under the dispersion relation (7.85).

$$D(\omega, \alpha) = \omega - \left[\frac{1}{3}(\alpha - i)^3 + i - \alpha V \right] \quad (7.85)$$

where we have also introduced a parameter V . The pinch points and branch points can be found by solving $d\omega/d\alpha = 0$, which yields

$$\alpha_{1,2} = i \pm \sqrt{V} \quad (7.86)$$

for the pinch points and

$$\omega_{1,2} = (1 - V)i \mp \frac{2}{3}V\sqrt{V} \quad (7.87)$$

for the associated branch points in the ω plane.

We set $V = 0.75$ and proceed with Briggs' method as outlined earlier. We will map lines of constant ω_i and lines of constant ω_r into the complex α plane by solving the cubic dispersion relation (7.85). The result is shown in Figure 7.9.

Clearly, a saddle point forms in the complex α plane that is marked by a symbol and corresponds to the solution of equation (7.86) for $V = 0.75$. Its branches originate in different half-spaces of the α plane. The corresponding branch point in the ω plane is also marked. We see that the branch point is clearly above the real ω -axis, proving the occurrence of an absolute instability.

Admittedly, this example is fairly simplistic. It nevertheless demonstrates the usefulness of Briggs' method to detect absolute instabilities. More complicated dispersion relations can be contrived that challenge the readers' knowledge of analytic function theory.

The relation between Briggs' method and the method of steepest descent

The method just outlined for the computation of absolute and convective stability characteristics is closely related to the method of steepest descent. In fact, the integral representation of the Green's function solution (7.74) suggests looking for saddle points of the phase function and evaluating the integral asymptotically according to standard techniques. It is important to also consider the global topology of the phase function; not all points with $\partial\omega/\partial\alpha = 0$ are associated with absolute instabilities. Failure to consider the global topology of the phase function may result in flawed calculations and incorrect conclusions about the absolute or convective nature of the instability.

When the Riemann sheets of the branch point ω_0 correspond to spatial branches located in the same α plane for high enough L , no pinching of F can occur as L is lowered. The corresponding branch point in the ω plane is not related to the absolute growth rate. Thus, care must be exercised to locate branch-point singularities pertaining to spatial branches originating from distinct halves of the α plane.

The method of steepest descent does not distinguish between branches originating in the same or different half-spaces. Additional analysis of the global topology of the phase function is necessary to focus on the correct type of saddle points in the α plane. For a more detailed treatment, including numerical examples, the reader is referred to Lingwood (1997).

7.2.3 The Cusp Map

We have seen that the asymptotic space-time evolution of a linear instability is governed by the location of pinch points in the complex α plane that are found by an analytic continuation of the Laplace inversion contour into the lower-half ω plane. This technique requires solving the dispersion relation for the spatial wave number α as a function of the frequency ω . This seems unfortunate, because the computation of ω as a function of α is, in most cases, much easier. It is the goal of this section to introduce a method for detecting absolute instabilities that solely relies on a mapping from the α plane to the ω plane. This technique is due to Kupfer *et al.* (1987), who refer to it as the cusp map in the complex-frequency plane.

Mappings between the α and ω planes

We will start by examining the mapping from the α plane to the ω plane. In general, dispersion relations are higher order polynomials (or transcendental) in the wave number α and thus the mapping of the F -contour into the ω plane is multivalued. Let us denote the image of F in the ω plane by $\omega(F)$. The reverse mapping of $\omega(F)$ back into the α plane will result in n branches $\alpha_k(\omega(F))$ with n as the highest order of α in the disper-

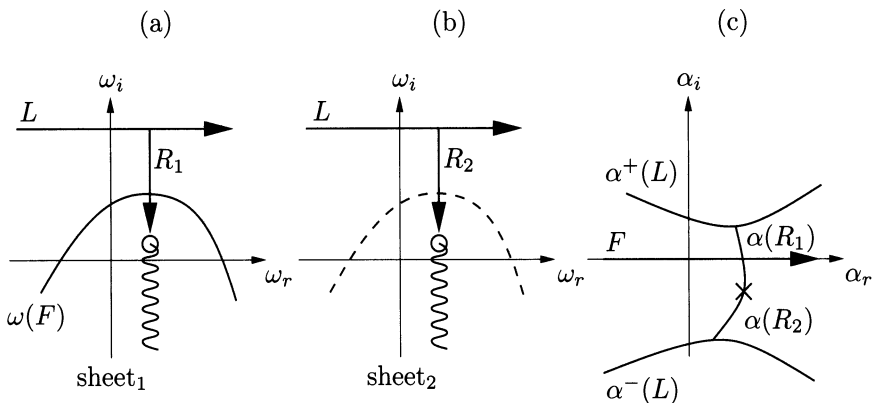
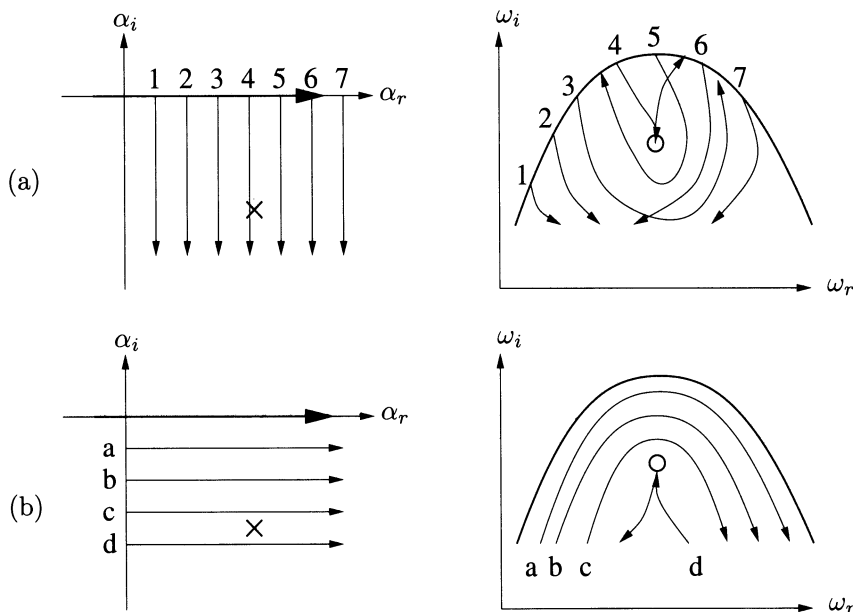


FIGURE 7.10. Sketch illustrating the cusp map method.

FIGURE 7.11. Outline of the numerical procedure for detecting branch points in the ω -plane used in the cusp map method.

sion relation². Nevertheless, the original contour F is recovered by one of the n branches. To make the mapping of the F -contour into the ω plane singlevalued we introduce n Riemann sheets in the complex ω plane and associate the n contours in the multisheeted ω plane with the n branches $\alpha_k(\omega(F))$ in the α plane.

The map between the ω and α plane is governed by the dispersion relation $D(\alpha, \omega) = 0$. For a pinch point in the complex α plane we have the additional constraints

$$\frac{\partial D(\alpha, \omega)}{\partial \alpha} = 0 \quad \frac{\partial^2 D(\alpha, \omega)}{\partial \alpha^2} \neq 0. \quad (7.88)$$

A point ω_0 in the complex ω plane that satisfies these conditions for a corresponding α_0 has only $n - 1$ image points in the complex α plane. In other words, two sheets in the ω plane connect at this specific point ω_0 . We will now concentrate on these two sheets. Let us introduce a vertical ray that connects the contour L in each of the two sheets to the point ω_0 (see Figure 7.10). We will call these rays R_1 and R_2 . They will help us determine whether the point ω_0 in the ω plane corresponds to a pinch point α_0 in the α plane: If and only if the images of the rays R_1 and R_2 in the complex α plane, i.e., $\alpha(R_1)$ and $\alpha(R_2)$ in Figure 7.10, originate on two different sides of F , the branch point at $\omega = \omega_0$ corresponds to a pinch point in the α plane. If the images $\alpha(R_1)$ and $\alpha(R_2)$ originate on different sides of F , but connect at one single point α_0 which is not on F , we must conclude that at least one of these images crosses F . If more than one crossing occurs, the total number of crossings by both images must be odd.

This criterion forms the basis of the cusp map procedure: By counting the number of times that each vertical ray, R_1 and R_2 , intersects the contour $\omega_k(F)$, we can determine whether the branch point ω_0 corresponds to a pinch point in the α plane.

The cusp map procedure

The procedure just described, which is completely general, may be used, together with the following procedure, to determine the stability characteristics of any dispersion relation. The procedure requires mapping a section of the α plane into a specified region located beneath $\omega(F)$. A set of vertical rays along the range of unstable wave numbers is mapped into the ω plane. These rays, originally parallel in the α plane, may have images that intersect, thus indicating a branch point. The singularity is identified by the angle-doubling property of its local map. This is the case in Figure 7.11(a), which shows the branch point nested at the edge of a typical “cusp”-like trajectory. If a branch cut is taken downward from the singularity, one ob-

²For dispersion relations that are transcendental in α , the order n tends to infinity.

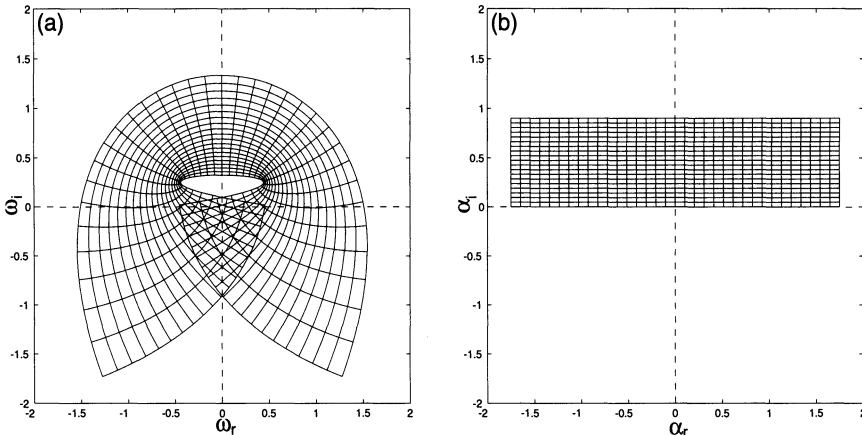


FIGURE 7.12. Mapping of the complex α -plane into the complex ω -plane under the dispersion relation (7.85).

tains a mapping consistent with the multisheeted structure implied by the contour $\omega(F)$. In this case the branch point is covered only once by $\omega(F)$ and thus corresponds to a pinch point. In many problems it is simpler to replace the vertical rays shown in Figure 7.11(a) with a set of horizontal contours that represent deformations of the Fourier integral path. In the ω plane, these contours will progress downward from $\omega(F)$ and form a cusp as they approach the singularity; see Figure 7.11(b). Once again the branch point is located by the angle-doubling (-tripling, etc.) property of its local map. This same procedure can be systematically generalized for dispersion relations with multiple unstable branches.

Applying this technique to the test dispersion relation, we will first map the F contour into the ω plane. A set of lines parallel and perpendicular to F will have images in the ω plane, as shown in Figure 7.12. The images form cusps at $\omega = \pm 2/3$. Both singularities are covered once by $\omega(F)$ so that each corresponds to a pinch point in the α plane.

7.2.4 Stability of a Two-Dimensional Wake

Mean flow and disturbance equations

To demonstrate the concept of absolute stability on a physical problem we consider the stability of a two-dimensional wake behind a stationary cylinder; see Figure 7.13. A linearized unsteady flow, modeled as viscous and incompressible, forms and is superimposed on the laminar flow field, which is assumed to be locally parallel. This last assumption is the most restrictive one, requiring in essence that at each section behind the cylinder

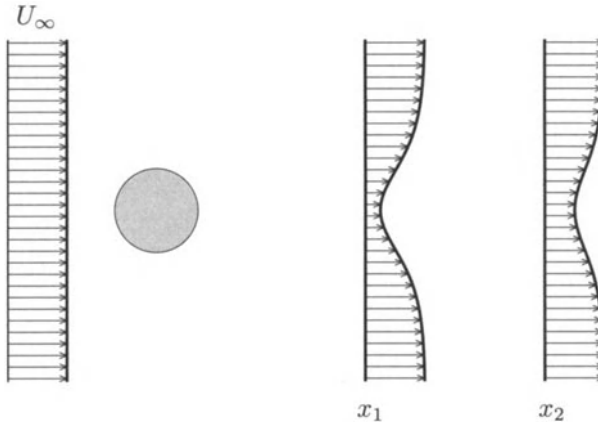


FIGURE 7.13. Sketch of wake geometry.

the properties of the wake are adequately represented, locally, by the stability properties of a parallel flow having the same average velocity profile. The analysis of the flow, therefore, is decomposed into several equivalent parallel-flow problems. Later in this chapter, we will briefly outline the modifications necessary to address effects of non-parallelism on the stability characteristics.

We follow Hultgren & Aggarwal (1987) and assume the nondimensional mean velocity of Gaussian form according to

$$U(y) = 1 - \lambda \exp(-y^2 \ln 2). \quad (7.89)$$

The parameter λ represents the local nondimensional wake velocity defect and will be fitted to mean velocity profiles measured at various distances behind the cylinder (see Figure 7.13). The mean flow profile is not realistic for the near-wake region, but it represents a convenient test example for the study of absolute instabilities in two-dimensional wakes. Other models of the mean flow have been suggested by Betchov & Criminale (1966), Mattingly & Criminale (1972), and Triantafyllou *et al.* (1986).

Absolute instability of Gaussian wakes

We then solve the Orr-Sommerfeld equation (3.14) governing the viscous instability of the wake profile for various downstream locations. The wake

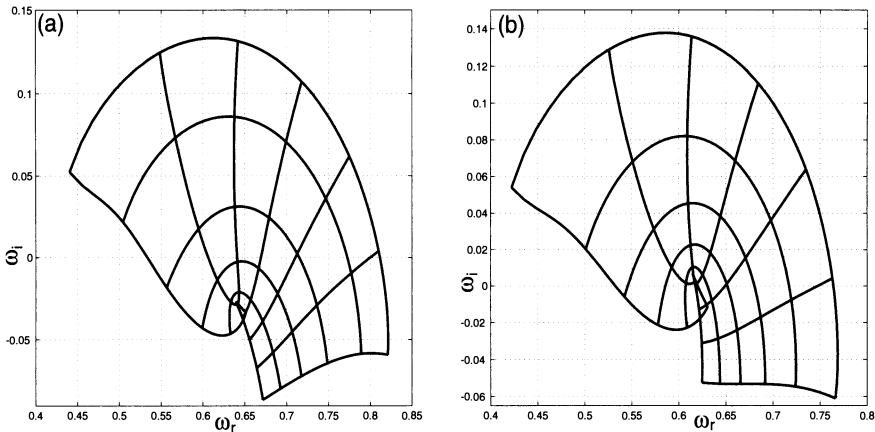


FIGURE 7.14. Mapping of the complex α -plane into the complex ω -plane under the dispersion relation for a Gaussian wake. The case $\lambda = 0.92$ (left) shows an absolutely stable flow; for $\lambda = 0.95$ (right) we observe an absolute instability. The Reynolds number is $\text{Re} = 400$.

Reynolds number $\text{Re}_w = \lambda U_\infty b / \nu$ will be based on the wake velocity defect and the local wake half-width b . This choice of Reynolds number is constant in the far wake and is therefore proportional to the drag coefficient of the body causing the wake. Keeping Re_w fixed and varying λ corresponds directly to changing the streamwise location in a given far-wake experiment.

As mentioned earlier, the stability analysis is local and can only be expected to yield meaningful results for disturbances whose streamwise length scale is much smaller than the characteristic length for the streamwise evolution of the mean flow. This cannot be expected to fully remain the case for small values of the Reynolds number. We will only consider two-dimensional perturbations and will ignore the presence of the continuous spectrum.

Hultgren & Aggarwal (1987) showed that the effect of viscosity on the growth rates is weak for wake Reynolds number larger than approximately 400. However, they observed a significant sensitivity of the growth rates to the velocity defect λ .

We choose a wake Reynolds number of $\text{Re}_w = 400$ and apply the cusp map technique in the frequency domain to investigate the presence of absolute instabilities. The Orr-Sommerfeld equation (3.14) for the Gaussian wake profile has been solved and an equispaced grid in the complex wave number (α) plane has been mapped into the complex frequency (ω) plane. The result of this map is shown in Figure 7.14 for two cases of the velocity defect λ .

In both cases, we observe the formation of a branch point in the frequency plane. The lines of $\alpha_r = \text{constant}$ reconnect to the $\alpha_i = 0$ curve, indicating

the existence of a branch point, while the lines of $\alpha_i = \text{constant}$ form a cusp as α_i is decreased. The location of the branch point will decide if the flow exhibits an absolute instability.

In the first case, the velocity defect parameter is $\lambda = 0.92$, and the branch point in the ω plane falls below the neutral line $\omega_i = 0$. The wake velocity profile is convectively unstable. On the other hand, for a velocity defect parameter of $\lambda = 0.95$, which corresponds to a position closer to the body, we observe the formation of a branch point above the $\omega_i = 0$ line. This indicates the existence of an absolute instability for this local mean velocity profile. We therefore conclude that as λ decreases in the streamwise direction, an initially absolute instability in the near-wake region will switch to a convective instability in the far-wake region. As a final note we wish to emphasize that the preceding analysis has employed a variety of approximations and simplification, and the results should therefore be interpreted cautiously. However, experimental measurements performed by Kovasznay (1949) have shown good qualitative and quantitative agreement with the presented results.

Hultgren & Aggarwal (1987) arrive at the same results using the analysis of pinch points in the α plane. For maps of the ω plane into the α plane, the reader is referred to this reference.

7.2.5 Stability of Rotating Disk Flow

As another example of absolute instability we will present a spatio-temporal stability analysis for rotating disk flow. Rotating disk flow is similar to boundary layer flow over a swept wing: Both boundary layers are three-dimensional with a laminar crossflow velocity component that is inflectional. The relation to swept-wing boundary layers has caused a great deal of interest from experimentalists and theoreticians and a large body of literature on the stability problem exists. A remarkable fact of transition in rotating boundary layers is that the onset of transition is very repeatable. Malik *et al.* (1981) tabulate locations for the onset of transition, as found by various experimentalists. The values show a scatter of less than 3 percent around an average Reynolds number of 513, despite various methods of investigation. These results contrast with the onset of transition of the boundary layer on a flat plate where the onset is sudden but the location is highly dependent on the disturbance environment. This contrast reinforces the idea that a well-defined location of absolute instability of the rotating-disk boundary layer may be triggering the nonlinear behavior characteristic of the onset of transition.

Basic flow

The disk will be modeled as an infinite planar disk rotating about the vertical z -axis at a constant angular frequency ω^* (see Figure 7.15).

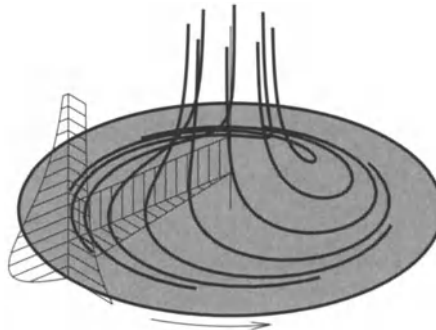


FIGURE 7.15. Sketch of rotating disk flow.

The mean flow has been computed by Karman (1921) as an exact similarity solution to the Navier-Stokes equations. Introducing the nondimensional distance from the disk in the form

$$\zeta = z \sqrt{\frac{\omega}{\nu}} \quad (7.90)$$

and assuming the velocity component and the pressure as

$$U^* = r^* \omega^* F(\zeta) \quad V^* = r^* \omega^* G(\zeta) \quad (7.91)$$

$$W^* = \sqrt{\nu \omega^*} H(\zeta) \quad P^* = \rho \nu \omega^* \Pi(\zeta) \quad (7.92)$$

we arrive at a system of nonlinear ordinary differential equations given as

$$2F + H' = 0 \quad (7.93)$$

$$F^2 + F'H - G^2 - F'' = 0 \quad (7.94)$$

$$2FG + HG' - G'' = 0 \quad (7.95)$$

$$\Pi' + HH' - H'' = 0 \quad (7.96)$$

which has to be solved numerically subject to the boundary conditions

$$\begin{aligned} F(0) &= H(0) = \Pi(0) = 0 & G(0) &= 1 \\ F(\infty) &= G(\infty) = 0. \end{aligned} \quad (7.97)$$

Disturbance equations

To formulate the linear stability problem we will perturb the mean flow by perturbations of infinitesimal amplitude

$$\bar{u}(r, \theta, t, z) = \frac{r}{\text{Re}} U(z) + u(r, \theta, t, z) \quad (7.98)$$

$$\bar{v}(r, \theta, t, z) = \frac{r}{\text{Re}} V(z) + v(r, \theta, t, z) \quad (7.99)$$

$$\bar{w}(r, \theta, t, z) = \frac{1}{\text{Re}} W(z) + w(r, \theta, t, z) \quad (7.100)$$

$$\bar{p}(r, \theta, t, z) = \frac{1}{\text{Re}^2} P(z) + p(r, \theta, t, z) \quad (7.101)$$

where $U = U^*/r^*\omega^*$, $V = V^*/r^*\omega^*$, $W = W^*(\nu\omega^*)^{1/2}$, and $P = P^*/\rho\nu\omega^*$. The Reynolds number is defined as the local Reynolds number where the stability analysis is applied, e.g., at $r = r_a$. Using the length scale $(\nu\omega^*)^{1/2}$ and velocity scale $r_a^*\omega^*$ we have

$$\text{Re} = r_a.$$

The Navier-Stokes equations are then linearized with respect to the small perturbation quantities. In order to make the linearized perturbation equations separable in the independent variables, it is necessary to ignore variations in the Reynolds number with radius. This involves replacing the variable r , which appears in coefficients of the linearized equations, by the Reynolds number Re . Terms of order $\mathcal{O}(\text{Re}^{-2})$ are then neglected. The perturbations are assumed to have a wavelike form, e.g.,

$$u = \hat{u}(z, \alpha, \omega, \beta) \exp[i(\alpha r + \beta\theta - \omega t)]. \quad (7.102)$$

The equations governing the dynamics of the perturbation quantities can be written as a system of six first-order equations by introducing new dependent variables; see Lingwood (1995). However, by dropping the Coriolis and curvature terms, which are of order Re^{-1} , we can derive an Orr-Sommerfeld equation for the velocity normal to the rotating disc. We have

$$[(\mathcal{D}^2 - \gamma^2)^2 - i\text{Re}(\alpha U + \bar{\beta}V - \omega)(\mathcal{D}^2 - \gamma^2) + i\text{Re}(\alpha U'' + \bar{\beta}V'')] \hat{w} = 0 \quad (7.103)$$

where $\gamma^2 = \alpha^2 + \bar{\beta}^2$, with $\bar{\beta} = \beta/\text{Re}$, and \mathcal{D} denotes differentiation with respect to z . This is the same form of the Orr-Sommerfeld equation that governs flow in a three-dimensional Falkner-Skan-Cooke boundary layer. If all terms of $\mathcal{O}(\text{Re}^{-1})$ are neglected and viscosity is considered to act only in the establishment of the mean flow, the preceding equation reduces further to the Rayleigh equation for rotating disk flow

$$[(\alpha U + \bar{\beta}V - \omega)(\mathcal{D}^2 - \gamma^2) - (\alpha U'' + \bar{\beta}V'')] \hat{w} = 0. \quad (7.104)$$

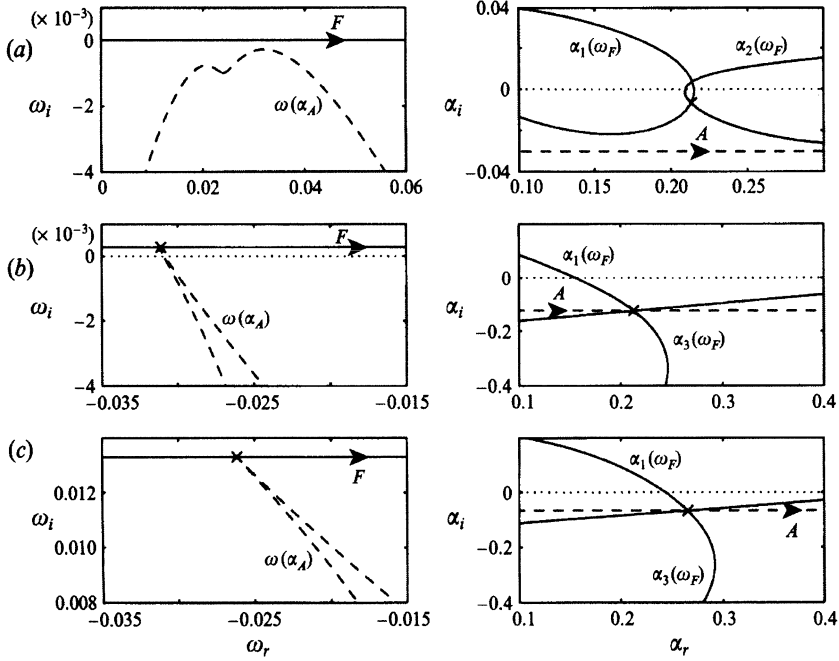


FIGURE 7.16. (a) Viscous temporal branch in the ω -plane (given by the A-line) and viscous spatial branches 1 and 2 in the α -plane (given by the F-line), for $Re = 515$ and $\beta = 6$, showing the branch point. (b) Viscous temporal branch in the ω -plane and viscous spatial branches 1 and 3 in the α -plane, for $Re = 530$ and $\beta = 67$, showing the pinch point. (c) Inviscid temporal branch in the ω -plane and inviscid spatial branches 1 and 3 in the α -plane, for $\bar{\beta} = 0.126$, showing the pinch point. From Lingwood (1995).

Numerical results

We solve the stability equations (both viscous sixth-order equation defined in Lingwood (1995) and the inviscid equation (7.104)) for rotating disk flow for the spatial wave number α that appears nonlinearly as the eigenvalue in these equations. As outlined in the previous sections, we then gradually lower the inversion contour in the complex ω plane and deform the inversion contour in the complex α plane so as to maintain causality. The appearance of a pinch point in the α plane for an inversion path with $\omega_i > 0$ indicates an absolute instability.

Figure 7.16 displays the results of the computations (Lingwood, 1995) in the ω plane and the α plane. The two upper plots show the starting point of the calculations for $Re = 515$ and $\beta = 6$. The inversion contour in the ω plane labeled F has been chosen high enough that all zeros of the dispersion relation lie below it. Evaluating the spatial eigenvalue problem for this choice of ω leads to the spatial branches displayed in the top-

right part of Figure 7.16. On the other hand, solving the temporal stability problem for α along the path marked as A in the α plane yields the curve $\omega(\alpha_A)$ in the ω plane. We proceed by manipulating F such that A will be pinched between two spatial branches. The middle figures show this situation for $Re = 530$ and $\beta = 67$. Because a pinch point in the α plane and an associated branch point in the ω plane have been identified for positive ω_i , we conclude that an absolute instability exists at this specific parameter combination. It is important that the pinch point in the α plane is formed by two branches α_1 and α_3 that originated from two different half-spaces (separated by the path A). For comparison, in the lower two plots, the inviscid equations for the same spanwise wave number have been solved, verifying the absolute instability.

A parameter study results in a radial absolute instability for Reynolds numbers larger than $Re = 510.26$ and suitable azimuthal wave number β .

Experimental results

To verify the theoretically obtained critical Reynolds number for the onset of an absolute instability in the radial direction, Lingwood (1996) conducted an experiment where the flow over a rotating disk was perturbed impulsively at a radial position well below that where an absolute instability is observed numerically. A three-dimensional wave packet consisting of *convectively* unstable modes forms and propagates in the positive radial direction. As the wave packet approaches the critical radius (corresponding to the critical Reynolds number of $Re_{crit} = 510$) for the onset of absolute instability, the group velocity of the packet tends to zero. The wave packet remains convectively unstable in the azimuthal direction and, in the presence of an absolute instability in the radial direction, triggers transition to turbulent fluid motion.

Figure 7.17 shows contours at the 0.008 level of the wave packet envelope amplitude for four disk revolutions. The wave packet has been generated at $Re \approx 311$ at $t = 0$, after which it spreads in the azimuthal and positive radial direction. The figure clearly shows the convective nature of the instability. At approximately $Re \approx 500$ one observes the breakdown of the packet, which conforms with the appearance of an absolute instability. Measurements of the leading and trailing edges of the wave packet are plotted in Figure 7.17, and lines have been fitted in a least-squares sense, to the data. Constraints at $Re = 311$ and (for the trailing edge) at $Re = 511$ have been imposed. The curves accurately describe the development of the wave packet in the radial and azimuthal coordinate directions. As mentioned earlier, the critical Reynolds number for transition to turbulence in rotating disk flow has been consistently observed by other investigators at a value of 513 ± 3 percent. Lingwood (1996) also observes a lack of sensitivity to the exact form of the disturbance environment, which is characteristic of an absolutely unstable flow.

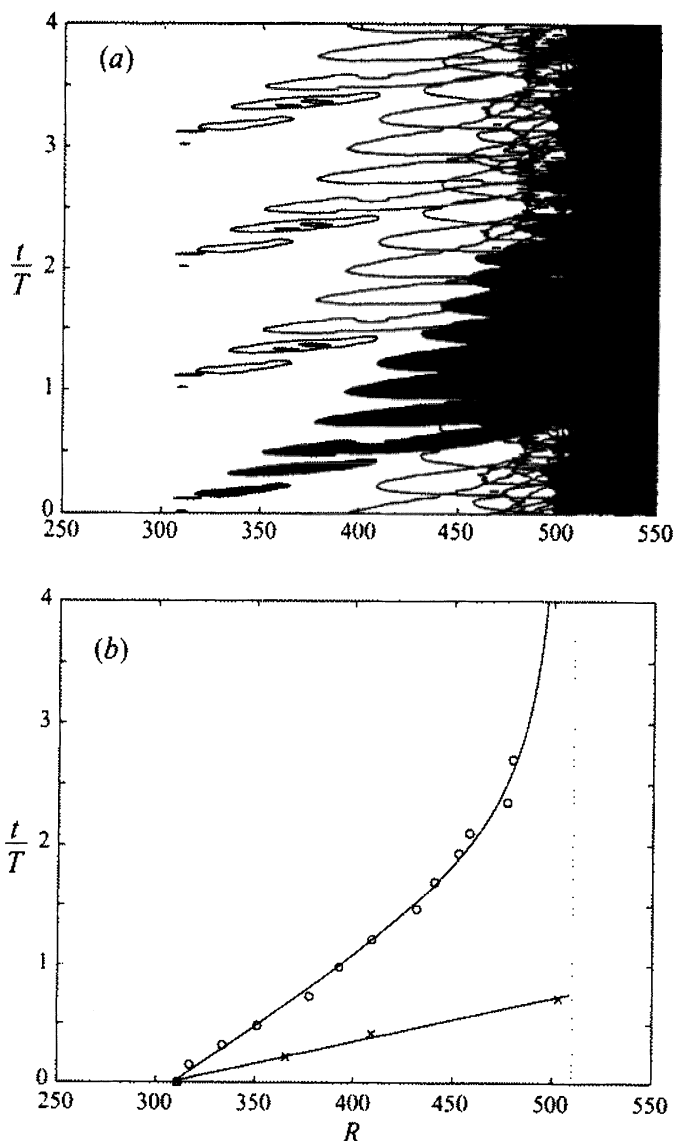


FIGURE 7.17. (a) Contour plot, at the 0.008 level, of the wave packet envelope at $z = 1, 3, \Omega = 1400$ r.p.m. (b) Leading edge (x) and trailing edge (o) of the wave packet trajectory, taken from (a), and least-squares fits to the experimental data (solid line). The critical Reynolds number for absolute instability, $Re = 510$, is indicated by a dotted line. From Lingwood (1996).

7.3 Spatial Initial Value Problem

In the previous two sections we analyzed the modal structure in a spatial and spatio-temporal setting. In this section we will investigate the spatial initial value problem. Various approximations will be introduced and discussed, and the influence of the most common effects neglected in modal theory will be investigated.

7.3.1 Primitive Variable Formulation

We will consider the governing equations for infinitesimal disturbances in parallel flows. Let $U_i = U(y)\delta_{1i}$ be the base flow, i.e., a flow in the x -direction that has a variation with y ; see Figure 2.1 defining the coordinate system and base flow. We will assume solutions of the form

$$q(x, y, z, t) = \hat{q}(x, y) \exp[i(\beta z - \omega t)] \quad (7.105)$$

which transforms the equations into

$$-i\omega\hat{u} + U \frac{\partial\hat{u}}{\partial x} + U'\hat{v} = -\frac{\partial\hat{p}}{\partial x} + \frac{1}{\text{Re}} \left(\frac{\partial^2}{\partial x^2} + \mathcal{D}^2 - \beta^2 \right) \hat{u} \quad (7.106)$$

$$-i\omega\hat{v} + U \frac{\partial\hat{v}}{\partial x} = -\mathcal{D}\hat{p} + \frac{1}{\text{Re}} \left(\frac{\partial^2}{\partial x^2} + \mathcal{D}^2 - \beta^2 \right) \hat{v} \quad (7.107)$$

$$-i\omega\hat{w} + U \frac{\partial\hat{w}}{\partial x} = -i\beta\hat{p} + \frac{1}{\text{Re}} \left(\frac{\partial^2}{\partial x^2} + \mathcal{D}^2 - \beta^2 \right) \hat{w} \quad (7.108)$$

$$\frac{\partial\hat{u}}{\partial x} + \mathcal{D}\hat{v} + i\beta\hat{w} = 0. \quad (7.109)$$

We will use the continuity equation (7.109) to eliminate the term $\partial^2 u / \partial x^2$. We obtain

$$\frac{\partial}{\partial x} \begin{pmatrix} \hat{u} \\ \hat{v} \\ \hat{v}_x \\ \hat{w} \\ \hat{w}_x \\ \hat{p} \end{pmatrix} = \begin{pmatrix} 0 & -\mathcal{D} & 0 & i\beta & 0 & 0 \\ 0 & 0 & 1 & 0 & 0 & 0 \\ 0 & -\text{Re}C & \text{Re}U & 0 & 0 & \text{Re}\mathcal{D} \\ 0 & 0 & 0 & 0 & 1 & 0 \\ 0 & 0 & 0 & -\text{Re}C & \text{Re}U & i\beta\text{Re} \\ C & -U' + U\mathcal{D} & -\mathcal{D}/\text{Re} & iU\beta & -i\beta/\text{Re} & 0 \end{pmatrix} \begin{pmatrix} \hat{u} \\ \hat{v} \\ \hat{v}_x \\ \hat{w} \\ \hat{w}_x \\ \hat{p} \end{pmatrix} \quad (7.110)$$

with

$$C = \frac{1}{\text{Re}}(\mathcal{D}^2 - \beta^2) + i\omega. \quad (7.111)$$

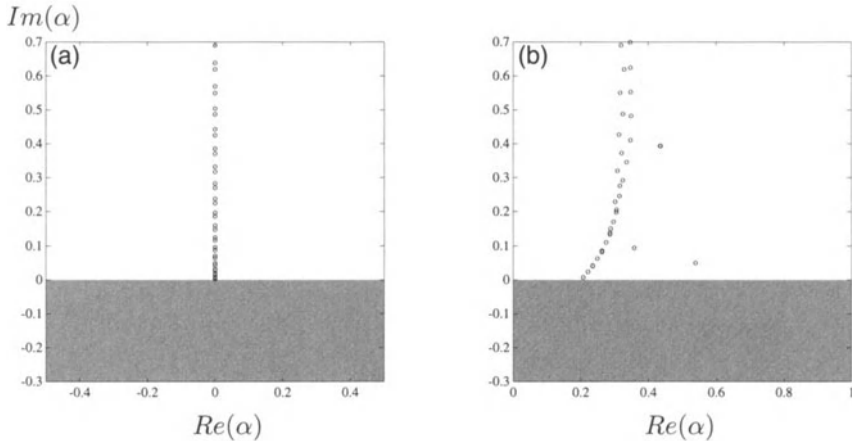


FIGURE 7.18. Spectrum of the spatial evolution operator for plane Poiseuille flow at $\text{Re} = 2000$. (a) $\beta = 1, \omega = 0$, (b) $\beta = 1, \omega = 0.2$. The shaded half-plane corresponds to the unstable domain.

This system of equation represents the three-dimensional analog of the system of equations (7.17) given earlier as a model problem. But in contrast, we assume neither a constant mean flow nor a periodic y -dependence as in (7.17). For this reason, the entries in the evolution matrix are functions of the normal coordinate direction or differential operators with respect to y .

7.3.2 Solution of the Spatial Initial Value Problem

Spatial eigenfunction expansion and optimal growth

The spatial initial value problem can be solved using an eigenfunction expansion in spatial eigenmodes. This approximation allows us to investigate the possibilities for spatial transient amplification. The spatial initial value problem may be written as

$$\frac{d\kappa}{dx} = i\Lambda\kappa \quad (7.112)$$

where $\Lambda = \text{diag}(\alpha_1, \dots, \alpha_N)$ is a diagonal matrix consisting of the spatial eigenvalues and $\kappa(x)$ are the coefficients in the eigenfunction expansion

$$\begin{pmatrix} \hat{u} \\ \hat{v} \\ \hat{w} \end{pmatrix} = \sum_{j=1}^N \kappa_j(x) \begin{pmatrix} \tilde{u} \\ \tilde{v} \\ \tilde{w} \end{pmatrix}_j \quad (7.113)$$

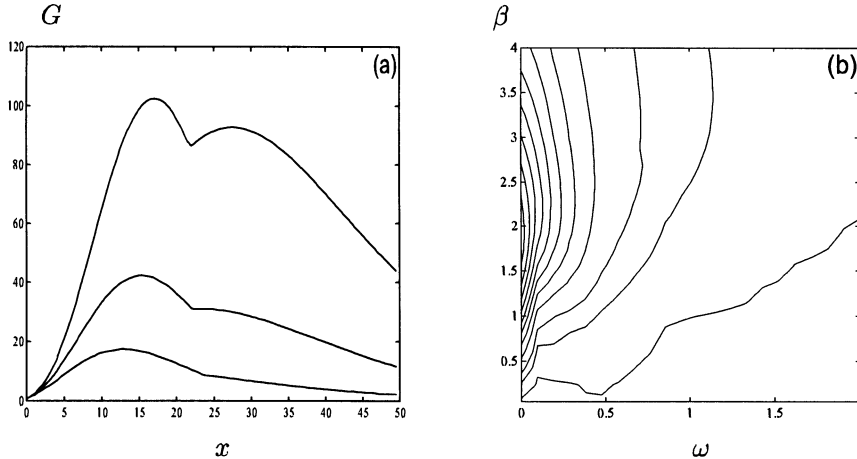


FIGURE 7.19. Transient spatial amplification: (a) maximum amplification of energy density versus streamwise location for $\text{Re} = 500, 1000, 2000, \beta = 2$, and $\omega = 0$. (b) G_{\max} as a function of frequency ω and spanwise wavenumber β for $\text{Re} = 2000$. The contour levels are 5, 10, 20, ..., 100.

with $(\tilde{u} \ \tilde{v} \ \tilde{w})_j^T$ as the j th vector eigenfunction of the discretized spatial evolution operator. We chose the primitive variable formulation of the eigenvectors. Another choice, which is equally valid, is using the normal velocity and normal vorticity. For the solution to be well posed, only spatial eigenmodes propagating in the downstream direction are included in the expansion. This is equivalent to using a reduced basis for the problem or, equivalently, to parabolizing the system.

The local energy density defined in terms of the vector eigenfunction expansion can be written

$$E(\kappa) = \kappa^H A \kappa = \kappa^H F^H F \kappa = \|F \kappa\|_2^2 \quad (7.114)$$

where

$$A_{ij} = \frac{1}{2} \int_{-1}^1 (\tilde{u}_i^* \tilde{u}_j + \tilde{v}_i^* \tilde{v}_j + \tilde{w}_i^* \tilde{w}_j) dy. \quad (7.115)$$

The kinetic energy is used as a measure of the disturbance. Because we are not interested in the transfer of energy, this choice will suffice. For a discussion of appropriate disturbance measures for spatial evolution problems, see Section 7.5.1.

The maximum possible energy amplification G is then given as

$$G(x) = \sup_{\kappa_0} \frac{E(\kappa)}{E(\kappa_0)} = \|F \exp(i\Lambda x) F^{-1}\|_2^2. \quad (7.116)$$

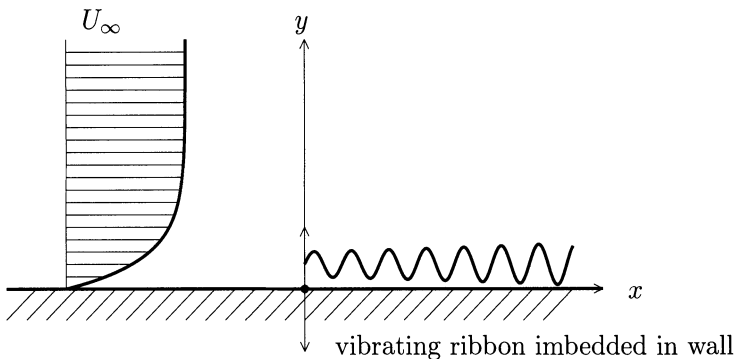


FIGURE 7.20. Sketch of vibrating ribbon in boundary layer flow.

The preceding analysis follows the temporal analog in Chapter 4.

Example: plane Poiseuille flow

A spectral collocation technique using Chebyshev polynomials was used to discretize the eigenvalue problem in the wall normal direction. Figures 7.18(a,b) show the spectrum of the spatial evolution operator for plane Poiseuille flow and two parameter combinations. The spectrum of the spatial evolution operator determines the growth or decay of infinitesimal disturbances far downstream ($x \rightarrow \infty$).

Figure 7.19 displays a plot of the maximum amplification $G(x)$ versus the streamwise location x for three different Reynolds numbers. Significant transient growth is observed before asymptotic decay of the disturbance dominates for large x . The curves in Figure 7.19(a) are composed of two separate growth curves for symmetric and antisymmetric \hat{v} -disturbances and the cusps in Figure 7.19(a) stem from a switching of the optimally amplified perturbation from a symmetric to an antisymmetric \hat{v} -disturbance. The peak G_{\max} of the amplification curves, i.e., $G_{\max} = \sup_{x \geq 0} G(x)$, has been plotted as a function of the frequency ω and the spanwise wave number β in Figure 7.19(b). The Reynolds number is $Re = 2000$, and G_{\max} has been found to be determined by symmetric \hat{v} -perturbations. Figure 7.19(b) shows that the largest amplification is achieved by steady disturbances, i.e., disturbances with frequency $\omega = 0$. The maximum occurs for $\beta \approx 2$.

7.3.3 The Vibrating Ribbon Problem

The excitation of spatially growing disturbances by a vibrating ribbon is a common experimental technique to investigate the response of a shear layer to harmonic forcing. Schubauer & Skramstad (1947) introduced this method to study the receptivity characteristics of a flat plate boundary layer. From a mathematical point of view, the vibrating ribbon problem is known as a signaling problem. We will follow the work of Ashpis & Reshotko (1990) and derive an expression for the response of the shear flow to a harmonic forcing using integral transform techniques.

The mathematical problem

The ribbon is described by an oscillatory source of vertical velocity embedded in the wall (see Figure 7.20)

$$v(x, 0, t) = \cos(\omega_0 t) \delta(x) H(t). \quad (7.117)$$

We use a Fourier transform in space and time. Because we model the vibrating ribbon by a step function in time, the Fourier transform in time is equivalent to a Laplace transform:

$$\tilde{v}(\alpha, y, \omega) = \iint_{-\infty}^{\infty} v(x, y, t) \exp[-i(\alpha x - \omega t)] dx dt \quad (7.118)$$

where α denotes the (complex) streamwise wave number and ω stands for the (complex) frequency. The solution to the normal velocity is governed by the Orr-Sommerfeld equation, which is given as

$$\{(\mathcal{D}^2 - \alpha^2)(\mathcal{D}^2 - \mu^2) + i\alpha \text{Re}U''\} \tilde{v} = 0 \quad (7.119)$$

with

$$\mu^2 = \alpha^2 + i\text{Re}[\alpha U - \omega]. \quad (7.120)$$

To complete the governing equations we have to Fourier transform the boundary conditions. We obtain

$$\tilde{v} = \frac{i\omega}{\omega^2 - \omega_0^2}, \quad \frac{\partial \tilde{v}}{\partial y} = 0; \quad \text{at } y = 0 \quad (7.121)$$

$$\tilde{v} = \frac{\partial \tilde{v}}{\partial y} = 0 \quad \text{as } y \rightarrow \infty \quad (7.122)$$

where we have used (7.117).

Equations (7.119)-(7.122) form a fourth-order ordinary differential equation with nonhomogeneous boundary conditions. Formally, the solution is given as a superposition of the four fundamental solutions of the differential equation. We will first solve the set of equations in the transformed variables and then transform to physical space.

Solution in the transformed domain

We have already determined the solution in the transformed domain in the limit $y \rightarrow \infty$ (see Section 3.2.3) where we found four fundamental solutions of exponential form

$$\tilde{v}_{1,3} = \exp[\mp\mu y] \quad \tilde{v}_{2,4} = \lim_{\epsilon \rightarrow 0} \exp[\mp\zeta y] \quad (7.123)$$

and the general solution to the equation for $y \rightarrow \infty$ as

$$\tilde{v} = C_1 \tilde{v}_1 + C_2 \tilde{v}_2 + C_3 \tilde{v}_3 + C_4 \tilde{v}_4. \quad (7.124)$$

Because $y > 0$ the fundamental solutions \tilde{v}_3 and \tilde{v}_4 are unbounded as $y \rightarrow \infty$. Consequently, we have to choose $C_3 = C_4 = 0$. The fundamental solutions \tilde{v}_1 and \tilde{v}_2 , on the other hand, decay as $y \rightarrow \infty$. The coefficients C_1 and C_2 follow from the boundary conditions at the wall (7.121). We have

$$C_1 = \frac{\tilde{v}'_{20}}{\Delta_0} \frac{i\omega}{\omega^2 - \omega_0^2} \quad C_2 = -\frac{\tilde{v}'_{10}}{\Delta_0} \frac{i\omega}{\omega^2 - \omega_0^2} \quad (7.125)$$

which yields

$$\tilde{v} = \frac{i\omega}{\omega^2 - \omega_0^2} \frac{\Delta}{\Delta_0} \quad (7.126)$$

where $\Delta \equiv \Delta(y; \alpha, \omega) = \tilde{v}_1 \tilde{v}'_{20} - \tilde{v}'_{10} \tilde{v}_2$, $\Delta_0 \equiv \Delta(0; \alpha, \omega)$, and $\tilde{v}_{j0} \equiv \tilde{v}_j(0; \alpha, \omega)$.

For the inversion to the physical domain we have to examine the singularities of \tilde{v} . In Section 3.2.3 we have already investigated the branch cut structure of \tilde{v} in the complex ω plane. In addition to these continuous singularities we have discrete singularities at $\omega = \pm\omega_0$ and at the zeros of $\Delta_0(\alpha, \omega)$, the dispersion relation of linear stability theory.

The solution $v(y; x, t)$ in the physical domain is obtained by evaluating the inversion integral

$$v(y; x, t) = \frac{1}{4\pi^2} \int_L \int_F \tilde{v} \exp[i(\alpha x - \omega t)] d\alpha d\omega \quad (7.127)$$

where F and L are appropriately chosen contours in the α and ω planes, respectively. In analogy with Briggs' method (Briggs, 1964) used for the investigation of absolute instability, we perform the integration in the α plane first, where F coincides with the real α -axis. The associated singularities in the ω plane are of discrete and continuous type. The discrete singularities in the ω plane are the solutions to the dispersion relation $\Delta_0(\alpha, \omega) = 0$ for real wave number α . The continuous singularities are defined by the straight-line branch cut for $\alpha = \alpha_r$ derived in Section 3.2.3.

The temporal inversion path has to be chosen above both discrete and continuous singularities. The branch cut singularity is always below the real ω -axis (recall (3.84)). However, the discrete singularities, i.e., the temporal eigenvalues, can move into the upper-half ω plane as the streamwise wave number is varied. The integration contour L has to lie in the upper-half ω plane above the maximum imaginary part of the least stable eigenvalue. We therefore choose L as the line defined by $\omega = i\sigma$ with $\sigma > \max_{\alpha_r} \omega_i(\alpha_r)$. The evaluation of the spatial and temporal part of the inversion integral now follows standard complex analysis procedures.

Spatial inversion

After choosing the integration path L we now proceed to evaluate the spatial part of the integral (7.127) and transform the solution of the vibrating ribbon problem from the α - to the x -domain. For positions downstream of the vibrating ribbon ($x > 0$ in our case) the integration contour has to be closed in the upper-half α plane. The presence of the two spatial branch cuts in the upper-half α plane (see Figure 7.21) requires the deflection of the semicircular contour around the two branch cuts. Similarly, for locations upstream of the vibrating ribbon ($x < 0$) the spatial integration contour is closed in the lower-half α plane with a corresponding deflection around the two branch cuts in the lower-half α plane. As the radius of the semicircular contour tends to infinity the spatial integral for $x > 0$ consists of three parts

$$\hat{v}(y; x, \omega) = \hat{v}_D + \hat{v}_{C_1} + \hat{v}_{C_2} \quad (7.128)$$

representing contributions from the discrete singularities

$$\hat{v}_D(y; x, \omega) = - \sum_j \frac{\omega}{\omega^2 - \omega_0^2} \left[\frac{\Delta}{\partial \Delta_0 / \partial \alpha} e^{i\alpha x} \right]_{\alpha=\alpha_j} \quad (7.129)$$

and contributions from the two continuous singularities (see Figure 7.21)

$$\hat{v}_{C_1}(y; x, \omega) = -\frac{1}{2\pi} \int_{I^+} \tilde{v} e^{i\alpha x} d\alpha - \frac{1}{2\pi} \int_{I^-} \tilde{v} e^{i\alpha x} d\alpha \quad (7.130)$$

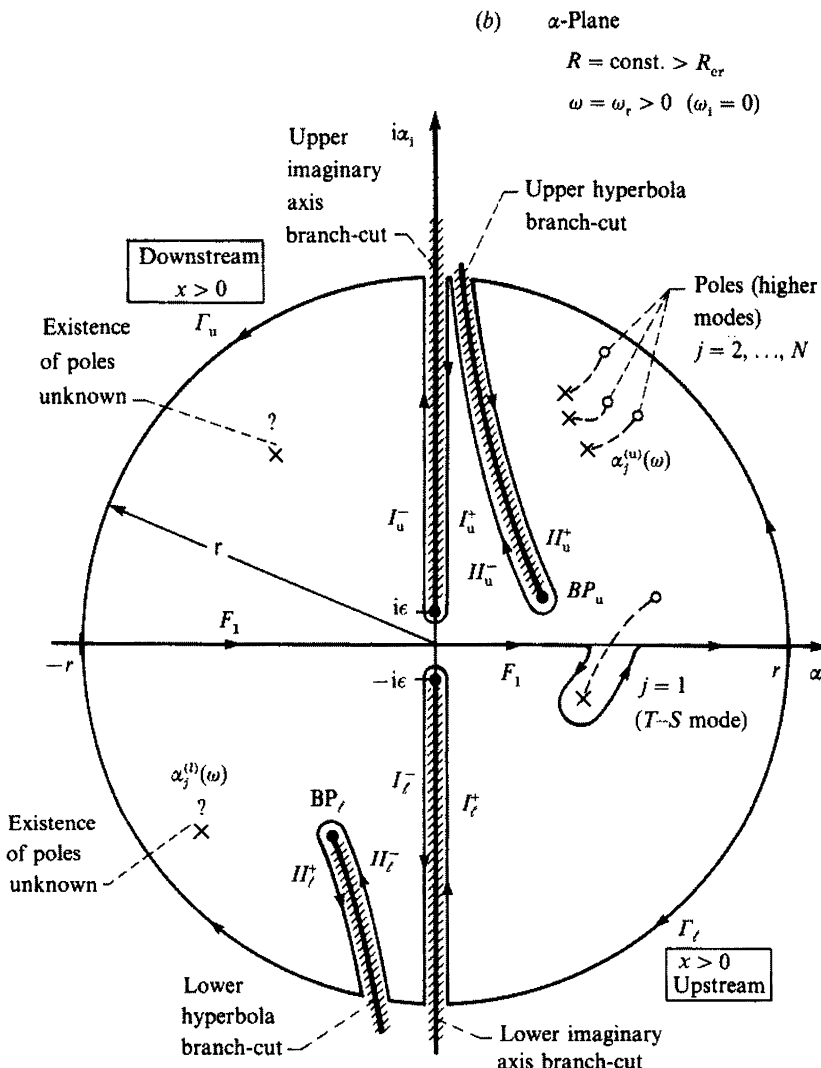


FIGURE 7.21. Closed integration contours in the α -plane. As ω varies along lines $\omega_r = \text{const.}$ the poles $\alpha_j(\omega)$ form the trajectories shown. The hyperbola branch cuts are shown for $\omega_i = 0$. From Ashpis & Reshotko (1990).

$$\hat{v}_{C_2}(y; x, \omega) = -\frac{1}{2\pi} \int_{\mathcal{I}^+} \tilde{v} e^{i\alpha x} d\alpha - \frac{1}{2\pi} \int_{\mathcal{I}^-} \tilde{v} e^{i\alpha x} d\alpha. \quad (7.131)$$

Similar expressions apply for the case $x < 0$.

Temporal inversion

The inversion of the spatial part of (7.127) is followed by the temporal inversion transforming the solution from the frequency domain to the time domain. Along the contour L the integral decreases to zero as t tends to infinity. The contributions to the velocity v thus stem from the part of the contour that encircles the poles at $\pm\omega_0$, and the solution is given as the sum of the residues at $\omega = \pm\omega_0$. We notice that the velocity $\hat{v}(y; x, \omega)$ contains terms of the form

$$G = \frac{\omega}{\omega^2 - \omega_0^2} g(y; x, \omega). \quad (7.132)$$

The sum of the residues at $\omega = \pm\omega_0$ for this general expression is simply $\text{Real}\{g(y; x, \omega_0)\}$ using the fact that $g(y; x, \omega_0) = g^*(y; x, -\omega_0)$. Applying this result yields the vertical velocity field:

$$v(y; x, t) = v_D + v_{C_1} + v_{C_2} \quad (7.133)$$

with

$$v_D(y; x, t) \sim - \sum_j \text{Im} \left\{ \left[\frac{\Delta}{\partial \Delta_0 / \partial \alpha} e^{i(\alpha_j(\omega)x - \omega_0 t)} \right]_{\omega=\omega_0} \right\} \quad (7.134)$$

as the contribution from the discrete spectrum and

$$v_{C_1}(y; x, t) \sim -\frac{1}{2\pi} \text{Im} \left\{ \int_0^\infty A_1(y; \sigma, \omega_0) e^{-\sigma x - i\omega_0 t} d\sigma \right\} \quad (7.135)$$

$$v_{C_2}(y; x, t) \sim \frac{1}{2\pi} \text{Re} \left\{ \int_0^\infty A_2(y; \sigma, \omega_0) E(\sigma) d\sigma \right\} \quad (7.136)$$

from the continuous part of the spectrum. v_{C_1} is the contribution from the branch cut located on the imaginary α -axis; v_{C_2} is the contribution from the hyperbolic branch cut labeled \mathcal{I}_u in Figure 7.21. The preceding expressions denote the time-asymptotic limit. The complex functions A_1 , A_2 , and E are given in Ashpis & Reshotko (1990).

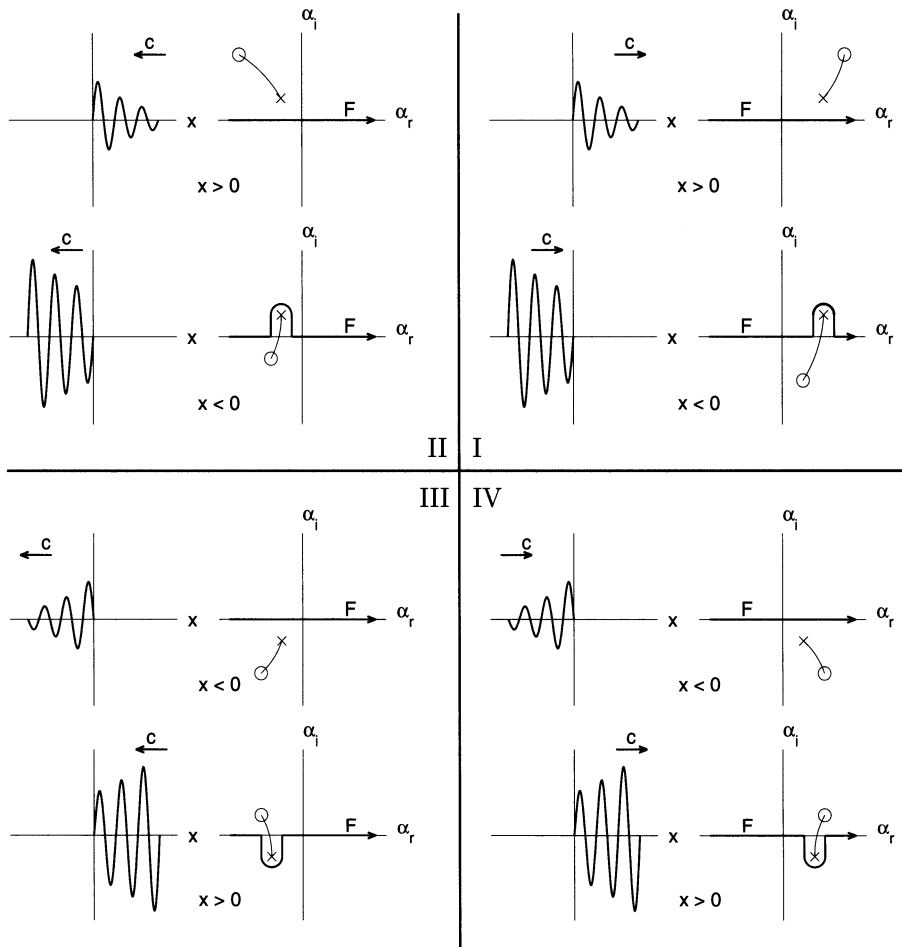


FIGURE 7.22. Effects of the location of the pole in the α -plane on its corresponding wave for $\omega_r > 0$; x: the α_j for $\omega_i = 0$; o: the α_j for $\omega = \omega_L$. Adapted from Ashpis & Reshotko (1990).

Discussion and interpretation of the results

The solution to the vibrating ribbon problem contains contributions from both the discrete and continuous spatial spectrum. The discrete part consists of solutions to the dispersion relation for a real frequency ω_0 and represents waves with wave number $\text{Real}\{\alpha_j(\omega_0)\}$ and corresponding phase velocity $\omega_0/\text{Real}\{\alpha_j(\omega_0)\}$. The spatial growth rate of these waves is given by $-\text{Im}\{\alpha_j(\omega_0)\}$. The amplitude K_j of the wave forced by the vibrating ribbon, i.e., the response of the j th eigenmode to the harmonic forcing, is taken from (7.134) as

$$K_j = \left[\frac{\Delta}{\partial \Delta_0 / \partial \alpha} \right]_{\alpha_j(\omega_0), \omega_0}. \quad (7.137)$$

The properties of the waves induced by the vibrating ribbon are governed by the location of the associated poles α_j in the complex α plane; see Figure 7.22. If a pole α_j lies above the spatial inversion contour F , the corresponding wave contributes to the downstream evolution of the response to the vibrating ribbon. Waves that correspond to poles in the right-half α plane have a positive phase velocity, while poles in the left-half α plane are associated with upstream traveling waves. Downstream of the ribbon waves exhibit spatial growth if $\text{Real}\{\alpha_j\}$ is negative; in the upstream region, a pole above the real α -axis is necessary for spatial growth. Figure 7.22 summarizes the different cases.

7.4 Nonparallel Effects

It is customary to use the parallel-flow approximation to describe the linear instability of boundary layer flows to small amplitude disturbances. In spite of the qualitative success of this assumption, parallel stability theory does not explain some important phenomena, and experiments have shown systematic differences with the theory. The effect of mean-flow nonparallelism on the stability of boundary layers is best illustrated by investigating the behavior of the growth rates for a given disturbance frequency rather than by investigating its effect on the critical Reynolds number.

The spatial formulation of the governing equations allows us to incorporate nonparallel effects in diverging flows such as boundary layers, jets and wakes into the stability analysis. There is a variety of ways to incorporate nonparallel effects mathematically, but a perturbation approach suggests itself for situations when the flow divergence is slow compared to the growth of disturbances in space.

7.4.1 Asymptotic Methods

Model problem

Before launching into the multiple-scale expansion for weakly nonparallel boundary flow, we will demonstrate the technique with the help of a simple model problem.

We will consider an inhomogeneous version of the Ginzburg-Landau equation, where we introduce a slowly varying function

$$\mu(X) \quad X = \epsilon x \quad \epsilon \ll 1 \quad (7.138)$$

to obtain the equation

$$\frac{\partial u}{\partial t} + U \frac{\partial u}{\partial x} = \mu(X)u + \gamma \frac{\partial^2 u}{\partial x^2}. \quad (7.139)$$

We seek solutions to this equation of the form

$$u = Q(X) \exp [i\Theta] = Q(X) \exp \left[\frac{i}{\epsilon} \int^X \alpha(s) \, ds - i\omega t \right] \quad (7.140)$$

which introduces a slowly varying amplitude and phase that will account for effects of the function $\mu(X)$. It then follows that

$$\frac{\partial u}{\partial t} = -i\omega Q \exp [i\Theta] \quad (7.141)$$

$$\frac{\partial u}{\partial x} = (i\alpha Q + \epsilon Q') \exp [i\Theta] \quad (7.142)$$

$$\frac{\partial^2 u}{\partial x^2} = (-\alpha^2 Q + i\epsilon\alpha' Q + 2i\epsilon\alpha Q' + \epsilon^2 Q'') \exp [i\Theta]. \quad (7.143)$$

We expand the slowly varying amplitude according to

$$Q(X) = Q_0(X) + \epsilon Q_1(X) + \epsilon^2 Q_2(X) + \mathcal{O}(\epsilon^3) \quad (7.144)$$

which is substituted into (7.139), and equal powers of ϵ are matched. To zeroth order we find the dispersion relation

$$D(\omega, \alpha) = \omega + U\alpha - i\mu(X) + i\gamma\alpha^2 = 0. \quad (7.145)$$

At the next order we find an amplitude equation for Q_0 ,

$$D(\omega, \alpha)Q_1 = -i(U - 2i\gamma\alpha)\frac{dQ_0}{dX} - \frac{i}{2}(2i\gamma)\frac{d\alpha}{dX}Q_0 = 0. \quad (7.146)$$

Using the dispersion relation formulated as $\omega = \omega(\alpha)$ we find the amplitude equation

$$\frac{\partial\omega}{\partial\alpha}\frac{dQ_0}{dX} + \frac{1}{2}\frac{\partial^2\omega}{\partial\alpha^2}\frac{d\alpha}{dX}Q_0 = 0. \quad (7.147)$$

This can be integrated to yield

$$Q_0(X) = A \exp \left[-\frac{1}{2} \int^X \left(\frac{\frac{\partial^2\omega}{\partial\alpha^2}\frac{d\alpha}{dX}}{\frac{\partial\omega}{\partial\alpha}} \right) dX \right] \quad (7.148)$$

which together with (7.140) gives the final solution of the model problem to this order. Evaluating the derivatives of the dispersion relation we find

$$u(x, t,) = A \exp \left[\int^X \frac{i\mu'(X)dX}{(2\alpha - iU)(U - 2i\gamma\alpha)} \right] \exp \left[\frac{i}{\epsilon} \int^X \alpha dX - \omega t \right]. \quad (7.149)$$

Multiple-scale analysis for boundary layer flow

Let us now find the nonparallel correction to the quasiparallel linear stability problem using multiple-scale analysis. The assumption behind this approach is that the mean boundary layer flow quantities vary slowly in the streamwise direction compared to the disturbance quantities. This introduces two length scales: the long scale, which is the length over which the mean flow varies, and the short scale, which is the length over which disturbance quantities vary. In the multiple-scale analysis, these two length scales are treated as independent variables and a solution is obtained by applying solvability conditions. This can be seen as a generalization of the method applied to the model problem in the previous section.

We will consider the evolution of a two-dimensional disturbance in a steady, incompressible flow over a flat plate described by the mean velocity

$$U = U(x, y) \quad V = V(x, y) \quad (7.150)$$

where we allow a slow variation in the streamwise direction x . We will nondimensionalize the equations of motion by the displacement thickness

of the boundary layer, the freestream velocity, and the kinematic viscosity, so that the Reynolds number is given as $\text{Re} = U_\infty \delta / \nu$. The linearized equation governing the evolution of infinitesimal disturbances reads

$$\frac{\partial}{\partial t} \nabla^2 v + U \frac{\partial}{\partial x} \nabla^2 v + \nabla^2 V \frac{\partial}{\partial y} u - V \frac{\partial}{\partial y} \nabla^2 v - \nabla^2 U \frac{\partial}{\partial x} v = \frac{1}{\text{Re}} \nabla^4 v \quad (7.151)$$

with boundary conditions

$$v = \frac{\partial v}{\partial y} = 0 \quad \text{at} \quad y = 0 \quad (7.152)$$

$$v \rightarrow 0 \quad \text{as} \quad y \rightarrow \infty. \quad (7.153)$$

We will employ a multiple-scale analysis using a small parameter ϵ characterizing the nonparallel nature of the mean velocity profile and represent the mean velocity in the form

$$U(x, y) = U_0(X, y) + \epsilon U_1(X, y) + \dots \quad (7.154)$$

$$V(x, y) = \epsilon V_1(X, y) + \dots \quad (7.155)$$

with X as the slow streamwise coordinate direction defined as

$$X = \epsilon x \quad \epsilon = \mathcal{O}(\text{Re}^{-1}) \ll 1. \quad (7.156)$$

To solve these equations using perturbation theory, we assume

$$v(x, y, t) = Q(X, y; \epsilon) \exp \left[\frac{i}{\epsilon} \int^X A(s; \epsilon) ds - iFt \right] \quad (7.157)$$

where Q and A stand for slowly varying parts of the normal velocity and of the streamwise wave number, respectively. We assume derivatives of Q and A with respect to the slow space scale to be of order one. The variation of the normal velocity v in the x -direction is not slow which is reflected in the ϵ^{-1} -term in the exponent. The frequency F in the preceding expression is related to ω by $F = \nu \omega / U_\infty^2$. The frequency F is taken as a real quantity in accordance with the spatial framework.

Next, we will expand the slowly varying amplitude Q and wave number A in a perturbation series according to

$$Q(X, y; \epsilon) = Q_0(X, y) + \epsilon Q_1(X, y) + \mathcal{O}(\epsilon^2) \quad (7.158)$$

$$A(X; \epsilon) = \alpha_0(X) + \epsilon \alpha_1(X) + \mathcal{O}(\epsilon^2). \quad (7.159)$$

Substituting into (7.151) and collecting terms of the same order in ϵ we obtain the following system of equations:

At order $\mathcal{O}(\epsilon^0)$ we have

$$\mathcal{L}(Q_0) = 0 \quad (7.160)$$

with homogeneous boundary conditions

$$\begin{aligned} Q_0 &= \frac{\partial Q_0}{\partial y} = 0 && \text{at } y = 0 \\ Q_0 &= \frac{\partial Q_0}{\partial y} = 0 && \text{at } y = \infty. \end{aligned} \quad (7.161)$$

The operator \mathcal{L} is the familiar Orr-Sommerfeld operator.

At the next order, $\mathcal{O}(\epsilon^1)$, we arrive at

$$\mathcal{L}(Q_1) = \mathcal{M}_1 \left(\frac{\partial Q_0}{\partial X} \right) + \mathcal{M}_2 \left(Q_0, \frac{\partial \alpha_0}{\partial X} \right) + i\alpha_1 \mathcal{M}_1(Q_0). \quad (7.162)$$

For the explicit forms of the operators $\mathcal{M}_{1,2}$ the reader is referred to El-Hady (1991). Solutions to this inhomogeneous system exist if the inhomogeneity is orthogonal to the solution of the problem adjoint to \mathcal{L} .

We obtain the solvability condition

$$\int_0^\infty \left[\mathcal{M}_1 \left(\frac{\partial Q_0}{\partial X} \right) + \mathcal{M}_2 \left(Q_0, \frac{\partial \alpha_1}{\partial X} \right) + i\alpha_1 \mathcal{M}_1(Q_0) \right] Q^+ dy = 0 \quad (7.163)$$

with

$$\mathcal{L}^+(Q^+) = 0 \quad (7.164)$$

as the adjoint Orr-Sommerfeld equation.

From this expression the first correction to the streamwise wave number can be extracted as

$$\alpha_1 = i \frac{\int_0^\infty \left[\mathcal{M}_1 \left(\frac{\partial Q_0}{\partial X} \right) + \mathcal{M}_2 \left(Q_0, \frac{d\alpha_0}{dX} \right) \right] Q^+ dy}{\int_0^\infty [\mathcal{M}_1(Q_0)] Q^+ dy}. \quad (7.165)$$

In order to evaluate this expression, we need to compute the quantities $\frac{\partial Q_0}{\partial X}$ and $\frac{d\alpha_0}{dX}$. We take the X -derivative of the Orr-Sommerfeld equation

$$\frac{\partial}{\partial X} \mathcal{L}(Q_0) = 0 \quad (7.166)$$

to obtain

$$\mathcal{L}\left(\frac{\partial Q_0}{\partial X}\right) = i \frac{d\alpha_0}{dX} \mathcal{M}_1(Q_0) + \mathcal{N}(Q_0) \quad (7.167)$$

subject to homogeneous boundary conditions

$$\begin{aligned} Q_0 &= \frac{\partial Q_0}{\partial y} = 0 && \text{at } y = 0 \\ Q_0 &= \frac{\partial Q_0}{\partial y} = 0 && \text{at } y = \infty. \end{aligned} \quad (7.168)$$

Again, a solution of this inhomogeneous problem exists only if the inhomogeneity is orthogonal to the adjoint problem, which allows us to solve for the slow variation of the streamwise wave number in the downstream direction. We get

$$\frac{d\alpha_0}{dX} = i \frac{\int_0^\infty \mathcal{N}(Q_0) Q^+ dy}{\int_0^\infty \mathcal{M}_1(Q_0) Q^+ dy}. \quad (7.169)$$

Substituting back we can solve equation (7.167) for the quantity $\frac{\partial Q_0}{\partial X}$ and evaluate the expression (7.165) for $\alpha_1(X)$.

For the leading-order approximation we then get

$$v(x, y, t) = C Q_0(X, y) \exp \left[i \int^x (\alpha_0 + \epsilon \alpha_1) ds - i F t \right]. \quad (7.170)$$

The definition of the spatial growth rate including nonparallel effects is not straightforward because it involves both growth due to the wave number α and growth due to changes in the amplitude Q . An additional difficulty arises from the y -dependence of the the growth component stemming from the amplitude function. In many cases experimental efforts provide guidance in the choice of the disturbance measure and the definition of the spatial growth rate. As a consequence, a unique neutral curve cannot be defined because it depends on the disturbance measure. We will come back to this difficulty when we discuss the parabolized stability equations (PSE) as a method for incorporating nonparallel effects into the spatial evolution of disturbances (see Section 7.4.3).

In general the growth rate of a disturbance is given as

$$\sigma_i = -\alpha_i - \epsilon \text{Im}(\alpha_1) + \epsilon \text{Real} \left\{ \frac{1}{M} \frac{\partial M}{\partial X} \right\}. \quad (7.171)$$

We recognize the first term as the spatial growth rate for parallel flow, while the second and third terms are the nonparallel corrections. The third term describes the distortion of the eigenfunction due to the nonparallel nature of the mean flow. Common choices for the disturbance measure M are the maximum of the streamwise velocity or the energy of the disturbance:

$$M(X) = \max_y u(X, y) \quad M(X) = \frac{1}{2} \int_0^\infty (u^2 + v^2 + w^2) dy. \quad (7.172)$$

The wave number correction due to the nonparallel nature of the mean flow is given by

$$\sigma_r = \alpha_r - \epsilon \text{Real}(\alpha_1) + \epsilon \text{Im} \left\{ \frac{1}{M} \frac{\partial M}{\partial X} \right\}. \quad (7.173)$$

It is worth mentioning that this analysis assumes the nonparallel correction to the growth rate to be $\mathcal{O}(1/\text{Re})$. While this assumption is valid for the basic boundary layer profile, it is not true for certain types of disturbances, for example, those near the lower branch, or with wavelengths relatively long compared to the plate length.

The effect of mean-flow nonparallelism on the boundary layer stability is demonstrated by presenting spatial disturbance growth rates at two streamwise locations, namely, $\text{Re} = 500$ and $\text{Re} = 1000$. The results (see Figure 7.23) are taken from El-Hady (1991) who considers the nonparallel effects for subsonic and supersonic boundary layers. Three curves are displayed. The first curve, labeled (a), is the parallel spatial growth rate, i.e., the first term in equation (7.171). The curve labeled (b) displays the spatial growth rate which accounts for nonparallel effects but discards the distortion effects of the eigenfunction. Finally, the curve labeled (c) is the entire nonparallel spatial growth rate, including contributions from the distortion of the eigenfunction. It is important to realize that curves (a) and (b) are independent of the normal coordinate y , as well as the normal disturbance velocity, but curve (c) is a function of both. The location to evaluate the effect of eigenfunction distortion has been chosen so as to maximize the mass-flow disturbance amplitude. This choice was guided by experimental measurements.

Triple-deck equations

The inclusion of nonparallel effects as demonstrated earlier has drawn some critique because the viscosity as the cause of nonparallelism is included

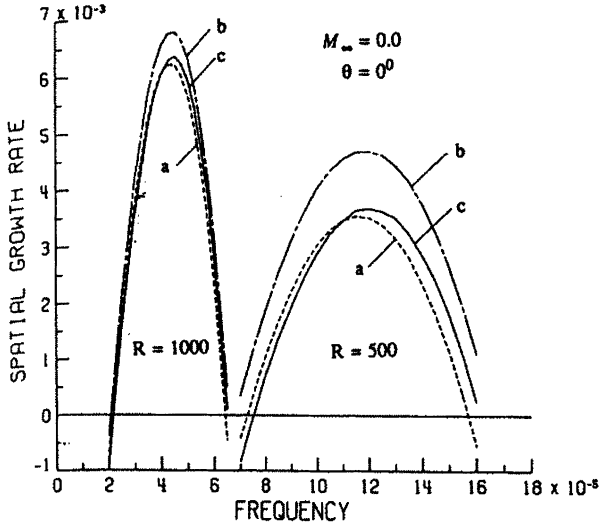


FIGURE 7.23. Variation of the spatial growth rates with frequency for two-dimensional waves. Curve (a): $-\alpha_i$; curve (b): $-\alpha_i - \epsilon \text{Im}(\alpha_1)$; curve (c): equation (7.171) based on $M(X) = \max_y u(X, y)$. From El-Hady (1991).

in the disturbance equations but neglected in the equations for the mean flow. A rational approach (van Dyke, 1975) has been suggested using triple-deck theory. Dividing the boundary layer into three regions in the normal direction allows the solution of simplified governing equations in each region (often called decks), and the subsequent asymptotic matching results in a uniform solution across the boundary layer. Nonparallel effects can easily be incorporated into the asymptotic equation hierarchy.

The scalings introduced in Section 3.2.4 give us a triple-deck structure where the lower deck (the viscous layer) has a thickness of order $\text{Re}_x^{-5/8}$, the middle deck (where the flow is inviscid but rotational) scales like $\text{Re}_x^{-1/2}$, and the upper deck where disturbances decay exponentially over a distance $1/\alpha$ scales like $\text{Re}_x^{-3/8}$ (see Figure 7.24).

We will not embark on a full asymptotic evaluation of nonparallel effects for boundary layer flow, but we will present the starting point of triple-deck asymptotics. We refer the interested reader to Smith (1979b), Smith (1979a), and Healey (1995). We will follow Healey (1998). It will be convenient to introduce $\epsilon = \text{Re}_x^{-1/8}$ as our small parameter. We then have a disturbance structure as follows:

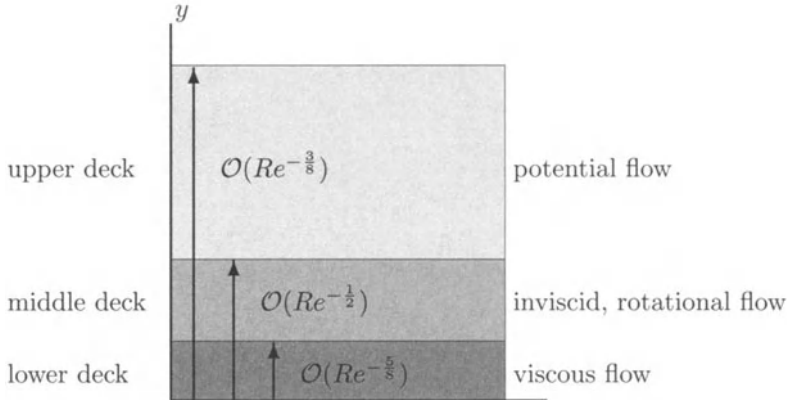


FIGURE 7.24. Sketch of triple deck structure and scaling for the lower branch of the neutral stability curve for Blasius boundary layer flow.

$$y = \epsilon^3 y_u \quad \text{for the upper deck} \quad (7.174)$$

$$y = \epsilon^4 y_m \quad \text{for the middle deck} \quad (7.175)$$

$$y = \epsilon^5 y_l \quad \text{for the lower deck} \quad (7.176)$$

$$\alpha = \epsilon^{-3} \bar{\alpha} \quad \text{with} \quad \bar{\alpha} = \bar{\alpha}(x) \quad (7.177)$$

$$\omega = \epsilon^{-2} \bar{\omega}. \quad (7.178)$$

We consider disturbances of the form

$$\hat{u} = u(x, y) \exp \left[i \left(\frac{1}{\epsilon^3} \int \bar{\alpha}(x) dx - \frac{i \bar{\omega}}{\epsilon^2} t \right) \right] = u(x, y) E \quad (7.179)$$

so that

$$\hat{u}_x = u_x E + \frac{i \bar{\alpha}}{\epsilon^3} u E \quad (7.180)$$

$$\hat{u}_t = -\frac{i \bar{\omega}}{\epsilon^2} u E. \quad (7.181)$$

The linearized disturbance equations for nonparallel flow can now be written:

$$u_x + \frac{i \bar{\alpha}}{\epsilon^3} u + v_y = 0 \quad (7.182)$$

$$\begin{aligned} \frac{i\bar{\omega}}{\epsilon^2}u + U_x u + U \left(u_x + \frac{i\bar{\alpha}}{\epsilon^3}u \right) + U_y v + V u_y = -p_x - \frac{i\bar{\alpha}}{\epsilon^3}p \\ + \epsilon^8 \left(u_{xx} + \frac{2i\bar{\alpha}}{\epsilon^3}u_x + \frac{i\bar{\alpha}_x}{\epsilon^3}u - \frac{\bar{\alpha}^2}{\epsilon^6}u + u_{yy} \right) \end{aligned} \quad (7.183)$$

$$\begin{aligned} \frac{i\bar{\omega}}{\epsilon^2}v + V_x u + U \left(v_x + \frac{i\bar{\alpha}}{\epsilon^3}v \right) + V_y v + V v_y = -p_y \\ + \epsilon^8 \left(v_{xx} + \frac{2i\bar{\alpha}}{\epsilon^3}v_x + \frac{i\bar{\alpha}_x}{\epsilon^3}v - \frac{\bar{\alpha}^2}{\epsilon^6}v + v_{yy} \right). \end{aligned} \quad (7.184)$$

Within each deck, these equations take simplified forms that can be solved analytically.

7.4.2 Parabolic Equations for Steady Disturbances

Continuing with our discussion of nonparallel effects we next present evolution equations of parabolic type in the streamwise coordinate direction for steady disturbances. These equations arise from linearizing parabolic equations about a nonparallel mean flow. The first example deals with algebraically growing/decaying modes for a (nonparallel) Blasius boundary layer; the second example investigates the local stability behavior of steady disturbances in flow along a concave wall.

Algebraic boundary layer modes

For the evolution of steady disturbances in space (using the boundary layer approximation) we have the equations

$$u_x + v_y + w_z = 0 \quad (7.185)$$

$$uu_x + vu_y + wu_z = \frac{1}{2}(U^2 + W^2)_x + u_{yy} \quad (7.186)$$

$$uw_x + vw_y + ww_z = \frac{1}{2}(U^2 + W^2)_z + w_{yy} \quad (7.187)$$

where we assume the following scaling: The streamwise and spanwise coordinates have been nondimensionalized by a characteristic reference length L and the associated velocities have been scaled with the freestream velocity U_∞ . The normal coordinate, on the other hand, is scaled with the local boundary layer thickness $\delta = \sqrt{L\nu/U_\infty}$ and the corresponding normal velocity has been nondimensionalized by $U_\infty/\text{Re}_\delta$ with Re_δ as the Reynolds number based on the boundary layer thickness and the freestream velocity, i.e., $\text{Re}_\delta = U_\infty\delta/\nu$. This scaling assumes spanwise velocities of the order of the streamwise disturbance velocity, $w \sim u$.

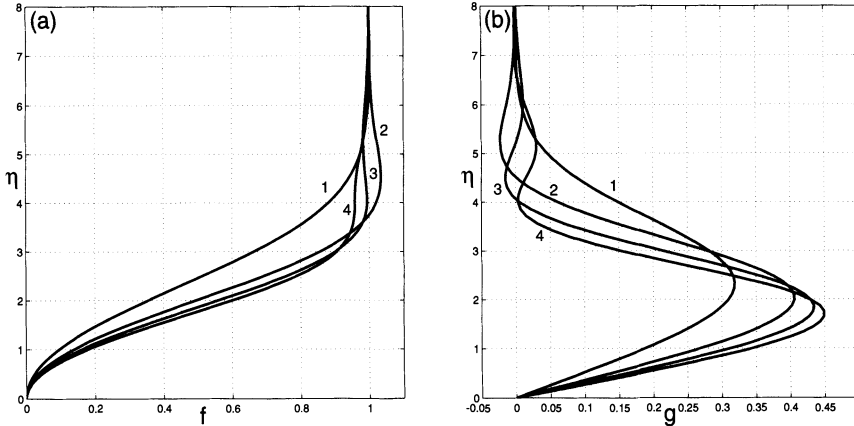


FIGURE 7.25. Similarity solutions for steady disturbances in Blasius boundary layer flow due to Libby & Fox (1964): (a) $f(\eta)$ and (b) $g(\eta)$.

Linearization about the Blasius solution $(U(x, y), V(x, y), 0)$ results in

$$\hat{u}_x + i\hat{v}_y + i\beta\hat{w} = 0 \quad (7.188)$$

$$U\hat{u}_x + V\hat{u}_y + U_x\hat{u} + U_y\hat{v} = \hat{u}_{yy} \quad (7.189)$$

$$U\hat{w}_x + V\hat{w}_y = \hat{w}_{yy} \quad (7.190)$$

where a Fourier transformation in the spanwise z -direction introduced the spanwise wave number β .

Using the similarity variable $\eta = y/\sqrt{x}$ and introducing

$$u = i\beta x^{-s+1} g(\eta) \quad (7.191)$$

$$v = i\beta x^{-s+1/2} \left[\frac{\eta}{2} g(\eta) + (s - \frac{3}{2}) f(\eta) \right] \quad (7.192)$$

$$w = x^{-s} h(\eta) \quad (7.193)$$

we can transform equations (7.188)-(7.190) into an eigenvalue problem for the exponent s , which is of the form

$$\mathcal{L}\mathbf{q} + s\mathcal{M}\mathbf{q} = 0 \quad (7.194)$$

with

$$\mathbf{q} = \begin{pmatrix} f \\ g \\ h \end{pmatrix} \quad \mathcal{M} = \begin{pmatrix} -F_{\eta\eta} & F_\eta & 0 \\ \frac{d}{d\eta} & -1 & 0 \\ 0 & 0 & F_\eta \end{pmatrix} \quad (7.195)$$

k	s_k	Type
1	0.786	Luchini
2	1.693	Luchini
3	2.000	Libby & Fox
4	2.627	Luchini
5	2.886	Libby & Fox
6	3.572	Luchini
7	3.814	Libby & Fox
8	4.525	Luchini
9	4.756	Libby & Fox
10	5.482	Luchini

TABLE 7.3. Eigenvalues s_k of equation (7.194).

$$\mathcal{L} = \begin{pmatrix} \frac{3}{2}F_{\eta\eta} & \frac{d^2}{d\eta^2} + \frac{1}{2}F\frac{d}{d\eta} - F_\eta & 0 \\ -\frac{3}{2}\frac{d}{d\eta} & \frac{3}{2}g & 1 \\ 0 & 0 & \frac{d^2}{d\eta^2} + \frac{1}{2}F\frac{d}{d\eta} \end{pmatrix} \quad (7.196)$$

and F is the solution to the Blasius equation

$$F_{\eta\eta\eta} + \frac{1}{2}FF_{\eta\eta} = 0. \quad (7.197)$$

The boundary conditions are

$$f(0) = g(0) = g(\infty) = h(0) = h(\infty) = 0. \quad (7.198)$$

From the structure of the eigenvalue problem (7.194) we conclude that there exist two fundamental types of eigenvalues. The first type investigated by Libby & Fox (1964) and Stewartson (1957) is characterized by eigenfunctions with $h = 0$; these modes are obtained by solving the upper 2×2 part of the stability operators. The largest eigenvalue of Libby-Fox type is 2, resulting in decaying perturbation velocities as x increases; in particular the streamwise disturbance velocity associated with the least stable Libby-Fox mode decays inversely proportional to the downstream coordinate, i.e., $u \sim x^{-1}$. The wall-normal profiles (as a function of the similarity variable η) for the first four Libby-Fox modes are displayed in Figure 7.25.

A second type of mode stemming from the system (7.194) is characterized by a nonzero spanwise velocity component. These modes were first

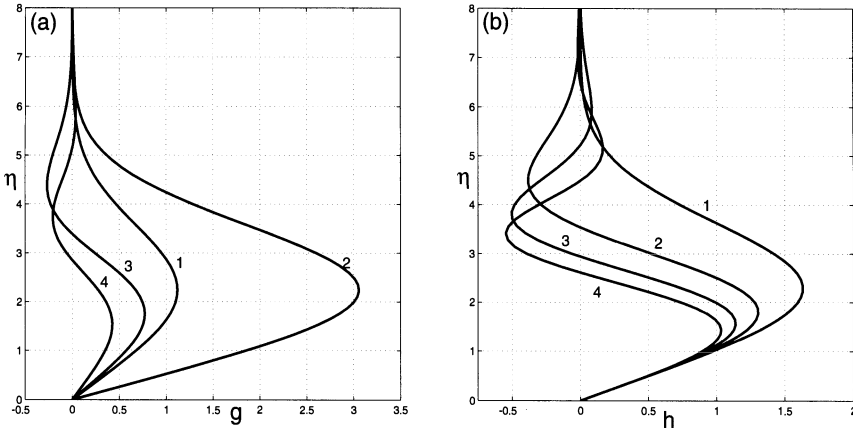


FIGURE 7.26. Similarity solutions for steady disturbances in Blasius boundary layer flow due to Luchini (1996). (a) $g(\eta)$ and (b) $h(\eta)$.

described by Luchini (1996). Eigenvalues of this type (together with Libby-Fox modes) are listed in Table 7.3. We observe that the two least stable modes are of Luchini-type, after which the type of mode alternates. In addition we note that the least stable eigenvalue is less than one resulting in a streamwise disturbance velocity that grows algebraically in the streamwise direction according to $u \sim x^{0.214}$. The corresponding eigenfunctions describing the wall-normal profile for the streamwise and spanwise disturbance velocities in the similarity variable η are depicted in Figure 7.26.

Two conclusions drawn from the preceding analysis are noteworthy. First, the perturbation stems from Prandtl's standard boundary layer approximation, where the explicit appearance of the Reynolds number has been eliminated by an appropriate scaling. Thus, instabilities based on these perturbations occur at *any* Reynolds number for which the boundary layer exists. This is in contrast to previously investigated flow instabilities that only develop within a certain Reynolds number regime.

Second, the mentioned algebraic instability, though weak in nature, has more practical consequences when considered as part of a superposition of decaying modes. A perturbation with initially zero longitudinal velocity can be thought of as a superposition of Libby-Fox and Luchini modes. As one progresses downstream the various modes grow (in the case of the least stable Luchini mode) or decay according to the eigenvalue s_k . Consequently, the subtle balance of eigenmodes to achieve zero u -velocity will cease to exist, and we will observe a strongly growing streamwise velocity component. In other words, it is not important how rapid the least stable mode grows, it is more important that it is not highly damped. Such an instability mechanism is not based on the slow growth of the least stable mode as $x^{0.214}$ but rather in the fast decay of all other modes. This mech-

anism is reminiscent of the transient growth mechanism resulting from a superposition of Orr-Sommerfeld and Squire modes.

Görtler vortices

Next we consider the linear stability of low-frequency disturbances in a high-Reynolds-number flow of a viscous, incompressible fluid over a concave surface of constant radius of curvature R ($R = +\infty$ corresponds to a flat plate). Again, we will use the boundary layer approximation of the steady, incompressible Navier-Stokes equations. These equations were first derived by Floryan & Saric (1982), and subsequently by Hall (1983) and others; for a detailed derivation see Bottaro & Luchini (1999).

The streamwise coordinate is nondimensionalized with the characteristic length scale L ; the streamwise velocity is nondimensionalized with the freestream velocity U_∞ . The wall-normal velocity is scaled with $\text{Re}^{-1}U_\infty$ and the corresponding coordinate is scaled with $\delta = (\nu L/U_\infty)^{1/2}$, where $\text{Re} = (U_\infty L/\nu)^{1/2}$. For large Reynolds numbers and small curvature parameter $\kappa = L/R$ we recover the Blasius boundary layer solution for the basic flow $U(x, y), V(x, y)$ to leading order.

We assume identical scalings for the disturbance velocities with the spanwise velocity and coordinate being scaled like the wall-normal components. This is in contrast to the last subsection where the spanwise coordinate was scaled the same way as the streamwise coordinate. If we linearize the Navier-Stokes equations around the Blasius solution, under the assumptions that the Reynolds number approaches infinity and the curvature parameter approaches zero, such that the Görtler number $G^2 = \text{Re}L/R$ is finite, we obtain

$$\frac{\partial u}{\partial x} + \frac{\partial v}{\partial y} + \frac{\partial w}{\partial z} = 0 \quad (7.199)$$

$$U \frac{\partial u}{\partial x} + \frac{\partial U}{\partial x} u + V \frac{\partial u}{\partial y} + \frac{\partial U}{\partial y} v = \left(\frac{\partial^2}{\partial y^2} + \frac{\partial^2}{\partial z^2} \right) u \quad (7.200)$$

$$U \frac{\partial v}{\partial x} + \frac{\partial V}{\partial x} u + V \frac{\partial v}{\partial y} + \frac{\partial V}{\partial y} v + 2G^2 U u + \frac{\partial p}{\partial y} = \left(\frac{\partial^2}{\partial y^2} + \frac{\partial^2}{\partial z^2} \right) v \quad (7.201)$$

$$U \frac{\partial w}{\partial x} + V \frac{\partial w}{\partial y} + \frac{\partial p}{\partial z} = \left(\frac{\partial^2}{\partial y^2} + \frac{\partial^2}{\partial z^2} \right) w. \quad (7.202)$$

Equations (7.199)-(7.202) are referred to as the Görtler equations which will be solved subject to the boundary conditions

$$u = v = w = 0 \quad \text{at} \quad y = 0 \quad (7.203)$$

$$u = w = p = 0 \quad \text{as} \quad y \rightarrow \infty. \quad (7.204)$$

Because the basic flow is independent of z we assume periodic disturbances in the spanwise direction. Using

$$(u, v, w, p) = (\hat{u} \cos \beta z, \hat{v} \cos \beta z, \hat{w} \sin \beta z, \hat{p} \cos \beta z) \quad (7.205)$$

the governing equations become

$$\hat{u}_x + \hat{v}_y + \beta \hat{w} = 0 \quad (7.206)$$

$$(U \hat{u})_x + V \hat{u}_y + U_y \hat{v} = \hat{u}_{yy} - \beta^2 \hat{u} \quad (7.207)$$

$$(V \hat{u} + U \hat{v})_x + (2V \hat{v})_y + \beta V \hat{w} + 2G^2 U \hat{u} + p_y = \hat{v}_{yy} - \beta^2 \hat{v} \quad (7.208)$$

$$(U \hat{w})_x + (V \hat{w})_y - \beta \hat{p} = \hat{w}_{yy} - \beta^2 \hat{w}. \quad (7.209)$$

These equations have a singularity at $x = 0$ (e.g., $V = \mathcal{O}(x^{-1/2})$) and we expect difficulties when starting the integration near the leading edge. Using the conservative form of the equations improves the situation because appropriate jump conditions can be derived across the leading edge similar to jump conditions for shock waves (see Luchini & Bottaro, 1998). Hence the starting point of the integration x_0 can be chosen as $x_0 = 0$. Because the equations are parabolic in x the solution can be obtained by a marching procedure that evolves the initial condition

$$\hat{u}(x_0, y) = u_0(y), \quad \hat{v}(x_0, y) = v_0(y) \quad (7.210)$$

to a downstream position $x > x_0$. The initial value of $\hat{w}(x_0, y)$ can be obtained from the equations of motion; only two initial conditions are independent.

To describe instabilities we need to introduce a disturbance measure. We typically monitor the perturbation energy defined as

$$E(x) = \int \hat{u}^2(x, y) dy \quad (7.211)$$

which leads to a local dimensionless growth rate defined as

$$\tilde{\sigma}(x) = \frac{x}{2E} \frac{dE}{dx}. \quad (7.212)$$

Although a definition of a local growth rate is possible, Hall (1983) points out that a unique neutral stability curve cannot be defined for all values of β , because it depends on the chosen initial condition and the choice of disturbance measure.

However, marching solutions clearly show exponential behavior sufficiently far downstream, with a local growth rate that is independent of the

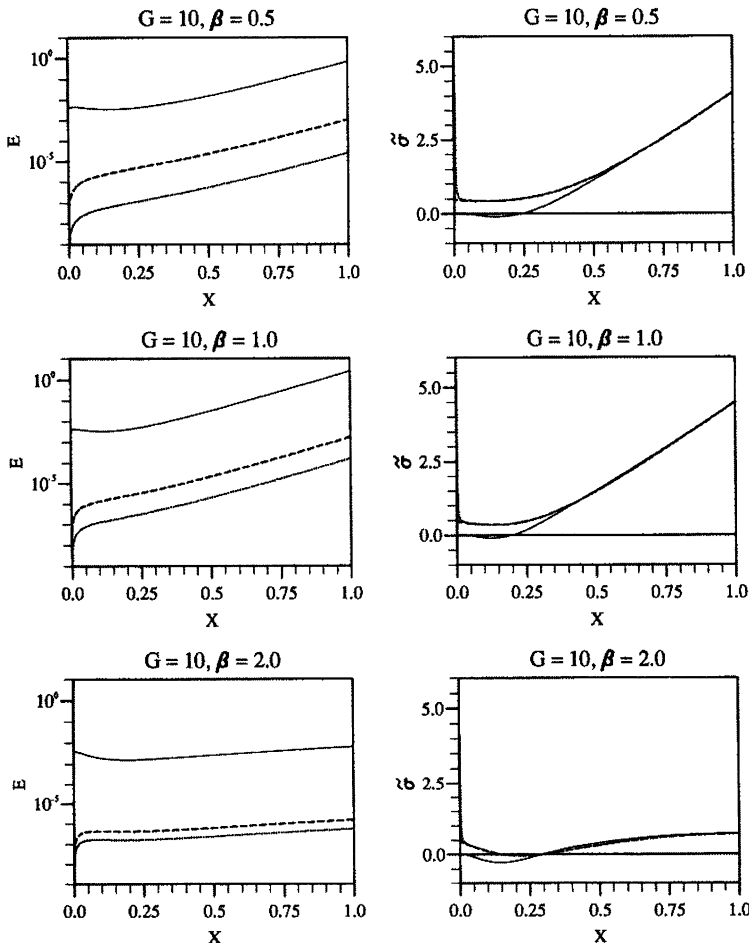


FIGURE 7.27. Left: energy curves as function of X for $G = 10$ and, from top to bottom, $\beta = 0.5, 1, 2$, obtained by a marching procedure. Right: corresponding amplification factors, from three different initial conditions. From Bottaro & Luchini (1999).

initial condition. Figure 7.27 demonstrates this fact by evolving three different initial conditions in the downstream direction using the parabolic equations given earlier. The energy quickly approaches an exponential growth regime, and the local growth rates for the different initial conditions, although distinct near the initial location, coincide farther downstream. Figure 7.27 illustrates this behavior over a range of spanwise wave numbers. The strong modal behavior far downstream has been taken as convincing evidence that a local stability analysis applies for sufficiently large x . Numerical experiments show that for $G > 7$ Görtler flow is amenable to local stability theory.

Bottaro & Luchini (1999) studied the Görtler equations using multiple-scale analysis. They assumed that the disturbances are in the form

$$\hat{u} = \epsilon e^{\varphi(x)/\epsilon} (\hat{u}_0(x, y) + \epsilon \hat{u}_1(x, y) + \dots) \quad (7.213)$$

$$\hat{v} = e^{\varphi(x)/\epsilon} (\hat{v}_0(x, y) + \epsilon \hat{v}_1(x, y) + \dots). \quad (7.214)$$

The scaling parameter ϵ emerges from a balance of the dominant terms in the streamwise and normal components of the Görtler equations and evaluates to the inverse of the Görtler number, i.e., $\epsilon = G^{-1}$. However, the resulting expansion is not uniformly valid in y because the small parameter ϵ appears in front of the highest normal derivative terms. To render the solution uniformly valid to leading order, Bottaro & Luchini (1999) added terms formally of higher order, which become dominant in parts of the normal coordinate direction. This is not a unique procedure, and the simplest form of a uniformly valid leading-order approximation are the original equations proposed by Görtler (1940).

The same difficulty arises in the derivation of the leading-order stability equations for the development of Tollmien-Schlichting waves in growing boundary layers. Rather than matching solutions of the Rayleigh equation to inner solutions for the wall and critical layers, some investigators have proposed a uniformly valid (in y) expansion instead. This expansion is essentially the same used by El-Hady and presented in Section 7.4.1.

The equations to leading order in the scaling parameter ϵ can be written in the form

$$-\sigma U \hat{u}_0 - \frac{\partial U}{\partial y} \hat{v}_0 + \epsilon \left(\frac{\partial^2 \hat{u}_0}{\partial y^2} - \beta^2 \hat{u}_0 \right) = 0 \quad (7.215)$$

$$-\sigma U \frac{\partial^2 \hat{v}_0}{\partial y^2} + \left(\beta^2 U + \frac{\partial^2 U}{\partial y^2} \right) \sigma \hat{v}_0 + 2\beta^2 U \hat{u}_0 + \epsilon \frac{\partial^4 \hat{v}_0}{\partial y^4} = 0 \quad (7.216)$$

where

$$\sigma(x) = \frac{d\varphi}{dx}. \quad (7.217)$$

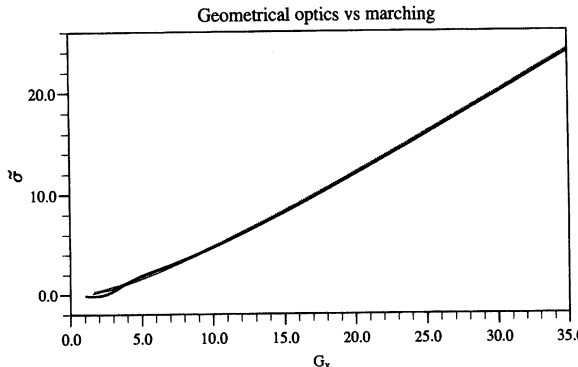


FIGURE 7.28. Strictly local results (solid line) and quasi-parallel correction (dotted line) compared to marching results. $\Omega = 210$. From Bottaro & Luchini (1999).

This establishes a system of homogeneous differential equations with σ as the eigenvalue. The coefficients – and the solutions – will depend on x parametrically. The next order correction to the equations are readily derived by continuing to higher order in the outlined perturbation approach. If the next order correction to the growth rate is needed, no higher-order equations need to be solved; it suffices to use the solvability condition to obtain that correction.

We will now define a locally scaled amplification factor of the instability according to

$$\tilde{\sigma}(x) = \frac{x\sigma(x)}{\epsilon}. \quad (7.218)$$

We furthermore scale the streamwise distance and spanwise wave number according to

$$G_x = Gx^{3/4} \quad \Lambda = G \left(\frac{2\pi}{\beta} \right)^{3/2}. \quad (7.219)$$

The scaling of the spanwise wave number leads to a nondimensional parameter that remains constant in the streamwise direction. This parameter is frequently used in experiments and numerical simulations. Figure 7.28 shows a comparison of growth rates obtained from the full parabolic equations (using a marching procedure) and growth rates obtained from the eigenvalue problem (7.215), (7.216). A spanwise scale of $\Lambda = 210$ has been chosen, which corresponds to the most linearly unstable wavelength for the Görtler problem. The close agreement of the curves (especially farther downstream) demonstrates the validity of local stability theory. For smaller

spanwise scales, small discrepancies between marching solutions and local stability analysis appear, which can be remedied by including nonparallel and higher-order terms in the multiple-scale analysis. For further details, the reader is referred to Bottaro & Luchini (1999).

With the establishment of the validity of local stability analysis, we can explore the behavior of the instability in the (G_x, Λ) plane. To this end, the eigenvalue problems derived from the asymptotic expansion can be solved for $\tilde{\sigma}$. The result, including some of the higher-order corrections calculated by Bottaro & Luchini (1999), is shown in Figure 7.29, where contours of constant (locally scaled) growth rates are displayed. The $\tilde{\sigma} = 0$ contour defines the boundary separating linearly stable from linearly unstable flow. The figure also contains an asymptotic approximation to the neutral stability curve valid for large values of β given by Hall (1983). This approximation has been obtained by a WKB expansion in the normal direction and is valid for large spanwise wave numbers β . It is given analytically as

$$G^2 = 2.95\beta^4 [1 + 0.96\beta^{-1} + \mathcal{O}(\beta^{-2})]. \quad (7.220)$$

Good agreement between the numerical and asymptotic results is observed. This part of parameter space is, however, of little interest because of the very low amplification factors at every location G_x for $\Lambda < 100$. A large body of experimental investigations (Bippes, 1978; Swearingen & Blackwelder, 1987; Pexieder, 1996) reports Görtler vortices with wavelengths Λ ranging from 200 to 600, unless even larger wavelengths are explicitly triggered by perturbations inherent to the installation (Aihara *et al.*, 1985).

7.4.3 Parabolized Stability Equations (PSE)

A set of equations known as the parabolized stability equations, or PSE, will be introduced in this section. The fundamental assumption of this theory is that the disturbances consist of a fast oscillatory part and an amplitude that varies slowly in the streamwise direction. A similar approximation is used in WKB and multiple-scale expansions of slowly varying boundary layer flows. The decomposition into fast and slow variations aims at a set of equations that is parabolic in the streamwise coordinate direction and is thus amenable to a numerical marching procedure. Starting with the Navier-Stokes equations which are not parabolic in space, appropriate approximations are called for to ensure the removal of all elliptic components. Once these approximations are carried out, the parabolized stability equations (PSE) can be solved at a fraction of the computational costs of direct numerical simulations, but with comparable accuracy. Special care has to be taken to ensure that PSE calculations stay within the region of validity of the underlying approximations.

The idea of solving parabolic evolution equations for boundary layer disturbances was first introduced by Floryan & Saric (1982) for steady Görtler

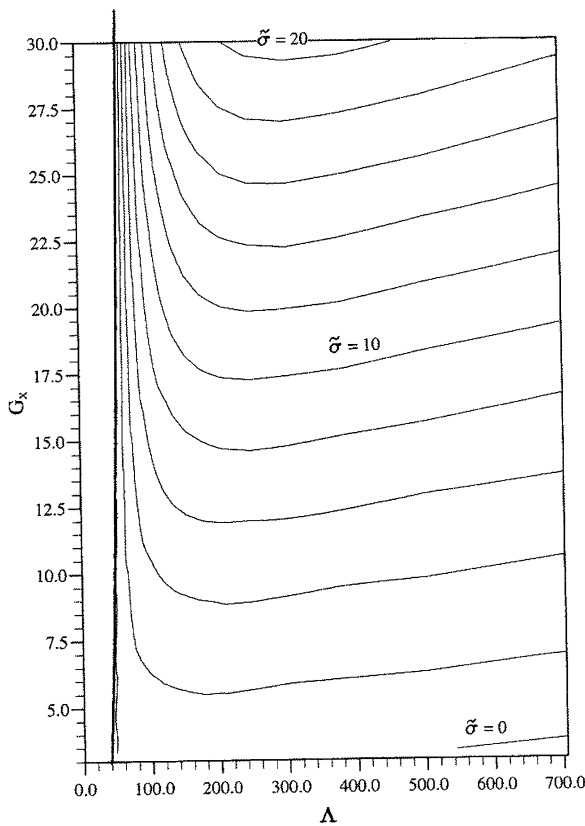


FIGURE 7.29. Curves of constant locally scaled growth factor in the Λ - G_x -plane and leading order asymptotic neutral curve (7.220) (thick line). From Bottaro & Luchini (1999).

vortices. Itoh (1986) derived a parabolic equation for small-amplitude Tollmien-Schlichting waves. Herbert and Bertolotti (Herbert & Bertolotti, 1987; Herbert, 1991; Bertolotti, 1991; Bertolotti *et al.*, 1992) developed this method further and derived the nonlinear parabolized stability equations (PSE). Simen (1992) – based on earlier work by Simen & Dallmann (1992) – independently developed a similar theory. His contribution was to consistently and in a general way model convectively amplified waves with divergent and/or curved wave-rays and wave-fronts propagating in nonuniform flow.

Approximation of the two-dimensional Navier-Stokes equations

We will start by applying the PSE approximation to the two-dimensional linear Navier-Stokes equations and analyze the characteristic structure of the approximation. We wish to obtain a spatial evolution equation with a parabolic evolution operator that takes into account streamwise varying flow quantities. We decompose the disturbance into an amplitude function and an exponential part according to

$$u(x, y, t) = \tilde{u}(x, y) \exp\left(i \int_{x_0}^x \alpha(\xi) d\xi - i\omega t\right) \quad (7.221)$$

with α as the complex streamwise wave number and similar expressions for the other flow variables. The two-dimensional Navier-Stokes equations linearized about a mean velocity profile $(U(x, y), V(x, y))$ for solutions of the form (7.221) then read

$$\tilde{u}_x + i\alpha\tilde{u} + \tilde{v}_y = 0 \quad (7.222)$$

$$\begin{aligned} -i\omega\tilde{u} + U\tilde{u}_x + i\alpha U\tilde{u} + U_x\tilde{u} + V\tilde{u}_y + U_y\tilde{v} &= -\tilde{p}_x - i\alpha\tilde{p} \\ + \frac{1}{\text{Re}} \left(\tilde{u}_{xx} + 2i\alpha\tilde{u}_x + i\frac{d\alpha}{dx}\tilde{u} - \alpha^2\tilde{u} + \tilde{u}_{yy} \right) \end{aligned} \quad (7.223)$$

$$\begin{aligned} -i\omega\tilde{v} + U\tilde{v}_x + i\alpha U\tilde{v} + V_x\tilde{u} + V\tilde{v}_y + V_y\tilde{v} &= -\tilde{p}_y \\ + \frac{1}{\text{Re}} \left(\tilde{v}_{xx} + 2i\alpha\tilde{v}_x + i\frac{d\alpha}{dx}\tilde{v} - \alpha^2\tilde{v} + \tilde{v}_{yy} \right) \end{aligned} \quad (7.224)$$

with boundary conditions

$$\tilde{u} = \tilde{v} = 0 \quad \text{at } y = y_{\min}, y_{\max}. \quad (7.225)$$

We will assume a mean flow that only varies slowly in the streamwise direction. This implies that the amplitude functions \tilde{u} , \tilde{v} , and \tilde{p} , and the wave

number, α , are also slowly varying functions of the streamwise coordinate x . We take

$$\frac{\partial}{\partial x}, \quad V \sim \mathcal{O}\left(\frac{1}{\text{Re}}\right) \quad (7.226)$$

while the size of other flow quantities is assumed to be order one. Neglecting all terms of order $\mathcal{O}(\text{Re}^{-2})$ and higher, we arrive at the following system of equations written in matrix form:

$$\frac{d}{dx} \begin{pmatrix} \tilde{u} \\ \tilde{v} \\ \tilde{p} \end{pmatrix} = \begin{pmatrix} -i\alpha & -\mathcal{D} & 0 \\ 0 & -\frac{c_1}{U} - \frac{V_y}{U} & -\frac{\mathcal{D}}{U} \\ -c_1 + i\alpha U - U_x & U\mathcal{D} - U_y & -i\alpha \end{pmatrix} \begin{pmatrix} \tilde{u} \\ \tilde{v} \\ \tilde{p} \end{pmatrix} \quad (7.227)$$

with

$$c_1 = i\alpha U - i\omega + V\mathcal{D} - \frac{1}{\text{Re}} (\mathcal{D}^2 - \alpha^2). \quad (7.228)$$

\mathcal{D} denotes the derivative with respect to the normal direction y . No second-order streamwise derivatives remain in the equations.

The form of the solution (7.221) assumes an x -dependent amplitude function and an x -dependent streamwise wave number α , thus causing an ambiguity. To remove this ambiguity we need to impose an auxiliary condition on the amplitude function. We choose

$$\int_{y_{\min}}^{y_{\max}} (\tilde{u}^* \tilde{u}_x + \tilde{v}^* \tilde{v}_x + \tilde{p}^* \tilde{p}_x) dy = 0. \quad (7.229)$$

This relation ensures that most of the x -variation of the disturbance will be accounted for by the exponential function. The streamwise variation of the amplitude functions remains small, in accordance with our original assumption.

Periodic y -dependence

It is instructive to analyze the eigenvalues of the PSE operator given in (7.227). To this end, we assume periodicity in the y -direction which significantly simplifies the PSE evolution operator and makes it amenable to a simple modal analysis. We get

$$\mathcal{L} = \begin{pmatrix} -i\alpha & -i\gamma & 0 \\ 0 & -\frac{c_4}{U} - \frac{V_y}{U} & -i\frac{\gamma}{U} \\ -c_4 + i\alpha U - U_x & i\gamma U - U_y & -i\alpha \end{pmatrix} \quad (7.230)$$

where γ is the vertical wave number and

$$c_4 = i\alpha U - i\omega + i\gamma V + \frac{\alpha^2}{\text{Re}} + \frac{\gamma^2}{\text{Re}}. \quad (7.231)$$

Again, we will consider the constant-coefficient case, i.e., $U_x = U_y = V_x = V_y = 0$. We obtain the eigenvalues and eigenvectors

$$\begin{aligned} \kappa_{1,2} &= -i\alpha \pm \gamma \\ \kappa_3 &= -i\alpha + \frac{i\omega}{U} - \frac{i\gamma V}{U} - \frac{\gamma^2}{U\text{Re}} - \frac{\alpha^2}{U\text{Re}} \end{aligned} \quad (7.232)$$

and

$$\Omega_{1,2} = \begin{pmatrix} 1 \\ \pm i \\ \pm i\alpha U - c_4 - U \end{pmatrix} \quad \Omega_3 = \begin{pmatrix} 1 \\ -\frac{\alpha U + ic_4}{U\gamma} \\ 0 \end{pmatrix}. \quad (7.233)$$

These eigenvalues and eigenvectors should be compared with those of the complete two-dimensional Navier-Stokes equations for constant mean flow and periodic y -dependence given in (7.21)-(7.24). We see that the first three eigenvalues, $\kappa_{1,2}$, and κ_3 , for the special case $\alpha = 0$, are identical to the first three eigenvalues given in (7.21)-(7.24). The group velocity corresponding to the third eigenvalue, κ_3 , is, in the limit of large $U\text{Re}$, given by

$$c_{g3} \approx U. \quad (7.234)$$

This is, to leading order, the group velocity of the third eigenvalue of the two-dimensional Navier-Stokes equations, which implies that the parabolization by the PSE approach eliminated one of the upstream propagating eigenmodes, namely, the fourth eigenvalue of equation (7.20) with group velocity $-U$. The eigenvalue associated with the upstream propagating pressure disturbances has been preserved. As will be shown later, the eigenmodes corresponding to the eigenvalues κ_1 and κ_2 cause numerical instabilities.

General formulation for three-dimensional flows

The same approximation (7.221) as shown earlier for the two-dimensional Navier-Stokes equations, can be applied to more complicated flows. We restrict ourselves to quasi three-dimensional flows (basic flows that are independent of the spanwise z -coordinate). Let us denote the general vector of disturbance quantities by $\mathbf{q} = (\hat{\mathbf{u}}, \hat{\mathbf{v}}, \hat{\mathbf{w}}, \hat{\mathbf{p}})^T$ and follow the assumptions of the previous section.

The first assumption involves the decomposition of the dependent variables into an amplitude function and an oscillating part, i.e.,

$$\mathbf{q} = \tilde{\mathbf{q}}(x, y)e^{i\Theta} \quad (7.235)$$

with

$$\Theta = \int_{x_0}^x \alpha(x') dx' + \beta z - \omega t. \quad (7.236)$$

Analogous to spatial local theory, the streamwise wave number α is complex. Both the amplitude function, $\tilde{\mathbf{q}}$, and the phase function, Θ , are allowed to vary in the streamwise direction.

The second assumption implies that a scale separation of $1/\text{Re}$ is introduced between the slow and fast x -variation similar to a multiple-scale analysis. Re is the local Reynolds number defined as $\sqrt{UL/\nu}$ with L as the characteristic length scale. It follows from this assumption that the x -dependence, the size of metric factors defining curvilinear coordinates, the basic and disturbance flow, and the normal basic flow velocity component V all scale with the small parameter $1/\text{Re}$. We can introduce the slow scale

$$X = x/\text{Re} \quad (7.237)$$

and the scalings

$$V(X, y) \sim \frac{1}{\text{Re}}, \quad \frac{\partial}{\partial x} \sim \frac{1}{\text{Re}} \quad \alpha = \alpha(X), \quad \tilde{\mathbf{q}} = \tilde{\mathbf{q}}(X, y). \quad (7.238)$$

Upon substitution into the governing equations, retaining terms up to $\mathcal{O}(\text{Re}^{-1})$, we obtain the general form of the linear parabolized stability equations. They describe the kinematics, nonuniform propagation, and amplification of wave-type disturbances with divergent or curved wave rays in a nonuniform basic flow. We obtain the following *nearly* parabolic equations for the amplitude functions

$$A\tilde{\mathbf{q}} + B\frac{\partial\tilde{\mathbf{q}}}{\partial y} + C\frac{\partial^2\tilde{\mathbf{q}}}{\partial y^2} + D\frac{\partial\tilde{\mathbf{q}}}{\partial x} = 0. \quad (7.239)$$

A, B, C , and D are functions of α, β, ω , mean flow, and, in general, metric quantities. For incompressible flow with small curvature terms in the streamwise direction the matrices A, B, C, D are given as

$$A = \begin{pmatrix} \Delta + \frac{1}{h_1} \frac{\partial U}{\partial x} & \frac{\partial U}{\partial y} + m_{12}U & 0 & \frac{i\alpha}{h_1} \\ -2m_{12}U & \Delta + \frac{\partial V}{\partial y} & 0 & 0 \\ 0 & 0 & \Delta & i\beta \\ \frac{i\alpha}{h_1} & m_{12} & i\beta & 0 \end{pmatrix} \quad (7.240)$$

$$B = \begin{pmatrix} V & 0 & 0 & 0 \\ 0 & V & 0 & 1 \\ 0 & 0 & V & 0 \\ 0 & 1 & 0 & 0 \end{pmatrix} \quad (7.241)$$

$$C = \begin{pmatrix} -\frac{1}{Re} & 0 & 0 & 0 \\ 0 & -\frac{1}{Re} & 0 & 0 \\ 0 & 0 & -\frac{1}{Re} & 0 \\ 0 & 0 & 0 & 0 \end{pmatrix} \quad (7.242)$$

$$D = \begin{pmatrix} \frac{U}{h_1} & 0 & 0 & \frac{1}{h_1} \\ 0 & \frac{U}{h_1} & 0 & 0 \\ 0 & 0 & \frac{U}{h_1} & 0 \\ \frac{1}{h_1} & 0 & 0 & 0 \end{pmatrix} \quad (7.243)$$

with

$$\Delta = -i\omega + \frac{i\alpha U}{h_1} + \frac{\alpha^2/h_1^2 + \beta^2}{Re} \quad (7.244)$$

where $h_1 = (R - y)/R$ is the scale factor taking into account effects from the curved geometry, and $m_{12} = -1/(R - y)$ is the metric term, R stands for the radius of curvature. For cases where R is much larger than the boundary layer thickness, the curvature parameters become $h_1 = 1$ and $m_{12} = -1/R = -\kappa$.

If the above parabolized stability equations are rescaled using boundary layer scalings we obtain the Görtler equations (with the exception of one term which is formally of higher order).

For compressible flow with arbitrary curvature the entries of the above matrices can be found in Hanifi *et al.* (1994).

Again, the ambiguity in the x -dependence of the amplitude function and the streamwise wave number is removed with the help of an auxiliary

condition which takes on the form

$$\int_0^\infty \tilde{\mathbf{q}}^H \frac{\partial}{\partial x} \tilde{\mathbf{q}} \ dy = 0. \quad (7.245)$$

This equation enforces the variation of the amplitude functions to remain small enough to justify the Re^{-1} -scaling of $\partial \tilde{\mathbf{q}} / \partial x$.

Definitions of growth rate

As mentioned earlier in the treatment of nonparallel effects, the physical growth rate for diverging flows will be dependent on the normal coordinate y and the disturbance quantity of interest. The growth rate σ of an arbitrary disturbance quantity ξ is given as

$$\sigma = \frac{1}{h_1} \left(-\alpha_i + \text{Real} \left[\frac{1}{\xi} \frac{\partial \xi}{\partial x} \right] \right) \quad (7.246)$$

where the first term on the right-hand side represents the contribution from the exponential part of the disturbance; the second term is the correction due to the changes of the amplitude function. Usually, ξ is taken to be the streamwise or normal velocity component, either at some fixed normal position or at the location where it reaches its maximum value. Alternatively, the disturbance kinetic energy E , defined as

$$E = \frac{1}{2} \int_0^\infty (|\tilde{u}|^2 + |\tilde{v}|^2 + |\tilde{w}|^2) \ dy \quad (7.247)$$

can be used as a measure for disturbance growth. In this case, equation (7.246) reads

$$\sigma = \frac{1}{h_1} \left(-\alpha_i + \frac{\partial}{\partial x} (\ln \sqrt{E}) \right). \quad (7.248)$$

The corresponding streamwise wave number is given by

$$\bar{\alpha} = \frac{1}{h_1} \left(\alpha_r + \text{Im} \left[\frac{1}{\xi} \frac{\partial \xi}{\partial x} \right] \right) \quad (7.249)$$

and the direction of wave propagation is described by the wave angle

$$\psi = \tan^{-1} \left(\frac{\beta}{\bar{\alpha}} \right). \quad (7.250)$$

The wave angle ψ also describes wave-front distortion or wave-ray curvature as ψ can vary in both the x - and y -directions.

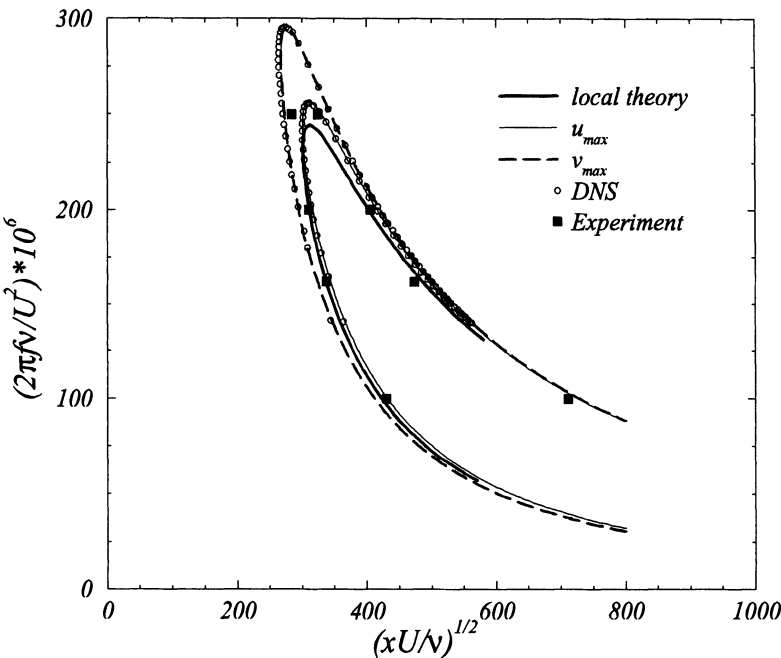


FIGURE 7.30. Neutral stability curves based on the maximum of \tilde{u} and \tilde{v} . The nonlocal results are compared to the DNS calculations (Berlin *et al.*, 1998) and experimental data (Klingmann *et al.*, 1993).

The nonparallel neutral curve for Blasius boundary layers

Berlin *et al.* (1998) calculated the neutral stability curves for two-dimensional disturbances in an incompressible flat plate boundary layer. The results are given in Figure 7.30. Two neutral curves for nonparallel boundary layer flow have been included. In one case, the maximum streamwise velocity has been used as a disturbance measure in the definition of the growth rate (7.246). In the other case, the growth rate based on the maximum normal velocity has been computed. The difference in the two neutral curves is quite appreciable but close agreement between the results from the direct numerical simulations and PSE calculations is observed. These results are also in good agreement with experimental data of Klingmann *et al.* (1993). For comparison the neutral curve based on local theory, i.e., the Orr-Sommerfeld equation (3.14) for parallel flow, is also displayed. The CPU time for the direct numerical simulations was approximately one hundred times higher than the CPU time for the PSE calculations.

Step-size restrictions

When discretizing the parabolized stability equations, caution is necessary when choosing a spatial step-size. We will demonstrate that a step-size restriction exists, requiring a *minimum* space step Δx for a numerically convergent scheme. For illustration, we revisit the two-dimensional Navier-Stokes equations with periodic y -dependence and constant mean flow (7.17). The evolution operator is a constant-coefficient matrix with eigenvalues and eigenvectors given in (7.21)-(7.24). After diagonalizing the system of equations, we are left with three decoupled evolution equations, which we will discretize in the streamwise direction using a backward Euler method. We get

$$\kappa_j^{n+1} = \kappa_j^n + \Delta x \lambda \kappa_j^{n+1} \quad (7.251)$$

$$\kappa_j^{n+1} = \frac{\kappa_j^n}{1 - \lambda \Delta x} \quad (7.252)$$

where κ_j is the j th eigenvector component and λ denotes the corresponding eigenvalue. To ensure time stability we have to require that

$$|1 - \lambda \Delta x| > 1. \quad (7.253)$$

Using the PSE approximation of the two-dimensional constant-coefficient Navier-Stokes equations, we identify the first two eigenvalues (7.232)

$$\lambda_{1,2} = \pm \gamma + \alpha_i - i\alpha_r \quad (7.254)$$

as the ones responsible for the space step restriction. The amplification factor of the backward Euler space discretization is

$$\frac{1}{[1 + (\alpha_i \pm \gamma) \Delta x] + i\alpha_r \Delta x} \quad (7.255)$$

which results in the space step restriction

$$\Delta x > \frac{1}{|\alpha_r|}. \quad (7.256)$$

For $|\alpha_r| \Delta x > 1$ the eigenvalues are outside the instability region for a backward Euler scheme for all values of γ (see Li & Malik, 1994).

Removal of the step-size restriction

The parabolized stability equations are nearly parabolic in space. The remaining ellipticity leads to step-size restrictions for numerical schemes. As

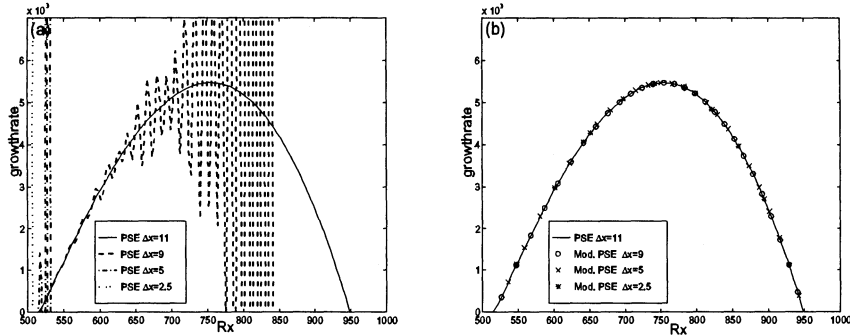


FIGURE 7.31. Growth rate versus streamwise position for boundary layer flow obtained from the PSE method: (a) instability due to step-size restriction; (b) stable computation. From Andersson *et al.* (1998).

the step size becomes too small, numerical instabilities arise in form of rapid oscillations in the solutions; see Figure 7.31. Andersson *et al.* (1998) suggested a modification of the parabolized stability equations, which makes the equations well-posed and eliminates the step-size problem. The modification is based on approximating the streamwise derivative by a first-order implicit scheme and including a term proportional to the leading truncation error of the numerical scheme.

As a direct consequence of the scaling of x -derivative terms the added truncation error is of order $\mathcal{O}(\text{Re}^{-2})$. Terms of this order were neglected in the original approximation; thus, adding of the truncation error does not violate the scaling of the governing equations at this order of approximation. We can introduce the new set of equations

$$(I - \Delta x \bar{\mathcal{L}} - s \bar{\mathcal{L}}) \tilde{\mathbf{q}}^{n+1} = (I - s \bar{\mathcal{L}}) \tilde{\mathbf{q}}^n \quad (7.257)$$

where s is a positive real number. Based on the earlier discussion, the difference between solutions of (7.239) and (7.257) is $\mathcal{O}(\text{Re}^{-2})$. Although s takes the place of Δx in the truncation error term, the added term is small, even if $s = \mathcal{O}(1)$. Andersson *et al.* (1998) found the critical step size for a stable numerical scheme as

$$\Delta x = \frac{1}{|\alpha_r|} - 2s. \quad (7.258)$$

This relation between the step size Δx , the streamwise wave number α_r , and the control parameter s defines a stability region in the $(\Delta x, s)$ plane as displayed in Figure 7.32. For a given α_r and Δx , a control parameter

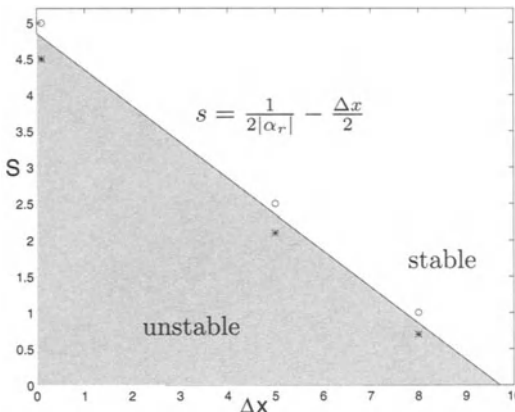


FIGURE 7.32. Numerical stability diagram in the $(\Delta x, s)$ -plane corresponding to stable or unstable marching conditions. From Andersson *et al.* (1998).

s in the stable area (Figure 7.32) will result in numerical stability despite the fact that Δx violates the original constraint (7.256). Numerical experiments have been performed for various parameter values s (as indicated by the symbols on both sides of the stability boundary in Figure 7.32), and the numerical stabilization scheme has proven itself highly effective in suppressing instabilities caused by too small a space step. This allows spatially accurate solutions to the parabolized stability equations without compromising the numerical stability of the scheme. The desired accuracy of the computations, rather than stability constraints, governs the choice of the spatial step size Δx .

7.4.4 Spatial Optimal Disturbances

Governing equations

Let us consider the linear stability of boundary layer flow at high Reynolds numbers. We are particularly interested in computing disturbances induced by moderate to high levels of freestream turbulence. Experiments suggest that these disturbances are elongated in the streamwise direction and vary only slowly in time which motivates the use of boundary layer approximations for the steady, incompressible Navier-Stokes equations.

If we assume spanwise periodicity, the governing equations correspond to the Görtler equations (7.206)-(7.209) derived earlier in this chapter with the Görtler number G set to zero. We have (omitting hats $\hat{\cdot}$)

$$u_x + v_y + \beta w = 0 \quad (7.259)$$

$$(Uu)_x + Vu_y + U_y v = u_{yy} - \beta^2 u \quad (7.260)$$

$$(Vu + Uv)_x + (2Vv)_y + \beta Vw + p_y = v_{yy} - \beta^2 v \quad (7.261)$$

$$(Uw)_x + (Vw)_y - \beta p = w_{yy} - \beta^2 w \quad (7.262)$$

with

$$u = v = w = 0 \quad \text{at} \quad y = 0 \quad (7.263)$$

$$u = w = p = 0 \quad \text{as} \quad y \rightarrow \infty. \quad (7.264)$$

The equations are parabolic in x for the (u, v, w) variables which allows us to numerically march an initial disturbance (v_0, w_0) in the downstream direction.

The optimization problem

Following Andersson *et al.* (1999) we look for optimally growing disturbances, i.e., the spatial counterpart to the temporal optimal disturbances discussed in Chapter 4. We will adopt an input-output point of view and consider the output

$$\mathbf{u}_{\text{out}} = \begin{pmatrix} u(x, y) \\ v(x, y) \\ w(x, y) \end{pmatrix} \quad (7.265)$$

at $x > x_0$ as a solution of the initial value problem (7.259)-(7.262) with the input data

$$\mathbf{u}_{\text{in}} = \begin{pmatrix} u_0(y) \\ v_0(y) \\ w_0(y) \end{pmatrix}. \quad (7.266)$$

Because the initial value problem is linear and homogeneous, we may write

$$\mathbf{u}_{\text{out}} = \mathcal{A}\mathbf{u}_{\text{in}} \quad (7.267)$$

where \mathcal{A} is a linear operator.

The downstream development of disturbances is studied by observing how the output \mathbf{u}_{out} changes with the input \mathbf{u}_{in} . First, we need to introduce a measure of disturbance size. A plausible measure is the disturbance energy,

$$E(\mathbf{u}) = \int_0^\infty (\text{Re } u^2 + v^2 + w^2) dy. \quad (7.268)$$

A Reynolds number scaling of the streamwise velocity disturbance is introduced to obtain similar weighting of all velocity components. Recall that the wall-normal and spanwise velocity disturbances are scaled with $\text{Re}^{-1/2} U_\infty$ in equation (7.259).

We will denote the norm and its associated inner product based on (7.268) as $E(\mathbf{u}) = \|\mathbf{u}\|^2 = (\mathbf{u}, \mathbf{u})$.

To calculate the optimal disturbance, we choose two streamwise locations $0 < x_0 < x_f$ and maximize the output disturbance energy at $x = x_f$ over all suitable input disturbances at $x = x_0$ with unit initial energy. The maximized quantity will be denoted the maximum spatial transient growth,

$$G(x_f) = \max_{\|\mathbf{u}_{\text{in}}\|=1} \|\mathbf{u}_{\text{out}}(x_f)\|^2. \quad (7.269)$$

Other norms than the one defined in (7.268) are possible; in fact, different norms could be used for the input and output data. The choice of norms is an important modeling issue and must be made based on physical considerations as it affects the outcome of the optimization.

Expression (7.269) may be further manipulated:

$$G(x_f) = \max_{\mathbf{u}_{\text{in}} \neq 0} \frac{\|\mathcal{A}\mathbf{u}_{\text{in}}\|^2}{\|\mathbf{u}_{\text{in}}\|^2} = \max_{\mathbf{u}_{\text{in}} \neq 0} \frac{(\mathcal{A}\mathbf{u}_{\text{in}}, \mathcal{A}\mathbf{u}_{\text{in}})}{(\mathbf{u}_{\text{in}}, \mathbf{u}_{\text{in}})}. \quad (7.270)$$

The maximum of $(\mathcal{A}\mathbf{u}_{\text{in}}, \mathcal{A}\mathbf{u}_{\text{in}})/(\mathbf{u}_{\text{in}}, \mathbf{u}_{\text{in}})$ is attained for some vector \mathbf{u}_{in} that satisfies the eigenvalue problem

$$\mathcal{A}^+ \mathcal{A} \mathbf{u}_{\text{in}} = \lambda_{\max} \mathbf{u}_{\text{in}} \quad (7.271)$$

where λ_{\max} denotes the largest eigenvalue. $G(x)$ is given by λ_{\max} . The operator \mathcal{A}^+ in equation (7.271) denotes the adjoint operator to \mathcal{A} with respect to the chosen inner product. We will calculate $G(x_f)$ by power iteration,

$$\mathbf{u}_{\text{in}}^{n+1} = \rho_n \mathcal{A}^+ \mathcal{A} \mathbf{u}_{\text{in}}^n, \quad (7.272)$$

where ρ_n is an arbitrary parameter used to scale the iterates to unit norm. This general method was used by Andersson *et al.* (1999) to find optimal spatial disturbances. In what follows we will adopt a slightly simplified version of the theory valid for large Reynolds numbers.

The large Reynolds number limit

To be consistent with the boundary layer approximation we will consider the large Reynolds number limit of the solution to the optimization problem, an approach first suggested by Luchini (2000). The input velocities close to the leading edge of the plate will be of the same order of magnitude. Due to the boundary layer scalings, where v_0 and w_0 are weighted with a factor $\sqrt{\text{Re}}$ compared to u_0 , the influence of u_0 on the solution of (7.259)-(7.262) can be neglected. In addition, for large Reynolds numbers, i.e., for large streamwise distances from the leading edge, the output component $u_1 = u(x_f)$ will be much larger than $v(x_f)$ and $w(x_f)$, again due to the boundary layer scalings. For the input and output variables this implies

$$\mathbf{u}_{in} = (0, v_0, w_0)^T \quad \mathbf{u}_{out} = (u_1, 0, 0)^T. \quad (7.273)$$

We now slightly redefine the norms, inner products, and the linear operator \mathcal{A} to incorporate the scalings for the large Reynolds number limit. We get

$$u_1 = \bar{\mathcal{A}}\mathbf{q} \quad \|u_1\|^2 = \int_0^\infty u_1^2 dy \quad \|\mathbf{q}\|^2 = \int_0^\infty (v_0^2 + w_0^2) dy \quad (7.274)$$

where $\mathbf{q} = (v_0(y), w_0(y))^T$. The optimization problem (7.270) now becomes

$$\frac{G(x_f)}{\text{Re}} = \max_{\|\mathbf{q}\|=1} \|u_1\|^2 = \max_{\mathbf{q}} \frac{(\bar{\mathcal{A}}\mathbf{q}, \bar{\mathcal{A}}\mathbf{q})}{(\mathbf{q}, \mathbf{q})} = \max_{\mathbf{q}} \frac{(\bar{\mathcal{A}}^+ \bar{\mathcal{A}}\mathbf{q}, \mathbf{q})}{(\mathbf{q}, \mathbf{q})} \quad (7.275)$$

where we have used the fact that the Reynolds number multiplies the streamwise velocity in the original definition of the norm (7.268). Consequently, the Reynolds number appears explicitly and the optimization becomes independent of the Reynolds number.

The adjoint equations

The action of the operator $\bar{\mathcal{A}}$ on a vector was defined earlier. To perform the power iterations, we need to determine the action of the adjoint operator $\bar{\mathcal{A}}^+$ on a vector. We will present an abridged derivation of the adjoint equation and refer the interested reader to Appendix C for details.

By definition of the adjoint operator $\bar{\mathcal{A}}^+$, we have

$$(\psi_1, \bar{\mathcal{A}}\mathbf{q}) = (\bar{\mathcal{A}}^+ \psi_1, \mathbf{q}) \quad (7.276)$$

for sufficiently differentiable functions $\psi_1(y)$ and $\mathbf{q}(y)$. The inner products can be written

$$(\psi_1, \bar{\mathcal{A}}\mathbf{q}) = \int_0^\infty \psi_1(y) u_1(y) dy \quad (\Phi, \mathbf{q}) = \int_0^\infty (\phi_2 v_0 + \phi_3 w_0) dy \quad (7.277)$$

where $\Phi = \bar{\mathcal{A}}^+ \psi_1$. We conclude that the action of the adjoint $\bar{\mathcal{A}}^+$ on ψ_1 is the vector $\Phi = (\phi_2, \phi_3)$ which is derived in Appendix C. Imposing the initial conditions

$$U(x_f, y) u^+(x_f, y) + V(x_f, y) v^+(x_f, y) + p^+(x_f, y) = \psi_1(y) \quad (7.278)$$

$$U(x_f, y) v^+(x_f, y) = 0 \quad (7.279)$$

$$U(x_f, y) w^+(x_f, y) = 0 \quad (7.280)$$

the adjoint equations become

$$v_y^+ + \beta w^+ = 0 \quad (7.281)$$

$$-p_x^+ - U u_x^+ - V v_x^+ - V u_y^+ = u_{yy}^+ + (V_y - \beta^2) u^+ \quad (7.282)$$

$$-U v_x^+ - 2V v_y^+ + U_y u^+ - p_y^+ = v_{yy}^+ - \beta^2 v^+, \quad (7.283)$$

$$-U w_x^+ - V w_y^+ + \beta V v^+ + \beta p^+ = w_{yy}^+ - \beta^2 w^+ \quad (7.284)$$

where $u^+(x, y)$, $v^+(x, y)$, $w^+(x, y)$, and $p^+(x, y)$ are functions defined on $x \geq x_0$, $y \geq 0$, with boundary conditions

$$\begin{aligned} u^+ &= v^+ = w^+ = 0 && \text{at } y = 0 \\ p^+ + 2V v^+ + v_y^+ &= u^+ = w^+ = 0 && \text{at } y = y_{\max}. \end{aligned} \quad (7.285)$$

The action of the adjoint operator is then given by

$$\phi_2(y) = U(x_0, y) v^+(x_0, y) \quad (7.286)$$

$$\phi_3(y) = U(x_0, y) w^+(x_0, y). \quad (7.287)$$

In equations (7.281)-(7.284) the x -derivative has opposite sign compared to equations (7.259)-(7.262). The parabolic nature of the equations demands that (7.281)-(7.284) be integrated backwards in space with initial conditions specified at $x = x_f$.

Optimization algorithm

The optimization problem (7.269) in the large Reynolds number limit becomes

$$G(x_f) = \max_{\|(0, v_0, w_0)\|=1} \operatorname{Re} \int_0^\infty u^2 dy. \quad (7.288)$$

It may be solved by power iteration outlined in (7.272). This amounts to the following three steps (see Figure 7.33):

- Given a current guess of the initial disturbance (v_0^n, w_0^n) , solve equations (7.259)-(7.262) using the boundary conditions (7.264) and initial conditions

$$u(x_0, y) = 0, \quad v(x_0, y) = v_0^n \quad \text{and} \quad w(x_0, y) = w_0^n.$$

- Given the solution $u(x_f, y)$ from step 1, solve (7.281)-(7.284) using the boundary conditions (7.285) and the initial conditions

$$\begin{aligned} U(x_f, y)u^+(x_f, y) + p^+(x_f, y) &= u(x_f, y) \\ v^+(x_f, y) &= 0 \\ w^+(x_f, y) &= 0 \end{aligned}$$

obtained from (7.278) where $\psi_1(y) = u(x_f, y)$.

- We then obtain the new initial disturbance (v_0^{n+1}, w_0^{n+1}) as

$$\begin{aligned} u_0^{n+1}(y) &= 0 \\ v_0^{n+1}(y) &= \rho_n U(x_0, y)v^+(x_0, y) \\ w_0^{n+1}(y) &= \rho_n U(x_0, y)w^+(x_0, y) \end{aligned}$$

from (7.286) where $v(y) = \phi_2(y)$ and $w(y) = \phi_3(y)$, and ρ_n is an arbitrary scaling parameter.

As pointed out earlier $G(x_f, \beta, \operatorname{Re})/\operatorname{Re} = \bar{G}(x_f, \beta)$ is independent of the Reynolds number. We can therefore conclude that the maximum spatial transient growth scales linearly with the Reynolds number in the large Reynolds number limit. The optimization has to be carried out for a single Reynolds number only, after which the results can be rescaled – within the validity of the boundary layer approximation – to obtain solutions for different Reynolds numbers.

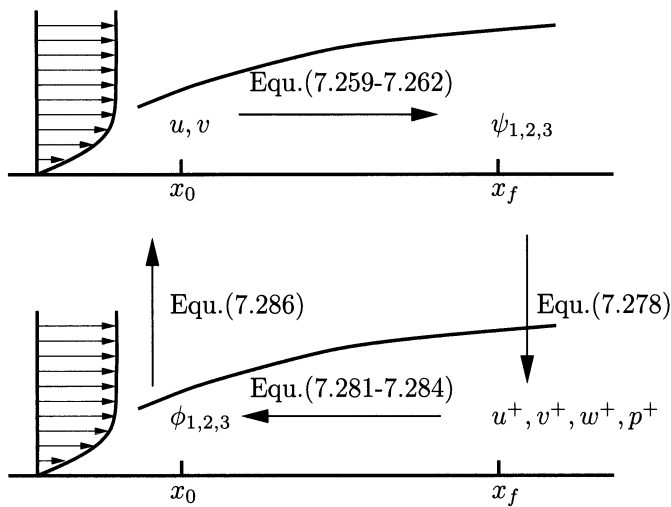


FIGURE 7.33. Sketch of optimization algorithm for computing spatial optimal disturbances.

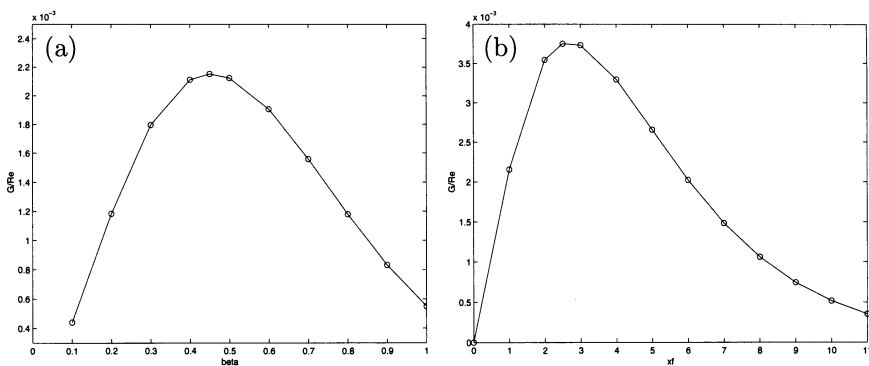


FIGURE 7.34. Maximum spatial transient growth for boundary layer flow (a) versus spanwise wave number, (b) versus streamwise distance.

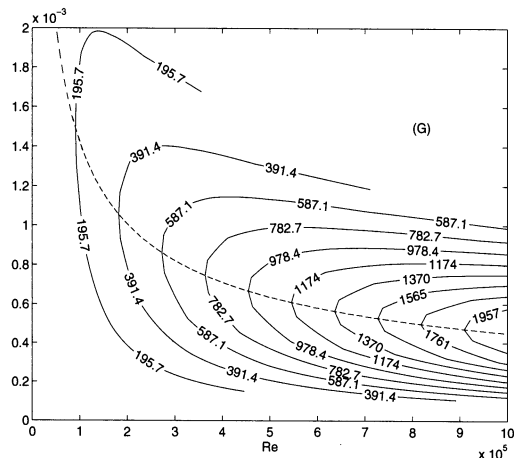


FIGURE 7.35. Contours of maximum spatial transient growth for boundary layer flow. From Andersson *et al.* (1999).

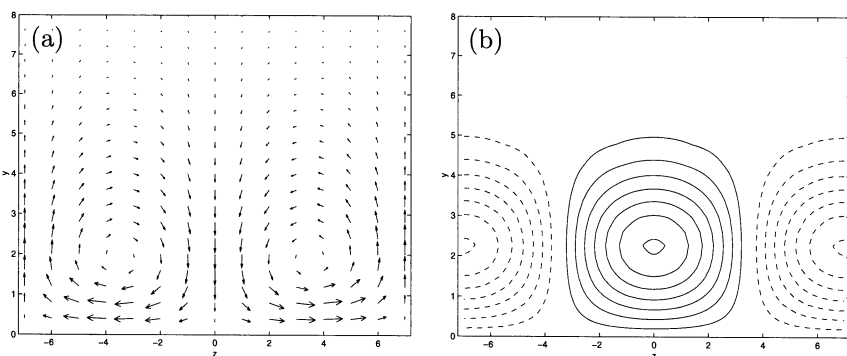


FIGURE 7.36. Spatial optimal disturbance for boundary layer flow: (a) velocity vectors in the y - z -plane at $x = x_0$; (b) contours of streamwise velocity at $x = x_f$. From Andersson *et al.* (1999).

Numerical examples

Using the optimization scheme outlined in the previous section we study the dependence of maximum transient spatial growth on the final position x_f and the spanwise wave number β . The initial position x_0 has been set to zero.

The dependence of transient growth on the spanwise wave number is shown in Figure 7.34(a) for a fixed final position of $x_f = 1$. We observe a pronounced peak at a spanwise wave number of $\beta \approx 0.45$. To probe the dependence on the downstream location x_f we choose a spanwise wave number of $\beta = 0.45$ and vary the variable x_f between 0 and 11. The result is shown in Figure 7.34(b). Again, there is a clear maximum of transient growth which occurs at $x_f \approx 2.5$ for this choice of parameters.

Using the results in Figure 7.34 we construct a contour plot containing isolines of constant maximum transient growth as a function of dimensionless spanwise wave number and Reynolds number. The spanwise wave number is nondimensionalized with the length scale ν/U_∞ and is denoted by $\bar{\beta}$. The results are given in Figure 7.35, together with a dashed curve, describing values of $\bar{\beta}$ for which the maximum growth (for a specific Reynolds number) is obtained. The explicit expression describing this dashed curve is

$$\bar{\beta} = \frac{0.45}{\sqrt{\text{Re}}} \quad (7.289)$$

which is derived using the scaling $\bar{\beta} = \beta^* \nu/U_\infty = \beta/\sqrt{\text{Re}}$ and the fact that the maximum was obtained for $\beta = 0.45$.

The initial condition that achieved the maximum spatial growth is seen in Figure 7.36(a) and the optimal downstream response is shown in Figure 7.36(b). Low-speed streaks in the streamwise velocity develop through the lift-up of low-velocity fluid elements near the wall. High-speed streaks are produced as high-speed fluid is pushed toward the wall. This is the spatial equivalent of the temporal transient growth found in Blasius boundary layer flow (see Section 4.4.2).

7.4.5 Global Instability

Absolute versus global instability

The concept of absolute and convective instability was discussed in Section 7.2. It applies only to parallel flows, i.e., flows invariant under translation in the streamwise direction x . The criterion used to discriminate between absolute and convective instability is based on the linear impulse response or the Green's function $G(x, t)$ in the laboratory frame. The instability is of absolute type if the Green's function $G(x, t)$ becomes infinite

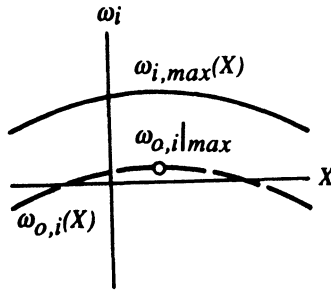


FIGURE 7.37. Sketch of global instability: pocket of absolute instability for a range of streamwise positions. From Huerre & Monkewitz (1990).

at any fixed location x in that particular frame as time evolves. The instability is of convective type if $G(x, t)$ approaches zero in that particular frame but tends to infinity in a different Galilean reference frame. In the laboratory frame, a convectively unstable flow will relax everywhere to the basic state as the disturbance is advected downstream (see Figure 7.6).

In many situations shear flows are not parallel but rather evolve in the streamwise direction. In this case the appropriate stability analysis is *global*, with the streamwise coordinate as an eigendirection. The x -dependence of the global eigenmodes is unknown, rather than assumed sinusoidal as in local stability analysis. When the base flow varies on a slow spatial scale $X = \epsilon x$ with $\epsilon \ll 1$, the concepts developed for parallel flows can be applied locally at each position X . Recent theoretical efforts have tried to establish a relationship between local and global instability properties for weakly divergent flows. In particular, using WKB theory ($\epsilon \ll 1$) the existence of a finite region of absolute instability has been identified as a necessary condition for global instability. The mathematical results show that self-sustained oscillations may arise through a feedback loop consisting of two unstable waves propagating downstream and upstream in the region of absolute instability.

General framework

In the next sections we will give a brief description of the most essential elements of global stability theory. For a more detailed treatment the reader is referred to Huerre & Rossi (1998).

Let us assume a general dispersion relation D in a slowly varying non-parallel flow. We write the associated differential equation

$$D[-i\frac{\partial}{\partial x}, i\frac{\partial}{\partial t}; X]v + \epsilon D_\epsilon[-i\frac{\partial}{\partial x}, i\frac{\partial}{\partial t}; X]v = \mathcal{O}(\epsilon^2). \quad (7.290)$$

Treating the slow streamwise variation X as a parameter, the leading-order local dispersion relation becomes

$$D(\alpha, \omega; X) = 0. \quad (7.291)$$

From this we can define the local absolute frequency as

$$\omega_0(X) = \omega(\alpha_0; X) \quad \frac{\partial \omega}{\partial \alpha}(\alpha_0; X) = 0 \quad (7.292)$$

and the most amplified temporal growth rate as

$$\omega_{\max} = \omega(\alpha_{\max}; X) \quad \frac{\partial \omega_i}{\partial \alpha}(\alpha_{\max}; X) = 0. \quad (7.293)$$

In what follows we will concentrate on the case where the flow exhibits a pocket of absolute instability in the streamwise direction, as shown in Figure 7.37. Starting point of the analysis is the impulse response or Green's function which satisfies

$$\left\{ D[-i\frac{\partial}{\partial x}, i\frac{\partial}{\partial t}; X] + \epsilon D_\epsilon[-i\frac{\partial}{\partial x}, i\frac{\partial}{\partial t}; X] \right\} G(x, t) = \delta(x)\delta(t). \quad (7.294)$$

Similar to the definition of absolute instability (see Section 7.2.1) we can define global instability based on properties of the Green's function $G(x, t)$. The basic flow is *globally unstable* if

$$\lim_{t \rightarrow \infty} G(x, t) \rightarrow \infty \quad \text{for some } x. \quad (7.295)$$

In globally unstable flows the long-time behavior will be dominated by global mode solutions, i.e., eigensolutions with an x -variation. In the case of a slowly varying x -dependence this amounts to solutions of the form

$$v(x, t) = \hat{v}(X)e^{-i\omega_G t} \quad (7.296)$$

where $\omega_{G,i} > 0$ is the global growth rate.

In the next section we will show how to calculate the global growth rate using properties of the local dispersion relation if the flow is slowly varying in the streamwise direction.

Derivation of global properties from local ones

Because we have assumed that the inhomogeneities in the flow are slowly varying, it is possible to derive global instability properties from the local

slowly varying dispersion relation. We follow Huerre & Rossi (1998) and introduce the temporal Fourier transform of the Green's function

$$G(x, t) = \frac{1}{2\pi} \int_L G(x, \omega) e^{-i\omega t} d\omega \quad (7.297)$$

where the contour L is taken above all singularities. We then assume an asymptotic expansion of $G(x, \omega)$ similar to the one used in the analysis of the nonparallel Ginzburg-Landau equation (see Section 7.4.1). We have

$$G^\pm(x, \omega) = [G_0^\pm + \epsilon G_1^\pm + \dots] \exp \left[\int^X \alpha^\pm(X, \omega) dX \right]. \quad (7.298)$$

In this expansion the superscripts \pm refer to the downstream and upstream propagating solutions, respectively.

Upon substitution of (7.298) into (7.294) we match equal powers of ϵ and recover the dispersion relation to zeroth order, with a $D(\alpha^-, \omega, X)$ branch associated with the upstream and a $D(\alpha^+, \omega, X)$ branch associated with the downstream propagating waves. In addition, we find, to first order, the amplitude equations for G^\pm ,

$$G_0^\pm(X) = A_0^\pm \exp \left\{ -i \int^X \frac{\delta\omega^\pm + \frac{i}{2}(D_{\alpha\alpha}^\pm/D_\omega^\pm)\alpha_X^\pm}{\omega_\alpha^\pm} dX \right\} \quad (7.299)$$

where subscripts denote derivatives with respect to the indicated variables and $\delta\omega = D_\epsilon/D_\omega$. The derivation is similar to the one of (7.148). Requiring the Green's function to be continuous on either side of the source at $x = 0$ we find that $A_0^+ = A_0^-$.

Global frequency selection criterion

We can now determine which global frequency will dominate the large-time behavior of $G(x, t)$. The solution (7.299) has a singularity at points of zero group velocity $\omega_\alpha = 0$. This is precisely the definition of the absolute frequency $\omega_0(X)$. Thus, for a fixed frequency the integral in (7.299) becomes singular at those positions. We may now proceed with the same reasoning as in Briggs' method in Section 7.2.2; we only need to replace the complex α -plane with the complex X -plane. Given the contour L in (7.297), the mapping to the X -plane given by the inverse of the function $\omega = \omega_0(X)$ exhibits branches on different sides of the real X -axis. Lowering L , the contours in the X -plane may be pinched between two different branches at a saddle point $X = X^S$, as seen in Figure 7.7 for the analogous case of absolute instability. At this point it is no longer possible to lower L any further without violating causality, and one has reached the dominant

singular contribution to the long-time asymptotics of $G(x, t)$. The saddle point is thus defined by

$$\frac{\partial \omega_0}{\partial X}(X^S) = 0. \quad (7.300)$$

This global frequency selection criterion (often called CHR criterion) has been derived by Chomaz *et al.* (1991) and may also be expressed in the alternative form

$$\frac{\partial \omega}{\partial \alpha}(\alpha^S, X^S) = 0 \quad \frac{\partial \omega}{\partial X}(\alpha^S, X^S) = 0 \quad \omega^S = \omega(\alpha^S, X^S) \quad (7.301)$$

where both the wave number and streamwise coordinate are assumed complex and the leading-order term in the global frequency $\omega_G \sim \omega^S$ is determined by the local dispersion relation.

Proceeding to the next order in the asymptotic expansion, the global eigenfunction and a correction to the global frequency can be determined. In fact, the correction yields a family of discrete global modes; see Huerre & Rossi (1998) for details.

A model problem: The Ginzburg-Landau equation

We will now exemplify global instability and the CHR criterion by analyzing the Ginzburg-Landau equation (7.139). We have

$$\frac{\partial u}{\partial t} + U \frac{\partial u}{\partial x} = \mu(X)u + \gamma \frac{\partial^2 u}{\partial x^2} \quad (7.302)$$

where $\mu(X) = \mu_0 + \mu_2 X^2/2$ with $\mu_2 < 0$. The local dispersion relation and maximum temporal growth rate become

$$\omega = \alpha U + i[\mu(X) - \gamma \alpha^2] \quad \omega_{i,\max} = \mu(X) \quad (7.303)$$

and using $\partial \omega / \partial \alpha = U - 2i\gamma\alpha$, the local absolute frequency and wave number become

$$\omega_0 = i[\mu(X) - \frac{U^2}{4\gamma}] \quad \alpha_0 = -i \frac{U}{2\gamma}. \quad (7.304)$$

Using these expressions it is a simple matter to determine the saddle point and evaluate the CHR criterion. We find

$$\omega^S = i \left[\mu_0 - \frac{U^2}{4\gamma} \right] \quad \alpha^S = -i \frac{U}{2\gamma} \quad X^S = 0. \quad (7.305)$$

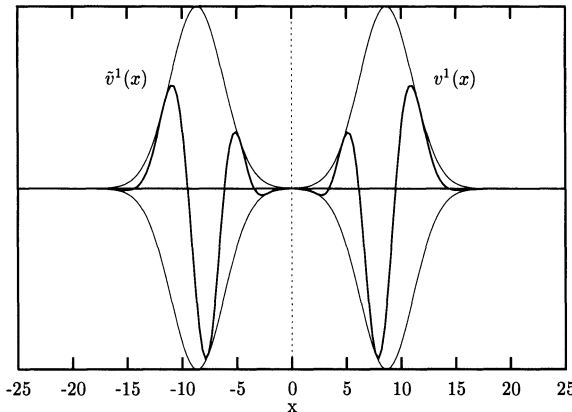


FIGURE 7.38. Global eigenfunctions of the Ginzburg-Landau equation: adjoint mode (left) and direct mode (right). From Cossu (private communication).

Proceeding to the next order it is possible to calculate the correction to the global frequency and the global eigenfunction. For this simple model problem the asymptotic solution at the next order is identical to the exact solution given by Cossu & Chomaz (1997):

$$v^n(X) = H_n[(\mu_2/2\gamma)^{1/4}X] \exp \left\{ \frac{1}{2} \left[\frac{U}{2\gamma} - \left(\frac{\mu_2}{2\gamma} \right)^{1/2} \right] X^2 \right\} \quad (7.306)$$

$$\omega_G^n = i \left[\mu_0 - \frac{U^2}{4\gamma} \right] - \epsilon (2\gamma\mu_2)^{1/2}(n + 1/2) \quad (7.307)$$

where H_n is the n th Hermite polynomial. For $\mu_0 < 0$ the flow is locally stable everywhere. A finite domain of local convective instability appears for $0 < \mu_0 < U^2/4|\gamma|^2$; for $\mu_0 > U^2/4|\gamma|^2$ the flow becomes absolutely unstable in part of this domain. In Figure 7.38 typical global eigenfunctions are shown.

Nonnormality and global modes

It is easy to verify that the linear operator associated with the Ginzburg-Landau equation is normal only if $U = 0$ or $\mu_2 = 0$. Otherwise the operator is nonnormal. Cossu & Chomaz (1997) developed the mathematical framework associated with transient behavior of damped and amplified nonnormal global modes for the Ginzburg-Landau equation. For the globally stable case, the flow can be thought of as a superposition of initially

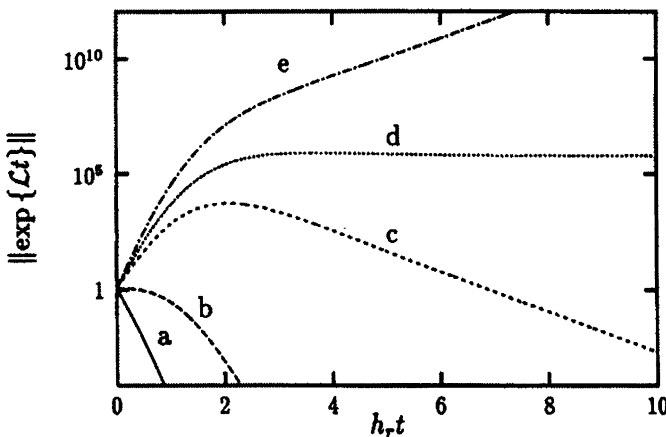


FIGURE 7.39. Growth curves for Ginzburg-Landau equation. Curve (a): the flow is everywhere locally stable ($\mu_0 < 0$); curve (b): locally stable everywhere except at one point ($\mu_0 = 0$); curve (c): finite region of local instability, but globally stable; curve (d): globally neutral; curve (e): globally unstable. From Cossu & Chomaz (1997).

excited nonnormal global modes whose amplitudes decrease in time. The resulting nonorthogonal superposition produces a wave packet which grows in time and moves in space according to the phases of the individual modes, but ultimately decays as time tends to infinity.

From a local point of view, compact perturbations will initially grow as if the flow were parallel and subsequently start to decrease in amplitude as they move away from the pocket of absolute instability. To confirm this intuition by a global analysis we use Hunt's solution (Hunt & Crighton, 1991) to the nonparallel Ginzburg-Landau equation governing the response $G(x, s, t)$ to an impulse applied at the location s at time $t = 0$. The transient growth may be estimated by the norm of the evolution operator as discussed in Chapter 4. Rather than using the energy norm, we choose the L_∞ -norm which measures the amplification of the maximum amplitude over x and is suitable for describing highly inhomogeneous disturbances. The L_∞ -norm of the evolution operator can be computed analytically:

$$\begin{aligned} \|e^{Lt}\|_\infty &= \sup_{-\infty \leq x \leq \infty} \int_{-\infty}^{\infty} |G(x, s, t)| \, ds \\ &= |c_1(t)| \sqrt{\frac{-\pi}{c_{2r}(t)}} \exp\left(\frac{U^2}{4|\gamma|^2[c_{3r}(t) - 2c_{2r}(t)]}\right). \end{aligned} \quad (7.308)$$

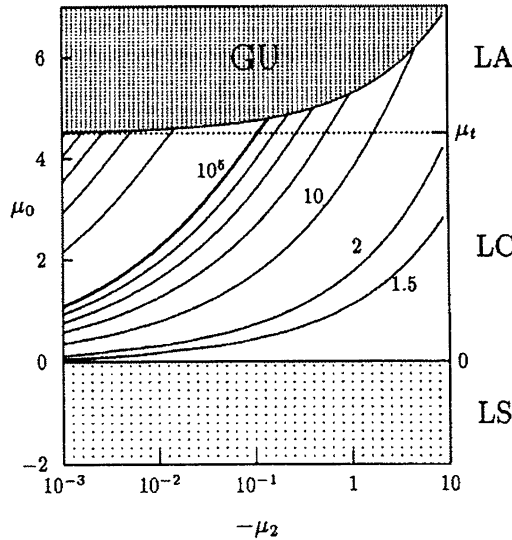


FIGURE 7.40. Maximum growth as a function of μ_0 and μ_2 . In the lower light gray region (LS) $\|\exp(\mathcal{L}t)\| = 1$; in the upper globally unstable region (GU) $\|\exp(\mathcal{L}t)\| = \infty$; in the locally convective (LC) and locally absolute (LA) regions the contour levels range from 1.5 to 10^{45} . From Cossu & Chomaz (1997).

where $c_1(t)$, $c_{2r}(t)$, and $c_{3r}(t)$ are given in Cossu & Chomaz (1997). Figure 7.39 shows the time evolution of $\|e^{\mathcal{L}t}\|$ for various values of μ_0 . The global transients are associated with wave packets that grow convectively but decay as they propagate out of the region of absolute instability. Once the parameter μ_0 is large enough and a global instability sets in, the wave packet does not propagate out of the domain but becomes associated with the most unstable global mode.

Figure 7.40 displays the regions of local stability, locally convective instability, locally absolute instability, and global instability in the (μ_2, μ_0) plane. This figure represents the global analog of the plots of G_{\max} in Chapters 4 and 6.

7.5 Nonlinear Effects

7.5.1 Nonlinear Wave Interactions

Model problem

Before we illustrate the effects of nonlinear wave interactions on the spatial evolution of disturbances we will consider the nonlinear, one-dimensional Burgers' equation as a model problem

$$u_t = u_{xx} + \frac{1}{2} (u^2)_x. \quad (7.309)$$

We first consider the temporal case and assume a periodic solution in space given by a Fourier series representation,

$$u = \sum_{k=-\infty}^{\infty} \hat{u}_k(t) \exp(i\alpha_k x) \quad (7.310)$$

where $\alpha_k = k\alpha$. If we substitute this expansion into Burgers' equation (7.309), we obtain

$$\frac{d}{dt} \hat{u}_k = -\alpha_k^2 \hat{u}_k - \frac{i}{2} \alpha_k \sum_{l+m=k} \hat{u}_l \hat{u}_m \quad (7.311)$$

where the sum is taken over all l and m such that their sum equals k . An equation governing the rate of change of the energy in each Fourier component, in this case represented by $|\hat{u}_k|^2$, can now be derived. If we multiply the preceding equation by \hat{u}_k^* (* indicates the complex conjugate operation) and add the complex conjugate of the same expression, we find

$$\frac{d}{dt} |\hat{u}_k|^2 = -2\alpha_k^2 |\hat{u}_k|^2 + \text{Im} \left[\alpha_k \hat{u}_k^* \sum_{l+m=k} \hat{u}_l \hat{u}_m \right]. \quad (7.312)$$

The last term represents the energy transfer within wave triads.

We now turn to the spatial case, where we instead assume a periodic solution in time, i.e.,

$$u = \sum_k \tilde{u}_k(x) \exp(-i\omega_k t) \quad (7.313)$$

with $\omega_k = k\omega_1$ and ω_1 as the fundamental frequency. Substituting into Burgers' equation results in

$$-i\omega_k \tilde{u}_k = \frac{d^2}{dx^2} \tilde{u}_k - \frac{1}{2} \frac{d}{dx} \sum_{l+m=k} \tilde{u}_l \tilde{u}_m \quad (7.314)$$

which is not in the form of an evolution equation in x . Such an equation can be formulated by introducing an additional variable, in this case $v = u_x$, and the previous equation can be written in the form

$$\frac{d}{dx} \begin{pmatrix} \tilde{u}_k \\ \tilde{v}_k \end{pmatrix} = \begin{pmatrix} 0 & 1 \\ -i\omega_k & 0 \end{pmatrix} \begin{pmatrix} \tilde{u}_k \\ \tilde{v}_k \end{pmatrix} + \begin{pmatrix} 0 \\ \frac{1}{2} \frac{d}{dx} \sum_{l+m=k} \tilde{u}_l \tilde{u}_m \end{pmatrix}. \quad (7.315)$$

An equation for the rate of change of the quantity $|\tilde{u}_k|^2 + |\tilde{v}_k|^2$ (which we will refer to as an energy) can now be found. We get

$$\begin{aligned} \frac{d}{dx} (|\tilde{u}_k|^2 + |\tilde{v}_k|^2) &= 2 \operatorname{Real} [\tilde{u}_k^* \tilde{v}_k] + 2 \operatorname{Im} [\omega_k \tilde{v}_k^* \tilde{u}_k] \\ &\quad + \operatorname{Real} \left[\tilde{v}_k^* \sum_{l+m=k} (\tilde{v}_l \tilde{u}_m + \tilde{u}_l \tilde{v}_m) \right]. \end{aligned} \quad (7.316)$$

The last term represents the transfer of energy between Fourier components in the spatial case.

Choice of norm

The model problem illustrates an important issue of stability calculations: the choice of the disturbance measure. In the previous analysis we used the kinetic energy for the temporal case, but chose a measure for the spatial case that also included spatial derivative terms. Consequently, the nonlinear transfer terms are different for the temporal and spatial case. In physical space, the transfer terms are $\frac{1}{2}u(u^2)_x$ for the temporal case, whereas in the spatial case the corresponding term is $\frac{1}{2}u_x(u^2)_x$. The previous analysis can be generalized to the Navier-Stokes equations.

These derivations suggest that the complete spatial initial value problem has to be taken into account in the derivation of meaningful disturbance measures, particularly when we are interested in the nonlinear transfer of the disturbance measure. By naively choosing temporal analogs for the spatial case one may calculate the transfer rates of quantities that are neither defined nor intended.

If streamwise velocity derivatives are not included in the disturbance measure for the spatial case, the measure may vanish for some Fourier components at particular streamwise positions, although the disturbance is nonzero in the vicinity of these locations. An example are local stagnation points. In contrast, if the kinetic energy in the temporal case is zero for a particular time, it will be zero for all subsequent times.

7.5.2 Nonlinear Parabolized Stability Equations

Asymptotic theories are used to incorporate nonlinear terms for nonparallel flows, and the analysis proceeds similar to the weakly nonlinear case

for parallel flows (see Section 5.3). The expansions, however, quickly become unwieldy. For this reason we will treat the nonlinear extension of the parabolized stability equations instead. Solution strategies for the linear parabolized stability equations have already been discussed earlier, and, conceptually, nonlinear terms can be added in a straightforward manner.

Formulation

We will deal with the incompressible Navier-Stokes equations for the nonlinear evolution of three-dimensional disturbances in a mean flow given by $(U(x, y), V(x, y), 0)$. We also include effects of small curvature in the streamwise direction, as in the linear parabolized stability equations (7.239-7.244).

Let $\mathbf{q} = (u, v, w, p)$ be the disturbance vector. We assume that the disturbances take the form

$$\mathbf{q} = \sum_m \sum_n \tilde{\mathbf{q}}_{mn}(x, y) \exp \left[i \int_{x_0}^x \alpha_{mn}(\xi) d\xi + in\beta z - im\omega t \right] \quad (7.317)$$

where α_{mn} and β are the streamwise and spanwise wave numbers, ω is the perturbation frequency, and $\tilde{\mathbf{q}}_{mn}$ is the amplitude function for the mode with $(m\omega, n\beta)$. This is the same disturbance form as was used for the linear parabolized stability equations.

There are now more unknowns than equations, one extra parameter (α_{mn}) for each wave number pair included in the calculation, and we need additional conditions to close the system of equations. Similar to the linear case, we require that the amplitude functions $\tilde{\mathbf{q}}_{mn}$ be slowly varying and introduce the familiar auxiliary condition for each wave number

$$\int_0^\infty \tilde{\mathbf{q}} \frac{\partial}{\partial x} \tilde{\mathbf{q}} dy = 0. \quad (7.318)$$

Substituting the expansion (7.317) into the nonlinear disturbance equations, assuming the same scalings (7.238) used for the linear PSE and performing a harmonic balance for the frequencies and spanwise wave numbers, we arrive at a set of coupled nonlinear equations of the form

$$A\tilde{\mathbf{q}}_{mn} + B \frac{\partial \tilde{\mathbf{q}}_{mn}}{\partial y} + C \frac{\partial^2 \tilde{\mathbf{q}}_{mn}}{\partial y^2} + D \frac{\partial \tilde{\mathbf{q}}_{mn}}{\partial x} = \mathbf{N}_{mn}. \quad (7.319)$$

with

$$\mathbf{N}_{mn} = \begin{pmatrix} \hat{N}_1 \\ \hat{N}_2 \\ \hat{N}_3 \\ 0 \end{pmatrix} \quad (7.320)$$

where \hat{N}_i is the Fourier transform (in t and z) of the nonlinear terms N_i which take the form

$$N_1 = -u \frac{\partial u}{\partial x} - v \frac{\partial u}{\partial y} - w \frac{\partial u}{\partial z} - \kappa uv \quad (7.321)$$

$$N_2 = -u \frac{\partial v}{\partial x} - v \frac{\partial v}{\partial y} - w \frac{\partial v}{\partial z} + \kappa u^2 \quad (7.322)$$

$$N_3 = -u \frac{\partial w}{\partial x} - v \frac{\partial w}{\partial y} - w \frac{\partial w}{\partial z} \quad (7.323)$$

The matrices A, B, C , and D have been given earlier for the linear problem (7.240)-(7.243); they depend nonlinearly on $\alpha_{mn}(x)$.

The boundary conditions for $n > 0$ specify zero velocities at the wall and at infinity. Special care has to be taken for the mean flow distortion ($m = n = 0$) and for zero streamwise wave numbers. It is necessary to use the traditional boundary layer scalings rather than the PSE scalings for those wave numbers. The associated boundary conditions do not specify $v = 0$ at infinity – as required by the boundary layer approximation.

In contrast to weakly nonlinear theories, the PSE formulation does not require a hierarchical ordering of terms based on amplitude. Convergence during the marching procedure is maintained by introducing new harmonics, when they are forced by a right-hand side that is greater than a preset threshold. This threshold is usually set at $\mathcal{O}(\text{Re}^{-2})$ or less, consistent with the order of the neglected streamwise derivatives.

Numerical computations start at some streamwise location x_0 where the velocity components are prescribed for a given wave number α_{mn} . The velocities and pressure at $x_0 + \Delta x$ are calculated using a backward Euler discretization in space. If the auxiliary condition (7.318) is not satisfied, a new α_{mn} is chosen and the equations are solved again. This iterative process continues until (7.318) is satisfied, after which the computation proceeds to the next streamwise location. During this iterative process, nonlinear terms are also updated and convergence is ensured before the solution proceeds downstream.

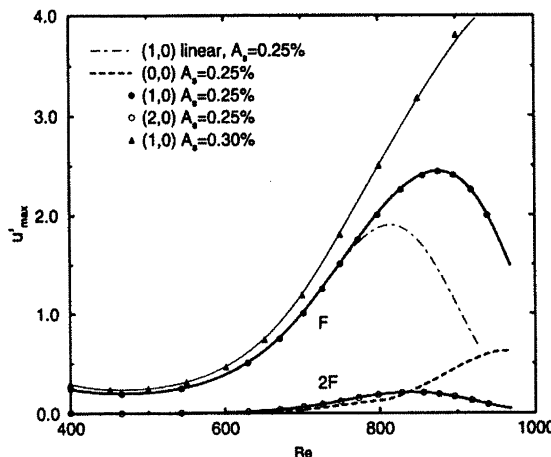


FIGURE 7.41. Amplitude of u'_{rms} versus Reynolds number for Tollmien-Schlichting waves at $F = 86$ and the first harmonic with $2F$ using initial Tollmien-Schlichting amplitudes of 0.25% (heavy lines) and 0.30% (thin lines) at $Re = 400$. The dashed line shows the linear result. Symbols denote results of the direct Navier-Stokes simulation. From Bertolotti *et al.* (1992).

7.5.3 Examples

Nonlinear development of Tollmien-Schlichting waves

As an example of the nonlinear evolution of small-amplitude disturbances we present the development of Tollmien-Schlichting waves into the finite-amplitude regime for Blasius boundary layer flow. Figure 7.41 displays the root-mean-square values of the streamwise velocity for a Tollmien-Schlichting wave and its higher harmonics (see Bertolotti *et al.*, 1992). We notice a distinct deviation from the linear computation as higher harmonics are introduced.

Saturated Görtler vortices

The nonlinear development of disturbances in Görtler flow is displayed in Figure 7.42. Starting with mode 1, the initial development follows the one predicted by linear theory. Farther downstream, higher harmonics and mode 0 (denoting the mean flow modification) rise sharply. At the same time, the evolution of the initial mode 1 substantially deviates from linear theory. As the finite-amplitude Görtler vortices develop we notice a saturation of the modes. The mode responsible for the mean flow modification contains the highest energy.

Isocontours of the streamwise velocity in the y - z plane are given in Figure 7.43, displaying the familiar structure of finite-amplitude Görtler vortices. Near the “stem” of the mushroom, low-momentum fluid is ejected from the wall and returns back toward the wall in the region of maximum wall shear.

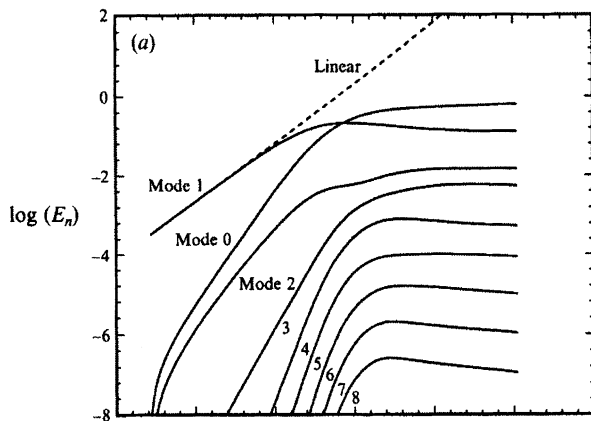


FIGURE 7.42. Nonlinear evolution of disturbance energy for various spanwise Fourier modes for Görtler flow. $\lambda_z = 0.9$ cm. From Li & Malik (1995).

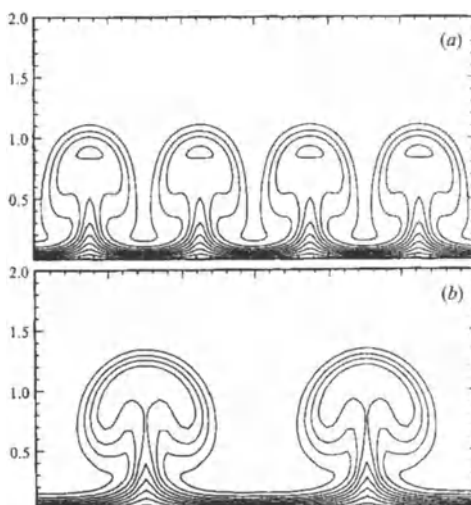


FIGURE 7.43. Variation of streamwise velocity in the y - z -plane due to the presence of Görtler vortices at $x = 100$ cm. (a) $\lambda_z = 0.9$ cm; (b) $\lambda_z = 1.8$ cm. Contours range from $u/u_e = 0.1$ to 0.9 in increments of 0.1. From Li & Malik (1995).

Supersonic jet flow

Malik & Chang (2000) studied axisymmetric supersonic jet flow for small Reynolds numbers using the nonlinear parabolized stability equations. They observed a strong interaction of the (least stable) helical modes which resulted in the rapid formation of streamwise vortices and a significant distortion of the mean flow.

7.6 Disturbance Environment and Receptivity

7.6.1 *Introduction*

Definition

In the previous sections of this chapter we have discussed various possible instabilities that may occur in boundary layer flows. However, in a physical situation these instabilities must start from a disturbance somewhere in the boundary layer environment. The entrainment process of disturbances into the boundary layer and the response of the boundary layer to a general disturbance environment is described by *receptivity* theory. Numerous experimental investigations have demonstrated that the transition process and the transitional Reynolds number depend strongly on the ambient perturbation environment. Reynolds noted that the transition location in pipe flow shifts upstream with increasing disturbance intensity of the incoming flow. It is generally recognized that many different types of external disturbances play an important role in the transition process such as natural freestream perturbations (vortical or acoustic), entropy (temperature) perturbations in supersonic flows, surface vibration, roughness elements on an otherwise streamlined surface, etc. The subsequent development of the disturbance inside the boundary layer depends not only on the source of ambient perturbations, but also on the intensity and spectral composition (in the frequency–wave number plane).

A recent extensive review of receptivity theory based on experiments, direct numerical simulations and theory, is given by Saric *et al.* (1994).

Receptivity at the leading edge and due to roughness and freestream turbulence

It is well known that acoustic disturbances in the freestream can excite instability waves inside the boundary layer (see Goldstein & Hultgren, 1989). Although the wavelength and propagation speed of acoustic waves are roughly two orders of magnitude larger than those of typical instability waves inside the boundary layer, Tollmien-Schlichting wave formation may occur in regions of strong local changes of characteristic flow quantities. Receptivity theory has to provide a mechanism that can convert the wave-

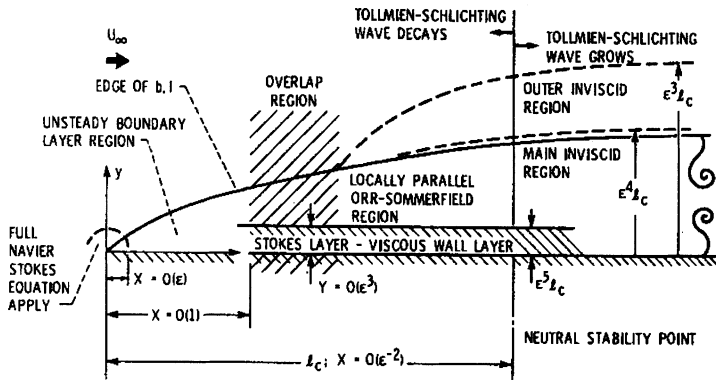


FIGURE 7.44. Sketch of asymptotic scalings for the leading-edge receptivity problem. From Goldstein & Hultgren (1989).

length of the acoustic disturbance into a typical wavelength of a Tollmien-Schlichting wave. It is assumed that Tollmien-Schlichting waves are forced by an interaction of acoustic perturbations with local heterogeneities of the mean flow such as short-scale variations in the streamwise direction. Hence receptivity to sound is inherently a nonparallel process and may occur in the leading-edge region where the boundary layer evolves over a distance that is short compared to the boundary layer thickness. Other possibilities of natural receptivity mechanisms are local streamwise changes that occur on a small streamwise length scale. Such heterogeneities may be two-dimensional roughness elements on the surface, rapid changes in surface curvature, or large pressure gradients.

Goldstein (1983) suggested that the linearized Navier-Stokes equations in the leading-edge region should be taken as

$$\frac{\partial u}{\partial t} + U \frac{\partial u}{\partial x} + V \frac{\partial u}{\partial y} + u \frac{\partial U}{\partial x} + v \frac{\partial U}{\partial y} = - \frac{\partial p}{\partial x} + \frac{1}{Re} \frac{\partial^2 u}{\partial y^2}. \quad (7.324)$$

This equation contains the terms $V \frac{\partial u}{\partial y}$ and $u \frac{\partial U}{\partial x}$, which represent the non-parallel mean flow effects. To effectively transform the wavelength and propagation speed of the sound wave these terms should be significant on a length scale comparable to the Tollmien-Schlichting wavelength. Progress has been made by approximating the Navier-Stokes equations by a multiple-deck structure (see Goldstein & Hultgren, 1989). An example of such a multiple-deck structure relevant to leading-edge receptivity of Tollmien-Schlichting waves can be seen in Figure 7.44 (see also Bodonyi (1990)). The small parameter ϵ is $Re_x^{-1/8}$ as in Section 7.4.1. Hammerton & Kerschen (1997) study boundary layer receptivity at a parabolic leading edge

for small Strouhal numbers S and report good agreement between asymptotic theory and numerical simulations for only very small values of S .

In the experimental study of Kachanov *et al.* (1979) the important role of the leading edge was demonstrated for the boundary layer receptivity to freestream fluctuations. It was shown that in the vicinity of the leading edge the nonvortical part of the fluctuation field – created by a vibrating ribbon positioned in the freestream below the stagnation streamline – transforms into a two-dimensional vortex with strong spanwise vorticity. This external vorticity field in turn leads to the generation of plane Tollmien-Schlichting waves in the starting boundary layer at the same frequency as the forcing.

In the case of nearly homogeneous freestream turbulence generated by a grid in a wind tunnel test section, the boundary layer is characterized by low-frequency perturbations and a slow decay of high-frequency fluctuations. Such wide-band distributions and stochastic variations result in a distinctly different excitation of the boundary layer compared to both acoustic and vibrational excitations.

Outline

In what follows we will briefly discuss the receptivity of the flat plate boundary layer to two-dimensional disturbances of low amplitude, which are typically present in freestream sound. Alternatively, one may consider the generation of Tollmien-Schlichting waves from a vibrating ribbon or suction/blowing slots as a receptivity problem. Finally we will investigate receptivity mechanisms for Görtler instabilities where three-dimensional roughness plays a crucial role. Receptivity to freestream turbulence, which is composed of highly three-dimensional vortical disturbances, is yet another receptivity scenario which will be discussed here and in Section 9.3.2.

Receptivity of bounded flows to blowing and suction will not be covered in this section. The interested reader is referred to Tumin (1996), Shan *et al.* (1999), and Ma *et al.* (1999).

The area of receptivity is a very active field of research characterized by many different approaches and the material presented below is intended to give only a brief cross section of current work in this field.

7.6.2 Nonlocalized and Localized Receptivity

General concept

An essential part of the transition process is the transformation of freestream disturbances into the small-amplitude perturbations that feed instabilities in the boundary layer (Figure 7.45). We will follow Crouch (1992*a,b*) and study the interaction of disturbances outside the boundary layer with instability waves inside the boundary layer in the presence of localized and nonlocalized streamwise changes of boundary layer characteristics. Both changes will be small compared to the mean flow such that linear theory

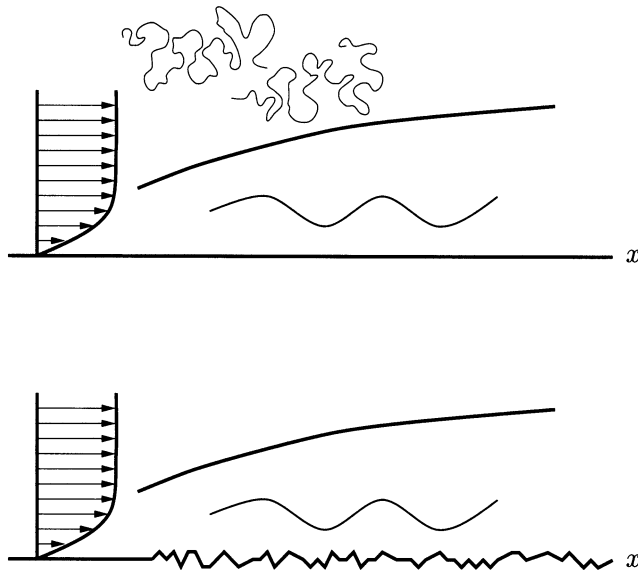


FIGURE 7.45. Receptivity to freestream disturbances and surface roughness.

applies. We will use a perturbation approach and develop a hierarchy of linear unforced and forced equations that we investigate for parametric resonances (see also Choudhari (1996)).

Before launching into this perturbation approach to boundary layer receptivity, we will first review and demonstrate the main features of driven oscillatory systems with locally varying frequencies. A simple model problem will mimic the underlying receptivity mechanism present in boundary layers.

A model problem

In the subsequent section we will derive an evolution equation for a Tollmien-Schlichting wave that is driven by a harmonic source term representing the combined forcing by the acoustic freestream disturbance and the wall roughness. As long as the forcing frequency does not coincide with the natural frequency of the Tollmien-Schlichting wave there is little interaction between external forcing and internal instability waves. However, as the Tollmien-Schlichting wave evolves downstream, its frequency changes and will at some location resonate with the forcing. In the neighborhood of this location a strong interaction between the Tollmien-Schlichting wave and the external forcing will cause a significant energy transfer into the Tollmien-Schlichting wave.

As a model problem for the receptivity analysis, we will study a forced harmonic oscillator to help demonstrate the approach taken to compute the response amplitude. We will consider the equation

$$\frac{d^2u}{dx^2} + \omega^2(x)u = \cos \Omega x \quad (7.325)$$

where the frequency ω varies slowly in x . This slow variation of the frequency allows us to compute local solutions for fixed frequencies ω . We obtain

$$u(x) = A \cos(\omega x + \beta) + \Lambda \cos \Omega x. \quad (7.326)$$

The first term represents the homogeneous solution with amplitude A and phase β . The second term is the particular solution with amplitude Λ given as $\Lambda = 1/(\omega^2 - \Omega^2)$. Due to the slow variation of the frequency ω , the amplitude A and the phase β are also slowly varying functions of x . To derive an evolution equation for A and β we apply the following procedure: starting with a complete solution at x_1 we compute an approximate solution at $x_2 = x_1 + \Delta x$ taking into account only the fast periodic terms. Comparing this solution to a local solution at x_2 yields the amplitude and phase at location x_2 in terms of their values at x_1 . We obtain

$$\begin{aligned} A_2^2 &= [A_1 \cos(\omega_1 x_2 + \beta_1) - (\Lambda_2 - \Lambda_1) \cos \Omega x_2]^2 \\ &\quad + \left[\frac{\omega_1}{\omega_2} A_1 \sin(\omega_1 x_2 + \beta_1) - \frac{\Omega}{\omega_2} (\Lambda_2 - \Lambda_1) \sin \Omega x_2 \right]^2 \end{aligned} \quad (7.327)$$

$$\beta_2 = \tan^{-1} \left[\frac{\omega_1 A_1 \sin(\omega_1 x_2 + \beta_1) - (\Lambda_2 - \Lambda_1) \Omega \sin \Omega x_2}{\omega_2 (A_1 \cos(\omega_1 x_2 + \beta_1) - (\Lambda_2 - \Lambda_1) \cos \Omega x_2)} \right] - \omega_2 x_2 \quad (7.328)$$

where the subscript ₁ and ₂ denote variables evaluated at x_1 and x_2 , respectively.

Starting with an initial amplitude and phase at $x = x_0$ we use the preceding equations together with (7.326) to compute the solution to the forced harmonic oscillator. As the frequency ω varies in the x -direction, the variables Λ , A , and β have to be adjusted accordingly.

An example will illustrate the response of a harmonic oscillator with slowly varying frequency to periodic forcing. We choose $\omega = 0.5 + 0.5(x/2\pi)$ and $\Omega = 1$. The initial conditions are $u(0) = \Lambda(0) = u'(0) = 0$, which is equivalent to setting $A(0) = 0$. Figure 7.46 shows the results of the computation. The amplitude A of the harmonic oscillator is displayed by the thick line in the upper half of the plot. The amplitude Λ of the particular

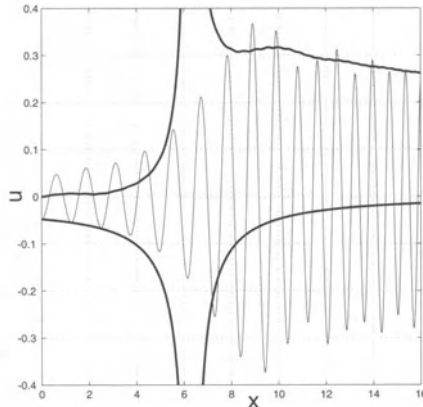


FIGURE 7.46. Receptivity model.

solution is shown as the thick line in the lower half of the plot. The oscillatory thin line displays the solution $u(x)$ given by (7.326) with (7.327) and (7.328). We notice that the solution consists of mostly the particular part for small x ; as we approach the location where $\omega = \Omega$ both amplitudes tend to infinity. After the resonance, the amplitude of the particular solution decays to zero following $\Lambda = 1/(\omega^2 - \Omega^2)$. The amplitude A of the harmonic oscillator, on the other hand, approaches a constant value. We also notice that prior to resonance $u(x)$ oscillates with the forcing frequency Ω ; after the resonance $u(x)$ oscillates with the natural frequency ω . In summary, we observe the rise of harmonic oscillations caused by a parametric resonance with a periodic external forcing.

We will see that the receptivity problem will follow the same principle and analysis: the external forcing, composed of acoustic freestream disturbances and wall roughness, will induce Tollmien-Schlichting waves inside the boundary layer by a parametric resonance.

Nonlocalized receptivity of boundary layers

Let us then apply a similar perturbation analysis to study the response behavior of an eigenmode to external forcing as the slowly varying spatial wave number (due to nonparallel flow) passes through resonance or near-resonance.

Consider the flow of two-dimensional disturbances in a parallel boundary layer (Crouch, 1992b) governed by

$$\mathcal{L}(\mathbf{v}) + \mathcal{N}(\mathbf{v}, \mathbf{v}) = 0 \quad (7.329)$$

with

$$\mathcal{L}(\mathbf{v}) = \frac{1}{\text{Re}} \nabla^4 \mathbf{v} - \frac{\partial}{\partial t} \nabla^2 \mathbf{v} \quad (7.330)$$

$$\mathcal{N}(\mathbf{v}, \mathbf{v}) = -\frac{\partial}{\partial x} (\mathbf{v} \cdot \nabla) \zeta \quad (7.331)$$

where $\omega = \nabla \times \mathbf{v} = (0, 0, \zeta)$ and $\mathbf{v} = (u, v, 0)$. Nondimensionalizing by the outer velocity U_∞ and the fixed reference length $\delta_{\text{ref}} = \sqrt{\nu x_f / U_\infty}$ we impose the boundary conditions

$$u \rightarrow 1 + \epsilon \exp[-i\omega_A t] \quad \text{as} \quad y \rightarrow \infty \quad (7.332)$$

and

$$u = v = 0 \quad \text{at} \quad y = \delta H(x). \quad (7.333)$$

The first boundary condition models an acoustic wave of amplitude ϵ and frequency ω_A ; the second boundary condition accounts for wall roughness of height δ . We will proceed by taking the Fourier transform of the roughness distribution $H(x)$. To simplify the following analysis we will consider a wavy wall consisting of a single mode, i.e.,

$$H(x) = \exp(i\alpha_W x) \quad (7.334)$$

where $\alpha_W = 2\pi/\lambda_W$ and λ_W is the characteristic wavelength of the surface perturbation. We have introduced two small parameters, ϵ and δ , and, using a perturbation approach, will seek solutions of the form

$$\mathbf{v}(x, y, t) = \mathbf{v}_0 + \epsilon \mathbf{v}_\epsilon + \delta \mathbf{v}_\delta + \epsilon \delta \mathbf{v}_{\epsilon\delta} + \dots \quad (7.335)$$

The lowest-order velocity \mathbf{v}_0 is the local Blasius boundary layer profile at the streamwise location x . Terms of order ϵ^2 and δ^2 have been neglected because the equations at order $\mathcal{O}(\epsilon\delta)$ completely determine the receptivity behavior.

Substituting the perturbation approach into the governing equation and boundary conditions leads to a set of homogeneous and inhomogeneous equations. At order $\mathcal{O}(\epsilon)$ we get

$$\mathcal{L}_0(\mathbf{v}_\epsilon) = 0 \quad (7.336)$$

$$u_\epsilon \rightarrow \exp(-i\omega_A t) \quad \text{as} \quad y \rightarrow \infty \quad (7.337)$$

$$u_\epsilon = v_\epsilon = 0 \quad \text{at} \quad y = 0 \quad (7.338)$$

which describes the forcing due to a time-periodic perturbation in the free-stream. At order $\mathcal{O}(\delta)$ we capture the effect of the spatially periodic wall roughness:

$$\mathcal{L}_0(\mathbf{v}_\delta) = 0 \quad (7.339)$$

$$u_\delta \rightarrow 0 \quad \text{as} \quad y \rightarrow \infty \quad (7.340)$$

$$u_\delta = -\frac{\partial u_0}{\partial y} \exp(i\alpha_W x) \quad (7.341)$$

$$v_\delta = 0 \quad \text{at} \quad y = 0. \quad (7.342)$$

where we linearized the boundary condition at the wall about $y = 0$. Finally, at order $\mathcal{O}(\epsilon\delta)$, we obtain an inhomogeneous problem

$$\mathcal{L}_0(\mathbf{v}_{\epsilon\delta}) = -\mathcal{N}(\mathbf{v}_\epsilon, \mathbf{v}_\delta) - \mathcal{N}(\mathbf{v}_\delta, \mathbf{v}_\epsilon) \quad (7.343)$$

$$u_{\epsilon\delta} \rightarrow 0 \quad \text{as} \quad y \rightarrow \infty \quad (7.344)$$

$$u_{\epsilon\delta} = -\frac{\partial u_\epsilon}{\partial y} \exp(i\alpha_W x) \quad (7.345)$$

$$v_{\epsilon\delta} = -\frac{\partial v_\epsilon}{\partial y} \exp(i\alpha_W x) \quad \text{at} \quad y = 0. \quad (7.346)$$

The linear operator \mathcal{L}_0 is defined as

$$\mathcal{L}_0(\mathbf{v}) = \mathcal{L}(\mathbf{v}) + \mathcal{N}(\mathbf{v}_0, \mathbf{v}) + \mathcal{N}(\mathbf{v}, \mathbf{v}_0). \quad (7.347)$$

The solution at order ϵ is assumed in the form

$$\mathbf{v}_\epsilon = \mathbf{v}_A \exp(-i\omega_A t) \quad (7.348)$$

and the solution to the $\mathcal{O}(\delta)$ problem is taken as

$$\mathbf{v}_\delta = \mathbf{v}_W \exp(i\alpha_W x) \quad (7.349)$$

where the time and space dependences are governed by the imposed forcing. Substituting into the $\mathcal{O}(\epsilon\delta)$ problem we obtain

$$\begin{aligned} \mathcal{L}_0(\mathbf{v}_{\epsilon\delta}) &= \left[-i\alpha_W v_W \frac{\partial^2 u_A}{\partial y^2} + \alpha_W^2 \left(\frac{\partial u_W}{\partial y} - i\alpha_W v_W \right) u_A \right] \\ &\quad \times \exp[i(\alpha_W x - \omega_A t)] \end{aligned} \quad (7.350)$$

where the right-hand side represents a traveling-wave disturbance resulting from the interaction of the acoustic mode and the wall mode. This equation

is in the form of a driven system similar to the model equation of the previous section. The corresponding boundary conditions are

$$u_{\epsilon\delta} \rightarrow 0 \quad \text{as } y \rightarrow \infty \quad (7.351)$$

$$u_{\epsilon\delta} = -\frac{\partial u_A}{\partial y} \exp[i(\alpha_W x - \omega_A t)] \quad (7.352)$$

$$v_{\epsilon\delta} = 0 \quad \text{at } y = 0. \quad (7.353)$$

We notice that \mathcal{L}_0 in the equation above is the Orr-Sommerfeld operator. To simplify the analysis, we will only consider a Tollmien-Schlichting wave and compute its response to the external forcing. We further assume that the wave number and frequency of the forcing (α_W, ω_A) are close to the wave number and frequency of the Tollmien-Schlichting wave (α_{TS}, ω_{TS}); under this near-resonant condition energy will be transferred into the Tollmien-Schlichting wave.

Following the model problem we will decompose the solution of the $\mathcal{O}(\epsilon\delta)$ problem into the sum of an eigenmode (homogeneous part) and a forced mode (particular part):

$$\mathbf{v}_{\epsilon\delta} = \mathbf{v}_{\epsilon\delta TS} + \mathbf{v}_{\epsilon\delta F}. \quad (7.354)$$

We will concentrate on the streamwise component of the forced mode which we assume of the form

$$u_{\epsilon\delta F} = \bar{\Lambda}_F(x) \bar{u}_F(y; x) \exp[i\phi_F(y; x) + i\psi_F(x)] \exp[i(\alpha_W x - \omega_A t)]. \quad (7.355)$$

The forced mode has the same spatial wave number and temporal frequency as the forcing. \bar{u}_F stands for the normalized response amplitude, and $\bar{\Lambda}_F$ denotes the maximum of the response. The phase profile is given by ϕ_F and the response phase ψ_F is the result of a normalization condition on ϕ_F . For the functions $\bar{\Lambda}_F, \bar{u}_F, \phi_F$ and ψ_F a weak dependence on the streamwise coordinate direction is assumed.

Proceeding to the homogeneous part of the solution we take the streamwise velocity component of the Tollmien-Schlichting eigenmode of the form

$$\begin{aligned} u_{\epsilon\delta TS} &= \bar{A}_{TS}(x) \bar{u}_{TS}(y; x) \exp[i\phi_{TS}(y; x) + i\psi_{TS}(x)] \\ &\times \exp \left[i \int_{x_0}^x \alpha_{TSr}(s) ds - i\omega_A t \right] \end{aligned} \quad (7.356)$$

where x_0 stands for a given upstream reference location. As before, the functions $\bar{A}_{TS}, \bar{u}_{TS}, \phi_{TS}$, and ψ_{TS} exhibit a weak dependence on the streamwise

coordinate direction. Exponential growth associated with the imaginary part of α_{TS} will be accounted for by the amplitude \bar{A}_{TS} .

The sum of homogeneous and particular part represents a traveling-wave disturbance with frequency ω_A :

$$\begin{aligned} u_{\epsilon\delta} &= A(x) \exp[i\psi(x)] \bar{u}(u; x) \exp[i\phi(y; x)] \exp[-i\omega_A t] \\ &= u_{\epsilon\delta F} + u_{\epsilon\delta TS}. \end{aligned} \quad (7.357)$$

It can be shown (see Crouch, 1992b) that near resonance the forced mode and the eigenmode have identical profiles except in a thin region near the wall. We therefore can extract an amplitude equation from (7.357).

$$\begin{aligned} A(x) \exp[i\psi(x)] &= \Lambda_F(x) \exp[i\alpha_W(x - x_0)] \\ &\quad + A_{TS}(x) \exp \left[i \int_{x_0}^x \alpha_{TSr}(s) ds \right] \end{aligned} \quad (7.358)$$

where

$$\Lambda_F = \bar{\Lambda}_F \exp[i\psi_F] \quad A_{TS} = \bar{A}_{TS} \exp[i\psi_{TS}] \quad (7.359)$$

are complex amplitudes. We like to emphasize that the above solutions are local solutions, i.e., the streamwise coordinate x appears as a parameter rather than an independent variable.

Similar to the model problem, we are particularly interested in the evolution of the amplitude A_{TS} as we move downstream, where contributions from the forcing and the inherent linear growth of the unforced problem should be identified. The solution of the equation will determine the effects of acoustic forcing in the freestream and wall roughness on the development of Tollmien-Schlichting instabilities in the boundary layer. The derivation of the amplitude equation proceeds similarly to the one given in Section 5.3.1 although now we incorporate weakly nonparallel rather than weakly nonlinear effects. For details the reader is referred to Crouch & Spalart (1995). The final equation governing the evolution of the forced Tollmien-Schlichting amplitude for weakly nonparallel flow reads

$$\frac{dA_{TS}}{dx} = -\alpha_{TSi} A_{TS} - \frac{d\Lambda_F}{dx} \exp \left[i\alpha_W(x - x_0) - i \int_{x_0}^x \alpha_{TSr}(s) ds \right]. \quad (7.360)$$

The right-hand side of the equation consists of two parts. The first part describes the linear spatial growth of the Tollmien-Schlichting wave, the second term represents the spatial growth rate due to the external forcing. This growth rate is proportional to the streamwise derivative of the forcing

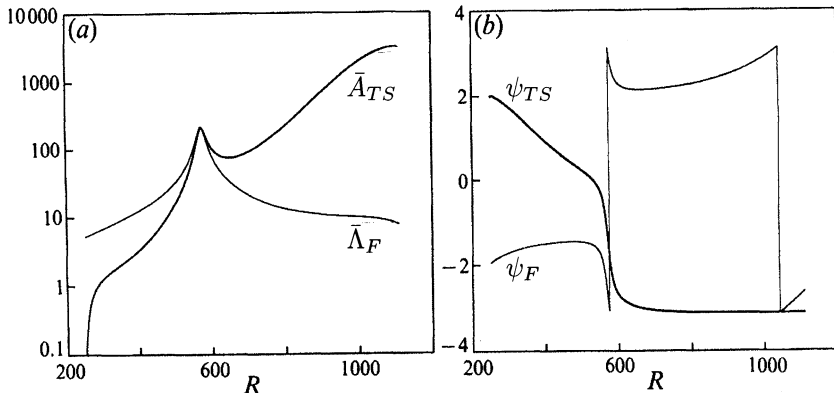


FIGURE 7.47. Streamwise variation of eigenmode (a) amplitude and (b) phase superimposed on the forced-mode response at $F = 56$, $\alpha_W = 0.174236$, $Re^* = 550$. From Crouch (1992b).

amplitude. Far from resonance, the streamwise derivative of the forcing amplitude Λ_F is rather small and influences the growth of the Tollmien-Schlichting amplitude only weakly. Near resonance, on the other hand, the variation of Λ_F in the streamwise direction is quite rapid, and the growth of the Tollmien-Schlichting wave is dominated by the external forcing.

Solving the preceding equation for $F = 56$, $\alpha_W = 0.174236$ and $Re = 550$ yields the results displayed in Figure 7.47. We observe a strong peak in the amplitude of the forced mode near branch I at $Re \approx 576$. Further downstream, the forced response decreases by more than an order of magnitude. The eigenmode, labeled A_{TS} in Figure 7.47(a), first increases rapidly before growing at a constant rate. As we approach a Reynolds number of about 500, a significant amount of energy is transferred to the eigenmode due to the rapid changes in $\bar{\Lambda}_F$ caused by near resonant conditions. Further downstream, the forcing of the eigenmode subsides, and we observe spatial growth due to linear theory. The phase functions of the forced mode and eigenmode are depicted in Figure 7.47. The phase of the eigenmode shows a characteristic shift of approximately π radians during the passage through near-resonance.

Localized receptivity of boundary layers

The same equations as given in the previous paragraph hold when considering the receptivity of boundary layer flow to a *localized* roughness distribution rather than a periodic array of roughness elements. We only have to modify the Fourier representation of the roughness distribution and the form of the solution at order $\mathcal{O}(\epsilon\delta)$. Rather than assuming a single-mode wavy wall we will consider a Fourier decomposition $\tilde{H}(\alpha)$ of a localized

surface irregularity given by $H(x)$. The streamwise velocity component at order $\mathcal{O}(\epsilon\delta)$ takes the form

$$u_{\epsilon\delta}(x, y, t) = \frac{1}{2\pi} \int_{-\infty}^{\infty} \tilde{H}(\alpha) \Lambda(\alpha) e^{i\Psi(\alpha)} \bar{u}_{\epsilon\delta}(\alpha, y) e^{i\Phi(\alpha, y)} e^{i(\alpha x - \omega_A t)} d\alpha. \quad (7.361)$$

Again, we take $\Lambda(\alpha) = \max |\tilde{u}_{\epsilon\delta}|/\tilde{H}(\alpha)$ as the receptivity measure. The integral is closed in the upper half-plane and is evaluated using residue theory. There will also be contributions from the continuous spectrum; we will neglect those contributions because only the response of the Tollmien-Schlichting wave is of interest to us. The integrand is singular at $\alpha = \alpha_{TS}$ and the corresponding residue will be denoted as $K(\alpha_{TS})$. The Tollmien-Schlichting wave amplitude at Reynolds number Re is then given as

$$A(Re) = |\epsilon\delta K(\alpha_{TS}) \tilde{H}(\alpha_{TS})|. \quad (7.362)$$

This expression is analogous to the “efficiency function” introduced by Goldstein (1983) using asymptotic techniques. Figure 7.48(a) shows the response residue $K(\alpha_{TS})$ as a function of the frequency. We use a scaled frequency S_0 defined as $S_0 = 10^{-6} F Re^{3/2}$, which arises in asymptotic theories of receptivity. For small frequencies, corresponding to locations upstream of branch I, the residues are independent of the frequency. This finding agrees with the asymptotic theory of Goldstein (1983). For larger values of S_0 , we observe a distinct frequency dependence of the residue curves which demonstrates that the Reynolds number scaling of S_0 does not fully capture the receptivity behavior downstream of branch I.

Figure 7.48(b) displays the receptivity amplitude $A(Re)/\epsilon$ as a function of the height of a rectangular surface irregularity. The nondimensional frequency is $F = 49.3$. We observe a linear dependence of the receptivity amplitude on the height. The symbols in Figure 7.48(b) represent experimental results. For small values of δ we have very good agreement between theory and experiment. For heights beyond $\delta \approx 0.3$ the experimental results deviate from the linear amplitude-height relation. Asymptotic studies (see Bodonyi & Smith, 1981) that are nonlinear in the surface height δ predict this type of behavior.

Receptivity to fundamental and subharmonic secondary instabilities of two-dimensional boundary layers has been investigated by Crouch (1997) where the finite-amplitude Tollmien-Schlichting wave has been included as part of the base flow leading to a nonhomogeneous system with periodic coefficients.

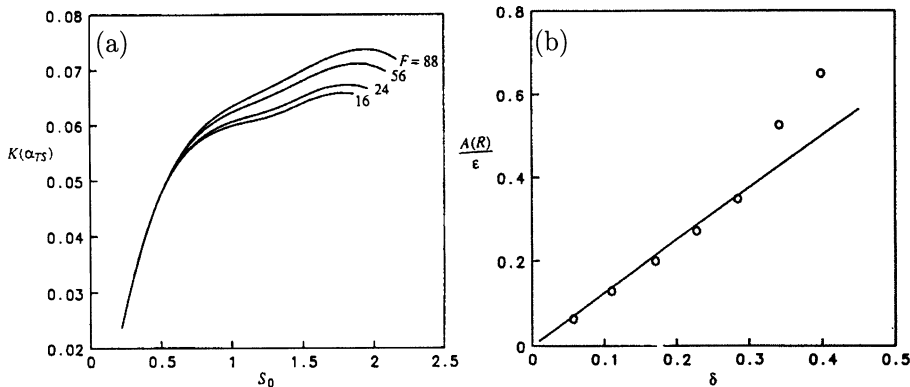


FIGURE 7.48. (a) Variation of the response residue $K(\alpha_{TS})$ as a function of the scaled frequency S_0 for different values of the frequency parameter F ; (b) Variation of the receptivity amplitude $A(\text{Re})/\epsilon$ with the hump height δ at $F = 49.34$, $\text{Re} = 582$, $d = 31.6$. Comparison to the experiments of Saric *et al.* (1991). From Crouch (1992a).

7.6.3 An Adjoint Approach to Receptivity

A different approach to receptivity is based in adjoint fields. In Section 3.3.1 we have introduced the adjoint Orr-Sommerfeld and Squire operators. We will now use the solutions of these adjoint operators to compute sensitivity measures for the solutions of the linearized Navier-Stokes equations and thus address the issue of receptivity to external forcing. The analysis closely follows the work of Hill (1995).

The Lagrange identity and generalized Green's theorem

We begin with the derivation of the Lagrange identity and the generalized Green's theorem – the two key elements of receptivity analysis based on adjoints.

The governing equations for linear velocity and pressure disturbances are given by

$$\frac{\partial \mathbf{v}}{\partial t} + \mathcal{L}\mathbf{v} + \nabla p = 0 \quad (7.363)$$

$$\nabla \cdot \mathbf{v} = 0 \quad (7.364)$$

with the linear operator \mathcal{L} defined as

$$(\mathcal{L}\mathbf{v})_i = U_j \frac{\partial v_i}{\partial x_j} + v_j \frac{\partial U_i}{\partial x_j} - \frac{1}{\text{Re}} \frac{\partial^2 v_i}{\partial x_j \partial x_j}. \quad (7.365)$$

The equations have been linearized about a steady flow \mathbf{U} , taken as the Blasius boundary layer flow, and the Reynolds number is based on the freestream velocity U_∞ and a characteristic length scale (such as the boundary layer displacement thickness). From the preceding equations we can derive the Lagrange identity

$$\begin{aligned} & \left[\left(\frac{\partial \mathbf{v}}{\partial t} + \mathcal{L}\mathbf{v} + \nabla p \right) \cdot \mathbf{v}^+ + (\nabla \cdot \mathbf{v}) p^+ \right] + \\ & \left[\mathbf{v} \cdot \left(\frac{\partial \mathbf{v}^+}{\partial t} + \mathcal{L}^+ \mathbf{v}^+ + \nabla p^+ \right) + p (\nabla \cdot \mathbf{v}^+) \right] = \frac{\partial}{\partial t} (\mathbf{v} \cdot \mathbf{v}^+) + \nabla \cdot \mathbf{J}(\mathbf{s}, \mathbf{s}^+) \end{aligned} \quad (7.366)$$

where \mathcal{L}^+ is the adjoint linearized Navier-Stokes operator and \mathbf{v}^+ and p^+ are the adjoint velocity vector and pressure, respectively. The variables \mathbf{s} and \mathbf{s}^+ stand for the variables (\mathbf{v}, p) and (\mathbf{v}^+, p^+) . The vector quantity $\mathbf{J}(\mathbf{s}, \mathbf{s}^+)$ is known as the bilinear concomitant:

$$\mathbf{J}_j(\mathbf{s}, \mathbf{s}^+) = v_i \sigma_{ij}^+ + \sigma_{ij} v_i^+, \quad (7.367)$$

where

$$\sigma_{ij} = p \delta_{ij} - \frac{1}{\text{Re}} \frac{\partial v_i}{\partial x_j} + U_j v_i \quad (7.368)$$

$$\sigma_{ij}^+ = p^+ \delta_{ij} + \frac{1}{\text{Re}} \frac{\partial v_i^+}{\partial x_j}. \quad (7.369)$$

The Lagrange identity is found by integration by parts similar to the derivation outlined in Appendix C. The second term in square brackets on the left-hand side of (7.366) defines the adjoint linearized Navier-Stokes equations. The integral over space and time of (7.366) represents the generalized Green's theorem applied to the linearized Navier-Stokes equations.

Choosing α, α^+ as streamwise wave numbers for the regular and adjoint problems, respectively, and ω, ω^+ as the corresponding frequencies, we assume a normal-mode form for the disturbance velocities and pressure. Upon substitution into the Lagrange identity (7.366), the left-hand side evaluates to zero yielding the following expression (see Grosch & Salwen, 1978)

$$-(\omega - \omega^+) \langle \phi_{\alpha\omega}, \phi_{\alpha^+, \omega^+}^+ \rangle + (\alpha - \alpha^+) [\phi_{\alpha\omega}, \phi_{\alpha^+, \omega^+}^+] = 0 \quad (7.370)$$

with

$$\begin{aligned}\left\langle \phi_{\alpha\omega}, \phi_{\alpha^+, \omega^+}^+ \right\rangle &= \int_0^\infty \mathbf{v} \cdot \mathbf{v}^+ dy \\ \left[\phi_{\alpha\omega}, \phi_{\alpha^+, \omega^+}^+ \right] &= \int_0^\infty \mathbf{J}_x(\mathbf{s}, \mathbf{s}^+) dy.\end{aligned}\tag{7.371}$$

These expressions define inner products for the temporal and spatial stability problem.

Response to a time-harmonic source distribution

We will use the Lagrange identity (7.366) to solve a general forced-response problem including sources of momentum and mass, as well as forcing through unsteady boundary conditions. We investigate the problem

$$-i\omega \hat{\mathbf{v}} + \mathcal{L} \hat{\mathbf{v}} + \nabla \hat{p} = \mathbf{q}(x, y; \omega) \tag{7.372}$$

$$\nabla \cdot \hat{\mathbf{v}} = \phi(x, y; \omega) \tag{7.373}$$

$$\hat{\mathbf{v}} = \mathbf{v}_b(x; \omega) \quad \text{on } y = 0 \tag{7.374}$$

where the source terms are assumed to be localized in x . Using the Lagrange identity (7.366), including these source terms, integrating both in the normal y -direction and the streamwise x -direction, and assuming a modal dependence $\sim \exp[i(\alpha x - \omega t)]$ for the regular and adjoint solutions, we obtain

$$\begin{aligned}a^{(2)} - a^{(1)} &= \int_{x_1}^{x_2} \int_0^\infty \mathbf{q}(x, y, \omega) \cdot \mathbf{v}_{\alpha\omega}^+(y) e^{-i\alpha x} dy dx \\ &\quad + \int_{x_1}^{x_2} \int_0^\infty \phi(x, y, \omega) p_{\alpha\omega}^+(y) e^{-i\alpha x} dy dx \\ &\quad + \int_{x_1}^{x_2} \mathbf{v}_b(x, \omega) \cdot \mathbf{S}_{\alpha\omega}^+ e^{-i\alpha x} dx\end{aligned}\tag{7.375}$$

where $a^{(1)}$ and $a^{(2)}$ denote the amplitudes of the mode $\phi_{\alpha\omega}$ at the streamwise locations x_1 and x_2 , respectively.

Any non-zero contribution from the right-hand side will influence the amplitude of the mode $\phi_{\alpha\omega}$. The first term accounts for effects of the momentum source weighted by the adjoint velocity vector. The second term represents the influence of the mass source with the adjoint pressure as the weight function. The last term describes the effects of boundary conditions with the adjoint quantity $\mathbf{S}_{\alpha\omega}^+$ as the weight function. $\mathbf{S}_{\alpha\omega}^+$ is referred to as the adjoint stress and is defined as

$$\mathbf{S}_{\alpha\omega}^+ = \left(p_{\alpha\omega}^+ \hat{\mathbf{y}} + \frac{1}{\text{Re}} \frac{\partial u_{\alpha\omega}^+}{\partial y} \hat{\mathbf{x}} \right)_{y=0}. \quad (7.376)$$

The adjoint stress is a measure of how efficient wall irregularities can excite normal modes. For more details on the derivation of (7.375) the reader is referred to Hill (1995).

The vibrating ribbon problem using the adjoint formulation

Expression (7.375) can be used to determine the response of a normal mode to any type of periodic and spatially localized forcing. In particular, we will revisit the vibrating ribbon problem of Section 7.3.3 and try to reproduce the receptivity results using the adjoint formulation.

The vibrating ribbon is placed in a Blasius boundary layer at $y = 0$. For $t > 0$, it induces a normal velocity field of the form

$$\mathbf{v}_b(x, t) = \delta(x) \exp[-i\omega t] \hat{\mathbf{y}}. \quad (7.377)$$

Using equation (7.375) the response to the vibrating ribbon is

$$\int_{x_1}^{x_2} \delta(x) \hat{\mathbf{y}} \cdot \mathbf{S}_{\alpha\omega}^+ e^{-i\alpha x} dx = p_{\alpha\omega}^+(0). \quad (7.378)$$

The result of Ashpis & Reshotko (1990) reads

$$\frac{i}{(\partial v / \partial \alpha)(0, \alpha, \omega)}. \quad (7.379)$$

Expressions (7.378) and (7.379) are equivalent: First we differentiate the linearized Navier-Stokes equations with respect to α . Substituting the partial derivatives of the dependent variables and the adjoint eigenfunctions into the Lagrange identity (7.366), we obtain

$$-i\hat{\mathbf{x}} \cdot \mathbf{J}(\mathbf{s}, \mathbf{s}^+) = \frac{\partial}{\partial y} (\hat{\mathbf{y}} \cdot \mathbf{J}(\mathbf{s}_\alpha, \mathbf{s}^+)). \quad (7.380)$$

Finally, we integrate over y from $y = 0$ to ∞ to obtain

$$\frac{i}{(\partial v / \partial \alpha)(0, \alpha, \omega)} = p_{\alpha\omega}^+(0) \quad \text{with} \quad [\phi_{\alpha\omega}, \phi_{\alpha\omega}^+] = 1 \quad (7.381)$$

which confirms the equivalence of the results obtained by Ashpis & Reshotko (1990) and the expression obtained by the adjoint technique.

Receptivity of boundary layers to surface roughness

In a similar way, the receptivity of Tollmien-Schlichting waves to surface roughness can be cast in the mathematical framework of adjoint fields. We will introduce a momentum source, taking into account nonparallel effects of the mean flow and a forcing applied at the boundary that models the presence of a localized patch of surface roughness. The forcing terms are (see Hill (1995))

$$\mathbf{q}(x, y; \omega) = -\hat{\mathbf{x}} \left(V \frac{du}{dy} + u \frac{\partial U}{\partial x} \right) - \hat{\mathbf{y}} u \frac{\partial V}{\partial x} \quad (7.382)$$

$$\phi(x, y; \omega) = 0 \quad (7.383)$$

$$\mathbf{v}_b(x; \omega) = -h(x) \frac{du}{dy} \hat{\mathbf{x}} \quad \text{on } y = 0 \quad (7.384)$$

with $u(y)$ as the profile of the freestream forcing and $h(x)$ representing the surface roughness.

The response of a Tollmien-Schlichting wave to this type of forcing is given as

$$A = - \int_{-X}^X \int_0^\infty \left(u_{\alpha\omega}^+ \left(V \frac{du}{dy} + u \frac{\partial U}{\partial x} \right) + v_{\alpha\omega}^+ u \frac{\partial V}{\partial x} \right) e^{-i\alpha x} dy dx \\ - \left(\frac{du}{dy} \right)_{y=0} (\hat{\mathbf{x}} \cdot \mathbf{S}_{\alpha\omega}^+) \hat{h}(\alpha) \quad (7.385)$$

which assumes that there is no incoming Tollmien-Schlichting wave from upstream. From this expression the amplitude of the Tollmien-Schlichting wave induced by the freestream disturbance and the surface roughness, i.e., $A = \Lambda \hat{h}(\alpha)$, can be calculated (see Hill (1995)).

Figure 7.49 shows a plot of $|\Lambda|$ as a function of $fRe^{3/2}$ (corresponding to the scaled frequency S_0 in Figure 7.48(a)) for various frequencies. The plot includes the asymptotic theory of Goldstein (1983), which is valid near and below branch I of the neutral stability curve in the inviscid limit. $|\Lambda|$ reaches a maximum at $fRe^{3/2} \approx 2$. For high frequencies, this maximum value is above the upper branch of the neutral stability curve; for low frequencies, the maximum is below the upper branch of the neutral stability curve. The receptivity calculations of Crouch (1992a) (see Figure 7.48) agree with the results shown in Figure 7.49.

7.6.4 Receptivity Using Parabolic Evolution Equations

In the previous section we used a modal approach to receptivity that addressed the problem of exciting an eigenmode by external forcing. This

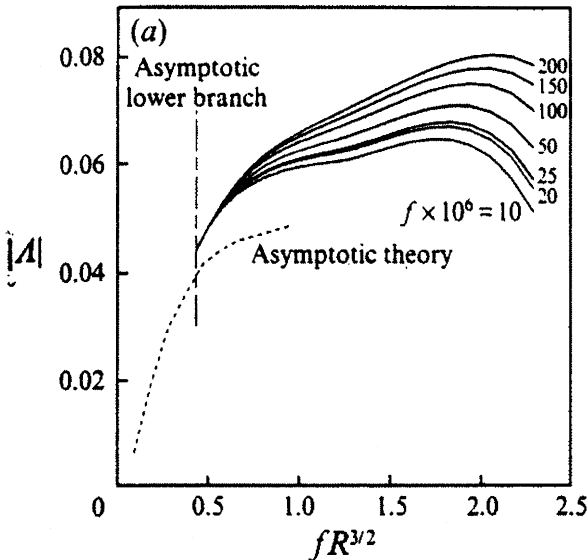


FIGURE 7.49. Plot of $|\Gamma|$ as a function of $fRe^{3/2}$ for various frequencies. Dashed line shows asymptotic theory (Goldstein), valid near the lower branch (chain-dashed line) as $Re \rightarrow \infty$. From Hill (1995).

approach eliminates the explicit x - and t -dependence and replaces it with an α - and ω -dependence. We will extend the idea of receptivity based on adjoint fields and apply it to spatially varying flows that are governed by parabolic evolution equations (see Luchini & Bottaro, 1998). We will first describe the general framework of the receptivity of a dominant (exponential) mode and then take the Görtler flow as an example of receptivity to wall disturbances. The receptivity to surface roughness through its interaction with freestream disturbances requires additional models of the interaction between the freestream disturbances and the roughness, as shown in the earlier sections.

The receptivity of a dominant mode

We can use the mathematical framework developed in Section 7.4.4 to compute receptivity characteristics. We will assume the presence of a dominant mode to which the flow is always attracted sufficiently far downstream. The question we consider is which inflow disturbances, wall disturbances, or momentum sources will optimally excite this dominant mode. We use the same notation as in Section 7.4.4 and label the input disturbance $\mathbf{u}_{\text{in}}(x_0, y)$, the evolution operator \mathcal{A} , and the output disturbance $\mathbf{u}_{\text{out}}(x_f, y)$ with $\mathbf{u}_{\text{out}} = \mathcal{A}\mathbf{u}_{\text{in}}$.

In the presence of a dominant mode we will converge to the same disturbance downstream, as long as the input disturbance has a nonzero projection onto the dominant mode. We introduce

$$\gamma \mathbf{h}(y) = \mathcal{A} \bar{\mathbf{u}}_{\text{in}} \quad (7.386)$$

where $\|\bar{\mathbf{u}}_{\text{in}}\| = 1$ and $\|\mathbf{h}(y)\| = 1$. If $\mathbf{h}(y)$ is a dominant mode, changing $\bar{\mathbf{u}}_{\text{in}}$ only changes the amplitude γ . The energy amplification of an input disturbance is then given as

$$\frac{E(x_f)}{E(x_0)} = \frac{\|\mathbf{u}_{\text{out}}\|^2}{\|\mathbf{u}_{\text{in}}\|^2} = (\mathcal{A} \bar{\mathbf{u}}_{\text{in}}, \mathcal{A} \bar{\mathbf{u}}_{\text{in}}) = \gamma^2 \|\mathbf{h}(y)\|^2 = \gamma^2. \quad (7.387)$$

It is now straightforward to calculate the disturbance that optimally excites the dominant mode. The maximum energy amplification $G(x_f)$ over the spatial interval $[x_0, x_f]$, using appropriate norms, can be expressed as

$$\begin{aligned} G(x_f) &= \max_{\|\mathbf{u}_{\text{in}}\|=1} \|\mathbf{u}_{\text{out}}\|^2 = \max(\mathcal{A} \bar{\mathbf{u}}_{\text{in}}, \mathcal{A} \bar{\mathbf{u}}_{\text{in}}) \\ &= \max \gamma(\mathbf{h}, \mathcal{A} \bar{\mathbf{u}}_{\text{in}}) = \max \gamma(\mathcal{A}^+ \mathbf{h}, \bar{\mathbf{u}}_{\text{in}}) \end{aligned} \quad (7.388)$$

where we have used (7.386) and the definition of the adjoint. Thus the maximum projection onto the dominant mode is given by the unit norm disturbance that is parallel to $\mathcal{A}^+ \mathbf{h}$, i.e.,

$$\bar{\mathbf{u}}_{\text{in}} = \frac{\mathcal{A}^+ \mathbf{h}}{\|\mathcal{A}^+ \mathbf{h}\|} \quad \text{and} \quad \gamma = \frac{\|\mathcal{A} \mathcal{A}^+ \mathbf{h}\|}{\|\mathcal{A}^+ \mathbf{h}\|}. \quad (7.389)$$

A question closely related to receptivity is the question of sensitivity of the output energy to changes in the input energy. Although it is possible to choose any input and output norms, but we will use the energy norm for simplicity. We define the objective function J as

$$J = \frac{E(x_f)}{E(x_0)} \quad (7.390)$$

and calculate the change in J as the unit input $\bar{\mathbf{u}}_{\text{in}}$ is changed by $\delta \mathbf{u}_{\text{in}}$. We have

$$\begin{aligned} \delta J &= (\mathcal{A} \delta \mathbf{u}_{\text{in}}, \mathcal{A} \bar{\mathbf{u}}_{\text{in}}) + (\mathcal{A} \bar{\mathbf{u}}_{\text{in}}, \mathcal{A} \delta \mathbf{u}_{\text{in}}) = \text{Real}\{(\mathcal{A} \bar{\mathbf{u}}_{\text{in}}, \mathcal{A} \delta \mathbf{u}_{\text{in}})\} \\ &= \text{Real}\{\gamma(\mathbf{h}, \mathcal{A} \delta \mathbf{u}_{\text{in}})\} = \text{Real}\{\gamma(\mathcal{A}^+ \mathbf{h}, \delta \mathbf{u}_{\text{in}})\}. \end{aligned} \quad (7.391)$$

Thus the projection of a change in initial condition onto the adjoint of the dominant mode yields the change in the objective function.

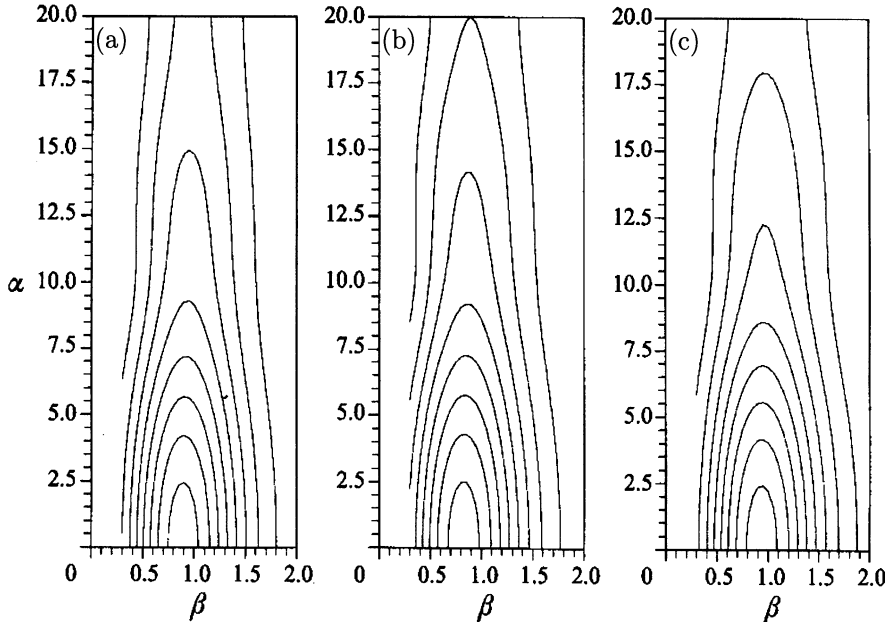


FIGURE 7.50. Contour plots of the receptivity in the spanwise-streamwise wave number space for (a) Φ_4 , (b) Φ_5 , and (c) Φ_6 . $G = 10$. From Luchini & Bottaro (1998).

Receptivity of Görtler vortices to wall disturbances

We will now apply the techniques of the previous section to the problem of Görtler flow and its receptivity to wall disturbances. We have derived the adjoint Görtler equations for zero Görtler number in Section 7.4.4. The adjoint equations for nonzero Görtler numbers are then given by adding the term $-2G^2 U v^+$ to the right-hand side of (7.282).

To assess the influence of wall disturbances on the development of Görtler vortices we introduce general wall boundary conditions of the form

$$u = u_W(x), \quad v = v_W(x), \quad w = w_W(x). \quad (7.392)$$

The derivation of the adjoint equations detailed in Appendix C has to be modified. We still take advantage of the large Reynolds number formulation, i.e., for large streamwise distances from the leading edge the streamwise component $u_1 = u(x_f)$ of the output will be much larger than the normal and spanwise components, $v(x_f)$ and $w(x_f)$. The wall boundary conditions are taken as input variables. We have

$$\mathbf{u}_{\text{in}} = (u_W(x), v_W(x), w_W(x))^T \quad \mathbf{u}_{\text{out}} = (u_1(y), 0, 0)^T. \quad (7.393)$$

To conform to the notation in Section 7.4.4 we define the evolution operator $\bar{\mathcal{A}}$ and norms as follows

$$u_1 = \bar{\mathcal{A}}\mathbf{q} \quad \|u_1\|^2 = \int_0^\infty u_1^2 dy \quad \|\mathbf{q}\|^2 = \int_{x_0}^{x_f} (u_W^2 + v_W^2 + w_W^2) dx \quad (7.394)$$

where $\mathbf{q} = \mathbf{u}_{in} = (u_W, v_W, w_W)^T$.

To derive the operator $\bar{\mathcal{A}}^+$ adjoint to $\bar{\mathcal{A}}$ with respect to the inner products based on the norms (7.394), let $\psi_1(y)$, $\phi_4(x)$, $\phi_5(x)$, and $\phi_6(x)$ be square-integrable functions. We recall that the definition of the adjoint implies

$$(\psi_1, \bar{\mathcal{A}}\mathbf{q}) = (\bar{\mathcal{A}}^+ \psi_1, \mathbf{q}) = (\Phi, \mathbf{q}) \quad (7.395)$$

where

$$(\psi_1, \bar{\mathcal{A}}\mathbf{q}) = \int_0^\infty \psi_1(y) u_1(y) dy \quad (7.396)$$

$$(\Phi, \mathbf{q}) = \int_{x_0}^{x_f} (\phi_4 u_W + \phi_5 v_W + \phi_6 w_W) dx. \quad (7.397)$$

The action of the adjoint $\bar{\mathcal{A}}^+$ on ψ_1 is given by the vector Φ . If these modifications are used in the derivation of the adjoint, we can identify the action of $\bar{\mathcal{A}}^+$ as

$$\phi_4(x) = \frac{\partial u^+}{\partial y}(x, 0) \quad (7.398)$$

$$\phi_5(x) = p^+(x, 0) \quad (7.399)$$

$$\phi_6(x) = \beta \frac{\partial w^+}{\partial y}(x, 0). \quad (7.400)$$

If wall disturbances are represented by a superposition of sinusoidal components, the Fourier transform of (7.398)-(7.400) yields a measure of receptivity to wall irregularities. Figure 7.50 shows the level curves of the absolute values of these Fourier transforms in the α - β plane for a Görtler number of $G = 10$. The wavelengths on the two axes are not directly comparable because of a ratio of \sqrt{Re} between their respective scales. Nevertheless, these curves point out the wave number range of maximum sensitivity, which occurs for $\alpha = 0$ and β close to one. For large spanwise wave numbers wall roughness is inefficient in exciting Görtler vortices. The above results can readily be used to find the receptivity of a specific input disturbance by calculating the inner product of that disturbance with the adjoint of the dominant mode. In this case, receptivity is defined as the response to a certain environmental disturbance, not necessarily to the one resulting in the largest amplification.

8

Secondary Instability

8.1 Introduction

Secondary instability theory deals with the stability analysis of finite-amplitude steady or quasi-steady states that resulted from an earlier primary instability. In many cases a secondary instability is a precursor of transition to turbulent flow. Consequently, secondary instability analysis is sometimes used for transition prediction. In this chapter we will mainly cover the theoretical framework of secondary instability analysis. The role of secondary instabilities in the transition process of various shear flows will be discussed in Chapter 9.

The concept of secondary instability can be described as follows. When disturbances grow to finite amplitudes due to a primary instability, they may saturate to a steady state and establish a new, often more complicated, mean flow. This mean flow in turn may become unstable to infinitesimal disturbances. The linear stability theory of this new modified mean flow is called secondary instability theory. The new stability problem will involve equations with periodic coefficients, and solutions can be found using Floquet analysis. Secondary instability theory can be applied even to quasi-steady mean flows as long as the computed secondary growth rates are significantly larger than the characteristic time scale of the quasi-steady mean flow.

This chapter starts with the secondary instability analysis of two-dimensional waves, discusses secondary instabilities of vortices and streaks, and concludes with a treatment of Eckhaus instabilities of vortices. Eckhaus

instability is a special case of secondary instability, which results in a rearrangement of finite-amplitude structures through merging and splitting. As we will see, the mathematical equations of these types of secondary instability problems have many features in common.

8.2 Secondary Instability of Two-Dimensional Waves

The secondary instability of two-dimensional waves discussed here will mainly deal with Tollmien-Schlichting waves. After deriving the governing stability equations we will study the various types of secondary instabilities and show results from computations and experiments. In what follows we will mainly follow Herbert (1988).

8.2.1 Derivation of the Equations

Mathematically, the secondary instability of Tollmien-Schlichting waves can be analyzed by assuming a base flow consisting of both the original laminar base flow and a finite-amplitude saturated Tollmien-Schlichting wave.

Equations governing the secondary instability of Tollmien-Schlichting waves

If we denote the streamwise and normal velocity components of the saturated Tollmien-Schlichting waves $Au^{2D}(x', y)$ and $Av^{2D}(x', y)$ and their phase speed C we have

$$U_i = [U(y) - C]\delta_{i1} + A[u^{2D}(x', y)\delta_{i1} + v^{2D}(x', y)\delta_{i2}] \quad (8.1)$$

where A is a measure of the amplitude of the waves and $x' = x - Ct$. If this expression is used as a base flow in the linearized Navier-Stokes equations we obtain the following equations governing the linear secondary instability of the finite-amplitude Tollmien-Schlichting waves

$$\begin{aligned} \frac{\partial u}{\partial t} + (U - C)\frac{\partial u}{\partial x'} + U'v + \frac{\partial p}{\partial x'} - \frac{1}{\text{Re}}\nabla^2 u \\ = -A\left[\frac{\partial}{\partial x'}(uu^{2D}) + \frac{\partial}{\partial y}(vu^{2D} + uv^{2D}) - u^{2D}\frac{\partial w}{\partial z}\right] \end{aligned} \quad (8.2)$$

$$\begin{aligned} \frac{\partial v}{\partial t} + (U - C) \frac{\partial v}{\partial x'} + \frac{\partial p}{\partial y} - \frac{1}{\text{Re}} \nabla^2 v \\ = -A \left[\frac{\partial}{\partial x'} (uv^{2D} + vu^{2D}) + \frac{\partial}{\partial y} (vv^{2D}) - v^{2D} \frac{\partial w}{\partial z} \right] \end{aligned} \quad (8.3)$$

$$\frac{\partial w}{\partial t} + (U - C) \frac{\partial w}{\partial x'} + \frac{\partial p}{\partial z} - \frac{1}{\text{Re}} \nabla^2 w = 0 \quad (8.4)$$

$$\frac{\partial u}{\partial x'} + \frac{\partial v}{\partial y} + \frac{\partial w}{\partial z} = 0. \quad (8.5)$$

This is a set of partial differential equations with periodic coefficients in x' due to the periodic nature of the saturated Tollmien-Schlichting waves.

General form of the solution

Floquet theory, applicable to differential equations with periodic coefficients, implies that solutions to these equations take the form

$$u(x', y, z, t) = \hat{u}(x', y) e^{\gamma x'} e^{\sigma t} e^{i\beta z} \quad (8.6)$$

where $\hat{u}(x', y)$ is a periodic function in x' with period $2\pi/\alpha$ and γ is the Floquet parameter. If $\hat{u}(x', y)$ is Fourier transformed in the x' -direction, the general form of the solution can be expressed as

$$u(x', y, z, t) = e^{\gamma x'} e^{\sigma t} e^{i\beta z} \sum_m \hat{u}_m(y) e^{im\alpha x'}. \quad (8.7)$$

Substituting into the governing equations (8.2)-(8.5) and expanding u^{2D} and v^{2D} in a Fourier series results in an infinite system of coupled ordinary differential equations that form an eigenvalue problem.

Classification of modes

The occurrence of two complex quantities, σ and γ , in the secondary instability problem leads to an ambiguity similar to the one associated with the Orr-Sommerfeld equation. Only two of the four real quantities σ_r , σ_i , γ_r , and γ_i are determined by the eigenvalue problem associated with the secondary instability. The remaining two must be chosen.

We observe that γ and $\gamma \pm in\alpha$ yield identical modes for any positive integer n to within a renumbering of the Fourier coefficients. Therefore it suffices to study $-\alpha/2 < \gamma_i \leq \alpha/2$. Introducing the parameter $\epsilon = \gamma_i/\alpha$, we can distinguish the following three cases:

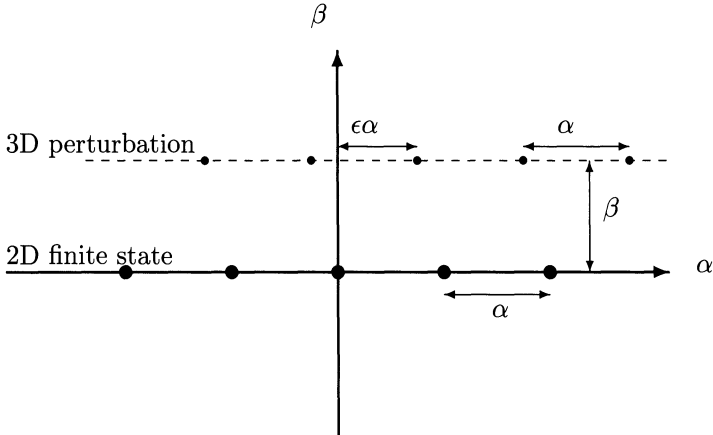


FIGURE 8.1. Sketch of secondary instability of two-dimensional waves in the (α, β) wave number plane.

1. Fundamental modes with $\epsilon = 0$,

$$u(x', y, z, t) = e^{\gamma_r x'} e^{\sigma t} e^{i\beta z} \sum_m \hat{u}_m(y) e^{im\alpha x'}. \quad (8.8)$$

2. Subharmonic modes with $\epsilon = 1/2$,

$$u(x', y, z, t) = e^{\gamma_r x} e^{\sigma t} e^{i\beta z} \sum_m \hat{u}_m(y) e^{i(m+\frac{1}{2})\alpha x'}. \quad (8.9)$$

3. Detuned modes with $0 < \epsilon < 1/2$,

$$u(x', y, z, t) = e^{\gamma_r x} e^{\sigma t} e^{i\beta z} \sum_m \hat{u}_m(y) e^{i(m+\epsilon)\alpha x'}. \quad (8.10)$$

The spatial period of the fundamental modes is identical to the period of the Tollmien-Schlichting waves, while the spatial period of the subharmonic waves is twice the period of the Tollmien-Schlichting waves. Figure 8.1 shows the wave numbers excited by the mean flow (large dots) and the perturbation (small dots) and gives a graphical description of the detuning parameter. The physical solution associated with the detuned case requires two complex conjugate modes with opposite detuning $\pm\epsilon$. Thus, the real disturbance contains wave numbers $m\alpha \pm \gamma_i$, and the sum of such wave number pairs matches the Tollmien-Schlichting wave number. Opposite detuning in wave numbers is associated with opposite detuning in frequency.

The real parts σ_r and γ_r govern the growth of the disturbance in time and space, respectively. It is convenient to measure disturbance growth in the laboratory frame x . We get

$$e^{\sigma_r t} e^{\gamma_r x'} = e^{(\sigma_r - \gamma_r C)t} e^{\gamma_r x}. \quad (8.11)$$

Temporal growth implies that $\gamma_r = 0$ and the growth rate is represented by σ_r , while σ_i can be interpreted as a frequency shift with respect to the Tollmien-Schlichting frequency. Modes with $\sigma_i = 0$ travel with the same phase speed as the Tollmien-Schlichting wave; in this case the detuning is given by γ_i .

Spatial growth in the laboratory frame implies that $\sigma_r = \gamma_r C$, and γ_r provides the spatial growth rate. γ_i is the shift in the streamwise wave number, and the detuning of the frequency is given by $\sigma_i - \gamma_i C$.

Secondary instability equations

We introduce (8.7) (and similar expressions for v and w) into the governing equations (8.2-8.5), and make the so-called shape assumption, implying that the Tollmien-Schlichting wave does not change shape as it saturates and that the \tilde{u}^{2D} and \tilde{v}^{2D} can be taken directly from solutions, \tilde{u}^{TS} and \tilde{v}^{TS} , of the linear Orr-Sommerfeld equation (3.20). This also implies that the Fourier series for \tilde{u}^{TS} and \tilde{v}^{TS} only contain the fundamental wave number which greatly simplifies the analysis. The equations governing the secondary instability become

$$\sigma\tilde{u}_m + i\alpha_m(U - C)\tilde{u}_m + \tilde{v}_m U' + i\alpha_m \tilde{p} - \frac{1}{Re}(\mathcal{D}^2 - k_m^2)\tilde{u}_m = N_v \quad (8.12)$$

$$\sigma\tilde{v}_m + i\alpha_m(U - C)\tilde{v}_m + \mathcal{D}\tilde{p} - \frac{1}{Re}(\mathcal{D}^2 - k_m^2)\tilde{v}_m = N_v \quad (8.13)$$

$$\sigma\tilde{w}_m + i\alpha_m(U - C)\tilde{w}_m + i\beta\tilde{p} - \frac{1}{Re}(\mathcal{D}^2 - k_m^2)\tilde{w}_m = 0 \quad (8.14)$$

$$i\alpha_m\tilde{u}_m + \mathcal{D}\tilde{v}_m + i\beta\tilde{w}_m = 0 \quad (8.15)$$

where

$$N_u = -A [i\alpha_m\tilde{u}_{m\pm 1}\tilde{u}^{TS} + \mathcal{D}(\tilde{v}_{m\pm 1}\tilde{u}^{TS} + \tilde{u}_{m\pm 1}\tilde{v}^{TS}) - i\beta\tilde{w}_{m\pm 1}\tilde{u}^{TS}] \quad (8.16)$$

$$N_v = -A [i\alpha_m(\tilde{u}_{m\pm 1}\tilde{v}^{TS} + \tilde{v}_{m\pm 1}\tilde{u}^{TS}) + \mathcal{D}(v_{m\pm 1}\tilde{v}^{TS}) - i\beta\tilde{w}_{m\pm 1}\tilde{v}^{TS}] \quad (8.17)$$

$$k_m = (m\alpha)^2 + \beta^2 \quad (8.18)$$

$$\alpha_m = m\alpha + \gamma_i \quad (8.19)$$

and $\tilde{u}_{m\pm 1} = \tilde{u}_{m+1} + \tilde{u}_{m-1}$.

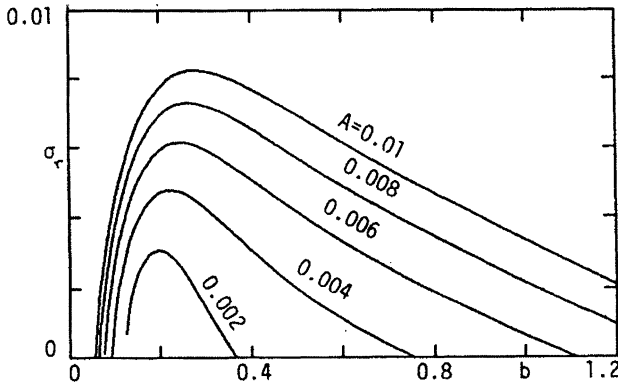


FIGURE 8.2. Subharmonic growth rate σ_r as a function of the spanwise wave number b for $F = 124$, $Re = 606$. From Herbert (1988).

These four equations can be reduced to two equations by applying manipulations used in the derivation of the Orr-Sommerfeld and Squire equations. It is also possible to reformulate the equations for the case of fundamental or subharmonic modes such that they contain only real coefficients (see Herbert, 1988).

The Fourier series needs to be truncated when a numerical solution is sought. For subharmonic modes the lowest possible truncation includes $m = 0$ and $m = -1$, which corresponds to the subharmonic wave numbers $\alpha/2$ and $-\alpha/2$, respectively. The lowest approximation for fundamental modes includes $m = 1$, $m = 0$, and $m = -1$, which corresponds to wave numbers α , 0, and $-\alpha$, respectively. In the fundamental case a streamwise-independent mode is included in the secondary instability disturbance.

8.2.2 Numerical Results

In the following numerical results the lowest possible truncation has been used for both the subharmonic and fundamental modes. In addition, the frequency parameter $F = 10^6 \alpha_r c_r / Re$ and the spanwise wave number $b = 10^3 \beta / Re$ are used. The amplitude A is measured as the maximum of the root-mean-square value of the streamwise disturbance velocity.

Subharmonic modes

The growth rate of the first temporal subharmonic mode as a function of the spanwise wave number is shown in Figure 8.2. At small amplitudes instability is restricted to a narrow band of spanwise wave numbers, while for larger amplitudes A the range of unstable waves broadens and shifts toward larger values of the spanwise wave number. There is a sharp cutoff at lower wave numbers.

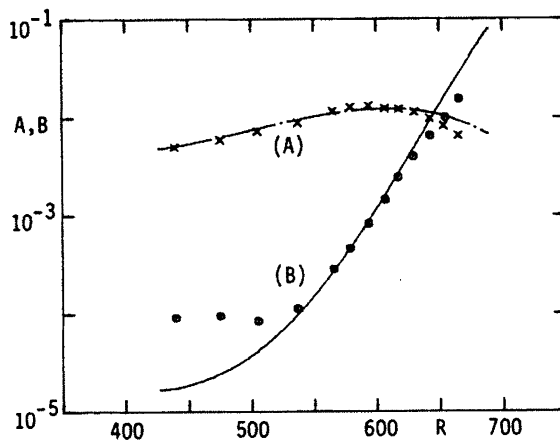


FIGURE 8.3. Amplitude variation with Re at $F = 124$, $b = 0.33$ for (A) the TS-wave ($A = 0.0044$) and (B) the subharmonic disturbance ($B = 1.26 \times 10^{-5}$). Comparison between theory (solid lines) and experiments by Kachanov & Levenschenko (1984) (x, o). From Herbert (1988).

The integrated growth rates for both the Tollmien-Schlichting wave and the subharmonic mode are compared to experiments by Kachanov & Levenschenko (1984) in Figure 8.3. The initial amplitude of the Tollmien-Schlichting wave was matched to the experimental value.

Comparison between fundamental and subharmonic modes

Numerical results indicate that subharmonic modes represent the most unstable secondary instability disturbances in Blasius boundary layers. Figure 8.4 shows secondary instability calculations and direct numerical simulations of fundamental and subharmonic modes. There is good agreement between the calculations and the experiments.

Because the fundamental mode is associated with a zero streamwise wave number component, it represents a spanwise varying mean component of the secondary instability disturbance. The spanwise position where the mean profile has its maximum is called the peak position, the location of the minimum is called the valley. Figure 8.5 shows measurements of the fundamental mode superimposed on the Tollmien-Schlichting wave. The difference between the peak and valley positions indicates the presence of the fundamental secondary instability disturbance.

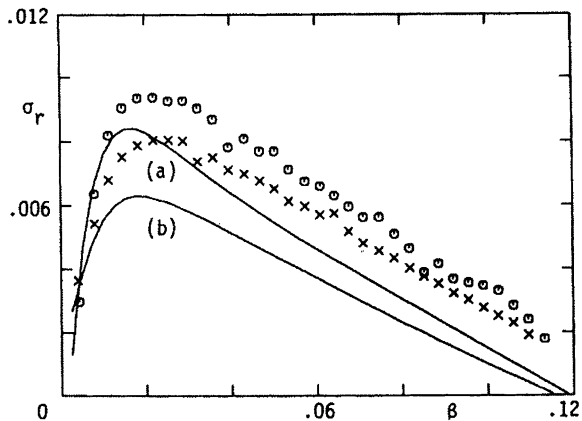


FIGURE 8.4. Growth rates of three-dimensional disturbances as a function of the spanwise wave number β for $F = 58.8$, $Re = 950$ and $A = 0.014$. Theory by Herbert: (a) subharmonic, (b) fundamental. DNS computations by Spalart & Yang: (o) subharmonic, (x) fundamental. From Spalart & Yang (1987).

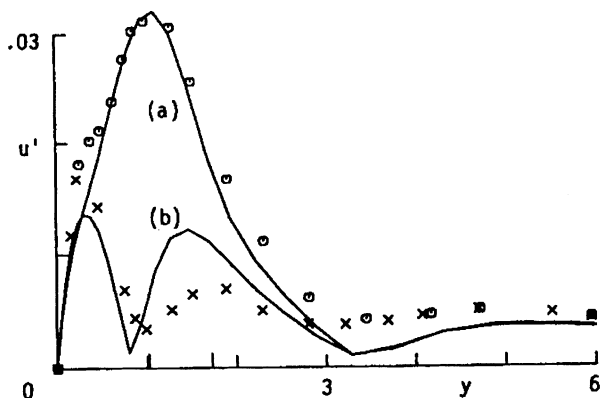


FIGURE 8.5. Distribution of streamwise disturbance velocity across the boundary layer for $F = 58.8$, $b = 0.243$ and $Re = 960$. Theory by Herbert: (a) peak, (b) valley. Experiment by Klebanoff *et al.*: (o) peak, (x) valley. From Herbert (1988).

8.2.3 Elliptical Instability

Flows with elliptical streamlines

When viewed in a frame of reference moving with the phase velocity of the two-dimensional Tollmien-Schlichting waves, the streamlines of the saturated flow show closed elliptical regions. Results of secondary instability calculations show that the largest disturbance amplitudes are concentrated in these regions. Pierrehumbert (1986) hypothesized that the ellipticity of these regions is essential for the rapid growth of secondary instabilities and tested this hypothesis by examining the stability of the flow

$$(U, V, 0) = ((\delta + 1/2)y, (\delta - 1/2)x, 0). \quad (8.20)$$

He found results that were in qualitative agreement with the secondary instability calculations for Tollmien-Schlichting waves.

Simple model of elliptical instability

Bayly (1986) proposed a simple model of the elliptical instability, which sheds light on the growth mechanisms involved. He noted that if $\delta = 0$ the flow given by (8.20) reduces to a state of rigid rotation that supports simple plane wave solutions in a rotating frame of reference. Such a solution for elliptical flow takes the form

$$(u_j, p) = (\tilde{u}_j, \tilde{p}) e^{ik_j(t)x_j} \quad (8.21)$$

where \tilde{u}_j , k_j and x_j are the three components of the perturbation velocity, wave number vector, and coordinate directions, respectively. Upon substitution into the inviscid disturbance equations we obtain

$$\frac{\partial \tilde{u}_j}{\partial t} + ik_n x_n \tilde{u}_j + i A_{mn} k_m k_n \tilde{u}_j + A_{mj} \tilde{u}_j = ik_j \tilde{p} \quad (8.22)$$

$$k_j \tilde{u}_j = 0 \quad (8.23)$$

where

$$\{A_{mn}\} = \begin{pmatrix} 0 & \delta + 1/2 & 0 \\ \delta - 1/2 & 0 & 0 \\ 0 & 0 & 0 \end{pmatrix}. \quad (8.24)$$

Equating terms linear in x_j we arrive at an equation for k_j , which has the solution

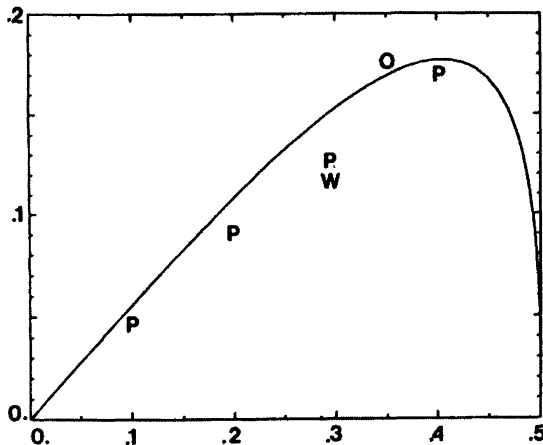


FIGURE 8.6. Growth rate of elliptical instability, maximized over angle and normalized by unit vorticity, as a function of the eccentricity parameter E . Solid line from Floquet theory (Landman & Saffman, 1987); points P are numerical results of Pierrehumbert (1986), point O is from Orszag & Patera (1983) and point W is from Pierrehumbert & Widnall (1982). From Bayly *et al.* (1988).

$$\begin{pmatrix} k_1 \\ k_2 \\ k_3 \end{pmatrix} = \begin{pmatrix} \sin \theta \cos \Omega t \\ E \sin \theta \cos \Omega t \\ \cos \theta \end{pmatrix} \quad (8.25)$$

with

$$E = \sqrt{(1/2 + \delta)/(1/2 - \delta)} \quad \Omega = \sqrt{1/4 - \delta^2} \quad (8.26)$$

and θ as the minimum angle between the wave vector and the y -axis.

By eliminating the pressure term and using the incompressibility constraint (8.23), an equation for \tilde{u}_j can be found

$$\frac{\partial \tilde{u}_j}{\partial t} = (2k_m k_n / k_i k_i - \delta_{mn}) A_{mn} \tilde{u}_j. \quad (8.27)$$

which can be analyzed by Floquet theory due to the periodicity of k_j . Waleffe (1990) showed that the known exponential solutions of this equation can be superimposed to form localized exponentially growing solutions with a remarkable resemblance to the numerical solutions of Pierrehumbert (1986).

Comparison with secondary instability results

Landman & Saffman (1987) noted that viscous effects could easily be added to the solutions of Bayly (1986). The growth rate of the elliptical instability, maximized over θ , is shown in Figure 8.6 together with the secondary

instability growth rates found by various other researchers. It is interesting that the simple elliptical instability model captures the main features of the secondary instability of two-dimensional Tollmien-Schlichting waves, thus indicating that the main reason Tollmien-Schlichting are unstable to three-dimensional perturbations lies in the elliptic streamlines found in the vicinity of their critical layers.

8.3 Secondary Instability of Vortices and Streaks

8.3.1 Governing Equations

General form of the disturbance equations

The breakdown of streaks and vortical flows may in many cases be understood by the growth and breakdown of secondary instability modes growing on finite-amplitude saturated vortices. Secondary instability calculations have been performed with basic flows taken from a number of flow situations and have produced rather similar results for Görtler vortices, crossflow vortices, vortices in rotating and curved channel flows, and boundary layer streaks.

In most secondary instability calculations of this type, the streamwise development of the mean flow is neglected, and the following parallel flow is used as a base flow

$$U_i = U(y, z)\delta_{1i} + V(y, z)\delta_{2i} + W(y, z)\delta_{3i} \quad (8.28)$$

where the y - z plane is perpendicular to the vortex axis. If this mean flow is used in the linearized Navier-Stokes equations we obtain the following equations governing the linear secondary instability of the spanwise periodic structure

$$\left[i\alpha U + \frac{\alpha^2}{Re} \right] \hat{u} + U_y \hat{v} + U_z \hat{w} + i\alpha \hat{p} + V \hat{u}_y + W \hat{u}_z - \frac{1}{Re} [\hat{u}_{yy} + \hat{u}_{zz}] = i\omega \hat{u} \quad (8.29)$$

$$\left[i\alpha U + \frac{\alpha^2}{Re} + V_y \right] \hat{v} + V_z \hat{w} + \hat{p}_y + V \hat{v}_y + W \hat{v}_z - \frac{1}{Re} [\hat{v}_{yy} + \hat{v}_{zz}] = i\omega \hat{v} \quad (8.30)$$

$$\left[i\alpha U + \frac{\alpha^2}{Re} + W_z \right] \hat{w} + W_y \hat{v} + \hat{p}_z + V \hat{w}_y + W \hat{w}_z - \frac{1}{Re} [\hat{w}_{yy} + \hat{w}_{zz}] = i\omega \hat{w} \quad (8.31)$$

$$i\alpha \hat{u} + \hat{v}_y + \hat{w}_z = 0. \quad (8.32)$$

We have assumed that the disturbances have exponential dependence in the streamwise direction (wave number α) and in time (angular frequency ω). There are a number of simplifications that can be made regarding the preceding equations. We will discuss some of them below.

Velocity-vorticity formulation for the streak instability

If we are dealing with a streak rather than a vortex-dominated mean flow, we may assume that the streamwise velocity component is much larger than the spanwise and normal components. Thus the latter two components can be neglected and the base flow takes the form $U_i = U(y, z)\delta_{1i}$. It has been found in numerical simulations of streaks that the streamwise velocity contributes more than 99 percent of the total energy of the streak (see, e.g., Reddy *et al.*, 1998). This assumption allows us to reformulate equations (8.29)-(8.32) in terms of the normal velocity and normal vorticity. After a derivation similar to the one leading to the Orr-Sommerfeld-Squire equations, we obtain

$$(-i\omega + i\alpha U)\hat{\nabla}^2\hat{v} + i\alpha U_{zz}\hat{v} + 2i\alpha U_z\hat{v}_z - i\alpha U_{yy}\hat{v} - 2i\alpha U_z\hat{w}_y - 2i\alpha U_{yz}\hat{w} - \frac{1}{Re}\hat{\nabla}^4\hat{v} = 0 \quad (8.33)$$

$$(-i\omega + i\alpha U)\hat{\eta} - U_z\hat{v}_y + U_{zy}\hat{v} + U_y\hat{v}_z + U_{zz}\hat{w} - \frac{1}{Re}\hat{\nabla}^2\hat{\eta} = 0 \quad (8.34)$$

where

$$\hat{\nabla}^2 = \frac{\partial^2}{\partial y^2} + \frac{\partial^2}{\partial z^2} - \alpha^2. \quad (8.35)$$

At a solid wall or in the freestream we have the boundary conditions $\hat{v} = \hat{v}_y = \hat{\eta} = 0$. The normal vorticity $\hat{\eta}$ is defined as $\hat{u}_z - i\alpha\hat{w}$. The spanwise velocity can be eliminated in this equation using the identity

$$-\alpha^2\hat{w} + \hat{w}_{zz} = -i\alpha\hat{\eta} - \hat{v}_{yz}. \quad (8.36)$$

The streak can be represented in the form

$$U(y, z) = \text{Real}\{U_0(y) + 2\sum_{k=1}^{\infty} U_k(y) e^{ik\beta z}\} \quad (8.37)$$

where it is assumed that the functions $\{U_k\}$ decay to zero rapidly as $k \rightarrow \infty$, and we assume that all U_k are real. The normal velocity and normal vorticity of the perturbation have the general form

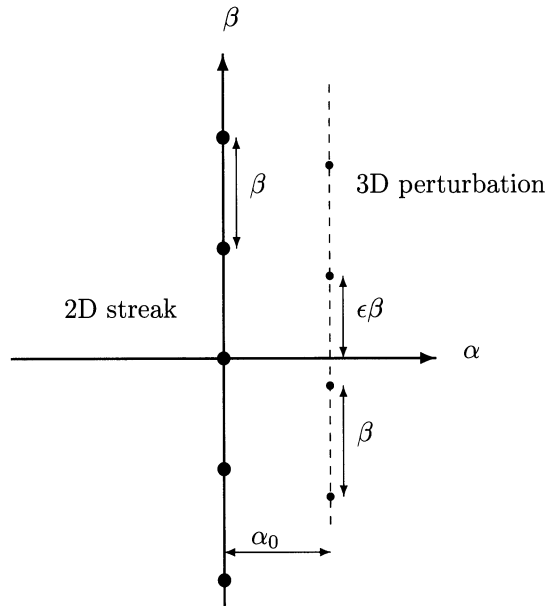


FIGURE 8.7. Sketch of secondary instability of two-dimensional vortex or streak in the (α, β) wave number plane.

$$\hat{v}(y, z) = \sum_{k=-m}^m \tilde{v}_k(y) e^{(ik\beta + \gamma)z} \quad (8.38)$$

$$\hat{\eta}(y, z) = \sum_{k=-m}^m \tilde{\eta}_k(y) e^{(ik\beta + \gamma)z} \quad (8.39)$$

where β is the fundamental spanwise wave number and γ is the Floquet detuning constant; see Figure 8.7 with $\epsilon = \gamma_i/\beta$. In this case, even and odd disturbances can be considered separately. We will discuss the classification of modes later.

It is instructive to compare the general form of the solution given above with the solution for the secondary instability of two-dimensional waves (see the previous section); compare Figures 8.7 and 8.1.

The inviscid limit

For base flows that are derived from a boundary layer approximation of the Navier-Stokes equations – such as Görtler vortices or streaks – the coefficients in the secondary instability equations that contain the normal V

or spanwise W velocities are of the same order as the viscous terms. In the inviscid limit ($\text{Re} \rightarrow \infty$) the governing equations thus greatly simplify, and one can readily derive a single partial differential equation for the disturbance pressure. If we first take the divergence of the momentum equations, take advantage of the continuity equation, and then use the normal and spanwise momentum equations, we find

$$(U - c)\hat{\nabla}^2\hat{p} - U_y\hat{p}_y - U_z\hat{p}_z = 0 \quad (8.40)$$

with boundary conditions $\hat{p}_y(y = 0) = \hat{p}(y = \infty) = 0$ and $\alpha = c/\omega$. For Görtler vortices this equation was derived by Hall & Horstman (1991). Earlier, Henningson (1987) used the same equations in an instability analysis of flows with spanwise variations in the mean velocity profile.

Once the pressure eigenfunctions are computed, the velocity components can be obtained from

$$i\alpha(U - c)\hat{v} = -\hat{p}_y \quad (8.41)$$

$$i\alpha(U - c)\hat{w} = -\hat{p}_z \quad (8.42)$$

$$i\alpha(U - c)\hat{u} + U_y\hat{v} + U_z\hat{w} = -i\alpha\hat{p}. \quad (8.43)$$

The pressure component \tilde{p} is expanded in an infinite sum of Fourier modes

$$\hat{p}(y, z) = \sum_{k=-\infty}^{\infty} \tilde{p}_k(y) e^{i(k+\epsilon)\beta z} \quad (8.44)$$

where β is the spanwise wave number of the primary disturbance field and ϵ is the detuning parameter shown in Figure 8.7.

We observe two symmetries: First, to within renumbering of the Fourier coefficients, ϵ and $\epsilon \pm n$ yield identical modes for any integer n . Second, the pressure equation is invariant under the reflection $z \rightarrow -z$. These symmetries allow us to restrict our study to values of ϵ between zero and one-half, with $\epsilon = 0$ corresponding to a fundamental instability mode, and $\epsilon = 0.5$ corresponding to a subharmonic mode. The first symmetry is also present in the secondary instability of two-dimensional waves, whereas the second symmetry is unique to the study of secondary instabilities for streaks and vortices and is only valid in the absence of a mean flow in the spanwise direction.

The mean field is also expanded as a sum of Fourier modes. For simplicity we include only the first Fourier component,

$$U(y, z) = U_0(y) + \frac{A}{2}U_1(y) e^{i\beta z} + \frac{A}{2}U_1(y) e^{-i\beta z}. \quad (8.45)$$

The expansion of the disturbance and mean field are introduced into equation (8.40) to yield an equation that holds for each integer k :

$$\begin{aligned} & \left\{ \frac{A}{2} U_1 [\mathcal{D}^2 - \beta^2(k-1+\epsilon)(k-3+\epsilon) - \alpha^2] - A U_{1,y} \mathcal{D} \right\} \tilde{p}_{k-1} \\ & + \{(U_0 - c) [\mathcal{D}^2 - \beta^2(k+\epsilon)^2 - \alpha^2] - 2 U_{0,y} \mathcal{D}\} \tilde{p}_k \\ & + \left\{ \frac{A}{2} U_1 [\mathcal{D}^2 - \beta^2(k+1+\epsilon)(k+3+\epsilon) - \alpha^2] - A U_{1,y} \mathcal{D} \right\} \tilde{p}_{k+1} = 0. \end{aligned} \quad (8.46)$$

The appropriate boundary conditions are:

$$\mathcal{D}\tilde{p}_k = 0 \text{ at } y = 0 \quad (8.47)$$

and

$$\mathcal{D}\tilde{p}_k \rightarrow 0 \text{ as } y \rightarrow \infty. \quad (8.48)$$

This problem consists of an infinite number of coupled ordinary differential equations, which must be truncated to find a numerical solution. The complete system must be solved numerically for arbitrary values of the detuning parameter ϵ . If, however, even and odd solutions in z are sought, the system of equations can be further simplified for fundamental and subharmonic modes. In this case the numerical effort is decreased considerably because the dimension of the matrices arising from the discretization is reduced to one-half.

In the fundamental ($\epsilon = 0$) case, even (odd) modes are obtained by imposing the condition $\tilde{p}_{-k} = \tilde{p}_k$ ($\tilde{p}_{-k} = -\tilde{p}_k$). This is equivalent to introducing either a cosine or a sine expansion

$$\hat{p}(y, z) = \sum_{k=0}^{\infty} \tilde{p}_k(y) \cos(\beta kz) \quad (8.49)$$

$$\hat{p}(y, z) = \sum_{k=1}^{\infty} \tilde{p}_k(y) \sin(\beta kz) \quad (8.50)$$

into equation (8.40).

In the case of subharmonic disturbances ($\epsilon = 0.5$) the spanwise periodicity of the fluctuations is twice that of the base flow. The subharmonic modes can also be decoupled into even and odd modes. In this case the cosine and sine expansions are:

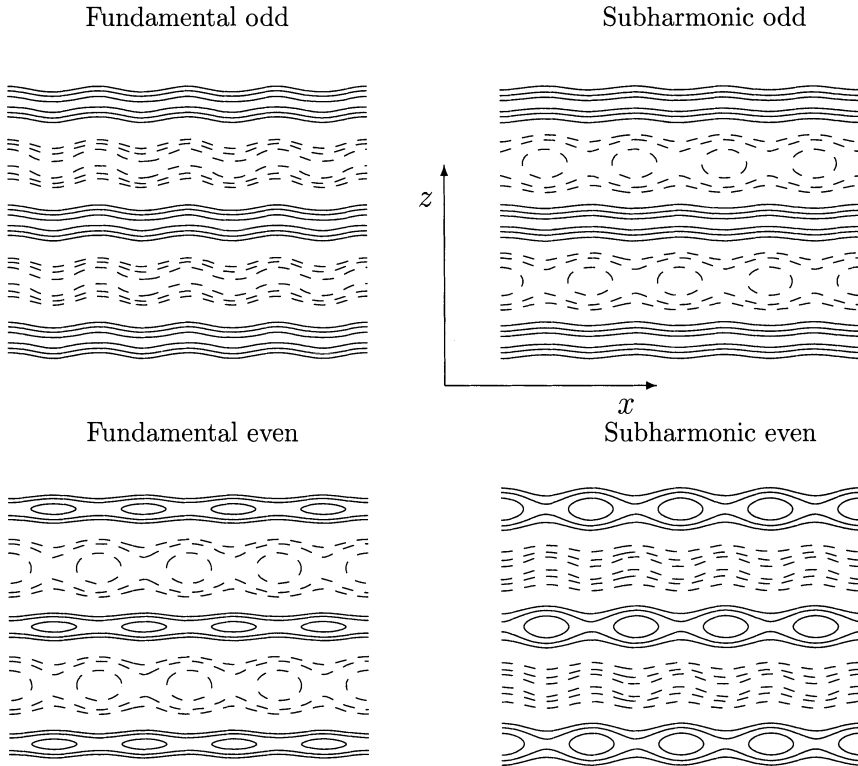


FIGURE 8.8. Sketch of streak instability modes in the $x - z$ plane over four streamwise and two spanwise periods, by contours of the total streamwise velocity. Low-speed streaks are drawn with dashed lines; solid lines are used for high-speed streaks.

$$\hat{p}(y, z) = \sum_{k=0}^{\infty} \tilde{p}_k(y) \cos(\beta z \frac{2k+1}{2}) \quad (8.51)$$

$$\hat{p}(y, z) = \sum_{k=0}^{\infty} \tilde{p}_k(y) \sin(\beta z \frac{2k+1}{2}). \quad (8.52)$$

These two expansions produce two systems of differential equations, which yield two different types of solutions. A sketch of the different fundamental and subharmonic modes is provided in Figure 8.8.

The equation for the pressure contains a number of singularities, which are easily evaluated by rewriting equation (8.46) as a system of first-order equations and evaluating its determinant. The singularities can be identified as the roots of the equation

$$\prod_{k=1}^K \{U_0 - c + AU_1 \cos\left(\frac{k\pi}{K+1}\right)\} = 0$$

where K is the number of Fourier modes. For small values of c_i the approximate location of each singularity in the complex y plane can be identified by a Taylor expansion around $y = y_r$, i.e.,

$$U_0(y_r) + AU_1(y_r; \beta) \cos\left(\frac{k\pi}{K+1}\right) = c_r + \dots$$

To first order, the locations of the singularities are given as

$$y_s = y_r + i \frac{c_i}{U_{0,y}(y_r) + AU_{1,y}(y_r) \cos(k\pi/(K+1))}. \quad (8.53)$$

These are the values of y for which the base flow velocity equals c , at the discrete spanwise locations imposed by the truncated Fourier expansion. When c_i changes sign, y_s crosses the real y -axis. This implies that the integration path must be deformed into the complex y -plane such that the singularities remain on the same side of the integration path as the growing modes. Complex contour integration is necessary when calculating neutral curves. Recall the discussion on computing neutral or damped solutions to the Rayleigh equation in Chapter 2.

8.3.2 Examples of Secondary Instability of Streaks and Vortices

Görtler vortices

We now turn to some results from an inviscid secondary instability analysis of Görtler vortices (see Li & Malik, 1995). The governing parameters were chosen to match the experimental efforts of Swearingen & Blackwelder (1987). A discussion of the full transition process will be postponed to Chapter 9.

The analysis of Li & Malik (1995) does not use the shape assumption; rather the complete nonlinear saturated Görtler vortex is taken as the base flow. The four types of modes discussed earlier were analyzed. Görtler vortices are solution of a boundary-layer type problem with V and W of order $\mathcal{O}(1/\text{Re})$ and the streamwise base flow of order $\mathcal{O}(1)$; the use of the inviscid pressure equation is thus justified.

Table 8.1 lists the frequency, wavelength and growth rate of the most unstable subharmonic and fundamental modes at $X = 85\text{cm}$. All the modes have comparable growth rates. Eigenfunctions for the two types of secondary instabilities reported in the experiment of Swearingen & Blackwelder (1987) are shown in Figure 8.9. The most unstable fundamental odd

		Streamwise	
	Frequency (Hz)	wavelength (cm)	Growth rate (s^{-1})
Fundamental (s)	253	1.41	187
Subharmonic (s)	233	1.63	107
Fundamental (v)	275	1.27	152
Subharmonic (v)	303	1.13	152

TABLE 8.1. Comparison of most unstable fundamental and subharmonic modes at $X = 85\text{cm}$, $\lambda_z = 0.9\text{cm}$ (s = sinuous (odd), v = varicose (even)). From Li & Malik (1995).

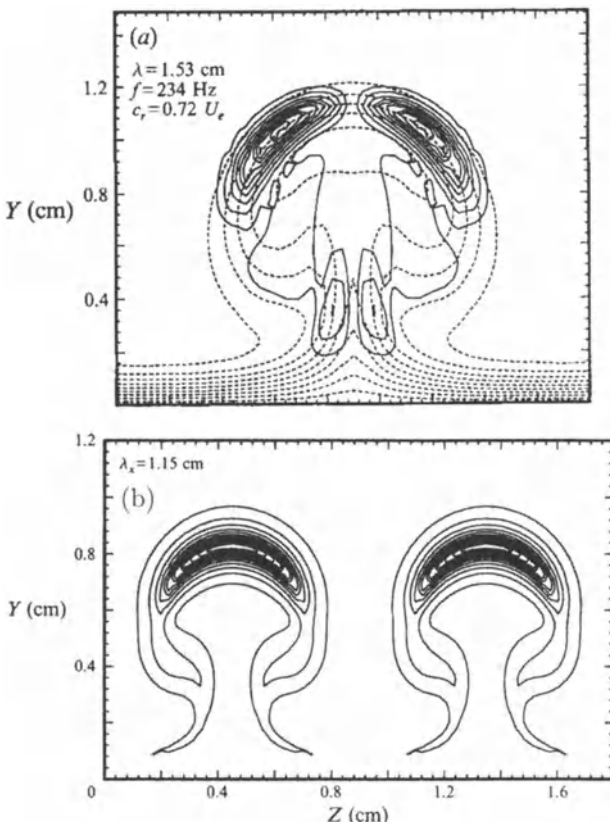


FIGURE 8.9. Streamwise velocity eigenfunctions (absolute value). (a) Most unstable odd mode for $X = 95\text{ cm}$. Dashed lines show the basic flow state.(b) Most unstable subharmonic even mode for $X = 85\text{ cm}$. Note that the absolute value of the eigenfunction shown in the lower figure is $2\pi/\beta$ periodic, although the function itself is $4\pi/\beta$ periodic. From Li & Malik (1995).

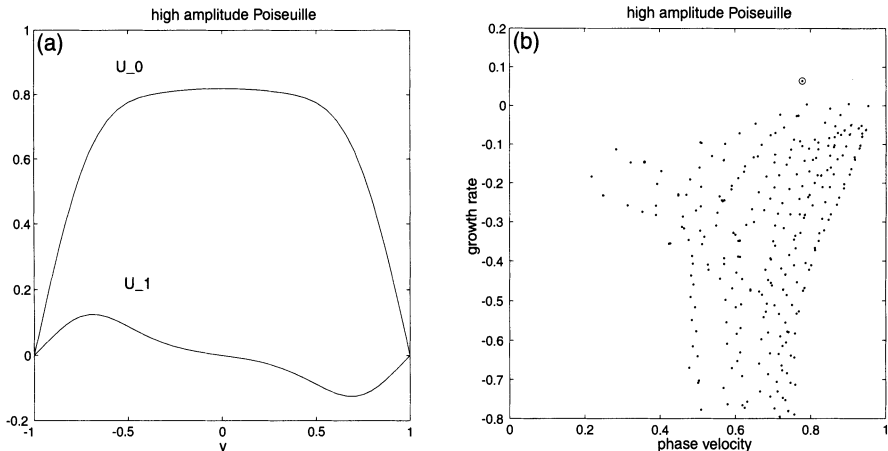


FIGURE 8.10. Poiseuille flow streak instability (a) Mean flow profile $U_0(y)$ and streak profile $U_1(y)$. (b) Spectra of the stability matrices for $\alpha_0 = 1$. The least stable mode is circled. From Reddy *et al.* (1998).

mode represents a sinuous oscillation of the vortex in-phase in the spanwise direction; the most unstable subharmonic even mode represents two horseshoe vortices 180° out-of-phase in the spanwise direction. These are also the two most unstable flow structures reported in Table 8.1, although the parameters are somewhat different.

A viscous secondary instability analysis of Görtler flow has been performed by Bottaro & Klingmann (1996) for parameters similar to the experiments by Swearingen & Blackwelder (1987). They found that the least stable secondary instability mode is sinuous and its streamwise velocity field correlates with the spanwise shear. In fact, the frequency and streamwise wave number of the least stable mode were found to scale with the spanwise shear as

$$|\partial U / \partial z|_{\max} / \omega_r \approx 1.2 \quad (8.54)$$

$$|\partial U / \partial z|_{\max} / \alpha \approx 0.8 \quad (8.55)$$

where $|\partial U / \partial z|_{\max}$ is the maximum value of $\partial U / \partial z$ in the x - y plane. These relations hold for a variety of downstream positions and spanwise wavelengths. It was also found that viscous effects on the sinuous mode were negligible, which justifies the inviscid approach of Li & Malik (1995). Further downstream the varicose instability becomes important which is consistent with the observation of horseshoe vortices in several experiments.

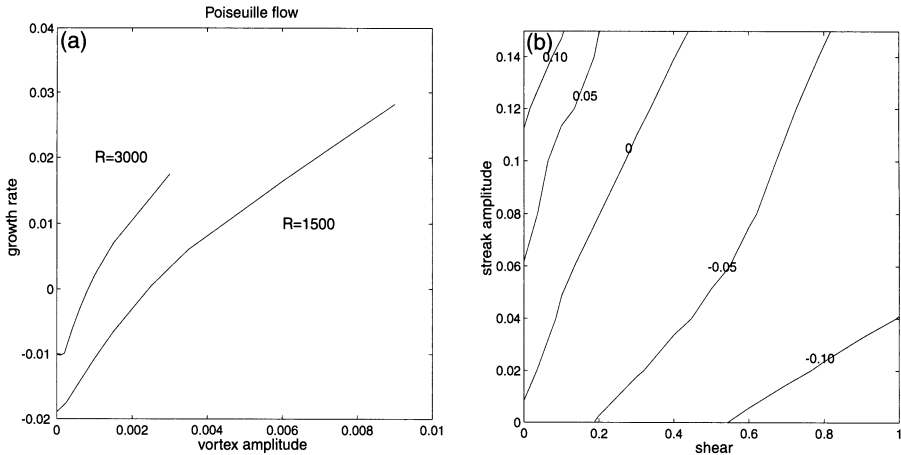


FIGURE 8.11. Growth rate for streak instability. (a) Maximum growth rate as a function of initial vortex amplitude for $\alpha = 1$ and $\beta = 2$. (b) Growth rate for least stable sinuous mode for model profile $U(y, z) = Sy + 2A_S \cos \beta z$ with $\alpha = 1$ and $\text{Re} = 500$. From Reddy *et al.* (1998).

Viscous instability of channel flow streaks

For channel flow streaks Reddy *et al.* (1998) demonstrated that the most unstable secondary instability mode is of fundamental even type. We will highlight some results of their analysis.

Figure 8.10(b) shows the spectrum of the secondary stability operator. We observe distinct differences between spectra of the linear and secondary stability operator. For laminar Poiseuille flow, the least stable linear mode, the Tollmien-Schlichting wave, has phase velocity of about 0.3 and is located near the walls; the least stable secondary mode, on the other hand, is a mode on the P -branch, and the phase velocity appears to be correlated to the mean velocity $U_0(y)$ at the center of the channel. Figure 8.10(a) shows the velocity profiles U_0 and U_1 that correspond to the spectrum in Figure 8.10(b). The mean profile has a maximum of about 0.8.

The essence of the streak breakdown can be understood by considering the stability of the velocity profile

$$U(z) = A_S \cos \beta_0 z \quad (8.56)$$

to perturbations in the x - z plane for inviscid flow (see Finlay *et al.*, 1988; Waleffe, 1995). The streak amplitude A_S is a constant, and we will further assume that $v = 0$ and all perturbations are independent of y . Using a one-term truncation, the eigenvalue is given as (see Waleffe, 1995)

$$c = i \frac{|\alpha_0 A_S|}{\sqrt{2}} \sqrt{\frac{\beta_0^2 - \alpha_0^2}{\beta_2^2 + \alpha_0^2}}. \quad (8.57)$$

The flow is unstable for $0 < \alpha_0 < \beta_0$ and is neutrally stable for $\alpha_0 \geq \beta_0$. We obtain qualitatively similar results if more terms are included in the expansion.

Results pertaining to Poiseuille flow are shown in Figure 8.11(a), and there are several noteworthy features.

For very small vortex amplitude the growth rate is independent of amplitude, because the flow is dominated by the mean flow $U_0(y, t)$, which is essentially the initial laminar profile $1 - y^2$. The least stable mode for the laminar flow is a varicose mode, located near the wall with phase velocity of about 0.3. As the initial vortex amplitude increases, the streaks become dominant and show a marked influence on the stability characteristics of the flow. The least stable mode is a sinuous mode, centered near $y = 0$ with phase velocity about one.

The qualitative features of the curves in Figure 8.11(a) are independent of the number of higher harmonics U_2, U_3, \dots included in the analysis. In fact, the behavior displayed in Figure 8.11(a) is preserved, even if U_0 is replaced by the laminar velocity profile $1 - y^2$. As the amplitude increases, the growth rate increases. The curves are approximately straight lines in qualitative agreement with (8.57) from the inviscid model problem. The slopes of the curves are approximately 8 and 16 for Reynolds numbers 1500 and 3000, respectively. The difference in slopes is due to the fact that a vortex of amplitude A_S will generate a streak with amplitude $|U_1| \approx \mathcal{O}(A_S \text{Re})$.

Reddy *et al.* (1998) investigated the effects of the shear and streak amplitudes on streak instability by computing growth rates for the model velocity profile:

$$U(y, z) = Sy + 2A_S \text{Real}\{e^{i\beta_0 z}\} = Sy + 2A_S \cos \beta_0 z \quad (8.58)$$

where S is the shear and A_S is the streak amplitude. Figure 8.11(b) plots contours of the growth rate for the least stable sinuous mode for $\alpha_0 = 1$, $\beta_0 = 2$, and $\text{Re} = 500$. For fixed streak amplitude, the growth rate increases as the shear decreases.

These results indicate that the mean shear plays a dual role in the spanwise inflectional instability. On one hand, mean shear is necessary for the creation of spanwise varying streaks. On the other hand, the mean shear has a stabilizing effect on the least stable sinuous mode. The secondary instability results of Reddy *et al.* (1998) for the plane Poiseuille and Couette flow problems show a behavior consistent with this result.

Crossflow vortices

The stability of crossflow vortices can also be treated by secondary instability theory. In this section we will concentrate on calculations of temporal secondary instability and leave the details of transition due to the breakdown of crossflow vortices to Chapter 9.

Koch *et al.* (2000) studied finite-amplitude stationary solutions of the Navier-Stokes equations for three-dimensional boundary layer flow. They used the methodology of Ehrenstein & Koch (1991) presented in Section 5.5.3 but used the nonlinear version of equations (6.16),(6.17) to calculate the finite-amplitude solutions. Using the base flow in (8.29)-(8.32), reformulated in terms of the normal velocity and normal vorticity, secondary instability calculations were performed. The computations were intended to complement experiments performed by the research group of Bippes (see, e.g., Nitschke-Kowsky & Bippes, 1988; Lerche, 1997).

Figure 8.12 shows various secondary instability modes calculated for the streamwise position of $x/c = 0.4$ in the experiment. The most amplified secondary mode with a frequency of $f^* = 1070$ Hz and wavelength $\lambda_{z\psi}^* = 11.49$ mm at its maximum is shown by the solid line. For comparison, the shaded area in the figure marks the growth rate of the primary instability. There are two additional unstable modes with almost equal growth rates. These are associated with the wall shear near the edge of the boundary layer. Their growth rates are displayed by dashed lines and show maxima at $f^* = 2392$ Hz, $\lambda_{z\psi} = 6.34$ mm and $f^* = 2849$ Hz, $\lambda_{z\psi} = 5.10$ mm, respectively. There is a fourth unstable mode, which can be correlated with the shear at the wall. The growth rate of this mode (shown as a dotted line) has a maximum at $f^* = 796.2$ Hz, $\lambda_{z\psi} = 8.35$ mm.

Figure 8.12 also contains iso-amplitude plots of the streamwise velocity for the four most amplified eigenfunctions, superimposed on the isolines of the base flow velocity. The maximum of the eigenfunctions are marked by a cross. These contour plots clearly link the modal amplitudes with the corresponding shear layers. Earlier work on the secondary instability of three-dimensional boundary layer flow by Fischer & Dallmann (1991) reported corresponding findings.

Similar results were found by Malik *et al.* (1999) who used the nonlinear parabolized stability equations to compute the secondary instability of crossflow vortices.

8.4 Eckhaus Instability

8.4.1 Secondary Instability of Parallel Flows

Eckhaus instability (Eckhaus, 1965) can be considered a special case of secondary instability. We will develop the governing equations for Eckhaus

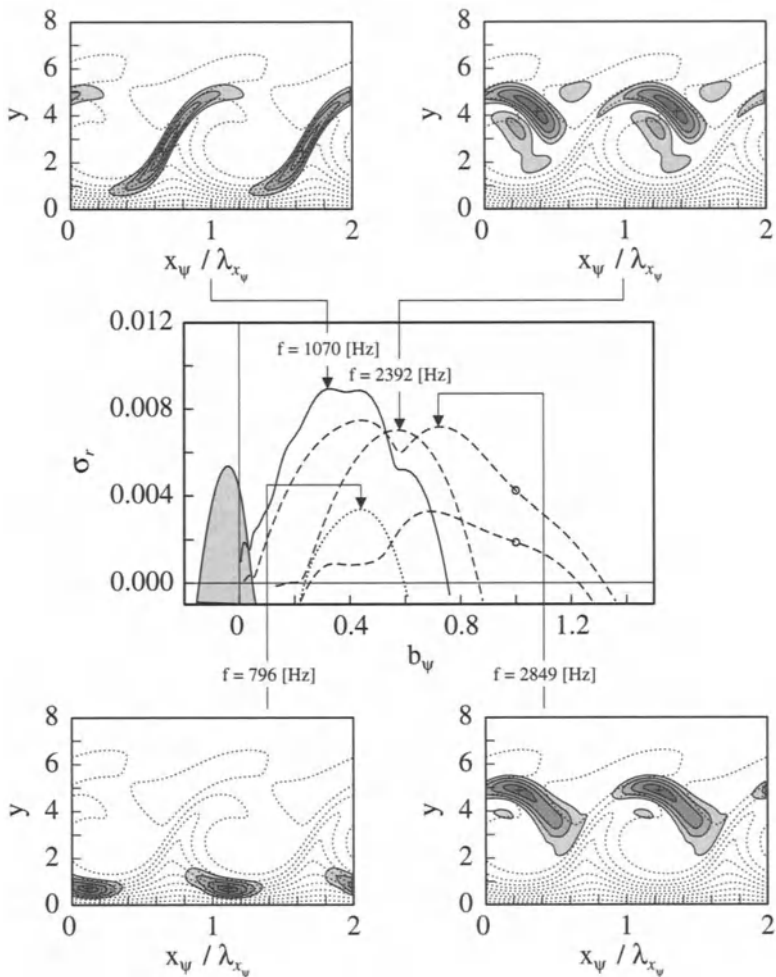


FIGURE 8.12. Temporal growth rates σ_r of secondary instability modes for cross-flow vortices versus spanwise wavenumber. Also shown are iso-amplitude plots of the four most amplified eigenfunctions, superimposed on the isolines of the base flow velocity. From Koch (2000).

instability by considering the stability of a finite-amplitude vortex to a similar small-amplitude vortex with a slight shift in the fundamental spanwise wave number. The theoretical framework is contained as a special case of the detuned secondary instability developed earlier in this chapter. If $\beta = 0$ in Figure 8.1 or $\alpha = 0$ in Figure 8.7 and $0 < \epsilon < 1$, we would recover Eckhaus instability theory for a spanwise or streamwise vortex, respectively. Eckhaus instability is also related to the sideband instability of water waves; see Benjamin & Feir (1967) and Stuart & DiPrima (1978).

Governing equations for Eckhaus instability in rotating channel flow

We will consider Eckhaus instability of rotating channel flow. The equations governing Eckhaus instability of the finite-amplitude vortices in rotating channel flow are given by (8.29),(8.30) with two additional terms added to account for rotation; all terms including a streamwise wave number are set to zero. We have

$$U_y \hat{v} + U_z \hat{w} + V \hat{u}_y + W \hat{u}_z - \frac{1}{\text{Re}} [\hat{u}_{yy} + \hat{u}_{zz}] = i\omega \hat{u} - 2 \text{Ro} \hat{v} \quad (8.59)$$

$$V_y \hat{v} + V_z \hat{w} + \hat{p}_y + V \hat{v}_y + W \hat{v}_z - \frac{1}{\text{Re}} [\hat{v}_{yy} + \hat{v}_{zz}] = i\omega \hat{v} + 2 \text{Ro} \hat{u} \quad (8.60)$$

$$W_z \hat{w} + W_y \hat{v} + \hat{p}_z + V \hat{w}_y + W \hat{w}_z - \frac{1}{\text{Re}} [\hat{w}_{yy} + \hat{w}_{zz}] = i\omega \hat{w} \quad (8.61)$$

$$\hat{v}_y + \hat{w}_z = 0 \quad (8.62)$$

where Ro is the rotation number. The disturbances can be written in the general form of detuned modes

$$\hat{u}(y, z) = \tilde{u}(y, z) e^{\gamma z} \quad (8.63)$$

where $\tilde{u}(y, z)$ is periodic in z with period $2\pi/\beta$ and $\gamma_i = \epsilon\beta$, which was earlier called the detuning parameter.

These equations are solved using the methods described for the secondary instability of two-dimensional waves, streaks, and vortices.

Examples of Eckhaus instability of rotating channel flow

Guo & Finlay (1991) calculated the Eckhaus instability of curved and rotating channel flows. Figure 8.13 shows the result for rotating channel flow for two rotation numbers. The Eckhaus stability boundary is determined by a change in sign of the Eckhaus growth rate ω_i as the parameters of the system are varied. Within the Eckhaus boundary, the growth rate is negative. In the vicinity of the Eckhaus boundary the numerical calculations

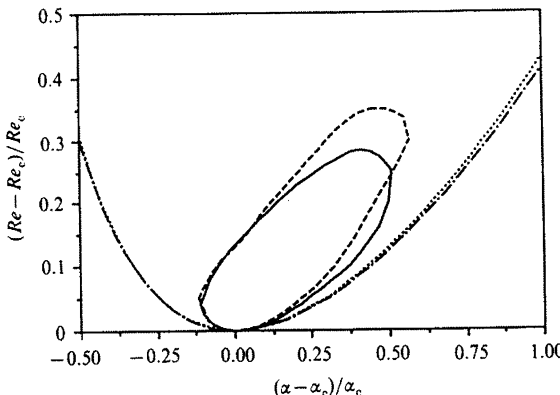


FIGURE 8.13. Eckhaus stability boundaries for rotating channel flow. Solid line: $Ro = 0.005$ ($Re_c = 198.95$, $\alpha_c = 2.01$). Dashed line: $Ro = 0.25$ ($Re_c = 44.30$, $\alpha_c = 2.46$). Dashed-dotted line: primary instability $Ro = 0.005$. Dotted line: primary instability $Ro = 0.25$. From Guo & Finlay (1991).

of Guo & Finlay (1991) showed that ω was purely imaginary, thus implying that the stability boundary is determined by non-oscillatory perturbations. Figure 8.13 shows that the Eckhaus stability region is a small closed region tangent to the neutral stability curve for the primary instability at $Re = Re_{crit}$. The stability region is only a weak function of the rotation number.

Eckhaus instabilities have also been observed in other flows, in particular Bénard convection (see Busse & Whitehead, 1971) where an elliptical region of Eckhaus stability – known as the “Busse balloon” – similar to the one in Figure 8.13 has been found.

8.4.2 Parabolic Equations for Spatial Eckhaus Instability

It is possible to generalize the Eckhaus instability for streamwise vortices by including spatial growth and nonparallel effects. Guo & Finlay (1991) derived parabolic equations similar to the parabolized stability equations (PSE) developed in Chapter 7.

Governing equations

The development of finite-amplitude vortices in curved geometries, such as curved channel or boundary layer flow, can be calculated using the steady parabolized Navier-Stokes equations or equivalently using the nonlinear parabolized stability equations (see Section 7.5.2). The solutions to these equations, i.e., Dean or Görtler vortices, provide the base flow for the secondary instability or Eckhaus instability calculations.

Once the spatially developing vortices are found, their stability to spanwise perturbations can be computed by substituting expressions of the form

$$u(x, y, z) = U(x, y, z) + \tilde{u}(x, y, z) e^{\gamma z} \quad (8.64)$$

into the Navier-Stokes equations and linearizing about the base flow given by $(U(x, y, z), V(x, y, z), W(x, y, z))$. The base flow and disturbances are taken periodic in z with period $2\pi/\beta$ and $\gamma_i = \epsilon\beta$. The resulting disturbance equations can again be parabolized and written in the form

$$2 \frac{\partial}{\partial x} (U\tilde{u}) + f_1 = \frac{1}{\text{Re}} (\tilde{u}_{yy} + \tilde{u}_{zz}) \quad (8.65)$$

$$\frac{\partial}{\partial x} (U\tilde{v}) + \frac{\partial}{\partial x} (V\tilde{u}) + f_2 = \tilde{p}_y + \frac{1}{\text{Re}} (\tilde{v}_{yy} + \tilde{v}_{zz}) \quad (8.66)$$

$$\frac{\partial}{\partial x} (U\tilde{w}) + \frac{\partial}{\partial x} (W\tilde{u}) + f_3 = \tilde{p}_z + \frac{1}{\text{Re}} (\tilde{w}_{yy} + \tilde{w}_{zz}) \quad (8.67)$$

$$\tilde{u}_x = -\tilde{v}_y - \tilde{w}_z - \gamma \tilde{w} \quad (8.68)$$

where

$$f_i = \frac{\partial}{\partial y} (V\tilde{u}_i + U_i\tilde{v}) + \left(\frac{\partial}{\partial z} + \gamma \right) (W\tilde{u}_i + U_i\tilde{w}) - \frac{1}{\text{Re}} \left(2\gamma \frac{\partial \tilde{u}_i}{\partial z} + \gamma^2 \tilde{u}_i \right) + C_i. \quad (8.69)$$

The index $i = 1, 2, 3$ represents the streamwise, normal, and spanwise directions, and the terms C_i denote nonlinear curvature terms.

Theoretically, the equations for the base flow should be solved first to obtain U_i , after which the disturbance equations can be solved using the stored base flow data. Because both sets of equations are parabolic in x , however, their solution can be marched downstream simultaneously, with the solution of the base flow being one step ahead of the disturbance equations.

From the spatially evolving disturbance the spatial energy growth rate can be calculated from

$$\sigma = (\ln E^{n+1} - \ln E^n) \frac{l}{2\Delta x} \quad (8.70)$$

where E is the kinetic energy density at $x = n\Delta x$ and l is the length scale used to normalize the growth rate.

Spatial Eckhaus instability of Dean vortices

Guo & Finlay (1991) studied the Eckhaus instability of Dean vortices at $\text{Re} = 2\text{Re}_{crit}$ in a curved channel with radius of curvature $\gamma_R = 0.975$. The

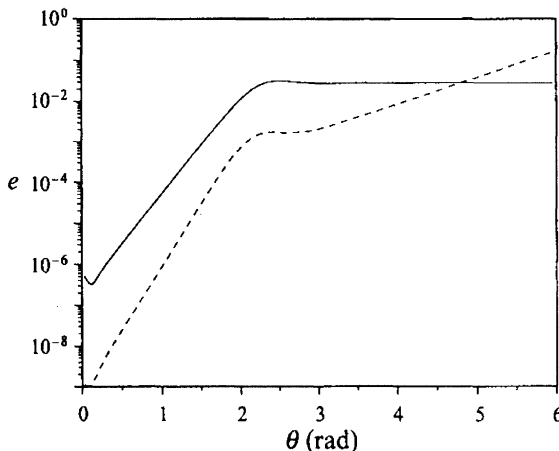


FIGURE 8.14. Spatial growth of the energies of the base Dean vortices for $\beta = 4$ (solid line) and the related perturbation ($\epsilon = 0.5$) of spatial Eckhaus instability (dashed line). From Guo & Finlay (1994).

initial condition for the base flow was taken as curved channel Poiseuille flow with a small perturbation added; the initial condition for the disturbance equations consisted of a similar small perturbation as added to the curved Poiseuille flow.

Figure 8.14 shows the evolution of energy for the base Dean vortices and the related perturbation of the spatial Eckhaus instability. The spanwise wave number of the base flow is twice that of the perturbation. For $\theta = x/\gamma_R < 1.5$ the growth rates of the Dean vortices and the perturbation are 0.071 and 0.09, which agree with the primary instability for the respective wave numbers. The growth rate of the perturbation remains near 0.09 until $\theta \approx 2$. At this point the base Dean vortices start to saturate. The Dean vortices are fully developed at $\theta \approx 3$, where the growth rate of the perturbation changes to 0.019 which is the spatial growth rate of the Eckhaus instability. Thus energy of the perturbation initially grows due to the primary instability, but once the base vortices have saturated, energy growth stems from an Eckhaus (secondary) instability. The energy of the perturbation continues to grow as the base Dean vortices saturate (see Figure 8.14).

9

Transition to Turbulence

9.1 Transition Scenarios and Thresholds

9.1.1 *Introduction*

We have spent several chapters discussing various type of instabilities in a number of flow situations. In this final chapter we will consider how these instabilities may trigger laminar-turbulent transition. The transition process is often complicated and can follow many possible routes. We shall try to classify these routes based on the mechanisms responsible for the disturbance growth. In this introductory section we will discuss three typical scenarios for the simplified flow situation of a parallel boundary layer growing in time; in the subsequent sections examples of more complicated flow situations will be given. First, however, we will briefly summarize some earlier attempts to classify transition.

Transition emanating from exponential instabilities

The traditional method of investigating the stability properties of a particular flow is based on eigenvalue problems. Consequently, instabilities arise as exponentially growing eigenmodes, e.g., Tollmien-Schlichting waves in a Blasius boundary layer or crossflow vortices in three-dimensional boundary layers. It seems then natural that early investigations of transition have used the growth of unstable eigenmodes as the starting point of their analysis. The growth of these exponential primary instabilities, together with

subsequent secondary instabilities, in many cases gives a good understanding of how a flow becomes turbulent.

However, there are a number of flow situations where difficulties arise. In some cases, transition to turbulence occurs in a parameter regime where no unstable eigenmodes exist. In other cases, the most unstable exponentially growing mode is observed in experiments. Transition that does not follow the traditional route of exponential instabilities has become known as bypass transition.

Bypass transition

We now have a better understanding of disturbance growth and transition scenarios that do *not* emanate from exponential instabilities, and we can use this understanding to better define bypass transition.

Originally, Morkovin (1969) coined the expression “bypass transition” in 1969 when he noted, “Apparently, we can bypass the TS-mechanism altogether if we can replace it with another strongly amplifying mechanism.” In this quote the “TS-mechanism” refers to the exponential growth of Tollmien-Schlichting waves. In an attempt to broaden the definition of bypass transition we propose to define bypass transition as *transition emanating from nonmodal growth mechanisms*.

Nonmodal growth mechanisms are associated with the nonnormal structure of the linear stability operator discussed in Chapter 4 and include, for example, algebraically or transiently growing disturbances. Often disturbances resulting from nonmodal growth are elongated in the streamwise direction and are a common feature in many transition processes. In particular, transition due to moderate to high levels of freestream turbulence is dominated by high-amplitude streaks in the streamwise velocity. Some researchers have previously reserved the term bypass transition for transition due to turbulence in the free stream. However, in view of the original meaning of bypass transition and our understanding that the growth of streaks is a linear nonmodal mechanism, the definition proposed above appears more appropriate.

Different stages in the transition process

In many cases the transition process can be divided into a number of stages. The first is usually the receptivity stage, which is associated with the initiation of disturbances in the flow. Receptivity (see Chapter 7) is often the most difficult process to include in transition prediction models for realistic flow situations. It entails knowledge about the ambient disturbance environment and the mechanisms by which (often) random disturbances are projected into growing eigenmodes or optimal disturbances, or how they otherwise force disturbances inside a boundary layer.

The next stage is the linear growth stage, where small disturbances are amplified until they reach a size where nonlinear effects become important.

This amplification can be in the form of exponential growth of eigenmodes, nonmodal growth of optimal disturbances, or nonmodal response to forcing.

Once a disturbance has reached a finite amplitude, it often saturates and transforms the flow into a new, possibly steady state. Only in a few cases does the primary instability lead the flow directly into a turbulent state. Instead, the new steady or quasisteady flow becomes a base flow on which secondary instabilities can grow.

As we saw in Chapter 8, the secondary instability stage can be viewed as a new instability of a more complicated flow. This stage of the transition process is in many cases more rapid than the stage where primary instabilities prevail.

The last stage is the breakdown stage where nonlinearities and/or higher (symmetry-breaking) instabilities excite an increasing number of scales and frequencies in the flow. This stage is often more rapid than both the linear stage and the secondary instability stage. Analysis of the breakdown stage is often difficult and is usually studied using physical or numerical experiments.

Dividing the transition process into these five stages (receptivity, linear growth, nonlinear saturation, secondary instability, and breakdown) certainly idealizes the situation because all stages cannot always be expected to occur in a nonambiguous manner. However, they often provide a good framework to view transition even for complicated flows.

9.1.2 Three Transition Scenarios

Three different transition scenarios for boundary layer flow will be introduced as they demonstrate typical features seen in more complicated flows. The starting point is laminar flow in a Blasius boundary layer at $\text{Re} = 500$. We will calculate the development of an initial disturbance using direct numerical simulations of the complete Navier-Stokes equations. The flow is taken as locally parallel but the boundary layer thickness is allowed to grow in time simulating a computational domain moving down the flat plate with a prescribed speed. In order for the simulation code to preserve the Blasius boundary layer as an undisturbed solution a small volume force has to be added to the Navier-Stokes equation; see Spalart & Yang (1987) for numerical details. Use of the temporal simulations gives a better chance to directly compare the results to the various stability theories presented earlier in this book.

In all three cases we use an initial condition consisting of one of the fastest growing disturbances in a given Fourier component. In addition, there are small-amplitude random perturbations added to nine of the lowest Fourier components. The initial disturbance is then followed in time. We will see that a number of concepts introduced earlier will be helpful in explaining the various phases of the disturbance evolution, such as primary instability, nonlinear interaction, and secondary instability.

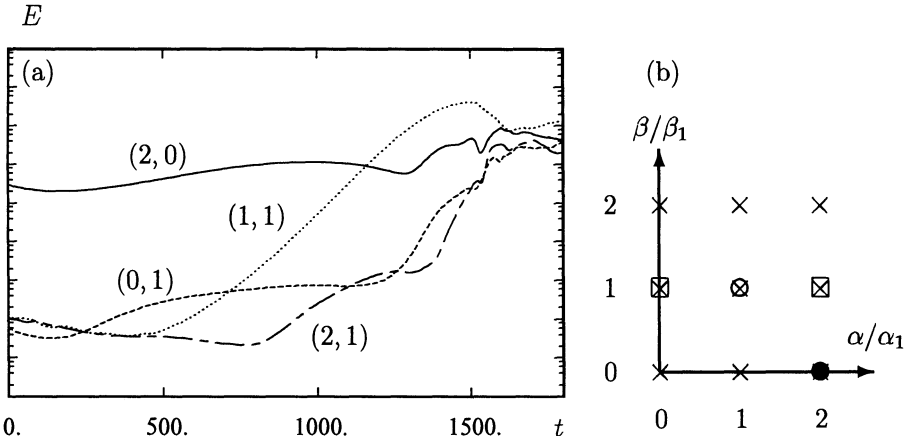


FIGURE 9.1. Energy in selected Fourier components for subharmonic Tollmien-Schlichting-wave secondary instability. Filled circle: initial Tollmien-Schlichting-wave; circle: subharmonic secondary instability mode; squares: fundamental secondary instability modes.

Scenario 1: Secondary instability of Tollmien-Schlichting waves

First we consider the secondary instability of a growing Tollmien-Schlichting wave. We initialize the Tollmien-Schlichting wave at a low amplitude in the wave number $(2, 0)$, meaning that the streamwise wave number is twice that of the fundamental one defined by the length of the computational box ($2\pi/L_x$); the spanwise wave number is zero. This wave is represented by a filled circle in Figure 9.1(b), where the Fourier components that contain random perturbations are marked with an \times . A contour plot of the streamwise velocity in a horizontal plane is seen in Figure 9.2(a) showing the two-dimensional wave and the random disturbances.

The evolution of the disturbance energy in time for four selected Fourier components can be seen in Figure 9.1(a). The Tollmien-Schlichting mode grows slightly, and although its amplitude measures only a few percent of the mean flow, it exhibits a secondary instability to a subharmonic mode, the open circle in Figure 9.1(b). The subharmonic nature of the instability is also seen in the staggered three-dimensional flow pattern in Figure 9.2(b) and (c). Later, modes associated with the fundamental secondary instability also grow; these modes are shown with open squares in Figure 9.1(b). This confirms the theoretical predictions, discussed in Section 8.2.2, that the subharmonic secondary instability is the first to be observed in a Blasius boundary layer.

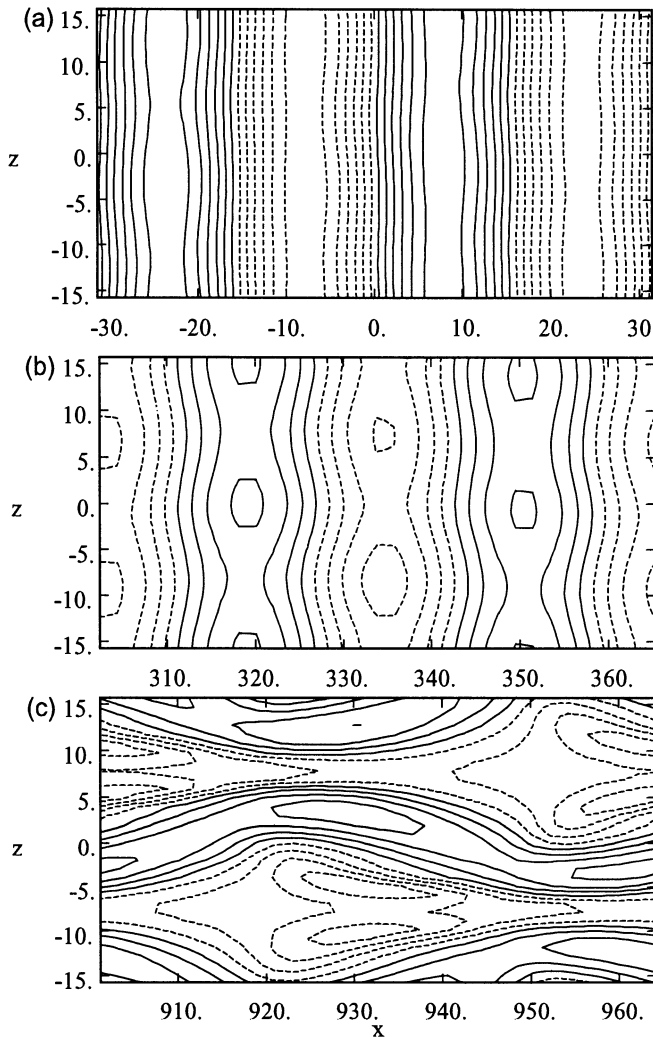


FIGURE 9.2. Contours of streamwise disturbance velocity for Tollmien-Schlichting-wave secondary instability at $y = 1.5$. (a) $t = 0$, (b) $t = 500$, (c) $t = 1400$. Dashed contours represent negative disturbance velocity.

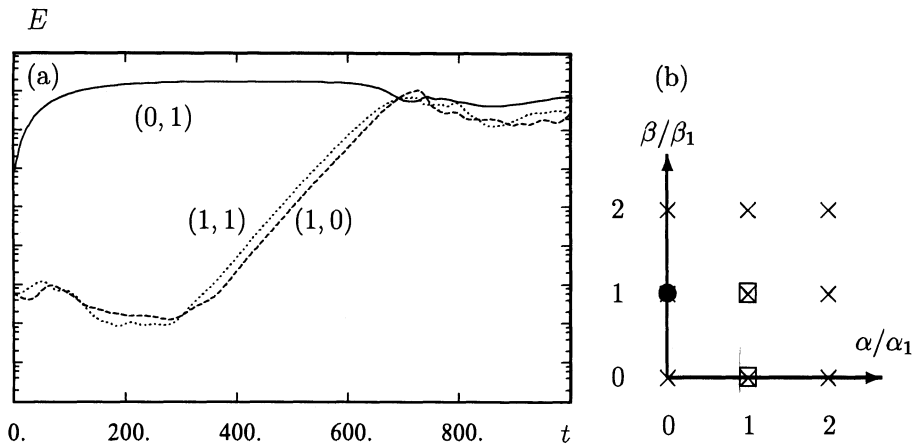


FIGURE 9.3. Energy in selected Fourier components for secondary instability of streaks. Filled circle: initial streak; squares: fundamental secondary instability modes.

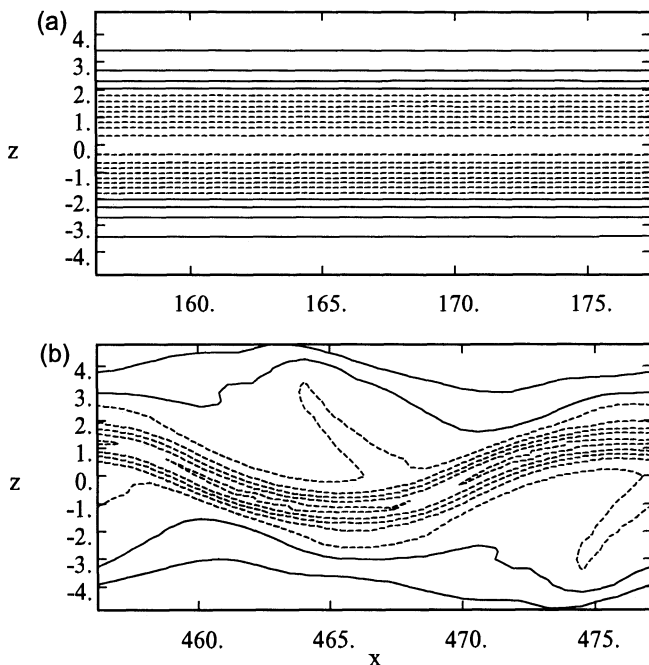


FIGURE 9.4. Contours of streamwise disturbance velocity for secondary instability of streaks at $y = 2$. (a) $t = 250$, (b) $t = 700$. Dashed contours represent negative disturbance velocity.

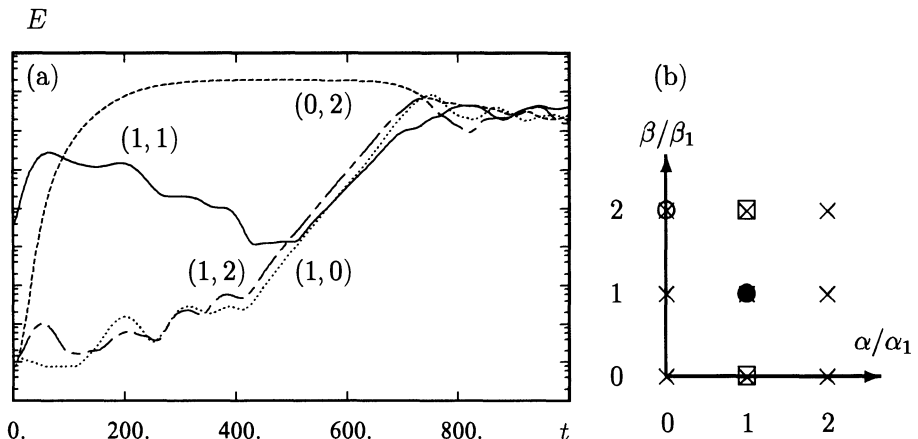


FIGURE 9.5. Energy in selected Fourier components for oblique breakdown. Filled circle: initial oblique waves; circle: nonlinearly forced streak; squares: fundamental secondary instability modes.

Scenario 2: Streak breakdown

Next, we consider the secondary instability of streaks produced by streamwise vortices. We start with a periodic array of streamwise vortices with wave number \$(0, 1)\$, the filled circle in Figure 9.3(b), and add low-amplitude random perturbations to nine of the lowest Fourier components. The streamwise vortices are chosen as optimal perturbations, implying that they are most effective in generating a streak. The energy of the Fourier component \$(0, 1)\$ experiences transient growth (Figure 9.3(a)) creating periodic streamwise streaks (Figure 9.4(a)). At about the time the streak reaches its maximum, a fundamental secondary instability (involving Fourier components marked with open squares in Figure 9.3(b)) starts to emanate from random disturbances. The secondary instability deforms the streak in a sinusuous manner and causes breakdown to turbulence; see Figure 9.4(b).

Scenario 3: Oblique transition

Finally, we consider the oblique transition scenario, where energy is seeded in a pair of oblique waves with Fourier component \$(1, 1)\$; see the filled circle in Figure 9.5(b). The flow is symmetric in the spanwise direction, implying that the Fourier component \$(1, -1)\$ is also initialized with equal energy (but is not shown in Figure 9.5(b)). The initial oblique waves are chosen as optimal disturbances. In addition, we have random disturbances in nine of the lowest Fourier components. The initial flow (Figure 9.6(a)) consists of a standing wave pattern in the spanwise direction.

As the flow develops, the oblique waves experience transient growth while generating streamwise vortices associated with the \$(0, 2)\$ component; see the open circle in Figure 9.5(b). The generated streamwise vortices, in

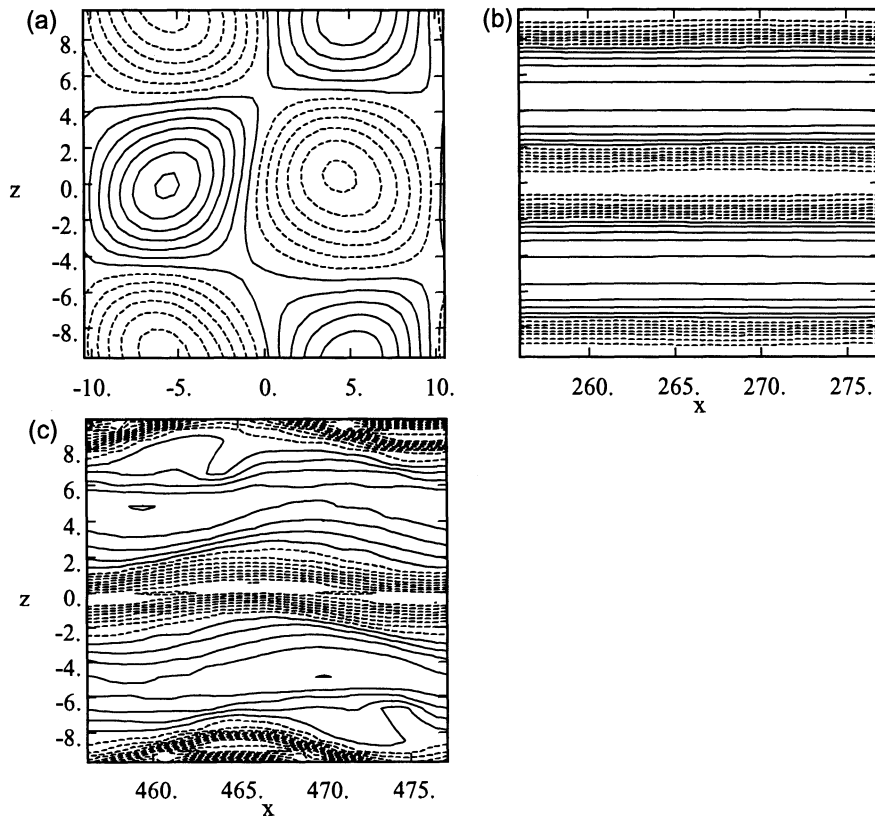


FIGURE 9.6. Contours of streamwise disturbance velocity for oblique transition at $y = 2$. (a) $t = 0$, (b) $t = 400$, (c) $t = 700$. Dashed contours represent negative disturbance velocity.

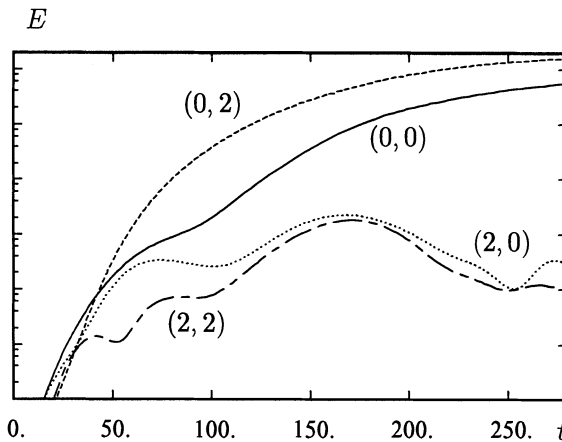


FIGURE 9.7. Energy in second-generation nonlinearly forced Fourier components for oblique breakdown. Full line: (0,0); dashed line: (0,2); dotted line: (2,0); chain dashed line: (2,2).

turn, generate streaks by the lift-up effect. As the streaks grow, the initial oblique waves start to decay and the flow field is dominated by the streaky structure; see Figure 9.6(b). From this point on, the development is similar to the streak breakdown, as a fundamental secondary instability develops on the streak, which starts to oscillate in a sinuous manner. A subharmonic secondary instability is also present, associated with the (1, 1) mode but the growth rate is slightly smaller than the fundamental one. Had the original oblique waves not decayed as much as they did, their remaining energy would have triggered a subharmonic varicose streak breakdown.

To better understand oblique transition we show the energy in all second-generation nonlinearly forced Fourier components in Figure 9.7. It is apparent that all modes are forced almost equally by the pair of oblique waves. However, their long term responses are very different. The (2, 2) and (2, 0) components, which are both damped and are not very sensitive to forcing, grow to a rather low energy. The (0, 0) component, or mean flow modification, experiences larger growth. This behavior is due to its low damping rate, essentially $\mathcal{O}(1/R)$ smaller than for the (2, 2) and (2, 0) components. However, the (0, 0) component is associated with a normal evolution operator and therefore has a low sensitivity to forcing. The (0, 2) component, on the other hand, has a low damping rate and is highly sensitive to forcing due to the nonnormal nature of the underlying operator for this wave number combination; see Sections 4.4 and 4.5. Thus, this component is the one experiencing the largest response to the forcing by oblique waves.

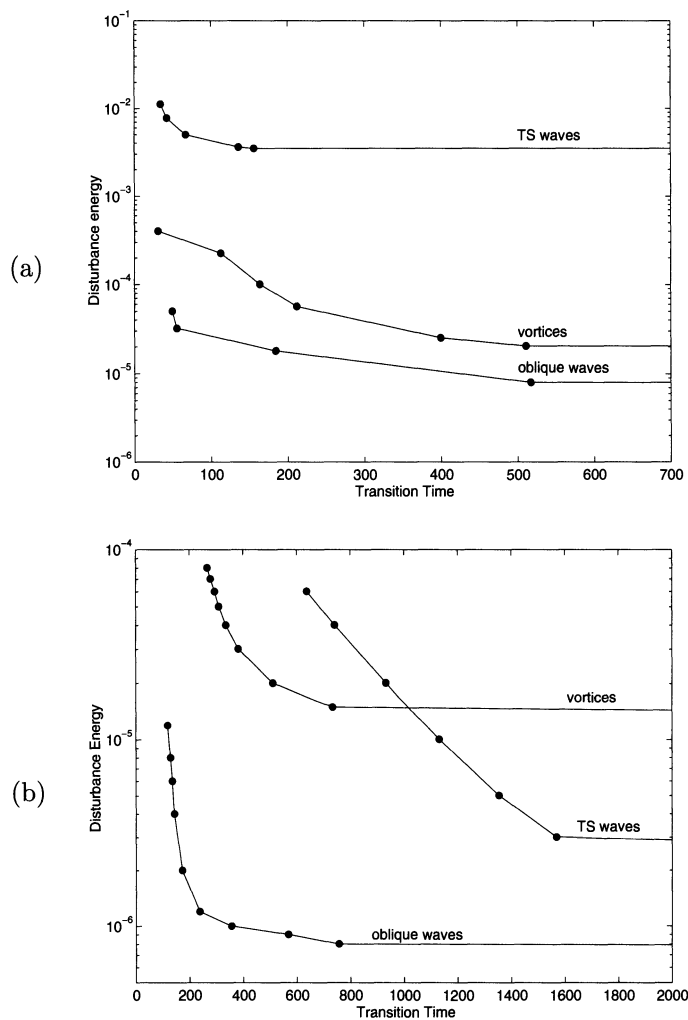


FIGURE 9.8. Initial disturbance energy versus transition time. (a) Plane Poiseuille flow at $Re = 1500$. (b) Temporally growing Blasius boundary layer at $Re = 500$. From Schmid *et al.* (1996).

9.1.3 The Most Likely Transition Scenario

Transition times

We have seen three different scenarios for laminar-turbulent transition in a Blasius boundary layer. One important question is the likelihood of each scenario in practice. The answer to this question depends, first of all, on the initial disturbance energy. Second, it depends on the time it takes for each scenario to achieve transition, and third, on the energy required for each scenario to reach a turbulent state.

In Figure 9.8 the time to reach transition is given as a function of the initial amplitude of the disturbances in the three cases considered here. We define the time for transition T as the time at which the friction coefficient c_f reaches the average of its laminar and turbulent value. If a turbulent state is not achieved, we define $T = \infty$. In addition to the Blasius boundary layer we will consider the transition times for the three scenarios in plane Poiseuille flow and investigate similarities and differences for the two different flows. The fundamental wave numbers chosen for the plane Poiseuille flow simulations are $\alpha = 1$, $\beta = 1$, except for the streamwise vortices, where $\beta = 2$.

For both flows the fastest transition and/or the lowest initial energy needed to achieve transition is associated with the oblique transition scenario. For moderate times, the streamwise vortex scenario is the second most likely candidate for transition, assuming equal initial excitation. The secondary instability of Tollmien-Schlichting waves is the most unlikely scenario, except for low-disturbance energies in the Blasius boundary layer. These results have been calculated at rather low Reynolds numbers. For plane channel flow the Reynolds number is within the experimentally observed Reynolds number range for transition, about $Re = 1000 - 2000$. For the Blasius boundary layer the Reynolds number is close to the value where Tollmien-Schlichting waves first become unstable. For higher Reynolds numbers the Tollmien-Schlichting wave scenario in the Blasius case will need less energy than the oblique waves in order to reach transition, although the scenario will require a long time to reach the turbulent state.

Figure 9.8 can be used to define threshold energies, because all the curves level off for small enough initial energies. Thresholds as a function of the Reynolds number have been calculated for plane Poiseuille flow and are presented in the next section.

Threshold amplitudes in plane Poiseuille flow

How do the transition thresholds compare for the secondary instability scenario, the streamwise vortex scenario, and the oblique wave scenario?

Figure 9.9 plots the threshold energy for transition in Poiseuille flow based on the three scenarios for $1500 \leq Re \leq 5000$. In addition, we compute a threshold for an initial field consisting of a two-dimensional optimal

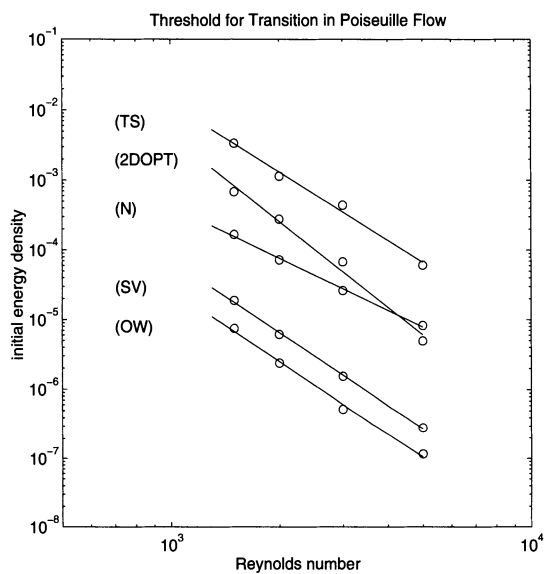


FIGURE 9.9. Threshold energy density for transition in Poiseuille flow for the three main scenarios, two-dimensional optimal disturbances (2DOPT), and random three-dimensional noise (N). The circles correspond to data from simulations. The lines are fits to the data. From Reddy *et al.* (1998).

disturbance and one initial field consisting only of a random combination of orthogonal (Stokes) modes with streamwise and spanwise wave numbers $0, \pm 1, \pm 2$ (the same wave numbers that contained random disturbances in the previous investigations).

The procedure to create the plot is straightforward. For each scenario, a full nonlinear simulation code is run with initial disturbances of varying energy density. Upper and lower bounds on the initial energy necessary for transition are determined and a plot of the average of these values is produced. For the simulations presented in Figure 9.9 only a fundamental-type breakdown is permitted for the Tollmien-Schlichting waves. If subharmonic-type breakdown is allowed, we find that the threshold is marginally lower.

The threshold transition energy for the initial oblique waves and the streamwise vortices are more than two orders of magnitude lower than for the Tollmien-Schlichting waves. The random initial perturbations have a threshold well below the one found for Tollmien-Schlichting waves and about the same as that for the two-dimensional optimal disturbance.

9.1.4 Conclusions

General conclusions

Several general conclusions can be drawn from our consideration of the three transition scenarios. Transition to turbulence is not a unique process; it is dependent on the initial or inflow disturbance environment and the type of flow one is interested in.

The lift-up process and the associated generation and breakdown of streaks, on the other hand, are generic processes that do not strongly depend on the type of shear flow under consideration. As soon as the initial or inflow condition contains streamwise vortices or disturbances that can generate streamwise vortices nonlinearly, we can expect large-amplitude streamwise streaks to be part of the transition process.

Because the presence of exponential instabilities is highly dependent on the details of the flow under consideration, one has to judge every flow individually to determine if the exponential instability will be able to compete with the generic growth of streaks.

In the zero pressure gradient boundary layer, for example, where the growth of the streaks and the exponential growth of Tollmien-Schlichting waves are comparable (for moderate Reynolds numbers), it is the initial disturbance spectrum, the initial amplitude distribution, and the threshold for secondary instability that determine the prevailing transition scenario. For flows with larger exponential growth rates, for example, those with strong inflection points in the mean velocity profile, one can expect the exponential growth to dominate the transition process.

Outline of the following sections

In what follows, we will consider the complete transition process in spatially evolving flows, as they would appear in realistic applications or in a controlled experiment. We will describe experimental results, either based on physical or numerical experiments (direct numerical simulations), and try to relate the flow features to the material discussed earlier in the book.

First, we consider the breakdown of exponentially growing two-dimensional waves. This has been the main focus of boundary layer instability and transition investigations over the last fifty years; a large body of knowledge has been gathered for this transition scenario.

Second, we discuss the transition scenario associated with the breakdown of large-amplitude streamwise streaks. Here, the growth mechanisms are different compared to the first scenario and the main flow features are at a 90° angle to the two-dimensional Tollmien-Schlichting waves and nearly independent of the streamwise direction.

Third, we discuss the scenario starting with two oblique waves. This scenario contains aspects of both of the preceding scenarios. The primary growth mechanism is similar to the second scenario, and surprisingly many features of the late stages are similar to those associated with the breakdown of two-dimensional waves.

Next, we consider the breakdown of streamwise vortices that exhibit short-term exponential growth. The vortices contain strong streak components but differ from the streak breakdown in that the vortices saturate and, in many cases, play an important role in the transition process. Nevertheless, the breakdown of these strong vortices shows many features common to the breakdown of streaks.

Finally, we discuss the breakdown of localized disturbances and the generation of turbulent spots, where we will see that all the growth mechanisms discussed earlier may be important, and many of the same flow features seen in the breakdown of single wave disturbances are also seen in the transition process of localized disturbances.

We conclude this chapter with a brief discussion of transition modeling issues.

9.2 Breakdown of Two-Dimensional Waves

9.2.1 *The Zero Pressure Gradient Boundary Layer*

K-type transition

Tollmien-Schlichting waves of small amplitude, i.e., of the order of a few tenths of a percent, seem to adhere to linear analysis quite well. They decay up to branch I, are amplified between branch I and II, and finally decay beyond branch II. However, the experimental study of Klebanoff *et al.*

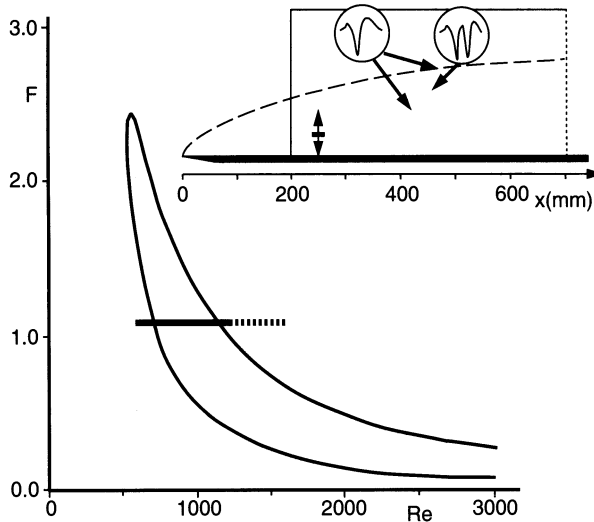


FIGURE 9.10. Position of the computational domain relative to the stability diagram of linear stability theory. Inset: position relative to the experiments by Kachanov & Levchenko (1984). The circles represent the different spike stages identified in the experiment. From Rist & Fasel (1995).

(1962) showed that initially two-dimensional Tollmien-Schlichting waves become three-dimensional when reaching an amplitude in u_{rms} of the order of 1 percent of U_∞ . The observed spanwise scale was of the same order as the streamwise wavelength of the Tollmien-Schlichting wave. By triggering the three-dimensionality through small pieces of tape below the vibrating ribbon, which was used to force the fundamental Tollmien-Schlichting mode, it was possible to study the three-dimensionality under controlled conditions. Klebanoff *et al.* (1962) defined the three-dimensional pattern as peak and valley regions. In the peak region they observed *spikes* prior to breakdown. Spikes are large-amplitude short-duration events that occur in the u -signal. These regions were identified as having instantaneous inflectional velocity profiles. The region for growth of three-dimensional structures in their experiment was about five Tollmien-Schlichting wavelengths, whereas the spike stage and breakdown to turbulence occurred over about one Tollmien-Schlichting wavelength. Both these processes were thus more rapid than the Tollmien-Schlichting wave growth. This transition scenario is called K-type secondary instability (K for Klebanoff).

Comparison between physical and numerical experiments

Many investigators have since considered this transition scenario, and we will describe in detail some careful numerical and physical experiments by Rist & Fasel (1995) and Kachanov & Levchenko (1984) with essentially

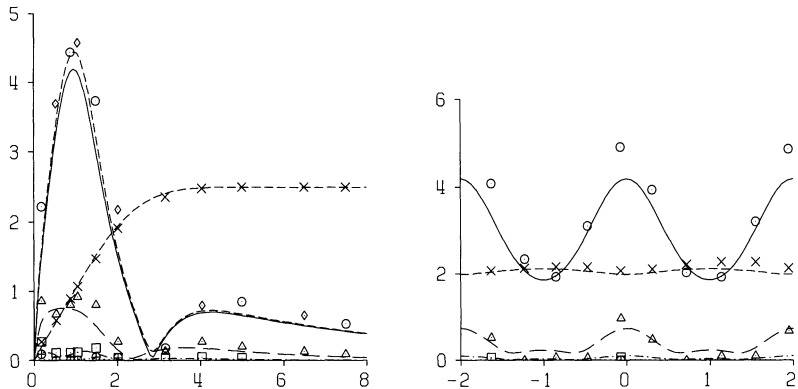


FIGURE 9.11. Comparison of amplitude distributions with the measurements of Kachanov & Levchenko (1984). From Rist & Fasel (1995).

the same parameters as the original experiments by Klebanoff *et al.* (1962). Figure 9.10 shows the position of the computational domain relative to the experiments and the neutral stability curve for Tollmien-Schlichting waves in the Blasius boundary layer. In the experiments the TS waves were generated by a vibrating ribbon and three-dimensionality was introduced by scotch tape, whereas in the simulations both the two- and three-dimensional waves were forced by blowing and suction at the wall. Figure 9.11 shows a detailed comparison of the normal and spanwise distribution of the streamwise velocity. The mean flow and the fundamental and higher-frequency components can be seen to show good quantitative agreement. In addition, we notice that the normal structure of the streamwise velocity disturbance still has the typical dual-peak structure, although the flow itself is highly three-dimensional.

The secondary instability stage

Having established the detailed agreement between the simulations and the experiments, we continue to show some additional flow features from the simulations. Figure 9.12 shows the development of the y -maxima of selected Fourier amplitudes in the downstream direction. The first digit refers to integer multiples of the fundamental frequency and the second digit to integer multiples of the fundamental spanwise wave number. The primary disturbance is the $(1,0)$ component, and the K-type secondary instability is primarily associated with the $(1,1)$ and $(0,1)$ components. Note the exponential growth of the three-dimensional disturbances, where the higher multiples of the fundamental frequency have growth rates that are approximately integer multiples of the growth rate of the fundamental. The exponential growth rate of the fundamental is compared with the spatial growth rate obtained from a Floquet analysis of the secondary K-type

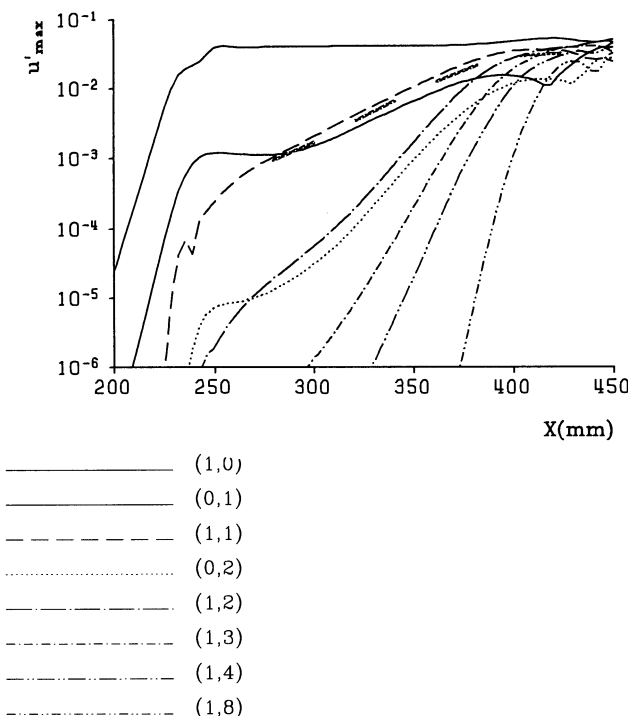


FIGURE 9.12. Development of the y -maxima of the streamwise velocity amplitudes in the downstream direction. From Rist & Fasel (1995).

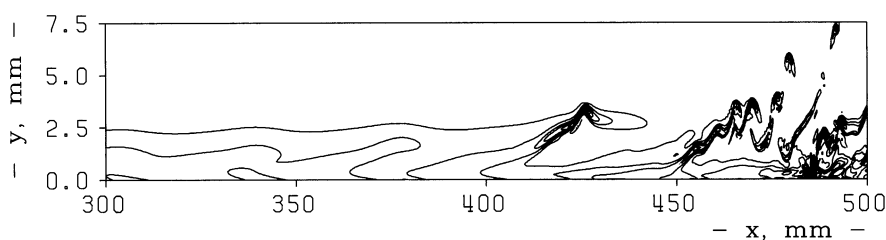


FIGURE 9.13. Instantaneous isolines of the spanwise vorticity component at the peak plane. From Rist & Fasel (1995).

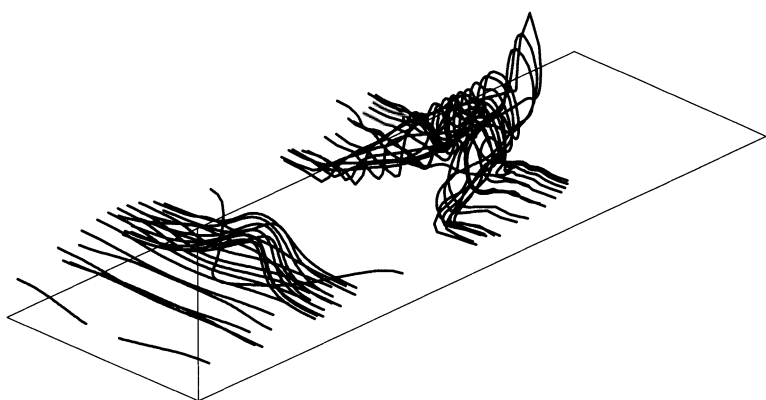


FIGURE 9.14. Timelines (particle paths) generated by marking wire placed at constant x and y in perspective view. From Rist & Fasel (1995).

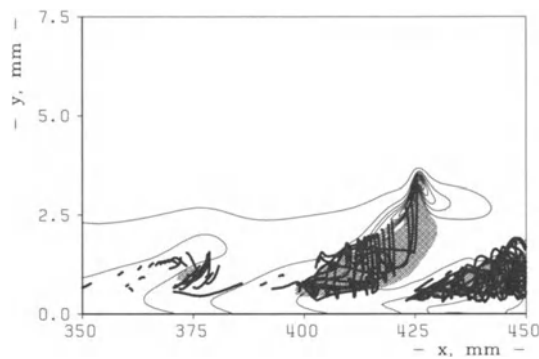


FIGURE 9.15. Comparison of instantaneous ω_z vorticity (isolines) with ω_x concentration (shaded area) and marker particles released in the peak plane, near the critical layer. From Rist & Fasel (1995).

instability, the long-dashed line in the figure; notice the good agreement far into the nonlinear stage of development.

The late stages of K-type transition

We conclude the description of the K-type breakdown by showing some detailed flow structures appearing at the late stages of the transition process. Figure 9.13 shows instantaneous isolines of the spanwise vorticity component for the peak plane, essentially indicating regions of high wall-normal shear. There are strong shear layers appearing in the outer flow region as the flow proceeds toward turbulence. These shear layers are associated with strong velocity spikes seen in measurements of the streamwise velocity at a constant normal position in the boundary layer. In addition to the strong shear layers there are so-called lambda-vortex (Λ -vortex) structures in the flow. These are identified by marked timelines (particle paths) of fluid particles. The vortex motion in the legs of the lambda vortex can be clearly seen; see Figure 9.14 .

The relationship between the shear layer and the Λ -vortex is illustrated in Figure 9.15, where a comparison of the isolines of instantaneous spanwise vorticity, concentration of streamwise vorticity (shaded area), and a projection of the marker particles from Figure 9.14, are shown. The timelines indeed identify the streamwise vorticity component of the Λ -vortex and the shear layer associated with the spike stage can be found directly above the head of the Λ -vortex.

Investigations of H-type transition

Investigations of the subharmonic or H-type (for Herbert) transition have been performed in both experiments and computations. Some investigators refer to this scenario as N-type (for Novosibirsk, where the experiments of this type of transition scenario were first carried out). Theoretically, this scenario is more likely to occur than the fundamental or K-type because of its higher growth rate (see Chapter 8). The temporal calculations presented in the first part of this chapter also showed that this was the case. In experiments, however, K-type is often seen in many cases where H-type is theoretically favored, due to the presence of low-amplitude streamwise vorticity in the background flow. Many flow structures in the late stages of H-type transition are similar to what is seen in K-type transition, e.g., the lambda-vortices that occur in a staggered pattern. We refer the interested reader to the end of the section on oblique, or O-type, transition, where a short discussion on the similarities and differences of K-, H-, and O-type transition scenarios in the Blasius boundary layer is presented.

For further reading and more references on K- and H-type transitions, see the reviews of Herbert (1988) and Kachanov (1994).

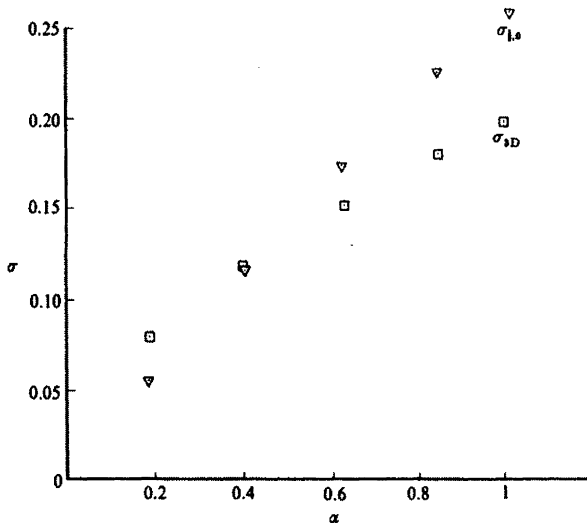


FIGURE 9.16. Subharmonic growth rate $\sigma_{\frac{1}{2},0}$ and three-dimensional growth rate σ_{3D} as a function of α for a mixing layer at $Re = 400$ and $\beta = 0.8$. Note that the wavenumber of the pairing mode is $\frac{1}{2}\alpha$. From Metcalfe *et al.* (1987).

9.2.2 Breakdown of Mixing Layers

There are a number of other flow situations and transition scenarios that start with two-dimensional waves; for example, flows with large exponential growth rates, typically associated with an inflectional mean velocity profile, such as the mixing layer or jet. We will next discuss temporal simulations of transition in mixing layers.

Secondary instability

The concept of secondary instability is also a fruitful one to consider for mixing layers. The primary instability in a mixing layer, which has been considered in detail in Chapter 3, is a strong inviscid exponential instability resulting from the inflectional mean profile. The finite-amplitude development of the disturbance is associated with the roll-up of the waves into a periodic array of strong vortices. These vortices can experience two different types of secondary instability. These two instabilities were simulated numerically by Metcalfe *et al.* (1987) by monitoring the growth of finite-amplitude disturbances on top of rolled-up finite-amplitude two-dimensional vortices.

Figure 9.16 shows the growth rate of a two-dimensional subharmonic Eckhaus-type secondary instability $\sigma_{\frac{1}{2}\alpha}$ compared to the growth rate of a three-dimensional elliptic-type secondary instability σ_{3D} . Both of these secondary instabilities have comparable growth rates, and it is a question

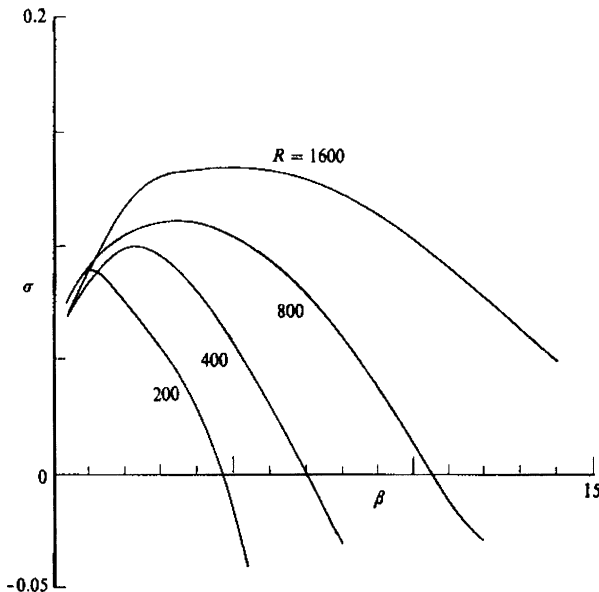


FIGURE 9.17. Three-dimensional growth rate σ_{3D} as a function of β for a mixing layer at various Reynolds numbers. The streamwise wavenumber α is 0.4. From Metcalfe *et al.* (1987).

of initial excitation which one is seen first. If the subharmonic secondary instability is predominant, the result is the growth of a disturbance with twice the wavelength of the initial vortices, producing a pairing of two vortices into a row of vortices twice as large. If the three-dimensional secondary instability is predominant, the result is the growth of spanwise perturbations on the two-dimensional vortices in conjunction with the appearance of secondary streamwise vortices connecting the original spanwise vortices. Figure 9.17 shows the growth rate of the three-dimensional secondary instability for various wave numbers and Reynolds numbers. Although the mean flow, $U(y) = \tanh y$, is both viscously and inviscidly stable for $\beta > 1$, the saturated two-dimensional vortices are strongly unstable at these scales.

We will now show the physical picture of these secondary instabilities following the calculations of Rogers & Moser (1992) and Moser & Rogers (1993).

Roll-up and pairing

The roll-up into an array of vortices by an initial condition consisting of a linear instability mode superimposed on a hyperbolic tangent mixing layer is shown in the first few frames of Figure 9.18. As the disturbance is growing, the spanwise vorticity is collecting into spanwise rollers at the expense of the vorticity in the braid regions located between a roller and

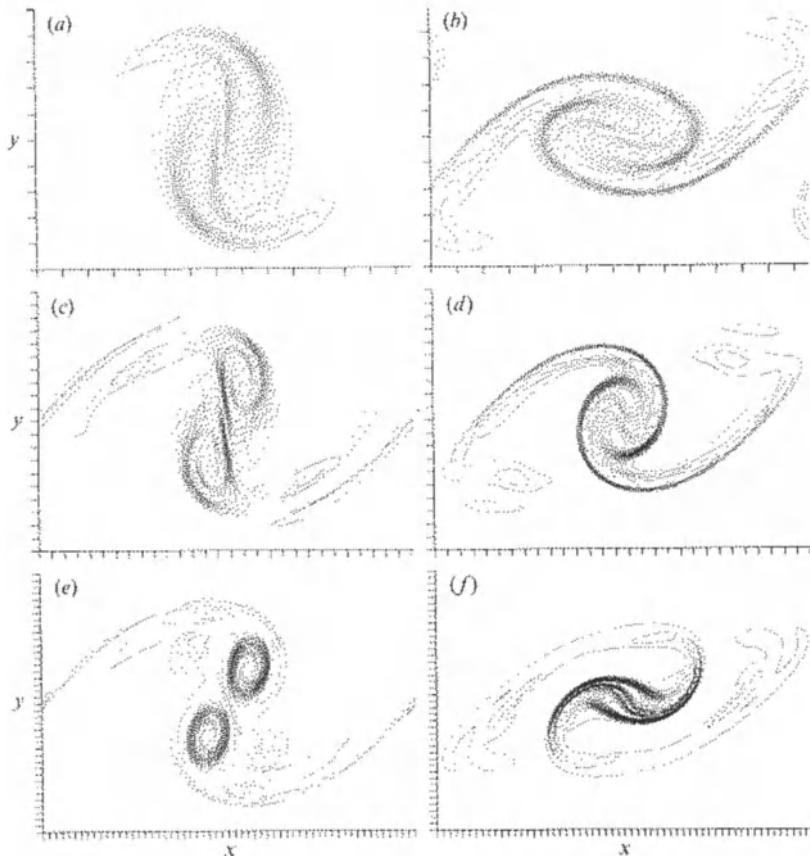


FIGURE 9.18. Roll-up and pairing of spanwise vortices in a hyperbolic tangent mixing layer. Displayed are contours of spanwise vorticity. From Moser & Rogers (1993).

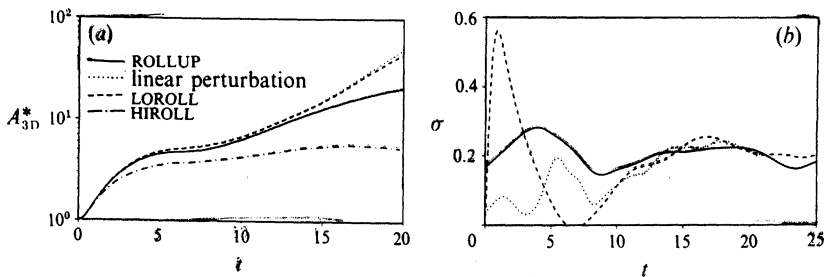


FIGURE 9.19. Evolution of a three-dimensional perturbation to the two-dimensional flow. (a) Amplitude of three-dimensional disturbance, $A_{3D}/A_{3D}(0)$, for linear, small ($A_{3D}(0) = 0.0166$), moderate ($A_{3D}(0) = 0.0832$) and high amplitude ($A_{3D}(0) = 0.3327$) cases. (b) Linear growth rate: —, elliptical flow analysis of Waleffe (1990); - - -, simulation of Rogers & Moser (1992). From Rogers & Moser (1992).

its periodic images. The roller quickly becomes roughly circular and as it continues to saturate changes into an elliptical form.

In the simulation just described, a small subharmonic disturbance was also added. As the vortex is rolling up, the subharmonic mode starts to grow, resulting in a pairing of two vortices seen in the latter frames of Figure 9.18. During this process, pairs of well-developed rollers come together, corotate, and eventually amalgamate. Both the number of rollers and the number of braid regions are thus halved, with the contents of every other braid region being absorbed into the new paired roller. The surviving braid region continues to be depleted of spanwise vorticity because all the vortical fluid is drawn into the paired roller.

The development of rib vortices and breakdown

Figure 9.19(a) shows the amplitude of the three-dimensional disturbance for four simulations with different initial amplitudes. It is interesting to note that although the amplitude is rather high for the moderate case, it can still almost be predicted by the linearized calculations.

The growth rate of the three-dimensional secondary instability is shown in Figure 9.19(b). The three-dimensional amplitude is measured by A_{3D} , which is the sum of the rms value in all oblique Fourier components of the three-dimensional disturbance. In addition, the growth rate from an application of the elliptical instability theory of Waleffe (1990) is shown. It is given by

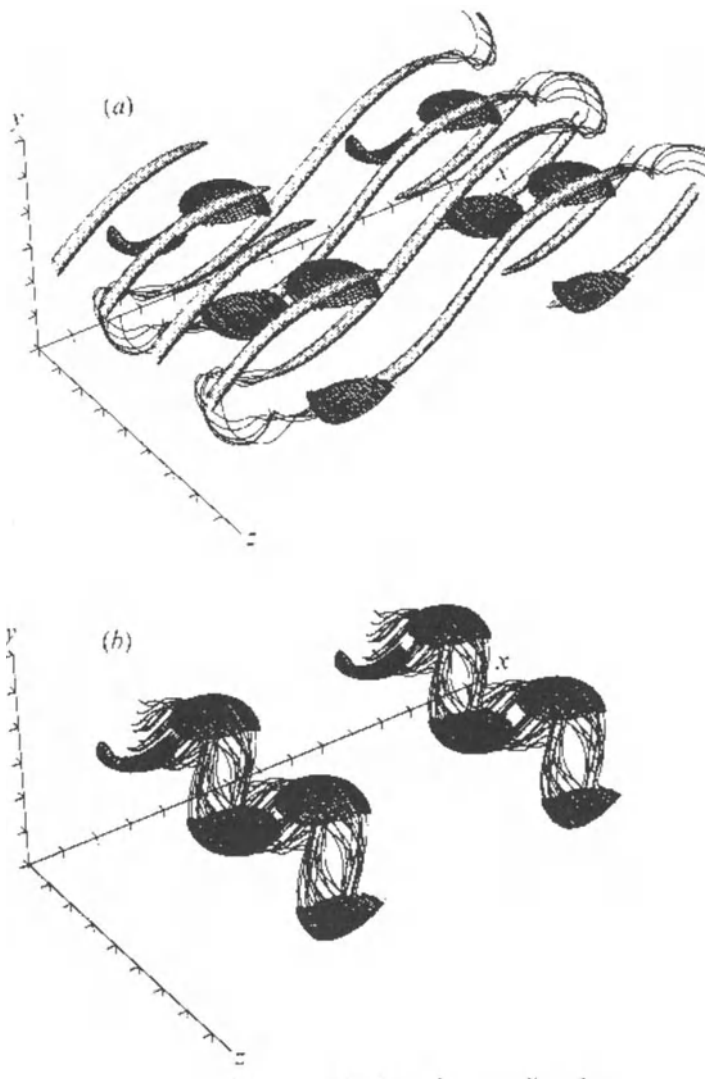


FIGURE 9.20. Surfaces of constant vorticity magnitude and vortex lines for moderate amplitude case at $t = 12.8$ from mixing layer simulations of Rogers & Moser (1992). Cross-hatched surfaces represent $\omega_z = -4.0$ and light surfaces in (a) show $(\omega_x^2 + \omega_y^2)^{1/2} = 4.0$. From Rogers & Moser (1992).

$$\sigma = \frac{9}{16} \gamma \sqrt{1 - 4\gamma^2/\omega_z^2} \quad (9.1)$$

where γ is the principal strain rate and ω_z is the spanwise vorticity, each evaluated at the center of the vortex. At $t = 15$ the two growth rates are almost identical, whereas for early times no agreement is expected because the mixing layer has not yet rolled up.

Once the three-dimensional disturbance reaches a finite amplitude, it produces a bending of the core of the rollers and of the so-called rib vortices extending in the streamwise direction in the braid region. The flow structures are shown in Figure 9.20, where the hatched cup-shaped surfaces contain large spanwise vorticity and the shaded surfaces visualize ω_x and ω_y of the same sign (alternating in the z -direction). Thus, the rib vortices occur in counterrotating pairs. The figures also show vortex lines going through the cup and rib regions, illustrating that the rollers are bent in a direction opposite to the vortex lines connecting the rib vortices. Caulfield & Kerswell (2000) modeled the braid region as a hyperbolic stagnation point and studied the nonlinear development of three-dimensional disturbances at these points.

9.3 Streak Breakdown

In this section we will discuss streak breakdown in channel and boundary layer flow. We will describe an experiment in channel flow where streaks have been artificially created and their secondary instability and transition to turbulence investigated. In boundary layer flow we will show streak breakdown results from both experiments and simulations: first, results for a single streak forced by blowing at the wall, and second, the initiation of streaks associated with moderate to high levels of freestream turbulence. The latter is one of the main practical applications where nonmodal growth mechanisms are responsible for the growth of the disturbances.

9.3.1 Streaks Forced by Blowing or Suction

Spatially evolving streaks in channel flow were created in the experiments of Elofsson *et al.* (1999), by applying suction through five slots (1 mm wide and 10 mm long) that were placed 15 mm apart. Downstream of the slots, phase-controlled disturbances were introduced through two holes 6 mm apart, which allowed for excitation of controlled secondary disturbances on the streaks.

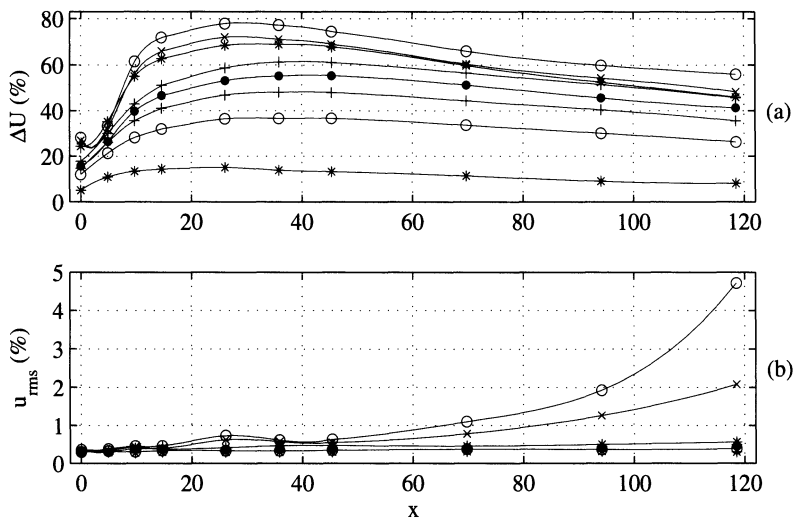


FIGURE 9.21. Evolution of (a) streak amplitude ΔU , (b) u_{rms} for $Re = 2000$. From Elofsson *et al.* (1999).

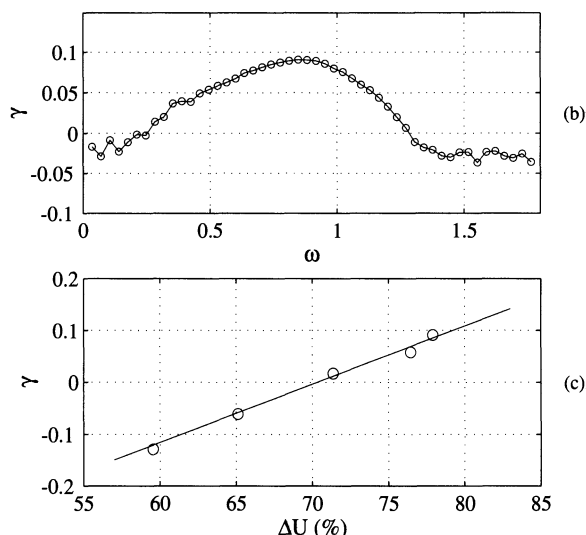


FIGURE 9.22. Dependence of growth rate (γ) on ΔU_{max} for $Re = 2000$ and frequency ω . From Elofsson *et al.* (1999).

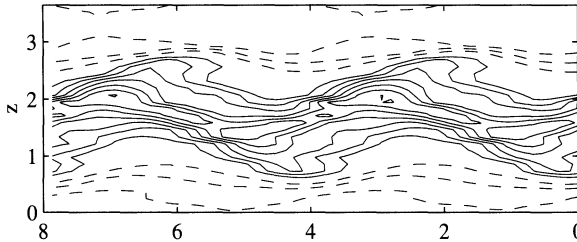


FIGURE 9.23. Contours of the phase-averaged velocity with spanwise average subtracted displayed in a $z-t$ -plane at $x = 93$. Forcing with $f_1 = 250\text{Hz}$ at $z = 1$ and $y = 2.4$. From Elofsson *et al.* (1999).

Secondary instability

In Figure 9.21 the overall evolution of ΔU and u_{rms} can be seen, where ΔU is the peak-to-peak value of the time-averaged mean flow, i.e., the streaks. These figures contain the results from several suction flow rates, resulting in streak amplitudes up to 78 percent of the centerline velocity. The data represent the maxima in each cross stream plane. The streak amplitude displays a rapid growth followed by a slow decay, and the u_{rms} remains constant with x , except for the two largest streak amplitudes where a significant growth can be seen for the farthest downstream positions.

In Figure 9.22, the dependence of the growth rate $\gamma = \ln(u/u_0)/(x - x_0)$ on the frequency ω and the streak amplitude ΔU are shown. The secondary instability is artificially introduced, and an amplification over a fairly wide frequency range can be seen. In addition, there exists a threshold in the streak amplitude of about 70 percent of U_{CL} , below which all time-periodic disturbances decay. We also observe a linear relationship between the streak amplitude and the growth rate.

Flow structures

The flow structures associated with the development of the streaks and their secondary instability can be seen in Figures 9.23 and 9.24. Figure 9.23 shows contours of the phase-averaged streamwise velocity in a $z-t$ plane. The sinuous nature of the secondary instability is preferentially triggered by operating the blowing and suction in the small holes out-of-phase. Under unforced conditions, it is still this type of instability mode that is observed. Figure 9.24 shows the contours of U_d and u_{rms} in cross stream planes. U_d is the time-averaged mean flow with its spanwise average subtracted. The maximum value of U_d decays slowly downstream while the maxima in u_{rms}

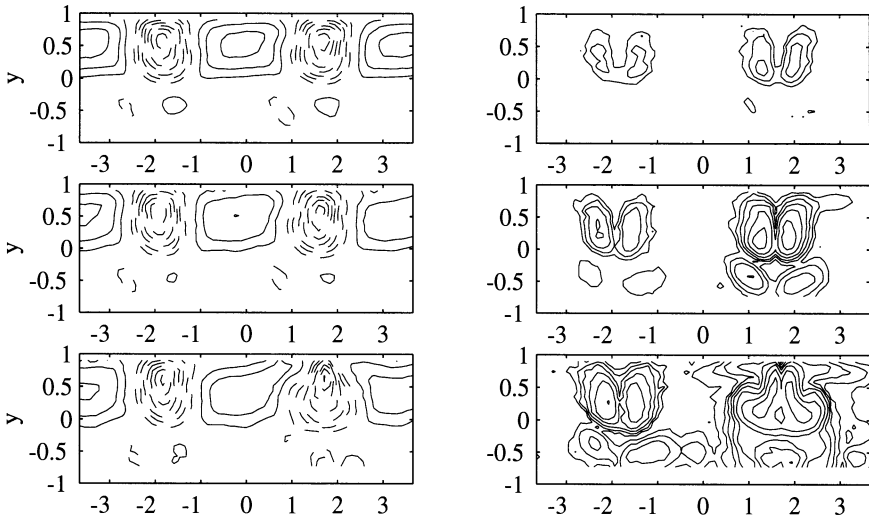


FIGURE 9.24. Contours of U_d (left) and U_{rms} (right) in y - z -planes at $x = 58$, 75 , 87 (from top to bottom). Forcing with $f_1 = 250\text{Hz}$ at $z = 1$ and $y = 2.4$. From Elofsson *et al.* (1999).

grow and appear in positions where the spanwise gradients of the streaks are large. At $x = 87$ both the streaks and the instability are highly deformed, showing that transition to turbulence is imminent.

It is interesting to compare these results with the streak breakdown in the temporal boundary layer described in Section 9.1.2 and with the temporal secondary instability calculations of streaks in channel flows presented in Chapter 8. It is clear that the temporal approximation gives a good qualitative view of the transition process, although it may be difficult to translate the large temporal secondary instability growth rates to corresponding spatial ones. It seems that it is indeed the sinuous secondary instability modes that are dominating. Another typical characteristic of streak breakdown is the large streak amplitudes that are required before they are susceptible to secondary instability and breakdown, about an order of magnitude larger than the amplitudes required for Tollmien-Schlichting waves to become susceptible to secondary instabilities.

Streaks formed by strong blowing at the boundary

The low-speed streaks in the experiment of Acarlar & Smith (1987) were forced by a strong steady blowing in a streamwise oriented slit at the wall in a boundary layer flow. The low-speed streaks developed a three-dimensional shear layer instability, which resulted in a periodic shedding of hair-pin vortices. This corresponds to a varicose secondary instability mode on the

single low-speed streak. The appearance of hair-pin vortices has also been found in numerical simulations by Singer & Joslin (1994), who used blowing to excite a turbulent spot. When streaks are created with large blowing at the boundary they seem to develop a varicose instability, whereas the streaks caused by smaller wall suction seem to be associated with a sinuous instability.

Asai & Nishioka (1995) introduced acoustically excited energetic hair-pin vortices at the leading edge of a flat-plate boundary layer and observed their subsequent development. They reported the occurrence of streamwise vortices in local three-dimensional wall shear layers.

Similarly, Levinski & Cohen (1995) studied the evolution of localized finite-amplitude vortex disturbances embedded in an external shear flow. Their analysis – based on the fluid impulse integral – showed the emergence of a growing vortex disturbance inclined at 45 degrees to the external flow direction in a plane normal to the transverse axis. Experiments confirmed their analysis.

9.3.2 Freestream Turbulence

The Klebanoff mode

The effect of freestream turbulence (FST) on the onset of transition was first investigated by Klebanoff (1971). Kendall (1985) summarizes the results as follows:

“Klebanoff recorded the fluctuation development in a flat plate layer at Re_x up to $2.1 \cdot 10^6$ for stream turbulence levels up to 0.3 percent. The turbulence was generated by means of various grids placed in the settling chamber of the tunnel. He showed that low frequency (in comparison with the most amplified TS-waves) fluctuations commenced growth at the plate leading edge and attained an amplitude of five percent at a station well ahead of the onset of transition, with the amplitude along the plate length varying in direct proportion to the boundary layer thickness.

“The broadband signal amplitude distribution through the layer resembled that which would result from a thickening/thinning oscillation of the layer, and Klebanoff referred to the low frequency motion as the breathing mode of the layer. He found by correlation methods that the broadband disturbances were quite narrow laterally, being no more than a few boundary layer thicknesses wide, although the scale depended upon that of the freestream turbulence and not upon the layer thickness.”

Kendall (1985) named this new disturbance-type Klebanoff mode. This summarizes the main features of the effect of freestream turbulence on a

boundary layer, and in the work by Kendall (1990) additional details of the disturbances are given. In flow visualizations, for example, he shows that these low-frequency oscillations are associated with long streaky structures inside the boundary layer.

Overview of the flow structures

The investigations of Klebanoff (1971) and Kendall (1985, 1990) were done with rather low freestream turbulence levels, $Tu < 1\%$ with the turbulence level defined as u_{rms}/U_∞ in the freestream. Streaky disturbances continue to be the main flow features as the freestream turbulence level increases, and in Figure 9.25 a smoke visualization of a boundary layer subjected to a freestream turbulence level of 2.2 percent demonstrates the presence of the typical streaky structures. Detailed studies and flow visualizations show that breakdown into turbulent spots occurs in regions where strong streaks exist. The breakdown occurs after a wavy motion of the streak has been observed, as can be seen in Figure 9.25. This breakdown seems to be associated with the same type of secondary instability described for channel flow streaks in the previous section. The transition region is then characterized by a random appearance of turbulent spots that grow in number and size downstream, until the boundary layer becomes fully turbulent.

Similar results have been reported by Westin *et al.* (1998) in their study of boundary layer receptivity to localized freestream disturbances. The appearance of streamwise vortices and the formation of streaks has been identified as the dominant mechanism.

In the simulations of Jacobs & Henningson (1999), shown in Figure 9.26, contours of the instantaneous streamwise velocity in a horizontal plane are displayed both inside and outside the boundary layer. At the inflow, small-scale turbulent fluctuations are seen at both positions. Above the boundary layer the intensity of the turbulence is seen to slowly decay downstream, from an initial intensity of about $Tu = 3\%$. Inside the boundary layer the turbulence is highly damped, and the same streaky structures as seen in the smoke visualizations appear. As we follow the streaks downstream, they break down into turbulent flow through the formation of turbulent spots. The simulations and experiments give the same overall picture of the transition process in boundary layers subjected to moderate levels of freestream turbulence.

Velocity measurements and correlations

Alfredsson & Matsubara (1996) and Westin *et al.* (1994) used hot-wire measurements for $Tu = 1.5\%$ and showed that the high frequencies in the freestream turbulence rapidly decay in the boundary layer while the low frequencies amplify; see Figure 9.27. It is the streaks that give rise to low-frequency disturbances when the streamwise velocity is measured by a stationary hot wire inside the boundary layer. The energy spectrum inside



FIGURE 9.25. Streaky structures observed through smoke visualization in a laminar boundary layer subjected to 2.2 % freestream turbulence. The flow is from bottom to top. Observe the sign of streak oscillations, breakdown and turbulent spot formation near the top edge of the photograph. From Alfredsson & Matsubara (2000).

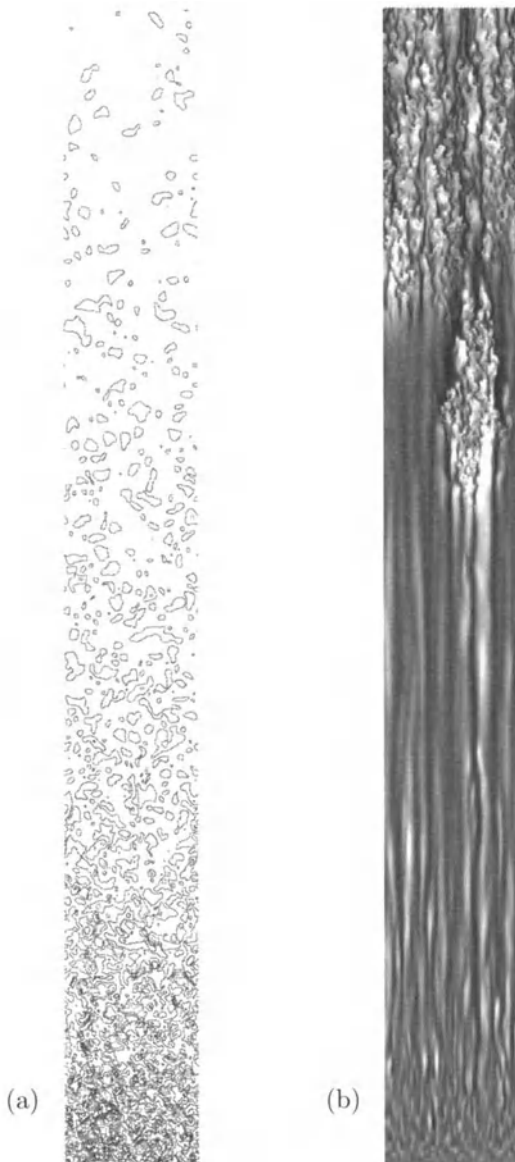


FIGURE 9.26. Contours of the streamwise velocity in the x - z -plane (a) above and (b) inside the boundary layer. The inflow Reynolds number is $Re = 278$; the flow is from bottom to top. The spanwise coordinate is stretched by a factor of two compared to the streamwise one. From Jacobs & Henningson (1999).

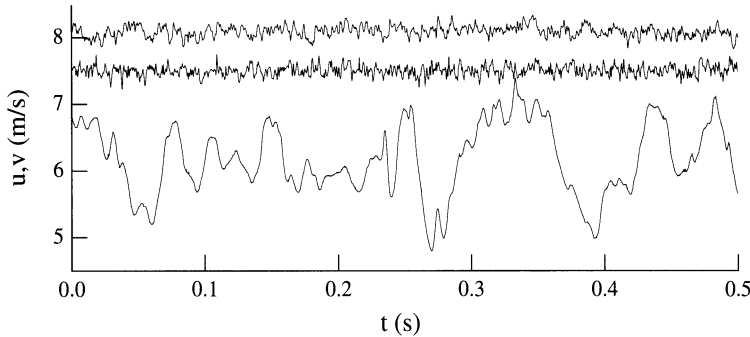


FIGURE 9.27. Comparison between velocity signals inside and outside a boundary layer subjected to freestream turbulence. The upper two traces are u and v measured in the freestream; the lower trace is u measured at $y/\delta^* = 1.5$. From Alfredsson & Matsubara (1996).

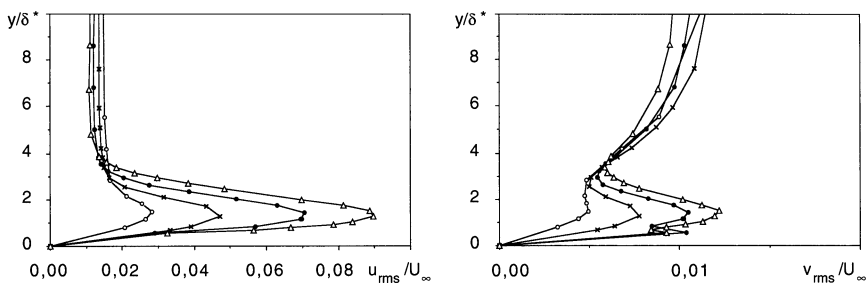


FIGURE 9.28. u_{rms} and v_{rms} -profiles for four different downstream positions in a boundary layer subjected to freestream turbulence. \circ : $x = 100\text{mm}$, \times : $x = 250\text{mm}$, \bullet : $x = 500\text{mm}$, Δ : $x = 800\text{mm}$. From Alfredsson & Matsubara (1996).

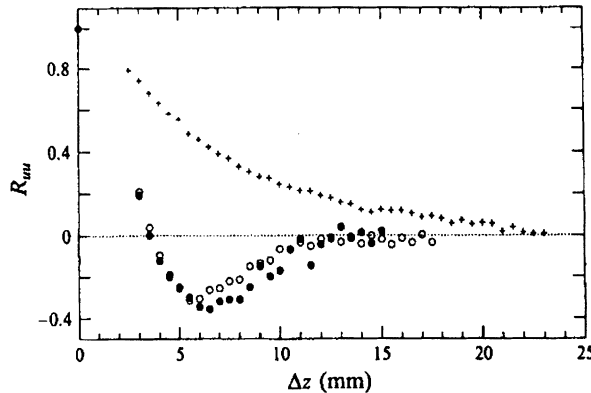


FIGURE 9.29. Spanwise correlations of the streamwise velocity in the boundary layer, measured close to the maximum of u_{rms} for $x = 500\text{mm}$ (○), $x = 1000\text{mm}$ (●). Spanwise correlation in the freestream at $x = 500\text{mm}$ (+). From Westin *et al.* (1994).

the boundary layer is dominated by contributions with frequencies much lower than in the turbulent freestream.

Westin *et al.* (1994) shows that although the u_{rms} levels inside the boundary layer may reach 10 percent or more before transition to turbulence occurs, the boundary layer profile is only slightly changed compared to the undisturbed flow. The rms profiles for both u and v are displayed in Figure 9.28 for four downstream positions. It is clearly demonstrated that the intensity increases in the downstream direction and that u_{rms} has a maximum in the center of the boundary layer. Several boundary layer thicknesses from the wall to the level of v_{rms} starts to decrease from its freestream value.

The spanwise distribution of the boundary layer perturbations is illustrated (Figure 9.29) by the correlation between two hot wire probes displaced in the spanwise direction. There is a marked anticorrelation at a spanwise probe separation approximately the size of the boundary layer thickness, corresponding to half the average spacing of the streaks.

The origin of streaks

In Figure 9.30, the results from the calculations of the optimal streak growth of Andersson *et al.* (1999) (described in Chapter 7) are plotted together with experimental data from Westin *et al.* (1994). The experimental data represent profiles of root-mean-square streamwise velocity perturbations seen in Figure 9.28. Because the experimentally measured streamwise rms values are mainly composed of low-frequency fluctuations, corresponding to elongated streaky structures, it is plausible to expect that they can be modeled by spatially growing steady streaks.

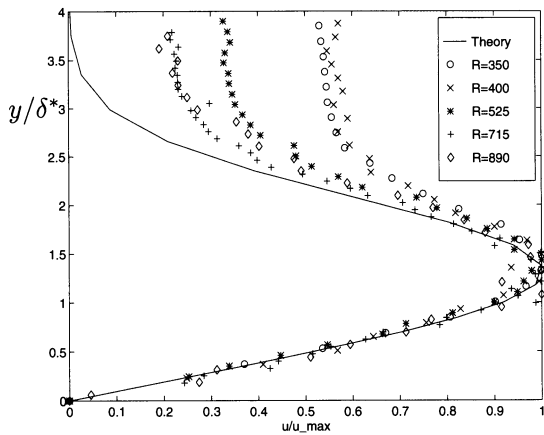


FIGURE 9.30. Streamwise velocity component of the downstream response of an optimal perturbation compared to experimental data. For the calculations, the parameters were taken as $x_f = 1$, $x_0 = 0$, $\beta = 0.45$ and $Re > 10^6$. From Andersson *et al.* (1999).

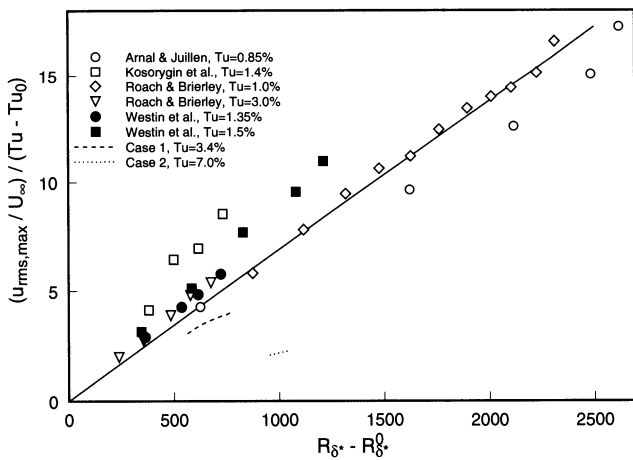


FIGURE 9.31. Downstream growth of u_{rms} versus Re_{δ^*} from various experiments. From Jacobs & Henningson (1999).

Recall that the maximum energy growth calculated by Andersson *et al.* (1999) scaled linearly with downstream distance. This implies that the amplitude growth scales linearly with the Reynolds number based on displacement thickness. Figure 9.31 shows the downstream growth of u_{rms} with Re_{δ^*} obtained from a number of different experiments. In the figure u_{rms} is scaled with $(Tu - Tu_0)U_0$ where $Tu_0 = 0.5\%$ and Re_0 is chosen so that the turbulence level is zero at the leading edge. A linear collapse of the data is clearly seen in Figure 9.31. In addition, the turbulence level of $Tu = 0.5\%$ is approximately the value below which the streak breakdown scenario ceases to exist.

The good agreement between the measured and calculated velocity profiles, as well as the approximately linear growth of the streak energy with downstream distance, indicate that the streak captured by the calculation is the Klebanoff mode. It also indicates the origin of the Klebanoff mode as a streamwise vortex situated outside the boundary layer at the leading edge. Detailed investigations of how particular freestream disturbances enter into a laminar boundary layer have also been performed by Bertolotti (1997), Goldstein & Wundrow (1998) and Leib *et al.* (1999).

However, there are other possible sources of boundary layer streaks. Berlin & Henningson (1999) showed that oblique disturbances in the free-stream could easily generate streamwise vortices and subsequent streaks inside the boundary layer. This is a nonlinear process and is most active at higher levels of freestream turbulence.

In a large-eddy simulation (LES) by Yang & Voke (1993), different free-stream conditions were imposed, and it was found that freestream fluctuations in the pressure (p) and normal velocity (v) are the most efficient in exciting perturbations in the boundary layer, whereas fluctuations in the streamwise velocity (u) are rather harmless. Thus measuring the turbulence intensity associated with the normal velocity may improve the correlations shown earlier, which are mostly based on measurements of the streamwise velocity only.

9.4 Oblique Transition

9.4.1 Experiments and Simulations in Blasius Flow

Overview of spatial oblique transition

Oblique transition has been studied in channel and boundary layer flows. In Section 9.1.2 the scenario was described for a temporally developing boundary layer. We will show that the same scenario exists and is a strong candidate for initiating laminar-turbulent transition in a spatially developing boundary layer.

The flow visualizations of Elofsson (1998), seen in Figure 9.32, gives a good overview of the scenario as it develops in space. In the lower part of the photograph a three-dimensional wave field is observed which farther downstream develops into the typical elongated structures associated with streamwise streaks. Breakdown is detected at the downstream end of the test section as a vortical motion associated with individual streaks develops.

The main Fourier components involved in spatially developing oblique transition correspond to those seen in Section 9.1.2, although now they are obtained by Fourier-transforming the solution in time and the spanwise direction rather than in the streamwise and spanwise directions. Figure 9.33 shows results from the direct numerical simulation of Berlin *et al.* (1994) in which results qualitatively similar to Elofsson & Alfredsson (1998) were obtained, although at a lower Reynolds number. At the inflow only the $(1, \pm 1)$ components are excited. The $(1, \pm 1)$ modes show a rapid initial growth as a result of zero initial normal vorticity. The $(0, 0)$, $(0, \pm 2)$, $(2, 0)$, and $(2, \pm 2)$ components subsequently grow due to nonlinear effects, because they are directly generated by the $(1, \pm 1)$ modes through triad interactions. The $(0, \pm 2)$ components grow more rapidly than the other modes and continue to grow until $x - x_0 \approx 100$. The latter part of this growth is due to the linear forcing of the streak (u component) by the vortex (v, w component). A second phase of rapid growth starts for modes with nonzero ω , eventually completing the transition process.

Figure 9.34 shows the streamwise shear in an x - y plane for the same numerical simulation. Strong shear layers can be seen, which closely resemble the spike stages found in the secondary instability of two-dimensional Tollmien-Schlichting waves. This and other similarities will be discussed in the following section.

Late stages of oblique transition

Detailed modeling of an experiment conducted in Göttingen, using direct numerical simulations of the Navier-Stokes equations, has shown that it is possible to obtain close agreement between numerical results and experimental efforts even at the late stages of disturbance development (Berlin *et al.*, 1999). We will show results from these investigations, focusing on the structures seen in the late stages of oblique transition.

Before the flow reaches a fully turbulent state, Λ -shaped structures consisting of pairs of streamwise counterrotating vortices are formed. These Λ -vortices are much stronger than the mean vortices causing the streak growth; one of these Λ -vortices is shown in Figure 9.35, where light and dark surfaces represent constant negative and positive streamwise vorticity, respectively. On the outside of the vorticity surfaces the disturbance flow is directed downward, whereas between the vorticity surfaces there is an upward motion. The lift-up of slow streamwise velocity between the vortices causes strong gradients in the streamwise velocity, which is shown

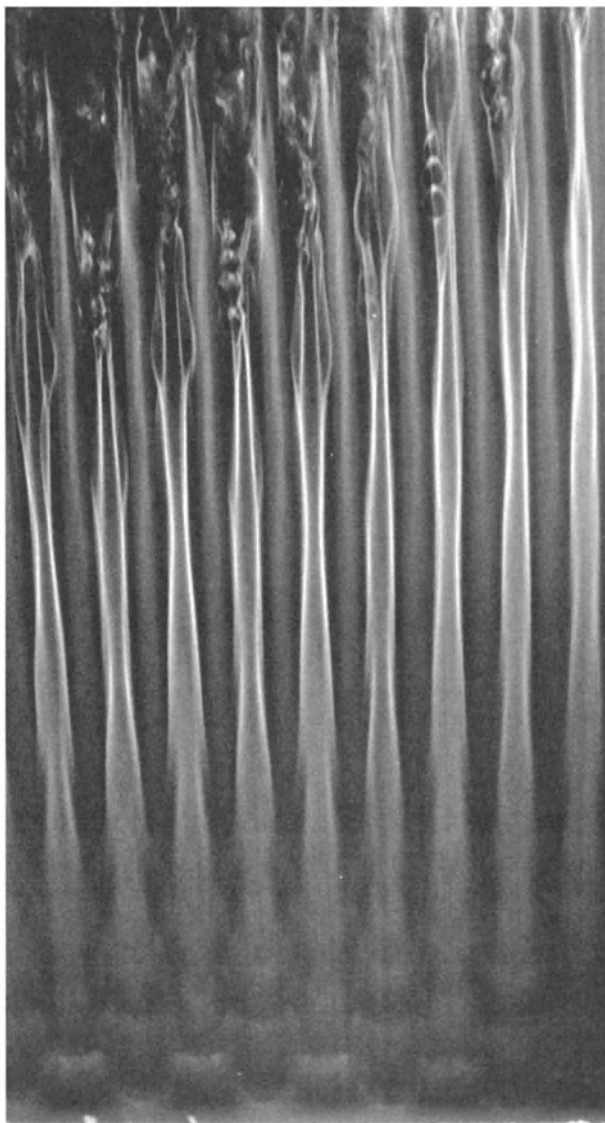


FIGURE 9.32. Smoke visualization of oblique transition; x - z -plane with flow from bottom to top. $U_\infty = 8.4 \text{ m/s}$ and $F = 69$. From Elofsson (1998).

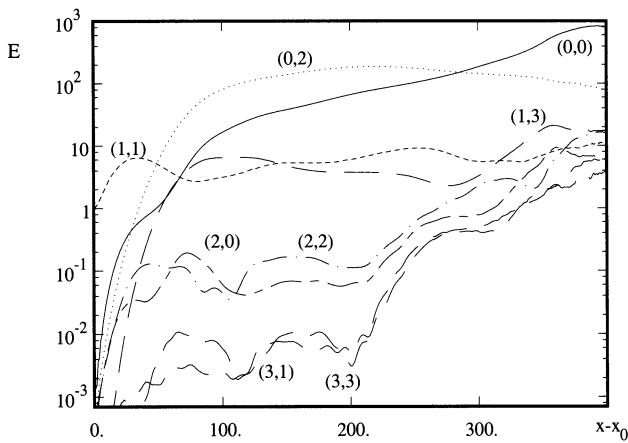


FIGURE 9.33. Energy in Fourier components with frequency and spanwise wavenumber $(\omega/\omega_0, \beta/\beta_0)$ as shown. The curves are normalized by the energy of the $(1,1)$ mode at the inflow. From Berlin *et al.* (1994).

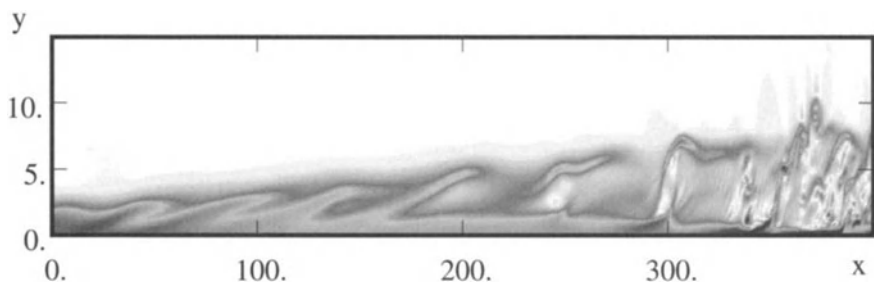


FIGURE 9.34. Streamwise shear in a x - y -symmetry plane for oblique transition. From Berlin *et al.* (1994).



FIGURE 9.35. Positive (light) and negative (dark) isosurfaces of streamwise vorticity in a Λ -vortex together with the associated high streamwise shear-layer (top). The white arrow at the wall marks the direction of the mean flow. From Berlin (1998).

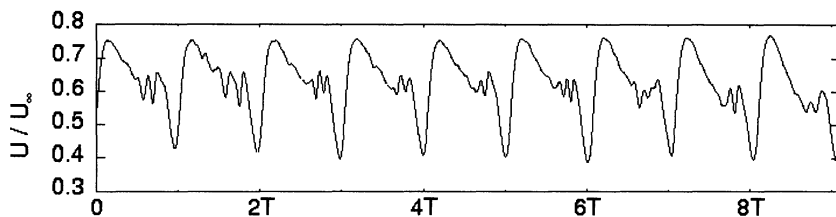


FIGURE 9.36. Time signal of the streamwise velocity at $z = -2.5$ mm, $x_v = 566$ mm, $y/\delta_r = 1.55$. From Berlin *et al.* (1999).

as a gray surface of constant $\partial u / \partial y$ in the figure. Λ -vortices are closely associated with the final breakdown. Inflectional velocity profiles, in both the normal and spanwise directions are associated with the Λ -vortices, and large velocity fluctuations and high u_{rms} values are first detected in their vicinity.

Measurements using hotwire probes positioned just to the side of the tip of the Λ -vortex show the first appearance of high-frequency oscillations. A time trace at such a position taken from the experiment is presented in Figure 9.36, where each fundamental cycle contains high-frequency oscillations.

Relation to K- and H-breakdown

The structures that we have identified in the late stage of oblique transition have many similarities with those found by previous investigators in the

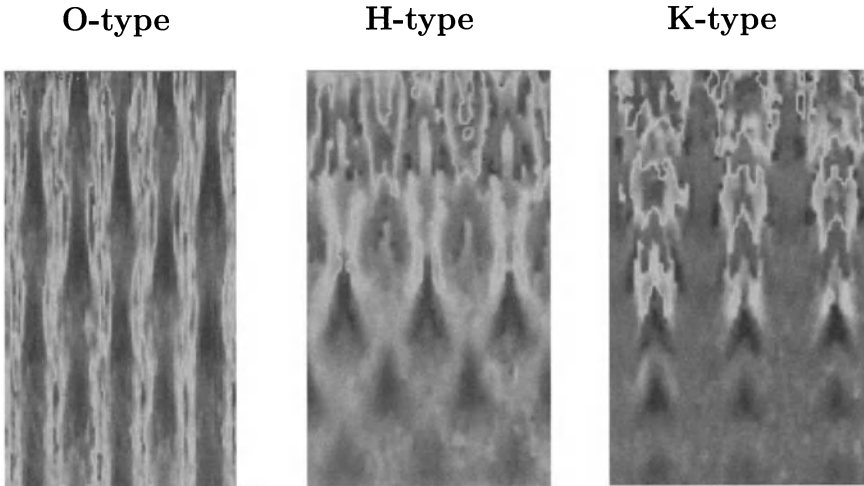


FIGURE 9.37. Instantaneous streamwise velocity fields from three transition scenarios measured with the PIV technique; from left to right: oblique transition, H-type transition and K-type transition. The flow direction is from the bottom to the top of the figures. Both Λ -shapes and streaks can be observed in all three scenarios. From Berlin *et al.* (1999).

corresponding stage of K- and H-type transition. We find, for example, Λ -vortices with strong shear layers on top, streamwise vortices deforming the mean flow, and inflectional profiles. PIV measurements of the instantaneous streamwise velocity from the three transition scenarios are compared in Figure 9.37. Both streaks and Λ -vortices can be observed in all three figures, but the amplitude relation between them differs.

Berlin *et al.* (1999) speculated that the pattern of Λ -vortices appearing in these three transition scenarios is independent of the presence of a Tollmien-Schlichting wave. Using a criterion of positive interference of the normal velocity between the streamwise vortices and the oblique waves, they were able to predict the appearance of Λ -vortices.

The experimental study of the late nonlinear stage of transition in Blasius boundary layers by Bake *et al.* (2000) further investigates the resemblance of K-type and H-type transition.

9.4.2 Transition in a Separation Bubble

Base flow characteristics

We will now consider the transition process in a laminar separation bubble. Rist & Maucher (1994) simulated a laminar separation bubble resulting from a local deceleration of the freestream velocity; see Figures 9.38 and 9.39(a). There is a strong increase in the shape factor and displacement thickness already upstream of the bubble that peaks in the middle of

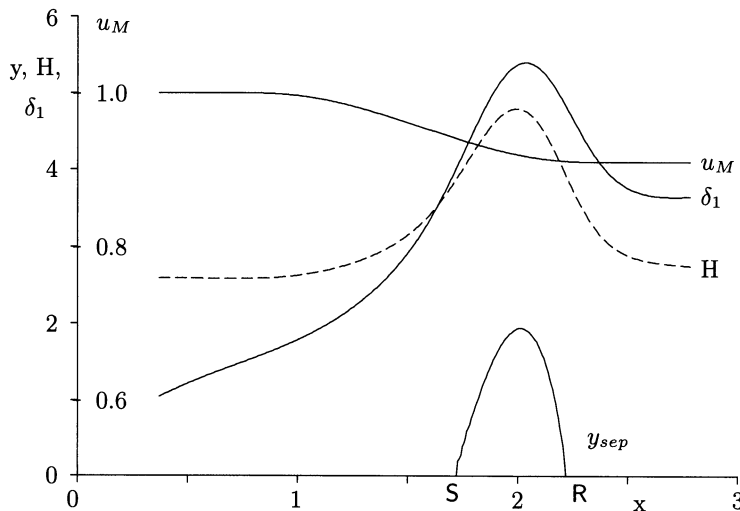


FIGURE 9.38. Base flow parameters for simulations of a laminar separation bubble: free-stream velocity u_M , shape factor H , displacement thickness δ_1 , separation streamline y_{sep} , separation point S, and reattachment point R. From Rist & Maucher (1994).

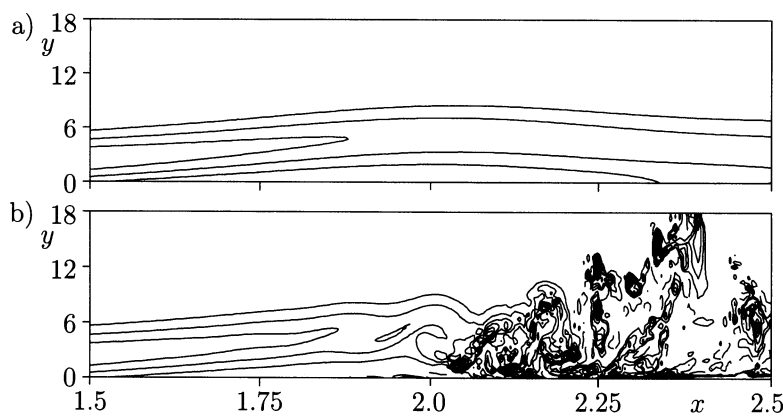


FIGURE 9.39. Vorticity of steady two-dimensional base flow (a) compared with three-dimensional instantaneous vorticity from O-type transition at $z = 0$ (b). From Rist & Maucher (1994).

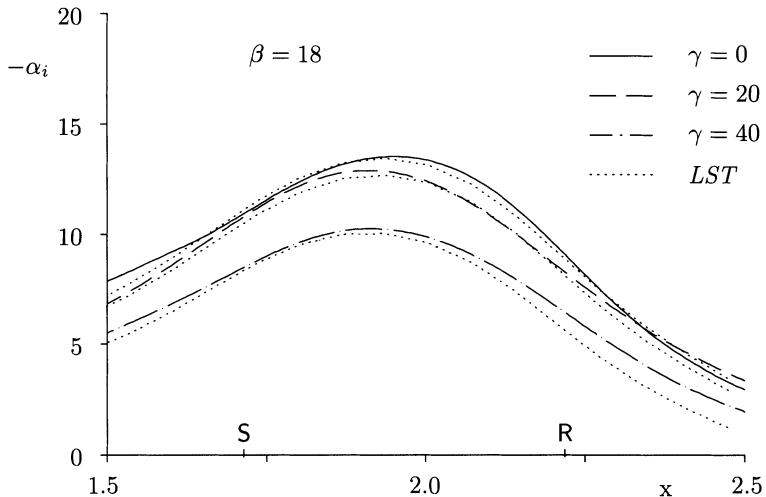


FIGURE 9.40. Comparison of DNS-amplification rates from a small-amplitude simulation with linear stability theory (*LST*). β stands for the frequency, γ denotes the spanwise wave number. From Rist & Maucher (1994).

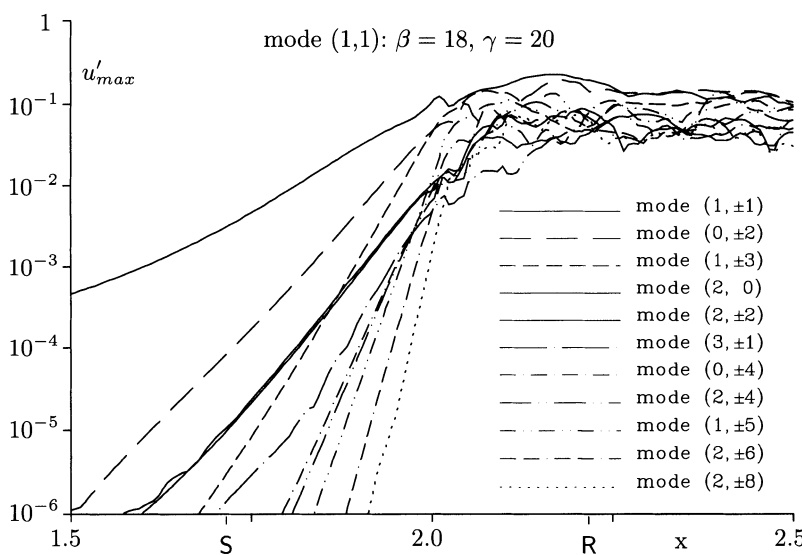


FIGURE 9.41. Amplification curves for large three-dimensional disturbance amplitudes (case O). β stands for the frequency, γ denotes the spanwise wave number. From Rist & Maucher (1994).

the separated region. Separation and reattachment, however, occur downstream of the largest gradient in the freestream velocity. In the separated region there exist sharp shear layers, and behind the bubble the flow asymptotically returns to Blasius boundary layer flow.

Linear stability theory calculations based on the Orr-Sommerfeld equation using local velocity profiles from the direct numerical simulations are shown in Figure 9.40. The plot reveals that the flow is most unstable to two-dimensional disturbances, although oblique waves are also unstable. The nonparallel effects are small because the Orr-Sommerfeld results show close correspondence to the growth rate calculated by introducing small wavelike disturbances in direct numerical simulations.

O-type transition

Rist & Maucher (1994) introduced different types of disturbances upstream of the bubble to study the complete transition process. If two-dimensional waves are introduced, large two-dimensional vortices start to shed from the bubble and the secondary instability and breakdown show similarities to those seen in the mixing layers reported in Section 9.2.2. However, if oblique waves are introduced upstream of the bubble, no large two-dimensional vortices are formed; instead the flow quickly becomes turbulent. Figure 9.39 shows a side view of the instantaneous vorticity from the complete transition simulation.

A detailed study of the amplitude in the individual Fourier components during this O-type transition is seen in Figure 9.41. The oblique mode (1,1) is growing exponentially, does not saturate until the flow reaches transition, and all other modes are nonlinearly generated from interactions with this mode. The second-generation modes (2,0), (2,2), and (0,2) are seen to have approximately twice the growth rate of the (1,1) mode; third-generation modes, of which (1,3) and (3,1) are shown, have about three times the growth rate. It is interesting to observe that it is again the modes that are most easily forced according to linear theory, i.e., (0,2) and (1,3), that attain the largest amplitudes. Thus, the rapid growth of the disturbance energy and the rapid transition can again be attributed to the same nonmodal growth mechanisms that were active during oblique transition in other flows. For O-type transition, there is no sign of a secondary instability of streaks, however, because the (1,1) mode is exponentially growing well into the transition region and is of larger amplitude than the forced (0,2) mode.

Spalart & Strelets (2000) conducted direct numerical simulations of transition in a separation bubble and observed a marked wavering of the shear layer followed by Kelvin-Helmholtz vortices which - without pairing - rapidly broke down due to three-dimensional instabilities. In the experimental investigation by Watmuff (1999) small-amplitude impulsive disturbances were introduced through a hole in the test surface. The resulting wave packet showed dispersive effects near the separation point, developed Kelvin-

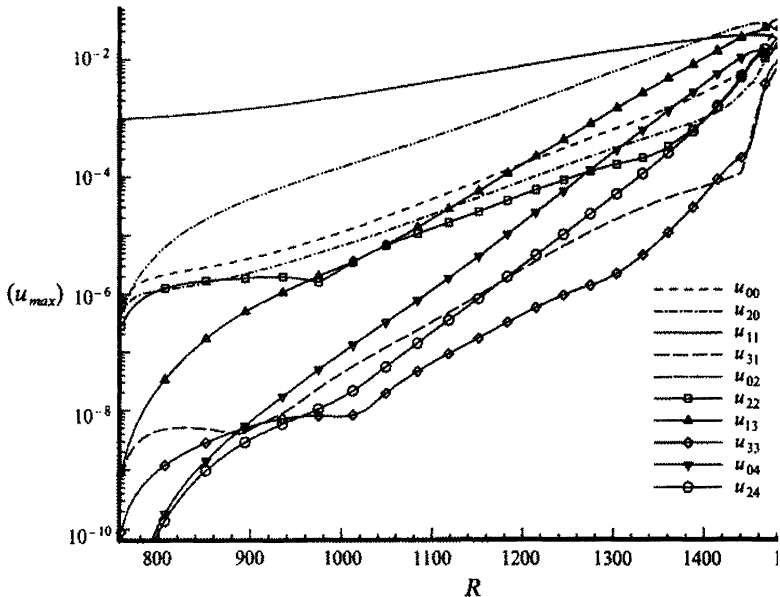


FIGURE 9.42. Evolution of maximum root-mean-square u -velocity perturbations for O-type transition. $\text{Ma} = 1.6$, $F = 0.2 \times 10^{-4}$ and $\beta/\text{Re} = 0.83 \times 10^{-4}$. From Chang & Malik (1994).

Helmholtz-type instability patterns near the reattachment point, and broke down into large-scale vortex loops further downstream.

9.4.3 Compressible Oblique Transition

For supersonic flows the most amplified linear wave is oblique with an angle of about 45° to 60° , see Section 6.5. Hence, small exponentially growing waves may interact nonlinearly to create growing streak components. This is similar to the transition scenario just described in the separation bubble because the oblique waves will be exponentially growing during the complete transition process. Fasel *et al.* (1993) showed that for a given initial energy this scenario was a much faster route to transition than for disturbances centered around two-dimensional waves.

Figure 9.42 shows the amplitude in a number of Fourier components in a nonlinear PSE calculation of Chang & Malik (1994). The $(1,1)$ modes are initialized at a rather low amplitude but quickly force high-amplitude perturbations in other wave components, particularly in the $(0,2)$ and $(1,3)$ components. Again, these are the modes associated with the most non-modal growth and are thus also the most easily forced. In the calculations of Chang & Malik (1994), O-type transition could occur for initial ampli-

tudes about two orders of magnitudes lower than for traditional H-type secondary instability.

9.5 Transition of Vortex-Dominated Flows

In this section we will consider laminar-turbulent transition in flows dominated by streamwise vortices. Because the vortices create streaks, these flows have many similarities with those considered in the previous section. On the other hand, in the flow situations studied in this section, the vortices themselves are part of the growing primary instability and play a crucial role in the transition process. We will consider Dean and Görtler vortices in flows with curvature and crossflow vortices in three-dimensional boundary layers.

9.5.1 *Transition in Flows with Curvature*

Dean vortices

In curved channels there exists a strong primary instability, as described in Section 6.2.1. The finite-amplitude development of this instability results in the formation of Dean vortices. The formation and breakdown of Dean vortices were considered experimentally by Matsson & Alfredsson (1990). Figure 9.43 shows the flow from the convex side of the channel. Close to the inlet the instability first arises in the form of a streaky structure, in this case showing streamwise vortices. The higher the Reynolds number, the closer to the inlet the Dean vortices appear and the faster they experience secondary instability, seen as a twisted pattern on top of the vortices in Figure 9.43. The secondary instability resulted in turbulence if the Reynolds number was high enough. Figure 9.44 shows the flow regimes found by Matsson & Alfredsson (1990). The boundaries between the different flow regimes were not distinct in their experiment.

Another aspect of the transition to turbulence of Dean vortices, also seen in Figure 9.43, is the merging and splitting of the vortices as they develop in the downstream direction. As we saw in Chapter 8, the developing Dean vortices are unstable to spanwise perturbations due to the Eckhaus instability mechanism. The nonlinear growth of these spanwise perturbations causes merging and splitting and as a result the wave numbers of the Dean vortices are changed. Because the first occurrence of vortex splitting and merging events depends on the initial perturbations at the channel entrance and the growth rates of the primary and Eckhaus instabilities, it is difficult to predict the favored wave numbers that prevail after the first onset of vortex splitting and merging. Guo & Finlay (1991) speculate that further downstream, as the splitting and merging of vortices continues to occur due to the instability of nonlinear Dean vortices with respect to spanwise

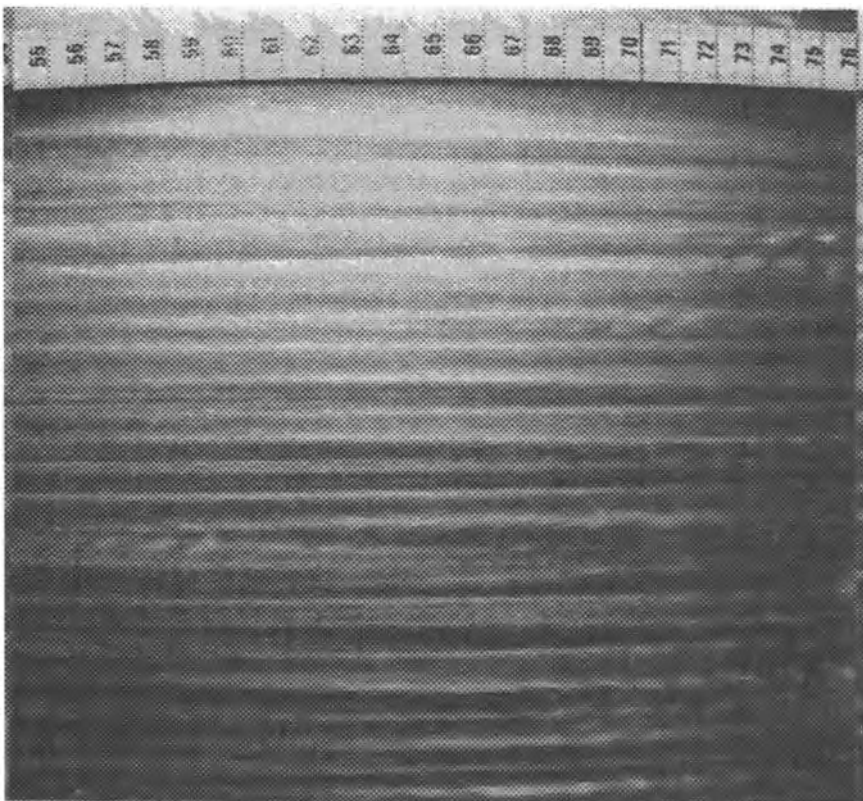


FIGURE 9.43. Flow visualization of curved channel flow at $Re = 960$ and $\gamma = 0.025$. From Matsson & Alfredsson (1990).

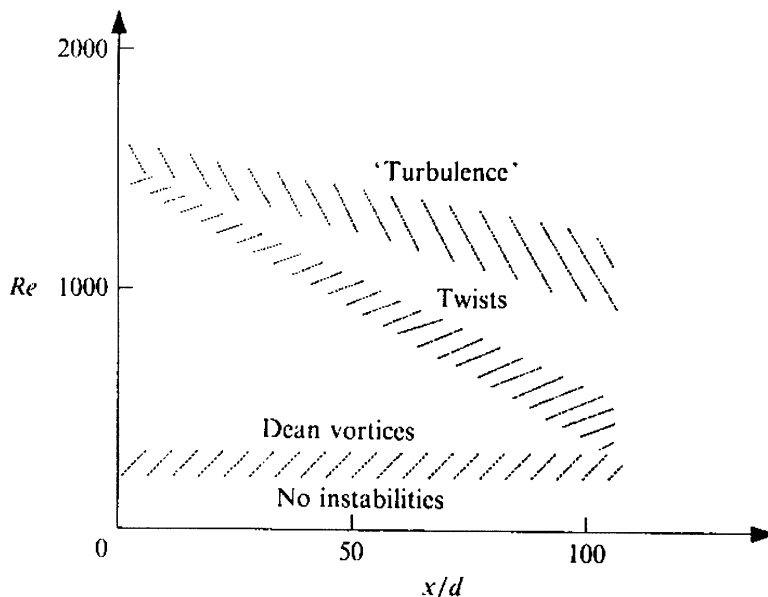


FIGURE 9.44. Observed flow regions for curved channel flow with $\gamma = 0.025$. From Matsson & Alfredsson (1990).

perturbations, the wave numbers that have the minimum Eckhaus growth rate are those most likely to be observed.

The perturbations needed for splitting and merging of Dean vortices can also originate from the interaction of vortices with different wave numbers. In Figure 9.45 Dean vortices with $\beta = 3$ and $\beta = 2.5$ reach a fully developed state at about $\theta = 2.5$. Then, near the interfaces between the two vortices with different wave numbers, a merging event among the vortices with $\beta = 3$ and a splitting event among the vortices with $\beta = 2.5$ begins to develop. The numerical calculations show a number of additional merging and splitting events as the flow proceeds downstream. These calculations used parabolized equations and therefore cannot be used to describe the secondary instability or the breakdown of these vortices. In this model the vortices would continue to split and merge as the flow developed downstream, without any subsequent transition to turbulence.

Görtler vortices

There are a number of similarities between the transition process in curved channel and curved boundary layer flows. Both flows have strong primary instabilities that result in finite-amplitude vortices. In curved boundary layer flow the vortices are called Görtler vortices. These vortices also experience merging and splitting as a result of an Eckhaus instability (Guo

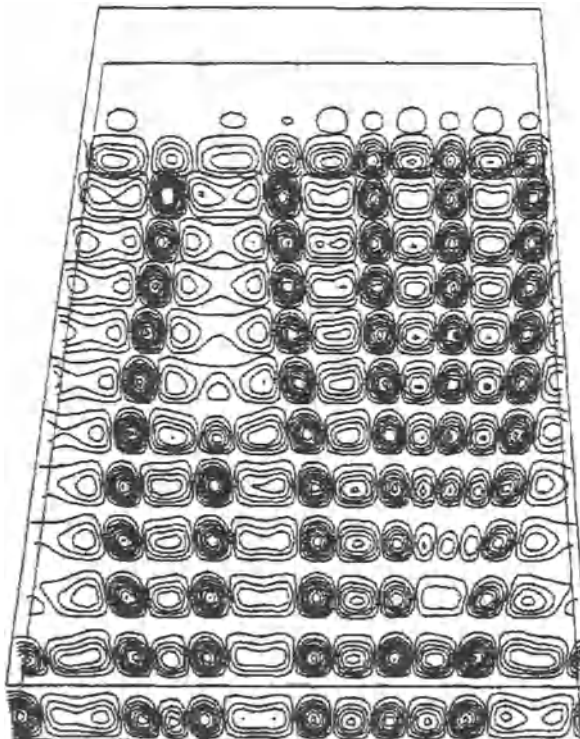


FIGURE 9.45. Contours of normal velocity of developing Dean vortices (shown in cross-stream planes from $\theta = 0.5$ to $\theta = 7.5$, with $\Delta\theta = 0.5$) in curved channel flow with $\gamma = 0.025$ and $Re = 2.186Re_c$. The simulations start with $\beta = 3.0$ for the right three vortices and with $\beta = 2.5$ for the left two vortex pairs. The flow proceeds downstream from top to bottom. Contours levels range from -0.08 to 0.08 in increments of 0.0105 . From Guo & Finlay (1991).

& Finlay, 1994), and they break down in conjunction with oscillatory secondary instabilities.

We will describe the careful flow visualization experiments of Swearingen & Blackwelder (1987) regarding the secondary instability of the Görtler vortices. It is evident from Figure 9.46 that the low-speed streaks developed by the vortex field experience periodic oscillations prior to transition. Two different modes of secondary instability were observed to precede the breakdown of the Görtler vortices in the experiments of Swearingen & Blackwelder (1987). Streak lines of the types seen in Figure 9.46(a) suggest that a horseshoe vortex structure is associated with development of the secondary instability, and the sinuous transverse oscillations of the streak lines seen in Figure 9.46(b) are an example of the second type of secondary instability.

It is interesting to compare these results with the secondary instability calculations of Li & Malik (1995), described in Section 8.3.2. They found four different modes of secondary instability, two of which are readily identified as the two seen in the experiments described above. The varicose fundamental mode of Li & Malik (1995) corresponds to the horseshoe vortex mode found by Swearingen & Blackwelder (1987), and the sinuous subharmonic mode in the calculations corresponds to the sinuous mode seen in the experiments. Both of these modes have high growth rates according to the calculations, although they do not represent the mode with the highest growth rate, which is a fundamental sinuous mode. Thus it is clear that the particular mode appearing is not just determined by the growth rate but also by the particular initial disturbance environment of the experimental set-up.

9.5.2 Direct Numerical Simulations of Secondary Instability of Crossflow Vortices

Small-amplitude stationary disturbances

The spatial structure of the crossflow instability will first be demonstrated by calculations of the evolution of small perturbations. We use a large computational domain in the spanwise direction and introduce random stationary disturbances along a line parallel to the leading edge. In Figure 9.47 the normal velocity associated with the crossflow eigenmode is shown. The disturbances grow downstream and appear to be inclined at about 45° . This corresponds to the most unstable direction for the zero-frequency (stationary) disturbance. At the end of the computational box in Figure 9.47 there are ten vortices, corresponding to a wavelength in the z -direction that is equivalent to the width of the computational box used in the rest of the direct numerical simulations presented in this section.

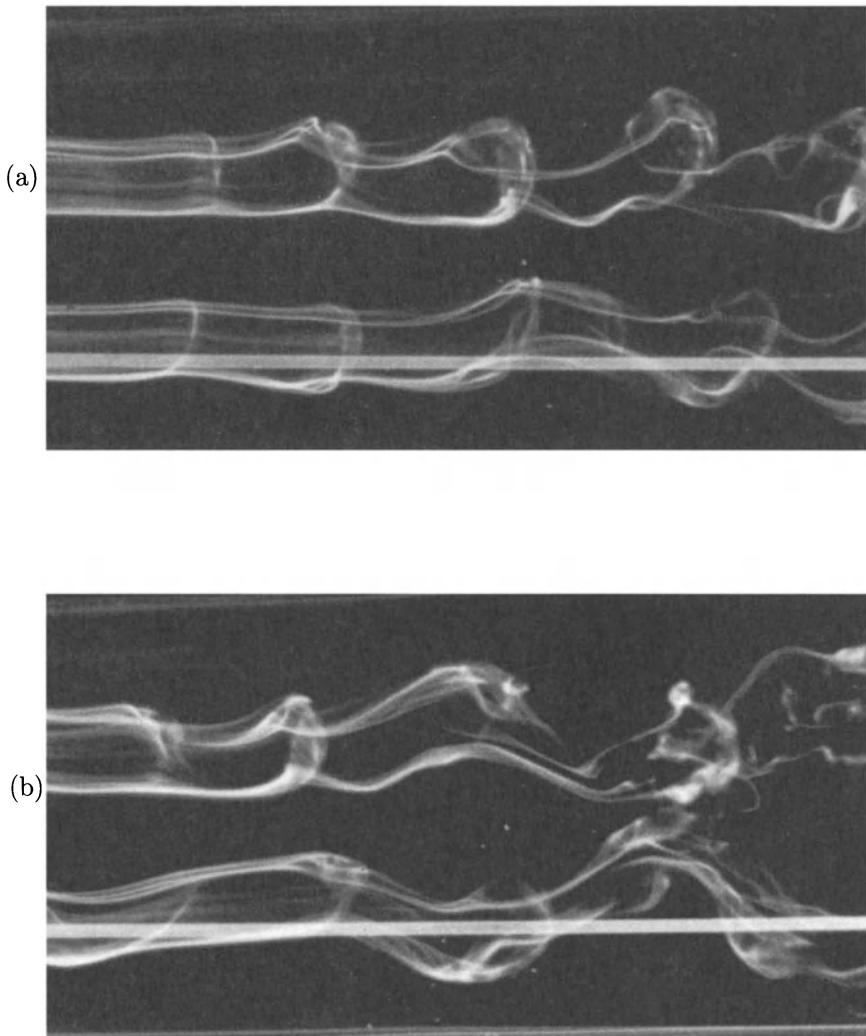


FIGURE 9.46. Instantaneous visualizations showing secondary instability modes: (a) fundamental varicose mode or horse shoe vortex, (b) dominant subharmonic sinuous mode. The smoke wire is located at $x = 54\text{cm}$ and $y/\delta_L = 0.3$. From Swearingen & Blackwelder (1987).

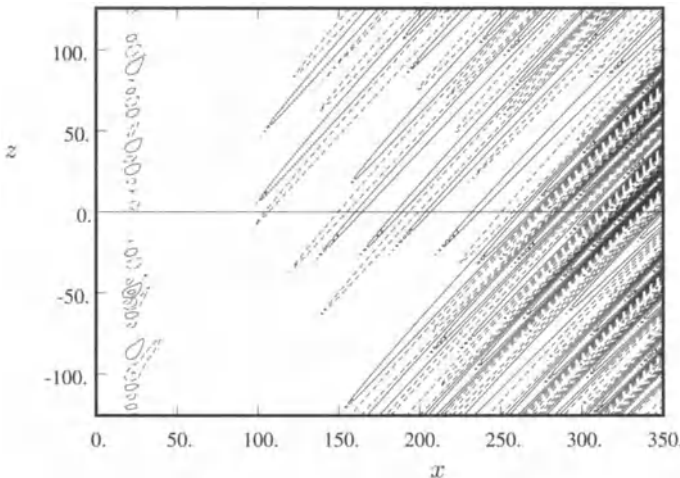


FIGURE 9.47. Contour lines of the normal disturbance velocity at $y = 0.5$. The spacing between the contours is 0.00005; the vortices are generated by random stationary disturbances at $x = 20.95$. From Höglberg & Henningson (1998).

Base Flow - Saturated Vortices

When the amplitude of the initial disturbance in the direct numerical simulation is increased, the crossflow vortices reach a saturated state, where the exponential disturbance growth is suppressed by nonlinear effects and the flow saturates. Contours of the chordwise velocity in an x - y plane are shown in Figure 9.48(a), where the strong saturated vortices can be clearly seen.

As a starting point of the investigations of the interaction between traveling and stationary crossflow modes a base flow with saturated crossflow vortices can be used. To this base flow one can add disturbances at different locations and with different spatial structures. The saturated vortices contain strong shear layers, as seen in Figure 9.48(a), which can be expected to support secondary instabilities. The shear layer at the bottom of the vortex is a result of high-speed fluid moving down with the vortex toward the wall into a region with lower velocities. The shear layer on the side and near the top of the vortex is the result of low-speed fluid being carried by the vortex into a region with fluid moving at higher velocities.

Low-frequency and high-frequency secondary instability

Figure 9.48(b) shows the response of the vortex to time-dependent random forcing.

In experiments by Kohama *et al.* (1991) and Deyhle & Bippes (1996), a high-frequency instability has been observed just prior to transition. The

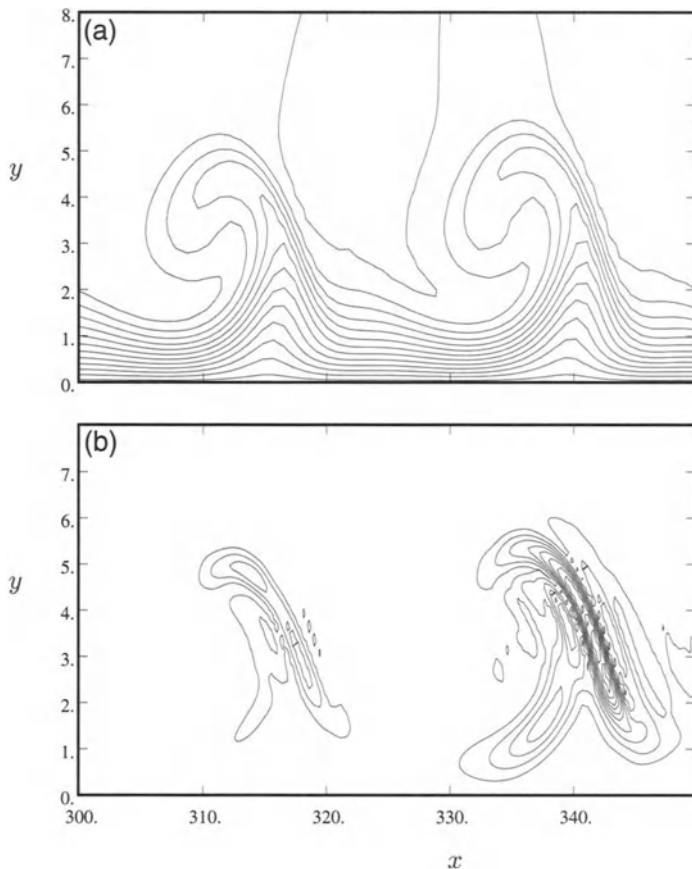


FIGURE 9.48. Crossflow vortices generated at $x = 20.95$ and their secondary instability. (a) Contours of chordwise velocity at $z = 0$. Contour spacing is 0.1. (b) Contours of u_{rms} at $z = 0$, with contour spacing of 0.001; non-stationary random-frequency disturbance generated at $x = 209.5$. From Högberg & Henningson (1998).

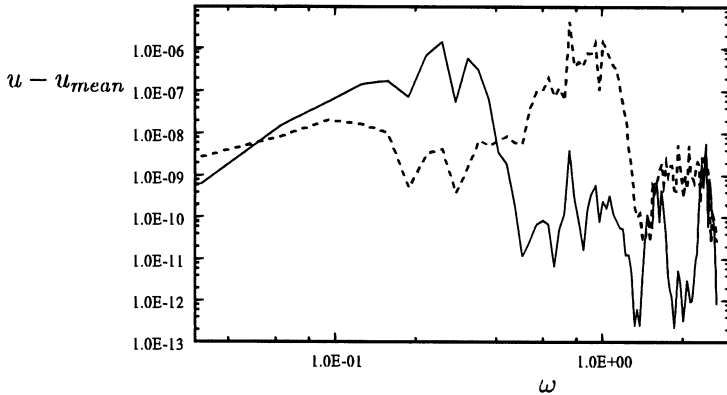


FIGURE 9.49. Frequency spectra at $x = 335$, $y = 1.0$, $z = 0$ (solid) and at $x = 337$, $y = 5.2$, $z = 0$ (dashed) for crossflow vortex flow with random-frequency disturbances at $x = 209.5$. From Högberg & Henningson (1998).

frequency of this instability was found to be about one order of magnitude higher than that of the most amplified traveling wave. Similar results were found in calculations by Malik *et al.* (1994).

To trigger this instability in our base flow a random disturbance generator was positioned where the vortex was close to saturation. The most unstable frequencies supported by the saturated vortex were found by adding a random disturbance to the base flow at $x = 209.5$. This disturbance triggered both low- and high-frequency instabilities (see Figure 9.48(b) for contours of the rms value of the chordwise velocity). The frequency spectra in Figure 9.49 show a peak for both a high and low frequency at different locations in the crossflow vortex. The high frequency ($\omega \approx 1.0$) is found in the upper part of the vortex and the low frequency ($\omega \approx 0.1$) at the bottom.

Small-amplitude harmonic oscillations for these frequencies were introduced in separate simulations. By integrating each solution far enough in time to obtain periodic solutions it is possible to calculate the respective growth rates. The growth rates are compared to the primary instabilities in Figure 9.50. The growth rate for the high-frequency secondary instability is considerably higher than the growth rates of the primary instabilities. It is also higher than the growth rate of the low-frequency mode. This indicates that the high-frequency secondary instability, when conditions are favorable, dominates the transition process, making it very rapid. One interesting aspect of the high-frequency instability is that the neutral point is located quite far downstream ($x \approx 270$). At that point the crossflow vortex is almost saturated.

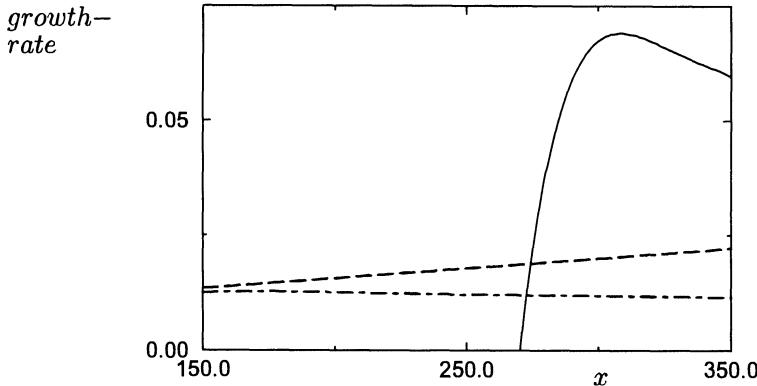


FIGURE 9.50. Growth rates for the secondary instabilities: zero-frequency primary disturbance (dash-dotted), low-frequency mode (dashed), and high-frequency secondary instability (solid). Smoothing was applied to the original data to obtain the growth rates. From Högberg & Henningson (1998).

Crossflow instabilities on supersonic ($\text{Ma} = 3.5$) highly swept wings were computed by Pruett *et al.* (2000) using direct numerical simulations and the parabolized stability equations.

9.5.3 Experimental Investigations of Breakdown of Crossflow Vortices

Stationary crossflow vortices

A physical experiment of the secondary instability of crossflow vortices was performed by Kawakami *et al.* (1999). Figure 9.51 shows the structure of the secondary instability modes obtained when phase-controlled periodic disturbances were superimposed on saturated stationary vortices. In Figure 9.51 the u_{rms} is filtered around the forcing frequencies and plotted along with the time averaged velocity in a y - z plane. It is clear that the high-frequency mode rides on top of the stationary vortex and the low-frequency mode is concentrated near the wall. These results are in complete agreement with those presented by Högberg & Henningson (1998). Note that the crossflow is directed in opposite directions in the two investigations.

Traveling crossflow modes

Further details of the high-frequency secondary instability of the saturated crossflow vortices were carefully investigated by Lerche (1997). He artificially triggered the high-frequency instability on saturated traveling crossflow vortices, referred to as (1,1) modes, and on a saturated combination of stationary and traveling crossflow vortices, referred to as (0,1)+(1,1) modes. Areas of high-frequency instability are marked by the black mesh

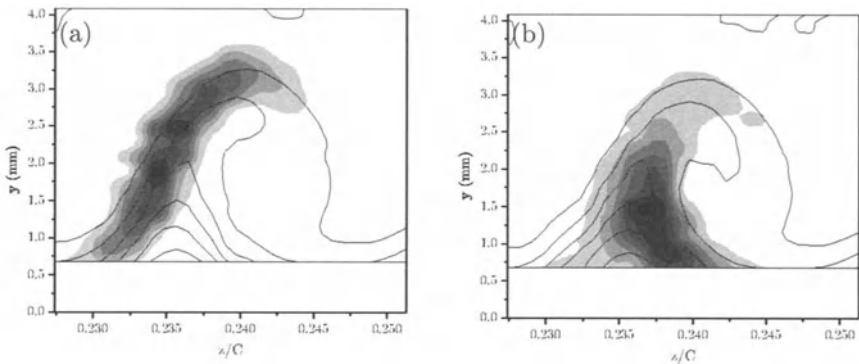


FIGURE 9.51. Distribution of u_{rms} filtered between (a) 120 Hz and 200 Hz, (b) 1460 Hz and 1540 Hz displayed in the y - z -plane at $x/C = 0.55$ for the forcing with $f=160$ Hz and $f=1500$ Hz, respectively. A roughness array with 12.5 mm spacing is located at $x/C = 0.2$. Contours of the mean velocity are superimposed. From Kawakami *et al.* (1999).

in Figure 9.52. The figure shows that for both cases the high-frequency areas are found in the same location (on top of the shear layer) as for the stationary vortices shown earlier. However, the combination of zero-frequency modes (0,1) and traveling crossflow modes (1,1) do not by themselves cause transition, but instead saturate into a state that is again susceptible to high-frequency secondary instabilities. Thus, the low-frequency mode discussed earlier will not take the flow to turbulence but rather to this new state. Breakdown seems to always be preceded by the high-frequency instability on top of the shear layers.

9.6 Breakdown of Localized Disturbances

In this section we will consider the breakdown of localized disturbances. We start with an experimental investigation of a wave packet in Blasius flow, and we continue with numerical experiments of two different disturbance types in both Blasius and adverse pressure gradient boundary layers.

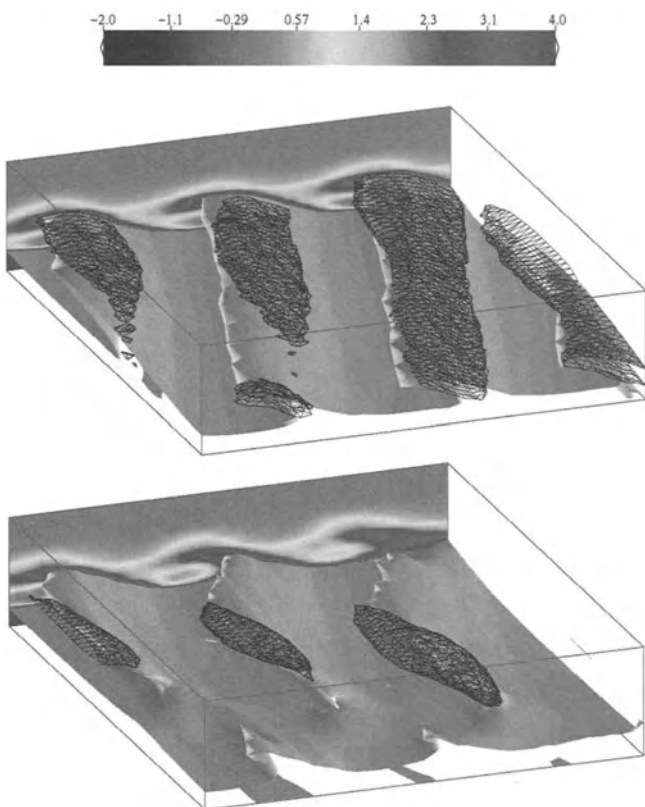


FIGURE 9.52. Isosurfaces of $\partial U_s / \partial z = 4.0$ and regions of high-frequency secondary instability (black mesh) for crossflow vortex flow. Top: case (1,1); bottom: case (0,1)+(1,1). From Lerche (1997).

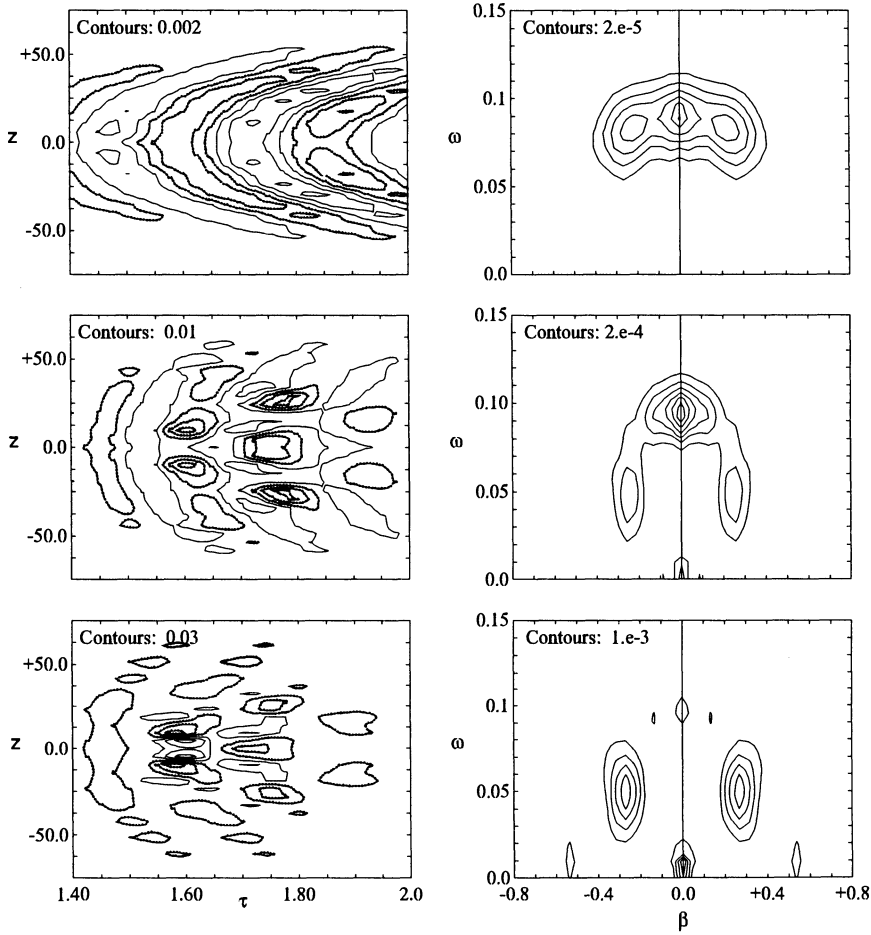


FIGURE 9.53. Overall view of the stages observed during the evolution of a wave packet. The left column depicts contours of streamwise velocity perturbations in the t - z -plane at $y/\delta^* = 0.5$. The three rows correspond to $x=170\text{cm}$, $x=250\text{cm}$ and $x=270\text{cm}$ (top to bottom). The three streamwise locations represent linear, subharmonic and early breakdown stages. Solid lines are positive contours; dotted lines show negative contours. The right column shows the corresponding wavenumber-frequency spectra of the ensemble-averaged velocity field. From Cohen *et al.* (1991).

9.6.1 Experimental Results for Boundary Layers

The linear stage

First we examine the development of a wave packet in a zero pressure gradient boundary layer. In the experiments by Cohen *et al.* (1991), a wave packet centered around the most unstable Tollmien-Schlichting wave is created by localized blowing and suction at the wall. Figure 9.53 shows a summary of the results. The three figures on the left show the streamwise velocity component at $y/\delta^* = 0.5$ in the t - z plane. The series of figures on the right show the corresponding two-dimensional wave number-frequency spectra. The linear stage of the wave packet is observed at $x = 170$ cm and is characterized by the smooth swept-back wave crests and a low amplitude (approximately 0.6 percent of U_∞ peak to peak). The spectrum indicates that most of the energy is concentrated in the two-dimensional modes, centered about a fundamental frequency $\omega_0 = 0.09$ that corresponds to the most amplified mode according to linear stability theory. This corresponds to the classical Gaster wave packet, see Gaster (1975).

The subharmonic stage

As we progress downstream, we see the onset of the first nonlinear effects. At $x = 250$ cm, oblique modes with a frequency half of the fundamental (i.e., subharmonic modes) gain energy, a development characterized by the appearance of strong peaks in the velocity perturbation on either side of the centerline. The peaks at the subharmonic ($\beta \approx 0.25$) grow out of background noise and are not associated with the local oblique maxima observed at $x = 170$ cm. Detailed investigations show that the vertical structure of each (β, ω) is still described well by the mode shape obtained from linear stability theory. In addition, the wave speeds of the observed three-dimensional subharmonic and two-dimensional fundamental structures approximately satisfy a subharmonic resonance criterion. This suggests that the subharmonic modes grow as part of a weakly nonlinear subharmonic resonance or secondary instability.

The breakdown stage

At $x = 270$ cm, the subharmonic part has now overtaken the fundamental as the primary location of disturbance energy and, as Figure 9.53 indicates, the $(0,0)$ peak has become much more pronounced than at the previous stages. We also see the growth of energy at $(2\beta_s, 0)$, where β_s indicates the spanwise scale of the subharmonic peak. This manifests itself in the velocity field by the appearance of strong spanwise variations and the increasingly streaky (low-frequency, high- β) structure of the velocity perturbations. By now the wave crests that defined the original wave packet, although still present, are no longer visible because their amplitude is too low to appear at these contour levels. Soon after this stage, a turbulent spot develops.

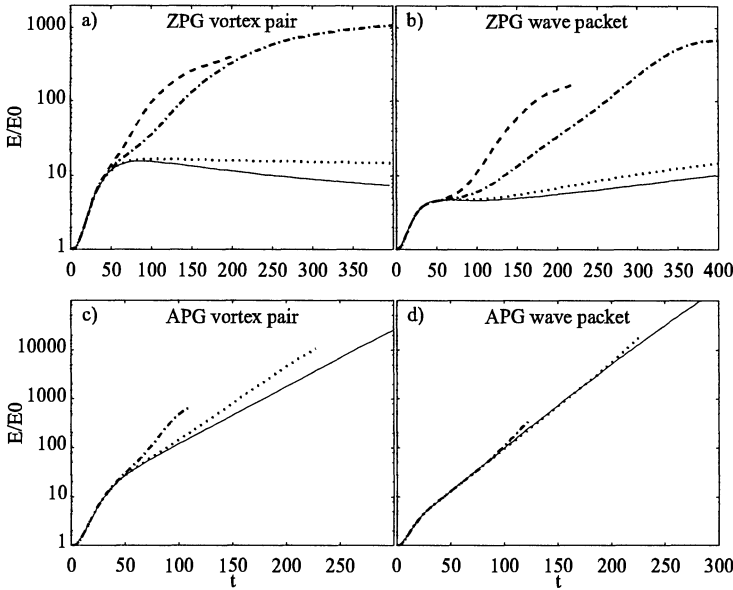


FIGURE 9.54. Kinetic disturbance energy versus time. (a) Zero pressure gradient vortex pair, (b) zero pressure gradient wave packet, (c) adverse pressure gradient vortex pair, (d) adverse pressure gradient wave packet. —: Linear case with $|v|_0 = 0.00001$, - - -: Finite-amplitude case with $|v|_0 = 0.001$, — - -: Finite-amplitude case with $|v|_0 = 0.005$, — —: Strong-amplitude case with $|v|_0 = 0.01$. The strong amplitude case is not included in the adverse pressure gradient results. From Beck *et al.* (1998).

9.6.2 Direct Numerical Simulations in Boundary Layers

Different initial amplitudes

We will consider the finite-amplitude evolution of various localized disturbances, some of which were discussed earlier in this book; see Chapters 4 and 5. A vortex pair and a wave packet disturbance in a zero pressure gradient and adverse pressure gradient boundary layer will be studied. In the adverse pressure gradient case we have a strong inflectional instability, whereas the low exponential growth rates for the Tollmien-Schlichting waves in the zero pressure gradient flow will have to compete with comparatively high transient growth of streaky structures.

The energy growth for the four different cases is depicted in Figure 9.54. In all figures, the upper curve corresponds to the largest, and the lower curve to the smallest initial amplitude. In the zero pressure gradient case, the second smallest initial amplitude $|v|_0 = 0.001$ is seen to yield a growth similar to the linear case. The third amplitude $|v|_0 = 0.005$ resulted in a qualitatively different growth and typically included substantial nonlinear

effects, while the fourth amplitude $|v|_0 = 0.01$ is rather substantial and caused rapid breakdown. The curves for this initial amplitude terminated around $t = 200$ when the disturbance was in the breakdown stage.

The exponential growth is of great importance in the finite-amplitude adverse pressure gradient cases. The exponential growth of the two-dimensional modes was succeeded by nonlinear interactions, visible as deviations from the approximately straight lines in Figure 9.54 (*c,d*). The onset of this strongly nonlinear regime was shifted to an earlier time when the initial amplitude was increased.

The zero pressure gradient vortex pair and wave packet

The main feature of the nonlinear evolution of the zero pressure gradient vortex pair, as seen in Section 5.5.4, is the streaky structure forced by the interaction of the oblique peaks in wave number space. The spectrum shows the emergence of a peak at a zero streamwise wave number as a result of such an interaction. This is similar to the forcing of streaks by the initial oblique waves in the oblique transition scenario.

The zero pressure gradient wave packet with $|v|_0 = 0.005$ exhibited rapid growth of the subharmonic modes, leading to breakdown around $t = 400$. The spectrum shows the emergence of a subharmonic at $(\alpha, \beta) = (0.16, 0.22)$. At $t = 200$, the subharmonics transferred a significant amount of energy into modes with small streamwise wave numbers. This behavior is analogous to the subharmonic breakdown observed in the experiments of (Breuer *et al.*, 1997).

Once the subharmonic oblique waves start to grow in the wave packet, the generation of streaks is very similar to the one observed for the vortex pair disturbance, i.e., nonlinear forcing of the streaks followed by an energy cascade along the spanwise wave number axis.

The adverse pressure gradient vortex pair and wave packet

Due to the presence of strong exponential growth for all disturbances, the adverse pressure gradient cases were different from the zero pressure gradient cases. Interestingly, the vortex pair was the first to enter the breakdown stage in the adverse pressure gradient cases. An initial amplitude of 0.005 was sufficient for the vortex pair to break down earlier than the wave packet. Initially, the vortex pair was centered around an oblique mode, which combined to generate streaky modes with a spanwise wave number close to twice the β value of the initial peak. The ability of the vortex pair to rapidly produce streaky structures made it more effective in causing breakdown than the wave packet, provided the initial amplitude was above a certain threshold.

The main aspect of the evolution of the adverse pressure gradient wave packet is the exponential growth of two-dimensional modes. Due to the large linear growth rate, it is difficult to observe any secondary instability.

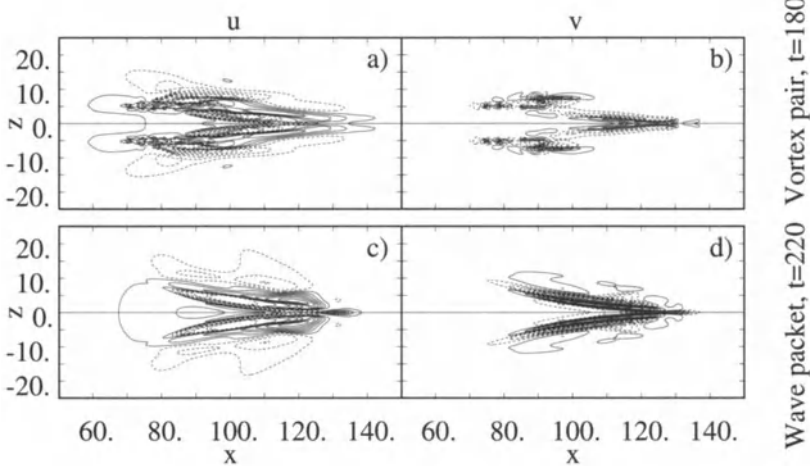


FIGURE 9.55. Contours of the streamwise velocity u (increment 0.05) and the normal velocity v (increment 0.01) at $y = 1$ for zero pressure gradient boundary layer with initial disturbance amplitude $|v|_0 = 0.01$. (a) u and (b) v at $t = 180$ for the vortex pair, (c) u and (d) v at $t = 220$ for the wave packet. From Beck *et al.* (1998).

Energy was concentrated in the primary two-dimensional mode almost up to breakdown. For amplitudes $|v|_0 = 0.001$ and lower, the wave packet reached breakdown earlier than the vortex pair.

The breakdown

Figure 9.55 shows the zero pressure gradient vortex pair breakdown in form of high-frequency, large-amplitude oscillations of the rear part of the streaks. A similar streak breakdown is observed at the pinched-off rear part of the adverse pressure gradient vortex pair (Figure 9.56(b)).

The visualization at $t = 180$ in Figure 9.55 shows that breakdown has occurred at the rear part of the streaky structure, in an off-centerline position. This corresponds to the position of maximum intensity of the streaky structure.

High-frequency instabilities were also observed above the head of the Λ -like structure ($x \simeq 130$, $y \simeq 4$, $z = 0$). In all cases except the zero pressure gradient vortex pair, breakdown occurred first in this spike region produced by the up-welling of fluid between the legs of the Λ -vortex. The shape of the spike regions was similar for the different cases; the length was approximately proportional to time and somewhat shorter for the wave packet.

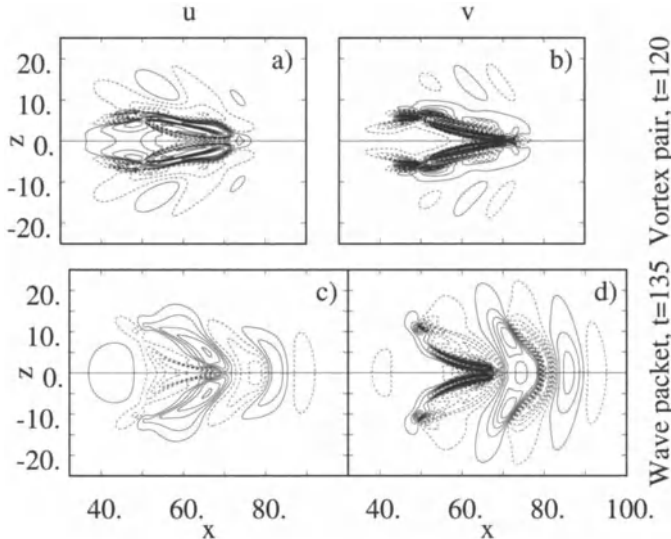


FIGURE 9.56. Contours of streamwise velocity u (increment 0.05) and normal velocity v (increment 0.01) at $y = 1$ for an adverse pressure gradient boundary layer with initial disturbance amplitude $|v|_0 = 0.005$. (a) u and (b) v at $t = 120$ for the vortex pair, (c) u and (d) v at $t = 135$ for the wave packet. From Beck *et al.* (1998).

It is evident that the streaks require surprisingly high amplitudes in order to break down. In the zero pressure gradient vortex pair case with $|v|_0 = 0.005$, they reached a streamwise velocity amplitude of about 30 percent without any sign of secondary instability. This need for high amplitudes for the onset of streak instability is in general agreement with similar results for other flows (see, e.g., Reddy *et al.*, 1998). For higher amplitudes, however, they do break down at the position of maximum intensity.

In the more unstable case of adverse pressure gradients, the threshold amplitude was lower than in the zero pressure gradient case. The ability of the vortex pair to cause rapid breakdown in the adverse pressure gradient case was due to the large component of oblique modes in the initial disturbance. Although the oblique modes were somewhat less unstable compared to the two-dimensional mode of the wave packet, they combined to generate streaky structures. These structures were probably subject to transient growth, and yielded an elongated A-like vortex of larger intensity than the surrounding wave packet.

Turbulent spots

When a localized vortex pair or wave packet has broken down, a localized area of turbulence – a turbulent spot – results. This turbulent region propagates downstream as it spreads out in the horizontal directions. A number

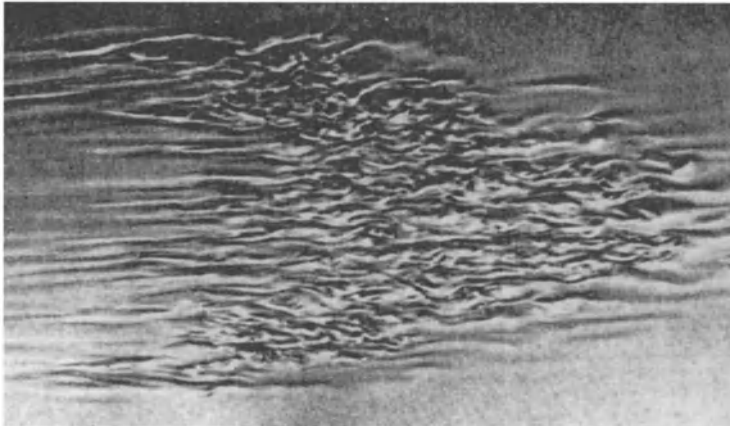


FIGURE 9.57. Flow visualization of a turbulent spot in a zero-pressure gradient boundary layer. Top view with flow from left to right. Experiment of Cantwell *et al.* (1978).

of physical and numerical experiments of turbulent spots have been performed to analyze such spots, primarily in channel or boundary layer geometries. For reviews see, e.g., Riley & Gad-el Hak (1985) and Henningson *et al.* (1994). Figures 9.57 and 9.58 show turbulent spots in a zero pressure gradient boundary layer and plane channel flow. Note that the boundary layer spot has an arrowhead shape pointing in the downstream direction, whereas the channel flow spot has a relaminarized front part.

Interesting wave phenomena have been found in conjunction with turbulent spots. For example, there are waves at the wingtips of turbulent spots in channels (Carlson *et al.*, 1982; Henningson & Alfredsson, 1987; Henningson, 1989). Their growth has been attributed to a local crossflow instability of the mean flow near the edge of the spot. Waves seen in the wake of boundary layer spots, on the other hand, are most likely associated with waves from the initial wave packet (see Chambers & Thomas, 1983).

General conclusions regarding the evolution of localized disturbances

For localized disturbances in flows with strong exponential instabilities, like those of the adverse pressure gradient flows discussed earlier, modal growth will dominate and transform the disturbance into a rapidly growing wave packet independent of the initial shape. With small initial amplitudes, two-dimensional waves are favored, while oblique waves yield faster transition for large initial amplitudes.

For flows with no or small exponential growth, like the zero pressure gradient case, the transient growth mechanisms – with associated streak development – dominate the disturbance evolution. Only in cases of very small initial amplitudes or for disturbances with no initial energy in $(0, \beta)$

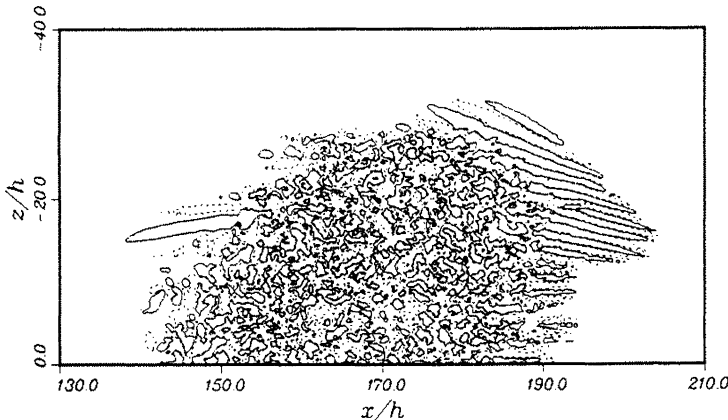


FIGURE 9.58. Top view of a turbulent spot in plane channel flow. Contours of the normal velocity from a numerical simulation by Henningson *et al.* (1987).

modes will there be a development similar to the adverse pressure gradient case.

9.7 Transition Modeling

With the various types of transition processes described in this chapter it may seem overoptimistic to expect simple but accurate transition models. It is clear that a universal method or methodology does not exist; instead we have to use various types of approximate models. In this section we will only briefly mention a few of the different models that have been used; we refer to articles dealing with applications. We start by briefly mentioning models that aim at understanding the physical mechanisms underlying transition and proceed to models used for transition prediction.

9.7.1 Low-Dimensional Models of Subcritical Transition

A number of low-dimensional models have been put forth to describe certain aspects of transition to turbulence. A class of models that was developed to investigate important aspects of subcritical transition and sustained turbulence will be discussed below.

Waleffe (1995) suggested that a 4×4 system should describe the essential ingredients. He argues that the key to understanding the transition problem in (subcritical) shear flows is the study of nonlinear (turbulent) sustainable states and their basin of attraction. We will introduce a dynamical system based on his model to illustrate how a simple 4×4 system can mimic a number of important characteristics of transitional flows.

A 4×4 model of transition in channel flows

Consider a model where $(u, v, w, n) = (0, 0, 0, 1) + (u', v', w', n')$ represents the laminar base flow plus a perturbation. The nonlinear disturbance equations derived from Waleffe's model (Waleffe, 1995) are (omitting primes)

$$\frac{d}{dt} \begin{pmatrix} u \\ v \\ w \\ n \end{pmatrix} = \begin{pmatrix} -\lambda u/\text{Re} & 1 & 0 & 0 \\ 0 & -\mu v/\text{Re} & 0 & 0 \\ 0 & 0 & -\nu w/\text{Re} & 0 \\ 0 & 0 & 0 & -\sigma n/\text{Re} \end{pmatrix} \begin{pmatrix} u \\ v \\ w \\ n \end{pmatrix} + \begin{pmatrix} -\gamma w^2 + vn \\ \delta w^2 \\ \gamma wu - \delta wv \\ -uv \end{pmatrix} \quad (9.2)$$

where the first term on the right-hand side is the linear operator and the last one contains the nonlinear interactions. The behavior of this system has many characteristics in common with subcritical transition.

First, all eigenmodes of the linear system decay, but because they are nonorthogonal (the linear operator is nonnormal) there is a potential for large transient growth. An $\mathcal{O}(1)$ streamwise vortex mode v drives the streak u to an amplitude $\mathcal{O}(\text{Re})$ before viscous decay sets in. This linear mechanism is the only source of disturbance energy in the model.

Second, the nonlinear terms are conservative and only redistribute the energy produced by the linear mechanism. For example, the energy produced in u by the transient growth is removed by the term vn , only to be immediately turned into a mean-flow modification n by the term $-uv$. Each nonlinear term has a corresponding one of opposite sign that will be associated with the same energy flux in an opposite direction. When deriving the disturbance energy equation, all nonlinear terms vanish.

Third, once the streak component u reaches sufficient amplitudes it becomes unstable to w -disturbances. The threshold amplitude for the secondary instability can easily be found from a linear stability analysis of the quasisteady streak solution $(u, 0, 0, n)$. The velocity component w grows exponentially if $u > \nu/\gamma\text{Re}$.

For the most part these characteristics describe well the behavior of disturbances governed by the full Navier-Stokes equations for subcritical transition in shear flows. In particular, the dynamical system (9.7.1) represents a good model for the streak breakdown scenario.

The equivalence of low-dimensional models

The model of Waleffe (1995) presented above is by no means the only one. Many researchers have tried to describe transition with low-dimensional models, many times citing large differences between their model and others.

In an interesting review of the characteristics of a number of these models, Baggett & Trefethen (1997) show that they are surprisingly similar.

The models reviewed by Baggett & Trefethen (1997) can be classified in two categories (see Figure 9.59). The first type of models is based on the idea that the nonmodal growth is the most important characteristic and that the form of the nonlinearities is less important. The only role of the nonlinearities is to trigger new nonmodal growth such that the evolution process is sustained and does not ultimately decay as the eigenvalues of the linear problem predict. Trefethen *et al.* (1993) refer to this process as bootstrapping.

The second type of models shown in Figure 9.59 is derived on the basis that the nonlinear terms must closely model the physical mechanisms at work in subcritical transition. In fact, Waleffe (1995) argues that the nonmodal growth mechanisms do not play an important role in subcritical transition. The nonlinear mechanisms are divided into a streak breakdown stage and a vortex regeneration phase.

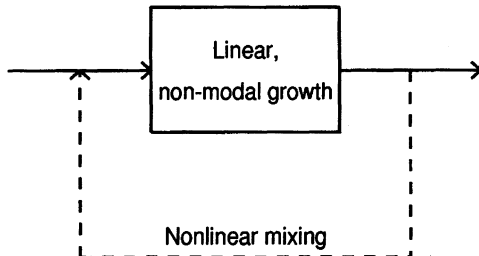
Baggett & Trefethen (1997) show that in practice there is little difference between these models. The upper-left arrow in the lower model in Figure 9.59, labeled streak formation, represents the linear growth mechanism based on nonmodal growth. The other two arrows in the lower model are consolidated into “nonlinear mixing” in the upper model. It may appear that the division of the nonlinear mixing into a breakdown phase followed by regeneration phase represents a fundamental difference between the two models. However, Baggett & Trefethen (1997) show that even when nonlinear mixing is modeled by arbitrary (random) quadratic interactions, these two phases usually emerge.

Transition thresholds versus Reynolds number

Low-dimensional models have been used to investigate the Reynolds number dependence of the threshold for transition. Based on their ideas of bootstrapping, Trefethen *et al.* (1993) conjectured that the threshold amplitude should scale like Re^α , with $\alpha < 1$.

Solutions of Waleffe’s model using initial disturbances that grow with the maximum rate are shown in Figure 9.60. It is clear that above a certain threshold, the solutions do not decay to the “laminar” state but rather exhibit a “transition to turbulence.” The Re -dependence of the threshold can be determined as Re^{-2} , which is observed in many of the other models discussed in Baggett & Trefethen (1997). Results from direct numerical simulations of plane Poiseuille flow described at the beginning of this chapter show threshold exponents between -1 and -2 . It is not difficult to construct a simple model with an arbitrary threshold exponent. Thus the threshold behavior in low-dimensional dynamical systems is a mathematical way of expressing a researcher’s physical understanding and interpretation of the transition process.

(a) Marburg/Cornell



(b) CTR/MIT

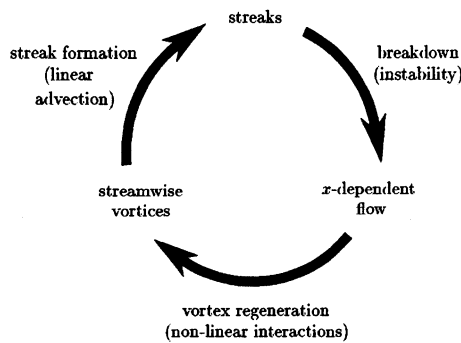


FIGURE 9.59. Schematic illustration of the ideas underlying two types of low-dimensional models of transition. Model (a) is abstract, depending only on certain general mathematical properties, whereas model (b) is physical, attempting to delineate the actual structures that interact in shear flows at high Reynolds number. From Baggett & Trefethen (1997).

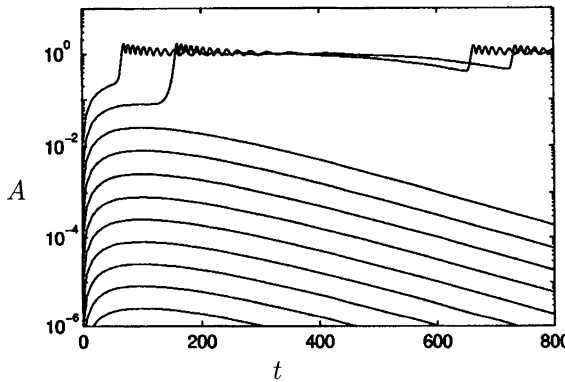


FIGURE 9.60. Evolution of disturbances governed by the model of Waleffe (1995) starting from various initial amplitudes. $\text{Re} = 100$, $\lambda = \mu = \nu = \sigma = \gamma = \delta = 1$.

9.7.2 Traditional Transition Prediction Models

The methods used today for predicting transition depend to some extent on empirical input. They are therefore limited to cases that are close to those for which the empirical input was taken and are usually unable to provide any physical modeling of the processes leading to transition.

Correlations

There are rudimentary methods that use information of the boundary layer velocity profile and/or Reynolds number to estimate the transition location. One of the simplest method that gives reasonable results for simple flows tries to correlate the transition location with the local momentum thickness. Michel (1952) proposed the formula

$$\text{Re}_{\theta,tr} = 2.9 \text{ Re}_{x,tr}^{0.4}$$

where $\text{Re}_{\theta,tr}$ is the Reynolds number based on the momentum thickness at transition and $\text{Re}_{x,tr}$ is the Reynolds number based on the streamwise distance at the transition location. A number of other transition correlations can be found in the book by White (1974).

The e^N -method

An improvement to the correlation methods was suggested by the observations of Michel (1952) that the transition point corresponds to the approximate location where the total amplification of Tollmien-Schlichting waves

is a given constant. This led van Ingen (1956) and Smith & Gamberoni (1956) to independently propose the so-called e^N -method. The idea is to find a correlation between the amplification of linear eigenmodes and the onset of transition.

The amplification is given by the N -factor: Transition takes place when the disturbance amplitude reaches e^N times the amplitude at the start of amplification (i.e., when the wave enters the unstable region in the F -Re plane for boundary layers). The method does not rely on the disturbance amplitude at the onset of exponential growth, which means that the receptivity process is not accounted for. However, after analyzing data from a large number of experiments, van Ingen (1956) and Smith & Gamberoni (1956) found that for transition in low-disturbance environments the onset and end of transition were fairly well described by N -factors around 8 and 11, respectively. They also reported that these values decreased with increasing freestream turbulence levels.

Figure 9.61 illustrates the calculation procedure for the e^N -method for the case of incompressible boundary layer flow. The amplitude development for various frequencies is followed along the streamwise coordinate direction and the x position at which an amplification of e^N is reached is taken as the transition location. For applications of this method, see Arnal (1987, 1999).

The e^N -method has been shown to fairly accurately predict transition for simple flows and has been used successfully for parametric studies of more complex flows. It should be kept in mind, however, that well before transition is reached the waves become nonlinear and that the e^N -method does not take nonlinear processes into account.

Modification of the e^N -method

Another newly developed technique is to base the N -factor on the growth calculated by the linear PSE method. This method allows nonparallel and curvature effects to be taken into account. Because it is still based on linear equations, it relies on some empirical input to determine when transition occurs. The computational effort using the linear parabolized stability equations is comparable to that of the e^N -method.

Crouch & Ng (2000) proposed a modified e^N -method for estimating the location of transition caused by crossflow instabilities. The method is based on a receptivity model, linear growth, and an amplitude correlation, and computational results agree well with experimental data.

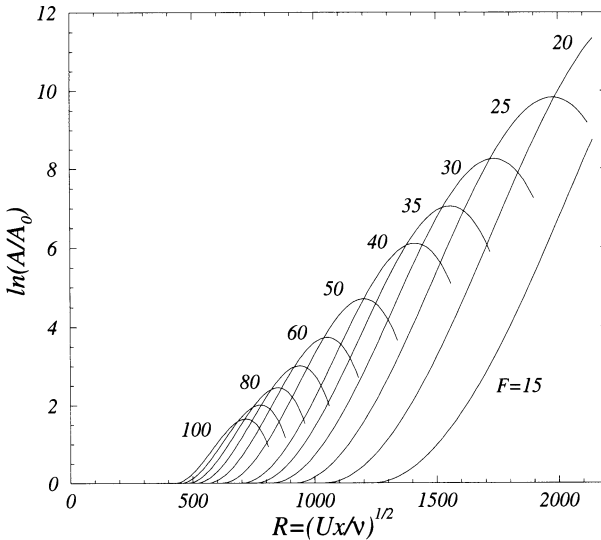


FIGURE 9.61. Illustration of e^N -method for Blasius boundary layer flow.

9.7.3 Transition Prediction Models Based on Nonmodal Growth

For higher freestream turbulence values, where nonmodal growth is the main cause of disturbance growth, other methods for transition prediction must be devised.

Correlations and a modified e^N -method

Correlation methods that incorporate the freestream turbulence level have been developed, and one of the most widely used model is the method of Abu-Ghanamm & Shaw (1980). This method gives correlations for both the start and end of transition for freestream turbulence levels between 0.3 percent and 5.0 percent and incorporates effects of pressure gradients and flow history. A simpler method that gives satisfactory results is the method of van Driest & Blumer (1963).

There have also been attempts to account for freestream turbulence in the e^N -method by correlating the freestream turbulence intensity to the N -factor. One such correlation was suggested by Mack (1984)

$$N = -8.43 - 2.4Tu \quad (9.3)$$

which gave reasonable transition locations for the range $0.1\% < Tu < 2\%$.

Methods using turbulence models

For high freestream turbulence levels (above 1%) turbulence models (both $k-\epsilon$ and Reynolds-stress-based models) have been used to predict transition. Although such models cannot take phenomena like nonmodal growth or secondary instability into account, the basic formulation should in principle be able to predict the diffusion of turbulent energy fluctuations in the freestream into the boundary layer. For a review of this subject see Savill (1996). The results seem to be fairly sensitive to the type and implementation of the initial and boundary conditions, and the turbulence models used for fully turbulent flows have to be modified to give predictions of the right order (Westin & Henkes, 1997).

A method based on spatial optimal growth

Using the optimal growth results presented in Chapter 7, we try to find a correlation between the transition Reynolds number, Re_T , and the turbulence level in the free stream, Tu .

Assuming isotropic turbulence, the freestream turbulence level is taken as $Tu = u'_{\text{rms}}/U_\infty$, where u' is the fluctuating streamwise velocity in the freestream. First, we assume that the input energy E_{in} into the optimal growth calculations is proportional to the freestream turbulence energy, i.e.,

$$E_{\text{in}} \sim Tu^2. \quad (9.4)$$

This assumption models the receptivity process.

Second, we assume that the initial disturbance grows with the optimal rate so that

$$E_{\text{out}} = GE_{\text{in}} = \bar{G} \operatorname{Re} E_{\text{in}}, \quad (9.5)$$

where \bar{G} is Reynolds number independent. Recall that the optimum growth was found to scale linearly with the Reynolds number for large enough Reynolds numbers.

Third, we assume that transition occurs when the output energy reaches a specific value, E_T ,

$$E_{\text{out}} = E_T. \quad (9.6)$$

Combining the assumptions we obtain

$$\sqrt{\operatorname{Re}_T} Tu = K \quad (9.7)$$

where K should be constant for moderate freestream turbulence levels. The experimental data used to verify this model are given in Table 9.1. We see

TABLE 9.1. Comparisons of different experimental studies

	$Tu(\%)$	Re_T	K
<hr/>			
Roach & Brierley (1992)			
T3AM	0.9	1,600,000	1138
T3A	3.0	144,000	1138
T3B	6.0	63,000	1506
Yang & Voke (1991)	5.0	51,200	1131
Matsubara (1997)			
grid A	2.0	400,000	1265
grid B	1.5	1,000,000	1500

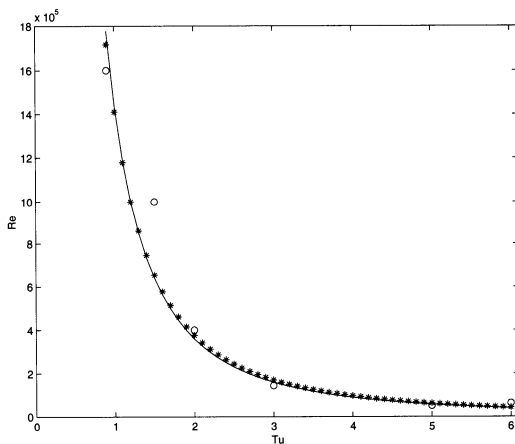


FIGURE 9.62. Transitional Reynolds number based on the distance to the leading edge versus freestream turbulence level (given in percent), for two transition prediction models and experimental data: — model based on optimal spatial growth with $K=1200$; (*) model proposed by van Driest & Blumer (1963); (o) experimental data from Table 9.1. From Andersson *et al.* (1999).

that K is approximately constant for a variety of freestream turbulence levels.

The model given by van Driest & Blumer (1963), who postulated that transition occurs when a maximum vorticity Reynolds number reaches a critical value, is compared to the model proposed by Andersson *et al.* (1999) and the experiments from Table 9.1 in Figure 9.62. White (1974) criticized the van Driest-Blumer model: "Since the concept of a critical vorticity Reynolds number is obviously questionable and not related to any fundamental rigorous analysis, we can regard the van Driest-Blumer correlation simply as an excellent semiempiricism." However, the assumptions underlying the van Driest-Blumer model can now be better understood from the theory of optimal spatial growth which should also provide a framework for continued improvement of transition prediction models.

9.7.4 Nonlinear Transition Modeling

To improve the empiricism contained in most of the models discussed so far, we need to include more of the physical processes in the transition modeling. Nonlinearities have to be incorporated into the model to describe the breakdown of the growing disturbances and the associated rise in skin friction. Of course, a full nonlinear calculation is not sufficient in itself unless one has information on the initial or inflow disturbance environment and the receptivity process.

Nonlinear PSE methods

The nonlinear version of the PSE technique can be used for more advanced transition prediction. This technique allows the calculation of disturbance growth from the linear stage to the strong nonlinear stage. No empirical input is needed to determine the onset of transition, but at the start of the computations the wave components and their initial amplitudes have to be chosen. The nonlinear calculations are of course computationally demanding, but much less so than for large-eddy simulations (LES) or direct numerical simulations (DNS) (see Hein *et al.* (1999)). Only little experience has been gained with nonlinear PSE so far, but a rapid development of this technique is expected.

In Figure 9.63 Chang & Malik (1994) show the variation of wall shear with Reynolds number from computations of the O-type transition process for supersonic boundary layers at various initial amplitudes. The transitional Reynolds number is found to increase with decreasing initial amplitude. Results such as these, which can readily be calculated using nonlinear PSE methodology, can be used for realistic transition prediction. The initial amplitude enters as a parameter that has to be estimated from the initial disturbance environment using appropriate assumptions about the receptivity process.

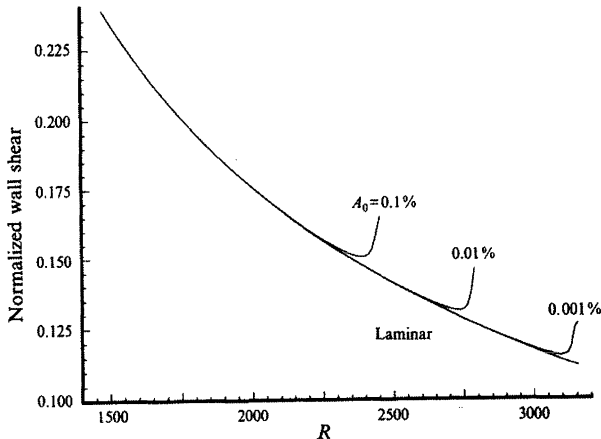


FIGURE 9.63. Average wall shear versus Reynolds number for various initial amplitudes of O-type transition. $\text{Ma} = 1.6$, $F = 0.06 \times 10^{-4}$ and $\beta/\text{Re} = 0.25 \times 10^{-4}$. From Chang & Malik (1994).

Methods based on DNS and LES

Although direct numerical simulations (DNS) or large-eddy simulations (LES) may be used in the future to determine the transition location in a wide range of flows, the cost of such calculations for engineering flows are currently overwhelming and can be foreseen to remain that way for some time. For simple flows, however, it appears that large-eddy simulations can be used for transition investigations with significant savings over full direct numerical simulations (see, e.g., Huai *et al.*, 1997).

Part III

Appendix

Appendix A

Numerical Issues and Computer Programs

A.1 Global versus Local Methods

Many problems in hydrodynamic stability theory result in eigenvalue problems. The asymptotic growth/decay rates are the imaginary part of the eigenvalues of the underlying stability operator, for an analysis of the transient behavior we found it advantageous to expand in eigenfunctions, the computation of the critical energy Reynolds number requires the solution of an eigenvalue problem, and the secondary growth rates for breakdown of vortices, Tollmien-Schlichting waves or streaks are the result of an eigenvalue computation.

From a numerical point of view, there are two general concepts of finding the eigenvalues of a discretized stability operator. The first method, the local method, starts with an initial guess for the eigenvalue and solves the original eigenvalue problem as an initial value problem. The initial guess is then adjusted until the boundary conditions are satisfied. The iteration procedure can be accelerated by common root finding methods. The second method, the global method, uses the fully discretized stability operator and supplies it to a matrix eigenvalue solver which results in the spectrum.

The advantage of the local method lies in its high accuracy, whereas the advantage of the global method lies in the fact that a large part of the spectrum rather than one eigenvalue is computed.

Below we will describe algorithms that have proven useful in the computation of eigenvalues for hydrodynamic stability problems.

A.2 Runge-Kutta Methods

A numerical method for the solution of the two-dimensional Orr-Sommerfeld equation will now be presented. With the use of Squire's transformation this can also be used to solve the three-dimensional version. For simplicity the assumption that the flow is contained between two parallel plates located at $y = \pm 1$ will be made. The equation together with the suitable boundary condition can be written

$$\Phi' = A(y)\Phi \quad (\text{A.1})$$

$$\Phi_1(\pm 1) = \Phi_2(\pm 1) = 0 \quad (\text{A.2})$$

where

$$\Phi = \begin{pmatrix} \Phi_1 \\ \Phi_2 \\ \Phi_3 \\ \Phi_4 \end{pmatrix} = \begin{pmatrix} \hat{v} \\ \hat{v}' \\ \hat{v}'' \\ \hat{v}''' \end{pmatrix} \quad (\text{A.3})$$

$$A = \begin{pmatrix} 0 & 1 & 0 & 0 \\ 0 & 0 & 1 & 0 \\ 0 & 0 & 0 & 1 \\ a & 0 & b & 0 \end{pmatrix} \quad (\text{A.4})$$

$$a = -i\alpha \operatorname{Re}(\alpha^2(U - c) + U'') - \alpha^4 \quad (\text{A.5})$$

$$b = i\alpha \operatorname{Re}(U - c) + 2\alpha^2. \quad (\text{A.6})$$

The general solution to the equation can be written

$$\Phi(y) = \gamma_1 \Phi^1 + \gamma_2 \Phi^2 + \gamma_3 \Phi^3 + \gamma_4 \Phi^4 \quad (\text{A.7})$$

where $\Phi^1, \Phi^2, \Phi^3, \Phi^4$ are the four linearly independent solutions and γ_i are the integration constants. Φ^i are chosen to satisfy

$$[\Phi^1(-1), \Phi^2(-1), \Phi^3(-1), \Phi^4(-1)] = \begin{pmatrix} 0 & 0 & 0 & 1 \\ 0 & 0 & 1 & 0 \\ 0 & 1 & 0 & 0 \\ 1 & 0 & 0 & 0 \end{pmatrix} \quad (\text{A.8})$$

Applying the boundary conditions at $y = -1$ and using the above conditions on the linearly independent parts of the solution we find that $\gamma_3 = \gamma_4 = 0$. From the boundary conditions at $y = 1$ we find

$$\begin{pmatrix} \Phi_1^1(1) & \Phi_1^2(1) \\ \Phi_2^1(1) & \Phi_2^2(1) \end{pmatrix} \begin{pmatrix} \gamma_1 \\ \gamma_2 \end{pmatrix} = 0. \quad (\text{A.9})$$

This means that the determinant of the matrix has to be zero for solutions to exist, i.e.,

$$d = \Phi_1^1(1)\Phi_2^2(1) - \Phi_1^2(1)\Phi_2^1(1) = 0. \quad (\text{A.10})$$

c must be chosen so that the dispersion relation above is satisfied.

The eigenvalue c can be found by a shooting procedure. A particular value of c is chosen, c_1 say, Φ^1 and Φ^2 are found by integration over y and the determinant is evaluated, d_1 say. This is done again for another value of c , c_2 say, resulting in another value, d_2 , of the determinant. If these values are sufficiently close to a correct eigenvalue, a better approximation can be found by linear extrapolation:

$$c = c_2 - d_2 \frac{c_1 - c_2}{d_1 - d_2}. \quad (\text{A.11})$$

This process can be repeated until the desired accuracy is obtained.

The integration method used is a fourth-order Runge-Kutta method which is defined as follows

$$g_1 = hA(y)\Phi(y) \quad (\text{A.12})$$

$$g_2 = hA(y + h/2)(\Phi(y) + g_1/2) \quad (\text{A.13})$$

$$g_3 = hA(y + h/2)(\Phi(y) + g_2/2) \quad (\text{A.14})$$

$$g_4 = hA(y + h)(\Phi(y) + g_3) \quad (\text{A.15})$$

$$\Phi(y + h) = \Phi(y) + (g_1 + 2g_2 + 2g_3 + g_4)/6 \quad (\text{A.16})$$

where $h = h(y)$ is the discretization step. For increased accuracy the step size h is not a constant; instead the grid points can be uniformly spaced in terms of the stretched coordinate $z = y \exp(y^2 - 1)$.

Because the matrix elements vary over several orders of magnitude the two linearly independent solutions Φ^1 and Φ^2 become increasingly collinear which will result in a loss of accuracy when the upper boundary conditions are applied. By orthonormalizing Φ^1 and Φ^2 this problem can be overcome. We will follow Conte (1966) in the outline of the orthonormalization process.

First we define the inner product in the usual manner

$$(\Phi^1, \Phi^2) = \sum_{j=1}^4 \Phi_j^1 \Phi_j^{2*} \quad (\text{A.17})$$

where the superscript * denotes the complex conjugate operation. The orthonormalization is done using the Gram-Schmidt procedure

$$\Psi^1 = \Phi^1 / \sqrt{(\Phi^1, \Phi^1)} \quad (\text{A.18})$$

$$t = \Phi^2 - (\Phi^2, \Psi^1) \Psi^1 \quad (\text{A.19})$$

$$\Psi^2 = t / \sqrt{(t, t)} \quad (\text{A.20})$$

where Ψ^j ($j = 1, 2$) are the new orthonormalized solution vectors. The above operation can be written in matrix form in the following way

$$[\Psi^1, \Psi^2] = [\Phi^1, \Phi^2] P \quad (\text{A.21})$$

where

$$P = \begin{pmatrix} p_{11} & p_{12} \\ 0 & p_{22} \end{pmatrix} \quad (\text{A.22})$$

$$p_{11} = 1 / \sqrt{(\Phi^1, \Phi^1)} \quad (\text{A.23})$$

$$p_{12} = -(\Phi^2, \Psi^1) / (\sqrt{(\Phi^1, \Phi^1)} \sqrt{(t, t)}) \quad (\text{A.24})$$

$$p_{22} = 1 / \sqrt{(t, t)} \quad (\text{A.25})$$

After the orthonormalization the new values Ψ^j are used as initial conditions. The above procedure can also be used when a forcing term is present. In the last step for this case the homogeneous part will be subtracted from the particular solution. However, the new particular solution should not be normalized since the forcing term itself is not rescaled. The equation for the horizontal disturbance velocity parallel to the wave front is a second-order inhomogeneous differential equation and will thus also have two solution vectors, the particular solution Φ^0 and the homogeneous solution vector Φ^1 , (the other solution has been set to zero using the boundary condition at $y = -1$). If orthonormalization of these solutions is necessary Φ^0 can be substituted for Φ^2 in the expressions above; in this case Ψ^0 should not be normalized.

The eigenvalue will be independent of the orthonormalization process since we are only changing the initial conditions to another set of linearly independent vectors. However, to obtain the eigenfunctions we have to make

use of the matrices P . Let us call the current discretized solution vectors u^1 and u^2 . Let y_n denote the points used in the orthonormalizations, let P_n stand for the corresponding matrices and call the total number of orthonormalizations N . We start by orthonormalizing at the endpoints which results in

$$[\Psi^1(1), \Psi^2(1)] = [u^1(1), u^2(1)]P_{N+1}. \quad (\text{A.26})$$

Next, we apply the upper boundary condition which gives

$$\Psi(1) = [\Psi^1(1), \Psi^2(1)]\gamma \quad (\text{A.27})$$

where γ is the two component column vector determined from (A.9). For the solution at locations between the endpoint and the previous orthonormalization (i.e., $y : y_N \leq y \leq y_{N+1}$) we apply the same transformation and obtain

$$\Psi(y) = [u^1(y), u^2(y)]P_{N+1}\gamma, \quad y_N \leq y \leq y_{N+1} \quad (\text{A.28})$$

$$= [u^1, u^2]\gamma_N \quad (\text{A.29})$$

with $\gamma_N = P_{N+1}\gamma$. The recovered solution between the two orthonormalizations, y_{n-1} and y_n say, will thus be

$$\Psi(y) = [u^1, u^2]\gamma_{n-1}, \quad y_{n-1} \leq y \leq y_n \quad (\text{A.30})$$

$$\gamma_{n-1} = P_n P_{n-1} \cdots P_{N+1}\gamma = P_n \gamma_N. \quad (\text{A.31})$$

By iterating backwards in this manner the entire solution can be recovered. The angle between the solution vectors could be used as a criterion for orthonormalization, but the following somewhat simpler criterion presents a viable alternative

$$\max \left(\sqrt{(u^1, u^1)}, \sqrt{(u^2, u^2)} \right) > M \quad (\text{A.32})$$

where M in our calculations has been set to 500.

A.3 Chebyshev Expansions

Spectral methods have had a significant impact on the accurate discretization of both initial value and eigenvalue problems. Especially in a bounded domain, the use of Chebyshev polynomials has been advantageous. Most

of the stability calculations shown in this book have been obtained by a Chebyshev discretization of the inhomogeneous coordinate direction. Below we will present the most useful relations for the discretization of derivatives and integrals.

Chebyshev polynomials can be defined in many ways, for example, in terms of trigonometric functions

$$T_n(y) = \cos(n \cos^{-1}(y)), \quad (\text{A.33})$$

as solutions of the singular Sturm-Liouville problem

$$\frac{d}{dy} \left(\sqrt{1-y^2} \frac{d}{dy} T_n(y) \right) + \frac{n^2}{\sqrt{1-y^2}} T_n(y) = 0, \quad (\text{A.34})$$

in terms of a recurrence relation

$$T_0(y) = 1, \quad T_1(y) = y, \quad T_{n+1}(y) = 2yT_n(y) - T_{n-1}(y), \quad (\text{A.35})$$

by a direct formula

$$T_n(y) = \frac{1}{2} \left[(y + \sqrt{y^2 - 1})^n + (y - \sqrt{y^2 - 1})^n \right], \quad (\text{A.36})$$

or by the so-called Rodrigues' formula

$$T_n(y) = \frac{(-1)^n 2^n n!}{(2n)!} \sqrt{1-y^2} \frac{d^n}{dy^n} \left[(1-y^2)^{n-(1/2)} \right]. \quad (\text{A.37})$$

For numerical purposes the definition in terms of trigonometric functions is most practical. Chebyshev polynomials satisfy an orthogonality condition of the form

$$\int_{-1}^1 \frac{T_n(y)T_m(y)}{\sqrt{1-y^2}} dy = C_n \delta_{nm} \quad C_0 = \pi, \quad C_n = \frac{\pi}{2} \quad (n \neq 0). \quad (\text{A.38})$$

We will approximate the dependent variables by a Chebyshev expansion

$$f(y) = \sum_{n=0}^N a_n T_n(y) \quad (\text{A.39})$$

and evaluate the Chebyshev polynomials at the extrema of the N -th Chebyshev polynomial given as

$$y_j = \cos\left(\frac{j\pi}{N}\right). \quad (\text{A.40})$$

These locations are also known as the Gauss-Lobatto points.

When discretizing ordinary or partial differential equations, derivatives of the solution are needed as well. These derivatives have to be expressed in terms of Chebyshev polynomials and the following recurrence relation between Chebyshev polynomials and their derivatives is used.

$$T_0^{(k)}(y_j) = 0, \quad (\text{A.41})$$

$$T_1^{(k)}(y_j) = T_0^{(k-1)}(y_j), \quad (\text{A.42})$$

$$T_2^{(k)}(y_j) = 4T_1^{(k-1)}(y_j), \quad (\text{A.43})$$

$$T_n^{(k)}(y_j) = 2nT_{n-1}^{(k-1)}(y_j) + \frac{n}{n-1}T_{n-1}^{(k)}(y_j) \quad n = 3, 4, \dots. \quad (\text{A.44})$$

with the superscript $k \geq 1$ denoting the order of differentiation.

The evaluation of scalar products requires formulas for the integration of functions that are represented as Chebyshev expansions on a Gauss-Lobatto grid. These formulas ensure spectral accuracy. We have

$$\int_{-1}^1 f(y) dy = \sum_{j=0}^N f(y_j) W(y_j), \quad (\text{A.45})$$

with $W(y_j)$ as the Chebyshev integration weight function which can be found as follows

$$f(y) = \sum_{n=0}^N a_n T_n(y) = \int_{n=0}^N c_n T_n(y) \sum_{j=0}^N \frac{b_j}{N} f(y_j) T_n(y_j). \quad (\text{A.46})$$

Integrating this expression with respect to y yields

$$\int_{-1}^1 f(y) dy = \frac{1}{N} \sum_{j=0}^N b_j f(y_j) \sum_{n=0}^N c_n T_n(y_j) \int_{-1}^1 T_n(y) dy. \quad (\text{A.47})$$

We have

$$\int_{-1}^1 T_n(y) dy = \frac{2}{1 - n^2} \quad n \text{ even} \quad (\text{A.48})$$

which results in

$$W(y_j) = \frac{b_j}{N} \left\{ 2 + \sum_{n=2}^N c_n \frac{1 + (-1)^n}{1 - n^2} \cos\left(\frac{n j \pi}{N}\right) \right\}. \quad (\text{A.49})$$

If a mapping $y = y(\hat{y})$ is used to transform the physical domain into the Chebyshev interval, the formula gets slightly modified

$$W(y_j) = \frac{b_j}{N} \sum_{n=0}^N c_n \cos\left(\frac{n j \pi}{N}\right) \int_{-1}^1 T_n(y) \frac{dy}{d\hat{y}} d\hat{y}. \quad (\text{A.50})$$

A.4 Infinite Domain and Continuous Spectrum

When solving stability problems on a semi-infinite or infinite domain, a mapping of the domain onto a finite domain is necessary before Chebyshev polynomials can be applied. The most frequently used mappings of a semi-infinite to a finite domain are algebraic

$$x = \frac{1 + \xi}{1 - \xi} \quad \xi = \frac{x - 1}{x + 1} \quad (\text{A.51})$$

or exponential

$$x = -\ln\left(\frac{1 - \xi}{2}\right) \quad \xi = 1 - 2e^{-x}. \quad (\text{A.52})$$

Investigations of different mappings have shown that algebraic maps are, in practice, more accurate and more robust than exponential ones.

To achieve the highest possible accuracy, it is sometimes important to control the number of points in a specified subsection of the physical domain. A rational map for the semi-infinite domain has proven successful in distributing grid points such that the near-wall region is sufficiently resolved. The map

$$y = a \frac{1 + \hat{y}}{b - \hat{y}} \quad (\text{A.53})$$

with

$$a = \frac{y_i y_{\max}}{y_{\max} - 2y_i} \quad b = 1 + \frac{2a}{y_{\max}} \quad (\text{A.54})$$

clusters grid points near the wall resulting in the accurate resolution of near-wall shear layers, and distributes half of the grid points in the interval $0 \leq y \leq y_i$.

Infinite intervals can be mapped to a finite domain using the map

$$x = -\cot(\xi/2) \quad (\text{A.55})$$

in conjunction with a Fourier series.

In conjunction with Chebyshev polynomials the mappings

$$x = \frac{\xi}{\sqrt{1 - \xi^2}} \quad (\text{A.56})$$

or

$$x = \tanh^{-1} \xi \quad (\text{A.57})$$

are most common for infinite domains..

A.5 Chebyshev Discretization of the Orr-Sommerfeld Equation

In this section we will present a spectral collocation method based on Chebyshev polynomials and apply it to the Orr-Sommerfeld equation. This method has been used extensively to compute the stability characteristics of shear flows presented throughout this book. The method is highly accurate and easy to implement.

The Orr-Sommerfeld equation reads

$$\left(-Uk^2 - U'' - \frac{k^4}{i\alpha\text{Re}} \right) \tilde{v} + \left(U + \frac{2k^2}{i\alpha\text{Re}} \right) \mathcal{D}^2 \tilde{v} - \frac{1}{i\alpha\text{Re}} \mathcal{D}^4 \tilde{v} = c (\mathcal{D}^2 \tilde{v} - k^2 \tilde{v}) \quad (\text{A.58})$$

with the boundary conditions

$$\tilde{v}(\pm 1) = \mathcal{D}\tilde{v}(\pm 1) = 0. \quad (\text{A.59})$$

We will expand the eigenfunctions in a Chebyshev series

$$\tilde{v}(y) = \sum_{n=0}^N a_n T_n(y). \quad (\text{A.60})$$

The derivatives of the eigenfunctions are obtained by differentiating the expansion above. We obtain for the second derivative, for example,

$$\mathcal{D}^2 \tilde{v}(y) = \sum_{n=0}^N a_n T_n''(y) \quad (\text{A.61})$$

and similarly for the fourth derivative. Upon substitution into the Orr-Sommerfeld equation we get

$$\left(U(y)k^2 - U''(y) - \frac{k^4}{i\alpha \text{Re}} \right) \sum_{n=0}^N a_n T_n(y) + \left(U(y) + \frac{2k^2}{i\alpha \text{Re}} \right) \sum_{n=0}^N a_n T_n''(y) - \frac{1}{i\alpha \text{Re}} \sum_{n=0}^N a_n T_n'''(y) = c \left(\sum_{n=0}^N a_n T_n''(y) - k^2 \sum_{n=0}^N a_n T_n(y) \right). \quad (\text{A.62})$$

We then require this equation to be satisfied at the Gauss-Lobatto collocation points $y_j = \cos(\pi j/N)$. This allows us to use the recurrence relations (A.41-A.44) to evaluate the derivatives of the Chebyshev polynomials.

The discretized boundary conditions read

$$\sum_{n=0}^N a_n T_n(1) = 0 \quad \sum_{n=0}^N a_n T_n(-1) = 0 \quad (\text{A.63})$$

$$\sum_{n=0}^N a_n T_n'(1) = 0 \quad \sum_{n=0}^N a_n T_n'(-1) = 0. \quad (\text{A.64})$$

The final result is a generalized eigenvalue problem of the form

$$\mathbf{A} \mathbf{a} = c \mathbf{B} \mathbf{a} \quad (\text{A.65})$$

with the right-hand side

$$c \mathbf{B} \mathbf{a} =$$

$$c \begin{pmatrix} T_0(1) & T_1(1) & \cdots \\ T'_0(1) & T'_1(1) & \cdots \\ T''_0(y_2) - k^2 T_0(y_2) & T''_1(y_2) - k^2 T_1(y_2) & \cdots \\ \vdots & \vdots & \vdots \\ T''_0(y_{N-2}) - k^2 T_0(y_{N-2}) & T''_1(y_{N-2}) - k^2 T_1(y_{N-2}) & \cdots \\ T'_0(-1) & T'_1(-1) & \cdots \\ T_0(-1) & T_1(-1) & \cdots \end{pmatrix} \begin{pmatrix} a_0 \\ a_1 \\ a_2 \\ \vdots \\ a_{N-2} \\ a_{N-1} \\ a_N \end{pmatrix} \quad (\text{A.66})$$

and similarly for the left-hand side $\mathbf{A} \mathbf{a}$. We have chosen to use the first, second, last and next-to-last row of \mathbf{B} to implement the four boundary conditions. The same rows in the matrix \mathbf{A} can be chosen as a complex multiple of the corresponding rows in \mathbf{B} . By carefully selecting this complex multiple, the spurious modes associated with the boundary conditions can be mapped to an arbitrary location in the complex plane.

The generalized eigenvalue problem can now be solved using standard software, e.g., LAPACK.

A.6 MATLAB Codes for Hydrodynamic Stability Calculations

Below are a suite of MATLAB routines (written by S. Reddy) to compute transient growth and spectral characteristics for plane Poiseuille and plane Couette flow.

MATLAB Driver Program

```
% osmat.m
%
% Program to compute the Orr-Sommerfeld matrix for three-
% dimensional Poiseuille or Couette flows and to compute
% energy matrix
%
```

```

% INPUT
%
% nosmod = number of Orr-Sommerfeld modes
% R = Reynolds number
% alp = alpha (streamwise wave number)
% beta = beta (spanwise wave number)
% iflow = type of flow (Poiseuille=1, Couette=2)
% nosmod = total number of modes for normal velocity
% iflag = flag
%           iflag = 1: compute the maximum growth and
%                   initial condition in time
%                   interval [0,T]
%           iflag = 2: compute the initial disturbance
%                   yielding maximum growth at time T
%
% OUTPUT
% d = 3D Orr-Sommerfeld matrix
% M = energy matrix
%
zi=sqrt(-1);

% input data

iflow=input('Poiseuille (1) or Couette flow (2) ');
nosmod=input('Enter N the number of OS modes: ');
R=input('Enter the Reynolds number: ');
alp=input('Enter alpha: ');
beta=input('Enter beta: ');
iflag=input(... '(1) Max growth in [Tmin,Tmax] (2) Max growth at T ');

if iflag==1,
    Tmin=input('Enter Tmin: ');
    Tmax=input('Enter Tmax: ');
    T=[Tmin Tmax];
else
    T=input('Enter T: ');
end;

% generate Chebyshev differentiation matrices

[D0,D1,D2,D4]=Dmat(nosmod);

% set up Orr-Sommerfeld matrices A and B

```

```

if iflow==1,
    [A,B]=pois(nosmod,alp,beta,R,D0,D1,D2,D4);
else
    [A,B]=couet(nosmod,alp,beta,R,D0,D1,D2,D4);
end;

% generate energy weight matrix

ak2=alp^2+beta^2;
M=energy(nosmod+1,nosmod+1,ak2);

% compute the Orr-Sommerfeld matrix (by inverting B)

d=inv(B)*A;

% compute the optimal

[flowin,flowot,gg]=optimal(d,T,M,ak2,iflag);
figure(1); semilogy(gg(:,1),gg(:,2));grid on

```

Computing Chebyshev Differentiation Matrices

```

function [D0,D1,D2,D4]=Dmat(N);

%
% Function to create differentiation matrices
%
% N      = number of modes
% D0     = zero'th derivative matrix
% D1     = first derivative matrix
% D2     = second derivative matrix
% D4     = fourth derivative matrix

%
% initialize

num=round(abs(N));

%
% create D0

D0=[];
vec=(0:1:num)';
for j=0:1:num

```

```

D0=[D0 cos(j*pi*vec/num)];
end;

% create higher derivative matrices

lv=length(vec);
D1=[zeros(lv,1) D0(:,1) 4*D0(:,2)];
D2=[zeros(lv,1) zeros(lv,1) 4*D0(:,1)];
D3=[zeros(lv,1) zeros(lv,1) zeros(lv,1)];
D4=[zeros(lv,1) zeros(lv,1) zeros(lv,1)];
for j=3:num
    D1=[D1 2*j*D0(:,j)+j*D1(:,j-1)/(j-2)];
    D2=[D2 2*j*D1(:,j)+j*D2(:,j-1)/(j-2)];
    D3=[D3 2*j*D2(:,j)+j*D3(:,j-1)/(j-2)];
    D4=[D4 2*j*D3(:,j)+j*D4(:,j-1)/(j-2)];
end;

```

Computing Orr-Sommerfeld Matrix for Poiseuille Flow

```

function [A,B]=pois(nosmod,alp,beta,R,D0,D1,D2,D4);
%
% Function to create Orr-Sommerfeld matrices using Chebyshev
% pseudospectral discretization for plane Poiseuille flow
% profile
%
% nosmod = number of modes
% alp    = alpha
% beta   = beta
% R      = Reynolds number
% D0     = zero'th derivative matrix
% D1     = first derivative matrix
% D2     = second derivative matrix
% D3     = third derivative matrix
% D4     = fourth derivative matrix

zi=sqrt(-1);

% mean velocity

ak2=alp^2+beta^2;
Nos=nosmod+1;
Nsq=nosmod+1;

```

```

vec=(0:1:nosmod)';
u=(ones(length(vec),1)-cos(pi*vec/nosmod).^2);
du=-2*cos(pi*vec/nosmod);

% set up Orr-Sommerfeld matrix

B11=D2-ak2*D0;
A11=-(D4-2*ak2*D2+(ak2^2)*D0)/(zi*R);
A11=A11+alp*(u*ones(1,length(u))).*B11+alp*2*D0;
er=-200*zi;
A11=[er*D0(1,:); er*D1(1,:); A11(3:Nos-2,:); ...
       er*D1(Nos,:); er*D0(Nos,:)];
B11=[D0(1,:); D1(1,:); B11(3:Nos-2,:); ...
       D1(Nos,:); D0(Nos,:)];

% set up Squire matrix and cross-term matrix

A21=beta*(du*ones(1,length(u))).*D0(1:Nos,:);
A22=alp*(u*ones(1,length(u))).*D0-(D2-ak2*D0)/(zi*R);
B22=D0;
A22=[er*D0(1,:); A22(2:Nsq-1,:); er*D0(Nsq,:)];
A21=[zeros(1,Nos); A21(2:Nsq-1,:); zeros(1,Nos)];

% combine all the blocks

A=[A11 zeros(Nos,Nsq); A21 A22];
B=[B11 zeros(Nos,Nsq); zeros(Nsq,Nos) B22];

```

Computing Orr-Sommerfeld Matrix for Couette Flow

```

function [A,B]=couet(nosmod,alp,beta,R,D0,D1,D2,D4);
%
% Function to create Orr-Sommerfeld matrices using Chebyshev
% pseudospectral discretization for plane Couette flow
% profile
%
% nosmod = number of even or odd modes
% alp    = alpha
% R      = Reynolds number
% D0     = zero'th derivative matrix
% D1     = first derivative matrix
% D2     = second derivative matrix

```

```
% D4      = fourth derivative matrix

zi=sqrt(-1);

% mean velocity

ak2=alp^2+beta^2;
Nos=nosmod+1;
Nsq=nosmod+1;
u=cos(pi*(0:1:Nos-1)'/(Nos-1));
du=ones(length(u),1);

% set up Orr-Sommerfeld matrix

B11=D2-ak2*D0;
A11=-(D4-2*ak2*D2+(ak2^2)*D0)/(zi*R);
A11=A11+alp*(u*ones(1,length(u))).*B11;
er=-200*zi;
A11=[er*[D0(1,:); D1(1,:)]; A11(3:Nos-2,:); ...
      er*[D1(Nos,:); D0(Nos,:)]];
B11=[D0(1,:); D1(1,:); B11(3:Nos-2,:); ...
      D1(Nos,:); D0(Nos,:)];

% set up Squire matrix and cross-term matrix

A21=beta*(du*ones(1,length(u))).*D0;
A22=alp*(u*ones(1,length(u))).*D0-(D2-ak2*D0)/(zi*R);
B22=D0;
A22=[er*D0(1,:); A22(2:Nsq-1,:); er*D0(Nsq,:)];

% combine all the blocks

A=[A11 zeros(Nos,Nsq); A21 A22];
B=[B11 zeros(Nos,Nsq); zeros(Nsq,Nos) B22];
```

Computing Energy Weight Matrix

```
function M=energy(Nos,Nsq,ak2);
%
% Program to compute the energy weight matrix for three-
% dimensional Poiseuille and Couette flows
%
```

```

% INPUT
% Nos      = Number of normal velocity modes
% Nsq      = Number of normal vorticity modes
%
% OUTPUT
% M        = weight matrix

M=eye(Nos+Nsq,Nos+Nsq);
Cos=two(Nos);
Dos=deven(Nos);
Wos=Dos'*Cos*Dos+ak2*Cos;
Wsq=two(Nsq);

[u,s,v]=svd(Wos); s=sqrt(diag(s));
Mos=diag(s)*u';

[u,s,v]=svd(Wsq); s=sqrt(diag(s));
Msq=diag(s)*u';

M=[Mos zeros(Nos,Nsq); zeros(Nsq,Nos) Msq];

```

Computing Two Norm Weight Matrix

```

function c=two(N);
%
% This program determines the two norm weight matrix c for
% Chebyshev polynomials. The matrix c is defined by
%
% c_{ij}= int_{-1}^1 T_{i}(x) T_{j}(x) dx,
%
% where T_k is a Chebyshev polynomial. The above product
% satisfies
%
% c_{ij}= 1/(1-(i+j)^2)+1/(1-(i-j)^2)   for i+j even
%           = 0                               for i+j odd
%
% Input
%
% N      = number of modes
%
% The maximum degree M of polynomials c_i,c_j satisfies
% M = N-1

```

```

%
num=round(abs(N));
c=zeros(num,num);

for i=(0:num-1)
    for j=(0:num-1)
        if rem(i+j,2)==0,
            p=1/(1-(i+j)^2)+1/(1-(i-j)^2);
            c(i+1,j+1)=p;
        else
            c(i+1,j+1)=0;
        end;
    end;
end;

```

Computing Chebyshev Conversion Matrix

```

function d1=deven(N);
%
% Compute matrix which converts Chebyshev coefficients of a
% polynomial to coefficients of derivative
%
% Reference:
% Gottlieb and Orszag, Numerical Analysis of Spectral
% Methods: Theory and Applications, SIAM, Philadelphia,
% 1977.
%
% d1 = derivative matrix (N,N)
% N = number of coefficients
%
num=round(abs(N));
d1=zeros(num,num);

for i=0:(num-1)
    for j=(i+1):2:(num-1)
        d1(i+1,j+1)=2*j;
    end;
end;

d1(1,:)=d1(1,:)/2;

```

Computing Transient Growth

```
function [flowin,flowot,gg]=optimal(d,T,M,ak2,iflag);  
%  
% This function computes the initial flow structure which  
% achieves the maximum transient energy growth  
%  
% INPUT  
% d      = 3D Orr-Sommerfeld operator  
% T      = time  
% M      = energy weight matrix  
% ak2    = alpha^2+beta^2  
% iflag   = flag  
%           iflag = 1: compute the maximum growth and  
%                   initial condition in time  
%                   interval [0,T]  
%           iflag = 2: compute the initial disturbance  
%                   yielding maximum growth at time T  
% OUTPUT  
% flowin = coefficients of optimal disturbance  
%           flowin(1:Nos)      = normal velocity  
%           coefficients  
%           flowin(Nos+1:Nos+Nsq) = normal vorticity  
%           coefficients  
% flowot  = coefficients of field at optimal time  
%           flowot(1:Nos)      = normal velocity  
%           coefficients  
%           flowot(Nos+1:Nos+Nsq) = normal vorticity  
%           coefficients  
  
global qb;  
  
% Phase 1: Compute eigenvalues and eigenfunctions of  
% Orr-Sommerfeld matrix and sort in order of descending  
% imaginary part. The function nlize normalizes the  
% eigenfunctions with respect to the weight matrix M.  
  
[xs,es]=iord2(d);  
xs=nlize(xs,M);  
  
% Phase 2: Choose which modes are to be used in optimal
```

```
% calculation. Modes with imaginary part > 1 are neglected.
% Modes with imaginary part < imin are neglected as well.

ishift=1;
imin=-1.5;

while imag(es(ishift))>1, ishift=ishift+1; end;

[n1,n2]=n9(es,imin);

cols=(ishift:n2);
xu=xs(:,cols);
eu=es(cols);
ncols=length(cols);
fprintf('Number of modes used: %1.0f \n',ncols);

% Phase 3: Compute the reduced Orr-Sommerfeld operator

[qb,invF]=qbmat(M,xu,eu);

% Phase 4: Compute the time for the maximum growth using
% the built-in Matlab routine 'fmin'

if iflag==1,
  gcheck=maxer(1/100);
  gcheck=gcheck^2;
  if gcheck<1,
    tformax=0;
    mgrowth=1;
  else
    ts=T(1);
    tf=T(2);
    options=[0 1e-3 1e-3];
    tformax=fmy(ts,tf,options);
    mgrowth=maxer(tformax);
    mgrowth=mgrowth^2;
  end;
  fprintf('Time for maximum growth: %e \n',tformax);
else
  tformax=T;
end;

% Phase 5: Compute the initial condition that yields the
% maximum growth. This is obtained by
% (1) computing the matrix exponential evaluated at the
```

```

%      optimal time;
% (2) computing the SVD of the matrix exponential
%      exp(-i*A*t)=USV.
% The initial condition that yields the maximum growth is
% the first column of V. To convert the initial condition
% to a vector of coefficients in the eigenfunction basis
% multiply by the matrix of eigenfunctions and inv(F)

evol=expm(tformax*qb);
[U,S,V]=svd(evol);
mgrowth=S(1,1)^2;
fprintf('Maximum growth in energy: %e \n',mgrowth);

flowin=sqrt(2*ak2)*xu*invF*V(:,1);
flowot=sqrt(2*ak2)*xu*invF*U(:,1);

for i=1:100,
    tid = ts + (tf-ts)/99*(i-1);
    gg(i,2) = norm(expm(tid*qb))^2;
    gg(i,1) = tid;
end

```

Computing Ordered Eigenvalues

```

function [xs,es]=iord2(d);
%
% This function computes the eigenvalues of a matrix d and
% orders the eigenvalues so that the imaginary parts are
% decreasing.
%
% INPUT
% d      = input matrix
%
% OUTPUT
% es     = ordered eigenvalues
% xs     = eigenvectors

[v,e]=eig(d);
e=diag(e);
[eimag,is]=sort(-imag(e));
xs=v(:,is);
es=e(is);

```

Normalizing Matrix Columns

```
function x=nlize(x,M);
%
% This function normalizes the columns of x such that
%
% || M x_i ||_2 = 1
%
% nc=size(x); nc=nc(2);
for i=1:nc
    x(:,i)=x(:,i)/norm(M*x(:,i));
end;
```

Selecting Eigenvalues

```
function [n1,n2]=n9(e,a);
%
% This function computes the number of eigenvalues
% satisfying
%
% a <= Imag(lambda) <= .5
%
% INPUT
% e    = eigenvalues ordered with decreasing imaginary
%       part
%
% OUTPUT
% n1  = position of first eigenvalue in the interval
% n2  = position of last eigenvalue in the interval

n1=1;

while imag(e(n1))>.5,
    n1=n1+1;
end;

n2=n1;
```

```

while imag(e(n2))>a,
    n2=n2+1;
end;

n2=n2-1;

```

Computing Transient Growth Matrix

```

function [qb,invF]=qbmata(M,xu,e)
%
% This function computes the matrix Q=-i*F*diag(e)*inv(F)
% which is used to compute the maximum transient growth
% (see Reddy and Henningson, "Energy Growth in Viscous
% Channel Flows", JFM 252, page 209, 1993).
%
% INPUT
% M      = energy weight matrix
% xu     = matrix of eigenfunctions (expansion coefficients)
% e      = vector of eigenvalues of the stability matrix
%
% OUTPUT
% qb     = output matrix Q
% invF   = inverse of F
%
%
% Phase 1: compute inner product of the eigenfunctions
%           in energy norm

work=M*xu;
A=work'*work;

% Phase 2: compute decomposition A=F^*F

[U,S,V]=svd(A);
s=sqrt(diag(S));
F=diag(s)*U';
invF=U*diag(ones(size(s))./s);

% Phase 3: compute Q=-i*F*diag(e)*inv(F)

qb=-sqrt(-1)*F*diag(e)*invF;

```

Computing Norm of Matrix Exponential

```
function a=maxer(t);
%
% This function computes the norm of the matrix exponential
% of qb*t

global qb;
a=-norm(expm(t*qb));
```

Maximizing Transient Growth

```
function t=fmy(t1,t2,options);
%
% This function uses the built-in function 'fmin' to find
% the maximum value of a function on the interval [t1,t2].
% The function is in the file maxer.m
%
% INPUT:
% t1,t2 = lower and upper bounds of interval
% options = input parameters for minimization routine
%
% OUTPUT
% t = value at which function maxer(t) is minimized

f1=maxer(t1);
f2=maxer(t2);

tt=fmin('maxer',t1,t2,options);

f3=maxer(tt);
f=[f1 f2 f3];
tm=[t1 t2 tt];
[y,is]=sort(f);
t=tm(is(1));
```

A.7 Eigenvalues of Parallel Shear Flows

Plane Poiseuille flow, $\text{Re} = 2000$

$\alpha = 1, \beta = 0$		$\alpha = 0.5, \beta = 1$		$\alpha = 0.25, \beta = 3$		$\alpha = 0, \beta = 2$	
c_r	c_i	c_r	c_i	c_r	c_i	c_r	c_i
Orr-Sommerfeld		Orr-Sommerfeld		Orr-Sommerfeld		Orr-Sommerfeld	
0.31210030	-0.01979866	0.37226932	-0.03737398	0.56329537	-0.08548514	-0.00507754	
0.42418427	-0.07671992	0.49935557	-0.09920592	0.83796079	-0.14010066	-0.01107002	
0.92078667	-0.0784706	0.88770220	-0.10945538	0.84492959	-0.14965217	-0.01982549	
0.92091806	-0.07820060	0.88808805	-0.10962449	0.58717755	-0.15289251	-0.03078177	
0.85717055	-0.13990151	0.79534673	-0.19331077	0.72738833	-0.22753394	-0.04449131	
0.85758968	-0.14031674	0.79830962	-0.19657914	0.73333862	-0.28917720	-0.06038365	
0.79399812	-0.20190508	0.72648153	-0.26096201	0.63548529	-0.36625533	-0.07903219	
0.79413424	-0.20232063	0.64779065	-0.26971348	0.62259513	-0.41560943	-0.09985929	
0.63912513	-0.22134137	0.70474692	-0.29872825	0.64672215	-0.44988239	-0.12344417	
0.53442105	-0.22356175	0.43320720	-0.30659209	0.66265886	-0.56491518	-0.14920592	
Squire		Squire		Squire		Squire	
0.98418861	-0.01631139	0.97763932	-0.02361068	0.96837728	-0.03974775	-0.00323370	
0.95256584	-0.04793417	0.93291797	-0.06833204	0.90513428	-0.10299426	-0.00693480	
0.92094306	-0.0795694	0.88819669	-0.11305351	0.84190728	-0.16629312	-0.01310331	
0.88932028	-0.11117972	0.84347472	-0.15777756	0.39061440	-0.21452290	-0.02173921	
0.24936056	-0.13725811	0.31232252	-0.16986946	0.39061296	-0.21452788	-0.03284251	
0.24936056	-0.13725811	0.31232252	-0.16986946	0.77824142	-0.23018702	-0.04641322	
0.85769752	-0.14280249	0.79871747	-0.20251584	0.70571029	-0.29246161	-0.06245133	
0.82607494	-0.17442537	0.75360282	-0.24701616	0.65305016	-0.31673071	-0.08095684	
0.79445264	-0.20605114	0.53467243	-0.27140532	0.65688684	-0.35866635	-0.10192975	
0.42863639	-0.22466515	0.53470480	-0.27146759	0.67269250	-0.4602968	-0.12537006	

TABLE A.1. PLANE POISEUILLE FLOW eigenvalues

Couette flow, $\text{Re} = 800$						
$\alpha = 1, \beta = 0$			$\alpha = 0.5, \beta = 1$		$\alpha = 0.25, \beta = 3$	
c_r	c_i	c_r	c_i	c_r	c_i	ω_i
Orr-Sommerfeld						
± 0.57647380	-0.129552206	± 0.47711120	-0.17057387	± 0.39990294	-0.25329463	-0.01269385
± 0.33837303	-0.2869889	± 0.18033226	-0.3689022	± 0.37283853	-0.48343132	-0.02767504
± 0.65474385	-0.31845690	± 0.55316723	-0.39709328	0.00000000	-0.48561430	-0.04956371
± 0.13853225	-0.41451617	0.00000000	-0.52654272	0.00000000	-0.56306665	-0.07695442
± 0.39155287	-0.44983177	± 0.21826018	-0.56176351	0.00000000	-0.72239155	-0.11122827
0.00000000	-0.51543904	0.00000000	-0.68690207	0.00000000	-0.92956625	-0.15095912
± 0.17496627	-0.56239996	0.00000000	-0.80374929	0.00000000	-1.17658449	-0.19758048
0.00000000	-0.64277951	0.00000000	-0.96841110	0.00000000	-1.44426340	-0.24964822
0.00000000	-0.69476878	0.00000000	-1.14407304	0.00000000	-1.73554371	-0.30861043
0.00000000	-0.80564720	0.00000000	-1.32986473	0.00000000	-2.04876750	-0.37301480
Squire						
± 0.78187852	-0.12718249	± 0.72518416	-0.16179000	± 0.65375374	-0.22021787	-0.00808425
± 0.61863618	-0.222143050	± 0.51951170	-0.28053505	± 0.39462265	-0.36982719	-0.01733701
± 0.48498831	-0.29855214	± 0.35112593	-0.37775262	± 0.18249973	-0.49241970	-0.03275826
± 0.36686964	-0.36678798	± 0.20230357	-0.46367578	0.00000000	-0.57627651	-0.0534802
± 0.25889370	-0.42912792	± 0.06726756	-0.54144268	0.00000000	-0.71401555	-0.08210628
± 0.15827968	-0.48721835	0.00000000	-0.65186131	0.00000000	-0.94254293	-0.11603305
± 0.06311251	-0.54178178	0.00000000	-0.80563552	0.00000000	-1.19022327	-0.15612832
0.00000000	-0.59624095	0.00000000	-0.97104292	0.00000000	-1.45959937	-0.20239209
0.00000000	-0.6958432	0.00000000	-1.14689443	0.00000000	-1.75143991	-0.25482436
0.00000000	-0.80694602	0.00000000	-1.3335240	0.00000000	-2.06630407	-0.31342514

TABLE A.2. COUETTE FLOW eigenvalues

Pipe Poiseuille flow, $Re = 2000$

$\alpha = 1, n = 0$		$\alpha = 0.5, n = 1$		$\alpha = 0.25, n = 2$		$\alpha = 0, n = 1$	
c_r	c_i	c_r	c_i	c_r	c_i	ω_i	
0.93675536	-0.06374551	0.84646970	-0.07176332	0.72551688	-0.14895301	-0.00734099	
0.93675445	-0.06374555	0.42653865	-0.10120107	0.37381075	-0.17973957	-0.01318731	
0.87350890	-0.12699110	0.30753390	-0.14961348	0.51310797	-0.19545604	-0.02460923	
0.87353385	-0.12701919	0.92769296	-0.15332927	0.85236191	-0.27489963	-0.03542500	
0.46474928	-0.12733652	0.74827192	-0.15401221	0.59574165	-0.29082257	-0.05174973	
0.24930527	-0.13770406	0.66105308	-0.23357367	0.60783255	-0.40189549	-0.06751036	
0.81026386	-0.19023731	0.84409924	-0.25072952	0.72720893	-0.41549788	-0.08876038	
0.81012530	-0.19098283	0.53491162	-0.28781712	0.64896591	-0.50429278	-0.10946009	
0.42850340	-0.22516774	0.46768245	-0.32736073	0.66139917	-0.61313884	-0.13564083	
0.74691455	-0.25352712	0.63139623	-0.33464114	0.66664316	-0.73870170	-0.16127756	
0.70634286	-0.25379497	0.75997902	-0.34520452	0.66017652	-0.86358022	-0.19239095	
0.73511224	-0.26390239	0.67575624	-0.43243735	0.66968104	-1.00995818	-0.22296378	
0.57089335	-0.28598470	0.67491966	-0.46947547	0.65952947	-1.15557527	-0.25901072	
0.685908153	-0.30991044	0.67065768	-0.56007978	0.67077599	-1.31762599	-0.29451918	
0.40118595	-0.33427144	0.66958056	-0.63844170	0.65971050	-1.48607071	-0.33550011	
0.68879517	-0.36815020	0.66947927	-0.72799068	0.67093631	-1.66460005	-0.37594393	
0.67317200	-0.37669040	0.66800877	-0.81713158	0.66029737	-1.85486324	-0.42185912	
0.69423205	-0.4362004	0.66915390	-0.91515764	0.67069161	-2.04976452	-0.46723813	
0.67232230	-0.47977566	0.66709014	-1.01401073	0.666099154	-2.26220681	-0.51808775	
0.67131307	-0.53467710	0.66899996	-1.12083979	0.67030895	-2.47485248	-0.56840184	

TABLE A.3. PIPE POISEUILLE FLOW eigenvalues

Blasius boundary layer flow, $\text{Re}_{\delta^*} = 800$

$\alpha = 1, \beta = 0$		$\alpha = 0.5, \beta = 0.1$		$\alpha = 0.25, \beta = 0.2$		$\alpha = 0.125, \beta = 0.3$	
c_r	c_i	c_r	c_i	c_r	c_i	c_r	c_i
Orr-Sommerfeld						Orr-Sommerfeld	
0.29440241	-0.08240950	0.39192905	-0.04349817	0.39065421	+0.00287572	0.42986402	-0.01526073
0.46408909	-0.16979273	0.48131508	-0.13904767	0.54772364	-0.23434181	0.67108511	-0.31529294
0.58341130	-0.21355653	0.28194476	-0.26456053	0.33866341	-0.31005379	0.43734404	-0.36626806
0.23752687	-0.21441674	0.64194579	-0.29009419	0.79181869	-0.37872068	0.86076659	-0.46712319
0.67030439	-0.28694526	0.51869001	-0.35381783	0.65749147	-0.40505900		
0.42182040	-0.29556202	0.81507495	-0.37808042				
0.78475538	-0.35409567	0.72900959	-0.42004769				
0.57920596	-0.35864989						
0.72486516	-0.40824449						
Squire						Squire	
0.15023935	-0.08789091	0.18934427	-0.10971644	0.23869653	-0.13769021	0.30108694	-0.17329180
0.26294369	-0.15227682	0.33172068	-0.19019408	0.41904327	-0.23747142	0.53079487	-0.29497981
0.35574122	-0.20409837	0.44962930	-0.25384742	0.57017612	-0.31360121	0.72806936	-0.38097627
0.43849974	-0.24866890	0.55577060	-0.30704908	0.70889059	-0.37342899	0.91630206	-0.43964252
0.51510271	-0.28789626	0.65531838	-0.35196883	0.84255313	-0.41937502		
0.58764090	-0.32268836	0.75120476	-0.38960568				
0.65744431	-0.3554522	0.84540756	-0.42054153				
0.72545592	-0.38077281						
0.79239966	-0.40457786						

TABLE A.4. BLASIUS BOUNDARY LAYER FLOW eigenvalues

Appendix B

Resonances and Degeneracies

B.1 Resonances and Degeneracies

The case of degenerate eigenvalues will be considered in this appendix.

Let us consider one double eigenvalue ω_d . In the degenerate case a generalized eigenfunction must be added to complete the set of expansion functions. This function $\partial\tilde{\mathbf{q}}_d$ and its adjoint satisfy the following equations (DiPrima & Habetler, 1969)

$$(\mathbf{L} - i\omega_d \mathbf{M}) \partial\tilde{\mathbf{q}}_d = i\mathbf{M}\tilde{\mathbf{q}}_d \quad (\text{B.1})$$

$$(\mathbf{L}^+ + i\omega_d^* \mathbf{M}) \partial\tilde{\mathbf{q}}_d^+ = -i\mathbf{M}\tilde{\mathbf{q}}_d^+ \quad (\text{B.2})$$

with boundary conditions analogous to the regular eigenvalue problem. The symbol ∂ indicates that the generalized eigenfunction can be considered as the derivative of the regular eigenfunction with respect to the eigenvalue. For a degeneracy between two Orr-Sommerfeld modes we obtain the problem studied by Shantini (1990).

The bi-orthogonality conditions for the case of degenerate eigenvalues are somewhat more involved but can be derived in a manner similar to the regular eigenvalue problem. After proper normalization we find the following relations.

$$\begin{aligned} (\mathbf{M}\tilde{\mathbf{q}}_d, \tilde{\mathbf{q}}_p^+) &= (\tilde{\mathbf{q}}_d, \mathbf{M}\tilde{\mathbf{q}}_p^+) = (\mathbf{M}\tilde{\mathbf{q}}_p, \tilde{\mathbf{q}}_d^+) \\ &= (\tilde{\mathbf{q}}_p, \mathbf{M}\tilde{\mathbf{q}}_d^+) = 0 \end{aligned} \quad (\text{B.3})$$

$$\begin{aligned} (\mathbf{M}\partial\tilde{\mathbf{q}}_d, \tilde{\mathbf{q}}_p^+) &= (\partial\tilde{\mathbf{q}}_d, \mathbf{M}\tilde{\mathbf{q}}_p^+) = (\mathbf{M}\tilde{\mathbf{q}}_p, \partial\tilde{\mathbf{q}}_d^+) \\ &= (\tilde{\mathbf{q}}_p, \mathbf{M}\partial\tilde{\mathbf{q}}_d^+) = \delta_{pd} \end{aligned} \quad (\text{B.4})$$

$$\begin{aligned} (\mathbf{L}\partial\tilde{\mathbf{q}}_d, \tilde{\mathbf{q}}_p^+) &= (\partial\tilde{\mathbf{q}}_d, \mathbf{L}^+\tilde{\mathbf{q}}_p^+) = (\mathbf{L}\tilde{\mathbf{q}}_p, \partial\tilde{\mathbf{q}}_d^+) \\ &= (\tilde{\mathbf{q}}_p, \mathbf{L}^+\partial\tilde{\mathbf{q}}_d^+) = i\omega_d\delta_{pd} \end{aligned} \quad (\text{B.5})$$

$$\begin{aligned} (\partial\tilde{\mathbf{q}}_d, \mathbf{L}^+\partial\tilde{\mathbf{q}}_d^+) - i\omega_d(\partial\tilde{\mathbf{q}}_d, \mathbf{M}\partial\tilde{\mathbf{q}}_d^+) \\ = (\mathbf{L}\partial\tilde{\mathbf{q}}_d, \partial\tilde{\mathbf{q}}_d^+) - i\omega_d(\mathbf{M}\partial\tilde{\mathbf{q}}_d, \partial\tilde{\mathbf{q}}_d^+) = i \end{aligned} \quad (\text{B.6})$$

The inner products in (B.3) are zero also for the case $p = d$, and the subscript d refers only to the eigenmode associated with the degenerate eigenvalue.

The solution to the linear initial value problem, assuming one degenerate eigenvalue ω_d , can be written in the form

$$\hat{\mathbf{q}} = K_d(t)\tilde{\mathbf{q}}_d + K_{d+1}(t)\partial\tilde{\mathbf{q}}_d + \sum_p K_p(t)\tilde{\mathbf{q}}_p \quad (\text{B.7})$$

where it is assumed that $p \neq d$, $p \neq d+1$. We introduce the expansion into the linear initial value problem, multiply by the adjoint eigenfunctions (including the generalized one) and integrate across the channel. Using the bi-orthogonality conditions and (B.3-B.6) we obtain a system of uncoupled equations for each K_p together with two coupled equations for K_d and K_{d+1} . The solution to this system is

$$K_p = K_p^0 e^{-i\omega_p t} \quad (\text{B.8})$$

$$K_d = (K_d^0 - iK_{d+1}^0 t)e^{-i\omega_d t} \quad (\text{B.9})$$

$$K_{d+1} = K_{d+1}^0 e^{-i\omega_{d+1} t}. \quad (\text{B.10})$$

The coefficients K_p^0 are identical to the coefficients found in Chapter 3, while the initial coefficients associated with the degenerate eigenvalue become

$$K_d^0 = (\mathbf{M}\hat{\mathbf{q}}^0, \partial\tilde{\mathbf{q}}_d^+) - K_{d+1}^0(\mathbf{M}\partial\tilde{\mathbf{q}}_d, \partial\tilde{\mathbf{q}}_d^+) \quad (\text{B.11})$$

$$K_{d+1}^0 = (\mathbf{M}\hat{\mathbf{q}}^0, \hat{\mathbf{q}}_d^+). \quad (\text{B.12})$$

The complete solution to the degenerate case thus can be written

$$\begin{aligned}\hat{\mathbf{q}} = & \sum_p (\mathbf{M}\hat{\mathbf{q}}^0, \tilde{\mathbf{q}}_p^+) \tilde{\mathbf{q}}_p e^{-i\omega_p t} + (\mathbf{M}\hat{\mathbf{q}}^0, \tilde{\mathbf{q}}_d^+) \partial\tilde{\mathbf{q}}_d e^{-i\omega_d t} + \\ & [(\mathbf{M}\hat{\mathbf{q}}^0, \partial\tilde{\mathbf{q}}_d^+) - (\mathbf{M}\hat{\mathbf{q}}^0, \tilde{\mathbf{q}}_d^+) (\mathbf{M}\partial\tilde{\mathbf{q}}_d, \partial\tilde{\mathbf{q}}_d^+) \\ & - it (\mathbf{M}\hat{\mathbf{q}}^0, \tilde{\mathbf{q}}_d^+)] \tilde{\mathbf{q}}_d e^{-i\omega_d t}.\end{aligned}\quad (\text{B.13})$$

Shantini (1990), using a Fourier-Laplace method, found the same expressions for a degeneracy between Orr-Sommerfeld modes. It is easy to generalize the result to vector eigenfunctions. Since they include both the Orr-Sommerfeld and Squire modes, the normal velocity - normal vorticity resonance studied by Benney & Gustavsson (1981) reduces to a degeneracy between vector modes of the linear system. The details regarding this type of degeneracy will be presented in the subsequent section. We close this section by presenting the special case of (B.13) when the initial condition only includes the generalized eigenfunction, i.e. $\hat{\mathbf{q}}^0 = \partial\tilde{\mathbf{q}}_d$, in which case

$$\hat{\mathbf{q}} = (\partial\tilde{\mathbf{q}}_d - it\tilde{\mathbf{q}}_d) e^{-i\omega_d t}. \quad (\text{B.14})$$

Reddy & Henningson (1993) assessed the importance of including the generalized eigenfunction when calculating optimal disturbances and found that the optimal disturbances varied smoothly across the degeneracy. Thus, it is sufficient to consider the regular eigenvalues close to the degeneracy to obtain an accurate representation of the solution; see Figure B.1.

B.2 Orr-Sommerfeld-Squire Resonance

If one of the degenerate modes is of Orr-Sommerfeld type and the other is a Squire mode, the degeneracy is identical to the resonance studied by Benney & Gustavsson (1981). It is interesting to see how this special case appears from a degeneracy of the vector eigenfunctions. We will follow Henningson & Schmid (1992) in this derivation. First we have to solve (3.28) to obtain the regular eigenfunction at the degeneracy. When ω is an eigenvalue of the homogeneous parts of both equations, the normal velocity has to be zero; otherwise the compatibility condition requiring the driving term of the normal vorticity equation to be orthogonal to the adjoint eigenfunction is not satisfied. Similarly, a solution to the equation governing the regular adjoint eigenfunction only exists when its normal vorticity is zero. We have the following equations governing the regular eigenfunctions at the degeneracy

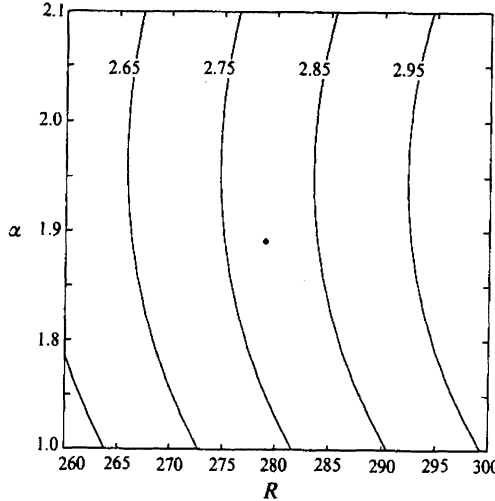


FIGURE B.1. Contours of G_{max} for plane Poiseuille flow in the neighborhood of the degeneracy at $\text{Re} \approx 279$ and $\alpha \approx 1.89$ (the dot), where the maximum growth is ≈ 2.80 . From Reddy & Henningson (1993).

$$\tilde{v}_d = 0 \quad (\text{B.15})$$

$$L_{SQ}\tilde{\eta}_d - i\omega_d\tilde{\eta}_d = 0 \quad (\text{B.16})$$

and

$$L_{OS}^+\tilde{v}_d^+ + i\omega_d^*M\tilde{v}_d^+ = 0 \quad (\text{B.17})$$

$$\tilde{\eta}_d^+ = 0. \quad (\text{B.18})$$

In component form the equations (B.1, B.2) for the generalized eigenfunctions at an Orr-Sommerfeld-Squire degeneracy now become

$$L_{OS}\partial\tilde{v}_d - i\omega_d M\partial\tilde{v}_d = 0 \quad (\text{B.19})$$

$$L_{SQ}\partial\tilde{\eta}_d - i\omega_d\partial\tilde{\eta}_d = -i\beta U'\partial\tilde{v}_d + i\tilde{\eta}_d \quad (\text{B.20})$$

and

$$L_{OS}^+\partial\tilde{v}_d^+ + i\omega_d^*M\partial\tilde{v}_d^+ = i\beta U'\partial\tilde{\eta}_d^+ - iM\tilde{v}_d^+ \quad (\text{B.21})$$

$$L_{SQ}^+\partial\tilde{\eta}_d^+ + i\omega_d^*\partial\tilde{\eta}_d^+ = 0 \quad (\text{B.22})$$

where we have used that $\tilde{v}_d = 0$ and $\tilde{\eta}_d^+ = 0$. This result implies that $\partial\tilde{v}_d$ is the solution to the Orr-Sommerfeld equation and $\partial\tilde{\eta}_d^+$ is the solution to

the adjoint Squire equation. The bi-orthogonality conditions governing the degenerate modes can now be evaluated in component form. It is easily verified that equation (B.3) is satisfied, while equation (B.4) becomes

$$\int_{-1}^1 \tilde{v}_p^{+*} M \partial \tilde{v}_d dy = \delta_{pd} \quad (\text{B.23})$$

$$\int_{-1}^1 \partial \tilde{\eta}_d^{+*} \tilde{\eta}_p dy = \delta_{pd} \quad (\text{B.24})$$

$$\int_{-1}^1 \left(\tilde{\zeta}_p^{+*} M \partial \tilde{v}_d + \tilde{\eta}_p^{+*} \partial \tilde{\eta}_d \right) dy = 0 \quad (\text{B.25})$$

$$\int_{-1}^1 \left(\partial \tilde{v}_d^{+*} M \tilde{v}_p + \partial \tilde{\eta}_d^{+*} \tilde{\xi}_p \right) dy = 0. \quad (\text{B.26})$$

The two last equations are identically zero when $p = d$. Equation (B.5), along with the above relations, can be used to derive

$$\begin{aligned} \beta \int_{-1}^1 U' \tilde{\eta}_p^{+*} \partial \tilde{v}_d dy &= -(\omega_d - \omega_p) \int_{-1}^1 \tilde{\zeta}_p^{+*} M \partial \tilde{v}_d dy \\ &= (\omega_d - \omega_p) \int_{-1}^1 \tilde{\eta}_p^{+*} \partial \tilde{\eta}_d dy \end{aligned} \quad (\text{B.27})$$

$$\begin{aligned} \beta \int_{-1}^1 U' \partial \tilde{\eta}_d^{+*} \tilde{v}_p dy &= (\omega_d - \omega_p) \int_{-1}^1 \partial \tilde{v}_d^{+*} M \tilde{v}_p dy \\ &= -(\omega_d - \omega_p) \int_{-1}^1 \partial \tilde{\eta}_d^{+*} \tilde{\xi}_p dy. \end{aligned} \quad (\text{B.28})$$

Finally, equation (B.6) yields

$$\beta \int_{-1}^1 U' \partial \tilde{\eta}_d^{+*} \partial \tilde{v}_d dy = 1. \quad (\text{B.29})$$

The last equation implies that the inhomogeneous terms in equations (B.20) and (B.21) are orthogonal to the solutions of the respective homogeneous operators. Thus, the compatibility condition is satisfied and solutions for both $\partial \tilde{\eta}_d$ and $\partial \tilde{v}_d^+$ can be found. To find $\partial \tilde{\eta}_d$, for example, we assume that it has an expansion in eigenmodes of the homogeneous operator (excluding the resonant term), and calculate the expansion coefficients using the bi-orthogonality condition for the normal vorticity. We find

$$\begin{aligned}\partial\tilde{\eta}_d &= \sum_{p \neq d} \int_{-1}^1 \tilde{\eta}_p^{+*} \partial\tilde{\eta}_d dy \tilde{\eta}_p \\ &= \sum_{p \neq d} \frac{\beta \int_{-1}^1 U' \tilde{\eta}_p^{+*} \partial\tilde{v}_d dy}{\omega_d - \omega_p} \tilde{\eta}_p\end{aligned}\quad (\text{B.30})$$

where equation (B.27) has been used to rewrite the expansion coefficient. An arbitrary amount of the eigenvector $\tilde{\eta}_d$ can be added to this solution. We have chosen to add zero, any other amount would only change the relative importance of the expansion coefficients multiplying the $\tilde{\eta}_d$ and $\partial\tilde{\eta}_d$ modes.

Using the above results the solution (B.14) at a $v\text{-}\eta$ degeneracy can be written

$$\begin{pmatrix} \hat{v} \\ \hat{\eta} \end{pmatrix} = \left[\begin{pmatrix} \partial\tilde{v}_d \\ \partial\tilde{\eta}_d \end{pmatrix} - it \begin{pmatrix} 0 \\ \tilde{\eta}_d \end{pmatrix} \right] e^{-i\omega_d t}. \quad (\text{B.31})$$

Finally, we will show that the expression for the $v\text{-}\eta$ degeneracy is recovered as the Orr-Sommerfeld and Squire eigenvalues approach each other. Let us consider two degenerate modes and expand (4.19) in a series with $\omega_r^{OS} - \omega_p^{SQ}$ as the small parameter. The algebraically growing term reads

$$\hat{\eta} = -i\beta \int_{-1}^1 U' \tilde{\eta}_p^{+*} \tilde{v}_r dy \{t - \mathcal{O}[(\omega_r^{OS} - \omega_p^{SQ})^2]\} \tilde{\eta}_p e^{-i\omega_d t} \quad (\text{B.32})$$

where $\omega_d = (\omega_r^{OS} + \omega_p^{SQ})/2$ and the expansion coefficients are set to one. As the degeneracy is approached

$$\begin{aligned}\tilde{\eta}_p &\rightarrow \tilde{\eta}_d \\ \tilde{\eta}_p^{+*} &\rightarrow \partial\tilde{\eta}_d^{+*} \\ \tilde{v}_r &\rightarrow \partial\tilde{v}_d.\end{aligned}\quad (\text{B.33})$$

The algebraically growing term in expression (B.31) can be recovered from equation (B.32), since (B.29) shows that β times the integral in (B.32) equals unity at the degeneracy.

Appendix C

Adjoint of the Linearized Boundary Layer Equation

C.1 Adjoint of the Linearized Boundary Layer Equation

In general, the adjoint of any bounded linear operator \mathcal{A} between two inner-product (Hilbert) spaces is defined through the relation

$$(\Psi, \mathcal{A}\mathbf{u}) = (\mathcal{A}^+\Psi, \mathbf{u}) \quad (\text{C.1})$$

where \mathbf{u} is an element in the domain of \mathcal{A} , and Ψ is an element in the space associated with the inner product in (C.1).

The operator $\bar{\mathcal{A}}^+$ is the adjoint of the operator $\bar{\mathcal{A}}$ with respect to the given inner products associated with the norms (7.274). Let $\psi_1(y)$, $\phi_2(y)$ and $\phi_3(y)$ be square-integrable functions, the definition of the adjoint implies

$$(\psi_1, \bar{\mathcal{A}}\mathbf{q}) = (\bar{\mathcal{A}}^+\psi_1, \mathbf{q}) = (\Phi, \mathbf{q}) \quad (\text{C.2})$$

where

$$(\psi_1, \bar{\mathcal{A}}\mathbf{q}) = \int_0^\infty \psi_1(y) u_1(y) dy \quad (\Phi, \mathbf{q}) = \int_0^\infty (\phi_2 v_0 + \phi_3 w_0) dy. \quad (\text{C.3})$$

Thus, the action of the adjoint $\bar{\mathcal{A}}^+$ on ψ_1 is the vector Φ . We have used the notation $u_1(y) = u(x_f, y)$.

We will derive an expression for the action of $\bar{\mathcal{A}}^+$ by integration by parts of the governing equations. Introducing compact notation, we start

by writing equations (7.259)-(7.262) as a system

$$(\mathbf{A}\mathbf{f})_x = \mathbf{B}_0\mathbf{f} + \mathbf{B}_1\mathbf{f}_y + \mathbf{B}_2\mathbf{f}_{yy} \quad (\text{C.4})$$

where

$$\mathbf{f} = (u, v, w, p)^T = \begin{pmatrix} \mathbf{u} \\ p \end{pmatrix}$$

$$\mathbf{A} = \begin{pmatrix} 1 & 0 & 0 & 0 \\ U & 0 & 0 & 0 \\ V & U & 0 & 0 \\ 0 & 0 & U & 0 \end{pmatrix} \quad \mathbf{B}_0 = \begin{pmatrix} 0 & 0 & -\beta & 0 \\ -\beta^2 & -U_y & 0 & 0 \\ 0 & -2V_y - \beta^2 & -\beta V & 0 \\ 0 & 0 & -V_y - \beta^2 & \beta \end{pmatrix}$$

$$\mathbf{B}_1 = \begin{pmatrix} 0 & -1 & 0 & 0 \\ -V & 0 & 0 & 0 \\ 0 & -2V & 0 & -1 \\ 0 & 0 & -V & 0 \end{pmatrix} \quad \mathbf{B}_2 = \begin{pmatrix} 0 & 0 & 0 & 0 \\ 1 & 0 & 0 & 0 \\ 0 & 1 & 0 & 0 \\ 0 & 0 & 1 & 0 \end{pmatrix}.$$

The initial condition for system (C.4) is

$$\mathbf{f}(x_0, y) = \begin{pmatrix} 0 \\ 0 \\ v_0 \\ w_0 \end{pmatrix}.$$

A remark on notation: Most variables in this section, \mathbf{f} , \mathbf{A} , and \mathbf{B}_1 for instance, are vector- or matrix functions of both the streamwise and wall-normal coordinates x and y , and we will sometimes use $\mathbf{f}(x)$ as shorthand for the function $y \mapsto \mathbf{f}(x, y)$ and $\mathbf{f}(y)$ for the function $x \mapsto \mathbf{f}(x, y)$.

Let

$$\mathbf{g} = (p^+, u^+, v^+, w^+)^T = (p^+(x, y), u^+(x, y), v^+(x, y), w^+(x, y))^T = \begin{pmatrix} p^+ \\ \mathbf{u}^+ \end{pmatrix}$$

be a smooth vector function defined on $x \geq x_0$, $y \geq 0$. We will impose further restrictions on \mathbf{g} as we proceed, allowing the identification of the components of \mathbf{g} as pressure- and velocity-like ‘adjoint’ variables, as the notation suggests. For now, however, \mathbf{g} could be any suitable function.

Taking the scalar product of the vector \mathbf{g} with equation (C.4), integrating over the domain $[x_0, x_f] \times [0, y_{\max}]$, and applying integration by parts yields

$$\begin{aligned} 0 &= \int_0^\infty \int_{x_0}^{x_f} \mathbf{g}^T [(\mathbf{A}\mathbf{f})_x - \mathbf{B}_0\mathbf{f} - \mathbf{B}_1\mathbf{f}_y - \mathbf{B}_2\mathbf{f}_{yy}] dx dy \\ &= \int_0^\infty \int_{x_0}^{x_f} \mathbf{f}^T [-\mathbf{A}^T \mathbf{g}_x - \mathbf{B}_0^T \mathbf{g} + (\mathbf{B}_1^T \mathbf{g})_y - \mathbf{B}_2^T \mathbf{g}_{yy}] dx dy \\ &\quad + \int_0^\infty \mathbf{f}^T(x_f) \mathbf{A}^T(x_f) \mathbf{g}(x_f) dy - \int_0^\infty \mathbf{f}^T(x_0) \mathbf{A}^T(x_0) \mathbf{g}(x_0) dy \\ &\quad - \int_{x_0}^{x_f} [\mathbf{f}^T(y) \mathbf{B}_1^T(y) \mathbf{g}(y) + \mathbf{f}_y^T(y) \mathbf{B}_2^T \mathbf{g}(y) - \mathbf{f}^T(y) \mathbf{B}_2^T \mathbf{g}_y(y)] dx \Big|_{y=0}^{y=y_{\max}}. \end{aligned} \quad (\text{C.5})$$

Now we require that \mathbf{g} satisfies the *adjoint equation*

$$-\mathbf{A}^T \mathbf{g}_x = \mathbf{B}_0^T \mathbf{g} - (\mathbf{B}_1^T \mathbf{g})_y + \mathbf{B}_2^T \mathbf{g}_{yy}$$

whose components are given in equation (7.281)-(7.284), i.e.,

$$\begin{aligned} v_y^+ + \beta w^+ &= 0 \\ -p_x^+ - U u_x^+ - V v_x^+ - V u_y^+ &= u_{yy}^+ + (V_y - \beta^2) u^+ \\ -U v_x^+ - 2V v_y^+ + U_y u^+ - p_y^+ &= v_{yy}^+ - \beta^2 v^+ \\ -U w_x^+ - V w_y^+ + \beta V v^+ + \beta p^+ &= w_{yy}^+ - \beta^2 w^+. \end{aligned} \quad (\text{C.6})$$

Appropriate boundary conditions for the adjoint equations can be deduced by expanding the last integral in (C.5),

$$\begin{aligned} &- \int_{x_0}^{x_f} [\mathbf{f}^T(y) \mathbf{B}_1^T(y) \mathbf{g}(y) + \mathbf{f}_y^T(y) \mathbf{B}_2^T \mathbf{g}(y) - \mathbf{f}^T(y) \mathbf{B}_2^T \mathbf{g}_y(y)] dx \Big|_{y=0}^{y=y_{\max}} \\ &= \int_{x_0}^{x_f} [v(y_{\max}) (v_y^+(y_{\max}) + 2V(y_{\max}) v^+(y_{\max}) + p^+(y_{\max})) \\ &\quad - u_y(y_{\max}) u^+(y_{\max}) - w_y(y_{\max}) w^+(y_{\max})] dx \\ &\quad + \int_{x_0}^{x_f} [u_y(0) u^+(x, 0) + v_y(0) v^+(0) + w_y(0) w^+(0) \\ &\quad - p(0) v^+(0)] dx \end{aligned} \quad (\text{C.7})$$

where the boundary conditions (7.264) have been used. Expression (C.7) vanishes if the boundary conditions (7.285), i.e.,

$$u^+ = v^+ = w^+ = 0 \quad \text{at } y = 0 \quad (\text{C.8})$$

$$p^+ + 2V v^+ + v_y^+ = u^+ = w^+ = 0 \quad \text{at } y = y_{\max}. \quad (\text{C.9})$$

are enforced. If \mathbf{g} satisfies equation (C.6) with the wall-normal boundary conditions (C.8), expression (C.5) reduces to

$$\int_0^\infty \mathbf{f}^T(x_f) \mathbf{A}^T(x_f) \mathbf{g}(x_f) dy = \int_0^\infty \mathbf{f}^T(x_0) \mathbf{A}^T(x_0) \mathbf{g}(x_0) dy. \quad (\text{C.10})$$

Choosing the initial conditions on the adjoint equations given in (7.286), i.e.,

$$\begin{aligned} U(x_f, y) u^+(x_f, y) + V(x_f, y) v^+(x_f, y) + p^+(x_f, y) &= \psi_1(y) \\ v^+(x_f, y) &= 0 \\ w^+(x_f, y) &= 0 \end{aligned} \quad (\text{C.11})$$

the left hand side of equation (C.10) reduces to

$$\int_0^\infty \mathbf{f}^T(x_f) \mathbf{A}^T(x_f) \mathbf{g}(x_f) dy = \int_0^\infty u_1 \psi_1 dy. \quad (\text{C.12})$$

Using the initial conditions on the right-hand side of (C.10) yields

$$\int_0^\infty \mathbf{f}^T(x_0) \mathbf{A}^T(x_0) \mathbf{g}(x_0) dy = \int_0^\infty [U(x_0) v_0 v_0^+ + U(x_0) w_0 w_0^+] dy. \quad (\text{C.13})$$

Matching this expression with (C.3) we obtain the action of the adjoint operator

$$\begin{aligned} \phi_2(y) &= U(x_0, y) v^+(x_0, y) \\ \phi_3(y) &= U(x_0, y) w^+(x_0, y). \end{aligned} \quad (\text{C.14})$$

Appendix D

Selected Problems on Part I

Chapter 2

1. Piecewise linear channel flow

Consider piecewise linear channel flow given by

$$U(y) = \begin{cases} 1 - y & 0 \leq y \leq 1 \\ 1 + y & -1 \leq y \leq 0 \end{cases} \quad (\text{D.1})$$

and determine the dispersion relation for waves in a inviscid fluid. What is the group velocity of the waves? Use the group velocity to show that short waves are found in the front of the dispersive disturbance and that long waves are in the back.

2. Numerical solution of the Rayleigh equation

Solve the Rayleigh equation numerically for the following velocity profiles:

- (a) Bickley jet, $U = 1/\cosh^2 y$, $-\infty < y < \infty$.
 - i) Verify that $v = 1/\cosh^2 y$, $\alpha = 2$, $c = 2/3$ represents a neutral symmetric solution and that $v = \tanh y / \cosh y$, $\alpha = 1$, $c = 2/3$ is a neutral antisymmetric solution.
 - ii) For parameter combinations that result in stable solutions the integration contour has to be extended into the complex plane,

around the critical layer singularity. Compute stable solutions of the Rayleigh equation for the Bickley jet.

- (b) Poiseuille flow, $U = 1 - y^2$, $-1 < y < 1$.

Plot the phase speed and growth rate as a function of the wavenumber for the odd and the even mode. Compare your results to the analytic dispersion relation for piecewise linear Poiseuille flow.

Hint: Write a local eigenvalue solver for the Rayleigh equation and declare all quantities complex. Then choose an appropriate integration path in the complex plane around the critical layer singularity.

Chapter 3

1. Stability of streamwise vortices

Show that the normal modes in plane Poiseuille flow for $\alpha = 0$ have zero phase speed and a decay rate inversely proportional to the Reynolds number. Note that these disturbances are slowly decaying streamwise vortices or streaks.

2. Three-dimensional mean velocity profile

- (a) Derive the Orr-Sommerfeld equation for a three-dimensional parallel mean flow, such as a Falkner-Skan-Cooke boundary layer. Assume that the mean velocity profile has the form

$$U = U(y) \quad W = W(y). \quad (\text{D.2})$$

Also derive the generalization of Squire's transformation for this mean flow.

- (b) Consider three-dimensional channel flow of the form

$$U = 1 - y^2 \quad W = (1 - y^2)y^2. \quad (\text{D.3})$$

Using the inflection point criterion, determine the region in wave number space (α, β) where the inviscid flow must be stable. Plot your results.

3. Benard convection I

The linearized equations for Benard convection between two infinite plates located at $y = 0$ and $y = 1$ are given as

$$\frac{\partial u_i}{\partial t} = -\frac{\partial p}{\partial x_i} + \text{Pr Ra } \theta \delta_{i2} + \text{Pr } \frac{\partial^2 u_i}{\partial x_j \partial x_j} \quad (\text{D.4})$$

$$\frac{\partial \theta}{\partial t} = v + \frac{\partial^2 \theta}{\partial x_j \partial x_j} \quad (\text{D.5})$$

$$\frac{\partial u_i}{\partial x_i} = 0. \quad (\text{D.6})$$

The boundary conditions are

$$\theta = v = \frac{\partial v}{\partial y} = 0 \quad \text{at} \quad y = 0, 1 \quad (\text{D.7})$$

for the rigid-rigid problem and

$$\theta = v = \frac{\partial^2 v}{\partial y^2} = 0 \quad \text{at} \quad y = 0, 1 \quad (\text{D.8})$$

for the free-free problem.

Derive a stability equation for the normal velocity v and compute solutions for both the rigid-rigid and the free-free problem.

4. Benard convection II

Show that the solution for the free-free Benard problem derived in the previous exercise

$$v = \text{Real}\{\tilde{v}(y)e^{i(\alpha x + \beta z)}e^{st}\} \quad (\text{D.9})$$

takes the form of counter rotating rolls in physical space. Recall that the horizontal velocities can be determined from continuity and the definition of the normal vorticity.

5. Stability of inviscid, stratified flow

Consider the stability of a parallel flow of an inviscid, stratified fluid. The governing, non-dimensionalized equations can be written,

$$\rho \left(\frac{\partial u}{\partial t} + u \frac{\partial u}{\partial x} + v \frac{\partial u}{\partial y} \right) = - \frac{\partial p}{\partial x} \quad (\text{D.10})$$

$$\rho \left(\frac{\partial v}{\partial t} + u \frac{\partial v}{\partial x} + v \frac{\partial v}{\partial y} \right) = - \frac{\partial p}{\partial y} - \frac{\rho}{F^2} \quad (\text{D.11})$$

$$\frac{\partial u}{\partial x} + \frac{\partial v}{\partial y} = 0 \quad (\text{D.12})$$

$$\frac{\partial \rho}{\partial t} + u \frac{\partial \rho}{\partial x} + v \frac{\partial \rho}{\partial y} = 0. \quad (\text{D.13})$$

We assume that there exists a basic state $U(y), P(y), \bar{\rho}(y)$ which is an exact solution to the above equations. Introduce wave-like disturbances and derive the linear stability equation for the normal velocity v ,

$$(U - c)(D^2 - \alpha^2)\hat{v} - U''\hat{v} + \frac{N^2\hat{v}}{(U - c)} = 0 \quad (\text{D.14})$$

where we have assumed that

$$\frac{\bar{\rho}'}{\bar{\rho}} \ll \frac{\bar{\rho}'}{\bar{\rho}F^2}. \quad (\text{D.15})$$

The parameter $N^2 = -\bar{\rho}'/\bar{\rho}F^2$ is known as the overall Richardson number.

Solve the equation for the simplified case $U = 0, N = \text{constant}$ and find the dispersion relation for internal gravity waves.

Chapter 4

1. Model problem for transient analysis

We will investigate a linear evolution equation of the form

$$\frac{d}{dt} \begin{pmatrix} v \\ \eta \end{pmatrix} = \begin{pmatrix} -\frac{1}{\text{Re}} & 0 \\ 1 & -\frac{2}{\text{Re}} \end{pmatrix} \begin{pmatrix} v \\ \eta \end{pmatrix} \quad (\text{D.16})$$

where the variables v and η resemble the normal velocity and normal vorticity, respectively, and Re denotes an equivalent Reynolds number. The influence of the velocity on the vorticity is accounted for by the off-diagonal term in the evolution operator.

Let the system matrix of the linear system (D.16) be called \mathbf{A} and $\mathbf{q} = (v, \eta)^T$, $\|\mathbf{q}\|^2 = v^2 + \eta^2$, and $G(t) = \max_{\mathbf{q}_0} \frac{\|\mathbf{q}(t)\|}{\|\mathbf{q}_0\|}$.

- (a) Show that the eigenvalues and normalized eigenvectors of the model equation are

$$\lambda_1 = -\frac{1}{\text{Re}} \quad \Phi_1 = \frac{1}{\sqrt{1 + \text{Re}^2}} \begin{pmatrix} 1 \\ \text{Re} \end{pmatrix} \quad (\text{D.17})$$

$$\lambda_2 = -\frac{2}{\text{Re}} \quad \Phi_2 = \begin{pmatrix} 0 \\ 1 \end{pmatrix} \quad (\text{D.18})$$

and that the complete solution can be written as

$$\begin{pmatrix} v \\ \eta \end{pmatrix} = \frac{A}{\sqrt{1 + \text{Re}^2}} \begin{pmatrix} 1 \\ \text{Re} \end{pmatrix} e^{-t/\text{Re}} + B \begin{pmatrix} 0 \\ 1 \end{pmatrix} e^{-2t/\text{Re}}. \quad (\text{D.19})$$

How are the constants A and B determined?

- (b) The formal solution of the initial value problem can be represented

$$\mathbf{q}(t) = e^{t\mathbf{A}} \mathbf{q}_0 \quad (\text{D.20})$$

with \mathbf{q}_0 as the vector consisting of the initial velocity and vorticity. Show that

$$G(t) = \|e^{t\mathbf{A}}\| \quad (\text{D.21})$$

where

$$e^{t\mathbf{A}} = \begin{pmatrix} e^{-t/\text{Re}} & 0 \\ -(e^{-2t/\text{Re}} - e^{-t/\text{Re}})\text{Re} & e^{-2t/\text{Re}} \end{pmatrix} \quad (\text{D.22})$$

Verify the results in Figure D.1(b) numerically.

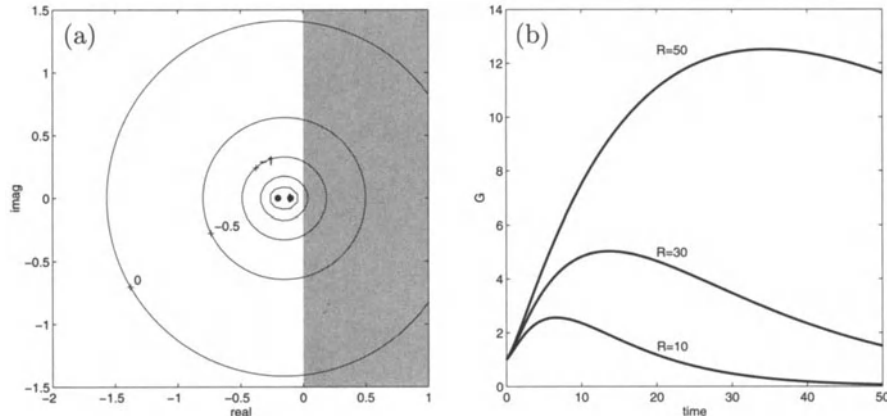


FIGURE D.1. Resolvent norm and growth curves for model problem. (a) Resolvent plot. (b) Maximum amplification for selected Reynolds numbers.

- (c) A number $z \in \mathbf{C}$ lies in the ε -pseudospectrum of a matrix \mathbf{A} , if $\|(z\mathbf{I} - \mathbf{A})^{-1}\| \geq \varepsilon^{-1}$. Show that the quantity $(z\mathbf{I} - \mathbf{A})^{-1}$, known as the resolvent, is given as

$$(z\mathbf{I} - \mathbf{A})^{-1} = \begin{pmatrix} \frac{\text{Re}}{z\text{Re} + 1} & 0 \\ \frac{\text{Re}^2}{(z\text{Re} + 1)(z\text{Re} + 2)} & \frac{\text{Re}}{z\text{Re} + 2} \end{pmatrix}. \quad (\text{D.23})$$

Verify the results in Figure D.1(a) numerically.

- (d) Recall that the reason for the large transient growth of the disturbance norm lies in the nonnormal nature of the evolution operator \mathbf{A} , show that $\mathbf{A}^T \mathbf{A} \neq \mathbf{A} \mathbf{A}^T$, and that the angle between the non-orthogonal eigenvectors are

$$\phi = \arccos\left(\frac{\text{Re}}{\sqrt{1 + \text{Re}^2}}\right) \quad (\text{D.24})$$

- (e) Let $\|\mathbf{q}\| = 1$ and show that the numerical range \mathcal{F} satisfies

$$\frac{d}{dt} \|\mathbf{q}\|^2 = -\frac{2(2v^2 + \eta^2)}{\text{Re}} + 2v\eta = \mathcal{F}, \quad (\text{D.25})$$

and that \mathcal{F}_{\max} satisfies

$$\mathcal{F}_{\max} = -\frac{1}{2\text{Re}} \left(3 - \frac{1}{\sqrt{1 + \text{Re}^2}} \right) + \frac{\text{Re}}{2\sqrt{1 + \text{Re}^2}} = \frac{dG}{dt} \Big|_{t=0} \quad (\text{D.26})$$

- (f) Let Re_G be the Reynolds number for which \mathcal{F}_{\max} is equal to zero, or, equivalently, the Reynolds number below which no transient growth can be expected. Verify that

$$\text{Re}_g = \sqrt{8} \quad \text{and thus} \quad \frac{dG}{dt} < 0 \quad \text{for } \text{Re} < \sqrt{8}. \quad (\text{D.27})$$

2. Algebraic growth of vorticity

An expression for the Fourier transformed normal vorticity ($\hat{\eta}$) for $\alpha = 0$ can be derived as

$$\hat{\eta} = \sum_m \tilde{\eta}_m \sum_j \frac{i\text{Re}\beta K_j}{\mu_m - \nu_j} \int_{-1}^1 U' \tilde{v}_j \tilde{\eta}_m dy \left(e^{-\mu_m t/\text{Re}} - e^{-\nu_j t/\text{Re}} \right) \quad (\text{D.28})$$

where $\alpha c_m = -i\mu_m/\text{Re}$ are the Squire eigenvalues and $\alpha c_j = -i\nu_j/\text{Re}$ are the Orr-Sommerfeld eigenvalues, both for $\alpha = 0$.

In Chapter 4 the first term in the expansion of the above expression for $t/\text{Re} \rightarrow 0$ has been calculated. We found that growth proportional to t resulted. Calculate the next term in the expansion and show that the maximum growth is proportional to Re and that this maximum occurs for times proportional to Re . Simplify your expressions as much as possible.

3. Algebraic instability

Derive the algebraic instability directly from the governing linearized inviscid disturbance equations in primitive variables. Assume a streamwise independent flow, i.e., $U_i = U(y)\delta_{i1}$ and $\partial/\partial x = 0$, but do not use Fourier-transformed variables.

Chapter 5

1. Nonlinear model equation

To investigate the effects of nonlinearities on transient growth we will consider the nonlinear system of equations for a disturbance described by $(v \ \eta)^T$

$$\begin{aligned} \frac{d}{dt} \begin{pmatrix} v \\ \eta \end{pmatrix} &= \begin{pmatrix} -1/\text{Re} & 0 \\ 1 & -2/\text{Re} \end{pmatrix} \begin{pmatrix} v \\ \eta \end{pmatrix} \\ &\quad + \sqrt{v^2 + \eta^2} \begin{pmatrix} 0 & 1 \\ -1 & 0 \end{pmatrix} \begin{pmatrix} v \\ \eta \end{pmatrix} \end{aligned} \quad (\text{D.29})$$

The parameter Re plays the role of the Reynolds number. The linear operator in the above system of equations will be referred to as \mathbf{A} .

- (a) Derive an equation for the 2-norm of $(v \ \eta)^T$ and interpret your result.
- (b) Use the expression for the resolvent of the linear operator \mathbf{A} given in (D.23) and plot the resolvent norm for various values of Re . What can be said about possible energy growth of the solutions to the disturbance equations? How does the resolvent norm vary with Re ?
- (c) Use the expression for the matrix exponential $e^{\mathbf{A}t}$ given in (D.22) and plot the growth function for various values of Re . How good is the bound on the growth derived above? How does $e^{\mathbf{A}t}$ vary with Re ? Calculate the initial conditions giving the optimal growth for a few selected parameter combinations.

Hint: $e^{\mathbf{A}t} = V e^{\Lambda t} V^{-1}$ where $\mathbf{A} = V \Lambda V^{-1}$ is the eigendecomposition of \mathbf{A} with V as the eigenvector matrix and Λ as the diagonal eigenvalue matrix.

- (d) Solve the nonlinear disturbance equations numerically and determine the threshold amplitude for transition as a function of Re . How does the threshold amplitude scale with Re ? Transition has occurred when the solution does not decay as t tends to infinity. Use optimal disturbances as initial conditions.

2. Energy method for Benard convection

- (a) Show that the energy equation for Benard convection reads

$$\begin{aligned} \frac{dE}{dt} &= - \int_V \left[u_i u_j \frac{\partial U_i}{\partial x_j} - \text{Pr} \left(\frac{\partial u_i}{\partial x_j} \right)^2 \right. \\ &\quad \left. + 2\text{Pr Ra } v\theta - \text{Pr Ra} \left(\frac{\partial \theta}{\partial x_j} \right)^2 \right] dV \end{aligned} \quad (\text{D.30})$$

- (b) Show that the Euler-Lagrange equations for this problem are identical to the linear stability equations for marginal stability of Benard convection.

3. Energy method for plane Couette flow

- (a) Derive the Reynolds-Orr equation for general shear flows.
- (b) Show that the corresponding Euler-Lagrange equations are

$$\frac{1}{2}u_j \left(\frac{\partial U_i}{\partial x_j} + \frac{\partial U_j}{\partial x_i} \right) = -\frac{\partial \lambda}{\partial x_i} + \frac{1}{\text{Re}} \nabla^2 u_i \quad (\text{D.31})$$

where λ is the Lagrange multiplier associated with the constraint from the continuity equation.

- (c) Let $U_i = y\delta_{i1}$, $\partial/\partial x = 0$, $u_i = \hat{u}_i(y) \exp[i\beta z]$ and show that the resulting equations can be identified with the Benard rigid-rigid problem. Deduce the energy Reynolds number Re_E for plane Couette flow for this case.
4. Comment on the differences in Ra_E and Ra_L for Benard convection and Re_E and Re_L for plane Couette flow.

Bibliography

- ABRAMOWITZ, M. & STEGUN, I. A. 1973 *Handbook of Mathematical Functions*. Dover Publications.
- ABU-GHANAMM, B. J. & SHAW, R. 1980 Natural transition of boundary layers – the effects of turbulence, pressure gradient, and flow history. *J. Mech. Eng. Sci.* **22**, 213–228.
- ACARLAR, M. S. & SMITH, C. R. 1987 A study of hairpin vortices in a laminar boundary layer. Part 2. Hairpin vortices generated by fluid injection. *J. Fluid Mech.* **175**, 43–48.
- AIHARA, Y., TOMITA, Y. & ITO, A. 1985 Generation, development and distortion of longitudinal vortices in the boundary layer along concave and flat plates. In *Laminar-Turbulent Transition* (ed. V. V. Kozlov), pp. 447–454. Springer-Verlag.
- ALFREDSSON, P. H. & MATSUBARA, M. 1996 Streaky structures in transition. In *Transitional Boundary Layers in Aeronautics*. (ed. R. Henkes & J. van Ingen), pp. 374–386. Elsevier Science Publishers.
- ALFREDSSON, P. H. & MATSUBARA, M. 2000 Freestream turbulence, streaky structures and transition in boundary layer flows. *AIAA 2000-2534*.
- ANDERSSON, P., BERGGREN, M. & HENNINGSON, D. 1997 Optimal disturbances in boundary layers. In *Progress in Systems Control*. Birkhäuser.

- ANDERSSON, P., BERGGREN, M. & HENNINGSON, D. 1999 Optimal disturbances and bypass transition in boundary layers. *Phys. Fluids* **11** (1), 134–150.
- ANDERSSON, P., HENNINGSON, D. & HANIFI, A. 1998 On a stabilization procedure for the parabolic stability equations. *J. Eng. Math.* **33**, 311–332.
- ARNAL, D. 1987 Transition description and prediction. In *Numerical simulation of unsteady flows and transition to turbulence* (ed. O. Pironneau, W. Rodi, I. Ryhming, A. Savill & T. Truong), pp. 303–316. Cambridge University Press.
- ARNAL, D. 1999 Transition prediction in industrial applications. In *Transition, Turbulence and Combustion Modelling* (ed. A. Hanifi, P. H. Alfredsson, A. V. Johansson & D. S. Henningson). ERCOFATAC Series, Vol. 6, Kluwer Academic Publishers, Dordrecht.
- ASAI, M. & NISHIOKA, M. 1995 Boundary-layer transition triggered by hairpin eddies at subcritical Reynolds numbers. *J. Fluid Mech.* **297**, 101–122.
- ASHPIS, D. E. & RESHOTKO, E. 1990 The vibrating ribbon problem revisited. *J. Fluid Mech.* **213**, 531–547.
- BAGGETT, J. S. & TREFETHEN, L. N. 1997 Low-dimensional models of subcritical transition to turbulence. *Phys. Fluids* **9**, 1043–1053.
- BAKE, S., FERNHOLZ, H. H. & KACHANOV, Y. S. 2000 Resemblance of K- and N-regimes of boundary-layer transition at late stages. *Europ. J. Mech. B* **19**, 1–22.
- BAMIEH, B. & DAHLEH, M. 1999 Disturbance energy amplification in three-dimensional channel flows. In *Proceedings of the 1999 American Control Conference, IEEE, Piscataway, NJ*, pp. 4532–4537.
- BAYLY, B. J. 1986 Three-dimensional instability of elliptical flow. *Phys. Lett. Rev.* **57**, 2160.
- BAYLY, B. J., ORSZAG, S. A. & HERBERT, T. 1988 Instability mechanisms in shear flow transition. *Ann. Rev. Fluid Mech.* **20**, 359–91.
- BECK, K. H., HENNINGSON, D. S. & HENKES, R. A. W. M. 1998 Linear and nonlinear development of localized disturbances in zero and adverse pressure gradient boundary layers. *Phys. Fluids* **10**, 1405–1418.
- BENJAMIN, T. B. 1961 The development of three-dimensional disturbances in an unstable film of liquid flowing down an inclined plane. *J. Fluid Mech.* **10**, 401–419.

- BENJAMIN, T. B. & FEIR, J. 1967 The disintegration of wave trains on deep water. Part 1. Theory. *J. Fluid Mech.* **27**, 417–430.
- BENNEY, D. J. & GUSTAVSSON, L. H. 1981 A new mechanism for linear and nonlinear hydrodynamic instability. *Stud. Appl. Math.* **64**, 185–209.
- BERGSTRÖM, L. 1993 Optimal growth of small disturbances in pipe Poiseuille flow. *Phys. Fluids A* **5**, 2710–2720.
- BERGSTRÖM, L. 1999 Interactions of three components and subcritical self-sustained amplification of disturbances in plane Poiseuille flow. *Phys. Fluids* **11**, 590–601.
- BERLIN, S. 1998 Oblique waves in boundary layer transition. PhD thesis, Royal Institute of Technology, Stockholm, Sweden.
- BERLIN, S., HANIFI, A. & HENNINGSON, D. S. 1998 The neutral stability curve for non-parallel boundary layer flow. In: Berlin, S.: Oblique waves in boundary layer transition, Dissertation, Royal Institute of Technology, Stockholm.
- BERLIN, S. & HENNINGSON, D. S. 1999 A nonlinear mechanism for receptivity of free-stream disturbances. *Phys. Fluids* **11**, 3749–3760.
- BERLIN, S., LUNDBLADH, A. & HENNINGSON, D. S. 1994 Spatial simulations of oblique transition. *Phys. Fluids* **6**, 1949–1951.
- BERLIN, S., WIEGEL, M. & HENNINGSON, D. S. 1999 Numerical and experimental investigations of oblique boundary layer transition. *J. Fluid Mech.* **393**, 23–57.
- BERTOLOTTI, F. P. 1991 Linear and nonlinear stability of boundary layers with streamwise varying properties. PhD thesis, Ohio State University, Department of Mechanical Engineering, Columbus, Ohio.
- BERTOLOTTI, F. P. 1997 Response of the blasius boundary layer to free-stream vorticity. *Phys. Fluids* **9** (8), 2286–2299.
- BERTOLOTTI, F. P., HERBERT, T. & SPALART, P. R. 1992 Linear and nonlinear stability of the Blasius boundary layer. *J. Fluid Mech.* **242**, 441–474.
- BESTEK, H., GRUBER, K. & FASEL, H. 1989 Self-excited unsteadiness of laminar separation bubbles by natural transition. In *The Prediction and Exploitation of Separated Flow*, pp. 14.1–14.16. Proceedings of the Royal Aeronautical Society.
- BETCHOV, R. & CRIMINALE, W. O. 1966 Spatial instability of the inviscid jet and wake. *Phys. Fluids* **9**, 359–362.

- BIPPES, H. 1978 Experiments on Görtler vortices. Proceedings of the Royal Aeronautical Society Conference on Boundary-Layer Transisiton and Control, Cambridge University, England.
- BOBERG, L. & BROSA, U. 1988 Onset of turbulence in a pipe. *Z. Naturforsch.* **43a**, 697–726.
- BODONYI, R. J. 1990 Nonlinear triple-deck studies in boundary layer receptivity. *Appl. Mech. Rev.* **43** (5), 158–165.
- BODONYI, R. J. & SMITH, F. T. 1981 The upper branch stability of the Blasius boundary layer, including non-parallel flow effects. *Proc. Roy. Soc. Lond. Ser. A* **375**, 65–92.
- BOTTARO, A. & KLINGMANN, B. G. B. 1996 On the linear breakdown of Görtler vortices. *Europ. J. Mech. B* **15** (3), 301–330.
- BOTTARO, A. & LUCHINI, P. 1999 Görtler vortices: are they amenable to local eigenvalue analysis? *Europ. J. Mech. B* **18** (1), 47–65.
- BOYCE, W. & DiPRIMA, R. 1997 *Elementary Differential Equations and Boundary Value Problems*. John Wiley & Sons.
- BREUER, K. S., COHEN, J. & HARITONIDIS, J. H. 1997 The late stages of transition induced by a low-amplitude wave packet in a laminar boundary layer. *J. Fluid Mech.* **340**, 395–411.
- BREUER, K. S. & HARITONIDIS, J. H. 1990 The evolution of a localized disturbance in a laminar boundary layer. Part I: Weak disturbances. *J. Fluid Mech.* **220**, 569–594.
- BREUER, K. S. & KURAISHI, T. 1994 Transient growth in two- and three-dimensional boundary layers. *Phys. Fluids* **6**, 1983–1993.
- BRIGGS, R. J. 1964 *Electron-Stream Interaction with Plasmas*. MIT Press, Cambridge.
- BROWN, W. B. 1961 A stability criterion for three-dimensional laminar boundary layers. In *Boundary Layer and Flow Control* (ed. G. Lachmann), , vol. 2, pp. 313–329. Pergamon Press, London.
- BROWN, W. B. 1962 Exact numerical solution of the complete linearized equations for the stability of compressible boundary layers. *Tech. Rep. NOR-62-15*. NorAir Report.
- BURRIDGE, D. & DRAZIN, P. 1969 Comments on 'Stability of pipe Poiseuille flow'. *Phys. Fluids* **12** (1), 264–265.
- BUSSE, F. H. & WHITEHEAD, J. A. 1971 Instabilities of convection rolls in a high Prandtl number fluid. *J. Fluid Mech.* **47**, 305–320.

- BUTLER, K. M. & FARRELL, B. F. 1992 Three-dimensional optimal perturbations in viscous shear flow. *Phys. Fluids A* **4**, 1637–1650.
- CANTWELL, B. J., COLES, D. & DIMOTAKIS, P. E. 1978 Structure and entrainment in the plane of symmetry of a turbulent spot. *J. Fluid Mech.* **87**, 641–672.
- CARLSON, D. R., WIDNALL, S. E. & PEETERS, M. F. 1982 A flow visualization study of transition in plane Poiseuille flow. *J. Fluid Mech.* **121**, 487–505.
- CARR, J. 1981 *Applications of Centre Manifold Theory*. Springer-Verlag.
- CASE, K. M. 1960 Stability of inviscid plane Couette flow. *Phys. Fluids* **3**, 143–148.
- CAULFIELD, C. P. & KERSWELL, R. R. 2000 The nonlinear development of three-dimensional disturbances at hyperbolic stagnation points: a model of the braid region in mixing layers. *Phys. Fluids* **12**, 1032–1043.
- CHAMBERS, F. W. & THOMAS, A. S. W. 1983 Turbulent spots, wave packets and growth. *Phys. Fluids* **26**, 1160–1162.
- CHANG, C.-L. & MALIK, M. R. 1994 Oblique-mode breakdown and secondary instability in supersonic boundary layers. *J. Fluid Mech.* **273**, 323–360.
- CHIN, R. W.-Y. 1981 Stability of flows down an inclined plane. PhD thesis, Harvard University, Division of Applied Sciences, Cambridge, Mass.
- CHOMAZ, J.-M., HUERRE, P. & REDEKOPP, L. G. 1991 A frequency selection criterion in spatially developing flows. *Stud. Appl. Math.* **84**, 119–144.
- CHOUDHARI, M. 1996 Boundary-layer receptivity to three-dimensional unsteady vortical disturbances in free stream. AIAA Paper 96-0181.
- COHEN, J., BREUER, K. S. & HARITONIDS, J. H. 1991 On the evolution of a wave packet in a laminar boundary layer. *J. Fluid Mech.* **225**, 575–606.
- CONTE, S. D. 1966 The numerical solution of linear boundary value problems. *Stud. Appl. Math.* **8** (3), 309–321.
- COOKE, J. C. 1950 The boundary layer of a class of infinite yawed cylinders. *Proc. Camb. Phil. Soc.* **46**, 645–648.
- CORBETT, P. & BOTTARO, A. 2000a Optimal linear growth in three-dimensional boundary layers. (submitted).

- CORBETT, P. & BOTTARO, A. 2000b Optimal perturbations for boundary layers subject to streamwise pressure gradient. *Phys. Fluids* **12** (1), 120–130.
- COSSU, C. & CHOMAZ, J.-M. 1997 Global measures of local convective instabilities. *Phys. Rev. Lett.* **78** (23), 4387–4390.
- CRAIK, A. D. D. 1971 Nonlinear resonant instability in boundary layers. *J. Fluid Mech.* **50**, 393–413.
- CRAIK, A. D. D. 1985 *Wave interactions and fluid flows*. Cambridge University Press.
- CROUCH, J. D. 1992a Localized receptivity of boundary layers. *Phys. Fluids* **4** (7), 1408–1414.
- CROUCH, J. D. 1992b Non-localized receptivity of boundary layers. *J. Fluid Mech.* **244**, 567–581.
- CROUCH, J. D. 1997 Excitation of secondary instabilities in boundary layers. *J. Fluid Mech.* **336**, 245–266.
- CROUCH, J. D. & NG, L. L. 2000 Variable N-factor method for transition prediction in three-dimensional boundary layers. *AIAA J.* **38**, 211–216.
- CROUCH, J. D. & SPALART, P. R. 1995 A study of non-parallel and non-linear effects on the localized receptivity of boundary layers. *J. Fluid Mech.* **290**, 29–37.
- DAVIS, S. H. & REID, W. J. 1977 On the stability of stratified viscous plane Couette flow. *J. Fluid Mech.* **80**, 509.
- DEYHLE, H. & BIPPES, H. 1996 Disturbance growth in an unstable three-dimensional boundary layer and its dependence on environmental conditions. *J. Fluid Mech.* **316**, 73–113.
- DIKII, L. A. 1960 The stability of plane-parallel flows of an ideal fluid. *Sov. Phys. Doc.* **135**, 1179–1182.
- DiPRIMA, R. C. 1967 Vector eigenfunction expansions for the growth of Taylor vortices in the flow between rotating cylinders. In *Nonlinear Partial Differential Equations* (ed. W. F. Ames), pp. 19–42. Academic Press.
- DiPRIMA, R. C. & HABETLER, G. J. 1969 A completeness theorem for non-selfadjoint eigenvalue problems in hydrodynamic stability. *Arch. Rat. Mech. Anal.* **32**, 218–227.
- DOLPH, C. L. & LEWIS, D. C. 1958 On the application of infinite systems of ordinary differential equations to perturbations to plane Poiseuille flow. *Q. Appl. Math.* **16**, 97–110.

- DOVGAL, A. V., KOZLOV, V. V. & MICHALKE, A. 1994 Laminar boundary layer separation: instability and associated phenomena. *Prog. Aerospace Sci.* **30**, 61–94.
- DRAZIN, P. G. & HOWARD, L. N. 1962 The instability to long waves of unbounded parallel shear flow. *J. Fluid Mech.* **14**, 257–283.
- DRAZIN, P. G. & REID, W. H. 1981 *Hydrodynamic Stability*. Cambridge University Press.
- VAN DRIEST, E. R. & BLUMER, C. B. 1963 Boundary layer transition: freestream turbulence and pressure gradient effects. *AIAA J.* **1**, 1303–1306.
- DUNN, D. W. & LIN, C. C. 1955 On the stability of the laminar boundary layer in a compressible fluid. *J. Aero. Sci.* **22**, 455–477.
- VAN DYKE, M. 1975 *Perturbation Methods in Fluid Mechanics*. Parabolic Press, Stanford.
- ECKHAUS, W. 1965 *Studies in Non-Linear Stability*. Springer-Verlag.
- EHRENSTEIN, U. & KOCH, W. 1991 Three-dimensional wavelike equilibrium states in plane Poiseuille flow. *J. Fluid Mech.* **228**, 111–148.
- EL-HADY, N. M. 1991 Nonparallel instability of supersonic and hypersonic boundary layers. *Phys. Fluids* **3** (9), 2164–2178.
- ELLINGSEN, T. & PALM, E. 1975 Stability of linear flow. *Phys. Fluids* **18**, 487–488.
- ELOFSSON, P. A. 1998 Experiment on oblique transition in wall bounded shear flows. PhD thesis, Royal Institute of Technology, Stockholm, Sweden.
- ELOFSSON, P. A. & ALFREDSSON, P. H. 1998 An experimental study of oblique transition in plane Poiseuille flow. *J. Fluid Mech.* **358**, 177–202.
- ELOFSSON, P. A., KAWAKAMI, M. & ALFREDSSON, P. H. 1999 Experiments on the stability of streamwise streaks in plane Poiseuille flow. *Phys. Fluids* **11** (4), 915–930.
- FARRELL, B. F. & IOANNOU, P. J. 1993 Stochastic forcing of the linearized Navier-Stokes equations. *Phys. Fluids A* **5** (11), 2600–2609.
- FARRELL, B. F. & IOANNOU, P. J. 1996 Generalized stability theory. II. Nonautonomous operators. *J. Atm. Sci.* **53**, 2041–2053.

- FASEL, H., THUMM, A. & BESTEK, H. 1993 Direct numerical simulation of transition in supersonic boundary layers: oblique breakdown. In *Transitional and Turbulent Compressible Flows* (ed. L. D. Kral & T. A. Zang), pp. 77–92. FED-Vol. 151, ASME.
- FINLAY, W. H., KELLER, J. B. & FERZIGER, J. H. 1988 Instabilities and transition in curved channel flow. *J. Fluid Mech.* **194**, 417–456.
- FISCHER, T. M. & DALLMANN, U. 1991 Primary and secondary stability analysis of a three-dimensional boundary layer flow. *Phys. Fluids A* **3**, 2378–2391.
- FJØRTOFT, R. 1950 Application of integral theorems in deriving criteria for instability for laminar flows and for the baroclinic circular vortex. *Geofys. Publ., Oslo* **17** (6), 1–52.
- FLORYAN, J. M., DAVIS, S. H. & KELLY, R. E. 1987 Instabilities of a liquid film flowing down an inclined plane. *Phys. Fluids* **30** (4), 983–989.
- FLORYAN, J. M. & SARIC, W. 1982 Stability of Görtler vortices in boundary layers. *AIAA J.* **20** (3), 316–324.
- FUJIMURA, K. 1989 The equivalence between two perturbation methods in weakly nonlinear stability theory for parallel shear flows. *Proc. Roy. Soc. Lond. A* **424**, 373–392.
- FUJIMURA, K. 1991 Methods of centre manifold and multiple scales in the theory of weakly nonlinear stability for fluid motions. *Proc. Roy. Soc. Lond. A* **434**, 719–733.
- GANTMACHER, F. R. 1959 *The Theory of Matrices*. Chelsea Pub. Co., New York.
- GASTER, M. 1962 A note on the relation between temporally-increasing and spatially-increasing disturbances in hydrodynamic stability. *J. Fluid Mech.* **14**, 222–224.
- GASTER, M. 1975 A theoretical model for the development of a wave packet in a laminar boundary layer. *Proc. Roy. Soc. Lond. Ser. A* **347**, 271–289.
- GASTER, M. 1982a The development of a two-dimensional wave packet in a growing boundary layer. *Proc. Roy. Soc. Lond. Ser. A* **384**, 317–332.
- GASTER, M. 1982b Estimates of the errors incurred in various asymptotic representations of wave packets. *J. Fluid Mech.* **121**, 365–377.
- GILL, A. E. 1965 Instability of 'top-hat' jets and wakes in compressible fluids. *Phys. Fluids* **8**, 1428–1430.

- GOLDSTEIN, M. E. 1983 The evolution of Tollmien-Schlichting waves near a leading edge. *J. Fluid Mech.* **127**, 59–81.
- GOLDSTEIN, M. E. & HULTGREN, L. S. 1989 Boundary-layer receptivity to long-wave freestream disturbances. *Ann. Rev. Fluid Mech.* **21**, 137–166.
- GOLDSTEIN, M. E. & WUNDROW, D. W. 1998 On the environmental realizability of algebraically growing disturbances and their relation to Klebanoff modes. *Theoret. Comput. Fluid Dynamics* **10**, 171–186.
- GÖRTLER, H. 1940 Über eine dreidimensionale instabilität laminarer grenzschichten an konkaven wänden. *Nachr. Ges. Wiss. Göttingen, N.F.* **2**, 1–26, translated in *Tech. Memor. Nat. Adv. Comm. Aero., Wash.* **1375**, (1954).
- GREGORY, N., STUART, J. T. & WALKER, W. S. 1955 On the stability of three-dimensional boundary layers with applications to flow due to a rotating disc. *Phil. Trans. R. Soc. Lond. A* **248**, 155–199.
- GREY, W. E. 1952 The effect of wing sweep on laminar flow. RAE TM Aero 255.
- GROSCH, C. E. & SALWEN, H. 1978 The continuous spectrum of the Orr-Sommerfeld equation. Part 1. The spectrum and the eigenfunctions. *J. Fluid Mech.* **87**, 33–54.
- GUO, Y. & FINLAY, W. H. 1991 Splitting, merging and wavelength selection of vortices in curved and/or rotating channel flow due to Eckhaus instability. *J. Fluid Mech.* **228**, 661–691.
- GUO, Y. & FINLAY, W. H. 1994 Wavenumber selection and irregularity of spatially developing nonlinear Dean and Görtler vortices. *J. Fluid Mech.* **264**, 1–40.
- GUSTAVSSON, L. H. 1978 On the evolution of disturbances in boundary layer flows. PhD thesis, Royal Institute of Technology, Stockholm, Sweden, (TRITA-MEK 78-02).
- GUSTAVSSON, L. H. 1979 Initial value problem for boundary layer flows. *Phys. Fluids* **22**, 1602–1605.
- GUSTAVSSON, L. H. 1982 Dynamics of three-dimensional disturbances in watertable flow. TECHNICAL REPORT 1982:036 T, Department of Fluid Mechanics, Luleå University of Technology, Sweden.
- GUSTAVSSON, L. H. 1986 Excitation of direct resonances in plane Poiseuille flow. *Stud. Appl. Math.* **75**, 227–248.

- GUSTAVSSON, L. H. 1991 Energy growth of three-dimensional disturbances in plane Poiseuille flow. *J. Fluid Mech.* **224**, 241–260.
- HAJ-HARIRI, H. 1988 Transformations reducing the order of the parameter in differential eigenvalue problems. *J. Comp. Phys.* **77**, 472–484.
- HALL, P. 1983 The linear development of Görtler vortices in growing boundary layers. *J. Fluid Mech.* **130**, 41–58.
- HALL, P. & HORSEMAN, N. J. 1991 The linear inviscid secondary instability of longitudinal vortex structures in boundary layers. *J. Fluid Mech.* **232**, 357–375.
- HAMMERTON, P. W. & KERSCHEN, E. J. 1997 Boundary layer receptivity for a parabolic leading edge. Part 2. The small-Strouhal-number limit. *J. Fluid Mech.* **353**, 205–220.
- HANIFI, A. & HENNINGSON, D. S. 1998 The compressible inviscid algebraic instability for streamwise independent disturbances. *Phys. Fluids* **10**, 1784–1786.
- HANIFI, A., HENNINGSON, D. S., HEIN, S., BERTOLOTTI, F. & SIMEN, M. 1994 Linear nonlocal instability analysis – the linear NOLOT code. FFA TN 1994-54, Technical Report from the Aeronautical Research Institute of Sweden (FFA), Bromma.
- HANIFI, A., SCHMID, P. J. & HENNINGSON, D. S. 1996 Transient growth in compressible boundary layer flow. *Phys. Fluids* **8**, 51–65.
- HEALEY, J. 1995 On the neutral curve of the flat-plate boundary layer: comparison between experiment, Orr-Sommerfeld theory and asymptotic theory. *J. Fluid Mech.* **288**, 59–73.
- HEALEY, J. 1998 Private communication.
- HEIN, S., STOLTE, A. & DALLMANN, U. C. 1999 Identification and analysis of nonlinear transition scenarios using NOLOT/PSE. *Z. Angew. Math. Mech.* **79**, S109–S112.
- HENNINGSON, D. S. 1987 Stability of parallel inviscid shear flow with mean spanwise variation. FFA-TN 1987-57, Aeronautical Research Institute of Sweden, Bromma.
- HENNINGSON, D. S. 1989 Wave growth and spreading of a turbulent spot in plane Poiseuille flow. *Phys. Fluids A* **1**, 1876–1882.
- HENNINGSON, D. S. 1996 Comment on “Transition in shear flows. Nonlinear normality versus non-normal linearity” [phys. fluids 7 3060 (1995)]. *Phys. Fluids* **8**, 2257–2258.

- HENNINSON, D. S. & ALFREDSSON, P. H. 1987 The wave structure of turbulent spots in plane Poiseuille flow. *J. Fluid Mech.* **178**, 405.
- HENNINSON, D. S., JOHANSSON, A. V. & ALFREDSSON, P. H. 1994 Turbulent spots in channel flows. *J. Eng. Mech.* **28**, 21–42.
- HENNINSON, D. S., LUNDBLADH, A. & JOHANSSON, A. V. 1993 A mechanism for bypass transition from localized disturbances in wall bounded shear flows. *J. Fluid Mech.* **250**, 169–207.
- HENNINSON, D. S. & SCHMID, P. J. 1992 Vector eigenfunction expansions for plane channel flows. *Stud. Appl. Math.* **87**, 15–43.
- HENNINSON, D. S., SPALART, P. & KIM, J. 1987 Numerical simulations of turbulent spots in plane Poiseuille and boundary layer flows. *Phys. Fluids* **30**, 2914–2917.
- HERBERT, T. 1977 Die Neutrale Fläche der Ebenen Poiseuille-Strömung. *Habilitationsschrift*, Universität Stuttgart.
- HERBERT, T. 1983 On perturbation methods in nonlinear stability theory. *J. Fluid Mech.* **126**, 167–186.
- HERBERT, T. 1988 Secondary instability of boundary layers. *Ann. Rev. Fluid Mech.* **20**, 487–526.
- HERBERT, T. 1991 Boundary-layer transition - analysis and prediction revisited. *AIAA Pap. No. 91-0737*.
- HERBERT, T. & BERTOLOTTI, F. 1987 Stability analysis of nonparallel boundary layers. *Bull. Am. Phys. Soc.* **32**, 2079.
- HILL, D. C. 1995 Adjoint systems and their role in the receptivity problem for boundary layers. *J. Fluid Mech.* **292**, 183–204.
- HÖGBERG, M. & HENNINSON, D. S. 1998 Secondary instability of cross-flow vortices in Falkner-Skan-Cooke boundary layers. *J. Fluid Mech.* **368**, 339–357.
- HORN, R. & JOHNSON, J. 1991 *Topics in Matrix Analysis*. Cambridge University Press.
- HOWARD, L. 1961 Note on a paper of John W. Miles. *J. Fluid Mech.* **10**, 509–512.
- HUAI, X., JOSLIN, R. D. & PIOMELLI, U. 1997 Large-eddy simulations of transition to turbulence in boundary layers. *Theoret. Comput. Fluid Dyn.* **9**, 149–163.

- HUERRE, P. & MONKEWITZ, P. A. 1990 Local and global instabilities in spatially developing flows. *Ann. Rev. Fluid Mech.* **22**, 473–537.
- HUERRE, P. & ROSSI, M. 1998 Hydrodynamic instabilities in open flow. In *Hydrodynamics and Nonlinear Instabilities* (ed. C. Godreche & P. Manneville). Cambridge University Press.
- HULTGREN, L. S. & AGGARWAL, A. K. 1987 Absolute instability of the Gaussian wake profile. *Phys. Fluids* **30** (11), 3383–3387.
- HULTGREN, L. S. & GUSTAVSSON, L. H. 1981 Algebraic growth of disturbances in a laminar boundary layer. *Phys. Fluids* **24**, 1000–1004.
- HUNT, R. E. & CRIGHTON, D. G. 1991 Instability of flows in spatially developing media. *Proc. Roy. Soc. Lond. A* **435**, 109–128.
- VAN INGEN, J. L. 1956 A suggested semi-empirical method for the calculation of the boundary layer transition region. *Tech. Rep. VTH-74*. Department of Aeronautical Engineering, University of Delft.
- ITOH, N. 1986 The origin and subsequent development in space of Tollmien-Schlichting waves in a boundary layer. *Fluid Dyn. Research* **1**, 119–130.
- JACOBS, R. G. & HENNINGSON, D. S. 1999 Evaluation of data from direct numerical simulations of transition due to freestream turbulence. Annual Research Briefs, Center for Turbulence Research.
- JOSEPH, D. D. 1968 Eigenvalue bounds for the Orr-Sommerfeld equation. *J. Fluid Mech.* **33**, 617–621.
- JOSEPH, D. D. 1976 *Stability of Fluid Motions I*. Springer-Verlag.
- JOSEPH, D. D. & CARMI, S. 1969 Stability of Poiseuille flow in pipes, annuli and channels. *Quart. Appl. Math.* **26**, 575–599.
- KACHANOV, Y., KOZLOV, V., LEVCHENKO, V. & MAKSIMOV, V. 1979 Transformation of external disturbances into the boundary layer waves. In *Proc. Sixth. Intl. Conf. on Numerical Methods in Fluid Dyn.*, pp. 299–307. Springer-Verlag.
- KACHANOV, Y. S. 1994 Physical mechanisms of laminar boundary-layer transition. *Ann. Rev. Fluid Mech.* **26**, 411–482.
- KACHANOV, Y. S. & LEVCHENKO, V. Y. 1984 The resonant interaction of disturbances at laminar turbulent transition in a boundary layer. *J. Fluid Mech.* **138**, 209–247.
- KARMAN, T. v. 1921 Über laminare und turbulente Reibung. *Z. Angew. Math. Mech.* **1**, 233–252.

- KATO, T. 1976 *Perturbation Theory for Linear Operators*. Springer-Verlag, Berlin.
- KAWAKAMI, M., KOHAMA, Y. & OKUTSU, M. 1999 Stability characteristics of stationary crossflow vortices in a three-dimensional boundary layer. *AIAA Paper* **99-0811**.
- KELLER, H. B. 1977 Numerical solution of bifurcation and nonlinear eigenvalue problems. In *Applications of Bifurcation Theory* (ed. P. H. Rabinowitz), pp. 359–384. Academic Press.
- KENDALL, J. M. 1985 Experimental study of disturbances produced in a pre-transitional laminar boundary layer by weak freestream turbulence. *AIAA Paper* **85-1695**.
- KENDALL, J. M. 1990 Boundary layer receptivity to freestream turbulence. *AIAA Paper* **90-1504**.
- KERCZEK, C. H. v. 1982 The stability of oscillatory plane Poiseuille flow. *J. Fluid Mech.* **116**, 91–114.
- KHORRAMI, M. R., MALIK, M. R. & ASH, R. L. 1989 Application of spectral collocation techniques to the stability of swirling flows. *J. Comp. Phys.* **81**, 206–229.
- KLEBANOFF, P. S. 1971 Effect of freestream turbulence on the laminar boundary layer. *Bull. Am. Phys. Soc.* **10**, 1323.
- KLEBANOFF, P. S., TIDSTROM, K. D. & SARGENT, L. M. 1962 The three-dimensional nature of boundary layer instability. *J. Fluid Mech.* **12**, 1–34.
- KLINGMANN, B. G. B., BOIKO, A., WESTIN, K., KOZLOV, V. & ALFREDSSON, P. 1993 Experiments on the stability of Tollmien-Schlichting waves. *Europ. J. Mech. B* **12**, 493–514.
- KOBAYASHI, R., KOHAMA, Y. & KUROSAWA, M. 1983 Boundary layer transition on a rotating cone in axial flow. *J. Fluid Mech.* **127**, 341–352.
- KOCH, W. 2000 Private communication.
- KOCH, W., BERTOLOTTI, F. P., STOLTE, A. & HEIN, S. 2000 Nonlinear equilibrium solutions in a three-dimensional boundary layer and their secondary instability. *J. Fluid Mech.* **406**, 131–174.
- KOHAMA, Y., SARIC, W. S. & HOOS, J. A. 1991 A high-frequency, secondary instability of crossflow vortices that leads to transition. Proceedings of the Royal Aeronautical Society Conference on Boundary-Layer Transition and Control, Cambridge University, England.

- KOVASZNAY, L. S. G. 1949 Hot-wire investigation of the wake behind cylinders at low Reynolds numbers. *Proc. Roy. Soc. Lond. A* **198**, 174–190.
- KREISS, G., LUNDBLADH, A. & HENNINGSON, D. S. 1993 Bounds for threshold amplitudes in subcritical shear flows. TRITA-NA 9307, Royal Institute of Technology, Stockholm, Sweden.
- KREISS, G., LUNDBLADH, A. & HENNINGSON, D. S. 1994 Bounds for threshold amplitudes in subcritical shear flows. *J. Fluid Mech.* **270**, 175–198.
- KUPFER, K., BERS, A. & RAM, A. K. 1987 The cusp map in the complex-frequency plane for absolute instabilities. *Phys. Fluids* **30**, 3075–3082.
- LANDAHL, M. T. 1975 Wave breakdown and turbulence. *SIAM J. Appl. Math.* **28**, 735–756.
- LANDAHL, M. T. 1980 A note on an algebraic instability of inviscid parallel shear flows. *J. Fluid Mech.* **98**, 243–251.
- LANDAHL, M. T. 1983 Theoretical modeling of coherent structures in wall bounded shear flows. Eighth Biennial Symposium on Turbulence, University of Missouri-Rolla.
- LANDAHL, M. T. 1993 Model for the wall-layer structure of a turbulent shear flow. *Europ. J. Mech. B* **12**, 85–96.
- LANDAU, L. D. & LIFSHITZ, E. M. 1959 *Fluid Mechanics*. Addison-Wesley.
- LANDMAN, M. J. & SAFFMAN, P. G. 1987 The three-dimensional instability of strained vortices in a viscous fluid. *Phys. Fluids* **30** (8), 2339–2342.
- LEES, L. & LIN, C. C. 1946 Investigation of the stability of the laminar boundary layer in a compressible fluid. NACA TN 1115.
- LEES, L. & RESHOTKO, E. 1962 Stability of the compressible laminar boundary layer. *J. Fluid Mech.* **12**, 555–590.
- LEIB, S. J., WUNDROW, D. W. & GOLDSTEIN, M. E. 1999 Effect of free-stream turbulence and other vortical disturbances on a laminar boundary layer. *J. Fluid Mech.* **380**, 169–203.
- LERCHE, T. 1997 Experimentelle Untersuchung nichtlinearer Strukturbildung im Transitionsprozess einer instabilen dreidimensionalen Grenzschicht. Fortschritt-Bericht VDI Reihe 7, no. 310.

- LEVINSKI, V. & COHEN, J. 1995 The evolution of a localized disturbance in external shear flows. I. Theoretical considerations and preliminary experimental results. *J. Fluid Mech.* **289**, 159–177.
- LI, F. & MALIK, M. R. 1994 Mathematical nature of parabolized stability equations. In *Laminar-Turbulent Transition* (ed. R. Kobayashi), pp. 205–212. Springer-Verlag.
- LI, F. & MALIK, M. R. 1995 Fundamental and subharmonic secondary instability of Görtler vortices. *J. Fluid Mech.* **297**, 77–100.
- LIBBY, P. A. & FOX, H. 1964 Some perturbation solutions in laminar boundary-layer theory. *J. Fluid Mech.* **17**, 433–449.
- LIN, C. C. 1946 On the stability of two-dimensional parallel flows. Part III. Stability in a viscous fluid. *Quart. Appl. Math.* **3** (4), 277–301.
- LIN, C. C. 1961 Some mathematical problems in the theory of the stability of parallel flows. *J. Fluid Mech.* **10**, 430–438.
- LINGWOOD, R. J. 1995 Absolute instability of the boundary layer on a rotating disk. *J. Fluid Mech.* **299**, 17–33.
- LINGWOOD, R. J. 1996 An experimental study of absolute instability of a rotating-disk boundary-layer. *J. Fluid Mech.* **314**, 373–405.
- LINGWOOD, R. J. 1997 On the application of the Briggs' and steepest-descent methods to a boundary-layer flow. *Stud. Appl. Math.* **98**, 213–254.
- LUCHINI, P. 1996 Reynolds number independent instability of the Blasius boundary layer over a flat surface. *J. Fluid Mech.* **327**, 101–115.
- LUCHINI, P. 2000 Reynolds number independent instability of the boundary layer over a flat surface: optimal perturbations. *J. Fluid Mech.* **404**, 289–309.
- LUCHINI, P. & BOTTARO, A. 1998 Görtler vortices: a backward-in-time approach to the receptivity problem. *J. Fluid Mech.* **363**, 1–23.
- LUNDBLADH, A. 1993a Private communication.
- LUNDBLADH, A. 1993b Simulation of bypass transition to turbulence in wall bounded shear flows. PhD thesis, Royal Institute of Technology, Stockholm, Sweden.
- MA, B., VAN DOORNE, C. W. H., ZHANG, Z. & NIEUWSTADT, F. T. M. 1999 On the spatial evolution of a wall-imposed periodic disturbance in pipe Poiseuille flow at $Re = 3000$. Part 1. Subcritical disturbance. *J. Fluid Mech.* **398**, 181–224.

- MACK, L. M. 1963 The inviscid stability of the compressible laminar boundary layer. In *Space Programs Summary*, , vol. 37-23, p. 297.
- MACK, L. M. 1964 The inviscid stability of the compressible laminar boundary layer. Part II. In *Space Programs Summary*, , vol. 4, p. 165.
- MACK, L. M. 1965 Stability of the laminar compressible boundary layer according to a direct numerical simulation. AGARDograph I (97).
- MACK, L. M. 1969 Boundary layer stability theory. Jet Propulsion Laboratory Report 900-277.
- MACK, L. M. 1975 Linear stability theory and the problem of supersonic boundary layer transition. *AIAA Journal* **13**, 278.
- MACK, L. M. 1976 A numerical study of the temporal eigenvalue spectrum of the Blasius boundary layer. *J. Fluid Mech.* **73**, 497–520.
- MACK, L. M. 1984 Boundary layer stability theory: Special course on stability and transition of laminar flow. AGARD Report 709, Paris, France.
- MALIK, M. R. 1989 Prediction and control of transition in supersonic and hypersonic boundary layers. *AIAA Journal* **27**, 1487–1493.
- MALIK, M. R. & CHANG, C.-L. 2000 Nonparallel and nonlinear stability of supersonic jet flow. *Comp. Fluids* **29**, 327–365.
- MALIK, M. R., LI, F. & CHANG, C.-L. 1994 Crossflow disturbances in three-dimensional boundary layers: non-linear development, wave interaction and secondary instability. *J. Fluid Mech.* **268**, 1–36.
- MALIK, M. R., LI, F., CHOUDHARI, M. M. & CHANG, C.-L. 1999 Secondary instability of crossflow vortices and swept-wing boundary-layer transition. *J. Fluid Mech.* **399**, 85–115.
- MALIK, M. R., WILKINSON, S. P. & ORSZAG, S. A. 1981 Instability and transition in rotating disk flow. *AIAA J.* **19**, 1131–1138.
- MASAD, J. A., NAYFEH, A. H. & AL-MAAITAH, A. A. 1992 Effect of heat transfer on the stability of compressible boundary layers. *Comp. Fluids* **21**, 43–61.
- MASLOWE, S. 1986 Critical layers in shear flows. *Ann. Rev. Fluid Mech.* **18**, 405–432.
- MATSSON, O. J. E. & ALFREDSSON, P. H. 1990 Curvature and rotation induced instabilities in channel flow. *J. Fluid Mech.* **210**, 537–563.
- MATSUBARA, M. 1997 Private communication.

- MATTINGLY, G. E. & CRIMINALE, W. O. 1972 The stability of an incompressible two-dimensional wake. *J. Fluid Mech.* **51**, 233–272.
- METCALFE, R. W., ORSZAG, S. A., BRACHET, M. E., MENON, S. & RILEY, J. J. 1987 Secondary instability of a temporally growing mixing layer. *J. Fluid Mech.* **184**, 207–243.
- MICHEL, R. 1952 ONERA Rep. 1/1578-A.
- MOORE, A. M. & FARRELL, B. F. 1993 Rapid perturbation growth on spatially and temporally varying oceanic flows determined using an adjoint method: application to the Gulf Stream. *J. Phys. Oceanography* **23**, 1682–1702.
- MORKOVIN, M. V. 1969 The many faces of transition. In *Viscous Drag Reduction* (ed. C. S. Wells). Plenum Press.
- MOSER, R. D. & ROGERS, M. M. 1993 The three-dimensional evolution of a plane mixing layer: pairing and transition to turbulence. *J. Fluid Mech.* **247**, 275–320.
- NAGATA, M. 1990 Three-dimensional finite-amplitude solutions in plane Couette flow: bifurcation from infinity. *J. Fluid Mech.* **217**, 519–527.
- NITSCHKE-KOWSKY, P. & BIPPES, H. 1988 Instability and transition of a three-dimensional boundary layer on a swept flat plate. *Phys. Fluids* **31**, 786–795.
- OLSSON, P. J. & HENNINGSON, D. S. 1994 Optimal disturbances in wavy-table flow. *Stud. Appl. Math.* **94**, 183–210.
- ORR, W. M. F. 1907 The stability or instability of the steady motions of a perfect liquid and of a viscous liquid. Part I: A perfect liquid. Part II: A viscous liquid. *Proc. R. Irish Acad. A* **27**, 9–138.
- ORSZAG, S. A. & PATERA, A. T. 1983 Secondary instability of wall-bounded shear flows. *J. Fluid Mech.* **128**, 347–385.
- O'SULLIVAN, P. L. & BREUER, K. S. 1994 Transient growth in circular pipe flow. Part I: Linear disturbances. *Phys. Fluids* **6**, 3643–3651.
- PEXIEDER, A. 1996 Effects of system rotation on the centrifugal instability of the boundary layer on a curved wall: an experimental study. PhD thesis, Ecole Polytechnique Federale de Lausanne, Lausanne, Switzerland.
- PIERREHUMBERT, R. T. 1986 Universal short-wave instability of two-dimensional eddies in an inviscid fluid. *Phys. Rev. Lett.* **57**, 2157.

- PIERREHUMBERT, R. T. & WIDNALL, S. E. 1982 The two- and three-dimensional instabilities of a spatially periodic shear layer. *J. Fluid Mech.* **114**, 59–82.
- POLL, D. I. A. 1985 Some observations on the transition process on the windward face of a long yawed cylinder. *J. Fluid Mech.* **150**, 329–356.
- PRUETT, C. D., CHANG, C. L. & STREETT, C. L. 2000 Simulation of crossflow instability on a supersonic highly swept wing. *Comp. Fluids* **29**, 33–62.
- RAYLEIGH, L. 1880 On the stability of certain fluid motions. *Proc. Math. Soc. Lond.* **11**, 57–70.
- RAYLEIGH, L. 1887 On the stability of certain fluid motions. *Proc. Math. Soc. Lond.* **19**, 67–74.
- REDDY, S. C. & HENNINGSON, D. S. 1993 Energy growth in viscous channel flows. *J. Fluid Mech.* **252**, 209–238.
- REDDY, S. C., SCHMID, P. J., BAGGETT, P. & HENNINGSON, D. S. 1998 On stability of streamwise streaks and transition thresholds in plane channel flows. *J. Fluid Mech.* **365**, 269–303.
- REDDY, S. C., SCHMID, P. J. & HENNINGSON, D. S. 1993 Pseudospectra of the Orr-Sommerfeld operator. *SIAM J. Appl. Math.* **53**, 15–47.
- REED, H. L. & SARIC, W. S. 1989 Stability of three-dimensional boundary layers. *Ann. Rev. Fluid Mech.* **21**, 235–284.
- RILEY, J. J. & GAD-EL HAK, M. 1985 The dynamics of turbulent spots. In *Frontiers of Fluid Mechanics*, pp. 123–155. Springer.
- RIST, U. & FASEL, H. 1995 Direct numerical simulation of controlled transition in a flat-plate boundary layer. *J. Fluid Mech.* **298**, 211–248.
- RIST, U. & MAUCHER, U. 1994 Direct numerical simulation of 2-d and 3-d instability waves in a laminar separation bubble. Proceedings of the AGARD Symposium on Application of Direct and Large Eddy Simulation to Transition and Turbulence, AGARD-CP-551.
- ROACH, P. E. & BRIERLEY, D. H. 1992 The influence of a turbulent free stream on zero pressure gradient transitional boundary layer development. In *Numerical Simulations of Unsteady Flows and Transition to Turbulence*, pp. 319–347. Cambridge University Press.
- ROGERS, M. M. & MOSER, R. D. 1992 The three-dimensional evolution of a plane mixing layer: the Kelvin-Helmholtz rollup. *J. Fluid Mech.* **243**, 183–226.

- ROMANOV, V. A. 1973 Stability of plane-parallel Couette flow. *Funktional Anal. i Proložen* **7** (2), 62–73, Translated in *Functional Anal. & Its Applications* **7**, 137 – 146 (1973).
- SALWEN, H. & GROSCH, C. E. 1981 The continuous spectrum of the Orr-Sommerfeld equation. Part 2. Eigenfunction expansions. *J. Fluid Mech.* **104**, 445–465.
- SARIC, W., REED, H. & KERSCHEN, E. 1994 Leading edge receptivity to sound: experiments, DNS, and theory. AIAA Paper 94-2222.
- SARIC, W. S., HOOS, J. A. & RADEZTSKY, R. H. 1991 Boundary-layer receptivity of sound with roughness. In *Boundary Layer Stability and Transition to Turbulence*, pp. 17–22. FED-Vol. 114.
- SAVILL, A. M. 1996 One-point closures applied to transition. In *Turbulence and Transition Modelling* (ed. M. Hallbäck, D. S. Henningson, A. V. Johansson & P. H. Alfredsson), pp. 233–268. Kluwer.
- SCHENSTED, I. V. 1961 Contribution to the theory of hydrodynamic stability. PhD thesis, University of Michigan, Ann Arbor.
- SCHLICHTING, H. 1933 Berechnung der Anfachung kleiner Störungen bei der Plattenströmung. *ZAMM* **13**, 171–174.
- SCHMID, P. J. 2000 Linear stability theory and bypass transition in shear flows. *Phys. Plasmas* **7**, 1788–1794.
- SCHMID, P. J. & HENNINGSON, D. S. 1994 Optimal energy density growth in Hagen-Poiseuille flow. *J. Fluid Mech.* **277**, 197–225.
- SCHMID, P. J. & KYTÖMAA, H. K. 1994 Transient and asymptotic stability of granular flow. *J. Fluid Mech.* **264**, 255–275.
- SCHMID, P. J., REDDY, S. C. & HENNINGSON, D. S. 1996 Transition thresholds in boundary layer and channel flow. In *Advances in Turbulence VI* (ed. S. Gavrilakis, L. Machiels & P. A. Monkewitz), pp. 381–384. Kluwer Academic Publishers.
- SCHUBAUER, G. B. & SKRAMSTAD, H. F. 1947 Laminar boundary layer oscillations and the stability of laminar flow. *J. Aero. Sci.* **14**, 69–78.
- SEN, P. K. & VENKATESWARLU, D. 1983 On the stability of plane Poiseuille flow to finite-amplitude disturbances, considering the higher-order Landau coefficients. *J. Fluid Mech.* **133**, 179–206.
- SHAN, H., MA, B., ZHANG, Z. & NIEUWSTADT, F. T. M. 1999 Direct numerical simulation of a puff and a slug in transitional cylindrical pipe flow. *J. Fluid Mech.* **387**, 39–60.

- SHANTINI, R. 1990 Degenerating Orr-Sommerfeld eigenmodes and development of three-dimensional perturbations. PhD thesis, Luleå University of Technology, Luleå, Sweden.
- SIMEN, M. 1992 Local and nonlocal stability theory of spatially varying flows. In *Instability, Transition and Turbulence*, pp. 181–201. Springer-Verlag.
- SIMEN, M. & DALLMANN, U. 1992 On the instability of hypersonic flow past a pointed cone – comparison of theoretical and experimental results at Mach 8. Deutscher Luft- und Raumfahrtkongress / DGLR-Jahrestagung, (29 September – 2 October, 1992, Bremen).
- SINGER, B. & JOSLIN, R. 1994 Metamorphosis of a hairpin vortex into a young turbulent spot. *Phys. Fluids* **6**, 3724–3736.
- SMITH, A. M. O. & GAMBERONI, N. 1956 Transition, pressure gradient and stability theory. *Tech. Rep. ES 26388*. Douglas Aircraft Co.
- SMITH, F. T. 1979a Nonlinear stability of boundary layers for disturbances of various sizes. *Proc. Roy. Soc. Lond. A* **368**, 573–589.
- SMITH, F. T. 1979b On the nonparallel flow stability of the Blasius boundary layer. *Proc. Roy. Soc. Lond. A* **366**, 91–109.
- SMYTH, W. D. 1992 Spectral energy transfers in two-dimensional anisotropic flow. *Phys. Fluids A* **4**, 340–349.
- SOIBELMAN, I. & MEIRON, D. I. 1991 Finite-amplitude bifurcations in plane Poiseuille flow: two-dimensional Hopf bifurcation. *J. Fluid Mech.* **229**, 389–416.
- SOMMERFELD, A. 1908 Ein Beitrag zur hydrodynamischen Erklärung der turbulenten Flüssigkeitbewegungen. In *Atti. del 4. Congr. Internat. dei Mat. III*, pp. 116–124. Roma.
- SPALART, P. R. & STRELETS, M. K. 2000 Mechanisms of transition and heat transfer in a separation bubble. *J. Fluid Mech.* **403**, 329–349.
- SPALART, P. R. & YANG, K. 1987 Numerical study of ribbon induced transition in Blasius flow. *J. Fluid Mech.* **178**, 345–365.
- SQUIRE, H. B. 1933 On the stability for three-dimensional disturbances of viscous fluid flow between parallel walls. *Proc. Roy. Soc. Lond. Ser. A* **142**, 621–628.
- STEWARTSON, K. 1957 On asymptotic expansion in the theory of boundary layer. *J. Math. Phys.* **36**, 137.

- STEWARTSON, K. & STUART, J. T. 1971 A nonlinear instability theory for a wave system in plane Poiseuille flow. *J. Fluid Mech.* **48**, 529–545.
- STUART, J. T. 1960 On the nonlinear mechanics of wave disturbances in stable and unstable parallel flows. Part 1. The basic behaviour in plane Poiseuille flow. *J. Fluid Mech.* **9**, 353–370.
- STUART, J. T. & DiPRIMA, R. C. 1978 The Eckhaus and Benjamin-Feir resonance mechanism. *Proc. Roy. Soc. Lond. Ser. A* **362**, 27–41.
- SWEARINGEN, J. D. & BLACKWELDER, R. F. 1987 The growth and breakdown of streamwise vortices in the presence of a wall. *J. Fluid Mech.* **182**, 255–290.
- SYNGE, J. 1938 Hydrodynamic stability. *Semicentenn. Publ. Amer. Math. Soc.* **2**, 227–269.
- TOLLMIEN, W. 1929 Über die Entstehung der Turbulenz. *Nachr. Ges. Wiss. Göttingen*, 21–44, (English translation NACA TM 609, 1931).
- TOLLMIEN, W. 1935 Ein allgemeines Kriterium der Instabilität laminarer Geschwindigkeitsverteilungen. *Nachr. Wiss. Fachgruppe, Göttingen Math.-phys. Kl.* 1 79–114, (English translation as 'General instability criterion of laminar velocity distributions', in *Tech. Memor. Nat. Adv. Comm. Aero. Wash.* No. 792 (1936)).
- TREFETHEN, A. E., TREFETHEN, L. N. & SCHMID, P. J. 1999 Spectra and pseudospectra for pipe Poiseuille flow. *Comput. Meth. Appl. Mech. Eng.* **175**, 413–420.
- TREFETHEN, L. N. 1992 Pseudospectra of matrices. In *Numerical Analysis 1991*, pp. 234–266. Longman.
- TREFETHEN, L. N., TREFETHEN, A. E., REDDY, S. C. & DRISCOLL, T. A. 1993 Hydrodynamic stability without eigenvalues. *Science* **261**, 578–584.
- TRIANTAFYLLOU, G. S., TRIANTAFYLLOU, M. S. & CHRYSSOSTOMIDIS, C. 1986 On the formation of vortex streets behind stationary cylinders. *J. Fluid Mech.* **170**, 461–477.
- TRITTON, D. & DAVIES, P. 1985 Instabilities in geophysical fluid dynamics. In *Hydrodynamic Instabilities and the Transition to Turbulence*, 2ed (ed. H. Swinney & J. Gollub), pp. 229–270. Springer-Verlag.
- TUMIN, A. 1996 Receptivity of pipe Poiseuille flow. *J. Fluid Mech.* **315**, 119–137.
- USHER, J. R. & CRAIK, A. D. D. 1975 Nonlinear wave interactions in shear flows. Part 2. Third-order theory. *J. Fluid Mech.* **70**, 437–461.

- WALEFFE, F. 1990 On the three-dimensional instability of strained vortices. *Phys. Fluids A* **2**(1), 76–80.
- WALEFFE, F. 1995 Transition in shear flows. Nonlinear normality versus nonnormal linearity. *Phys. Fluids* **7**, 3060–3066.
- WATMUFF, J. H. 1999 Evolution of a wave packet into vortex loops in a laminar separation bubble. *J. Fluid Mech.* **397**, 119–169.
- WATSON, J. 1960 On the nonlinear mechanics of wave disturbances in stable and unstable parallel flows. Part 2. The development of a solution for plane Poiseuille and for plane Couette flow. *J. Fluid Mech.* **9**, 371–389.
- WESTIN, K. J. & HENKES, R. A. W. M. 1997 Applications of turbulence models to bypass transition. *J. Fluids Eng.* **119**, 859–866.
- WESTIN, K. J. A., BAKCHINOV, A. A., KOZLOV, V. V. & ALFREDSSON, P. H. 1998 Experiments on localized disturbances in a flat plate boundary layer. Part 1. The receptivity and evolution of a localized freestream disturbance. *Europ. J. Mech. B* **17**, 823–846.
- WESTIN, K. J. A., BOIKO, A. V., KLINGMANN, B. G. B., KOZLOV, V. V. & ALFREDSSON, P. H. 1994 Experiments in a boundary layer subject to free-stream turbulence. Part I: Boundary layer structure and receptivity. *J. Fluid Mech.* **281**, 193–218.
- WHITE, F. M. 1974 *Viscous Fluid Flow*. McGraw-Hill, New York.
- YANG, Z. Y. & VOKE, P. R. 1991 Numerical simulation of transition to turbulence. *Tech. Rep. ME-FD/91.01*. University of Surrey, Dept. Mech. Eng.
- YANG, Z. Y. & VOKE, P. R. 1993 Large-eddy simulation of transition under turbulence. *Tech. Rep. ME-FD/93.12*. University of Surrey, Dept. Mech. Eng.
- YIH, C. S. 1963 Stability of flow down an inclined plane. *Phys. Fluids* **6**, 321–334.
- ZAHN, J. P., TOOMRE, J., SPIEGEL, E. A. & GOUGH, D. O. 1974 Non-linear cellular motions in Poiseuille channel flow. *J. Fluid Mech.* **64**, 319–345.

Index

- absolute instability, 270
 - branch points, 275
 - Briggs' method, 273
 - cusp map, 278
 - global instability, 337
 - pinch points, 275
 - rotating disk flow, 284
 - steepest descent method, 278
 - two-dimensional wake, 281
- adjoint equation, 86, 304, 332, 363
- adjoint operator, 85, 111, 231
- algebraic growth, 100, 105
- algebraic instability, 47
- amplitude expansion, 162, 185
- asymptotic results, 78
 - Blasius flow, 82
 - localized disturbances, 149
 - nonparallel effects, 301
 - plane Poiseuille flow, 81
 - triple-deck theory, 82
- β -cascade, 188, 461
- bi-orthogonality, 87, 509
- bifurcation
 - from infinity, 185
- Hopf, 214
- subcritical, 165
- supercritical, 165
- Blasius boundary layer flow
 - asymptotic results, 82
 - linear stability, 66
 - neutral curve, 71
 - optimal growth, 118
- bounds
 - Kreiss matrix theorem, 140
 - on eigenvalues, 94
 - on matrix exponential, 139
 - on maximum response, 128
- branch
 - A,P,S-branch, 64
 - lower branch, 73, 414
 - upper branch, 73, 414
- Briggs' method, 273
- cusp map, 278
- Busse balloon, 397
- bypass transition, 402
- Case solution, 49
- center manifold expansion, 160, 179
- compressibility, 237

- compressible boundary layer
 - linear stability, 246
 - neutral curve, 246
 - transient growth, 249
- continuous spectrum
 - inviscid, 43, 48
 - Laplace transform, 77
 - viscous, 74, 107
- convective instability, 270
- Couette flow
 - Case solution, 49
 - linear stability, 66
- Craik's resonance, 168
- critical Reynolds number
 - table, 6
- critical layer, 19, 78
- critical Reynolds number
 - definition, 5
- crossflow vortices, 205, 450
 - breakdown, 455
 - secondary instability, 394, 452
- curved channel flow, 446
 - linear stability, 207
 - optimal growth, 210
 - small curvature approximation, 208
- curved rotating channel flow
 - linear stability, 213
 - neutral curve, 214
- cusp map, 278
- Dean vortices, 446
 - Eckhaus instability, 398
- dispersion relation
 - spatial branch, 271
 - temporal branch, 271
- disturbance equations
 - linear
 - inviscid, 15
 - disturbance environment, 351
 - disturbance equations
 - linear
 - viscous, 55, 102
 - nonlinear, 2
 - disturbance group velocity, 34, 97
- disturbance kinetic energy
 - definition, 3
- disturbance measure, 102, 218, 250, 346
- Eckhaus instability, 394, 446, 448
 - Busse balloon, 397
 - Dean vortices, 398
 - rotating channel flow, 396
 - sideband instability, 396
- elliptical instability, 381, 423
- energy inner product, 110
- energy norm, 89, 110
- energy Reynolds number, 189
- energy theory, 188
 - constraints, 191
- equilibrium states, 180
- Falkner-Skan boundary layer
 - linear stability, 198
 - optimal growth, 200
- Falkner-Skan-Cooke boundary layer
 - linear stability, 203
 - optimal growth, 205
- Fjørtoft's criterion, 21
- Floquet theory, 227, 373
- Fredholm alternative, 163, 170, 304
- freestream turbulence, 429
- Görtler flow, 313
 - transition, 448
- Görtler vortices, 448
 - linear stability, 313
 - receptivity, 370
 - saturation, 349
 - secondary instability, 389
- Gaster's transformation, 264
- Ginzburg-Landau equation, 167
 - global instability, 341
- global instability, 337
 - frequency selection criterion, 340
- Ginzburg-Landau equation, 341
 - nonnormality, 342
- Green's theorem, generalized, 363

- group velocity, 97
- group velocity, 34
- Gulf Stream, 234
- Hagen-Poiseuille flow
 - linear stability, 66
 - optimal growth, 114
- harmonic point source, 266
- Hartree parameter, 199, 204
- Howard's semicircle theorem, 22
- inflection point criterion, 21
 - compressible, 241
- initial value problem
 - compressible, 237
 - inviscid, 38
 - Laplace transform, 42
 - nonlinear, 155
 - spatial, 290
 - viscous, 99
 - continuous formulation, 106
 - discrete formulation, 108
- Kelvin-Helmholtz instability
 - inviscid, 29
- Klebanoff mode, 429, 436
- Lagrange identity, 363
- Landau coefficients, 163
- Landau equation
 - derivation, 162
 - stability, 165
 - steady states, 164
- lift-up effect, 46, 144
- localized disturbance
 - asymptotic results, 149
 - breakdown, 456
 - inviscid, 50
 - linear evolution, 144
 - nonlinear evolution, 185
 - transition, 456
 - viscous, 144
- Lyapunov equation, 137
- Lyapunov exponent, 235
- Mathieu's equation
- Lyapunov exponent, 236
- stability, 223
- transient growth, 228
- matrix exponential, 111
- maximum energy growth
 - bounds, 139
 - temporal, 112
- maximum growth rate, 132
- maximum response, 126
 - bounds, 128
 - stochastic forcing, 133
- mixing layer
 - damped inviscid solutions, 45
 - inviscid stability, 32
 - piecewise linear approximation, 26
 - rib vortices, 423
 - roll-up and pairing, 421
 - transition, 420
- neutral curve
 - Blasius boundary layer flow, 71
 - compressible boundary layer, 246
 - curved channel flow, 210
 - curved rotating channel flow, 214
 - Falkner-Skan boundary layer, 200
 - Falkner-Skan-Cooke boundary layer, 205
 - nonparallel effects, 326
 - oscillating channel flow, 226
 - parallel flow, 71
 - plane Poiseuille flow, 71
 - rotating channel flow, 212
 - water table flow, 221
 - nonlinear effects, 344
 - nonlinear equilibrium states, 180
 - nonlinear stability, 153
 - nonnormality, 93
 - nonparallel effects, 300
 - multiple-scale analysis, 302
 - neutral curve, 326

- triple-deck theory, 306
- numerical range, 132
- oblique transition, 436, 444, 445
- optimal disturbance
 - general, 230
 - spatial, 329
 - temporal, 119
- optimal growth, 111
 - Reynolds number dependence, 120
 - spatial, 472
- optimal growth rate, 126
- optimal response, 126, 128
 - Reynolds number dependence, 129
 - stochastic forcing, 133
- Orr mechanism, 120
- Orr-Sommerfeld equation, 56
 - adjoint, 85
- oscillating channel flow
 - linear stability, 224
 - neutral curve, 226
- oscillatory flow
 - linear stability, 223
 - transient growth, 226
- parabolized stability equations
 - linear, 318
 - nonlinear, 346, 474
 - step-size restriction, 327
- peak position, 379
- permanent scar, 50
- piecewise linear velocity, 24
 - boundary layer, 29
 - jump conditions, 25
 - mixing layer, 26
- pipe flow, 61
 - linear stability, 66
 - optimal growth, 114
- plane Poiseuille flow
 - asymptotic results, 81
 - linear stability, 64
 - neutral curve, 71
 - optimal growth, 113
- pressure equation, 17, 55
- PSE
 - linear, 318
 - nonlinear, 346, 474
 - step-size restriction, 327
- pseudo-eigenvalues, 93
- Rayleigh equation, 17
 - compressible, 241
 - logarithmic singularity, 20, 45
- Rayleigh's criterion, 21
 - compressible, 241
- receptivity, 351
 - adjoint approach, 363, 368
 - asymptotic theory, 351
 - localized, 361
 - nonlocalized, 356
- relative Mach number, 240
- resolvent, 126
- resonant triad interaction, 167
- Reynolds number dependence
 - optimal growth, 120
 - optimal response, 129
- Reynolds-Orr equation, 7, 189
 - consequences, 9
 - derivation, 7
 - energy theory, 189
- rotating channel flow
 - neutral curve, 212
- rotating channel flow
 - Eckhaus instability, 396
 - linear stability, 211
 - optimal growth, 212
- rotating curved channel flow
 - linear stability, 213
- rotating disk flow
 - absolute instability, 284
- secondary instability, 373
 - channel flow streaks, 392
 - crossflow vortices, 394, 452
 - Dean vortices, 398
 - detuned mode, 375
 - Eckhaus instability, 394, 446,
- 448

- elliptical instability, 381, 423
- fundamental mode, 375
- Görtler vortices, 389
- mixing layer, 420
- peak position, 379
- rotating channel flow, 396
- shape assumption, 377
- streaks, 383, 392, 407, 427
 - inviscid, 385
- subharmonic mode, 375
- Tollmien-Schlichting waves, 374,
 - 404
 - fundamental, 379
 - subharmonic, 378
- two-dimensional waves, 374
- valley position, 379
- vortices, 383
- separation bubble, 202, 441
- shape assumption, 377
- sideband instability, 396
- spatial analysis, 253
- spatial evolution
 - concept, 6
- spectrum
 - Blasius boundary layer flow, 66
 - bounds on eigenvalues, 94
 - continuous
 - spatial, 262
 - temporal, 74
 - continuous operator, 69
 - Couette flow, 66
 - pipe flow, 66
 - plane Poiseuille flow, 64
 - pseudo-eigenvalues, 93
 - sensitivity, 89
 - spatial, 255
 - unresolved, 92
- Squire equation, 56
 - adjoint, 88
 - forced, 103
- Squire's theorem, 59
- Squire's transformation, 58
- stability
 - complex flows, 197
 - compressible, 237
 - conditional, 3
 - definition, 3
 - global, 3
 - monotonic, 5
 - nonlinear, 153
 - unsteady flow, 223
 - energy growth rate, 235
 - general, 229
 - Lyapunov exponent, 235
 - oscillatory, 223
- stability problem
 - compressible, 238
 - higher modes, 244
 - spatial, 253
 - temporal, 17, 57
 - weakly nonlinear, 160
- steepest descent method, 266
- steepest descent method, 96, 278
- stochastic forcing, 133
- streaks
 - breakdown, 425
 - origin, 434
 - secondary instability, 383, 392, 407, 427
 - inviscid, 385
- surface tension effects, 216
- swept Hiemenz flow
 - linear stability, 205
- three-wave interactions, 167
- threshold amplitudes, 411
- Tollmien's solutions, 20, 44, 79
- Tollmien-Schlichting waves, 66, 69, 244
 - saturation, 349
 - secondary instability, 374, 404, 414, 419
- transition, 401
 - bypass, 402
 - crossflow vortices, 450
 - curved channel flow, 446
 - Dean vortices, 446
 - flows with curvature, 446
 - freestream turbulence, 429

- from exponential instabilities, 401
- from nonmodal growth, 402
- Görtler flow, 448
- Klebanoff mode, 429, 436
- localized disturbances, 456
- mixing layer, 420
- modeling, 465
 - based on nonmodal growth, 471
 - correlations, 469
 - e^N -method, 469
 - nonlinear models, 474
- oblique transition, 407, 436, 444
- compressible, 252, 445
- incompressible, 436
- scenarios, 403
- separation bubble, 441
- stages, 402
- streak breakdown, 425
- threshold amplitudes, 411
- Tollmien-Schlichting waves, 414
 - fundamental, 414, 440
 - H-type, 419, 440
 - K-type, 414, 440
 - subharmonic, 419, 440
- turbulent spot, 463
- two-dimensional waves, 414
 - Blasius boundary layer, 414
 - mixing layer, 420
- vortex-dominated flows, 446
- transition modeling, 465
 - based on nonmodal growth, 471
 - correlations, 469
 - e^N -method, 469
 - low-dimensional dynamical systems, 465
 - nonlinear models, 474
- transition prediction, 469
- transition scenarios, 401
- transition threshold, 411
- transition time, 411
- triple-deck theory
 - nonparallel effects, 306
- turbulent spot, 463
- unsteady flow, 223
- valley position, 379
- vector modes, 59
- velocity-vorticity formulation
 - inviscid, 16
 - nonlinear, 155
 - pipe flow, 62
 - viscous, 55, 155
- vibrating ribbon problem, 294, 366
- wake flow
 - absolute instability, 281
- water table flow
 - linear stability, 216
 - neutral curve, 221
 - optimal growth, 221
- wave packet
 - asymptotic results, 96
 - inviscid evolution, 33
 - real axis approximation, 97
 - viscous evolution, 96
- wave triad interactions, 172, 344
 - Craik's resonance, 168
 - energy conservation, 175
 - resonance condition, 167
- weakly nonlinear stability, 160
 - amplitude expansion, 162
 - center manifold expansion, 179
 - Ginzburg-Landau equation, 167
 - Landau coefficients, 163
 - multiple-scale analysis, 160

Applied Mathematical Sciences

(continued from page ii)

61. *Sattinger/Weaver*: Lie Groups and Algebras with Applications to Physics, Geometry, and Mechanics.
62. *LaSalle*: The Stability and Control of Discrete Processes.
63. *Grasman*: Asymptotic Methods of Relaxation Oscillations and Applications.
64. *Hsu*: Cell-to-Cell Mapping: A Method of Global Analysis for Nonlinear Systems.
65. *Rand/Armbruster*: Perturbation Methods, Bifurcation Theory and Computer Algebra.
66. *Hlaváček/Haslinger/Necas/Lovíšek*: Solution of Variational Inequalities in Mechanics.
67. *Cercignani*: The Boltzmann Equation and Its Applications.
68. *Temam*: Infinite-Dimensional Dynamical Systems in Mechanics and Physics, 2nd ed.
69. *Golubitsky/Stewart/Schaeffer*: Singularities and Groups in Bifurcation Theory, Vol. II.
70. *Constantin/Foias/Nicolaenko/Temam*: Integral Manifolds and Inertial Manifolds for Dissipative Partial Differential Equations.
71. *Catin*: Estimation, Control, and the Discrete Kalman Filter.
72. *Lochak/Meunier*: Multiphase Averaging for Classical Systems.
73. *Wiggins*: Global Bifurcations and Chaos.
74. *Mawhin/Willem*: Critical Point Theory and Hamiltonian Systems.
75. *Abraham/Marsden/Ratiu*: Manifolds, Tensor Analysis, and Applications, 2nd ed.
76. *Lagerstrom*: Matched Asymptotic Expansions: Ideas and Techniques.
77. *Aldous*: Probability Approximations via the Poisson Clumping Heuristic.
78. *Dacorogna*: Direct Methods in the Calculus of Variations.
79. *Hernández-Lerma*: Adaptive Markov Processes.
80. *Lawden*: Elliptic Functions and Applications.
81. *Bluman/Kumei*: Symmetries and Differential Equations.
82. *Kress*: Linear Integral Equations, 2nd ed.
83. *Bebernes/Eberly*: Mathematical Problems from Combustion Theory.
84. *Joseph*: Fluid Dynamics of Viscoelastic Fluids.
85. *Yang*: Wave Packets and Their Bifurcations in Geophysical Fluid Dynamics.
86. *Dendrinos/Sonis*: Chaos and Socio-Spatial Dynamics.
87. *Weder*: Spectral and Scattering Theory for Wave Propagation in Perturbed Stratified Media.
88. *Bogaevski/Povzner*: Algebraic Methods in Nonlinear Perturbation Theory.
89. *O'Malley*: Singular Perturbation Methods for Ordinary Differential Equations.
90. *Meyer/Hall*: Introduction to Hamiltonian Dynamical Systems and the N-body Problem.
91. *Straughan*: The Energy Method, Stability, and Nonlinear Convection.
92. *Naber*: The Geometry of Minkowski Spacetime.
93. *Colton/Kress*: Inverse Acoustic and Electromagnetic Scattering Theory, 2nd ed.
94. *Hoppensteadt*: Analysis and Simulation of Chaotic Systems, 2nd ed.
95. *Hackbusch*: Iterative Solution of Large Sparse Systems of Equations.
96. *Marchioro/Pulvirenti*: Mathematical Theory of Incompressible Nonviscous Fluids.
97. *Lasota/Mackey*: Chaos, Fractals, and Noise: Stochastic Aspects of Dynamics, 2nd ed.
98. *de Boor/Höllig/Riemenschneider*: Box Splines.
99. *Hale/Lunel*: Introduction to Functional Differential Equations.
100. *Sirovich* (ed): Trends and Perspectives in Applied Mathematics.
101. *Nusse/Yorke*: Dynamics: Numerical Explorations, 2nd ed.
102. *Chossat/Iooss*: The Couette-Taylor Problem.
103. *Chorin*: Vorticity and Turbulence.
104. *Farkas*: Periodic Motions.
105. *Wiggins*: Normally Hyperbolic Invariant Manifolds in Dynamical Systems.
106. *Cercignani/Illner/Pulvirenti*: The Mathematical Theory of Dilute Gases.
107. *Antman*: Nonlinear Problems of Elasticity.
108. *Zeidler*: Applied Functional Analysis: Applications to Mathematical Physics.
109. *Zeidler*: Applied Functional Analysis: Main Principles and Their Applications.
110. *Diekmann/van Gils/Verduyn Lunel/Walther*: Delay Equations: Functional-, Complex-, and Nonlinear Analysis.
111. *Visintin*: Differential Models of Hysteresis.
112. *Kuznetsov*: Elements of Applied Bifurcation Theory, 2nd ed.
113. *Hislop/Sigal*: Introduction to Spectral Theory: With Applications to Schrödinger Operators.
114. *Kevorkian/Cole*: Multiple Scale and Singular Perturbation Methods.
115. *Taylor*: Partial Differential Equations I, Basic Theory.
116. *Taylor*: Partial Differential Equations II, Qualitative Studies of Linear Equations.
117. *Taylor*: Partial Differential Equations III, Nonlinear Equations.

(continued on next page)

Applied Mathematical Sciences

(continued from previous page)

- 118. *Godlewski/Raviart*: Numerical Approximation of Hyperbolic Systems of Conservation Laws.
- 119. *Wu*: Theory and Applications of Partial Functional Differential Equations.
- 120. *Kirsch*: An Introduction to the Mathematical Theory of Inverse Problems.
- 121. *Brokate/Sprekels*: Hysteresis and Phase Transitions.
- 122. *Gliklikh*: Global Analysis in Mathematical Physics: Geometric and Stochastic Methods.
- 123. *Le/Schmitt*: Global Bifurcation in Variational Inequalities: Applications to Obstacle and Unilateral Problems.
- 124. *Polak*: Optimization: Algorithms and Consistent Approximations.
- 125. *Arnold/Khesin*: Topological Methods in Hydrodynamics.
- 126. *Hoppensteadt/Izhikevich*: Weakly Connected Neural Networks.
- 127. *Isakov*: Inverse Problems for Partial Differential Equations.
- 128. *Li/Wiggins*: Invariant Manifolds and Fibrations for Perturbed Nonlinear Schrödinger Equations.
- 129. *Müller*: Analysis of Spherical Symmetries in Euclidean Spaces.
- 130. *Feintuch*: Robust Control Theory in Hilbert Space.
- 131. *Eriksen*: Introduction to the Thermodynamics of Solids, Revised ed.
- 132. *Ihlenburg*: Finite Element Analysis of Acoustic Scattering.
- 133. *Vorovich*: Nonlinear Theory of Shallow Shells.
- 134. *Vein/Dale*: Determinants and Their Applications in Mathematical Physics.
- 135. *Drew/Passman*: Theory of Multicomponent Fluids.
- 136. *Cioranescu/Saint Jean Paulin*: Homogenization of Reticulated Structures.
- 137. *Gurtin*: Configurational Forces as Basic Concepts of Continuum Physics.
- 138. *Haller*: Chaos Near Resonance.
- 139. *Sulem/Sulem*: The Nonlinear Schrödinger Equation: Self-Focusing and Wave Collapse.
- 140. *Cherkaev*: Variational Methods for Structural Optimization.
- 141. *Naber*: Topology, Geometry, and Gauge Fields: Interactions.
- 142. *Schmid/Henningson*: Stability and Transition in Shear Flows.